UNIVERSITY OF OKLAHOMA

GRADUATE COLLEGE

INSTABILITY ANALYSIS OF A LOW-DENSITY GAS JET INJECTED INTO A HIGH-DENSITY GAS

A DISSERTATION

SUBMITTED TO THE GRADUATE FACULTY

in partial fulfillment of the requirements for the

degree of

DOCTOR OF PHILOSOPHY

By

Anthony Layiwola Lawson
Norman, Oklahoma
2001

UMI Number: 3022971

Bell & Howell Information and Learning Company
300 North Zeeb Road
P.O. Box 1346
Ann Arbor, MI 48106-1346

INSTABILITY ANALYSIS OF A LOW-DENSITY GAS JET INJECTED INTO A HIGH-DENSITY GAS

A DISSERTATION APPROVED FOR THE SCHOOL OF AEROSPACE AND MECHANICAL ENGINEERING

BY

[illegible]

Ajay Ajay K. Agrawal.

[illegible]

[illegible]

[illegible]

ACKNOWLEDGEMENTS

To God, be the glory! Words can not express the amount of gratitude the author owes the Almighty One – it is by His grace that this work was accomplished; may His name be forever glorified (Amen).

The author wishes to thank his advisor, Dr. R. N. Parthasarathy, for his guidance and recommendations during the preparation of the dissertation. He respectfully thanks Dr. Ajay Agrawal, Dr. M.-C. Altan and Dr. S. R. Gollahalli of the School of Aerospace and Mechanical Engineering, and Dr. S. O. Osisanya of the School of Petroleum and Geological Engineering for serving on his dissertation defense committee. Also, his gratitude goes out to Dr. F.-C. Lai who served on his PhD dissertation committee but was absent from the defense committee due to sabbatical leave. He sincerely appreciates the assistance received from the members of the School of Aerospace and Mechanical Engineering staff.

The author thanks Dr. Ajay Agrawal and Kasyap Pasumarthi of the Microgravity Combustion Laboratory for providing the rainbow schlieren image used in Chapter 3 of this report. Also, he expresses his gratitude to Ben Baird and the Combustion and Flame Dynamics Laboratory for their support and advice during the visualization experiments.

Finally, the author wishes to thank all his friends in general and particularly the entire ACF team, Yinka Akinshola, Busola Alagbala (a worthy companion and friend indeed), Kola Ayeni, Monojit Bhattachariya, Kemi Harris (for your generosity & concern), Kunle Ogunlade, Opeoluwa Oke (for your advice and listening ear), Jumoke Oladunni, Jumoke Olowu, Mrs. Augusta Osisanya (Mama mi ni Norman), Kasyap Pasumarthi, and members of his family for their encouragement and support during the preparation of the dissertation.

The financial support of this study by the NASA Microgravity Fluid Physics program is gratefully acknowledged.

TABLE OF CONTENTS

LIST OF TABLES

LIST OF FIGURES

NOMENCLATURE

English Symbols

C_1	constant of integration of equation (2.27)
C_2	constant of integration of equation (2.28)
d	nozzle diameter in Cetegen (1997-2)
D	jet diameter
D_b	binary diffusivity coefficient
Fr	Froude number; $Fr^2 = \dfrac{U_j^2}{gR}\dfrac{\rho_j}{(\rho_\infty - \rho_j)}$
g	acceleration due to gravity
G	non-dimensional coefficient of the buoyancy term in the pressure disturbance equation; $G = \dfrac{1}{Fr^2 \dfrac{R}{\theta}\left(\dfrac{\rho_\infty}{\rho_j} - 1\right)}$
i	$\sqrt{-1}$
k	wavenumber
Δk	step-size of the real and imaginary parts of the wavenumber
m	azimuthal wavenumber
N	parameter that controlled the jet mixining layer thickness in Monkewitz and Sohn (1988)
P	Prandtl number

p	pressure
r	radial coordinate
r_o	low-density jet exit radius
Δr	lateral shift between the inflexion points of velocity and density profiles
R	radius of the jet shear layer
R_e	radius of the jet exit
Ri	Richardson number; $Ri = \frac{gD}{U_j^2}\frac{\left(\rho_\infty - \rho_j\right)}{\rho_j}$
Ri_1	Richardson number; $Ri_1 = \frac{\rho_j}{\rho_\infty} Ri$
S	Density ratio
Sc	Schmidt number; $Sc = \frac{\upsilon}{D_b}$
t	time
T	temperature
u	jet axial velocity component
U	jet base velocity
U_c	jet base centerline velocity
v	jet radial velocity component
w	jet azimuthal velocity component

x	axial coordinate
Y_j	local mass fraction of injected gas

Greek Symbols

δ_{ij}	Kronecker delta
∇	del operator
ϕ	azimuthal coordinate
λ	wavelength
Λ	velocity ratio in Monkewitz and Sohn (1988); $\Lambda = \frac{U_j - U_\infty}{U_j + U_\infty}$
μ	fluid viscosity
υ	fluid kinematic viscosity
ρ	fluid mass density
ρ_j	fluid mass density of low-density gas
ρ_∞	fluid mass density of high-density ambient gas
θ	shear layer momentum thickness
Ω	angular frequency

Superscripts

$(\ )'$ fluctuations

$(\bar{\ })$ averaged variable

$(\hat{\ })$ amplitude of variable

$(\tilde{\ })$ dimensional variable

Subscripts

∞ ambient gas property

j low-density gas property

ABSTRACT

The objective of this study was to determine the effects of buoyancy on the absolute instability of low-density gas jets injected into high-density gas mediums. Most of the existing analyses of low-density gas jets injected into a high-density ambient have been carried out neglecting effects of gravity. In order to investigate the influence of gravity on the near-injector development of the flow, a linear temporal stability analysis and a spatio-temporal stability analysis of a low-density round jet injected into a high-density ambient gas were performed. The flow was assumed to be isothermal and locally parallel; viscous and diffusive effects were ignored. The variables were represented as the sum of the mean value and a normal-mode small disturbance. An ordinary differential equation governing the amplitude of the pressure disturbance was derived. The velocity and density profiles in the shear layer, and the Froude number (signifying the effects of gravity) were the three important parameters in this equation. Together with the boundary conditions, an eigenvalue problem was formulated. Assuming that the velocity and density profiles in the shear layer to be represented by hyperbolic tangent functions, the eigenvalue problem was solved for various values of Froude number. The temporal growth rates and the phase velocity of the disturbances were obtained. It was found that the presence of variable density within the shear layer resulted in an increase in the temporal amplification rate of the disturbances and an increase in

the range of unstable frequencies, accompanied by a reduction in the phase velocities of the disturbances. Also, the temporal growth rates of the disturbances were increased as the Froude number was reduced (i.e. gravitational effects increased), indicating the destabilizing role played by gravity. The spatio-temporal stability analysis was performed to determine the nature of the absolute instability of the jet. The roles of the density ratio, Froude number, Schmidt number, and the lateral shift between the density and velocity profiles on the jet's absolute instability were determined. Comparisons of the results with previous experimental studies show good agreement when the effects of these variables are combined together. Thus, the combination of these variables determines how absolutely unstable the jet will be. Experiments were carried out to observe the qualitative differences between a round low-density gas jet injected into a high-density gas (helium jet injected into air) and a round constant density jet (air jet injected into air). Flow visualizations and velocity measurements in the near-injector region of the helium jet show more mixing and spreading of the helium jet than the air jet. The vortex structures develop and contribute to the jet spreading causing the helium jet to oscillate.

Chapter 1

Introduction

1.1: General statement of the problem

Low-density gas jets injected into higher density ambient gases are encountered in many engineering and technical applications such as plumes of diffusion flames, fuel leaks, engine and industry exhaust, propulsion in space, materials processing, and in natural phenomena such as fires and volcanic eruptions. Recent experimental studies (Monkewitz et al, 1990; Subbarao and Cantwell, 1992; Kyle and Sreenivasan, 1993; Cetegen and Kasper, 1996) indicate that at certain conditions, low-density gas jets injected into high-density gases may sustain an absolute instability leading to highly periodic oscillations as illustrated in Figure 1.1. Figure 1.1 contains four photographs of the schlieren image of a weakly excited helium jet in ambient air taken over several cycles (Subbarao and Cantwell, 1992). Subbarao and Cantwell (1992) excited the jet using a loudspeaker located in the pipe system before the nozzle. The leftmost photograph is multiply exposed 16 times, while the other three photographs are single-shot exposed and several thousand cycles apart. In the multiply exposed photograph the outline of the large-scale structure of jet is not blurred and the location of the vortices within the shear layer are coincident with those of the single-shot exposed photographs even after several cycles. Indicating the periodic nature with which the structures are repeated.

This phenomenon is similar to the buoyancy-induced flickering observed in diffusion flames (for example Buckmaster and Peters, 1986; Chen et al., 1988; Cetegen and Dong, 2000). It is thus plausible that the periodicity observed in the oscillations of low-density gas jets injected into a high-density medium is related to buoyancy effects. Therefore, an investigation of the influence of gravity on the disturbances in the near-injector region of low-density jets is necessary. The effects of buoyancy on the formation and characteristics of the near-injector large-scale structures need to be understood further. This study aims to highlight as well as improve the understanding of the nature of flow instability in low-density round gas jets injected into high-density gases.

1.2: Related studies

Round jets with homogeneous shear layers have been studied extensively in the past. A gas, say air, injected into air of equal density (isothermal flow) develops a shear layer at the interface between the jet and the surrounding air. The near-injector region of a round jet, as influenced by disturbances, has a direct influence on the flow development in the far-field of the jet. Several authors (Crow, 1972, Moore, 1977, Ffowcs-Williams, 1978) have shown that linear stability analysis models the large-scale structures of the near-injector region well. Batchelor and Gill (1962) studied the stability of steady unbounded axisymmetric single-phase jet flows of the wake-jet type with nearly parallel streamlines. The instantaneous velocity and pressure equations for a small disturbance to a unidirectional jet were derived and the results were obtained in the form of a Fourier series with respect to time in cylindrical coordinates. The critical Reynolds number of the jet was obtained based on these assumptions.

Mollo-Christensen (1967) measured space-time correlations between different frequency bands with bandpass filters tuned to different frequencies in a turbulent jet. The power spectral density of velocity fluctuations in the near-injector region shear layer was measured and it was found that the spectrum of forced instability oscillations showed sharp distinct peaks at the forcing frequency as well as at subharmonic frequencies. The near-injector region of the jet responded to the pressure field associated with pressure fluctuations downstream of the jet. Thus, it was suggested that knowing the phase speeds of the disturbance waves, the maxima and decay parameters for different frequency components and the power spectral density of pressure fluctuations at the jet, the far-field power spectrum could be computed. Crow and Champagne (1971) also observed the evolution of a large-scale orderly pattern in the noise-producing region of a jet. Mollo-Christensen (1967) and Crow and Champagne (1971) found that the near-injector large-scale structure of jet turbulence was well modeled by linear stability theory. Morerecent developments in the understanding of turbulent shear flows have shown that coherent structures control the dynamics of the flow. In the case of free shear flows, such as mixing layers and jets, it has also been shown that external forcing techniques can be used to control the global development of these flows. Gaster et al. (1985) applied the inviscid stability theory to model the large-scale vortex structures that occurred in a forced mixing layer. The comparison between experimental data and computational models showed that the agreement in both amplitude and phase velocity of the disturbances across the various sections of the flow was excellent on a purely local basis. Armstrong et al. (1977) and Stromberg et al. (1980) found that the large-scale structure of turbulence in a circular jet was dominated by the axisymmetric and the first order azimuthal components. The results of linear stability calculations were successfully applied to these two components to describe the near-field structure of a turbulent jet.

Early studies of jet instability were reviewed by Michalke (1984). These studies were carried out to understand the transition from laminar flow to turbulence and to describe the evolution of the large-scale coherent structures in the near-injector field. The analysis was based on the locally parallel flow assumption and the neglect of fluid viscosity, heat conduction and dissipation, and gravitational effects. Small disturbances in the form of normal modes were introduced in the equations of motion and the equations were linearized. The disturbance equations could then be reduced to one equation governing the amplitude of the pressure disturbance. This equation was solved for specified axial velocity and temperature profiles, and the unstable wavenumbers were documented as a function of frequency. The critical Reynolds number denoting the transition from laminar to turbulent flow was found. Also, the streak line patterns obtained using the results of the linear stability analysis were in good agreement with the first-stage of the vortex rolling-up process that was observed experimentally in the near-injector field. Cohen and Wygnanski (1987) concluded that the linear stability analysis was able to correctly predict the local distribution of amplitudes and phases in an axisymmetric jet that was excited by external means. The analysis was also capable of predicting the entire spectral distribution of velocity perturbations in an unexcited jet over a short distance in the streamwise direction.

Monkewitz and Sohn (1988) re-examined the linear inviscid stability analysis of compressible heated axisymmetric jets with particular attention to the impulse response of the flow. Monkewitz and Sohn (1988) assumed a velocity profile

$$u = 1 - \Lambda + \frac{2\Lambda}{1 + \left(e^{r^2 \ln 2} - 1\right)^N}$$

where Λ was the co-flow velocity ratio given as

$$\Lambda = \frac{U_c - U_\infty}{U_c + U_\infty},$$

with U_c being the centerline velocity and U_∞ the ambient gas uniform velocity, N was a jet parameter that controlled the jet mixing layer thus indicated the axial location of the jet and thickness, r was the radial direction from the jet axis. They used the concept of the turbulent Prandtl number proposed by Reichardt (Schlichting, 1979) to specify a relationship between the density profile and the velocity profile as

$$\frac{\dfrac{1}{\rho}-1}{\dfrac{1}{S}-1}=\left(\frac{u+2\Lambda-1}{2\Lambda}\right)^{P}$$

where S was the ratio of the mass density at the jet centerline to that of the ambient gas and, P was the Prandtl number. Two different responses were identified based on the results. In one case, the flow was absolutely unstable, when a locally generated small disturbance grew exponentially at the site of the disturbance and eventually affected the entire flow region. In the other case termed convective instability, the disturbance was convected downstream leaving the mean flow undisturbed. Monkewitz and Sohn (1988) documented the boundaries between the absolute and convective instability assuming locally parallel flow, infinite Froude number, and zero Eckert number. It was shown that heated (low-density) jets injected into ambient gas of high density developed an absolute instability and became self-excited when the jet density was less than 0.72 times the ambient gas density. Monkewitz and Sohn (1988) also studied the effect of the azimuthal wavenumber on the absolute stability of the hot jet. The critical density ratio (demarcating absolute and convective stability) was much lower, about 0.35, for the first azimuthal wavenumber mode than that for the axisymmetric wavenumber mode. This indicated the dominance of the axisymmetric mode during jet instability for high density ratios.

Yu and Monkewitz (1990) carried out a similar analysis for two-dimensional inertial jets and wakes with non-uniform density and axial velocity profiles. Again, gravitational effects were neglected and the flow was assumed to be locally parallel. They assumed a velocity profile of

$$u = 1 - \Lambda + \frac{2\Lambda}{1 + \sinh^{2N}\left(y \sinh^{-1} 1\right)}$$

and for the temperature they used a profile, similar to the velocity profile, of

$$T = 1 + \frac{\left(S^{-1} - 1\right)}{1 + \sinh^{2N}\left(y \sinh^{-1} 1\right)}$$

where, y was the direction normal to the flow axis and other symbols are as specified above for the Sohn and Monkewitz (1988) discussion. An ideal gas was assumed to produce the variable density by heating. It was found that the absolute frequencies and wavenumbers of small disturbances in the near-injector region scaled with the jet/wake width and not on the thickness of the individual mixing layers, suggesting that the absolute instability was brought about by the interaction of the two mixing layers.

Jendoubi and Strykowski (1994) considered the stability of axisymmetric jets with external co-flow and counterflow using linear stability analysis. The boundaries between absolute and convective instability were distinguished for various parameters: jet-to-ambient velocity ratio, density ratio, jet Mach number, and the shear layer thickness. Jendoubi and Strykowski (1994) assumed a hyperbolic tangent velocity profile of the form

$$U(r) = 1 + \Lambda \tanh\left[\frac{D}{8\theta}\left(\frac{1}{r} - r\right)\right]$$

where D was a characteristic diameter of the jet, θ the momentum thickness, Λ the co-flow velocity ratio similar to that of Monkewitz and Sohn (1988) and r, the radial distance from the jet axis. The temperature distribution was assumed to satisfy the Busemann-Crocco relation (Schlichting, 1979) and thus the density profile was given as

$$\rho(r) = \frac{S}{1 + \left(\frac{1-S}{2\Lambda}\right)(U - 1 - \Lambda) + \left(\frac{\gamma - 1}{2}\right)\left(\frac{M}{1+\Lambda}\right)^2 \left(\Lambda^2 - 1 + 2U - U^2\right)}$$

with S being the density ratio, M the centerline Mach number and γ the specific heat ratio. Two distinct axisymmetric instability modes were identified: the first became absolutely unstable in the presence of co-flow whereas the other mode required counterflow to become absolutely unstable. The onset of global self-excitation identified in laboratory jets agreed reasonably well with the predictions.

Kyle and Sreenivasan (1993) performed experiments at low Richardson numbers to study the instability and breakdown of axisymmetric helium/air mixtures emerging into ambient air. Kyle and Sreenivasan (1993) made high-speed motion pictures of the jet by illuminating the flow with a continuous laser sheet. They made velocity measurements of the flow using a laser-Doppler velocimeter in the forward scatter-mode. The velocity profile of the jet approximated the Blasius profile. A hot wire anemometer operated on the constant temperature mode was also used to obtain velocity measurements in air jets (constant density within the shear layer). Kyle and Sreenivasan (1993) observed an intense oscillating instability (the oscillating mode) of the jet when the ratio of the jet exit density to the ambient fluid density was less than 0.6. From the high-speed films, they found that the overall structure of the oscillating mode repeated itself with "extreme" regularity which often extended to the fine-scale structure of the jet.

Raynal et al. (1996) carried out experiments with variable-density plane jets issuing into ambient air. A range of density ratios (0.14 to 1) and a range of Reynolds numbers based on the slot width and the jet fluid viscosity (250 to 3000) were studied. It was found that when the jet to ambient fluid density ratio was less than 0.7, the jets exhibited self-excited oscillations. The frequency and amplitude of these oscillations scaled with the nozzle width and not the thickness of the shear layer, indicating that the oscillatory behavior was a whole-jet phenomenon. Theoretical results based on the analysis of Yu and Monkewitz (1990) indicated the presence of absolute instability for density ratios less than 0.94 for plane jets, which was different from the value of 0.7 observed in experiments. Raynal et al. (1996) attempted to explain this discrepancy by taking into account the differences in the location of the inflection points in the density and velocity profiles for the cases of heated jets injected into air and the isothermal helium-air jets injected into air. It was found that the difference in the profiles alone could not entirely account for the discrepancy, and that the difference in the location of the inflexion points of the velocity and density profiles was important. The growth rate of the absolute instability was maximum when the inflection points in the density and velocity profiles coincided with one another. Also, a critical value for the difference the difference in the location of the inflexion points of the velocity and density profiles was noted, above which the absolute instability became convectively unstable.

Richards et al. (1996) used Mie scattering to visualize helium-air jets injected into air. Jets at varying density ratios and Reynolds number were studied. Intense mixing and vortex interactions characterized the self-excited helium jets at a density ratio of 0.14. Using an aspirating probe, concentration measurements at several radial locations were obtained that provided evidence of side-jets which produce vigorous mixing.

Note that gravitational effects have been neglected in all of the analyses listed above. The neglect of gravitational effects has been justified by the authors because of the small magnitude of the Richardson number based on the jet velocity and jet diameter. However, within the shear layer where the density and velocity change from jet to ambient values, the gravitational effects may not be negligible. Literatureon the effects of gravity and/or buoyancy on the stability characteristics of low-density gas jets injected in higher density ambient gases is limited.

Early studies of buoyant planar and axisymmetric jets are reviewed by

Gebhart et al. (1984). Hamins et al. (1992) used a shadowgraph technique to observe the near-field behavior of a non-reacting buoyant helium plume discharged from a round tube into air. Hamins et al. (1992) compared the pulsations in non-reacting helium plumes to the pulsations in diffusion flames. Pulsations in the non-reacting helium plume were not observed until a minimum flow rate that was much greater than the flow rate required to initiate pulsations in the flames. Like methane flames, the location of the formation of the vortex structures depended on the helium exit velocity. The Strouhal number-Froude number relationship for the non-reacting helium plume was $St \propto \left(\frac{1}{Fr}\right)^{0.38}$,unlike that for the flames which was $St \propto \left(\frac{1}{Fr}\right)^{0.57}$. The Strouhal number was defined as $St = fD/V$; where, f is the pulsation frequency, D is the jet diameter and V is the exit velocity. While the Froude number was defined as $Fr = V^2/(gD)$; where g is the acceleration due to gravity. Hamins et al. (1992) concluded that difference in the Strouhal number Froude number relations was due to the difference in the density profiles in the shear layers of the non-reacting and reacting flows.

Subbarao and Cantwell (1992) performed experiments on a co-flowing buoyant jet to study the scaling properties and effects of Richardson number and Reynolds number, independently, on the natural frequency of the jet. A helium jet, with a parabolic exit velocity profile, was injected into co-flowing air at half the helium jet velocity. The presence of co-flow eliminated the random meandering usually present in buoyant plumes with no co-flow. The jet exhibited periodic oscillations; even the fine-scale structure of these oscillations was highly regular and repeatable at high Richardson numbers. The Strouhal number defined as

$$St = \frac{fD}{U_j}$$

was plotted as a function of the square root of the Richardson number and was separated into three regimes. Note, for the graph, Subbarao and Cantwell (1992) defined the Richardson number as

$$Ri = \frac{gD}{U_j^2}\left(\frac{1-\frac{\rho_j}{\rho_\infty}}{\frac{\rho_j}{\rho_\infty}}\right).$$

At low Richardson numbers, the flow Strouhal number scaled with an inertial timescale, D/U_j, while at high Richardson numbers the Strouhal number scaled with a buoyancy timescale, $[\rho_j D/g(\rho_\infty - \rho_j)]^{0.5}$. Between the Richardson numbers of 0.7 and 1, a transition regime occurred. Subbarao and Cantwell (1992) defined a "buoyancy Strouhal number" as

$$St_B = \frac{\frac{fD}{U_j^2} - K_1}{\sqrt{Ri}}$$

where, K_1 is an empirical constant. Subbarao and Cantwell (1992) suggested that at high Richardson numbers the "buoyancy Strouhal number" was constant, at a value of 0.136.

Recently, Cetegen and coworkers studied buoyant plumes experimentally. Cetegen and Kasper (1996) performed experiments on the oscillatory behavior of axisymmetric buoyant plumes of helium and helium-air mixtures. The effects of varying nozzle diameters, source velocities and plume densities were investigated. Cetegen and Kasper (1996) observed that the plume boundaries exhibited periodic oscillations that were repeatable and evolved into toroidal vortices similar to those found in pool fires. When Strouhal number was defined as $St = \frac{fD}{U_j}$ and Richardson number defined as $Ri_1 = \frac{\left(\rho_\infty - \rho_j\right)gD}{\rho_\infty U_j^2}$ Cetegen and Kasper (1996) determined that three regimes could be identified for the Strouhal number, St, of buoyant jets: For $Ri_1 < 100$, $St = 0.8Ri_1^{0.38}$; for $Ri_1 > 500$, $St = 2.1Ri_1^{0.28}$; and for $100 < Ri_1 < 500$ a transition regime occurred. Cetegen and Kasper (1996) explained that the effect of turbulent mixing on local plume density and a resulting change of the convection speed of the vortices were the reasons for the different observed flow regimes. Cetegen (1997-1) investigated the effect of sinusoidal forcing on an axisymmetric buoyant plume. Helium and helium-air mixtures were again used. A loud speaker was used upstream of the plumes to force them. The plumes responded readily to the imposed oscillations with the toroidal vortices forming at the frequency of forcing. Mushroom-shaped small-scale vortex pairs were observed in the early part of the forced plumes that were not observed in unforced plumes. As the plumes evolved downstream, the frequency spectra became more broadband and contained frequencies other than the imposed one and its harmonics.

Cetegen (1997-2) used digital particle image velocimetry to measure the velocity field of a naturally pulsating plume of helium-air mixture in the presence of co-flowing air. The density ratio of the plume was 0.25, source velocity was 0.05 m/s and Richardson number of 283. The Richardson number was defined as $Ri = \frac{gd}{V^2}\frac{(\rho_\infty - \rho_j)}{\rho_\infty}$, where g is the acceleration due to gravity, d is the nozzle diameter (d = 10 cm), V is the source velocity, ρ_j is the plume density and ρ_∞ is the ambient air density. The oscillation frequency of the plume was between 3 and 4.5 Hz. Velocity measurements were performed in a phase resolved manner so as to characterize different phases of the plume. The velocity field around the toroidal vortex at 1.5 cm from the nozzle exit was characterized. Cetegen (1997-2) observed that the formation of the toroidal vortex structure occurs at about an axial location of $0.5d$. The vortex then convects downstream and significantly affects the flow field in its vicinity.

Pasumarthi (2000) conducted experiments to investigate the flow structure of a pulsating helium jet injected into air using quantitative rainbow schlieren deflectometry. Pasumarthi (2000) observed the flickering of the helium jet that revealed periodic global oscillations in the flow field. Like Subbarao and Cantwell

(1992), Pasumarthi (2000) observed that the Richardson number had a more significant effect on the flow structure than the jet exit Reynolds number. His data revealed a linear relationship between the Strouhal number $\left(\frac{fD}{U_j}\right)$ and Richardson number, defined as $\frac{gD}{U_j}\left(\frac{\rho_\infty - \rho_j}{\rho_j}\right)$, for the range of Richardson numbers, 0.5 to 6.5, investigated.

1.3: Objectives

The present study extends the work of Buckmaster and Peters (1986) to consider the effects of gravity on the instability of a low-density gas injected into a high-density ambient. The specific objectives of the study were:

1. To perform a linear temporal stability analysis of low-density round jets injected into high-density ambient gases.
2. To determine the effects of buoyancy on the instabilities of the jet.
3. To determine the nature of the instabilities, whether absolute or convective, and to demarcate the boundary separating the two modes of instability.

The dissertation begins with a description of the theoretical method that was used. Next, an experiment that was carried out to determine the velocity profile of helium (low-density gas) injected into air (high-density gas) in the near-injector region is discussed. The results of the stability analysis with the effects of the varying density in the shear-layer and buoyancy on the stability characteristics of low-density jets are presented. The absolute stability of low-density gases injected into high-density ambient gases is described in the subsequent section. The dissertation ends with a summary, conclusions, and recommendations for further study.

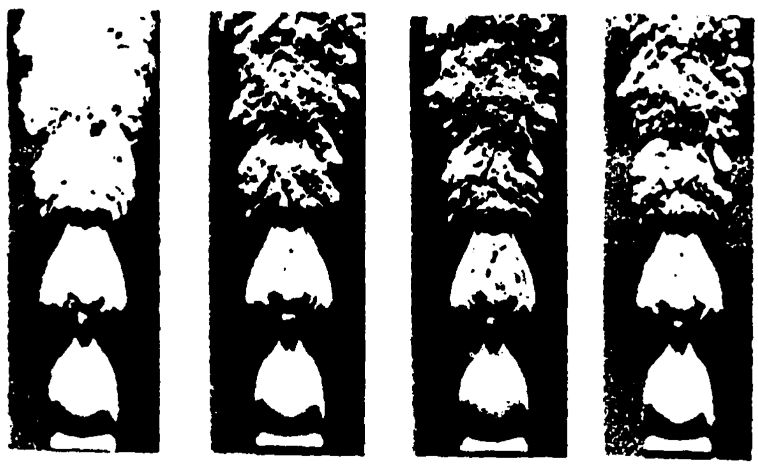

Figure 1.1: Schlieren photographs of a helium jet in ambient air at Reynolds number = 790 and Richardson number = 1.6 (Subbarao and Cantwell, 1992)

Chapter 2

Theory

2.1: General description

The present analysis considers a round jet of low-density gas discharged into a high-density ambient gas medium. The basic jet flow is assumed to be a locally inviscid parallel flow with an axial velocity component varying radially. In order to simplify the analysis, the flow is assumed to be isothermal. The radial velocity of the jet is considered small and, therefore, neglected. This corresponds to the "locally-parallel" assumption normally used in the linear stability analysis. As noted in the literature review, most of the existing analyses on low-density gas discharged into a high-density ambient assume negligible effects of buoyancy. The self-excited oscillations that are observed in these jets are analogous to the flickering of flames, known to be buoyancy induced. Thus, an analysis considering the effects of buoyancy, along the lines of Buckmaster and Peters (1986) is performed. Buckmaster and Peters (1986) performed a linear stability analysis on a diffusion flame taking into account the natural convection within the neighborhood of the hot flame sheet. The analysis of this study differs from that of Buckmaster and Peters (1986) in several ways. First, the near-injector velocity and density profiles are used in the analysis. Second, an axisymmetric configuration is studied. Finally, whereas Buckmaster and Peters (1986) solved for the neutral temporal stability characteristics, the boundary between absolute and convective instability is demarcated in this study.

2.2: Linear stability analysis

A simple method of investigating the instability characteristics of a nonparallel round jet with mean flow profiles evolving slowly in the axial direction is the linear stability analysis applied at each axial location. The normal mode assumption is made for the disturbances and their radial dependence is then determined by a set of ordinary differential equations derived from the conservation equations coupled with the boundary conditions at the jet axis and a radial location far away from the jet.

An eigenvalue problem is thus posed with either the wavenumber, k or frequency, Ω as the eigenvalue. The eigenvalue solution of the problem depending on the mean flow velocity and density profiles, along with other relevant flow parameters and fluid properties, at any axial location can then be determined. For a spatial linear stability analysis, the complex wavenumber eigenvalues are determined for specified real frequencies. For a temporal linear stability analysis, on the other hand, the complex frequency eigenvalues are determined for specified real wavenumbers. Thus, the spatial linear stability analysis determines the downstream evolution of a constant amplitude harmonic input while the temporal stability analysis determines the evolution of a spatially periodic pattern with time

(Yu, 1990). For a spatio-temporal linear stability analysis, both the frequency and wavenumber are considered complex. If the complex wavenumbers are specified, the complex frequency eigenvalues are determined and vice versa.

The spatio-temporal linear stability along with the Briggs-Bers criterion (Briggs, 1964; Bers, 1975, 1983) can be used to determine the absolute stability and the nature of the absolute stability of the jet. The jet is said to be absolutely unstable when the complex frequency eigenvalue is a saddle point and its imaginary part is greater than zero. If its imaginary part is less than zero, the jet is convectively unstable. A description of how the saddle point was located in the complex frequency domain is given in Section 2.4 of this report.

2.3: Formulation

Consider a round jet (radius R) of a low-density gas (density ρ_j) injected vertically upward with velocity U_j into an ambient quiescent gas of density ρ_∞ at atmospheric pressure as illustrated in the schematic diagram of Figure 2.1.

Representing the velocity components by $(\tilde{u}, \tilde{v}, \tilde{w})$, in cylindrical coordinates $(\tilde{x}, \tilde{r}, \phi)$ centered at the origin of the jet, and the pressure by p the conservation equations governing the flow are :

$$\frac{\partial \tilde{\rho}}{\partial t} + \frac{\partial(\tilde{\rho}\tilde{u})}{\partial \tilde{x}} + \frac{1}{\tilde{r}}\frac{\partial(\tilde{r}\tilde{\rho}\tilde{v})}{\partial \tilde{r}} + \frac{1}{\tilde{r}}\frac{\partial(\tilde{\rho}\tilde{w})}{\partial \phi} = 0 \qquad (2.1)$$

$$\tilde{\rho}\left[\frac{\partial \vec{v}}{\partial t}+\vec{v}\bullet\nabla\vec{v}\right]=-\nabla p+g\left(\rho_{\infty}-\tilde{\rho}\right)\delta_{i1}+\nabla\bullet\left(\mu\nabla\vec{u}\right) \tag{2.2}$$

where g is the acceleration due to gravity and δ_{i1} is the Kronecker delta function with i = 1 representing the axial direction. The binary mass diffusion equation for the diffusion of the injected gas in the ambient gas medium is given in terms of the local mass fraction of the injected gas, Y_j (Gebhart, 1993):

$$\tilde{\rho}\left[\frac{\partial Y_j}{\partial t}+\vec{v}\bullet\nabla Y_j\right]=\nabla\bullet\left[\tilde{\rho}D_b\nabla Y_j\right] \tag{2.3}$$

where D_b is the binary diffusivity coefficient.

The flow is assumed to be locally parallel, and the variables are represented as the sum of the base state value and a fluctuation:

$$\begin{aligned}
\tilde{u}&=\overline{u}(\tilde{r})+u'\\
\tilde{v}&=v'\\
\tilde{w}&=w'\\
\tilde{p}&=p'\\
\tilde{\rho}&=\overline{\rho}(\tilde{r})+\rho'
\end{aligned} \tag{2.4}$$

The effects of viscosity on the large-scale structures in the near-injector region are negligible (Crow and Champagne, 1971). Substitution of equations (2.4) into equations (2.1) and (2.2), linearization, and the neglect of viscous and diffusive terms yields

$$\frac{\partial \rho'}{\partial t}+\bar{u}\frac{\partial \rho'}{\partial \bar{x}}+\bar{\rho}\frac{\partial u'}{\partial \bar{x}}+\frac{1}{\bar{r}}\frac{\partial(\bar{r}\bar{\rho}v')}{\partial \bar{r}}+\frac{\bar{\rho}}{\bar{r}}\frac{\partial w'}{\partial \phi}=0 \tag{2.5}$$

$$\bar{\rho}\left[\frac{\partial u'}{\partial t}+\bar{u}\frac{\partial u'}{\partial \bar{x}}+v'\frac{d\bar{u}}{d\bar{r}}\right]=-\frac{\partial p'}{\partial \bar{x}}-g\rho' \tag{2.6}$$

$$\bar{\rho}\left[\frac{\partial v'}{\partial t}+\bar{u}\frac{\partial v'}{\partial \bar{x}}\right]=-\frac{\partial p'}{\partial \bar{r}} \tag{2.7}$$

$$\bar{\rho}\left[\frac{\partial w'}{\partial t}+\bar{u}\frac{\partial w'}{\partial \bar{x}}\right]=-\frac{1}{\bar{r}}\frac{\partial p'}{\partial \phi} \tag{2.8}$$

The density of the mixture is related to the mass fraction by

$$\bar{\rho}=\frac{\rho_j}{Y_j+(1-Y_j)S}$$

where ρ_j is the density of the injected gas and S is the density ratio ρ_j/ρ_∞ (ρ_∞ is the density of the ambient gas medium). Rewriting Y_j in terms of ρ, we have

$$Y_j=\frac{1}{1-S}\left(\frac{\rho_j}{\bar{\rho}}-S\right)$$

Therefore,

$$\frac{\partial Y_j}{\partial t}=-\frac{\rho_j}{\bar{\rho}^2(1-S)}\frac{\partial \bar{\rho}}{\partial t}$$

$$\frac{\partial Y_j}{\partial \bar{x}}=-\frac{\rho_j}{\bar{\rho}^2(1-S)}\frac{\partial \bar{\rho}}{\partial \bar{x}}$$

$$\frac{\partial Y_j}{\partial \bar{r}}=-\frac{\rho_j}{\bar{\rho}^2(1-S)}\frac{\partial \bar{\rho}}{\partial \bar{r}}$$

Substituting the above expressions in equation (2.3), we obtain

$$-\frac{\rho_j}{\tilde{\rho}(1-S)}\left(\frac{\partial\tilde{\rho}}{\partial t}+\tilde{v}\bullet\nabla\tilde{\rho}\right)=\nabla\bullet\left[\left(-\frac{\rho_j}{\tilde{\rho}(1-S)}\right)D_h\nabla\tilde{\rho}\right] \tag{2.9}$$

The effects of viscosity and diffusivity on the large-scale structures in the near-injector region are negligible (Crow and Champagne, 1971). Neglecting the diffusive term, and linearizing equation (2.9), we obtain

$$\frac{\partial\rho'}{\partial t}+\bar{u}\frac{\partial\rho'}{\partial\tilde{x}}+v'\frac{d\bar{\rho}}{d\tilde{r}}=0 \tag{2.10}$$

Using equation (2.10), equation (2.5) reduces to

$$\bar{\rho}\left[\frac{\partial u'}{\partial\tilde{x}}+\frac{1}{\tilde{r}}\frac{\partial(\tilde{r}v')}{\partial\tilde{x}}+\frac{1}{\tilde{r}}\frac{dw'}{d\phi}\right]=0 \tag{2.11}$$

Normal mode disturbances are assumed given by

$$(u',v',w',p',\rho')=\left[\hat{u}(\tilde{r}),\hat{v}(\tilde{r}),\hat{w}(\tilde{r}),\hat{p}(\tilde{r}),\hat{\rho}(\tilde{r})\right]e^{i(\tilde{k}\tilde{x}-\tilde{\Omega}t+m\phi)} \tag{2.12}$$

where $i=\sqrt{-1}$; $\hat{u},\hat{v},\hat{w},\hat{p},\hat{\rho}$ are the amplitudes of the disturbances; $\tilde{k}$ is the wavenumber; $\tilde{\Omega}$ is the frequency, and m is the azimuthal wavenumber. For temporal linear stability analysis, the wavenumber, $\tilde{k}$, is real while the frequency $\tilde{\Omega}=\tilde{\Omega}_r+i\tilde{\Omega}_i$ is complex. The real part $\tilde{\Omega}_r$ is proportional to the disturbance frequency and the imaginary part $\tilde{\Omega}_i$ is the temporal growth rate of the disturbance. The disturbance gets amplified if $\tilde{\Omega}_i$ is positive. The ratio of $\tilde{\Omega}_r$ to k represents the wave speed, c_{ph} of the disturbance.

Substituting the expressions (2.12) in equations (2.6), (2.7), (2.8), (2.10) and (2.11), we obtain

$$\bar{\rho}\left[i\left(\tilde{k}\bar{u}-\tilde{\Omega}\right)\hat{u}+\hat{v}\frac{d\bar{u}}{d\bar{r}}\right]=-i\tilde{k}\hat{p}-g\hat{\rho} \tag{2.13}$$

$$i\bar{\rho}\left(\tilde{k}\bar{u}-\tilde{\Omega}\right)\hat{v}=-\frac{d\hat{p}}{d\bar{r}} \tag{2.14}$$

$$i\bar{\rho}\left(\tilde{k}\bar{u}-\tilde{\Omega}\right)\hat{w}=-i\frac{m\hat{p}}{\bar{r}} \tag{2.15}$$

$$i\left(\tilde{k}\bar{u}-\tilde{\Omega}\right)\hat{\rho}+\hat{v}\frac{d\bar{\rho}}{d\bar{r}}=0 \tag{2.16}$$

$$i\tilde{k}\hat{u}+\frac{1}{\bar{r}}\frac{d\left(\bar{r}\hat{v}\right)}{d\bar{r}}+\frac{im}{\bar{r}}\hat{w}=0 \tag{2.17}$$

From equations (2.14), (2.15) and (2.16), we have

$$\hat{v}=i\frac{1}{\bar{\rho}\left(\tilde{k}\bar{u}-\tilde{\Omega}\right)}\frac{d\hat{p}}{d\bar{r}} \tag{2.18}$$

$$\hat{w}=-\frac{m\hat{p}}{\bar{r}\bar{\rho}\left(\tilde{k}\bar{u}-\tilde{\Omega}\right)} \tag{2.19}$$

$$\hat{\rho}=i\frac{\hat{v}\dfrac{d\bar{\rho}}{d\bar{r}}}{\left(\tilde{k}\bar{u}-\tilde{\Omega}\right)}=-\frac{\dfrac{d\hat{p}}{d\bar{r}}\dfrac{d\bar{\rho}}{d\bar{r}}}{\bar{\rho}\left(\tilde{k}\bar{u}-\tilde{\Omega}\right)^2} \tag{2.20}$$

and, from equation (2.13) we have

$$\hat{u}=-\frac{\tilde{k}\hat{p}}{\bar{\rho}\left(\tilde{k}\bar{u}-\tilde{\Omega}\right)}+i\frac{g\dfrac{d\hat{p}}{d\bar{r}}\dfrac{d\bar{\rho}}{d\bar{r}}}{\bar{\rho}^2\left(\tilde{k}\bar{u}-\tilde{\Omega}\right)^3}-\frac{\dfrac{d\hat{p}}{d\bar{r}}\dfrac{d\bar{u}}{d\bar{r}}}{\bar{\rho}\left(\tilde{k}\bar{u}-\tilde{\Omega}\right)^2} \tag{2.21}$$

Substituting equations (2.18) to (2.21) in equation (2.17) we get the following equation for the pressure disturbance:

$$\frac{d^2\hat{p}}{d\tilde{r}^2}+\left[\frac{1}{\tilde{r}}-\frac{2\frac{d\bar{u}}{d\tilde{r}}}{\bar{u}-\frac{\tilde{\Omega}}{\tilde{k}}}-\frac{1}{\bar{\rho}}\frac{d\bar{\rho}}{d\tilde{r}}\left(1+\frac{ig}{\tilde{k}\left(\bar{u}-\frac{\tilde{\Omega}}{\tilde{k}}\right)^2}\right)\right]\frac{d\hat{p}}{d\tilde{r}}-\left(\tilde{k}^2+\frac{m^2}{\tilde{r}^2}\right)\hat{p}=0 \qquad (2.22)$$

For the varicose mode disturbance (m = 0) equation (2.22) reduces to

$$\frac{d^2\hat{p}}{d\tilde{r}^2}+\left[\frac{1}{\tilde{r}}-\frac{2\frac{d\bar{u}}{d\tilde{r}}}{\bar{u}-\frac{\tilde{\Omega}}{\tilde{k}}}-\frac{1}{\bar{\rho}}\frac{d\bar{\rho}}{d\tilde{r}}\left(1+\frac{ig}{\tilde{k}\left(\bar{u}-\frac{\tilde{\Omega}}{\tilde{k}}\right)^2}\right)\right]\frac{d\hat{p}}{d\tilde{r}}-\tilde{k}^2\hat{p}=0 \qquad (2.23)$$

The variables are nondimensionalized as follows

$$P=\frac{\hat{p}}{\rho_r U_j^2} \qquad Fr^2=\frac{U_j^2}{gR}\frac{\rho_j}{\rho_r-\rho_j}$$

$$r=\frac{\tilde{r}}{\theta} \qquad x=\frac{\tilde{x}}{\theta}$$

$$\Omega=\frac{\tilde{\Omega}\theta}{U_j} \qquad k=\tilde{k}\theta$$

$$U=\frac{\bar{u}}{U_j} \qquad \rho=\frac{\bar{\rho}}{\rho_r}$$

where θ *is* the momentum boundary layer thickness defined as

$$\theta=\int_0^{\infty}\left(\frac{\bar{u}-U_\infty}{U_j-U_\infty}\right)\left(1-\frac{\bar{u}-U_\infty}{U_j-U_\infty}\right)d\tilde{r} \qquad (2.24)$$

Nondimensionalizing equation (2.23) gives the nondimensionalized pressure disturbance equation

$$\frac{d^2P}{dr^2}+\left[\frac{1}{r}-\frac{2\frac{dU}{dr}}{U-\frac{\Omega}{k}}-\frac{1}{\rho}\frac{d\rho}{dr}\left(1+i\frac{1}{Fr^2\frac{R}{\theta}\left(\frac{\rho_\infty}{\rho_j}-1\right)k\left(U-\frac{\Omega}{k}\right)^2}\right)\right]\frac{dP}{dr}-k^2P=0 \quad (2.25)$$

It should be noted that with no density gradient equation (2.25) reduces to the equation governing the instability of constant-density jets (Michalke, 1984). Also, as $r \to \infty$, and if gravitational effects are neglected, equation (2.25) is identical to the equation used by Yu and Monkewitz (1990) and Raynal et al. (1996) in the analysis of plane jets. Inclusion of buoyancy effects indicates that the stability characteristics are altered by the additional term present in equation (2.25). The pressure disturbance must vanish at large radial distances from the jet and the pressure disturbance is finite at the jet axis (r = 0) therefore

$$\begin{aligned} &P(\infty) \to 0 \\ &P(0) \text{ is finite} \\ &\frac{dP(0)}{dr}=0 \quad \text{due to symmetry} \end{aligned} \qquad (2.26)$$

An eigenvalue problem is posed, for specified mean velocity and density profiles, by equation (2.12) along with the boundary conditions (2.26). As $r \to 0$ and $r \to \infty$, $\frac{dU}{dr}$ and $\frac{d\rho}{dr}$ equal zero and the pressure disturbance equation (2.25) reduces to the modified Bessel equation. The solutions of the modified Bessel equation satisfying the boundary conditions (2.26), as $r \to 0$ and $r \to \infty$, are

$$P^{(i)} = C_1 I_m(kr) \tag{2.27}$$

$$P^{(o)} = C_2 K_m(kr) \tag{2.28}$$

respectively, where the superscripts i and o represent the inner and outer solutions respectively. I_m and K_m are the modified Bessel functions of the order m and C_1 and C_2 are arbitrary constants.

Following Monkewitz and Sohn (1988), the base axial velocity and the density profiles are specified as a function of the local jet radius. The basic jet velocity profile, $U(r)$, is given by Michalke and Hermann (1982),

$$\frac{\bar{u}(\bar{r}) - U_\infty}{U_j - U_\infty} = 0.5\left\{1 - \tanh\left[0.25\frac{R}{\theta}\left(\frac{\bar{r}}{R} - \frac{R}{\bar{r}}\right)\right]\right\} \tag{2.29}$$

where U_j is the injected jet uniform velocity and U_∞ is the uniform co-flow velocity. For this study the co-flow velocity was set to zero for a quiescent ambient gas and R is the radius of the jet defined as the radial location corresponding to the center of the shear layer where $\bar{u} = 0.5(U_j + U_\infty)$. The momentum boundary layer thickness, θ, is defined as

$$\theta = \int_0^\infty \left(\frac{\bar{u} - U_\infty}{U_j - U_\infty}\right)\left(1 - \frac{\bar{u} - U_\infty}{U_j - U_\infty}\right) d\bar{r} \tag{2.30}$$

R/θ is the jet parameter that characterizes the jet velocity profile at various axial positions. As shown by Crighton and Gaster (1976),

$$\frac{R}{\theta} = \frac{100}{3\frac{\tilde{x}}{R} + 4} \tag{2.31}$$

for no co-flow. The values of the jet parameter used in this study are 25, 10 and 5 corresponding to $\tilde{x}/(2R)$ = 0, 1 and 2.67. This is within the near-injector region of the jet and allows for the effects of buoyancy to manifest as the jet proceeds downstream from R/θ = 25 (Subbarao and Cantwell, 1992). Figure 2.2 illustrates the basic jet velocity profiles at these three locations. The shear layer widens as the jet proceeds downstream from R/θ = 25 to R/θ = 5 indicating the downstream development of the jet.

A hyperbolic tangent profile is also assumed for the basic density profile in the shear layer,

$$\frac{\bar{\rho}(r)}{\rho_\infty} = 1 + \left(\frac{\rho_j}{\rho_\infty} - 1\right)\left\{0.5\left(1 - \tanh\left[0.25\frac{R}{\theta}\left(\frac{\bar{r}}{R} - \frac{R}{\bar{r}}\right)\right]\right)\right\} \tag{2.32}$$

Figure 2.3 illustrates the density profiles at R/θ = 10 for ρ_j/ρ_∞ = 1, 0.6, and 0.14.

The effects of buoyancy on the jet were studied by investigating the variation of the real and imaginary parts of both the complex wavenumber and frequency with the Froude number, Fr. Froude number is the ratio of the inertia force to buoyancy force and is defined as

$$Fr^2 = \frac{U_j^2}{gR}\frac{\rho_j}{\rho_\infty - \rho_j} \tag{2.33}$$

2.4: Method of solution

To solve the disturbance equation (2.25), a fourth-order Runge-Kutta scheme with automatic step-size control is used to integrate the equation (2.25). The infinite integration domain, $0 < r < \infty$ is divided into two finite domains: an inner domain $R \geq r \geq 0$ and an outer domain $r_\infty \geq r \geq R$, where R is the jet radius and r_∞ is a specified large radius where the gradients of the velocity and density are small. A shooting method is used to determine $\Omega(k)$ such that both P and $\frac{dP}{dr}$ are continuous at $r = R$. A parabolic complex zero-search procedure was used to vary Ω for a specified k until the matching conditions were satisfied to a minimum accuracy within 10^{-10}. Fortran 90/95 computer programs were used to solve the eigenvalue problem, and a listing of the source codes can be found in Appendix B. The Briggs-Bers criterion (Briggs, 1964; Bers, 1975, 1983) is used to determine the nature of the instability (whether absolute or convective) by determining the saddle points in the complex (Ω, k) domain and verifying the satisfaction of the pinching requirements. This is done using the mesh-searching technique described by Li and Shen (1996). The theory behind the demarcation of absolute and convective instability is well documented (Briggs, 1964; Bers, 1975, 1983; Li and Shen, 1996). The steps involved in this technique are listed below:

1. **The search is restricted in the *k*-plane.**

This is important because if the region is too small the saddle points or pinch points may be missed and if it is too large the grid may be too coarse for the saddle points or pinch points to be located. Thus, appropriate ranges for the real and imaginary values of k must be selected. To select the appropriate ranges, the temporal stability solution is first determined. If there is a pinch point, $k^o = k_r^o + ik_i^o$ within the region selected, the corresponding growth rate, Ω_i^o of the absolute instability will be less than or equal to the maximum temporal disturbance growth rate, $\Omega_{i,\,max}^t$ (Bers, 1983) and the real part of the pinch point, k_r^o will be less than or equal to the wavenumber corresponding to neutral stability, $k_{r,\,c}^t$ (Li and Shen, 1996). Thus, the estimates for the k region are determined using the wavenumber corresponding to neutral stability, $k_{r,\,c}^t$ and the maximum temporal disturbance growth rate, $\Omega_{i,\,max}^t$. Therefore, Ω^o will lie in either the first or fourth quadrants of the Ω-plane (see Figure 2.4), while k^o will lie in the fourth quadrant of the k-plane (see Figure 2.5).

2. **The disturbance equation for $\Omega(k)$ is solved.**

The disturbance equation (2.25) is solved numerically, as discussed at the beginning of section 2.4, within the search region in the k-plane determined in the previous step. Complex wavenumbers are specified and the corresponding complex frequency eigenvalue solutions are determined. This is done by starting at wavenumbers with $k_i^t = 0$ (the temporal stability solution) and decreasing the value k_i for several k_r within the search region.

3. **The saddle point is found.**

A contour plot of various constant Ω_r or Ω_i on the k-plane is used to determine the saddle point, Ω^s. The saddle point is the point within the Ω_r or Ω_i domain, which is a minimum along the k_r-axis and a maximum along the k_i-axis, or vice versa. Mathematically, the saddle point can be obtained from

$$\frac{D\Omega}{Dk} = \frac{\partial\Omega_r}{\partial k_r} - i\frac{\partial\Omega_r}{\partial k_i} = 0 \tag{2.34}$$

or

$$\frac{D\Omega}{Dk} = \frac{\partial\Omega_i}{\partial k_r} + i\frac{\partial\Omega_i}{\partial k_i} = 0 \tag{2.35}$$

In this study the saddle points were determined by inspection of the contour plots. Figure 2.6 is a contour plot of Ω_r for $R/\theta = 10$, $Fr = \infty$ and $\rho_j/\rho_\infty = 0.14$ in the k-plane and Figure 2.7 shows the 3-D depiction that illustrates the saddle point.

4. **The pinch point is determined**

The same contour plot of various constant Ω_r on the k-plane from the previous step is used to determine the pinch point, k^o. The pinch points are double roots in k. If two k-roots merge to k^o from opposite sides of the k_r-axis or k_i-axis as Ω tends to Ω^s from above $\Omega_{i,max}'$, k^o is a pinch point.

For normal mode disturbance, any disturbance variable q' is represented as given in equation (2.12) by

$$q' = \hat{q}(r)e^{i[(k_r+ik_i)x-(\Omega_r+i\Omega_i)t]}$$

$$\therefore q' = \left[\hat{q}(r) e^{(\Omega_i t - k_i x)} \right] e^{i[k_r x - \Omega_r t]} \tag{2.36}$$

Thus, for negative k_i the flow system is said to be absolutely unstable if $\Omega_i^o > 0$ (since the amplitude of the disturbance will grow with time and space), otherwise it is convectively unstable. The boundaries demarcating the absolute and convective instabilities were computed as a function of shear-layer thickness, and specified velocity and density profiles. Particular attention was devoted to the effects of buoyancy in the form of the Froude number and the ratio of the density of the jet to that of the ambient gas.

The convergence of the saddle points as the step-size of k (Δk) is reduced is illustrated in Table 2.1 for a density ratio of 0.14 and Froude number of infinity at $R/\theta = 10$. The saddle point converges to $\Omega = 0.05638 + i0.01808$ as Δk tends to 0.0005. Thus, accuracy of the saddle point is at least five decimal places. This was the lowest accuracy of all the saddle points determined in this report.

Table 2.1: Convergence of (Ω^o, k^o) as step-size Δk of k_r and k_i is reduced for $R/\theta = 10$, S = 0.14 and Fr = ∞

Δk	k_r^o	$-k_i^o$	Ω_r^o	Ω_i^o
0.025	0.075	0.1	0.05624	0.01776
0.01	0.07	0.09	0.05638	0.01808
0.005	0.07	0.09	0.05638	0.01808
0.0025	0.07	0.09	0.05638	0.01808
0.0001	0.071	0.089	0.05638	0.01808
0.0005	0.0705	0.0895	0.05638	0.01808

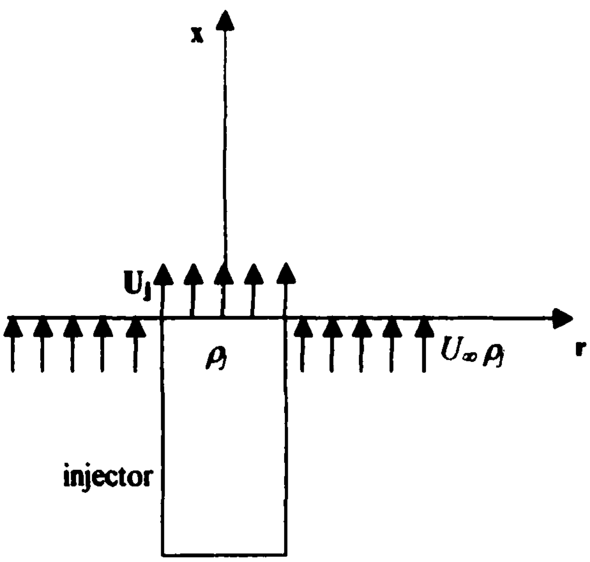

Figure 2.1: Schematic of a low-density round gas jet injected vertically upwards into a high-density ambient gas

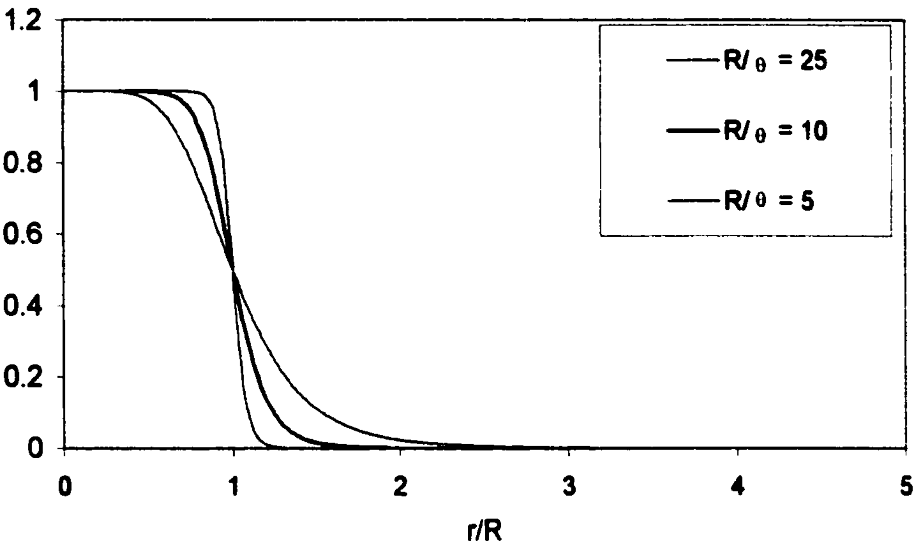

Figure 2.2: Nondimensionalized basic jet velocity profile for S = 1 at R/θ = 25, 10 and 5

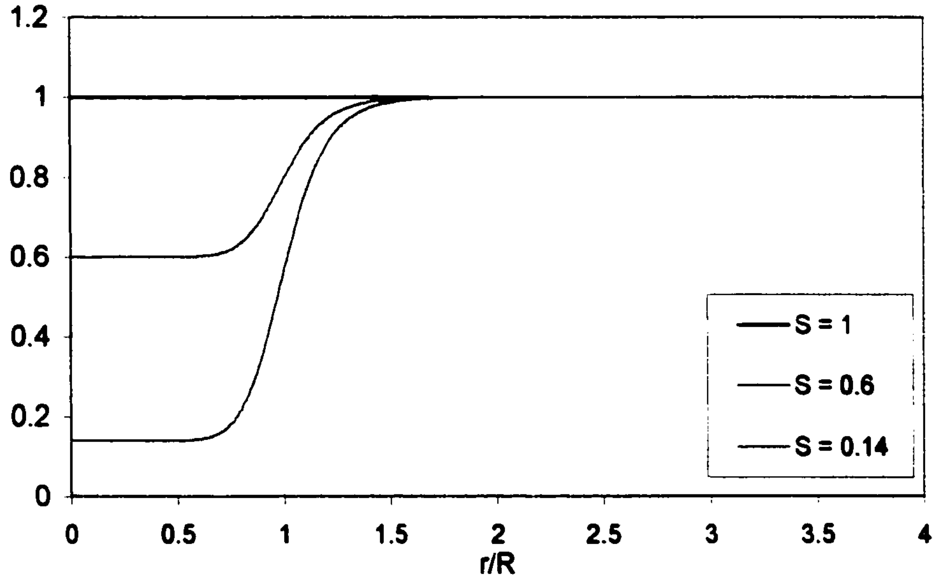

Figure 2.3: Nondimensionalized basic density profile vs r/R for R/θ = 10 at S = 1, 0.6 and 0.14

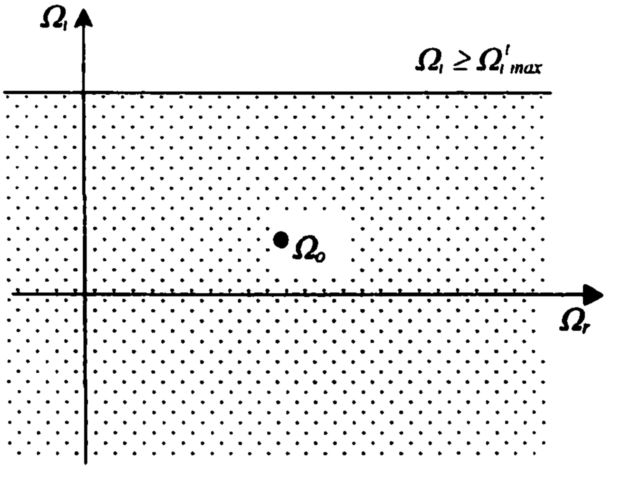

Figure 2.4: Solution region on the Ω-plane

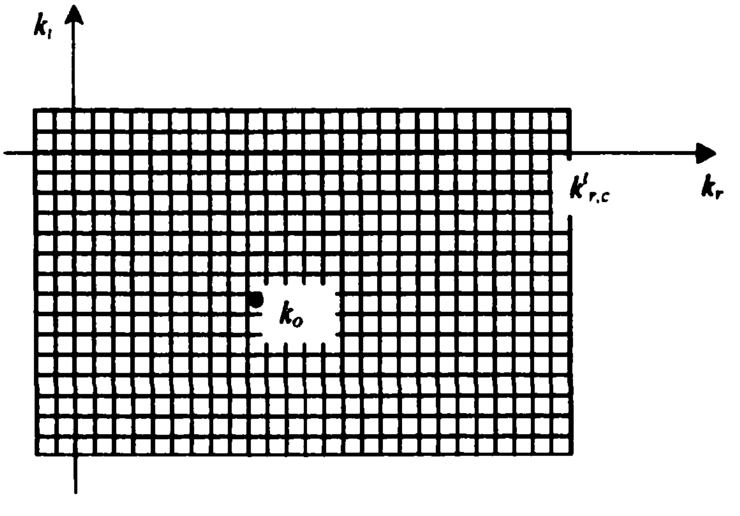

Figure 2.5: Mesh on the k-plane

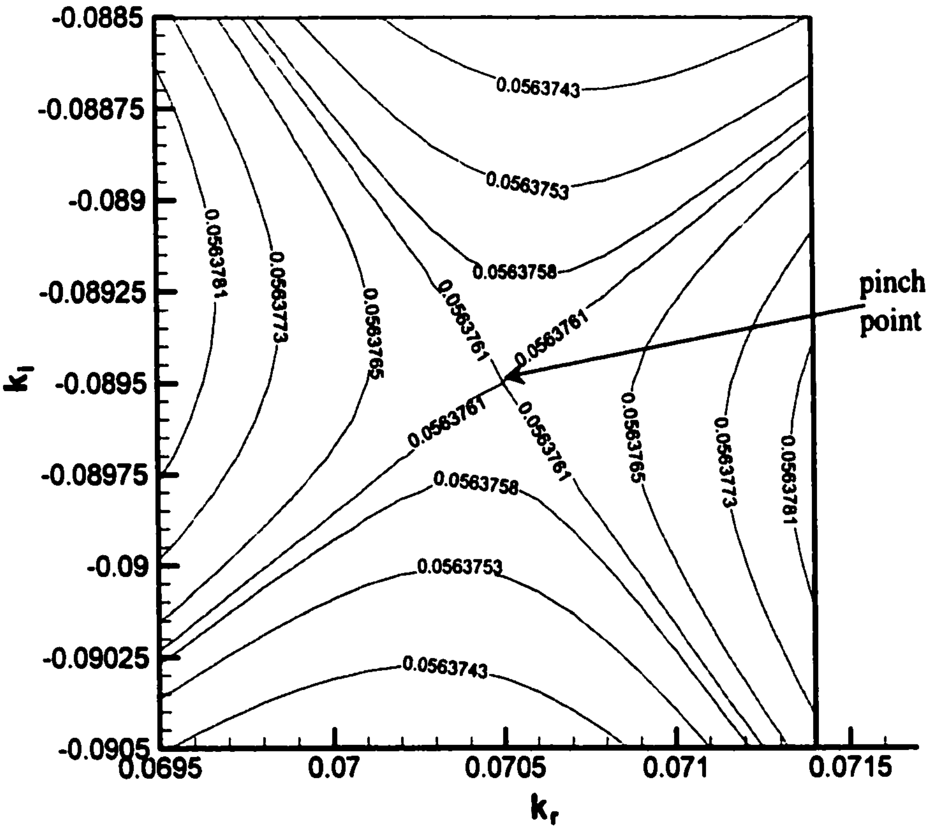

Figure 2.6: Contour plot of Ω_r for $R/\theta = 10$, $Fr = \infty$ and $\rho_j/\rho_\infty = 0.14$ in the k-plane illustrating the pinch point

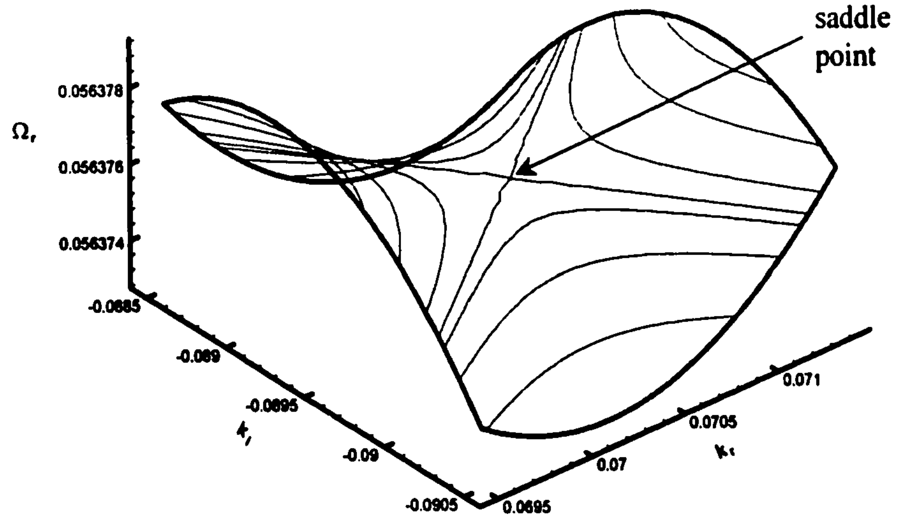

Figure 2.7: 3-D plot of Ω_r for $R/\theta = 10$, $Fr = \infty$ and $\rho_j/\rho_\infty = 0.14$ illustrating the saddle point

Chapter 3

Experiments on low-density round gas jets injected into a high-density ambient gas

3.1: Introduction

The mean velocity profile of a low-density gas injected into a high-density ambient gas varies with the axial location. A round jet experiment was set up to investigate the velocity profile of a real low-density gas injected into a high-density ambient gas in the near-injector region. In this chapter, the jet exit radius R_e and jet centerline velocity U_c are used as the characteristic length and velocity respectively.

The flow system consisted of a gas discharged from a round pipe into the quiescent ambient medium. The jet was operated at Reynolds numbers within the laminar flow regime. The velocity profile in the near-injector region of an isothermal round helium jet discharged into air (with a density ratio of 0.14) was studied and compared to that of an isothermal air-in-air round jet. Photographs of the jets were also studied to observe the visual differences between the helium-in-air and air-in-air jets.

3.2: Test facility

Figure 3.1 is a sketch of the test facility. A listing of the apparatus is provided in Table 3.1. A gas cylinder fitted with a compressed gas cylinder pressure regulator to monitor the cylinder exit pressure served as the source. The flow passed through a flow meter and a needle valve (for fine control) before entering an atomizer that provided water drops as seed particles. The flow carrying the water drops exited into the injector pipe.

The injector pipe was similar in design to that used by a counterpart team for microgravity experiments at the NASA Glenn Research Center. A schematic diagram of the injector arrangement is illustrated in Figure 3.2. The injector pipe consisted of a 180-degree curved inlet pipe section, a 0.254-m long horizontal section and a 0.254-m long vertical section as shown in Figure 3.2, with an exit diameter of 0.01905 m. The injector pipe could be traversed in the three orthogonal directions. The vertical motion was achieved using a screw jack assembly (least count = 0.25" and maximum traverse distance = 5.5") and the lateral motion in the horizontal plane was achieved by two Unislides assembled perpendicular to each other (one with a least count = 0.01" and maximum traverse = 12" and the other with a least count = 0.01 cm and maximum traverse = 28 cm). Positioning uncertainties of the injector pipe were mainly due to the least counts of the lab jack and the Unislide assembly. Two stainless steel screens (mesh size = 24 mesh per inch) located at the 90-degree elbow, as shown in Figure 3.2, were used to straighten the flow and eliminate large eddies.

The flow meters were calibrated using a Pitot-static tube connected to a pressure transducer that was connected to a multimeter. The Pitot-static tube's outside diameter was 0.0078 m (about 41% of the jet exit diameter). The length of the Pitot-static tube from the total pressure port to just beyond the static pressure ports was placed vertically along the jet axis in the injector pipe upstream of the jet exit to measure the jet centerline velocity. The centerline velocity of a parabolic pipe flow velocity profile is twice the bulk velocity. The bulk velocity was then used to determine the flow rate and compared to flow rate data obtained from the flow meters. The calibration curves for both the helium and air flow meters are illustrated in Figure 3.3. The maximum uncertainty in the calibration data for the helium flow meter is about 3 SLPM while that for the air flow meter is about 0.4 SLPM. Both calibration curves have correlation (R^2-) factors greater than 0.97. Thus, the calibration curves fit the data well. The equation for the helium flow meter calibration curve (dimensions in SLPM) is

$$y = 1.1592x \tag{3.1}$$

where, x and y are the coordinate labels of the abscissa and ordinate respectively. The equation for the air flow meter calibration curve (dimensions in SLPM) is

$$y = 0.9417x \tag{3.2}$$

3.3: Instrumentation

3.3.1: LDV system and data acquisition

A TSI two-beam Laser Doppler Velocimetry (LDV) system with a 2-Watt argon ion laser was used to measure the jet velocities. The LDV system is identical to that used by Chan (1998) without the discriminator system. A schematic of the general arrangement of the LDV system is illustrated in Figure 3.4 with a summary of the components given in Table 3.2.

A dispersion prism was used to separate the green (λ = 514.5 nm) and the blue (λ = 488 nm) components from the argon ion laser beam. In this study, only one component of velocity was of interest; therefore, the blue beam was blocked off and not used. The green beam was divided into two parallel beams in a vertical plane and then focused at a point above the injector pipe. Thus, the velocity in the vertical plane at the focus could be measured. One beam from the two parallel green beams was passed through a Bragg-cell frequency shifter to allow for measurements of positive and negative velocities. The properties of the LDV measuring volume are tabulated in Table 3.3.

The flow was seeded with water droplets from the TSI six-jet atomizer. As pressurized helium or air passes through the six-jet atomizer the gas forms high-velocity jets through six 0.015-inch-diameter orifices. The pressure drop from the jets draws water up from a reservoir through narrow tubes and the water is broken up into droplets by the high-velocity jets. The larger droplets impinge on spherical impactors and fall into the water reservoir while the smaller droplets make no contact and form an aerosol that exits through the atomizer outlet. The outlet diameter of the atomizer was 1 inch and tapered on the inside. Gas entered the TSI six-jet atomizer through a built-in pressure regulator (least count = 2 psi) at the inlet. Cetegen and Kasper (1996) used a TSI six-jet atomizer in their study on the oscillatory behavior of helium plumes and using a phase Doppler particle sizer they measured the water droplets from the six-jet atomizer to be less than 2 μm in diameter. The particle number density varied with flow rate. At a flow rate of 72 SLPM, the particle number density is about 10^{10} particles per liter of gas medium (TSI Inc., 2000-1). The scattered light from the LDV volume was collected in an on-axis forward scatter mode to enable a high signal-to-noise ratio. The scattered light was collected by a dichroic mirror in the receiving optics, then filtered by a narrow-band pass filter and focused onto a photomultiplier.

The signal from the photomultiplier was processed using a TSI Model IFA 655 digital burst correlator. The TSI Model IFA 655 digital burst correlator distinguished the signal burst from the noise, based on signal-to-noise ratio (TSI Inc., 2000-2). The electronics of the processor was verified by measuring known signals from a 2-MHz signal generator (BK Precision Model # 3022) with the LDV system. As illustrated in Figure 3.5, data from the LDV system agree well with those from the signal generator. There was no significant difference between the data - the maximum difference between the data was 0.2% at very low velocities.

Chan (1998) also verified the LDV system by measuring the velocity of the edge of a 0.0508 m rotating disk and comparing the data with measurements obtained from a stroboscope (Ametek Model 1965). The calibration curve that was obtained showed that the difference between the two measurements was less than 7% and within a 95% confidence interval (Chan, 1998). The calibration curve is reproduced in Figure 3.5a courtesy of Chan (1998).

3.3.2: Data processing

Signals from the LDV system were digitally transferred from the digital burst correlator to an AMD-processor-based IBM compatible personal computer (PC). In the PC the processed signals were stored and statistically analyzed using the Flow Information Display (FIND) software from TSI, Inc. Using the FIND software the number of data points collected and the time-out window which stopped data acquisition could be specified. Thus, the data rates from the LDV system could be monitored. A time-out window of 200 seconds and 5000 data points to be collected was specified and the FIND software stopped data acquisition whenever either value was achieved. The water droplets used to seed the flow were less concentrated in the shear layer region than in the neighborhood of the jet axis (the potential core) thus it took longer to gather LDV data in the shear layer region than in the potential core. In the potential core it took less than 20 seconds to gather

5000 data points while in the shear layer it took longer time.

3.3.3: Flow visualization

For flow visualization purposes, a cylindrical lens (focal length = 0.01322 m), located as depicted in Figure 3.6, was used to form a laser sheet from the green beam of the argon laser of the LDV system. At the jet, the laser sheet was estimated to be 0.092075 m wide and 0.003175 m thick. The cross-section of the jet was illuminated by the scattering of the laser light of the laser sheet from the water droplets used to seed the flow. Photographs were taken by first recording a movie on a Maxell Digital 8 tape at 30 fps and then recording the images of each frame on a memory stick using a Sony digital video camera.

3.3.4: Test Conditions

The operating range of the test conditions in the study is tabulated in Table 3.4. The velocity profiles of two jet flows were studied: a helium jet discharged into quiescent air (S = 0.14) and an air jet discharged into quiescent air (constant density jet; S = 1). The constant density jet was used as a baseline. Previous studies (Sohn and Monkewitz, 1988; Kyle and Sreenivasan, 1993; and Raynal et al., 1996) indicate that at a density ratio of 0.14 the jet is absolutely unstable while at a density ratio of 1 the jet is not absolutely unstable (but, may be convectively unstable).

Velocity measurements of the helium jet discharged into air (helium-air system) and the air jet discharged into air (air-air system) were obtained, with the LDV system, at two axial locations: x/R_e = 0.5 (very near the jet exit) and x/R_e = 2.5. At each axial location, the velocity measurements were obtained at radial locations, with an increment in the radial location of about r/R_e = 0.27. The measurements were repeated five times, and averaged, at each axial location to enable an error analysis of the data. Velocity data obtained from measuring devices in any experiment are prone to bias errors and random errors.

Parthasarathy (1985) reported the several bias errors associated with the use of LDV to obtain velocity measurements as directional ambiguity, directional bias, concentration bias, velocity bias, and gradient bias. Directional ambiguity occurs when the LDV system is unable to determine the direction in which the seeds of the flow are crossing the fringes in the measuring volume due to a stationary or slow-moving fringe pattern. In this study, directional ambiguity was eliminated using a frequency shifter with the fringes moving at 1 MHz. The concentration bias in this study was not significant because the flow was seeded uniformly and the mixing of the water droplets did not affect the results since signals from the drops were only present for a fraction of the time. The amount of particles crossing the measuring volume depends on the velocity of the flow resulting in more high-velocity seeds being counted than the low-velocity seeds. The measurements in this study were number-averaged and the results biased towards the high velocities causing a velocity bias. According to a study on velocity bias in LDV measurements by Ahmed et al. (1995), the differences between the bias-corrected data, obtained from constant time-interval and time between velocity sampling, and the biased number-averaged data were insignificant for round jets (less than 2%) thus velocity bias was ignored in the error analysis. Gradient bias is due to the finite size of the measuring volume. The velocity measurements obtained from the LDV system are the average velocities of the seeds crossing the measuring volume at a given instance due to the finite size of the measuring volume. In his analysis, Parthasarathy (1985) determined that the gradient bias error is largest where the velocity gradients are large like near the edge of the jet, but the gradient biasing of the mean and fluctuating velocities throughout the jet were insignificant (less than 1%). Thus, based on this analysis, the bias errors in the LDV measurements of the velocities were negligible in the experiments of this study.

Random errors (or precision errors) are introduced when the velocities are determined from a limited number of valid signals from the LDV system. Increasing the sample size and time of data acquisition can reduce the random errors. In this study, the sample size was 5000 and cutoff time for data acquisition was 200 seconds. Acquisition of the data was then repeated five times at each axial location to reduce the random errors. The random errors were determined using the following equation (Wheeler and Ganji, 1996)

$$P = t_{0.025} \frac{s_x}{\sqrt{N}} \tag{3.3}$$

where, the student's t value $t_{0.025}$ = 2.776 (for N = 5 and 95% confidence interval), s_x is the standard deviation of the data, and N = 5. The major contribution to uncertainty in the velocity data was thus the random errors.

Results of the velocity measurements are compared to the parabolic velocity profile (fully developed laminar pipe flow) and the hyperbolic tangent velocity profile (a velocity profile assumed for jet flow in the near-injector region) and are presented below.

3.4: The mean flow

3.4.1: Axisymmetry of the mean flow

The measurements of the mean velocity profile of the helium-air system and the air-air system at x/R_e = 0.5 are presented in Figures 3.7 and 3.8 respectively. In both figures, the axisymmetry of the jets is apparent within the uncertainty of the data. The differences of corresponding data on each side of the jet axis (r/R_e = 0) are within a maximum of 6% of the jet mean centerline velocity for both figures. In Figure 3.8, the uncertainty of the data within the shear-layer (region in the neighborhood of the jet radius) is higher than in the regions near the axis of the jet and far away from the axis of the jet. For the helium-air system (Figure 3.7), however, the uncertainties at all radial locations appear to be high. Further investigation indicated that the helium jet was self-excited and the velocity profiles measured at different times showed significant changes. This is attributable to the vigorous mixing and ambient air entrainment peculiar to the absolutely unstable helium-air flow when compared to the air-in-air jet flow, which is not absolutely unstable.

3.4.2: The mean velocity profile

The mean velocity profile of a fully developed laminar pipe flow is parabolic while that within the near-injector region of an initially laminar jet with a potential core can be represented by a hyperbolic tangent profile. Thus, the parabolic profile and hyperbolic tangent profile are plotted along with the experimental data for comparison purposes in Figures 3.7 and 3.8. For both flow systems, at $x/R_e = 0.5$, the exit mean velocity profiles lie between the parabolic and hyperbolic tangent profiles illustrating the effect of the pipe flow velocity profile on the jet. Near the center of the jet the profile is nearly flat suggesting that the pipe flow upstream of the jet exit was not fully developed. This was as a result of the injector pipe design. The injector pipe was designed to fit in a space-constrained set-up for microgravity experiments in the NASA Glenn Research Center drop tower. Thus the pipe length upstream of the jet exit was not long enough to allow for a fully developed flow before the jet was discharged. Away from the center of the jet the deviation from the parabolic profile in the Figures 3.7 and 3.8 is due to the relaxation and entrainment of air.

Figures 3.9 and 3.10 illustrate the mean velocity profiles of the helium-air and air-air systems, respectively, at $x/R_e = 2.5$. Again, for both flow systems, the data lie between the parabolic and hyperbolic tangent profiles. The influence of the high disturbance amplitude of the self-excited helium-air flow system on the uncertainty values is observed again at this axial location. Comparison of the mean velocity profiles for both jets at this axial location to those at the $x/R_e = 0.5$ show the spreading of the jets at $x/R_e = 2.5$. The radial location at which the velocity profile tends to zero is increased by about 25% and 80% for the helium-air system and air-air system respectively. The air jet appears to have spread further than the helium jet, which does not seem to agree with the large spreading usually associated with absolutely unstable jets like the helium jets discharged in air observed in previous studies (see Subbarao and Cantwell, 1992 and Cetegen and Kasper, 1996). Upon further examination of the structure of the helium jets reported in the previous studies it is observed that the boundaries of the helium jets oscillate periodically. This oscillation is an entire jet phenomenon with the jet expanding at one axial location and then contracting at a downstream location from that axial location at a given time. The flow visualization images discussed in section 3.6 of this report also illustrate this.

3.5: Profiles of the standard deviation of axial velocity

Figures 3.11 and 3.12 are the profiles of the standard deviation of the velocity nondimensionalized by the mean centerline velocity at $x/R_e = 0.5$ for the helium-air and air-air flow systems respectively. As discussed in section 3.4 above, the error bars are wider for radial locations near the jet axis in the helium-air system than those in the air-air system. The standard deviation of the velocity is an indication of the amplitude of the velocity disturbance. For the helium-air system, the maximum standard deviation is 0.071; about 78% more than that of the air-air system (which is 0.04). Thus, the amplitude of the velocity disturbance in the helium-air flow system was greater than in the air-air system. This is similar to the findings of Kyle and Sreenivasan (1993) in their study on absolutely unstable variable-density jets. And, it suggests that the disturbances in an absolutely unstable round jet are greater than those of a jet that is not absolutely unstable. This may also be due to the acceleration of the helium flow at the jet exit due to buoyancy. The radial location from the jet axis where the maximum standard deviation occurs in the helium-air system is 0.054; about 48% less than that of the air-air system which is at r/R_e = 0.08. Due to the more energetic disturbances of the absolutely unstable helium jet, the velocity fluctuations are higher and they occur nearer the center of the jet. Even at the center of the jet the amplitude of the velocity disturbance in the absolutely unstable helium jet is about 25% greater than those of the air jet. Downstream, at the axial location corresponding to $x/R_e = 2.5$ (see Figures 3.13 and 3.14), the amplitude of the velocity disturbance at the center of the helium jet are about 88% more than those of the air jet. Also, at x/R_e = 2.5, the amplitude of the velocity disturbance of the air jet peaks around the jet radius with the amplitudes within the neighborhoods of the center of the jet and far away from the jet radius being at least 50% less than the maximum value. For the helium jet, on the other hand, the amplitudes of the velocity disturbance at radial locations from the jet center to the jet radius are within 23% of the maximum value and beyond the jet radius the amplitudes taper off. Thus, for the air-jet-in-air flow system which is not absolutely unstable the disturbances are highest within the shear layer while for the helium-jet-in-air flow system that is absolutely unstable the effect of the disturbance is felt in the entire jet.

3.6: Flow visualization

The objective of the flow visualization was to show the global differences in the appearance of the helium jet discharged into air compared to the air jet injected into air. Figures 3.15 and 3.16 show the sequences of movie frames of a helium jet and air jet respectively. Both were injected into air from the injector pipe shown in Figure 3.2. The helium jet was at a Froude number of 4.88 and a Reynolds number of 664 while the air jet was at a Froude number (defined as $Fr^2 = \frac{U_j^2}{gR_e}$ for a constant density jet) of 3.18 and a Reynolds number of 1193. The first frame in

Figure 3.15 (Frame # 01.30.00) shows the spreading of the helium jet. At about 3.67 diameters downstream of the jet exit (top of the frame) the jet has spread by about 167%. On the other hand, in Figure 3.16 at the same downstream location in any of the frames for the air jet there is no significant spreading observed. Also, the higher intensity light region (the potential core) in the helium jet is 30% narrower than that of the air jet at this downstream location. And, there is a wider band of the annular shear layer in the helium jet than in the air jet. Note that the radial extent of the jet that is seen in the frames is limited by the spread of the water droplets used to seed the jet. The light from laser sheet is scattered by the water droplets and captured by the video camera. Thus, this spreading of the helium jet downstream is indicative of the strong mixing associated with absolutely unstable jets. The droplets are spread further into the ambient air surrounding the helium jet.

We also notice the pulsating of the helium jet. The development of the vortex structures appears to cause the pulsations of the helium jet. In Figure 3.15, as we proceed from the first frame to the second frame, the lower vortices have moved up and grown in size. By the fourth frame new vortices are formed nearer the jet exit and the vortex pairing process starts again in the seventh frame (see Frame # 01.30.06). This vortex pairing process repeats almost every seven frames causing the helium jet to oscillate. The oscillation frequency observed is thus 4.3Hz. Due to the limit of the frame rate of the camera (30 fps), 4.3 Hz must be one of the harmonic frequencies but may not be the first harmonic. A camera with a faster frame rate may be needed to determine the first harmonic frequency. Thus, the helium jet is absolutely unstable since the disturbances grow with time and space unlike the air jet, which did not exhibit any visually growing disturbances. Also, the vortex structures are symmetric about the helium jet axis suggesting that the disturbances are of the varicose mode.

A rainbow schlieren image of a helium jet at a Froude number of 1.2 and Reynolds number of 164 discharged from an injector pipe similar to that in Figure 3.2 into quiescent air at a flow rate of 15.6 SLPM is shown in Figure 3.17. The rainbow schlieren image was gratefully obtained from the counterpart team of this study and provided to illustrate the vortex structures in an absolutely unstable jet. The lighter regions in the rainbow schlieren image are regions of varying gas concentration (or density) within the shear layer of the jet. Thus the dark region in the middle of the jet is the potential core and the other dark region surrounding the outer boundary of the shear layer is the ambient air. The narrow potential core and wide shear layer are again observed in the rainbow schlieren image. The pulsating of the jet due to the development of the vortex structures can also be observed. In the figure, the jet bulges at the axial location coinciding with the center of the vortex structures and then narrows at the top of the vortex structures. The rainbow schlieren image confirms the observations of the absolutely unstable helium jet of the experiments described above.

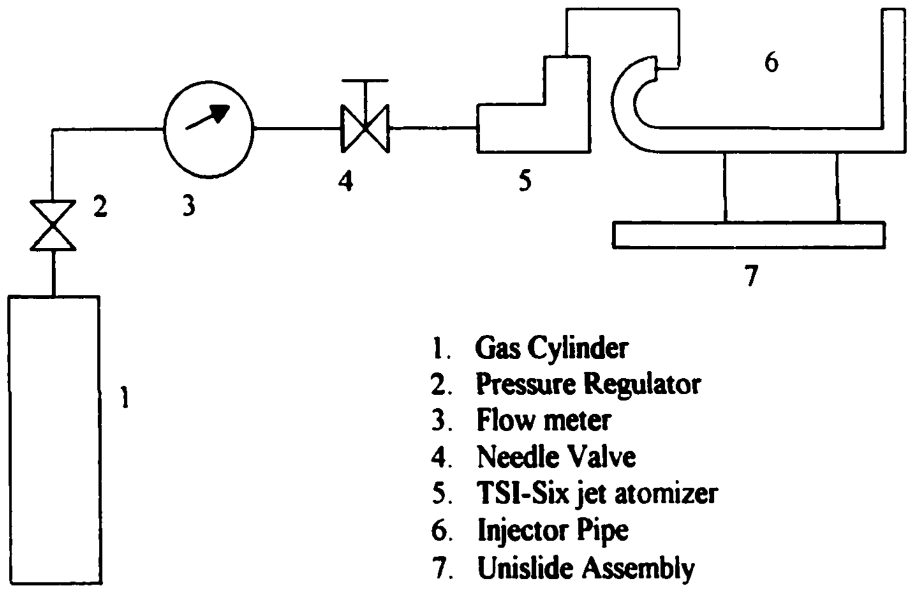

Figure 3.1: Test facility

Table 3.1: List of apparatus of the test facility

Apparatus	Variable measured	Manufacturer	Model	Least count
Compressed gas cylinder pressure regulators: • Helium • Compressed air	Pressure Pressure	Fischer Scientific Airgas	Fisherbrand 10-573-J 300-3-346-V	10 psi 5 psi
Flow meter • Helium • Air	Flow rate Flow rate	Fathom Technologies Fathom Technologies	GR-112-1-A-PV-5241 GR-112-1-A-PV-5477	0.1 SLPM 0.1 SLPM
Needle valve		Swagelok	B-1RF4	
Six-jet atomizer		TSI	9306	
Lab jack	Height	Fischer Scientific	19090-002	Maximum height = 5.5"
Unislide assembly	Lateral motion	Velmex, Inc.	• A6018W1-S6-TL-RC • A4000	• 0.01" (Maximum traverse = 12") • 0.01 cm (Maximum traverse = 28 cm)
Pitot-static tube	Velocity			
Multimeter	Voltage		DM-301	0.0001 V
Pressure transducer		Validyne	CD280	
Digital video camera	Flow visualization	Sony	DCR-TRV 530	30 fps

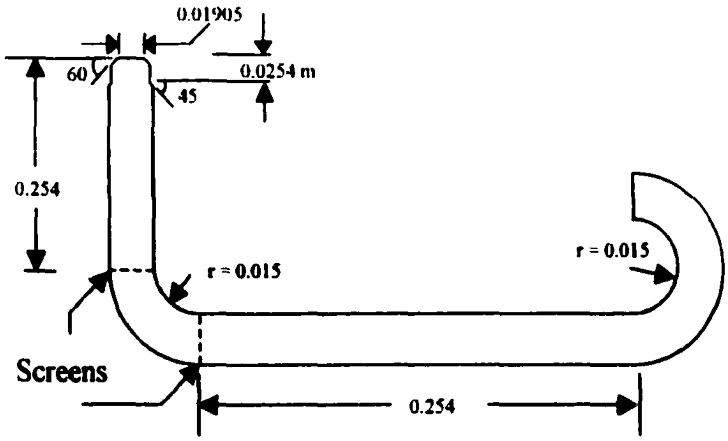

Figure 3.2: Schematic of the injector pipe

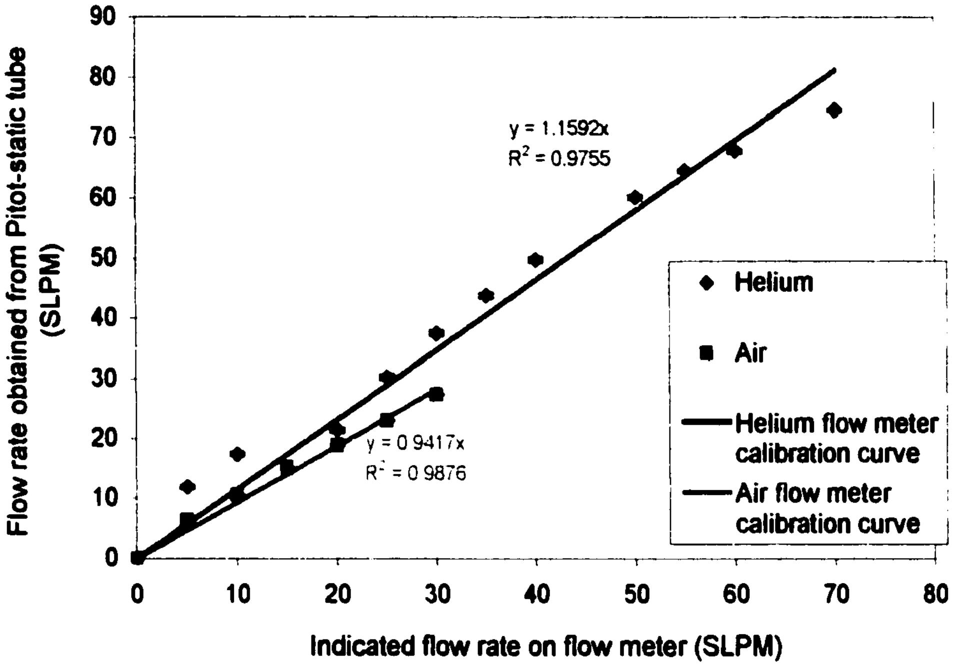

Figure 3.3: Calibration of helium and air flowmeters using a Pitot-static tube

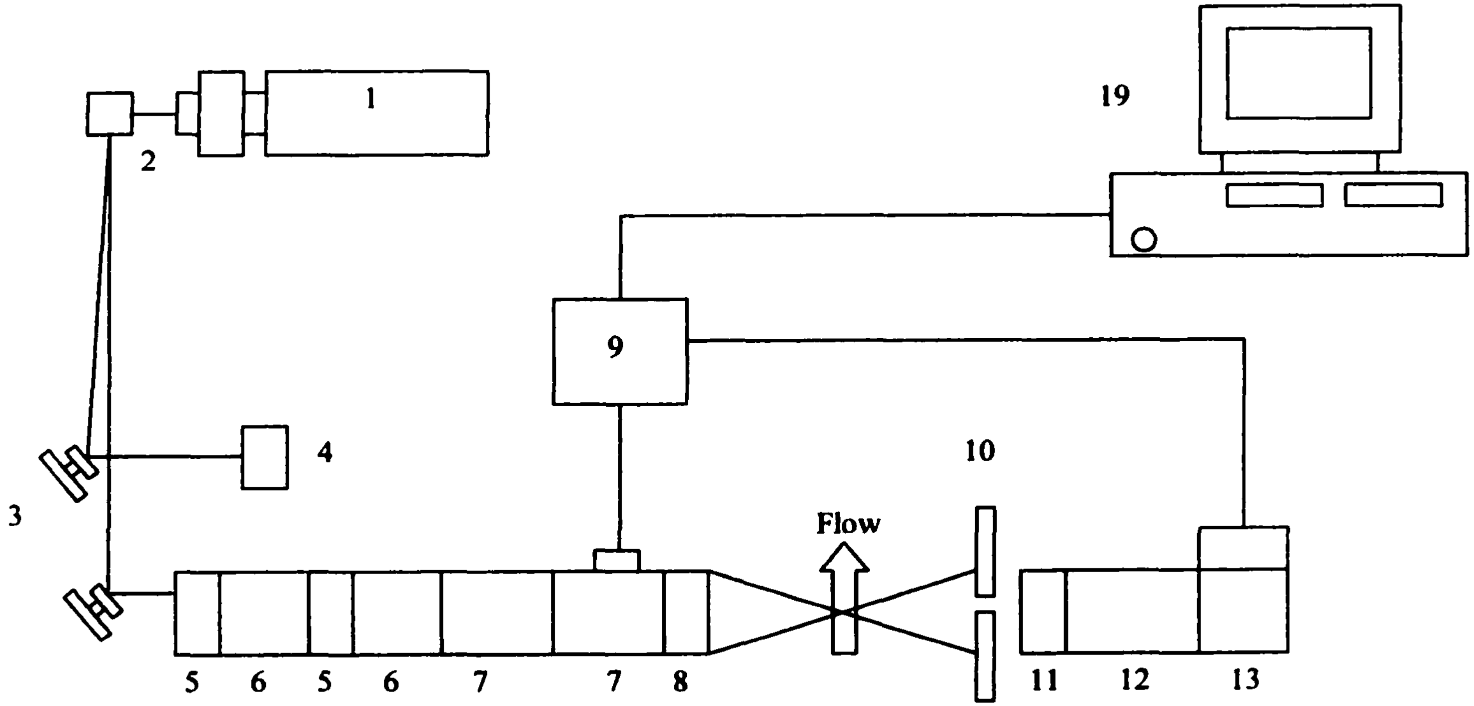

1. Argon-ion Laser
2. Dispersion Prism
3. Mirror Assembly
4. Stopper
5. Polarization Rotator
6. Beam Splitter
7. Bragg cell Shifter
8. Focusing Lens
9. Frequency Shifter
10. Beam Stop
11. Collecting Lens
12. Receiving Optics
13. Photomultiplier

Figure 3.4: Schematic diagram of the Laser Doppler Velocimetry system

Table 3.2: Components of the Laser Doppler Velocimetry system

Component	Manufacturer	Model	Specification/Function
Argon ion laser	Lexel Laser, Inc.	95-2	TEM_{00} model, 514.5 to 457.9 nm wavelength, 1.3 mm beam diameter, 2.5 maximum power
Dispersion prism	TSI	905 and 906	Separate the blue and green components of the laser
Mirror	TSI	907	
Polarization rotator	TSI	9102-11 and –12	
Beam splitter	TSI	915-1	50 mm beam spacing
Frequency shifter	TSI	9186A	Bragg cell 2 kHz to 10 MHz frequency shifting
Focusing lens	TSI	9167-350	349.8 mm focal length
Receiving module	TSI	9140	
Collecting lens	TSI	9167-350	349.8 mm focal length
Photomultiplier	TSI	9162	Photodetector with 0.25-mm diameter aperture
Photomultiplier power supply	TSI	9165	
Oscilloscope	Tektronix	465	Monitor real-time sampling
Digital burst correlator	TSI	IFA 655	Signal conditioning and processing
16-bit DMA interface board	TSI	6261	Transfer data from signal processor to PC
IBM-compatible personal computer (PC)	AuthenticAMD		266 MHz AMD-K6 processor
FIND program	TSI	FIND for Windows version 1.4	

Table 3.3: Properties of LDV laser and measuring volume

Element	Characteristics
Beam color	Green
Beam diameter ($D_{e^{-2}}$)	1.3 mm
Wavelength	514.5 nm
Beam spacing	50 mm
Beam half angle	4.09°
Fringe spacing	3.61 μm
Measuring volume diameter	0.18 mm
Length of measuring volume	2.47 mm

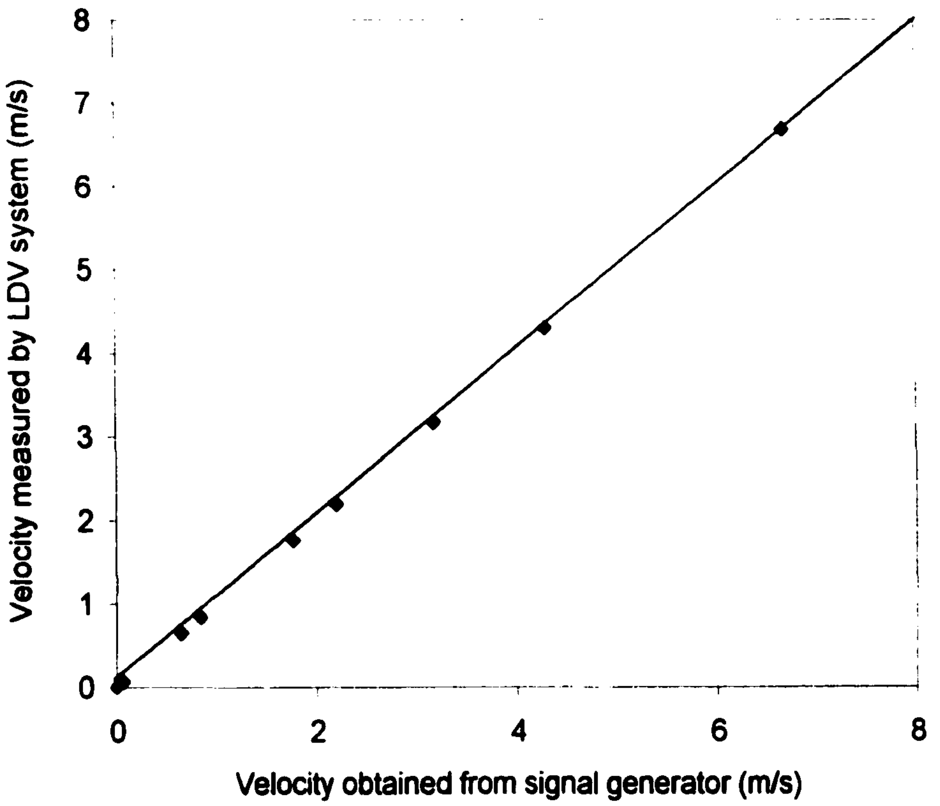

Figure 3.5: Verification of LDV measurements

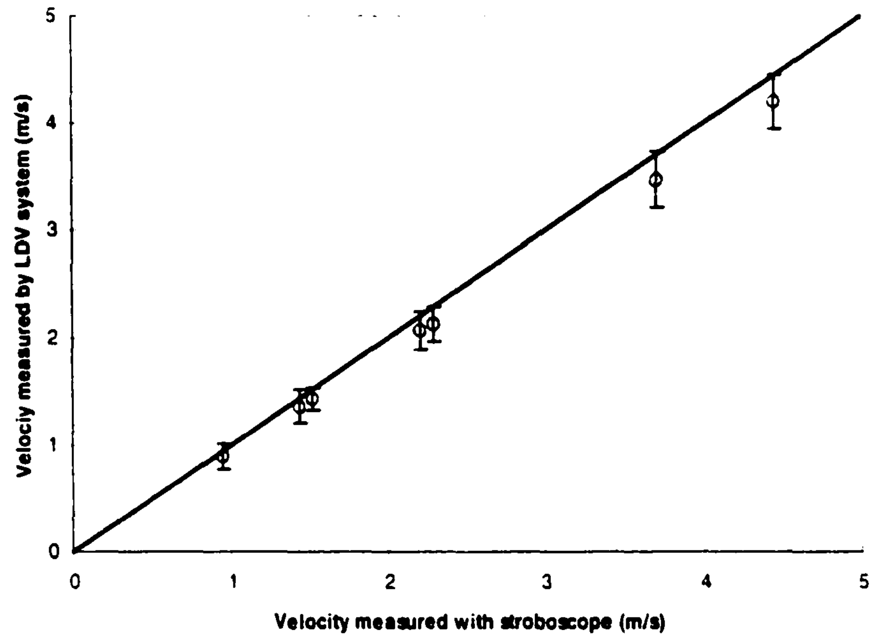

Figure 3.5a: Verification of LDV measurements within 2 standard deviations by rotating disk experiment (Chan, 1998)

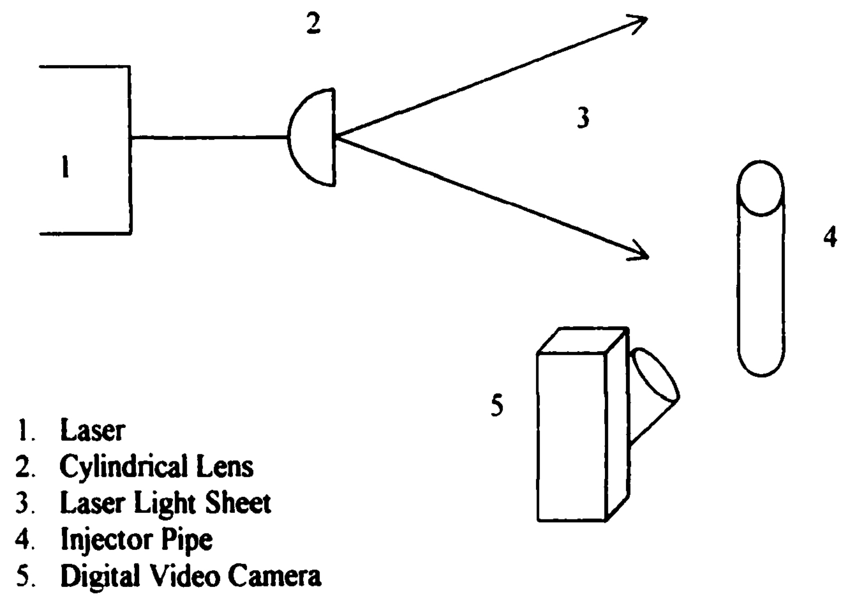

Figure 3.6: Experimental configuration for visualization of jet cross-section

Table 3.4: Operating range of test conditions

Density ratio	Flow rate (SLPM)	Bulk velocity (m/s)	Reynolds number	Froude number
For velocity measurements:				
0.14	62	3.63	652	$\frac{U_j}{\sqrt{gR}}\frac{\rho_j}{(\rho_r-\rho_j)} = 4.79$
1	8.11	0.47	583	$\frac{U_j}{\sqrt{gR}} = 1.55$
For flow visualization:				
0.14	63.2	3.70	664	$\frac{U_j}{\sqrt{gR}}\frac{\rho_j}{(\rho_r-\rho_j)} = 4.88$
1	16.6	0.97	1193	$\frac{U_j}{\sqrt{gR}} = 3.18$

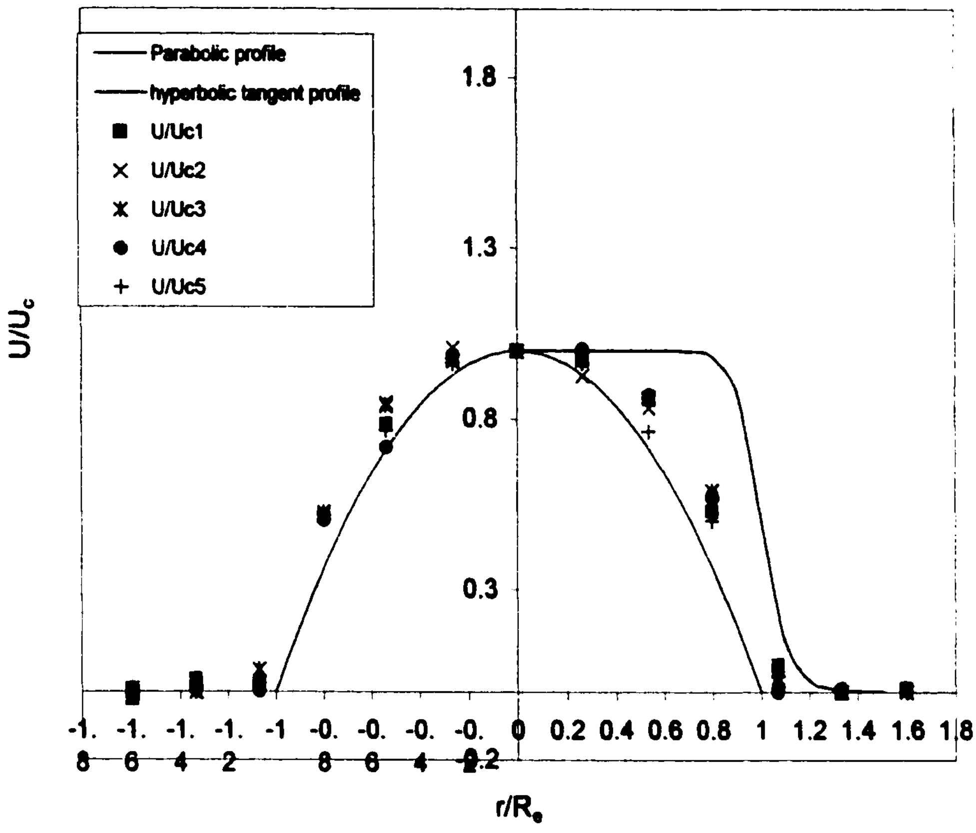

Figure 3.7: Mean velocity profiles for He-air system measured five different times at $x/R_e = 0.5$

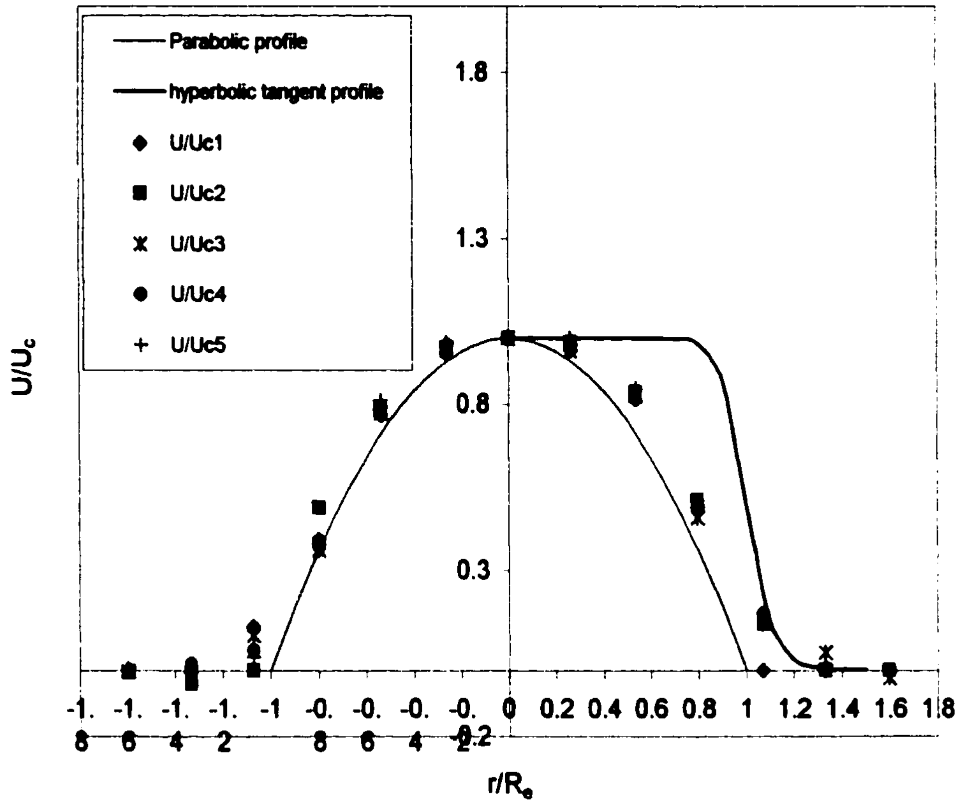

Figure 3.8: Mean velocity profiles for air-air system measured five different times at $x/R_e = 0.5$

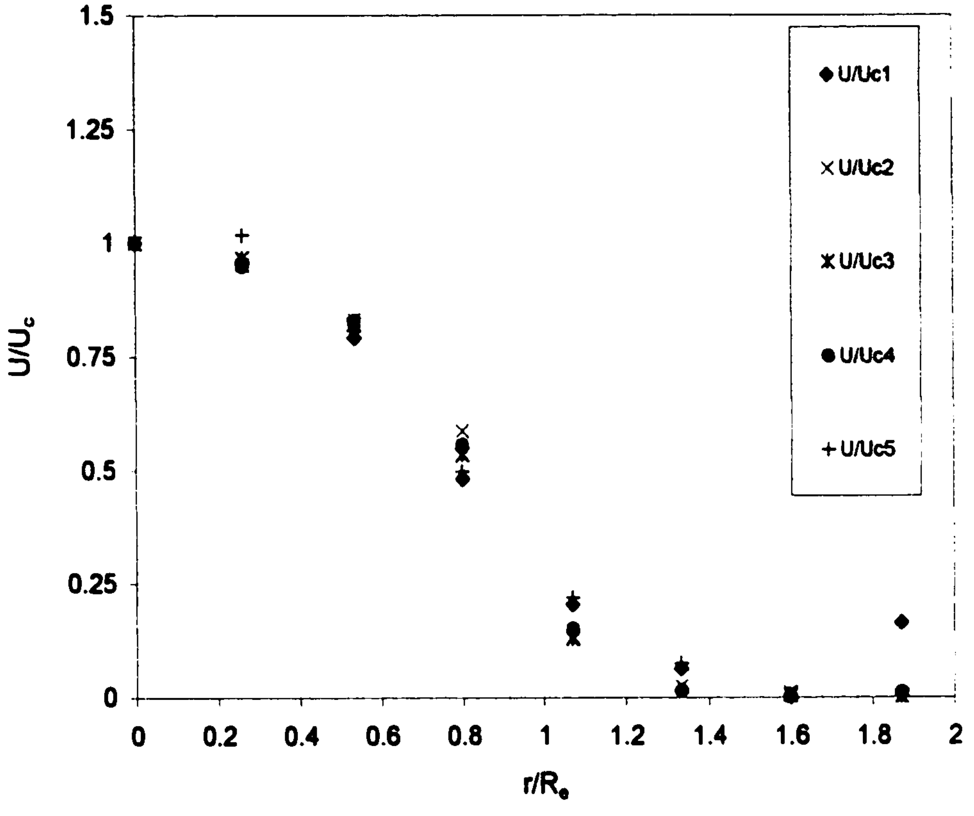

Figure 3.9: Mean velocity profiles for He-air system measured five different times at $x/R_e = 2.5$

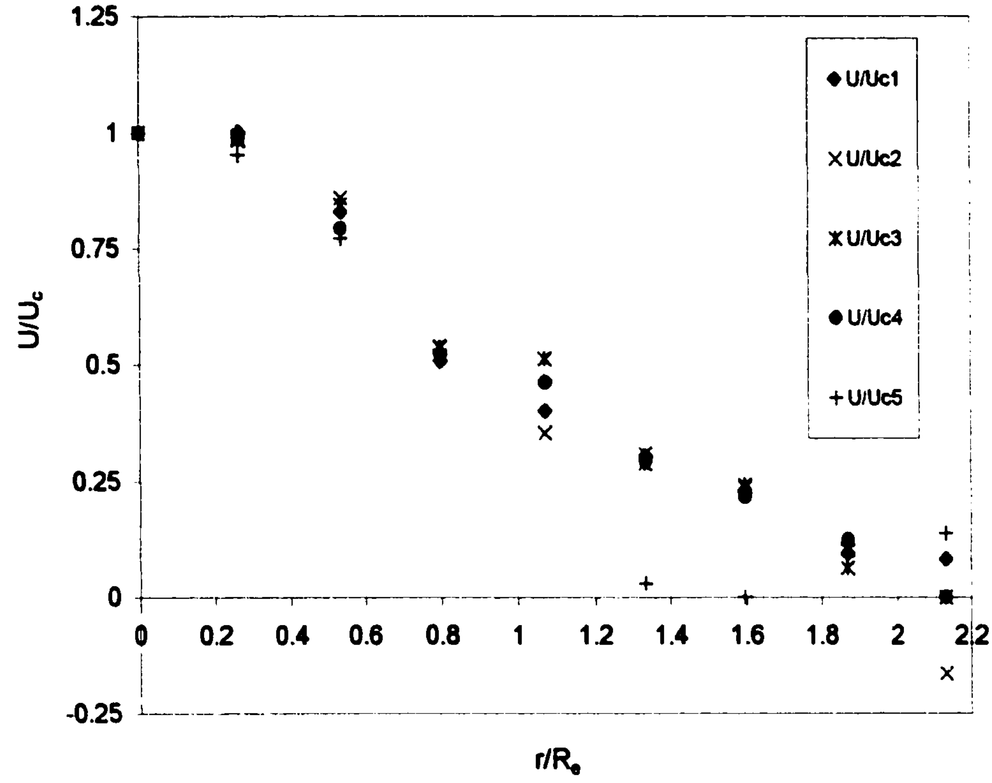

Figure 3.10: Mean velocity profiles for air-air system measured five different times at $x/R_e = 2.5$

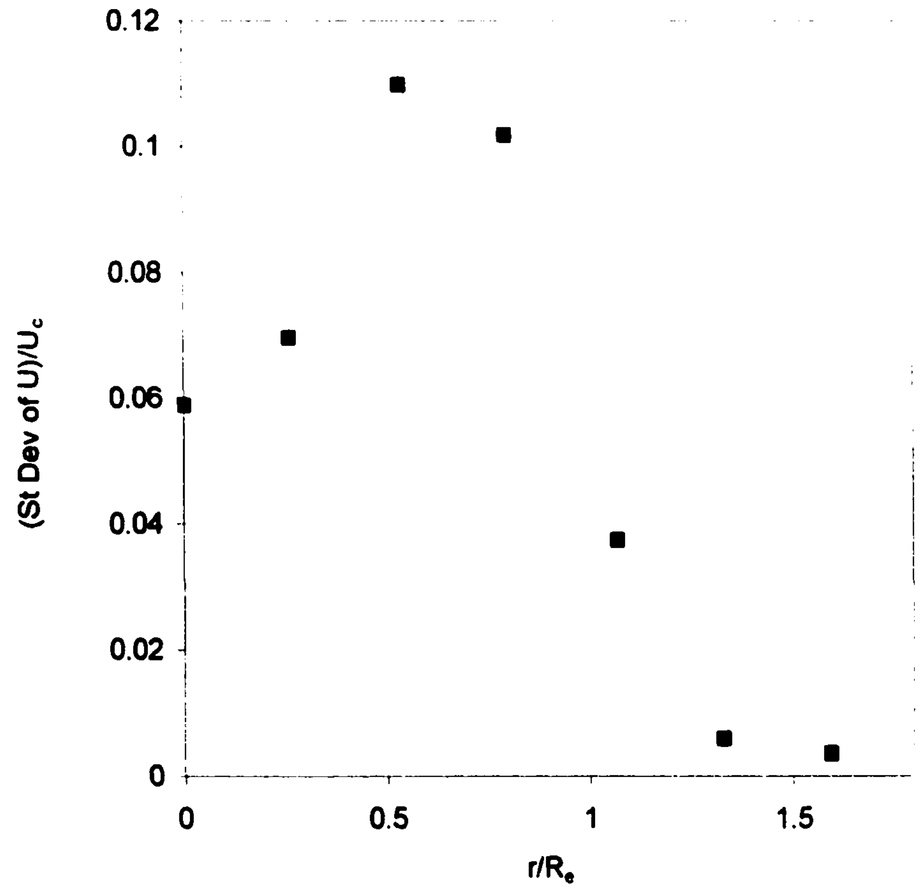

Figure 3.11: (Standard deviation of the velocity)/U_c vs r/R_e for He-air system at $x/R_e = 0.5$

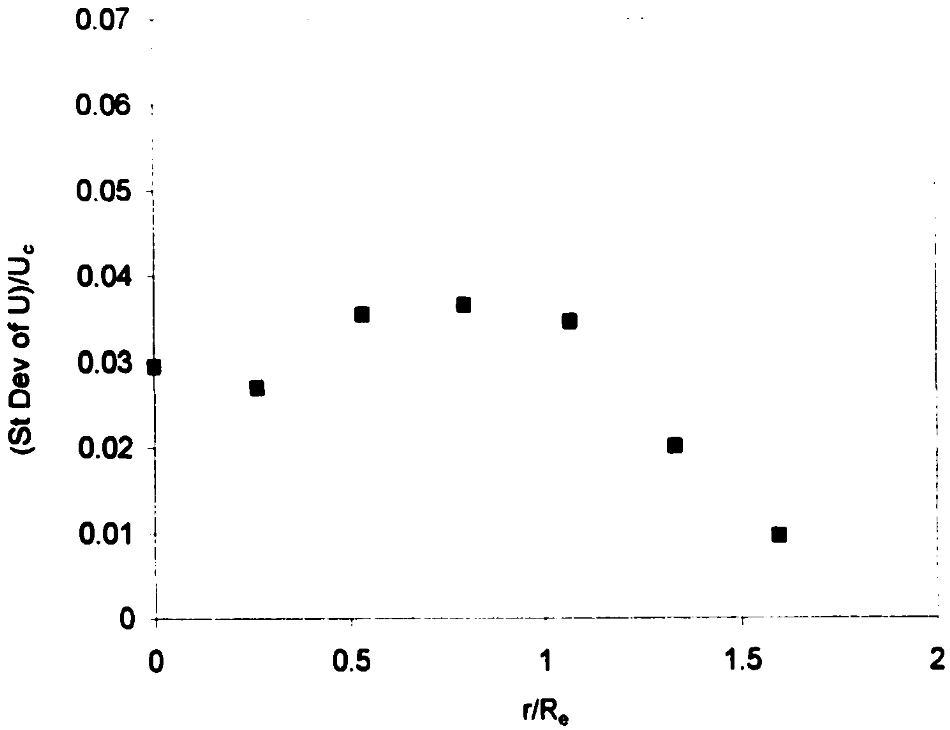

Figure 3.12: (Standard deviation of the velocity)/U_c vs r/R_c
for air-air system at $x/R_c = 0.5$

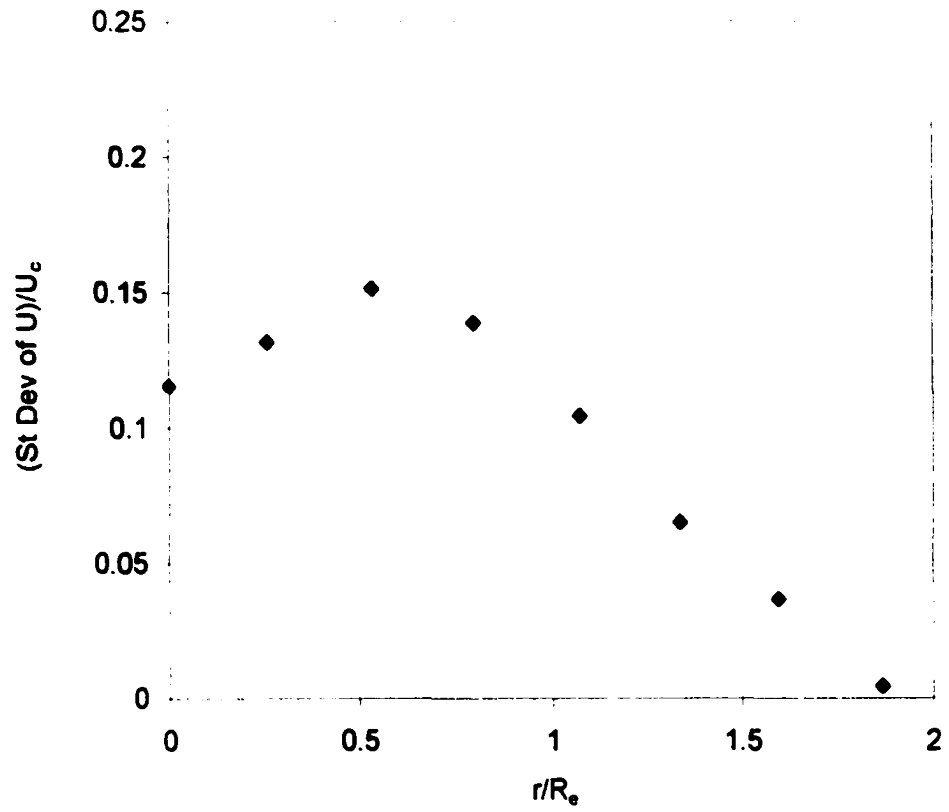

Figure 3.13: (Standard deviation of the velocity)/U_c vs r/R_e for He-air system at $x/R_e = 2.5$

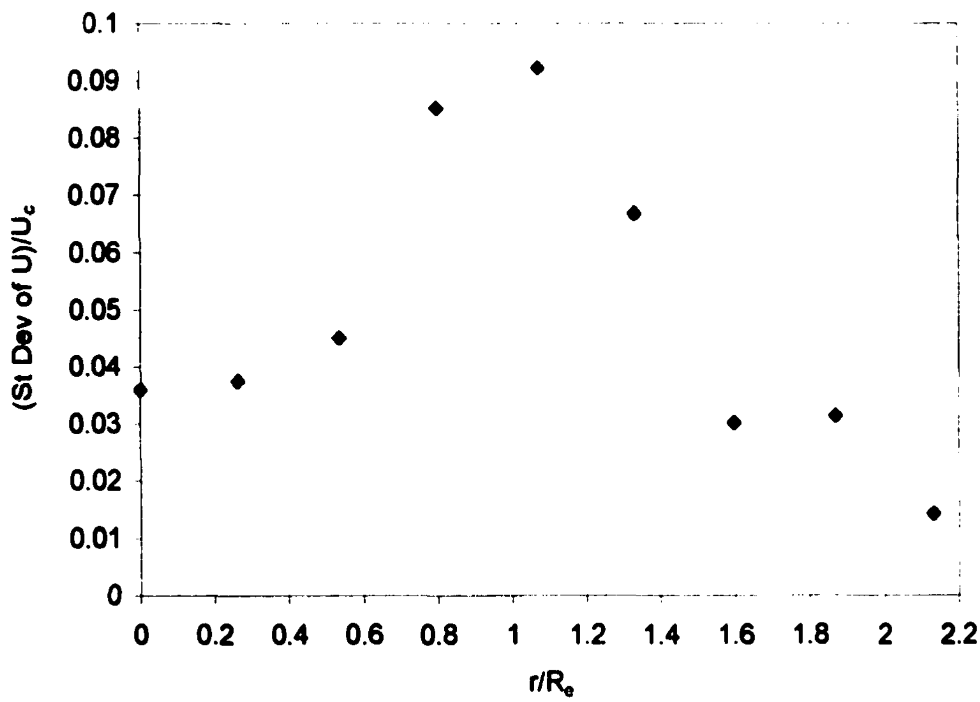

Figure 3.14: (Standard deviation of the velocity)/U_c vs r/R_c
for air-air system @ $x/R_c = 2.5$

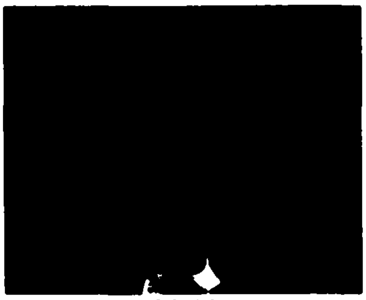

Frame = 01.30.00

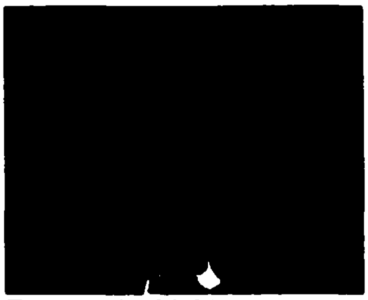

Frame = 01.30.01

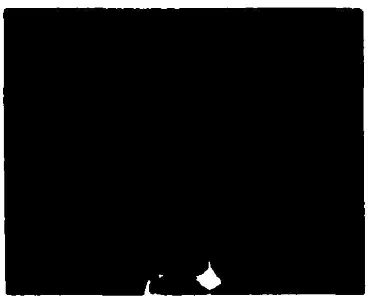

Frame = 01.30.02

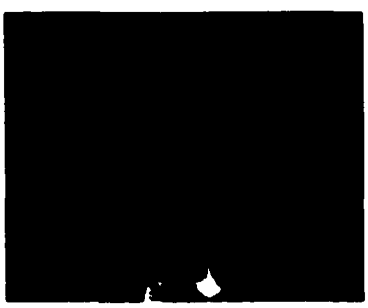

Frame = 01.30.03

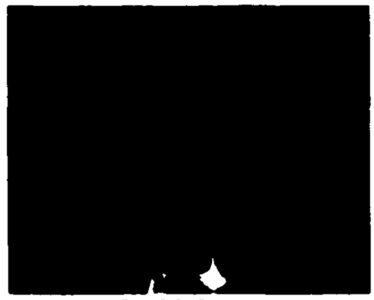

Frame = 01.30.04

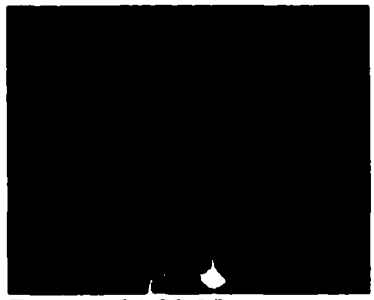

Frame = 01.30.05

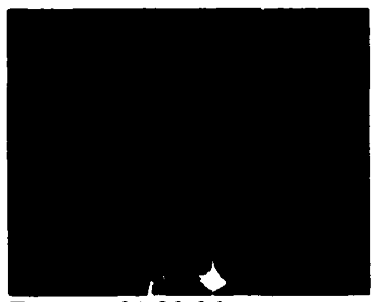

Frame = 01.30.06

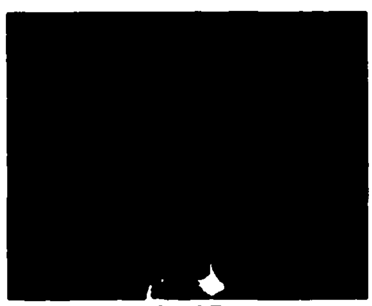

Frame = 01.30.07

Figure 3.15: Sequence of frames from the video of the helium jet injected into air (flow rate = 63.2 SLPM) at a framing rate of 30 fps

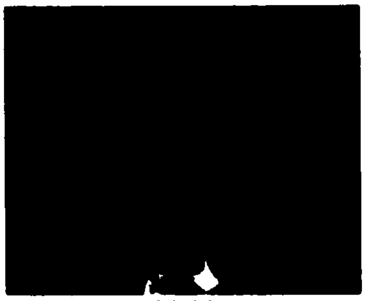
Frame = 01.30.08

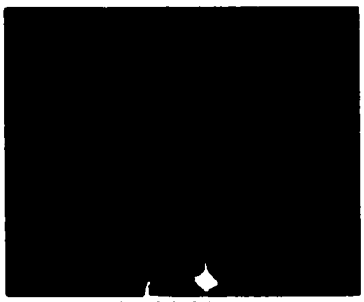
Frame = 01.30.09

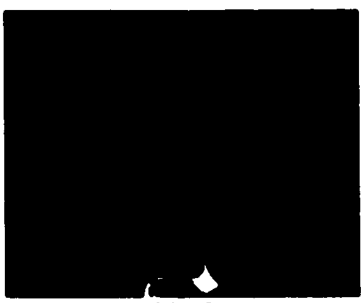
Frame = 01.30.10


Frame = 01.30.11

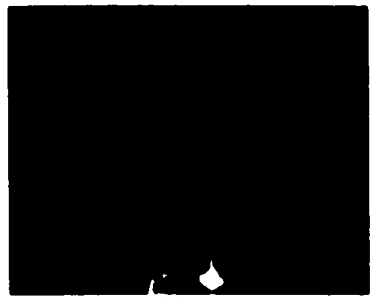
Frame = 01.30.12

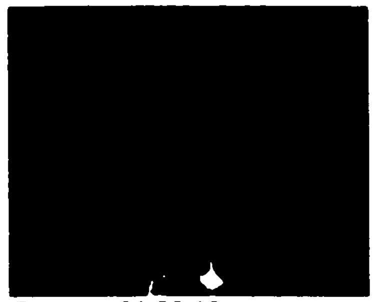
Frame = 01.30.13

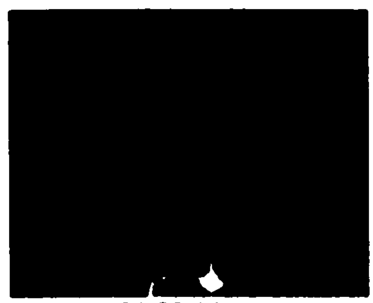
Frame = 01.30.14

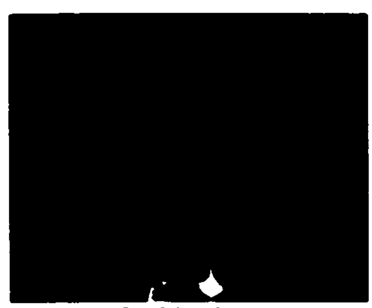
Frame = 01.30.15

Frame = 01.30.16

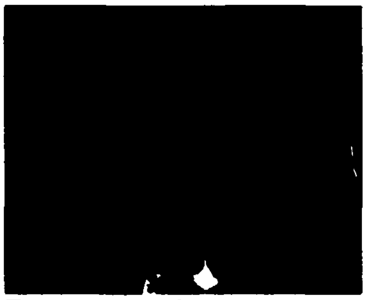

Frame = 0.07.20

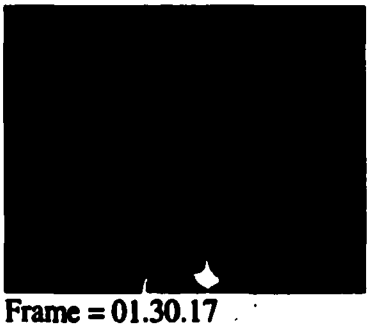

Frame = 01.30.17

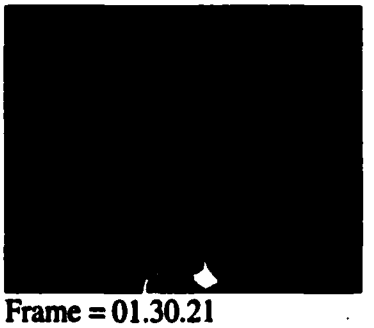

Frame = 01.30.21

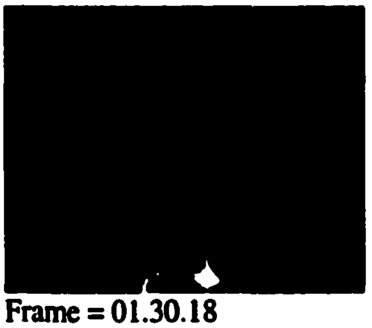

Frame = 01.30.18

Frame = 01.30.22

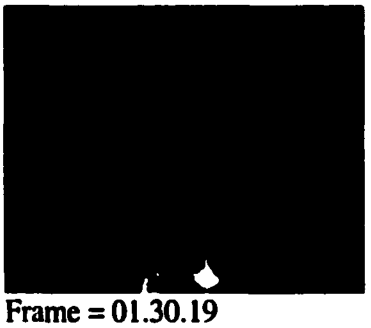

Frame = 01.30.19

Frame = 01.30.23

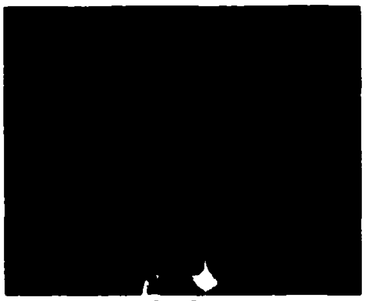
Frame = 01.30.24

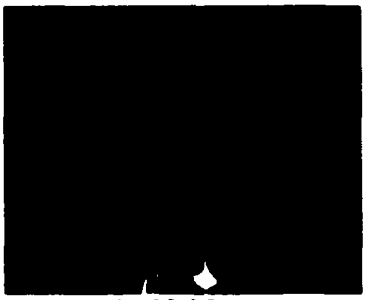
Frame = 01.30.25

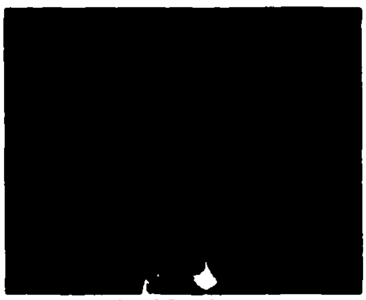
Frame = 01.30.26

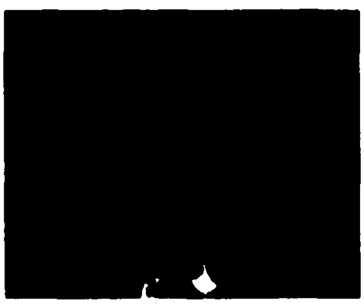
Frame = 01.30.27

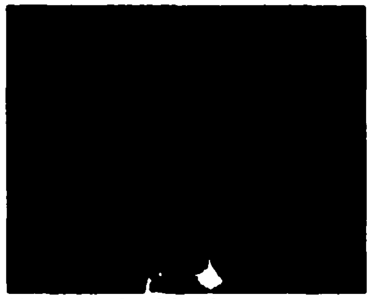
Frame = 01.30.28

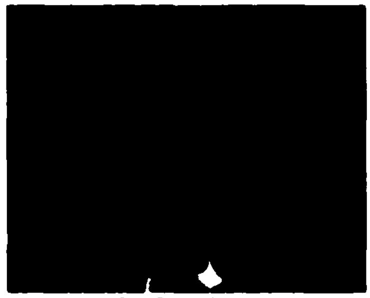
Frame = 01.30.29

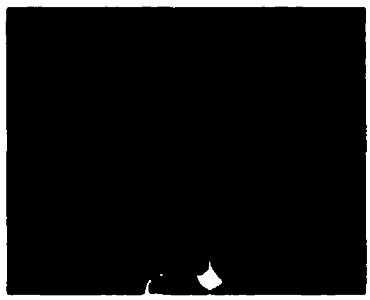
Frame = 01.31.00

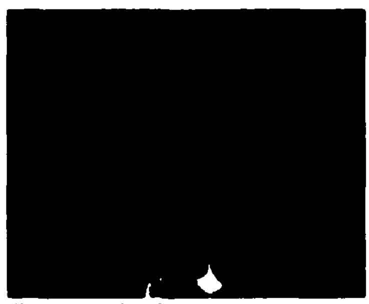
Frame = 01.31.01

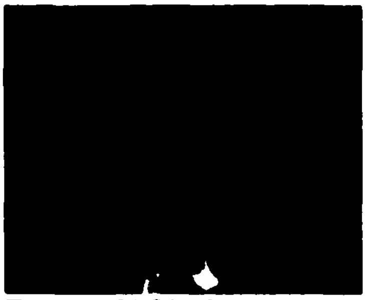
Frame = 01.31.02

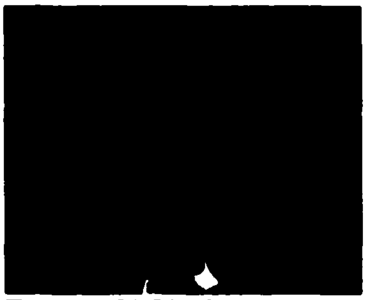
Frame = 01.31.03

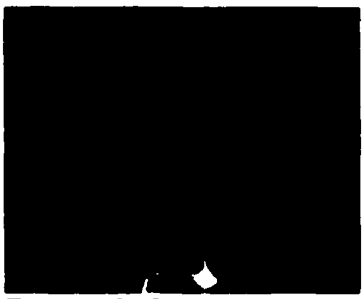
Frame = 01.31.04

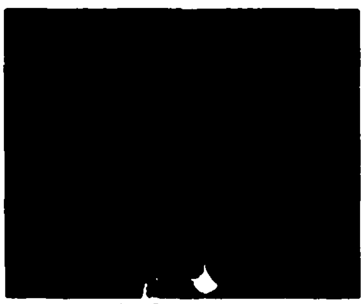
Frame = 01.31.05

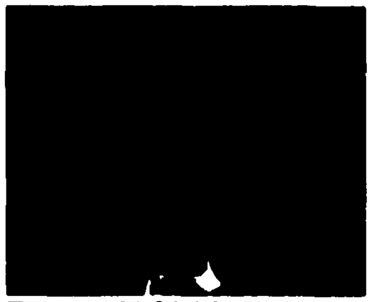
Frame = 01.31.06

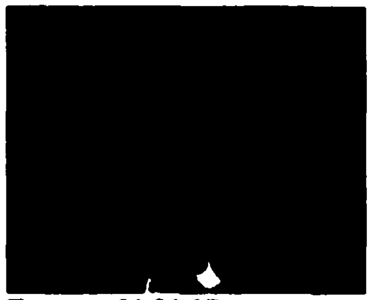
Frame = 01.31.07

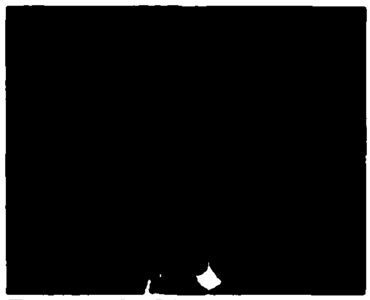
Frame = 01.31.08

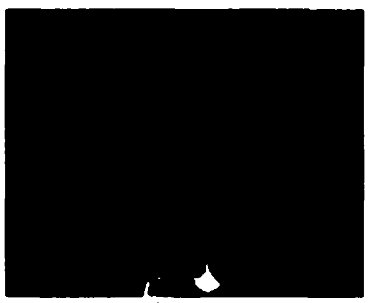
Frame = 01.31.09


Frame = 01.31.10


Frame = 01.31.11

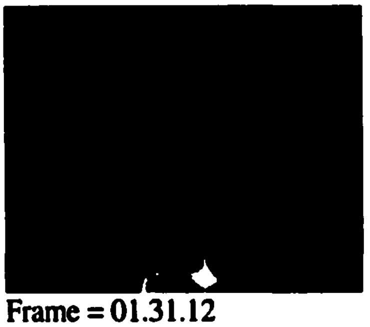
Frame = 01.31.12

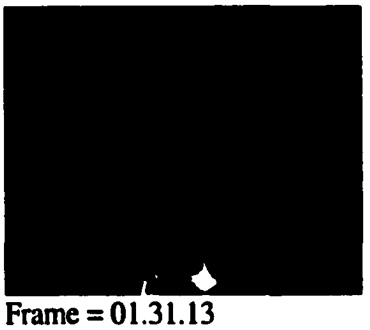
Frame = 01.31.13

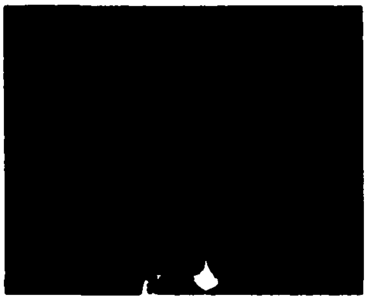
Frame = 01.31.14


Frame = 01.31.15


Frame = 01.31.16


Frame = 01.31.17

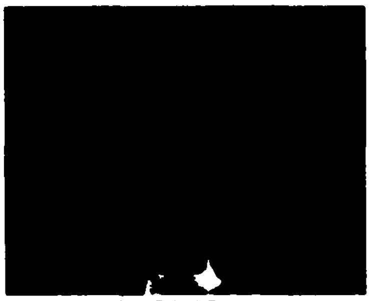
Frame = 01.31.18

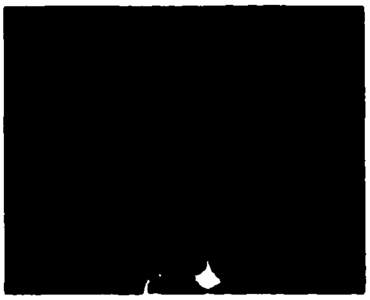
Frame = 01.31.19

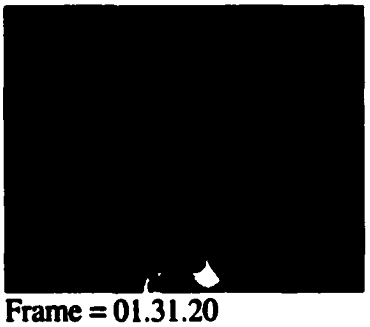
Frame = 01.31.20

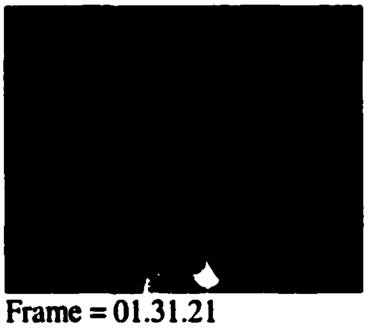
Frame = 01.31.21

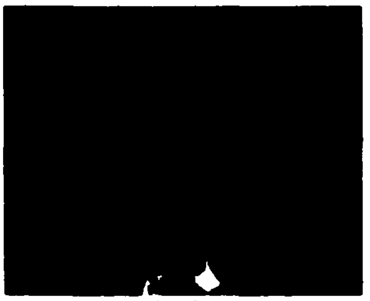
Frame = 01.31.22

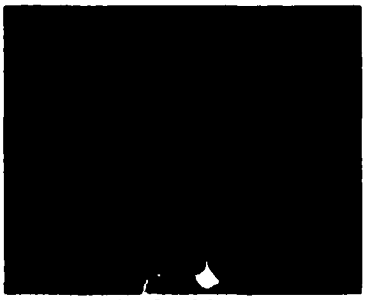
Frame = 01.31.23


Frame = 01.31.24


Frame = 01.31.25

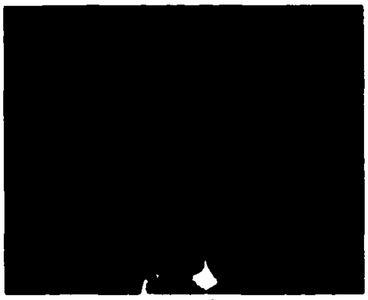

Frame = 01.31.26

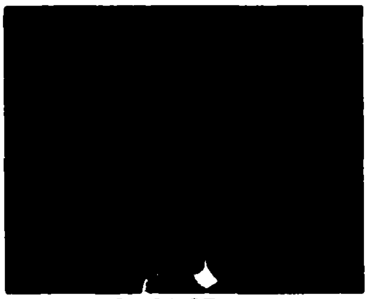

Frame = 01.31.27

Frame = 01.31.28

Frame = 01.31.29

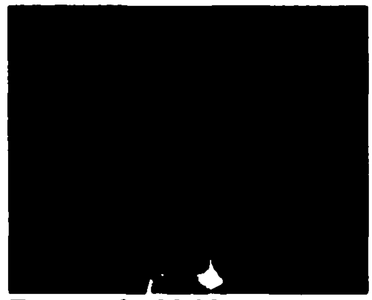

Frame = 01.32.00

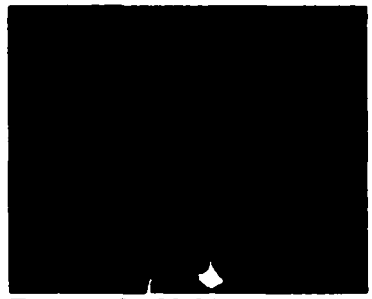

Frame = 01.32.01

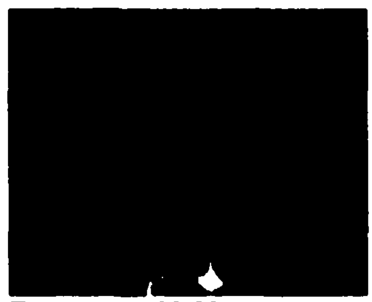

Frame = 01.32.02

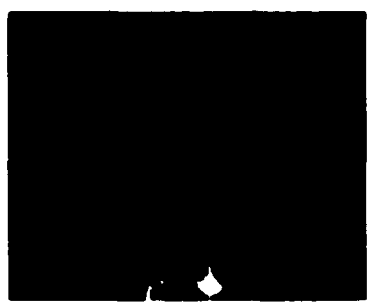

Frame = 01.32.03

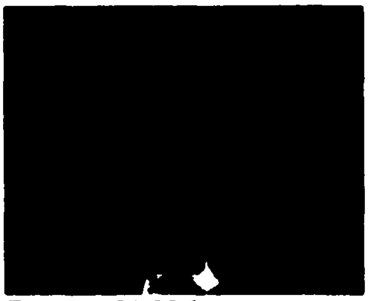
Frame = 01.32.04

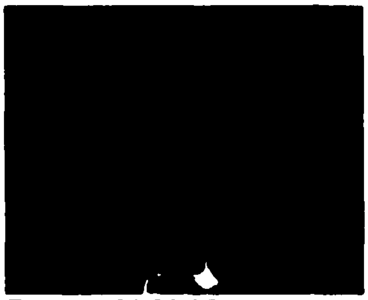
Frame = 01.32.05


Frame = 01.32.06

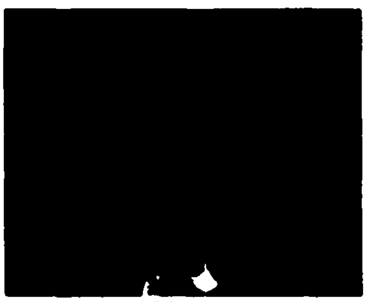
Frame = 01.32.07

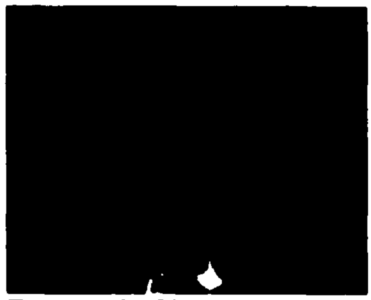
Frame = 01.32.08

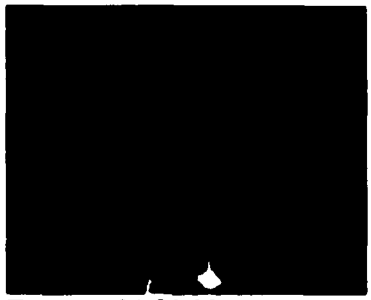
Frame = 01.32.09

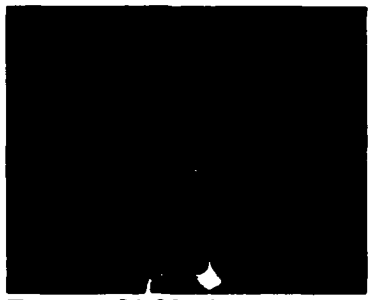
Frame = 01.32.10

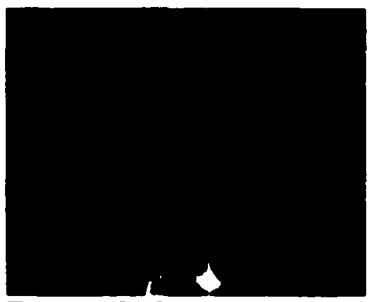
Frame = 01.32.11

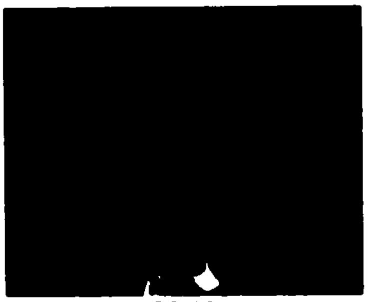
Frame = 01.32.12


Frame = 01.32.13

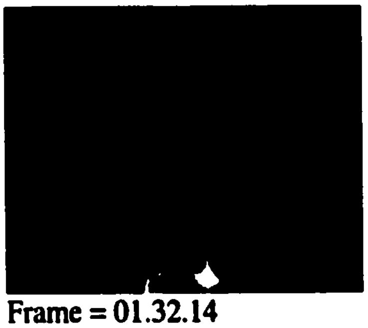
Frame = 01.32.14

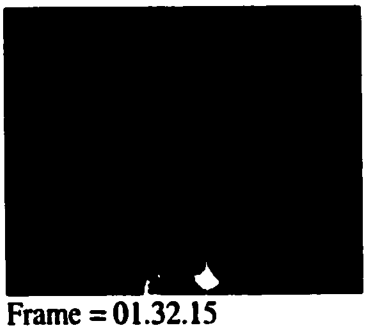
Frame = 01.32.15


Frame = 01.32.16


Frame = 01.32.17

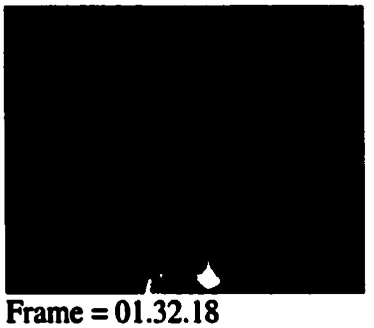
Frame = 01.32.18

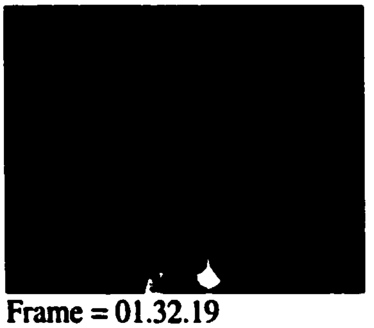
Frame = 01.32.19

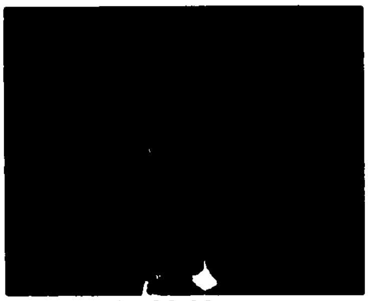
Frame = 01.32.20

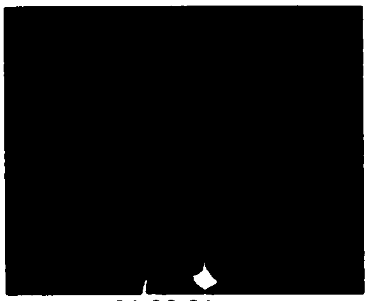
Frame = 01.32.21

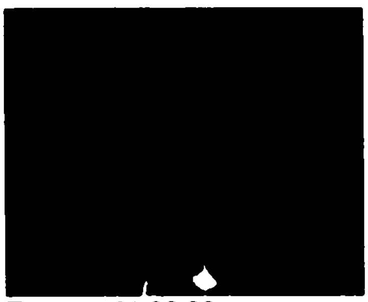
Frame = 01.32.22


Frame = 01.32.23

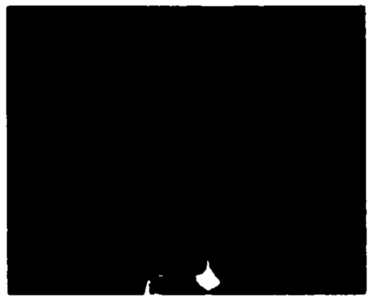
Frame = 01.32.24

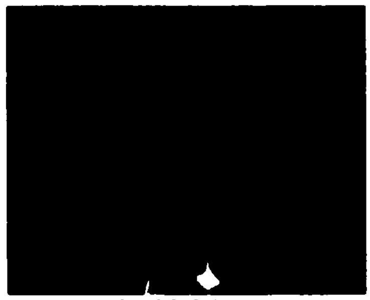
Frame = 01.32.25


Frame = 01.32.26

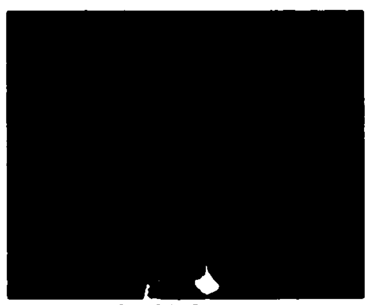
Frame = 01.32.27


Frame = 01.32.28

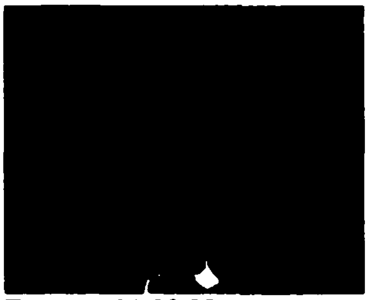
Frame = 01.32.29

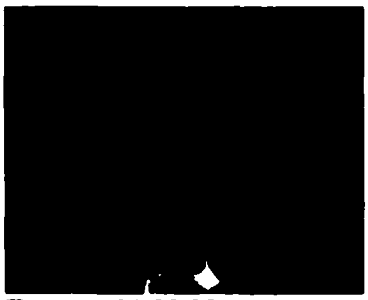
Frame = 01.33.00

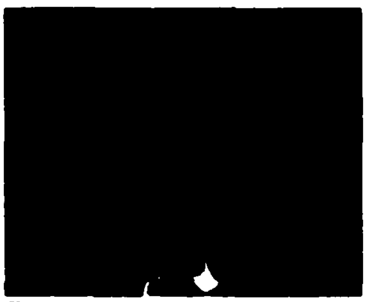
Frame = 01.33.01

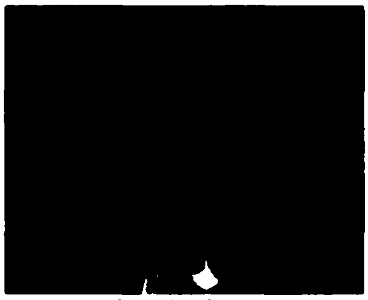
Frame = 01.33.02

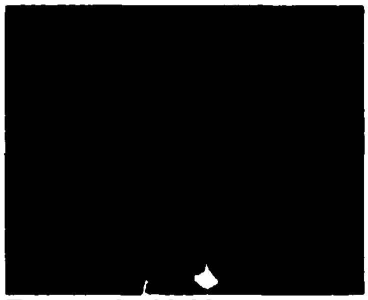
Frame = 01.33.03


Frame = 01.33.04


Frame = 01.33.05

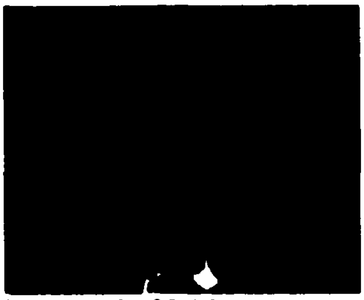
Frame = 01.33.06

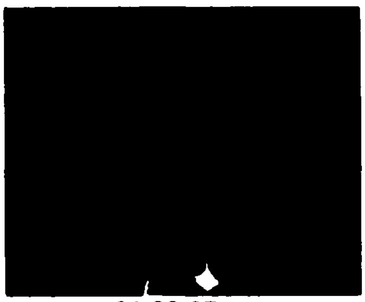
Frame = 01.33.07

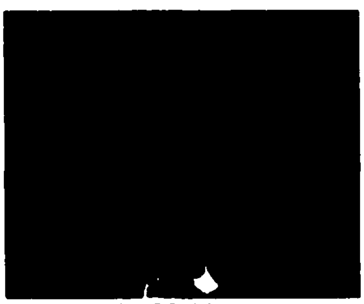
Frame = 01.33.08

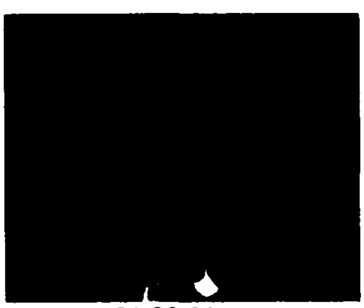
Frame = 01.33.09

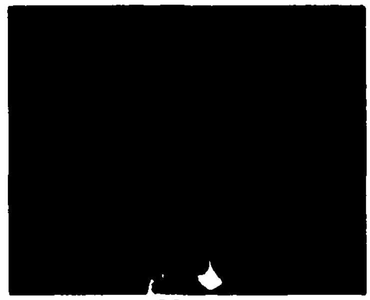
Frame = 01.33.10

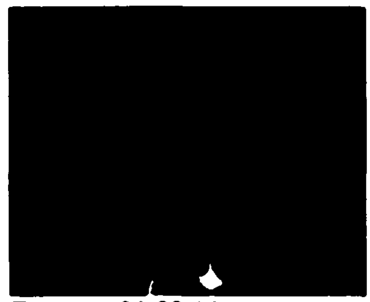
Frame = 01.33.11


Frame = 01.33.12

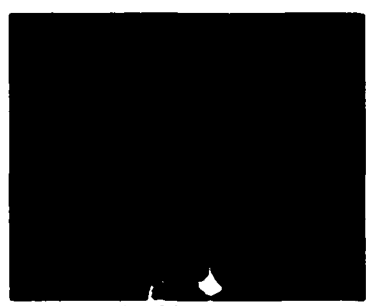
Frame = 01.33.13

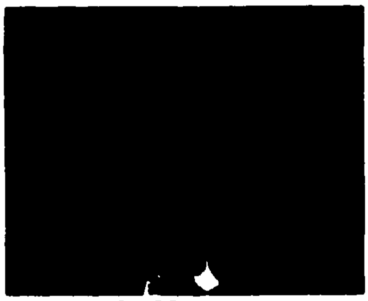

Frame = 01.33.14

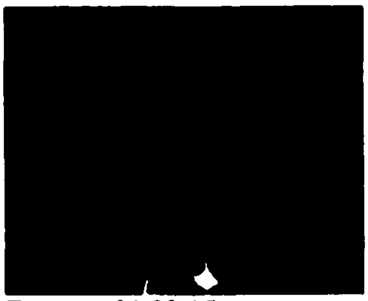

Frame = 01.33.15

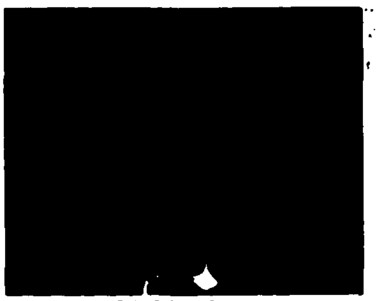

Frame = 01.33.16

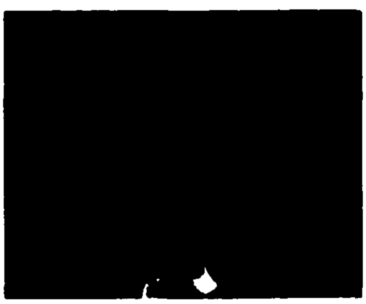

Frame = 01.33.17

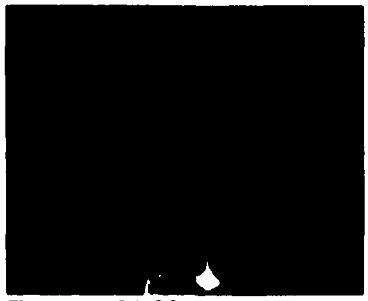

Frame = 01.33.18

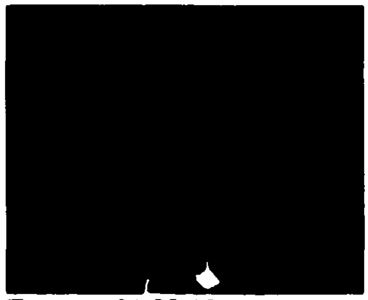

Frame = 01.33.19

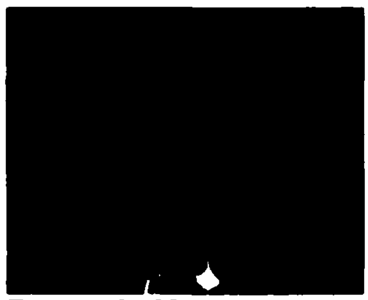

Frame = 01.33.20

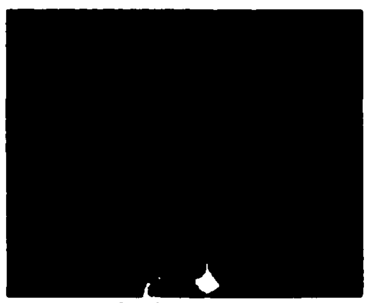

Frame = 01.33.21

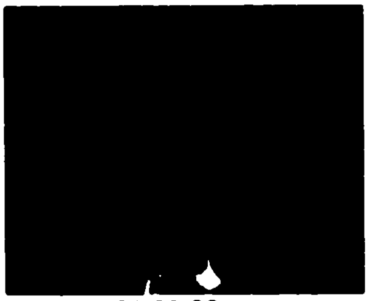
Frame = 01.33.22

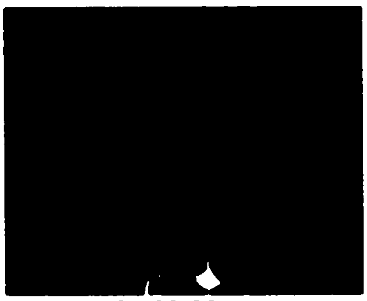
Frame = 01.33.23

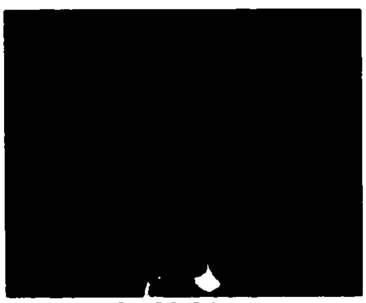
Frame = 01.33.24

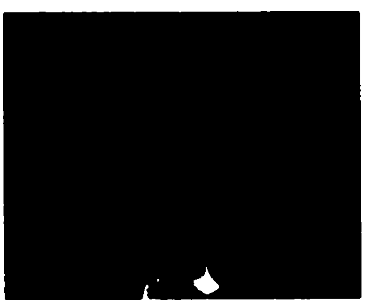
Frame = 01.33.25

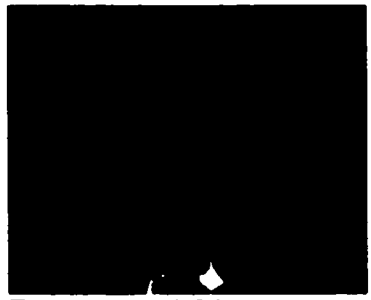
Frame = 01.33.26

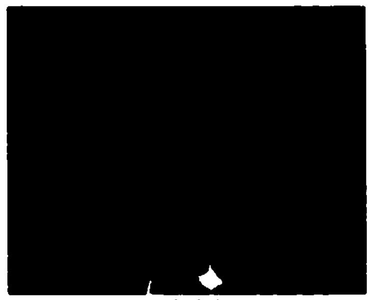
Frame = 01.33.27

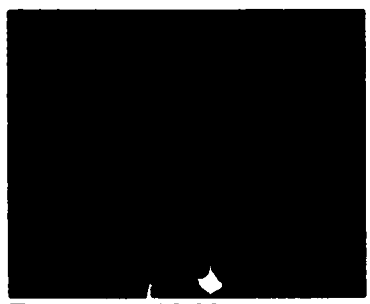
Frame = 01.33.28

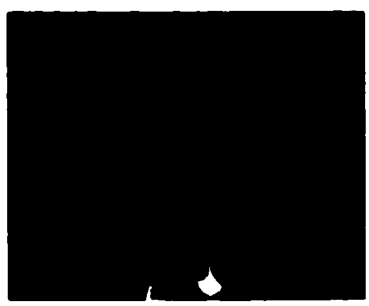
Frame = 01.33.29

Frame = 01.34.00

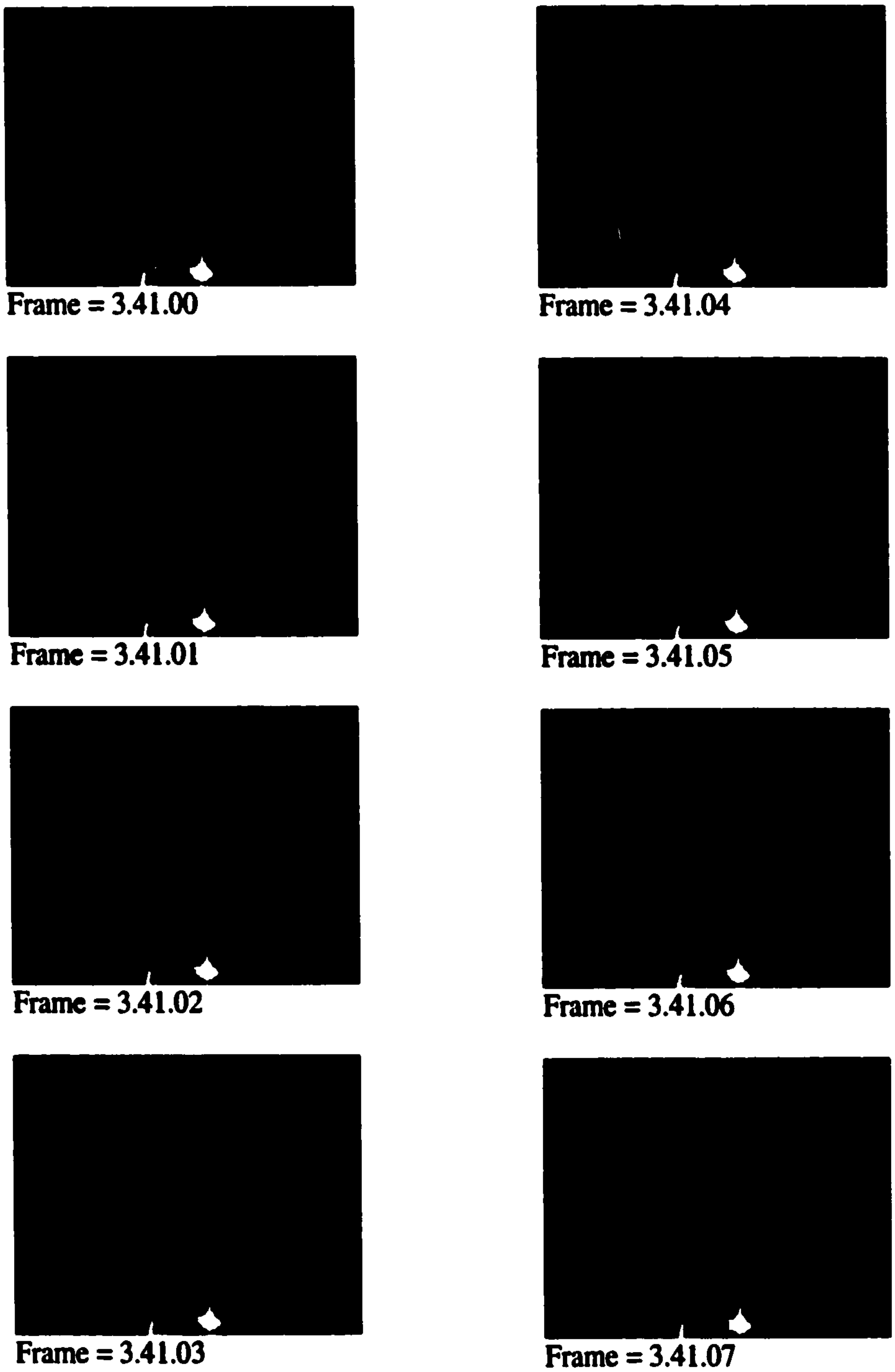

Figure 3.16: Sequence of frames from the video of the air jet injected into quiescent air (flow rate = 16.6 SLPM) at a framing rate of 30 fps

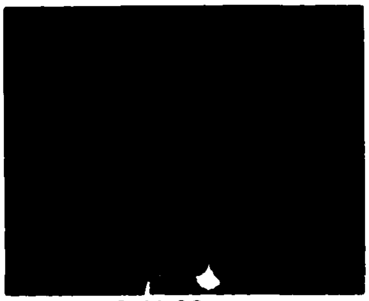

Frame = 3.41.08

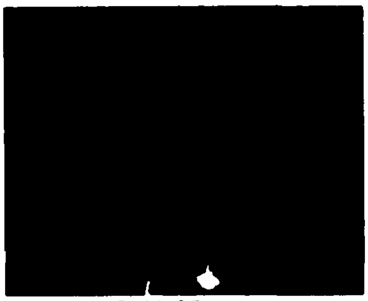

Frame = 3.41.09

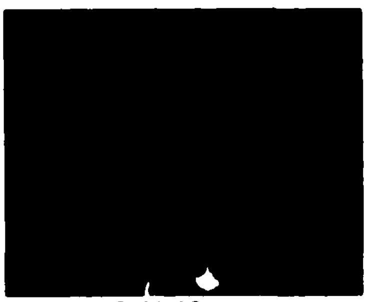

Frame = 3.41.10

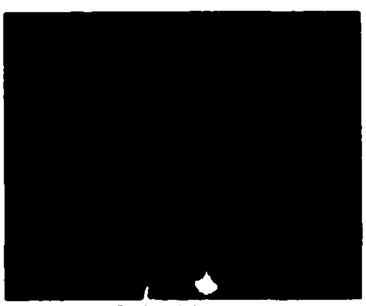

Frame = 3.41.11

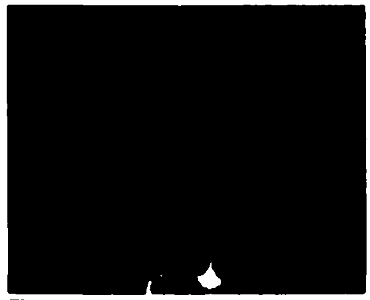

Frame = 3.41.12

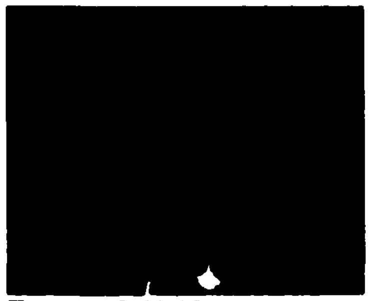

Frame = 3.41.13

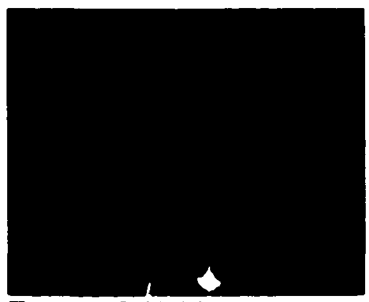

Frame = 3.41.14

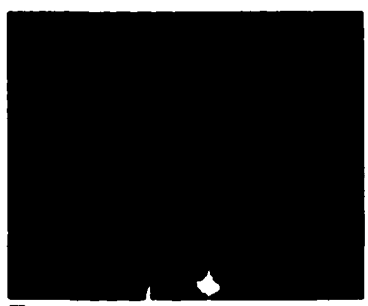

Frame = 3.41.15

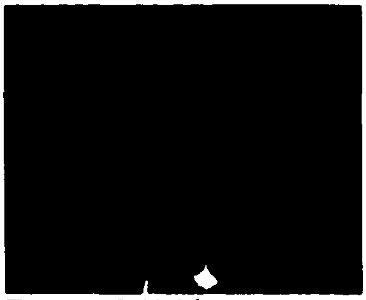
Frame = 3.41.16


Frame = 3.41.17

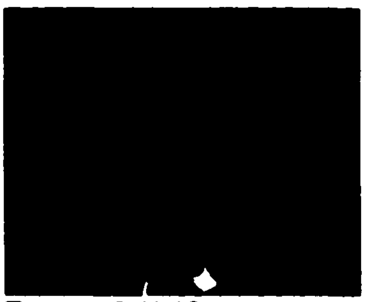
Frame = 3.41.18

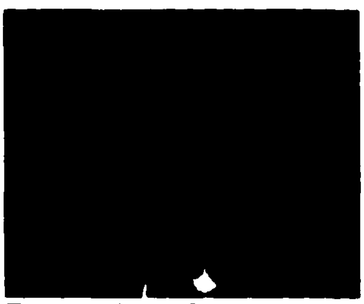
Frame = 3.41.19

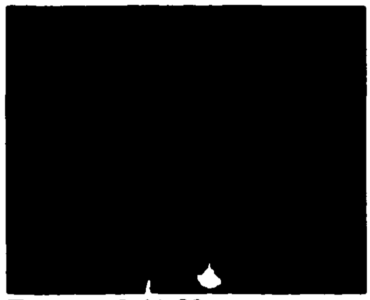
Frame = 3.41.20

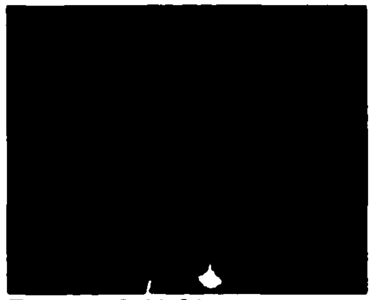
Frame = 3.41.21

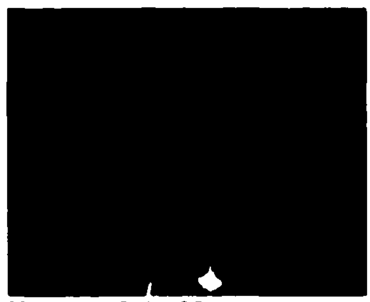
Frame = 3.41.22

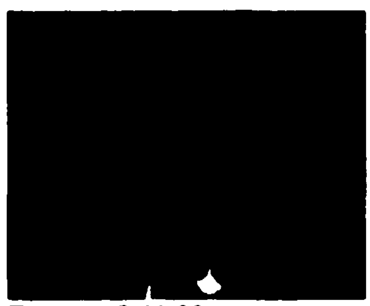
Frame = 3.41.23

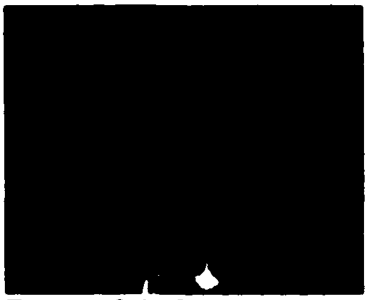
Frame = 3.41.24

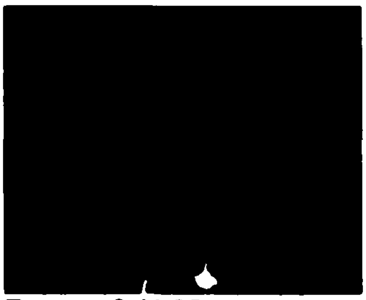
Frame = 3.41.25

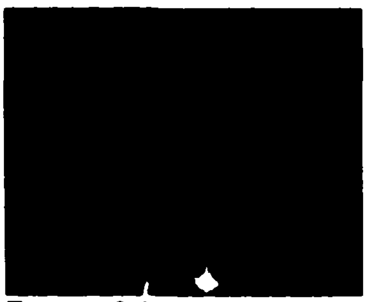
Frame = 3.41.26

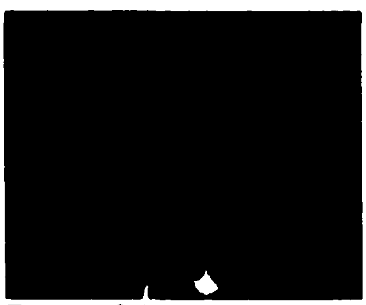
Frame = 3.41.27

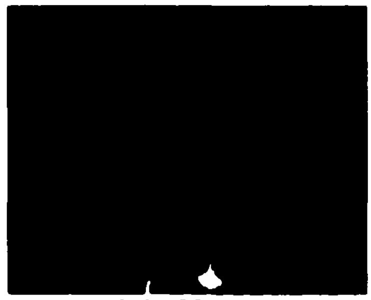
Frame = 3.41.28

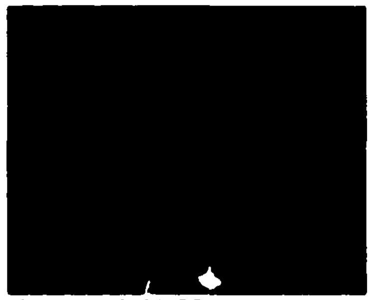
Frame = 3.41.29

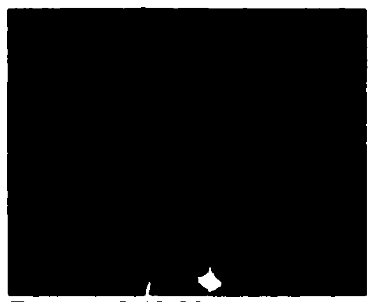
Frame = 3.42.00

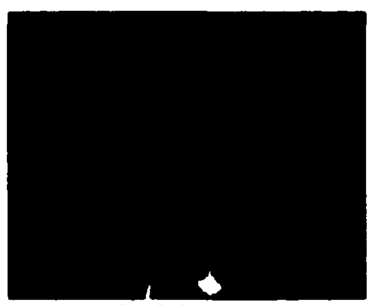
Frame = 3.42.01


Frame = 3.42.02

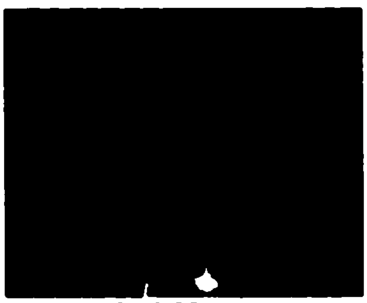
Frame = 3.42.03

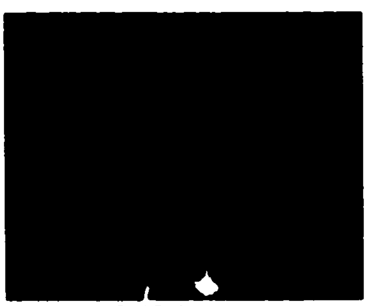
Frame = 3.42.04


Frame = 3.42.05

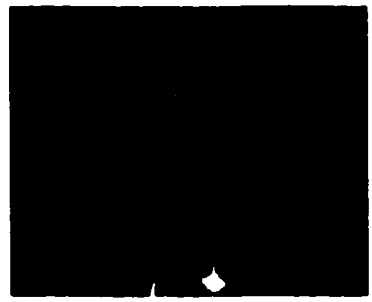
Frame = 3.42.06

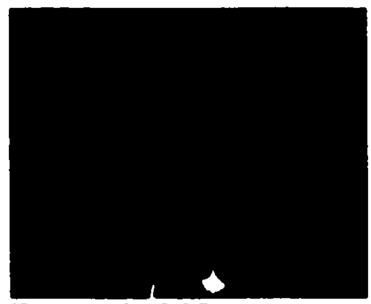
Frame = 3.42.07

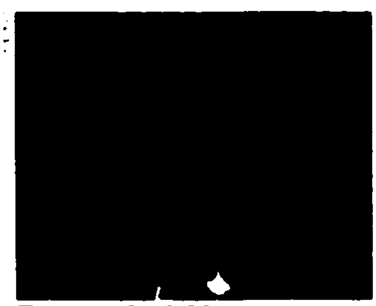
Frame = 3.42.08


Frame = 3.42.09

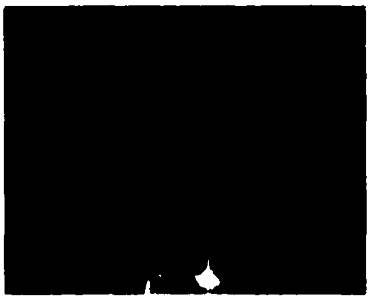
Frame = 3.42.10

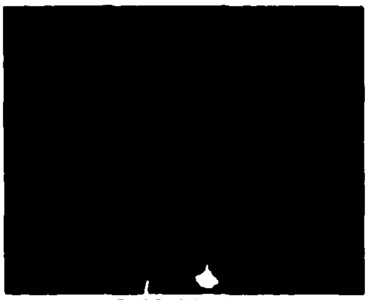
Frame = 3.42.11


Frame = 3.42.12

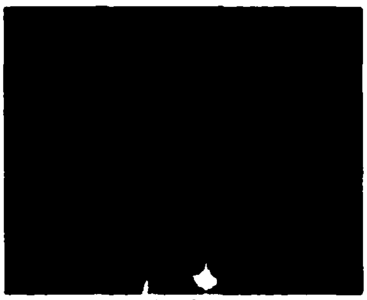
Frame = 3.42.13

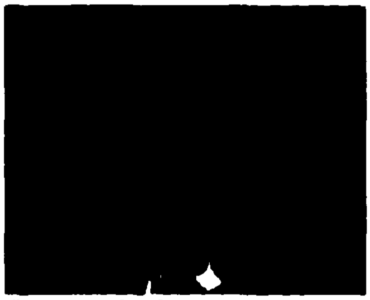
Frame = 3.42.14

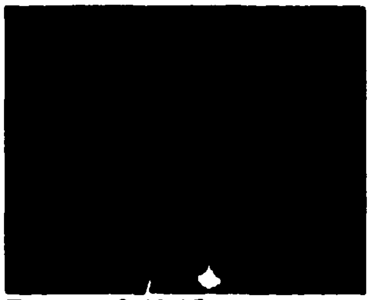
Frame = 3.42.15

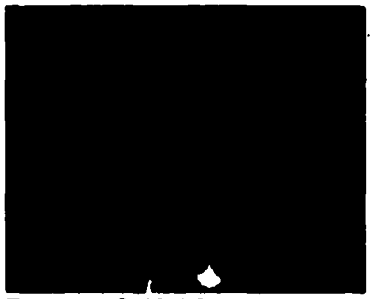
Frame = 3.42.16

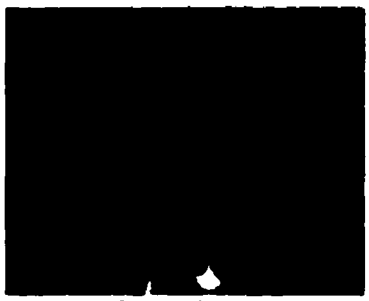
Frame = 3.42.17

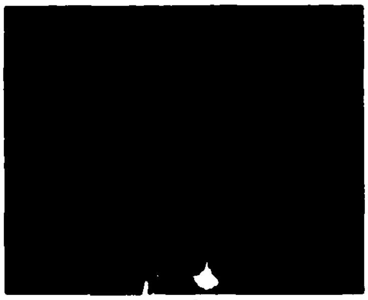
Frame = 3.42.18

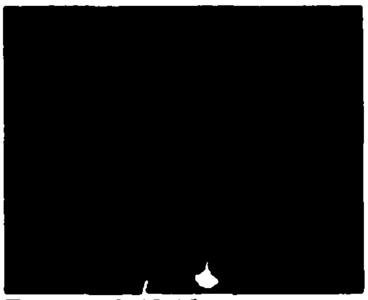
Frame = 3.42.19

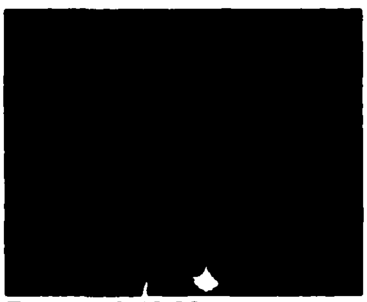
Frame = 3.42.20

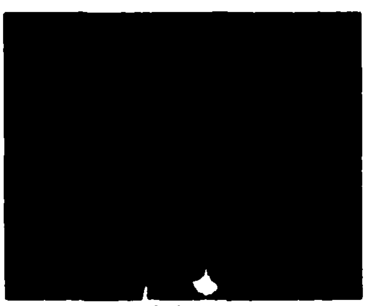
Frame = 3.42.21

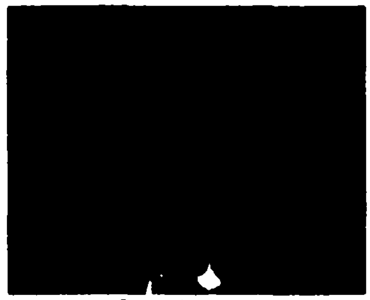
Frame = 3.42.22

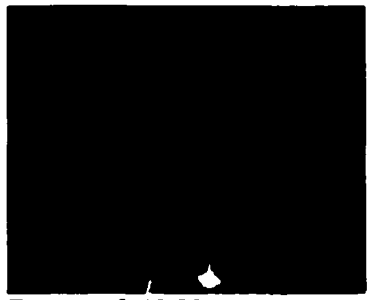
Frame = 3.42.23

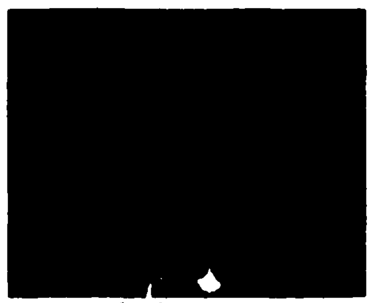
Frame = 3.42.24

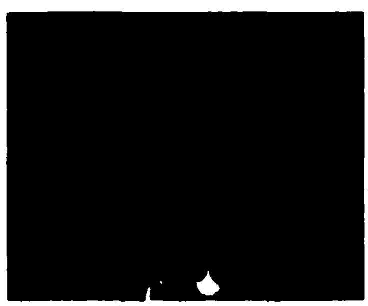
Frame = 3.42.25

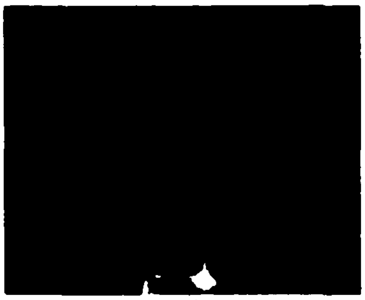
Frame = 3.42.26

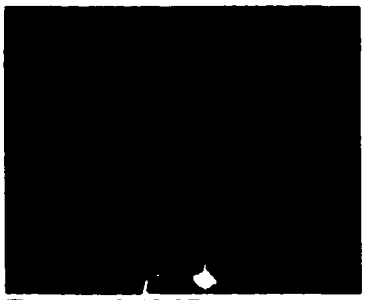
Frame = 3.42.27

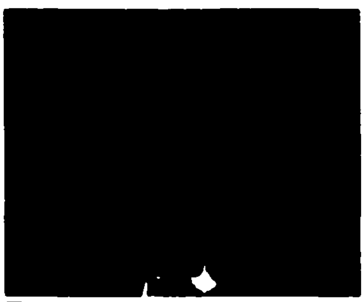
Frame = 3.42.28

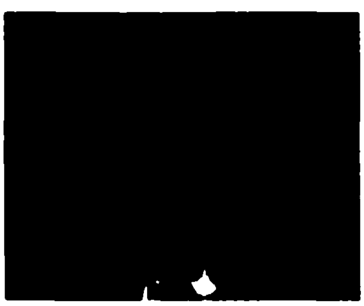
Frame = 3.42.29

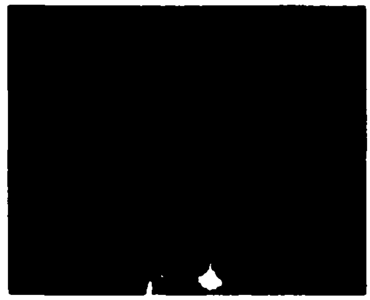
Frame = 3.43.00

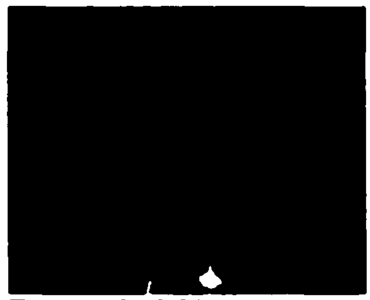
Frame = 3.43.01

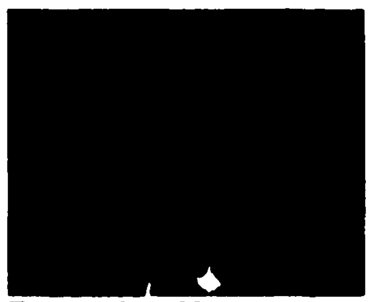
Frame = 3.43.02


Frame = 3.43.03

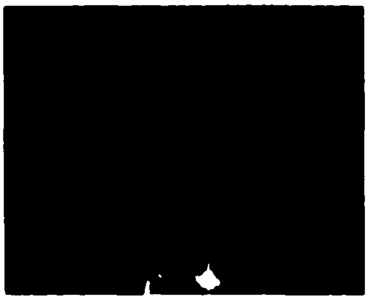
Frame = 3.43.04

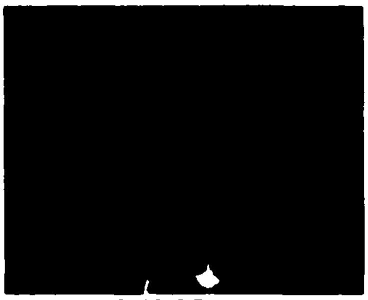
Frame = 3.43.05

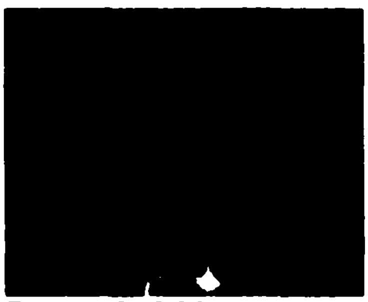
Frame = 3.43.06

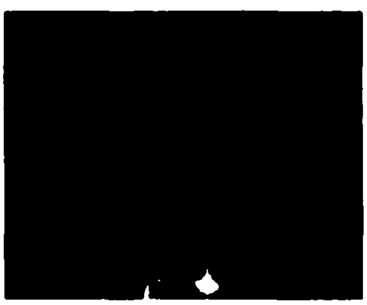
Frame = 3.43.07

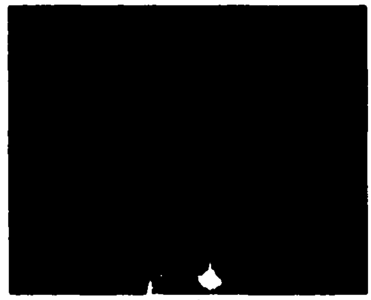
Frame = 3.43.08

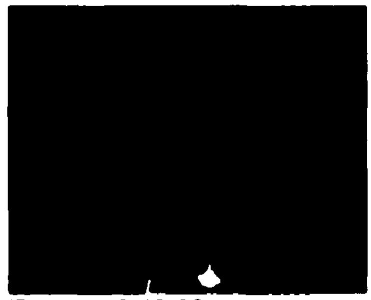
Frame = 3.43.09

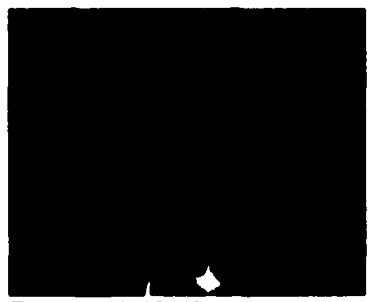
Frame = 3.43.10

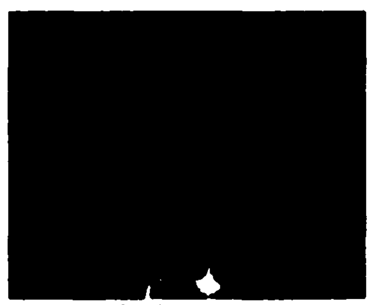
Frame = 3.43.11

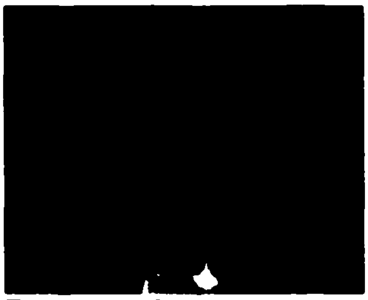
Frame = 3.43.12

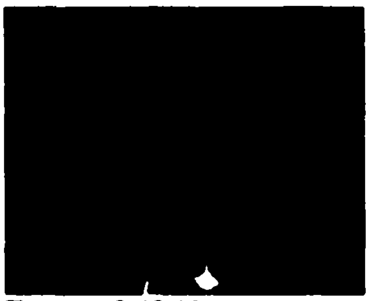
Frame = 3.43.13

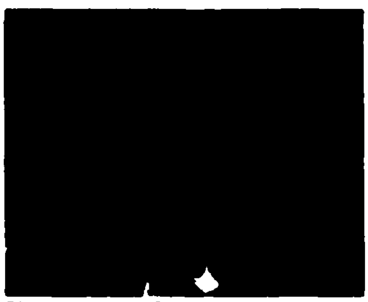
Frame = 3.43.14

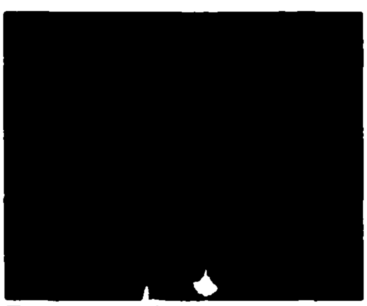
Frame = 3.43.15

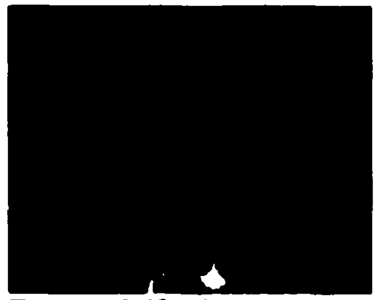
Frame = 3.43.16

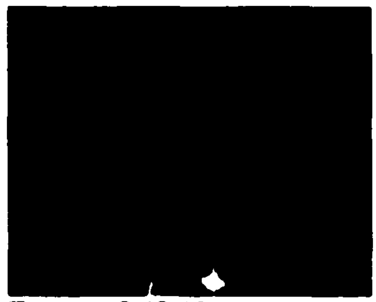
Frame = 3.43.17

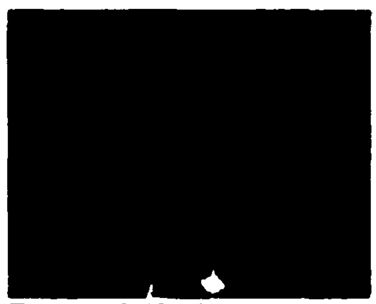
Frame = 3.43.18

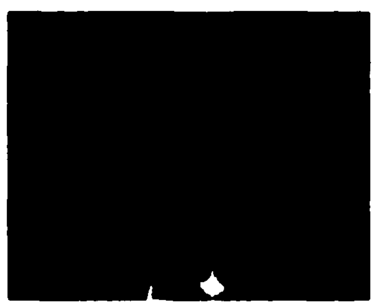
Frame = 3.43.19

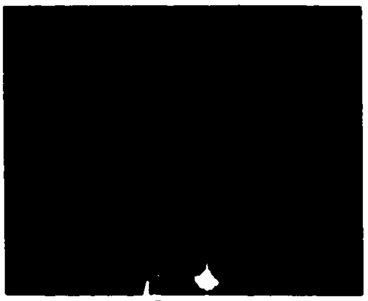

Frame = 3.43.20

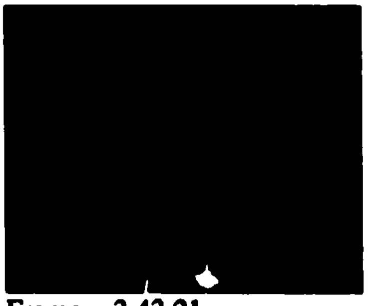

Frame = 3.43.21

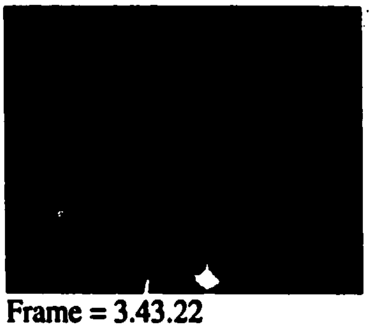

Frame = 3.43.22

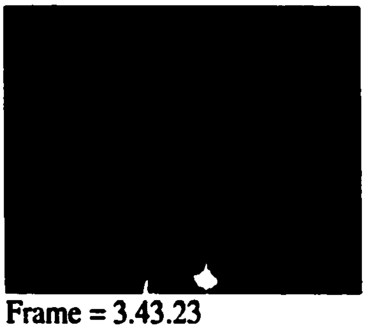

Frame = 3.43.23

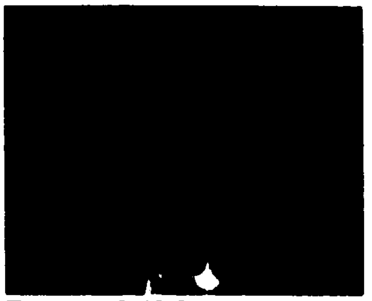

Frame = 3.43.24

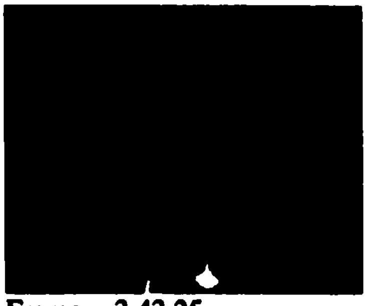

Frame = 3.43.25

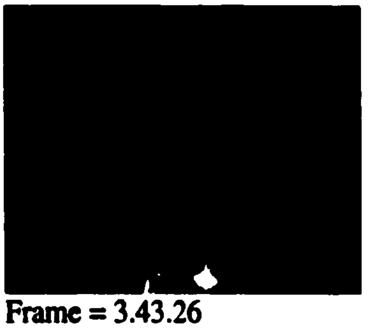

Frame = 3.43.26

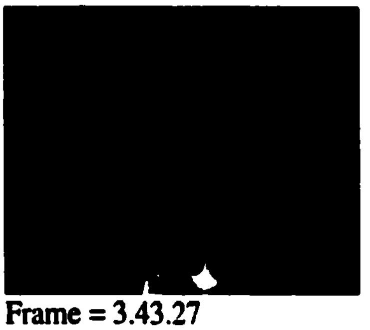

Frame = 3.43.27

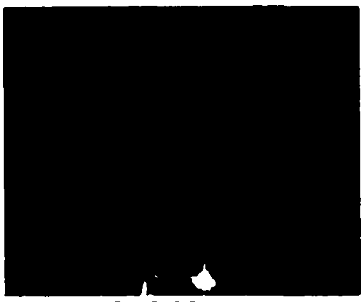
Frame = 3.43.28

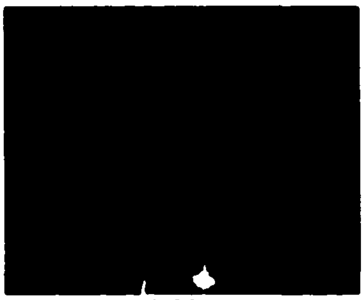
Frame = 3.43.29


Frame = 3.44.00

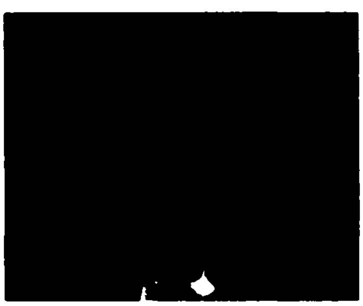
Frame = 3.44.01

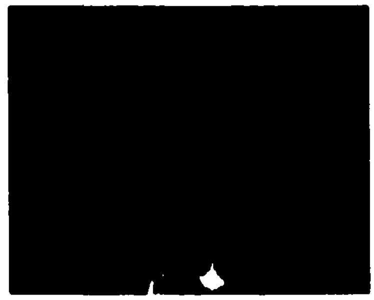
Frame = 3.44.02

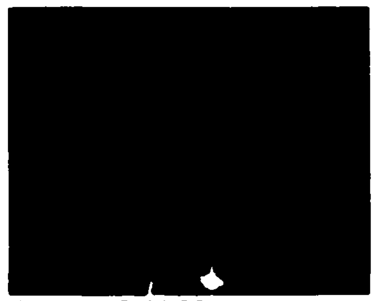
Frame = 3.44.03

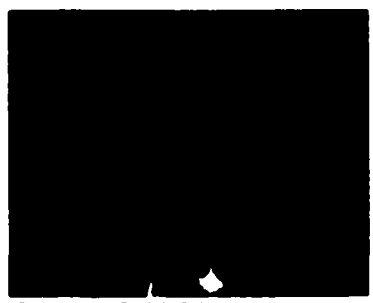
Frame = 3.44.04

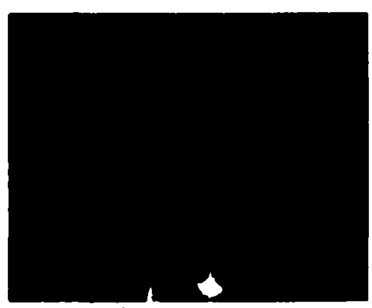
Frame = 3.44.05

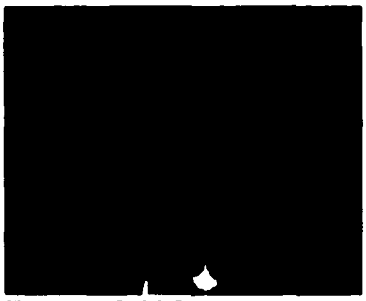
Frame = 3.44.06

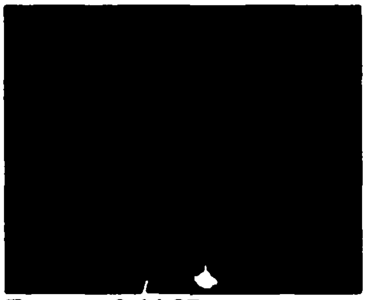
Frame = 3.44.07

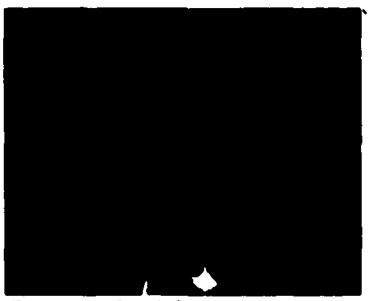
Frame = 3.44.08

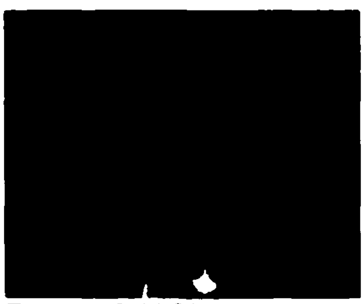
Frame = 3.44.09

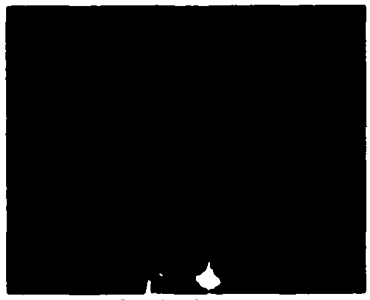
Frame = 3.44.10

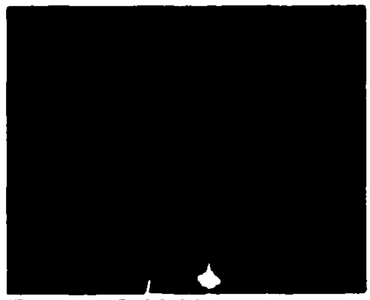
Frame = 3.44.11

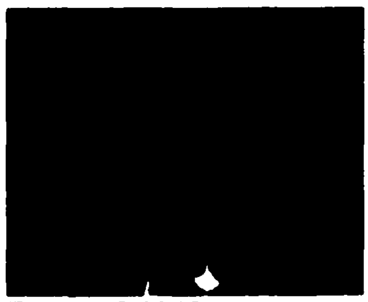
Frame = 3.44.12

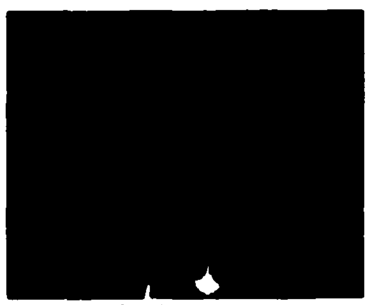
Frame = 3.44.13


Frame = 3.44.14


Frame = 3.44.15

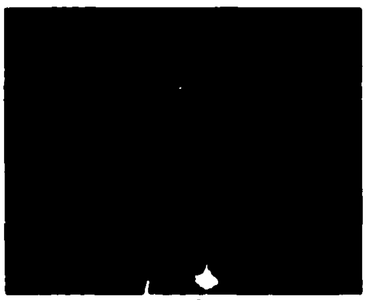
Frame = 3.44.16

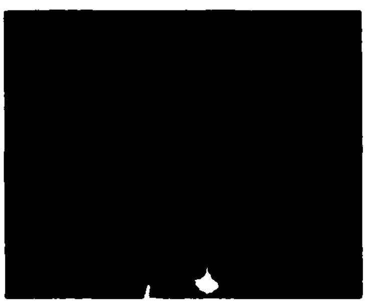
Frame = 3.44.17

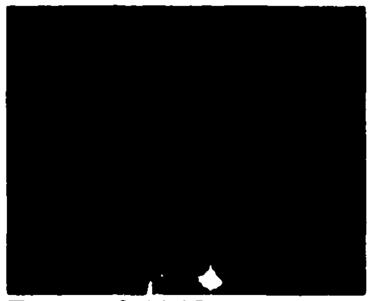
Frame = 3.44.18

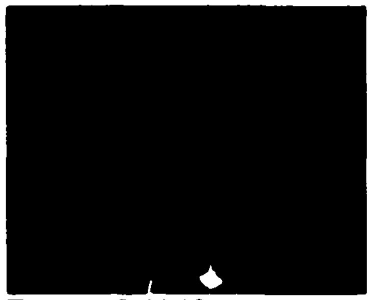
Frame = 3.44.19

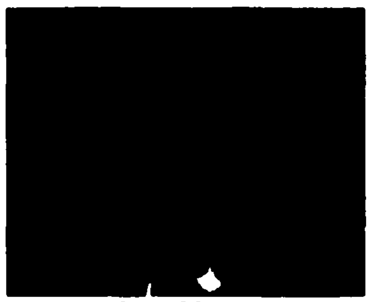
Frame = 3.44.20

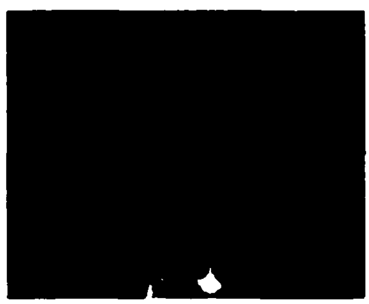
Frame = 3.44.21

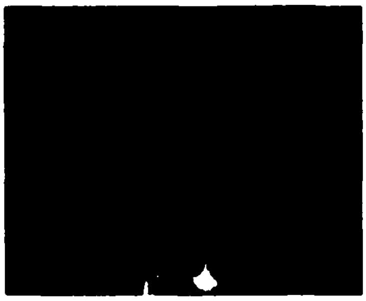
Frame = 3.44.22

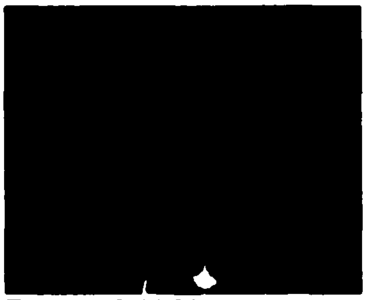
Frame = 3.44.23

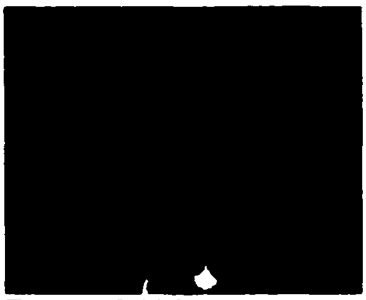
Frame = 3.44.24

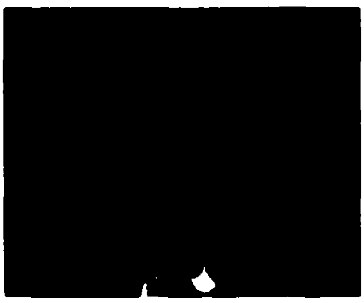
Frame = 3.44.25

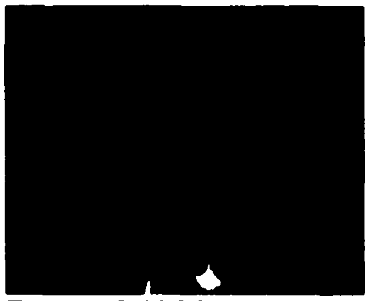
Frame = 3.44.26

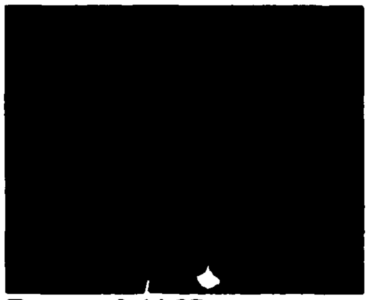
Frame = 3.44.27

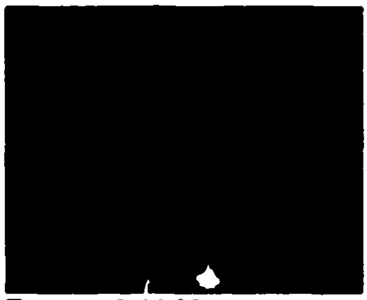
Frame = 3.44.28

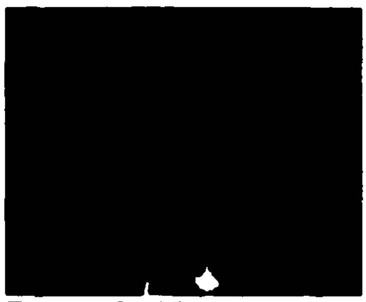
Frame = 3.44.29

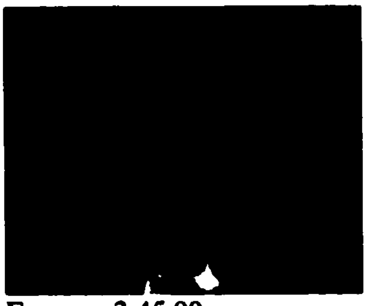

Frame = 3.45.00

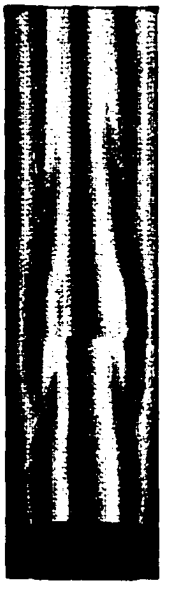

Figure 3.17: Rainbow schlieren image of a helium jet injected into quiescent air at a flow rate of 15.6 SLPM, Reynolds number = 164 and Froude number = 1.2 (courtesy of the Microgravity Combustion Laboratory, University of Oklahoma)

Chapter 4

Results of stability analysis

Preliminary calculations confirmed the conclusion of Monkewitz and Sohn (1988) that the varicose mode (m = 0) is more absolutely unstable than the sinuous mode (m = 1) in the near-injector region of round jets. This is illustrated in Figure 4.A1. Figure 4.A1 depicts the variation of the absolute temporal growth rate Ω_i^o with density ratio of an inviscid top-hat jet bounded by a cylindrical vortex sheet at m = 0 and m = 1. At all density ratios studied, Ω_i^o values are higher for the varicose mode than for the sinuous mode. Also, the density ratio at which Ω_i^o first becomes positive, as density ratio is reduced, is higher for the varicose mode (at a density ratio of 0.66) than for the sinuous mode (at a density ratio of 0.35). In their experiments on round variable-density gas jets, Kyle and Sreenivasan (1993) also observed that the shear layer in the near-injector region was always axisymmetric due to the varicose mode of the disturbance waves. Therefore, the following results on the instability of a low-density round gas jet injected into a high-density ambient gas concentrate on the varicose mode (m = 0).

4.1: <u>Temporal stability analysis</u>

A temporal stability analysis was carried out for two reasons:

1. To investigate the effects of the inhomogeneous shear-layer and buoyancy on the evolution of the disturbances with time.
2. To determine the limits in the complex wavenumber k-plane for the mesh-searching process used to determine the saddle points for the absolute stability analysis.

The near-injector region was investigated at axial locations along the jet represented by the jet parameter (R/θ) values of 10 $\left(\text{corresponding to } \frac{x}{2R} = 1\right)$ and 5 $\left(\frac{x}{2R} = 2.67\right)$, the value of 10 being closer to the injector exit. The density ratio, $S = \frac{\rho_j}{\rho_r}$, was varied from 1 (homogeneous shear-layer) to 0.14 (helium jet discharged into air), while varying the Froude number from infinity (no buoyancy) to 1.

The imaginary part of the complex frequency, Ω_i, is the temporal growth rate of the amplitude of the disturbance wave. The wavenumber k is the reciprocal of the wavelength. The temporal growth rate, Ω_i, the phase velocity, c_{ph}, and the wavenumber k were normalized using the shear-layer momentum thickness θ and the jet exit velocity U_j.

4.1.1: Effect of density ratio

In order to investigate the effect of an inhomogeneous shear layer only on the evolution of the jet instabilities with time, the Froude number was fixed at infinity (negligible gravity effect) and the density ratio (S) was varied from 1 to 0.14. A density ratio of 1 signifies a constant density shear-layer, e.g. air jet injected into air, while a density ratio less than 1 corresponds to the case of a low-density gas jet injected into a high-density ambient gas.

The variation of the normalized temporal growth rate of the instabilities with the normalized wavenumber at $R/\theta = 10$ and 5 is presented in Figures 4.1 and 4.3, respectively, for m = 0 (the axisymmetric disturbance mode) and Froude number (Fr) = infinity. Note that the normalized wavenumber is equal to the ratio of the circumference of a jet of radius equal to the shear-layer momentum thickness to the disturbance wavelength. At $R/\theta = 10$, as the density ratio is reduced from 1 to 0.14, the range of unstable wavenumbers is increased by about 20%. This implies that the range of unstable wavelengths decreases when the gas jet density is reduced relative to the ambient gas density. The values of the temporal growth rates are also increased. The maximum growth rate is increased by about 21%, as the density ratio is decreased from 1 to 0.14. A decrease in the jet density results in the steepening of the density gradient in the shear layer, which leads to additional generation of vorticity, thus causing an increase in the disturbance growth rate. Also, the maximum growth rate occurs at a higher wavenumber with a decrease in the density ratio. The wavenumber corresponding to the maximum growth rate is increased by about 8.3%, as the density ratio is decreased from 1 to 0.14. The disturbance wave with the maximum growth rate is usually assumed to dominate the flow and so will be the disturbance that is observed in experiments. Thus, the above results imply that the disturbance wavelength that is observed in experiments is reduced (by about 8%) in the presence of a higher density ambient gas.

As the jet proceeds downstream from $R/\theta = 10$ to $R/\theta = 5$, the disturbance growth rates for the constant density jet decrease by 10%, but for the case of density ratio 0.14 this decrease is 35%. This implies that the growth rate of the disturbance wave is a function of both the density ratio and the downstream location . Trends similar to those observed at $R/\theta = 10$ are seen at this location also as the density ratio is reduced.

Figures 4.2 and 4.4 depict the variation of the phase velocity of the disturbances with wavenumber at $R/\theta = 10$ and 5 respectively. The phase velocity of the disturbance decreases with increasing wavenumber, indicating that the disturbances move with a velocity less than the jet velocity. Also, as the density ratio is reduced, the phase velocity decreases at all unstable wavenumbers. Note that the phase velocity is equal to the ratio of the real part of the frequency to the wavenumber. With this in mind, the unstable frequencies can be determined by multiplying the phase velocity by their corresponding wavenumbers. It can be thus seen that the range of unstable frequencies increases as the density ratio is reduced;

i.e., the frequency spectrum of the fluctuations now contains additional frequencies.

The above results were computed for the case of infinite Froude number. However, when a low-density gas jet is injected into a high-density medium, buoyancy plays an important role. Thus, we proceed to determine the effects of buoyancy on the jet instability.

4.1.2: Effect of buoyancy

The effects of buoyancy on the jet temporal instability were determined by considering finite values of the Froude number in the analysis. The Froude number is the ratio of the inertial forces due to the jet momentum to the buoyancy forces acting on the jet. To study the effect of buoyancy on the jet temporal instability the density ratio was fixed at 0.14 (corresponding to a helium jet injected into air), while the Froude number was varied from infinity (negligible buoyancy) to 1; as the Froude number is reduced, the effects of buoyancy on the jet are increased.

Figures 4.5 and 4.7 display the variation of the temporal growth rates with wavenumber at $R/\theta = 10$ and 5 respectively, as the Froude number (Fr) is reduced from infinity to 1. The temporal growth rates for the constant-density jet are included as a baseline for comparison. At all Froude numbers, the temporal growth rates exceed those of the constant-density jet at both $R/\theta = 10$ and 5. Also, the wavenumber corresponding to the maximum growth rates exceed those of the constant-density jet, even though this appears to be due to the change in density ratio. When the effect of changing the Froude number alone is considered, no significant change in the wavenumber corresponding to the maximum growth rate is observed, except for Fr = 1 at R/θ=5. Thus, it seems that gravity does not have a "significant" effect on the wavenumber corresponding to the maximum growth rate at Fr $\geq$ 1.

In Figure 4.5, at R/θ = 10, as the Froude number is reduced from infinity to 5, no significant change is observed in the values of the temporal growth rates. The growth rates are increased, though, as the Froude number is reduced further. The maximum growth rate increases by about 4.4%, when the Froude number is reduced from infinity to 2, but the range of unstable wavenumbers is not altered. At a Froude number of unity, the maximum growth rate is increased by about 18%, while the range of unstable wavenumbers is increased by a mere 3.4%. Results for various Froude numbers at a downstream location, are given in Figures 4.7 and 4.8. A comparison of Figures 4.7 and 4.5 indicates that the temporal growth rates decrease for Froude numbers equal to infinity, 10, 5, and 2 as the jet proceeds downstream. The maximum growth rates decrease by about 7% for Fr = ∞ and 10, by about 6.4% for Fr = 5, and by about 2.3% for Fr =2. At Fr = 1, however, the maximum growth rate increases by about 14% while the wavenumber corresponding to the maximum growth rate is decreased by about 8%. As the Froude number is further reduced at this axial location, trends similar to those for R/θ = 10 are observed, except at Fr = 1 where there is a change in the wavenumber corresponding to the maximum growth rate. Before we attempt to explain this phenomenon at Fr = 1, we shall consider the phase velocities.

Figures 4.6 and 4.8 display the variation of the phase velocities of the disturbances at various Froude numbers for $R\ \theta = 10$ and 5 respectively. Again, the constant-density case is included as a baseline. At $R\ \theta = 10$, the influence of Froude number on the phase velocity, it seems, is to lower the phase velocities when compared to those of the constant density jet at most wavenumbers. But, at Fr = 1, for wavenumbers less than 0.02 the phase velocities are increased, and are even greater than 1. This suggests that disturbances at these low wavenumbers move with a velocity faster than the jet. Subbarao and Cantwell (1992) observed the formation of "secondary vortex-ring-like structures" at a Richardson number of 1.6 (equivalent to Fr = 1.12) that accelerated rapidly upward within the core fluid and increased the entrainment and breakdown of the jet. The increased phase velocities at low wavenumbers may be associated with these secondary vortex-ring-like structures. As the jet moves downstream from $R/\theta = 10$ to $R/\theta = 5$, the increased phase velocities are evident at Fr = 2, with phase-velocities at Fr = 1 increasing further by about 18% for these low wavenumbers.

In order to understand the effect of buoyancy on the jet instability, the definition of Froude number and the extra term in the disturbance equation (2.25) due to gravity need to be analyzed. Froude number in this study is defined as

$$Fr^2 = \frac{U_j^2}{gR}\frac{\rho_j}{\rho_\infty - \rho_j} \tag{4.1}$$

Thus, it appears that when the buoyancy force is of equal magnitude to the inertial force, there is a significant effect of gravity on the jet instability. To confirm this, the Froude number was reduced further to 0.2 for $R/\theta = 10$ in Figures 4.9 and 4.10. Figure 4.9 indicates the temporal growth rate variation with wavenumber. The growth rates and range of unstable wavenumbers are further increased with reducing Froude number. When Fr is reduced from infinity to 0.5, the maximum growth rate is increased by about 74% and the range of unstable wavenumbers is increased by about 14%, while the wavenumber corresponding to the maximum growth rate is decreased by about 8%. The maximum growth rate and range of unstable wavenumbers are increased by 187% and 31% respectively when Fr is reduced to 0.3 from infinity, while the wavenumber corresponding to the maximum growth rate is increased by about 8%. Reducing Fr from infinity to 0.2 results in a 350% increase in the maximum growth rate, 55% increase in the range of unstable wavenumbers and a 46% increase in the wavenumber corresponding to the maximum growth rate. Thus for Fr < 1, the growth rates are dramatically increased, signifying that the jet becomes highly unstable for buoyancy-driven jet flows. This has been observed in experiments conducted by Cetegen and Kasper (1996).

In Figure 4.10, the phase velocities are plotted as a function of wavenumber. As Fr is reduced below 1 to 0.2, the range of low wavenumbers corresponding to phase velocities greater than 1 is increased from 0.02 to 0.04. Also, the maximum phase velocity is almost doubled at Fr = 0.2. These results can be understood in light of the extra term in equation (2.25) due to the presence of gravity. The non-dimensional coefficient of the buoyancy term in this equation is

$$G = \frac{1}{Fr^2 \frac{R}{\theta}\left(\frac{\rho_\infty}{\rho_j} - 1\right)} \tag{4.2}$$

The variation of G, equation (4.2), with Froude number for R/θ = 10 and 5 is indicated on Figure 4.11 at a density ratio of 0.14. At both R/θ = 10 and 5, for Froude numbers less than 1, G increases almost exponentially. Note that when Fr, equation (4.1), is substituted for in equation (4.2) it is apparent that $G = \frac{g}{\left(U_j^2 / \theta\right)}$ which is the ratio of buoyancy force per unit mass to inertial force per unit mass. Thus, G can be defined as a non-dimensional number that compares the acceleration of the large-scale structures of the jet due to buoyancy to that due to inertial forces. Also, the values of G at R/θ = 5 are about double those at R/θ = 10. Hence, the reason for the increase in growth rates at Fr = 1 as the jet proceeds downstream from R/θ = 10 to R/θ = 5 instead of decreasing as in the case of higher Fr values. Thus, the effect of buoyancy at low Fr values is to cause the jet instabilities to increase exponentially. This could explain the reason for the abrupt breakdown of the jet large-scale structures noticed in helium-jets-in-air experiments by Subbarao and Cantwell (1992) and Cetegen and Kasper (1996).

4.2: <u>Absolute instability analysis</u>

A spatio-temporal stability analysis was also carried out to determine the absolute instability of the jet. The effects of the inhomogeneous shear-layer and buoyancy on the nature of the absolute instability (whether absolutely or convectively unstable) of the jet were investigated. This was done by first studying the effect of varying the density ratio from 0.99 to 0.14, while varying the Froude number from infinity to 0.5 and keeping the Schmidt number constant at 1. The hypothesis for the influence of Schmidt number Sc, analogous to the turbulent Prandtl number discussed by Reichardt (Schlichting, 1979) was used to study the effects of dissimilar density and velocity profiles on the nature of the jet absolute instability. The effect of varying the Schmidt number while varying the Froude number for a density ratio of 0.14 was studied. Previous results of two-dimensional jets (Raynal et al., 1996) indicate that the shift in the velocity and density profiles may have a significant effect on the instabilities. Therefore, the effect of the lateral shift in the velocity and density profiles was investigated for a density ratio of 0.14 and Schmidt number equal to 1. Finally, the results of the spatio-temporal stability analysis were compared to the experimental findings of Subbarao and Cantwell (1992) and Pasumarthi (2000).

The complex frequency Ω and the complex wavenumber k are normalized using the shear-layer momentum thickness θ and the velocity difference $\Delta U = U_j - U_\infty$. The contour plots in the k-plane illustrating the pinch points for the absolute stability results can be found in Appendix A.

Monkewitz and Sohn (1988), assuming negligible buoyancy effects, studied the effect of variable density on the absolute instability of hot round jets; the mean velocity and density profiles that were used in the analysis were different from those used in this study. Therefore, a comparison of the two sets of results was made to determine the effects of the assumed forms of the velocity and density profiles. Also, such a comparison is useful to validate the method of solution used in this study. The results for the saddle points (Ω^o, k^o) are given for $R/\theta = 25$ and 10 in tables 4.1 and 4.2, where subscripts "i" and "r" indicate the imaginary and real parts respectively. The trends of the results agree with those of Monkewitz and Sohn (1988). The major differences between the two results occur at the axial location corresponding to $R/\theta = 25$. At $R/\theta = 25$, the difference in the k_r^o values between the two results is about 30%; for the $-k_i^o$ values the maximum difference is about 2%; while for the Ω_r^o and Ω_i^o values the maximum difference is about 13% and 550% respectively. A major contribution to these differences, apart from the difference in density and velocity profiles used in the studies, is from the least counts of the graphs in Monkewitz and Sohn (1988). The least counts of the graphs, normalized using the momentum thickness θ and jet velocity U_j, are 0.04 for the k_r^o

and $-k_i^o$ results, 0.02 for the Ω_r^o results, and 0.002 for the Ω_i^o results. In light of these least counts the differences between the Monkewitz and Sohn (1988) data and the data from the present study can be understood. The trends of both results, however, are similar. Having gained confidence in the present method, we now discuss the effect of the variable density on the nature of the absolute instability of the jet.

4.2.1: Effect of density ratio

When the jet is absolutely unstable, initially localized disturbances grow with time and space, and eventually contaminate the entire flow. On the other hand, if the jet is convectively unstable the disturbances grow as they are convected downstream. The imaginary part Ω_i^o of the complex absolute frequency, in this study, denotes the absolute temporal growth rate of the disturbances. When Ω_i^o is positive (and the Briggs-Bers criterion is satisfied) the jet is absolutely unstable while for a negative Ω_i^o the jet may be convectively unstable. A constant-density jet (such as an air-in-air jet) may be convectively unstable; as the density ratio is reduced (a low-density jet injected into a high-density gas medium), the nature of instability of the jet is changed from convective instability to absolute instability. This density ratio, at which the jet first becomes absolutely unstable, is referred to as the critical density ratio (S_c). In Figure 4.12, for example, this is the density ratio at which $\Omega_i^o = 0$. The real part Ω_r^o of the absolute complex frequency is the frequency corresponding to the absolute temporal growth rate of the disturbance. The imaginary part k_i^o of the complex wavenumber is the absolute spatial growth rate of the disturbances. A negative k_i^o indicates the absolute spatial growth rate of the disturbances while a positive k_i^o denotes the absolute spatial decaying rate of the disturbances. Note that for an absolutely unstable flow k_i^o will be negative. The real part of the complex wavenumber is the absolute wavenumber of the disturbances. It should be noted that the word "absolute" when used in conjunction with the disturbance wavenumber or growth rate in this study is synonymous with the phenomenon of "absolute instability or stability."

Figure 4.12 depicts the variation of the absolute temporal growth rate of the disturbances with the density ratio at $R/\theta = 10$ and 5 with Froude number fixed at infinity (no buoyancy effects). At $R/\theta = 10$, the growth rate is increased by about 201%, as the density ratio is reduced from 0.99 to 0.14 . The critical density ratio, S_c, at this location is 0.525. The absolute growth rates of the jet disturbance are positive for density ratios below 0.525 indicating that the jet is absolutely unstable. However, for density ratios above 0.525 the absolute growth rates are negative meaning the jet is convectively unstable.

As the jet proceeds downstream from an axial location corresponding to $R/\theta = 10$ to $R/\theta = 5$, the absolute temporal growth rates decrease for all density ratios. The absolute temporal growth rates are decreased by about 76% at a density ratio of 0.14 and by about 316% at a density ratio of 0.99 (the other extreme of the range of density ratios studied). The percentage decrease in the growth rates for density ratios between 0.14 and 0.99 is increased from 76% to 316%. Trends similar to those observed at $R/\theta = 10$ for the growth rates are also observed at $R/\theta = 5$, but the critical density ratio is decreased to 0.17. Figure 4.13 illustrates the change in critical density ratio as the jet proceeds from $R/\theta = 10$ to $R/\theta = 5$.

The variation of the real part of the absolute frequency Ω_r^o as the density ratio is increased from 0.14 to 0.99 for $R/\theta = 10$ and 5 is illustrated in Figure 4.14. At $R/\theta = 10$ and 5, Ω_r^o is increased by about 107% and 62%, respectively, as the density ratio increased from 0.14 to 0.99. Ω_r^o is increased as the flow proceeds from $R/\theta = 10$ to 5 at all density ratios. At extremes of the range of density ratios investigated (0.14 and 0.99) Ω_r^o is increased by about 83% and 43%, respectively, as the flow proceeds from $R/\theta = 10$ to 5.

The absolute spatial growth rates $-k_i^o$ are plotted against density ratio for $R/\theta = 10$ and 5 in Figure 4.15. At $R/\theta = 10$, the absolute spatial growth rate is increased by about 76% as the density ratio is increased from 0.14 to 0.99. At $R/\theta = 5$, the absolute spatial growth rate is increased by about 71% as the density ratio is increased from 0.14 to 0.99. And, as the jet proceeds downstream from $R/\theta = 10$ to $R/\theta = 5$, the absolute spatial growth rates are increased by about 65% at density ratio = 0.14 and by about 60% at density ratio = 0.99.

Figure 4.16 illustrates the variation of the real part of the absolute wavenumber k_r^o as the density ratio is increased from 0.14 to 0.99 for R/θ values of 10 and 5. At R/θ = 10, k_r^o is increased by about 47% as the density ratio is increased from 0.14 to 0.99 while at R/θ = 5, k_r^o is increased by about 27% as the density ratio is increased from 0.14 to 0.99. And, as the jet proceeds from R/θ = 10 to R/θ = 5, k_r^o is increased by about 70% and 47% at density ratios of 0.14 and 0.99 respectively.

The above trends of the real and imaginary parts of the saddle points (Ω^o, k^o) are similar to those presented by Monkewitz and Sohn (1988) in their study on the absolute instability of hot jets at an axial location of x/R = 2 (R/θ = 10), with buoyancy effects neglected. Next, buoyancy effects are introduced and the influence of buoyancy on the jet instability is discussed.

4.2.2: Effect of buoyancy

Figures 4.17 and 4.22 illustrate the variation of the absolute temporal growth rate of the disturbances with the density ratio for several Froude numbers at R/θ = 10 and 5 respectively. At both R/θ = 10 and 5, as the Froude number is reduced from infinity the absolute temporal growth rate varies with the density ratio only, but below a Froude number of 2 the absolute temporal growth rate varies with both the density ratio and Froude number. For R/θ = 10, the absolute temporal growth rate is increased as the density ratio is reduced for large Froude numbers. As the density ratio is reduced from 0.14 to 0.99, the absolute temporal growth rate is increased by about 200% at Fr = ∞ and 10. At Fr = 5, the absolute temporal growth rate is increased by about 188%. For Fr = 2, 1.58, and 1, the absolute temporal growth rates are enhanced by about 131%, 99%, and 20% respectively. Below a Froude number of unity, this trend is reversed.. At Fr = 0.75 and 0.5, the absolute temporal growth rates are increased by about 28% and 76% respectively, as the density ratio is increased from 0.14 to 0.99. The absolute temporal growth rates are higher at each density ratio as the Froude number alone is decreased below Fr = 5. For Fr $\geq$ 5, there is no significant change in the absolute temporal growth rates due to changes in the Froude number, indicating that the jet is momentum-driven at Fr $\geq$ 5 and that effects of buoyancy are small. At R/θ = 5, the trend is reversed at Froude numbers below 0.75 and the same trends observed at R/θ = 10 are observed at this downstream location also.

As noted earlier, the critical density ratio below which the jet is absolutely unstable for a given Froude number is of interest. Figures 4.18 and 4.23 depict the variation of the critical density ratio with Froude number at R/θ = 10 and 5 respectively. At R/θ = 10, at large Froude numbers, the critical density ratio tends to 0.525, and the "critical Froude number" below which the jet is absolutely unstable for all density ratios studied is 1.58. Thus, at density ratios less than 0.525

the jet is absolutely unstable at this location and for Fr < 1.58 any low-density gas jet injected into a high density ambient gas becomes absolutely unstable at R/θ = 10. For R/θ = 5 (Figure 4.23), as the Froude number tends to a large value, the critical density ratio tends to 0.17 and the "critical Froude number" is 1.015. Thus the critical density ratio and critical Froude number appear to be functions of the shear layer width and thus the axial location downstream of the jet.

The real part of frequencies corresponding to the absolute temporal growth rates of the saddle points discussed above are depicted in Figures 4.19 and 4.24 for R/θ = 10 and 5 respectively. Note that the real part of the normalized frequency Ω_r^o might be interpreted as the Strouhal number expressed in terms of the shear-layer momentum thickness, θ and the velocity difference, $\Delta U = U_j - U_\infty$. At R/θ = 10, Ω_r^o is increased by about 105% at Fr ≥ 1.58 as the density ratio is increased from 0.14 to 0.99. Below the critical Fr = 1.58, at this axial location, Ω_r^o is increased by about 102%, 105%, and 112% at Fr = 1, 0.75 and 0.5 respectively as the density ratio is increased from 0.14 to 0.99. Above the critical Fr, Ω_r^o does not change significantly with Fr, although it is a function of density ratio; whereas, below the critical Fr at this location Ω_r^o depends on both the density ratio and Fr, suggesting that the critical Fr demarcates two jet flow regimes. For values less than the critical Fr, the flow is momentum-driven, while at values greater than the critical Fr the flow is within the buoyancy-driven regime. Similar Strouhal number regimes were observed by Subbarao and Cantwell (1992) in their experiments on helium jets discharged into a co-flowing air. The same trends are noticed at the axial location corresponding to $R/\theta = 5$, and again the dependence on Fr is noticed below the critical Fr, at this location, of 1.015.

The variation of the spatial growth rates $-k_i^o$ corresponding to the saddle point as a function of the density ratio is illustrated in Figures 4.20 and 4.25 for $R/\theta = 10$ and 5, respectively, at several Fr values from ∞ to 0.5. At $R/\theta = 10$, the absolute spatial growth rates are increased by about 80% as the density ratio is increased from 0.14 to 0.99 for all Fr values studied. There is no significant change in the absolute spatial growth rates as Fr is decreased except at Fr = 0.5 for density ratios above 0.3. Even then the largest increase in the absolute spatial growth rate at this Fr is only about 6% at a density ratio of 0.99. The absolute spatial growth rates do not vary significantly as Fr is reduced from ∞ to 0.75 at each density ratio, implying that the spatial growth rates do not depend on Fr within this range of Fr values. As the jet proceeds downstream to $R/\theta = 5$, the absolute spatial growth rates are increased within a range of about 67% - 46% for the Froude numbers studied;. the change at lower density ratios is greater than at higher density ratios. The same trends are observed as in the case for $R/\theta = 10$ as the density ratio is increased, and there is no significant dependence of the absolute spatial growth rates on Fr at this location, for any of the density ratios studied.

The real part of the wavenumber k_r^o is plotted against density ratio for several Fr in Figures 4.21 and 4.26 for $R/\theta = 10$ and 5 respectively. This value is inversely proportional to the wavelength of the disturbance that is observed in experiments. For an R/θ value of 10, when the density ratio is increased from 0.14 to 0.99, k_r^o is increased by about 48% for Fr ≥ 1.58; and about 56%, 65%, and 78% for Fr = 1, 0.75, and 0.5, respectively. For all Fr ≥ 1.58 (the critical Fr) k_r^o does not vary with Fr significantly at each density ratio. At lower Fr values, however, k_r^o is a function of both Fr and the density ratio, except at S = 0.14. As the jet proceeds to $R/\theta = 5$ from $R/\theta = 10$, k_r^o is increased within a range of about 71% - 46% for all Fr values. Again the limits of the range are the percentage increases at density ratios of 0.14 and 0.99 respectively. The same trends for k_r^o are observed at this axial location as at the $R/\theta = 10$ location except that the dependence on Fr is observed at Fr values less than 1.015, the critical Fr at this location.

From the discussions above it is clear that there is a critical Froude number, which depends on axial location, below which Ω_r^o and k_r^o exhibit a dependence on the Froude number. This is also the Froude number below which the flow is absolutely unstable for all density ratios studied.

4.2.3: Effect of co-flow

Figure 4.27 illustrates the effect of co-flow on the absolute temporal growth rates of the jet flow at $R/\theta = 10$ for $\rho_j/\rho_\infty = 0.14$ and Fr = ∞, 10, 5, 2, 1, 0.75 and

0.5. Results are presented for co-flow velocity ratios of $U_\infty/\Delta U$ = 0, 0.5 (corresponding to $U_\infty = 0.33U_j$), and 1 (corresponding to $U_\infty = 0.5U_j$). As the co-flow is increased ($U_\infty/\Delta U$ is increased from 0 to 1), it is observed that the absolute temporal growth rates of the disturbances decrease linearly at each Fr. An increase in co-flow leads to a decrease in the magnitude of mean shear that serves as the driving force for the instability, thus, resulting in a decrease in the growth rates. As $U_\infty/\Delta U$ is increased from 0 to 1, at this axial location, the absolute growth rates are reduced by about 414% for Fr > 2, and about 359%, 257%, 204%, and 137% at Fr = 2, 1, 0.75 and 0.5 respectively. Though the effect of co-flow is felt less as Fr is decreased, it is obvious from Figure 4.27 that the presence of co-flow tends to make the previously absolutely unstable flow become convectively unstable. The variation of the real part of the complex absolute frequency Ω_r^o at the saddle points with co-flow is illustrated in Figure 4.28 for $\rho_j/\rho_\infty = 0.14$ and Fr = ∞, 10, 5, 2, 1, 0.75 and 0.5 at an axial location corresponding to $R/\theta = 10$. An increase in co-flow causes Ω_r^o to increase. As $U_\infty/\Delta U$ is increased from 0 to 1, Ω_r^o is increased by about 53% at all Fr. Note again the reducing effect of co-flow as Fr decreased below 10.

The change in absolute spatial growth rate $-k_i^o$ as co-flow is increased is illustrated in Figure 4.29 for $\rho_j/\rho_\infty = 0.14$ and Fr = ∞, 10, 5, 2, 1, 0.75 and 0.5 at R/θ = 10. As co-flow is increased from 0 to 1, the absolute spatial grow rates are decreased by about 25% for all Fr values. Thus, not only does co-flow make the jet less absolutely temporally unstable it also reduces the absolute spatial growth rate of the disturbances. Figure 4.30 depicts the variation of the real part of the wavenumber k_r^o with co-flow velocity ratio for $\rho_j/\rho_\infty = 0.14$ and Fr = ∞, 10, 5, 2, 1, 0.75 and 0.5 at $R/\theta = 10$. As co-flow is increased from 0 to 1, k_r^o is decreased by about 82% for all Fr values studied. Thus, as co-flow increased the wavelengths of the disturbances increased.

For an inhomogeneous jet flow involving two gases of different mass densities, such as a helium jet injected into air for instance, there is a concentration gradient in the shear-layer between the two gases. In the presence of a concentration gradient there will be mass transfer of one gas to the other by diffusion. In this case, the density profile and the velocity profile within the shear layer may not be identical and could be completely different due to a difference in momentum and mass diffusion. The Schmidt number signifies the ratio of the rate of momentum transfer to the rate of mass transfer of a flow.

The concept of turbulent Prandtl number in the form proposed by Reichardt and discussed by Schlichting (1979) was used by Monkewitz and Sohn (1988) to specify the relationship between the velocity and density profiles. The same analogy can be used for a relationship between the transfers of momentum and mass.

Thus,

$$\frac{\bar{\rho}(r)-\rho_{\infty}}{\rho_{j}-\rho_{\infty}}=\left(\frac{\bar{u}(r)-U_{\infty}}{U_{j}-U_{\infty}}\right)^{Sc} \tag{4.3}$$

where, $Sc=\frac{\upsilon}{D_b}$ is the Schmidt number. The basic density profile in the shear layer is thus,

$$\frac{\bar{\rho}(r)}{\rho_{\infty}}=1+\left(\frac{\rho_{j}}{\rho_{\infty}}-1\right)\left\{0.5\left(1-\tanh\left[0.25\frac{R}{\theta}\left(\frac{r}{R}-\frac{R}{r}\right)\right]\right)\right\}^{Sc} \tag{4.4}$$

Figure 4.31 depicts the density profiles at several Sc for $R/\theta = 10$ and $\rho_j/\rho_\infty = 0.14$. The effect of Sc on the absolute stability of the jet flow is discussed in the next section. Also, the effect of a lateral shift Δr between the inflexion points of the density and velocity profiles, with Schmidt number set at Sc = 1, on the absolute instability of the jet was investigated and is discussed in the subsequent section. This was done by replacinging r in the density profile equation (2.32) with $(r + \Delta r)$ like was done by Raynal et al. (1996) for plane variable-density jets. Thus,

$$\frac{\bar{\rho}(r)}{\rho_{\infty}}=0.5\left\{2+\left(\frac{\rho_{j}}{\rho_{\infty}}-1\right)\left(1-\tanh\left[0.25\frac{R}{\theta}\left(\frac{\{r+\Delta r\}}{R}-\frac{R}{\{r+\Delta r\}}\right)\right]\right)\right\} \tag{4.5}$$

The density profiles at several Δr for $R/\theta = 10$ and $\rho_j/\rho_\infty = 0.14$ are illustrated in Figure 4.32.

4.2.4: <u>Effect of Schmidt number</u>

The variation of the absolute temporal growth rate as a function of Schmidt number Sc is illustrated in Figure 4.33 for $\rho_f/\rho_\infty = 0.14$ and Fr = ∞, 10, 5, 2, 1, 0.75 and 0.5 at $R/\theta = 10$. The absolute temporal growth rates decrease for large changes of Sc from the value of 1. As Sc is decreased to 0.05 from 1, the absolute growth rates are reduced by about 152% for Fr > 1, and about 132%, 124%, and 117% for Fr = 1, 0.75 and 0.5 respectively at this axial location. And, as Sc is increased from 1 to 10, the absolute temporal growth rates are reduced by about 40% for Fr > 1, and by about 37%, 32%, and 24% for Fr = 1, 0.75 and 0.5 respectively. Data from Pasumarthi (2000) suggests an average kinematic viscosity of 8.64 x 10^{-5} m^2/s, at room temperature, for helium round jets discharged into air. At room temperature, the binary diffusion coefficient for a helium-in-air system is 7.44 x 10^{-5} m^2/s (Geankoplis, 1972), so the Schmidt number at these conditions is about 1.16. This value is within the neighborhood of Sc = 1, thus it is necessary to study the absolute instability for small changes from Sc = 1. For a small change in Sc from 1 the variation of the absolute temporal growth rate as a function of Sc is complex. For instance, at Fr > 1, as Sc is increased from 1 to 1.2 the absolute temporal growth rate is increased slightly before decreasing as Sc is increased further. While at Fr = 0.5, as Sc is reduced from 1 to 0.6 the absolute temporal growth rate is increased slightly before decreasing as Sc is decreased further. This complex dependence of the absolute growth rates on Sc within the neighborhood of Sc = 1 makes it difficult to compare results with experiments. Note also, that at Sc values less than 0.21 the flow is convectively unstable for all Fr greater than 1. For Fr $\leq$ 1, the flow becomes convectively unstable at Sc values less than 0.1.

Figure 4.34 depicts the variation of the real part of the frequency Ω_r^o corresponding to the saddle point as Sc changed for ρ_j/ρ_∞ = 0.14 and Fr = ∞, 10, 5, 2, 1, 0.75 and 0.5 at R/θ = 10. At each Fr value, as Sc is increased from 0.05 to 10, a minimum value of Ω_r^o occurs at a Schmidt number value. The Schmidt number corresponding to the minimum value of Ω_r^o varies with the Froude number. At Fr > 1, the minimum value of Ω_r^o occurs at a constant value of Sc = 0.6. Whereas, at Fr = 1, 0.75 and 0.5, the Sc values corresponding to the minimum value of Ω_r^o are about 0.4, 0.21, and 0.1 respectively. Below the Schmidt number corresponding to the minimum Ω_r^o, Ω_r^o is reduced as Fr is decreased from ∞ to 0.5, but above the Schmidt number corresponding to the minimum Ω_r^o, Ω_r^o is increased as Fr is decreased from ∞ to 0.5.

The variation of the absolute spatial growth rate $-k_i^o$ as Schmidt number Sc is increased from 0.05 to 10 is illustrated in Figure 4.35 for ρ_j/ρ_∞ = 0.14 and Fr = ∞, 10, 5, 2, 1, 0.75 and 0.5 at R/θ = 10. At this location, as Sc is increased from 0.05 to 10 $-k_i^o$ is decreased by about 43% for Fr values greater than 2; by about 46% at Fr = 2 and 1; and by about 48% at Fr = 0.75 and 0.5. This indicates that increasing the Schmidt number causes the jet to be less absolutely spatially unstable.

The variation of k_r^o as Schmidt number Sc is increased from 0.05 to 10 is illustrated in Figure 4.36 for $\rho_j/\rho_\infty = 0.14$ and Fr = ∞, 10, 5, 2, 1, 0.75 and 0.5 at $R\theta$ = 10. The variation of k_r^o as Sc is increased from 0.05 to 1 is complex even as Fr is reduced, but above Sc = 1 k_r^o is decreased as Sc is increased from 1 to 10 and there is only a slight dependence of k_r^o on Fr for Sc $\geq$ 1.

4.2.5: <u>Effect of lateral shift between velocity and density profiles</u>

Raynal et al. (1996) showed that for plane jets the lateral shift between the inflexion points of the velocity and density profiles has a greater effect on the jet absolute stability than the difference in the profiles. Plane jets and round jets differ due to the requirement of the boundary condition at the jet center, but it was necessary to confirm the effect of the lateral shift between the velocity and density profiles on round jets. The results of the analysis are presented below.

The variation of the absolute temporal growth rate as a function of the lateral shift Δr is presented in Figure 4.37 for $\rho_j/\rho_\infty = 0.14$ and Fr = ∞, 10, 5, 2, 1, 0.75 and 0.5 at $R\theta$ = 10. For Fr = ∞, 10, and 5, there is no significant change in the absolute temporal growth rates and the maximum absolute temporal growth rate occurs at Δr = 0. At Fr values less than 5 the growth rates are increased with the maximum growth rate increasing by about 18%, 88%, 160% and 302% as the Fr value is decreased from ∞ to 2, 1, 0.75 and 0.5 respectively. And, the Δr corresponding to the maximum absolute temporal growth rate occurs at Δr = -1.25 for Fr = 2 and at -2.5 for Fr $\leq$ 1. Thus, as Fr is decreased the effect of the lateral shift between the velocity and density profiles becomes more pronounced and whether the jet becomes more absolutely unstable or not depends on the location of the inflexion point of the density profile relative to that of the velocity profile. Observing the change in the absolute temporal growth rate due to the influence of Δr and that due to the influence of Sc, we see that the effects of Δr and Sc on the absolute instability of the jet is complex. Thus, the combined effects of both Sc and Δr need to be considered when analyzing the absolute instability of a round jet. This means that the specific density and velocity profiles used in the stability analysis of absolutely unstable round jets affect the absolute instability of the jet, and are important.

Figure 4.38 depicts the variation of Ω_r^o as a function of Δr for $\rho_j/\rho_\infty = 0.14$ and Fr = ∞, 10, 5, 2, 1, 0.75 and 0.5 at $R/\theta = 10$. As Δr is increased from a value of 0 to 5, Ω_r^o is increased by about 53% for the Fr values studied. For $\Delta r > 0$ the increase in Ω_r^o is a linear function of Δr. As Δr is decreased from a value of 0 to –2.5, Ω_r^o is decreased by about 20% for Fr $\geq$ 5; by about 28% for Fr = 2; and by about 38% for Fr $\leq$ 1. Again, it is obvious that the relative position of the density profile to the velocity profile affects the absolute frequency (or Strouhal number) of the jet in a complex manner.

The variation of the absolute spatial growth rate $-k_i^o$ as a function of Δr for $\rho_f/\rho_x = 0.14$ and Fr = ∞, 10, 5, 2, 1, 0.75 and 0.5 at $R\theta = 10$ is depicted in Figure 4.39. As the lateral shift is increased from $\Delta r = 0$ to $\Delta r = 5$, the absolute spatial growth rate first decreases until a minimum value is reached and then it increases. For Fr > 0.5 the minimum absolute spatial growth rate value within this range of Δr values occurs at $\Delta r = 1.25$, and at $\Delta r = 2.5$ for Fr = 0.5. As Δr is decreased from $\Delta r = 0$ to $\Delta r = -1.25$ the absolute spatial growth rates are increased by about 4% for Fr > 1; by about 9% at Fr = 1; by about 12% at Fr = 0.75; and by about 18% at Fr = 0.5. As the lateral shift is decreased to a value of $\Delta r = -2.5$, the absolute spatial growth rate is decreased by about 3.5% for Fr > 1; but the spatial growth rate is increased by about 19%, 35%, and 57% for Fr = 1, 0.75, and 0.5 respectively.

Figure 4.40 depicts the variation of k_r^o as a function of Δr for $\rho_f/\rho_x = 0.14$ and Fr = ∞, 10, 5, 2, 1, 0.75 and 0.5 at $R\theta = 10$. As the lateral shift is increased from $\Delta r = 0$ to $\Delta r = 5$, k_r^o is first decreased to a minimum value at $\Delta r = 2.5$ and then is increased to a value close to that at $\Delta r = 0$ at $\Delta r = 5$ for all Fr values. As Δr decreased from $\Delta r = 0$ to $\Delta r = -2.5$, k_r^o is decreased by about 8% for Fr > 2; but increased by about 9% for Fr = 2 and by about 39% at Fr ≤ 1.

4.3: Effects of Froude number and density ratio on disturbance amplitudes and the vorticity

Now, the effects of density ratio and Froude number on the radial distributions of the absolute values of the amplitudes of the pressure disturbance, the derivative of the pressure disturbance, the axial velocity disturbance, the radial velocity disturbance and the vorticity in the azimuthal direction will be discussed. Results discussed are at an axial location corresponding to $R/\theta = 10$.

4.3.1: Pressure disturbance and derivative of the pressure disturbance

Figures 4.41 and 4.42, obtained from results of the linear spatio-temporal stability analysis, illustrate the radial variation of the absolute values of the amplitudes of the pressure disturbance and that of the derivative of the pressure disturbance respectively, as density ratio (S) is decreased from 0.99 to 0.14 while Froude number (Fr) is decreased from infinity to unity at a downstream location corresponding to $R/\theta = 10$. As the density ratio is decreased from S = 0.99 to S = 0.14, the pressure is increased and the radial distance from the jet center to where the pressure drops to zero is increased by about 40% at both Froude numbers. There is no significant effect of Froude number on the radial distribution of the pressure values within the shear-layer. For Fr = ∞, as the density ratio is decreased from S = 0.99 to S = 0.14, the absolute values of the amplitude of the pressure derivative are first decreased until a non-dimensionalized radial location of r = 20 is reached. Beyond this radial location the pressure derivative values are increased as S is decreased from 0.99 to 0.14. Also as the density ratio is decreased to 0.14, the radial location from the jet center where the pressure derivative dropped to zero is increased by about 27%. As in the case of the pressure distribution, there is no significant effect of Fr on the radial distribution of the pressure derivative.

Figures 4.43 and 4.44 are the counterparts of Figures 4.41 and 4.42 for results obtained from the linear temporal stability analysis. At $Fr = \infty$, as S is decreased from 0.99 to 0.14, the pressure disturbance within the shear-layer is increased with the maximum pressure disturbance occurring at the jet radius for both density ratios. The maximum pressure disturbance is increased by about 52% as S is decreased from 0.99 to 0.14. Reducing the density ratio had the effect of increasing the pressure disturbance within the shear-layer. As Fr is decreased from infinity to 1, with S constant at 0.99, the pressure disturbance is increased, with the maximum pressure disturbance increasing by about 13% at the jet radius. Thus, increasing the influence of gravity has the effect of increasing the pressure disturbance within the shear-layer at a density ratio of 0.99. At a density ratio of 0.14, as the Froude number is decreased from infinity to 1, no significant change in the pressure disturbance is observed except at the jet radius where the maximum pressure disturbance occurred. At the jet radius, the maximum pressure disturbance is decreased by about 3%. Comparing Figure 4.41 to Figure 4.43, we see that the absolute values of the amplitude of the pressure disturbance in the case of the results from the spatio-temporal stability analysis is always less than 1 at all radial locations while that for the temporal stability analysis is greater than 1 within the shear-layer. Also, the radial locations from the jet axis where the pressure disturbance drops to zero in the results from the spatio-temporal stability analysis are about 133% (for S = 0.14) and about 67% (for S = 0.99) of those for the temporal stability analysis. In Figure 4.44, the absolute value of the amplitude of the derivative of the pressure disturbance is increased within the shear-layer as the density ratio is decreased from 0.99 to 0.14 at both Fr = ∞ and 1. Thus, reducing the density ratio has the effect of increasing the derivative of the pressure disturbance within the shear-layer. As the Fr value is reduced from infinity to 1, the derivative of the pressure disturbance increased within the shear-layer for S = 0.99, but does not change significantly for S = 0.14 within the shear-layer, except at the peaks where the absolute value of the amplitude of the derivative of the pressure disturbance is decreased.

4.3.2: Axial and radial velocity disturbances

Equations (2.18) and (2.21) are rewritten below for the amplitudes of the radial $\hat{v}$ and axial $\hat{u}$ components of the velocity disturbances

$$\hat{u} = -\frac{k\hat{p}}{\bar{\rho}\left(\bar{u}\tilde{k}-\tilde{\Omega}\right)} - \frac{\frac{d\bar{u}}{d\bar{r}}\frac{d\hat{p}}{d\bar{r}}}{\bar{\rho}\left(\bar{u}\tilde{k}-\tilde{\Omega}\right)^2} + i\frac{g\frac{d\bar{\rho}}{d\bar{r}}\frac{d\hat{p}}{d\bar{r}}}{\bar{\rho}^2\left(\bar{u}\tilde{k}-\tilde{\Omega}\right)^3} \qquad (4.6)$$

$$\hat{v} = i\frac{\frac{d\hat{p}}{d\bar{r}}}{\bar{\rho}\left(\bar{u}\bar{k} - \bar{\Omega}\right)} \tag{4.7}$$

The variation of the absolute value of the amplitude of the axial velocity disturbance in the radial direction as density ratio is decreased from S = 0.99 to S = 0.14 while Froude number is decreased from infinity to unity, obtained from the linear spatio-temporal stability analysis results for $R/\theta = 10$, is illustrated in Figure 4.45. As the radial distance increased from the jet axis, the absolute value of the amplitude of the axial velocity disturbance is decreased, until a region within the neighborhood of the jet radius (r = 10 at this axial location) where it varies in a wave-like manner and then continues decreasing to zero at a radial location at about five times the jet radius. At the jet axis (r = 0), as the density ratio is decreased from a value of S = 0.99 to S = 0.14 with Fr held constant at infinity, the absolute value of the amplitude of the axial velocity disturbance is increased by about 507%, while at Fr = 1 it is increased by about 518%. Kyle and Sreenivasan (1993) in their experiments on round variable-density jets with negligible buoyancy observed that the value of the centerline axial velocity disturbance became extraordinarily large (compared to constant that of a constant density jet) as the density ratio was lowered below the critical density ratio.

Figure 4.46 depicts the variation of the absolute value of the amplitude of the radial velocity disturbance with the radial distance as density ratio is decreased from S = 0.99 to S = 0.14 while Froude number is decreased from infinity to unity; obtained from the linear spatio-temporal stability analysis results for $R_\theta = 10$. All the curves start at zero at the jet axis, increase to a maximum near the jet radius and then decrease again to zero at a radial location far from the jet axis. Thus, at the jet axis there is no radial component of the velocity disturbance, but within the shear-layer the radial component of the velocity disturbance increases (due to mixing and entrainment of the ambient gas by the jet) to a maximum at the jet radius, where the center of the vortex structures usually occurs, and then decreases to zero far away from the jet where no disturbances exist. At Fr = ∞, as the density ratio is decreased from a value of S = 0.99 to S = 0.14, the maximum value of the absolute value of the amplitude of the radial velocity disturbance is increased by about 53% and the radial location corresponding to the maximum value is decreased by about 28%. Also, as S is decreased from 0.99 to 0.14, at Fr = ∞, the radial location far away from the jet axis where the absolute value of the amplitude of the radial velocity disturbance decreased to zero is increased by about 40%. Similar trends are observed at Fr = 1 although the maximum value of the absolute value of the amplitude of the radial velocity disturbance is increased by about 46%.

Figures 4.47 and 4.48 are the counterparts of Figures 4.45 and 4.46, respectively, for results obtained from the linear temporal stability analysis. The same trends observed in Figures 4.45 and 4.46 are observed in Figures 4.47 and 4.48, except that the wave-like variation within the neighborhood of the jet radius is more pronounced in Figure 4.47 than in Figure 4.45 and the radial locations away from the jet axis where the curves reduce to zero occur at the same location for all the curves from the linear temporal stability analysis (this radial location is even about 40% less than that for S = 0.99 of the results from the linear spatio-temporal stability analysis). Also the maximum values are about an order of magnitude higher than in the results from the linear spatio-temporal stability analysis.

4.3.3: <u>Vorticity in the azimuthal direction</u>

The angular velocity of the vortices in the shear-layer is directly proportional to the vorticity. An investigation of the effects of density ratio and Froude number on the vorticity will help understand the increased mixing and entrainment associated with absolutely unstable round jets.

The component in the azimuthal direction is the only component of the vorticity present for the varicose mode disturbance. The vorticity component in the azimuthal direction is given by

$$\omega_\theta = \frac{dv}{d\bar{x}} - \frac{du}{d\bar{r}} \tag{4.8}$$

Substitution of equations (2.4) into equation (4.8) yields, for the amplitude of the vorticity,

$$\hat{\omega}_\theta = i\bar{k}\hat{v} - \frac{d\bar{u}}{d\bar{r}} - \frac{d\hat{u}}{d\bar{r}} \tag{4.9}$$

Substituting equations (4.6) and (4.7) in equation (4.9), and simplifying, we obtain

$$\hat{\omega}_{\theta} = -\frac{d\bar{u}}{d\bar{r}} - \left[\frac{\bar{k}\frac{d\bar{\rho}}{d\bar{r}}}{\bar{\rho}^2\left(\bar{u}\bar{k}-\bar{\Omega}\right)} + \frac{\bar{k}^2\frac{d\bar{u}}{d\bar{r}}}{\bar{\rho}\left(\bar{u}\bar{k}-\bar{\Omega}\right)^2} \right]\hat{p}$$

$$+\left\{ \begin{array}{l} \dfrac{\frac{d^2\bar{u}}{d\bar{r}^2}}{\bar{\rho}\left(\bar{u}\bar{k}-\bar{\Omega}\right)^2} - \dfrac{\frac{d\bar{u}}{d\bar{r}}\frac{d\bar{\rho}}{d\bar{r}}}{\bar{\rho}^2\left(\bar{u}\bar{k}-\bar{\Omega}\right)^2} - \dfrac{2k\left(\frac{d\bar{u}}{d\bar{r}}\right)^2}{\bar{\rho}\left(\bar{u}\bar{k}-\bar{\Omega}\right)^3} \\ +ig\left[\dfrac{2\left(\frac{d\bar{\rho}}{d\bar{r}}\right)^2}{\bar{\rho}^3\left(\bar{u}\bar{k}-\bar{\Omega}\right)^3} - \dfrac{\frac{d^2\bar{\rho}}{d\bar{r}^2}}{\bar{\rho}^2\left(\bar{u}\bar{k}-\bar{\Omega}\right)^3} + \dfrac{3k\frac{d\bar{u}}{d\bar{r}}\frac{d\bar{\rho}}{d\bar{r}}}{\bar{\rho}^2\left(\bar{u}\bar{k}-\bar{\Omega}\right)^4} \right] \end{array} \right\}\frac{d\hat{p}}{d\bar{r}} \qquad (4.10)$$

$$+\left[\frac{\frac{d\bar{u}}{d\bar{r}}}{\bar{\rho}\left(\bar{u}\bar{k}-\bar{\Omega}\right)^2} - i\frac{g\frac{d\bar{\rho}}{d\bar{r}}}{\bar{\rho}^2\left(\bar{u}\bar{k}-\bar{\Omega}\right)^3} \right]\frac{d^2\hat{p}}{d\bar{r}^2}$$

Our attention is drawn to the increased number of terms in equation (4.10) due to the variable density. Also, for a constant density there is no effect of gravity on the vorticity.

The variation of the absolute value of the amplitude of the vorticity with the radial location as density ratio is decreased from S = 0.99 to S = 0.14 while Froude number is decreased from infinity to unity, obtained from the linear spatio-temporal stability analysis results for $R/\theta = 10$, is illustrated in Figure 4.49. Notice that, for all the cases shown, the vorticity is within the region of the shear-layer of the jet only. At Fr = ∞, as the density ratio is reduced from S = 0.99 to S = 0.14, the vorticity is increased with the maximum value of the absolute value of the amplitude of the vorticity increasing by about 500%. The radial location corresponding to the maximum value also increases by about 20% as density ratio is reduced from S = 0.99 to S = 0.14. Also, notice that the curve at S = 0.14 has two humps unlike that at S = 0.99 which has one peak. The same trend is noticed at Fr = 1 as density ratio is reduced from S = 0.99 to S = 0.14. The increase in vorticity as the density ratio is reduced helps explain the increased mixing observed in experiments on absolutely unstable jets by previous researchers (see Monkewitz et al., 1990; Subbarao and Cantwell, 1992; Kyle and Sreenivasan, 1993; Cetegen and Kasper, 1996). As the Froude number is reduced from infinity to unity, at S = 0.99, the maximum value of the absolute value of the amplitude of the vorticity is almost doubled; but at S = 0.14 the maximum value only increases by about 11%. Thus the Froude number has a greater influence on the vorticity at the high-density ratio value.

Figure 4.50 is the counterpart of Figure 4.49 obtained from the linear temporal stability analysis. Again, the vorticity is restricted to the shear-layer. At Fr = ∞, as the density ratio is reduced from a value of S = 0.99 to S = 0.14, the maximum value of the absolute value of the amplitude of the vorticity is increased by about 650% and the radial location corresponding to the maximum values is increased by about 22%. At Fr = 1, the maximum value of the absolute value of the amplitude of the vorticity is almost doubled as the density ratio is reduced from S = 0.99 to S = 0.14, and the radial location corresponding to the maximum values is, again, increased by about 22%. As the Froude number is decreased from Fr = ∞ to Fr = 1, at S = 0.99, the maximum value of the absolute value of the amplitude of the vorticity is increased by about 525% and there is no significant effect of Fr on the radial location corresponding to the maximum values. The same trends are observed at S = 0.14, except that the maximum value of the absolute value of the amplitude of the vorticity is increased by about 60%.

4.4: Comparison with experimental data

The Strouhal number variation with Richardson number is usually used in experimental studies on buoyant low-density gas jets to describe the pulsating frequency of the jets (Subbarao and Cantwell, 1992; Cetegen and Kasper, 1996; Pasumarthi, 2000). The Strouhal number is a nondimensional frequency that describes the pulsating oscillation frequency of the jet. Thus the Strouhal number results of this absolute stability analysis are compared to experimental findings of Subbarao and Cantwell (1992) and Pasumarthi (2000). In order to do this an attempt was made, with the experimental results in mind, to determine the best combination of the variables that affect the absolute instability of the jet. When a jet is absolutely unstable the resulting disturbances of an initially localized impulse eventually contaminate the entire flow (Yu and Monkewitz, 1990). It was observed in the paper by Monkewitz and Sohn (1988) that the axial location where the maximum absolute growth rate occurs depends on the density ratio for Fr = ∞. In this chapter it was observed that the axial location corresponding to the maximum absolute temporal growth rate also depends on the Froude number. Although, the variation of the maximum absolute temporal growth rate with axial location was not studied it was observed in Figure 4.12 that the absolute temporal growth rate decreases as the jet proceeds downstream and so using results obtained at the jet exit (where, $x = 0$ and $R/\theta = 25$) was favored. Next an Sc value of 1.43 (for a helium jet injected into ambient air) and $\Delta r = 12.5$ (corresponding to a dimensional $\Delta r = 0.5R$ at $R/\theta = 25$) was also favored. These values while not being values obtained from the experiments used in the comparison are not physically unrealistic.

The comparison of Strouhal number versus Richardson number ($2/Fr^2$) data of this study with the experimental data of Subbarao and Cantwell (1992) for a helium jet discharged into ambient air at a velocity twice the co-flow velocity is illustrated in Figure 4.51. To show the effect of combining the factors affecting the absolute instability of a round jet, Strouhal number results for "Sc = 1 & $\Delta r = 0$" and "Sc = 1.43 & $\Delta r = 12.5$" are compared to the data from Subbarao and Cantwell (1992). When the Strouhal numbers from the "Sc = 1 & $\Delta r = 0$" combination are compared to those of Subbarao and Cantwell (1992) the data do not seem to agree well especially at high Richardson numbers. The data from Subbarao and Cantwell (1992) is about an order of magnitude higher than the Strouhal numbers from the "Sc = 1 & $\Delta r = 0$" combination. Considering the effects of Sc and Δr using the

Strouhal numbers for the "Sc = 1.43 & Δr = 12.5" combination, there is closer agreement with the Subbarao and Cantwell data. The Strouhal numbers for the "Sc = 1.43 & Δr = 12.5" combination are within the same order of magnitude of those of Subbarao and Cantwell (1992). The Strouhal numbers for the "Sc = 1.43 & Δr = 12.5" combination are over ten times those from the "Sc = 1 & Δr = 0" combination, thus it appears that when Schmidt number and the lateral shift between the velocity and density profiles are taken into consideration there is better agreement with experimental data taking into account experimental uncertainties.

Figure 4.52 depicts the comparison of results from this study to those of Pasumarthi (2000) and Kyle and Sreenivasan (1993) for a helium jet injected into air. Note that the experiments by Kyle and Sreenivasan (1993) were at negligible buoyancy (Ri = 0) and at high Reynolds numbers. Again the effect of combining the factors affecting the absolute instability of a round jet is apparent. From the comparison with experimental data above the importance of combining the factors affecting the absolute instability of a round jet at the axial location where the maximum absolute growth rate occurs is obvious. Unfortunately, the experimental studies above did not document the values of these variables.

Table 4.1: Comparison of absolute stability results for R/θ = 25 (x/R = 0.0)

S	k_r^o	k_i^o	Ω_r^o	Ω_i^o
	Monkewitz and Sohn (1988) data			
1	0.026	-0.072	0.068	-0.0102
0.72	0.026	-0.070	0.062	-0.0018
0.66	0.026	-0.068	0.059	0.0002
0.5	0.026	-0.064	0.054	0.006
	Data from present study			
1	0.0340	-0.0730	0.0599	-0.0064
0.72	0.0341	-0.0684	0.0538	-0.0001
0.66	0.0340	-0.0671	0.0521	0.0013
0.5	0.0334	-0.0630	0.0467	0.0052

Table 4.2: Comparison of absolute stability results for R/θ = 10 (x/R = 2.0)

S	k_r^o	k_i^o	Ω_r^o	Ω_i^o
	Monkewitz and Sohn (1988) data			
1	0.097	-0.155	0.115	-0.0135
0.72	0.100	-0.140	0.100	-0.0065
0.66	0.099	-0.135	0.095	-0.005
0.5	0.098	-0.120	0.085	0
	Data from present study			
0.99	0.1037	-0.1578	0.1165	-0.0183
0.72	0.1000	-0.1450	0.1054	-0.0084
0.66	0.0990	-0.1415	0.1025	-0.0059
0.5	0.0949	-0.1312	0.0934	0.0012

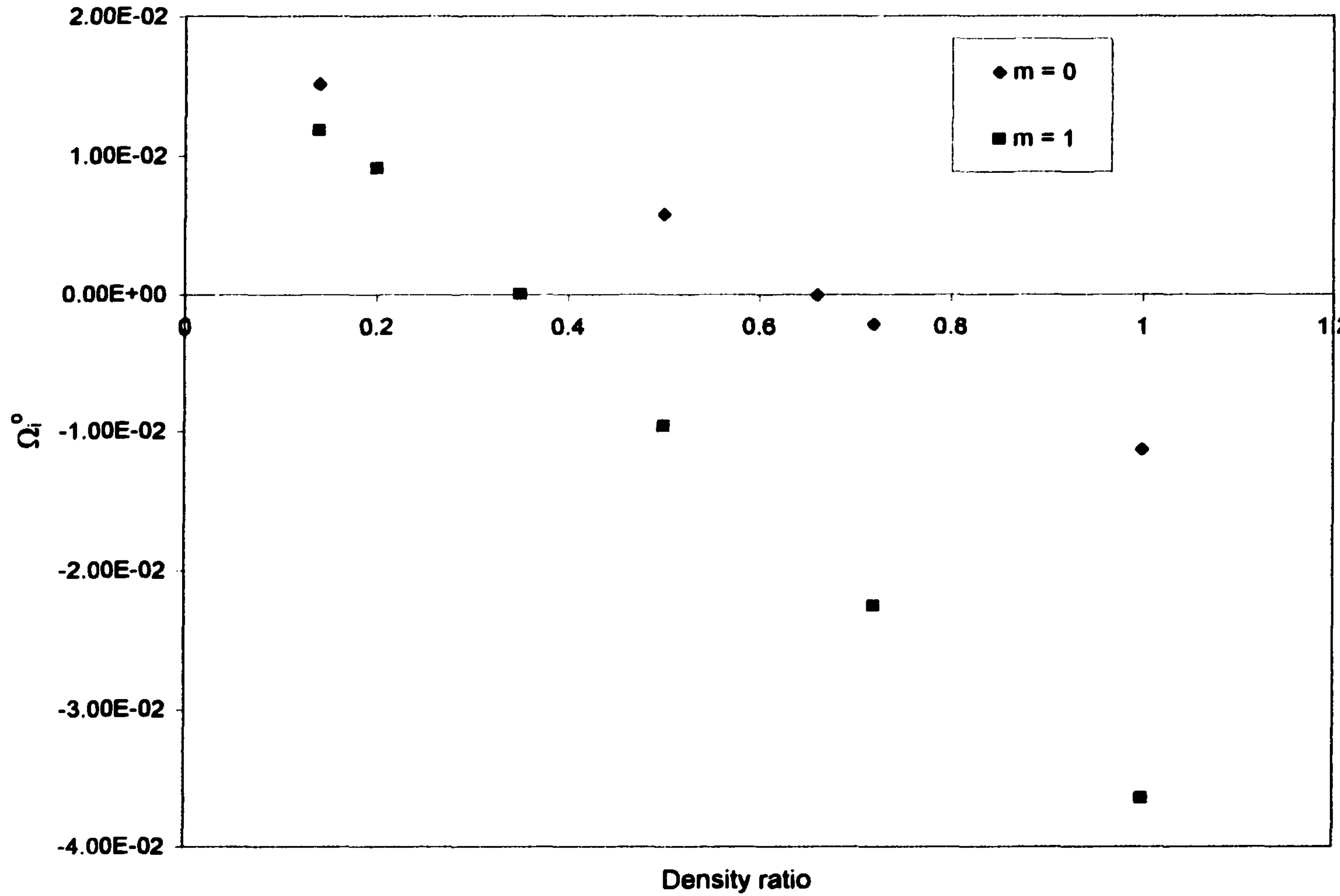

Figure 4.A1: Ω_i^o vs density ratio for m = 0 and m = 1
of an inviscid top-hat jet bounded by a cylinderical vortex sheet

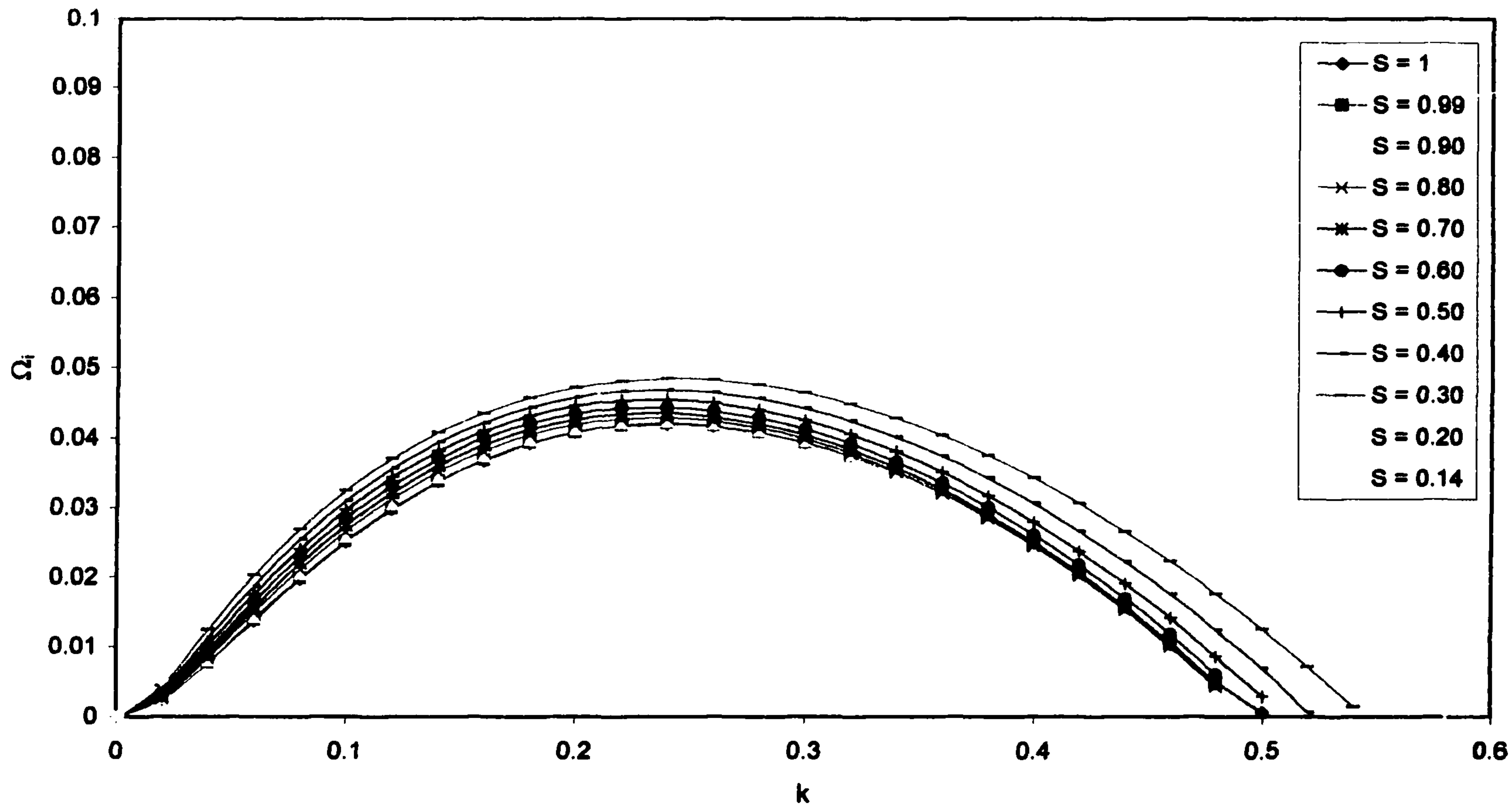

Figure 4.1: Temporal growth rate Ω_i as a function of wavenumber k
for m = 0, R/θ = 10, Fr = infinity, S = 1, 0.99, 0.9, 0.8, 0.7, 0.6, 0.5, 0.4, 0.3, 0.2, 0.14

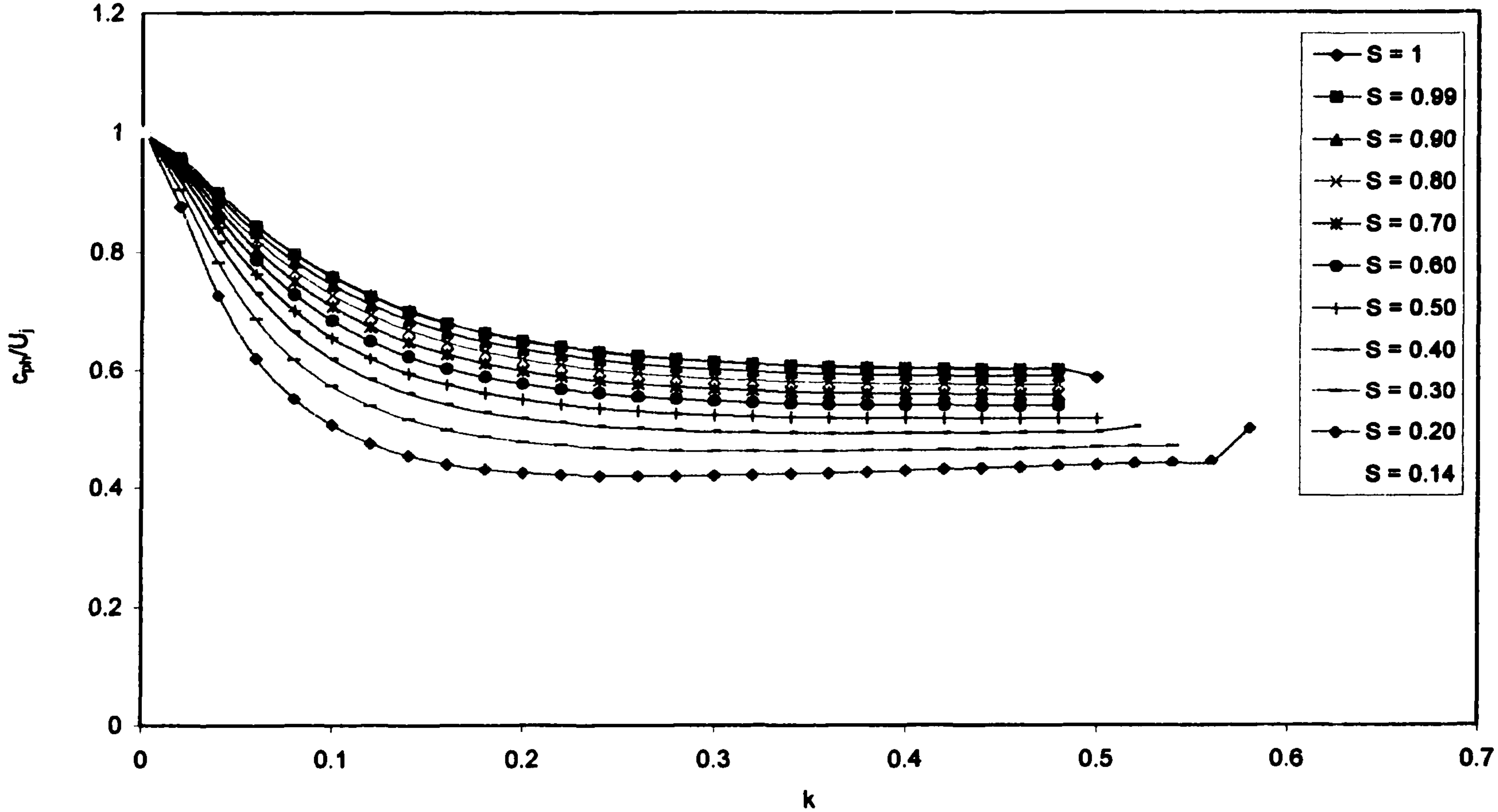

Figure 4.2: Phase velocity c_{ph} as a function of wavenumber k
for m = 0, R/θ = 10, Fr = infinity, S = 1, 0.99, 0.9, 0.8, 0.7, 0.6, 0.5, 0.4, 0.3, 0.2, 0.14

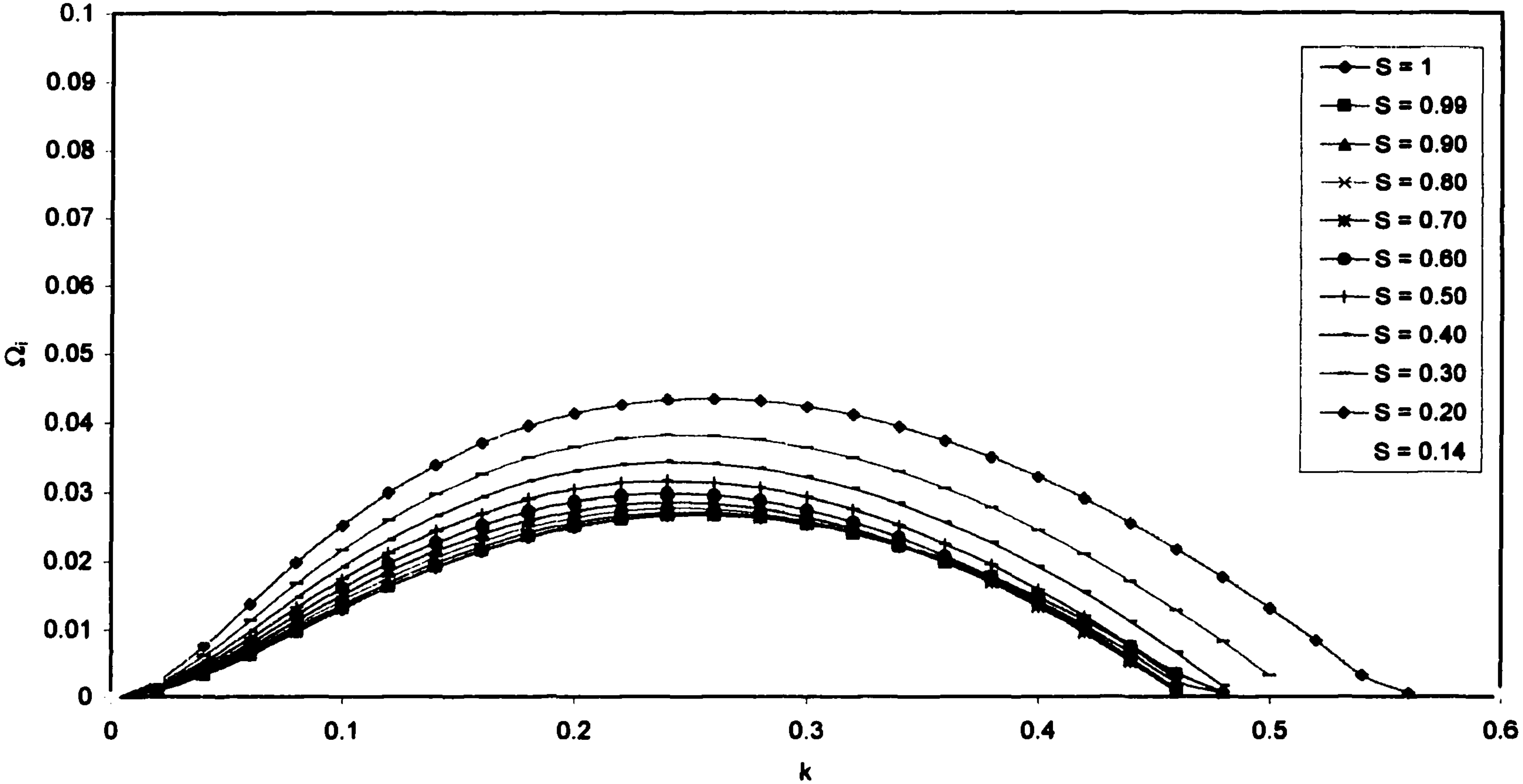

Figure 4.3: Temporal growth rate Ω_i as a function of wavenumber k for m = 0, R/θ = 5, Fr = infinity, S = 1, 0.99, 0.9, 0.8, 0.7, 0.6, 0.5, 0.4, 0.3, 0.2, 0.14

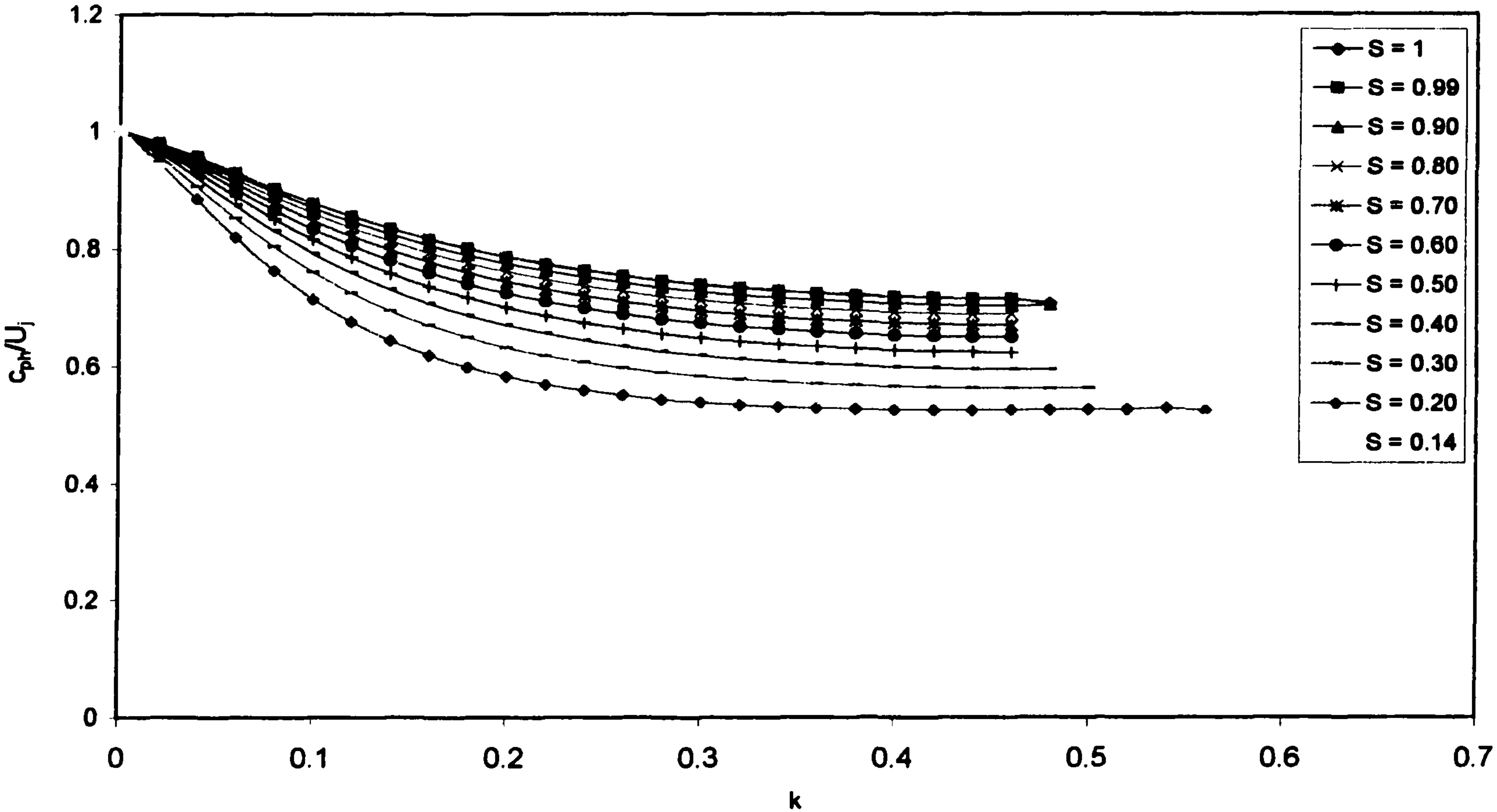

Figure 4.4: Phase velocity c_{ph} as a function of wavenumber k
for m = 0, R/θ = 5, Fr = infinity, S = 1, 0.99, 0.9, 0.8, 0.7, 0.6, 0.5, 0.4, 0.3, 0.2, 0.14

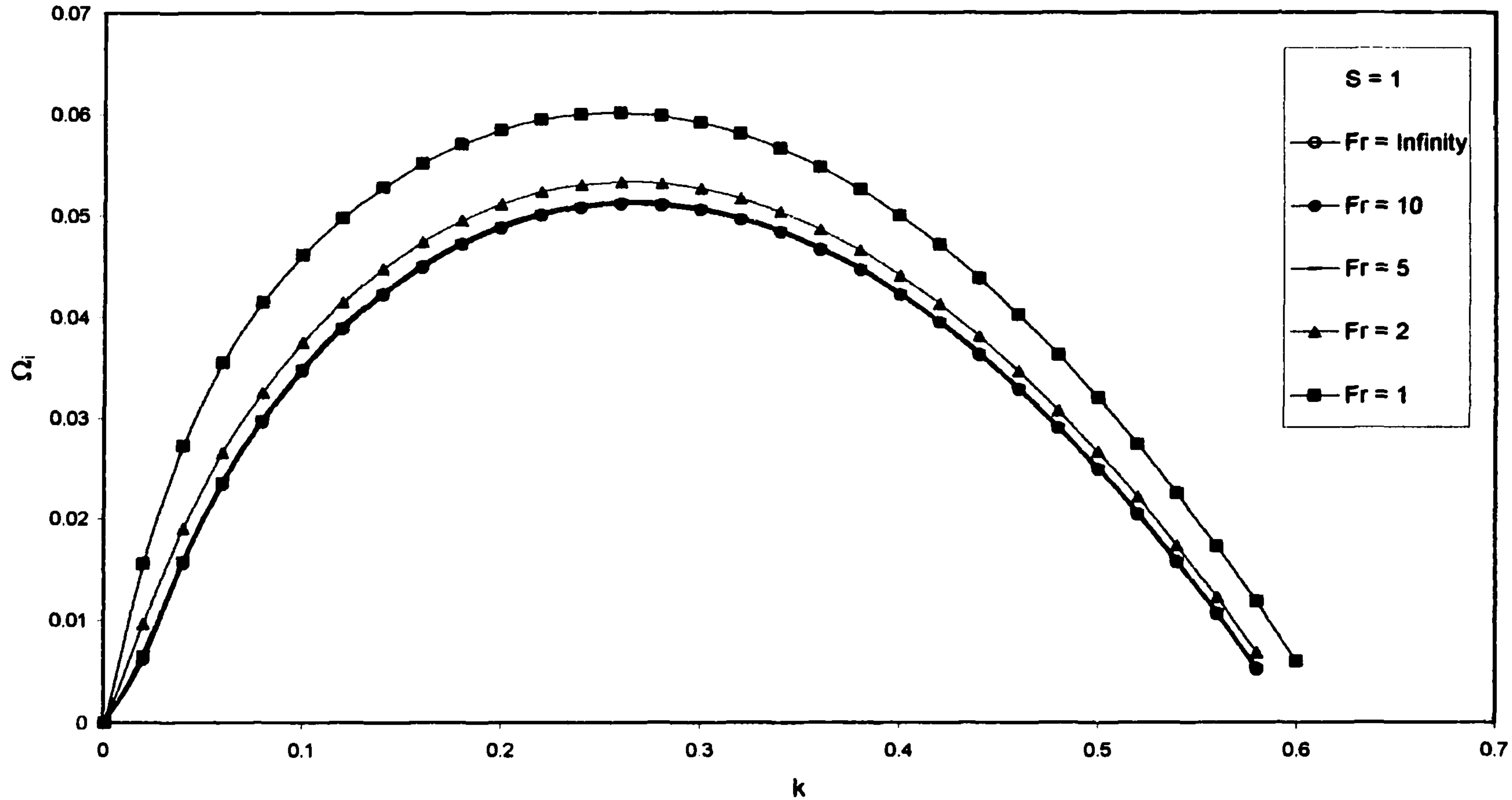

Figure 4.5: Temporal growth rate Ω_i as a function of wavenumber k
for m = 0, R/θ = 10, S = 1 and 0.14, Fr = Infinity, 10, 5, 2, 1

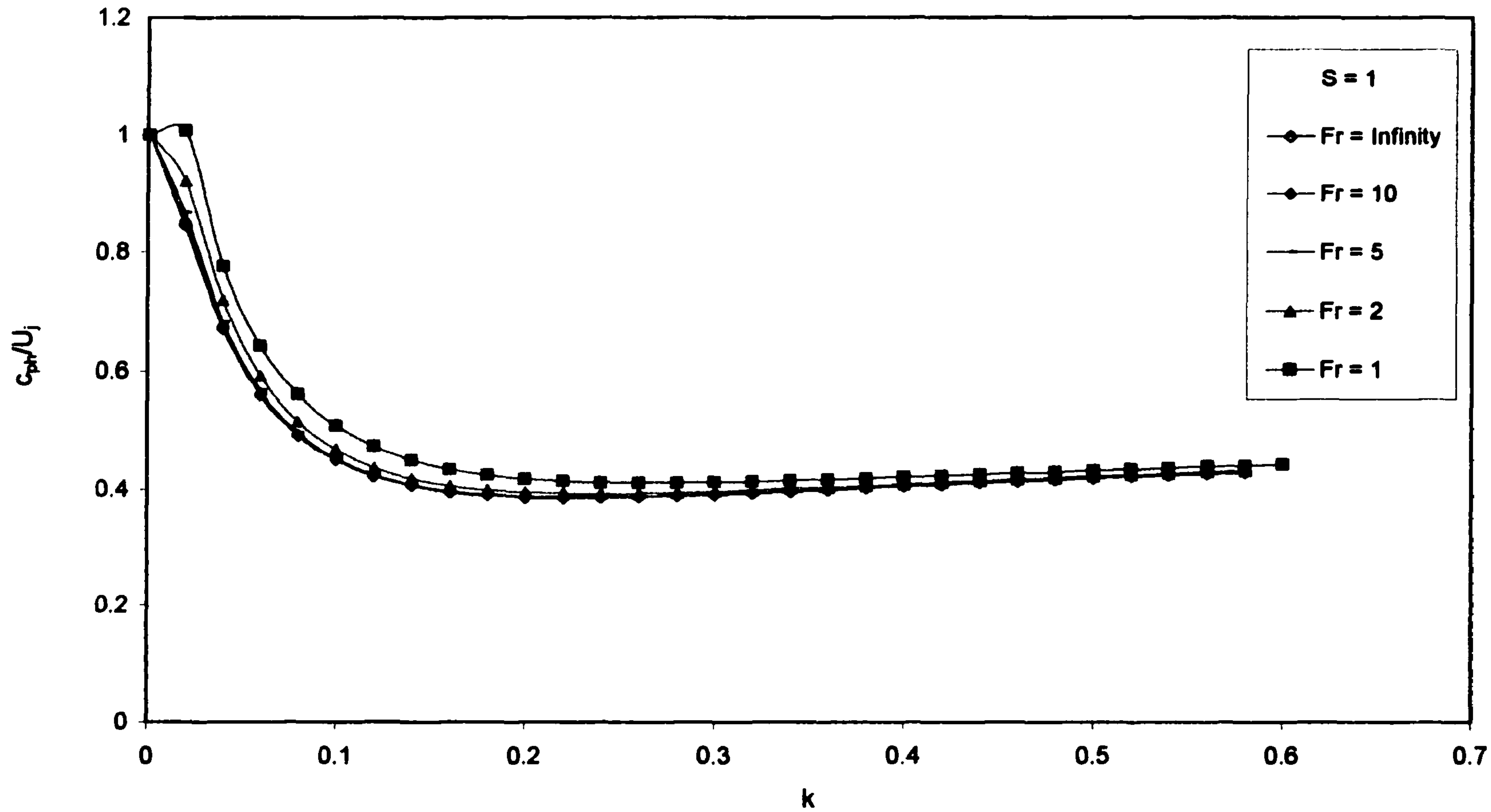

Figure 4.6: Phase velocity c_{ph} as a function of wavenumber k
for m = 0, R/θ = 10, S = 1 and 0.14, Fr = Infinity, 10, 5, 2, 1

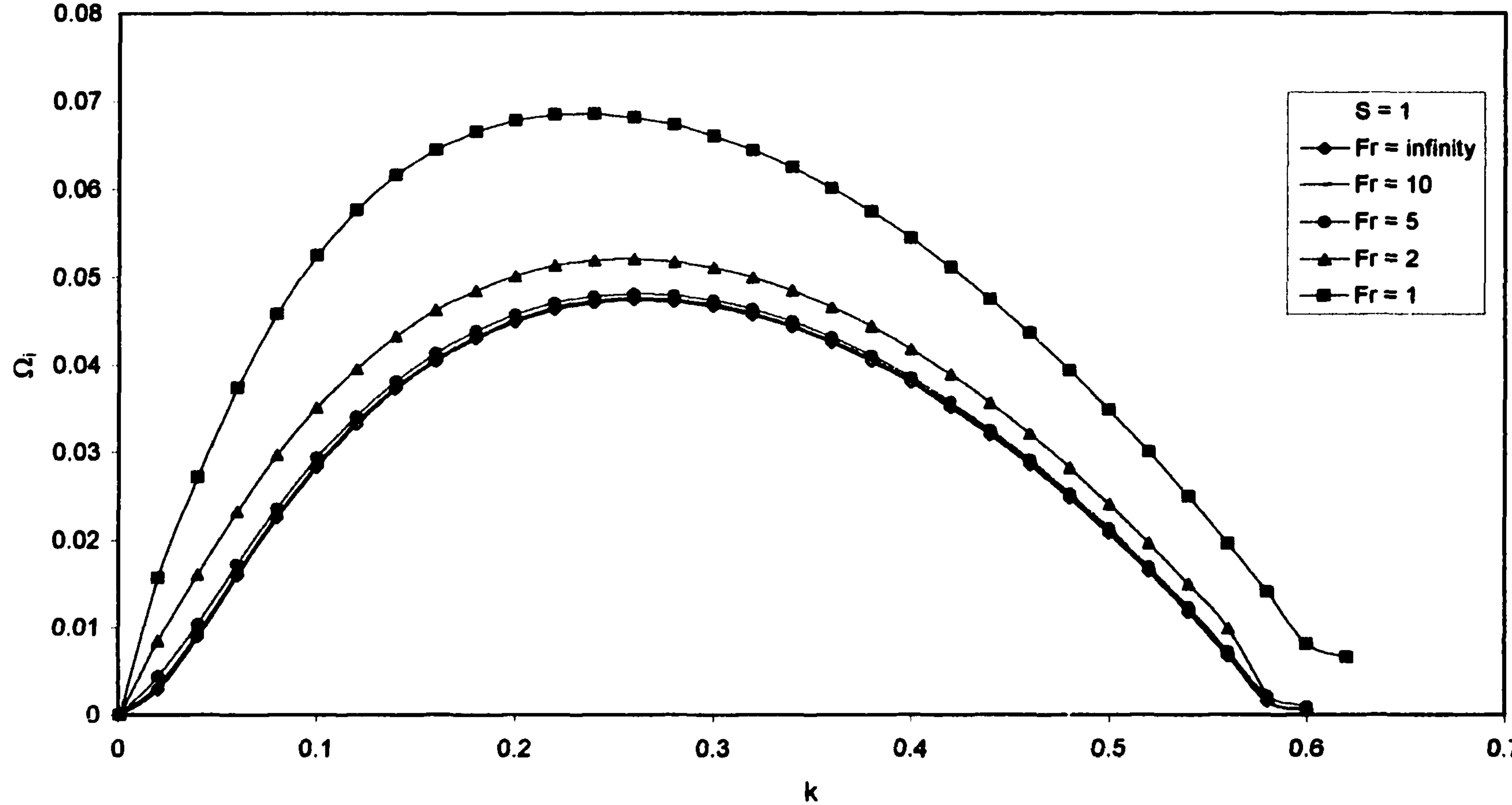

Figure 4.7: Temporal growth rate Ω_i as a function of wavenumber k
for m = 0, R/θ = 5, S = 1 and 0.14, Fr = Infinity, 10, 5, 2, 1

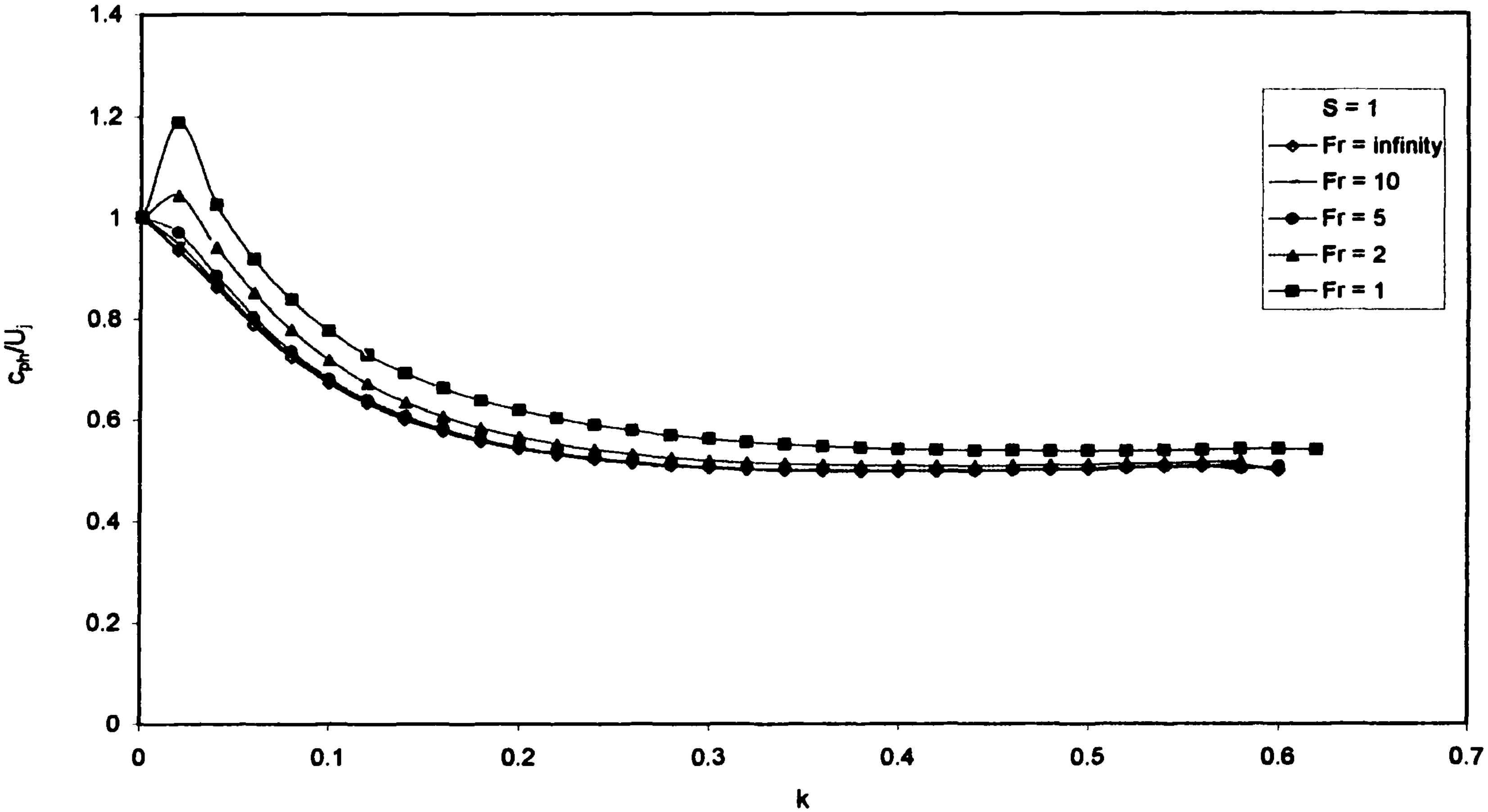

Figure 4.8: Phase velocity c_{ph} as a function of wavenumber k
for m = 0, R/θ = 5, S = 1 and 0.14, Fr = Infinity, 10, 5, 2, 1

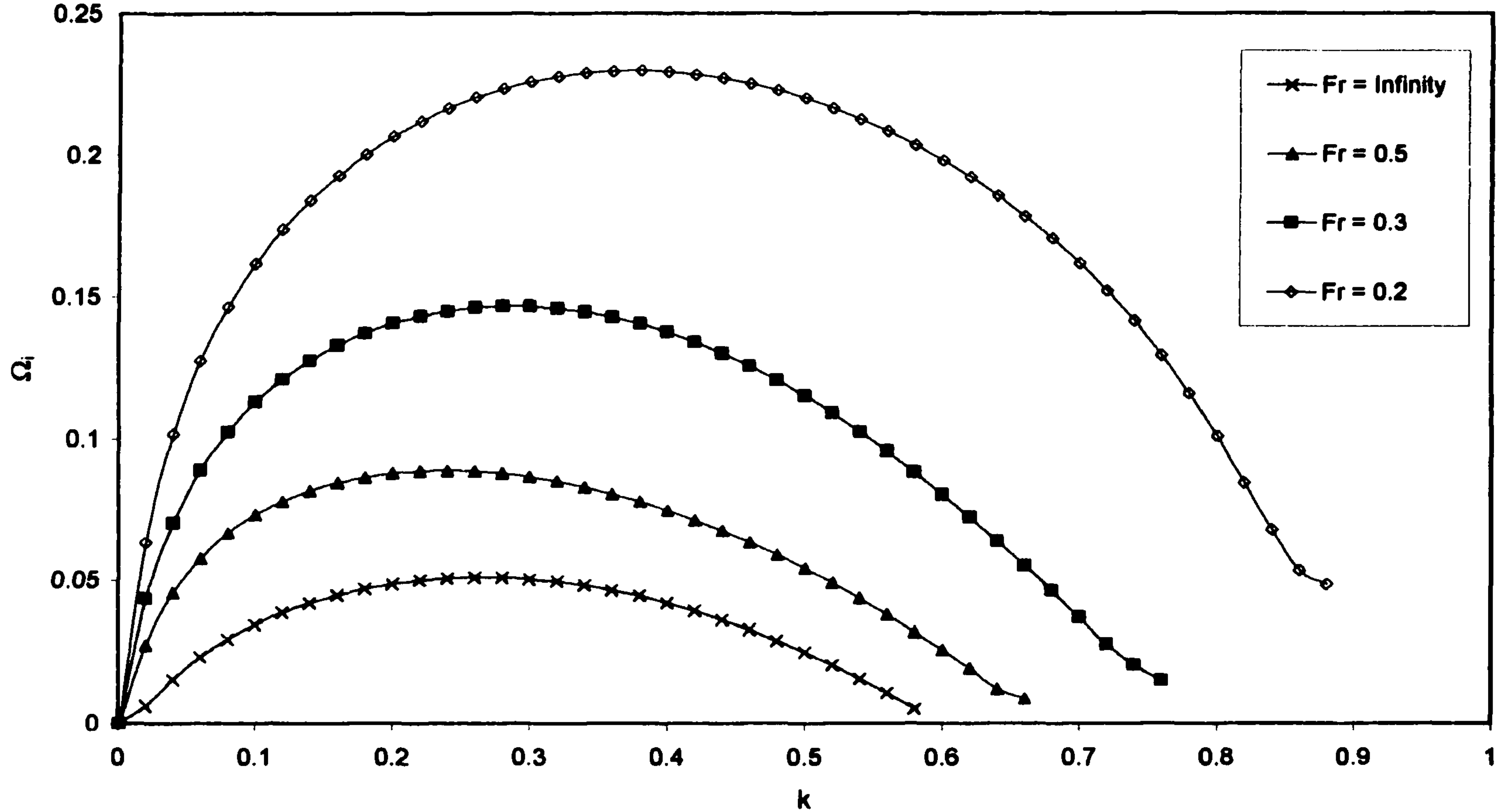

Figure 4.9: Temporal growth rate Ω_i as a function of wavenumber k
for m = 0; R/θ = 10; S = 0.14 with Fr = Infinity, 0.5, 0.3, 0.2

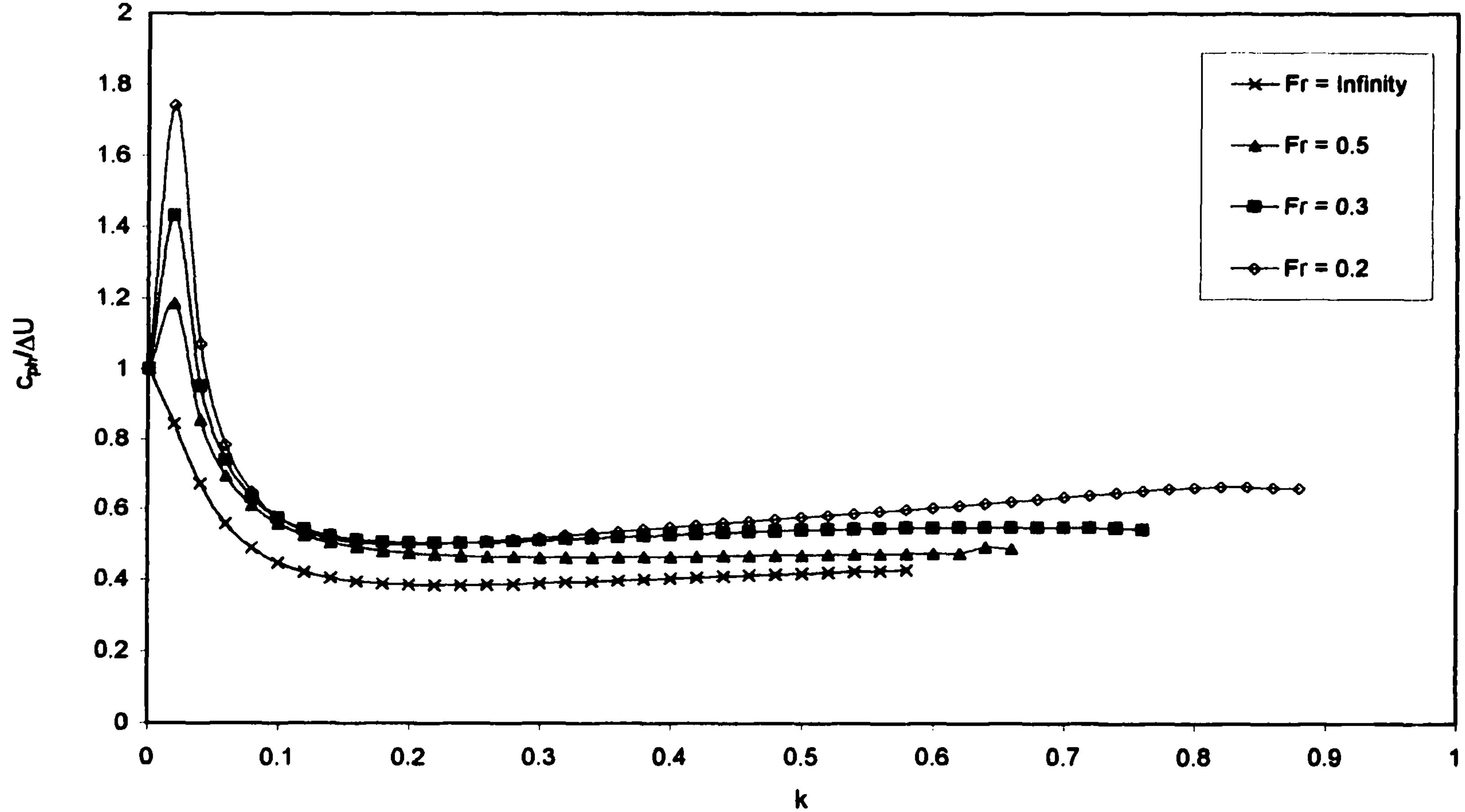

Figure 4.10: Phase velocity c_{ph} as a function of wavenumber k for m = 0; R/θ = 10; S = 0.14 with Fr = Infinity, 0.5, 0.3, 0.2

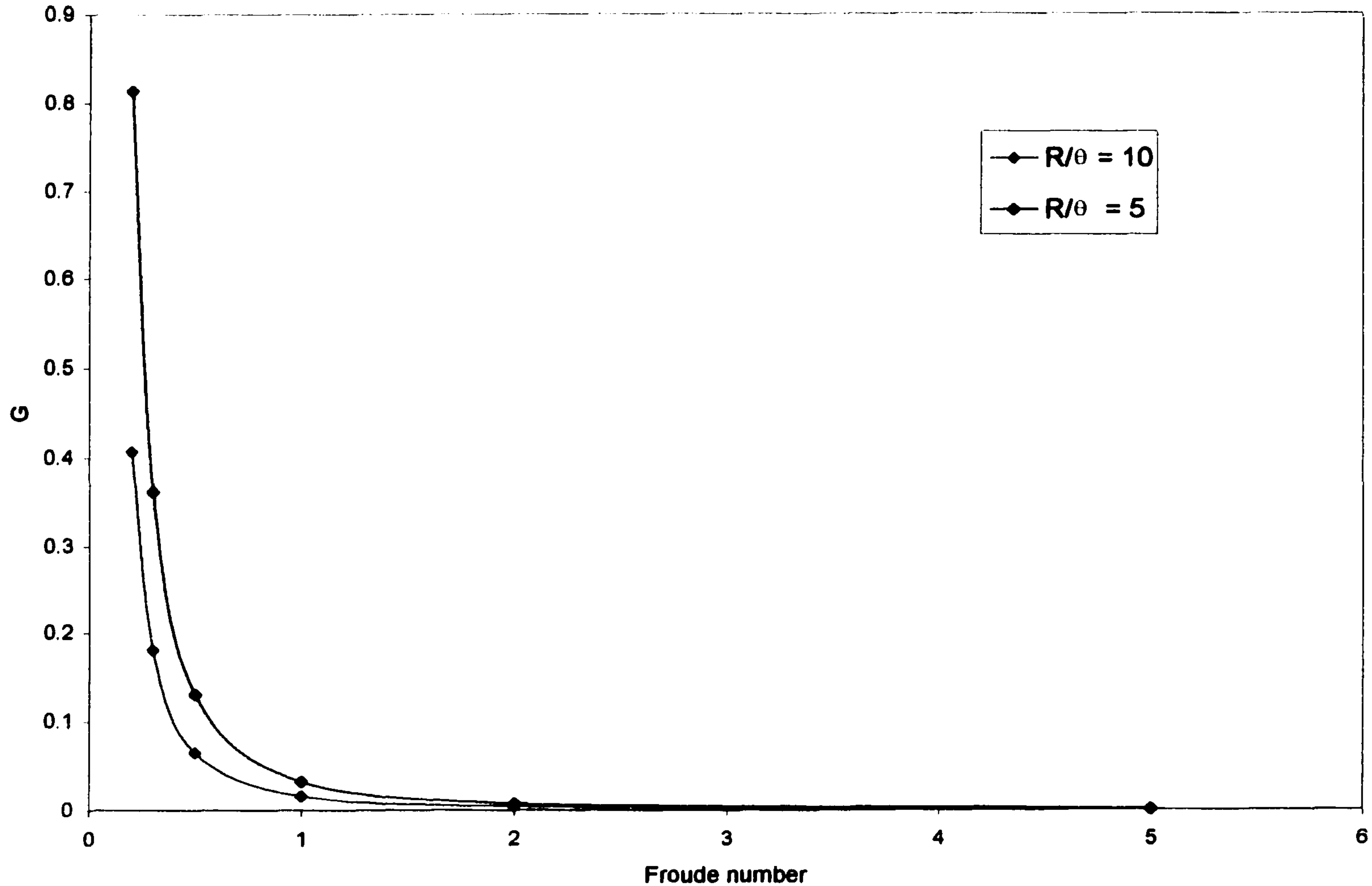

Figure 4.11: G vs Froude number for S = 0.14 at R/θ = 10 and 5

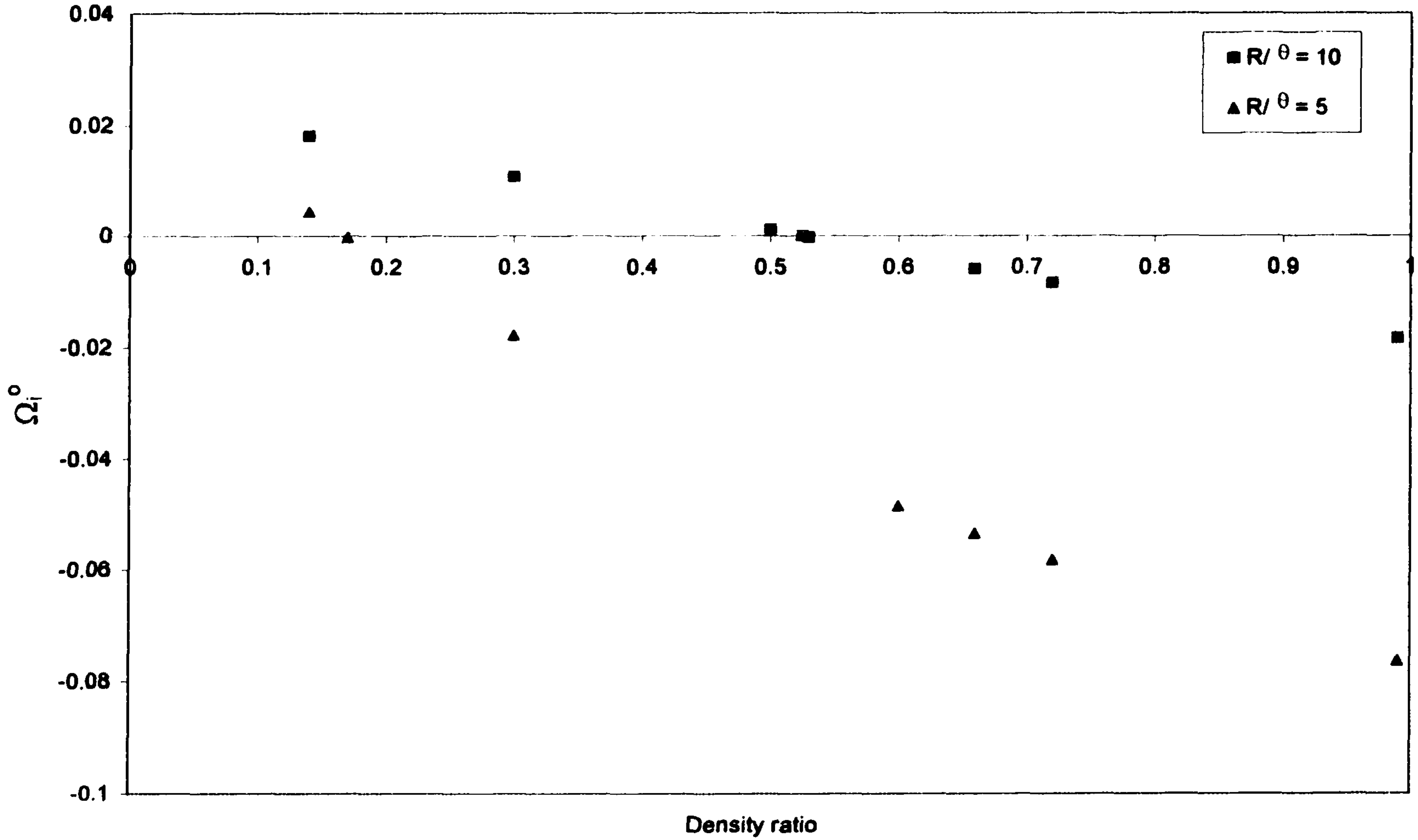

Figure 4.12: Ω_i^o vs density ratio at Fr = infinity

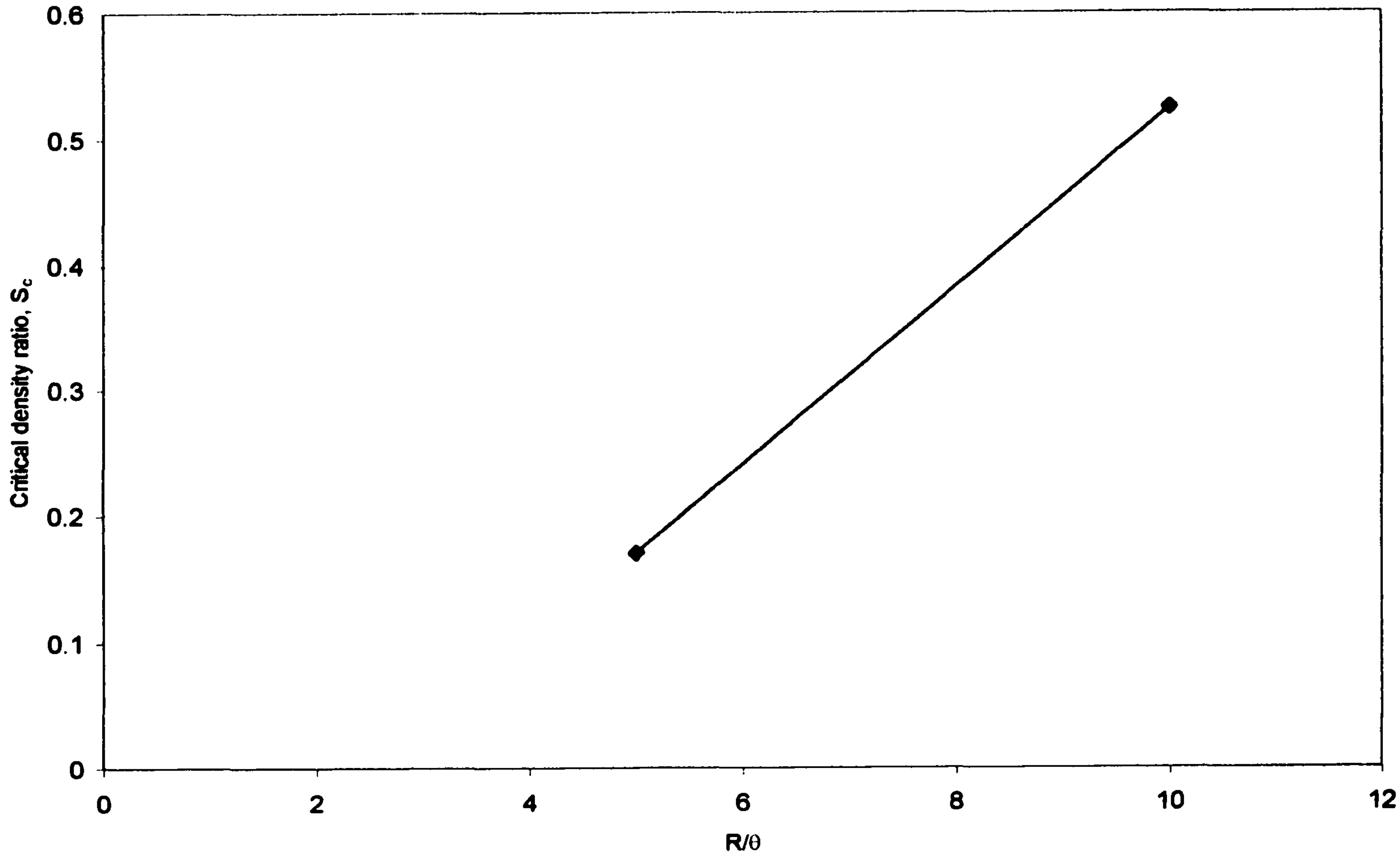

Figure 4.13: Critical density ratio, S_c vs R/θ at Fr = infinity

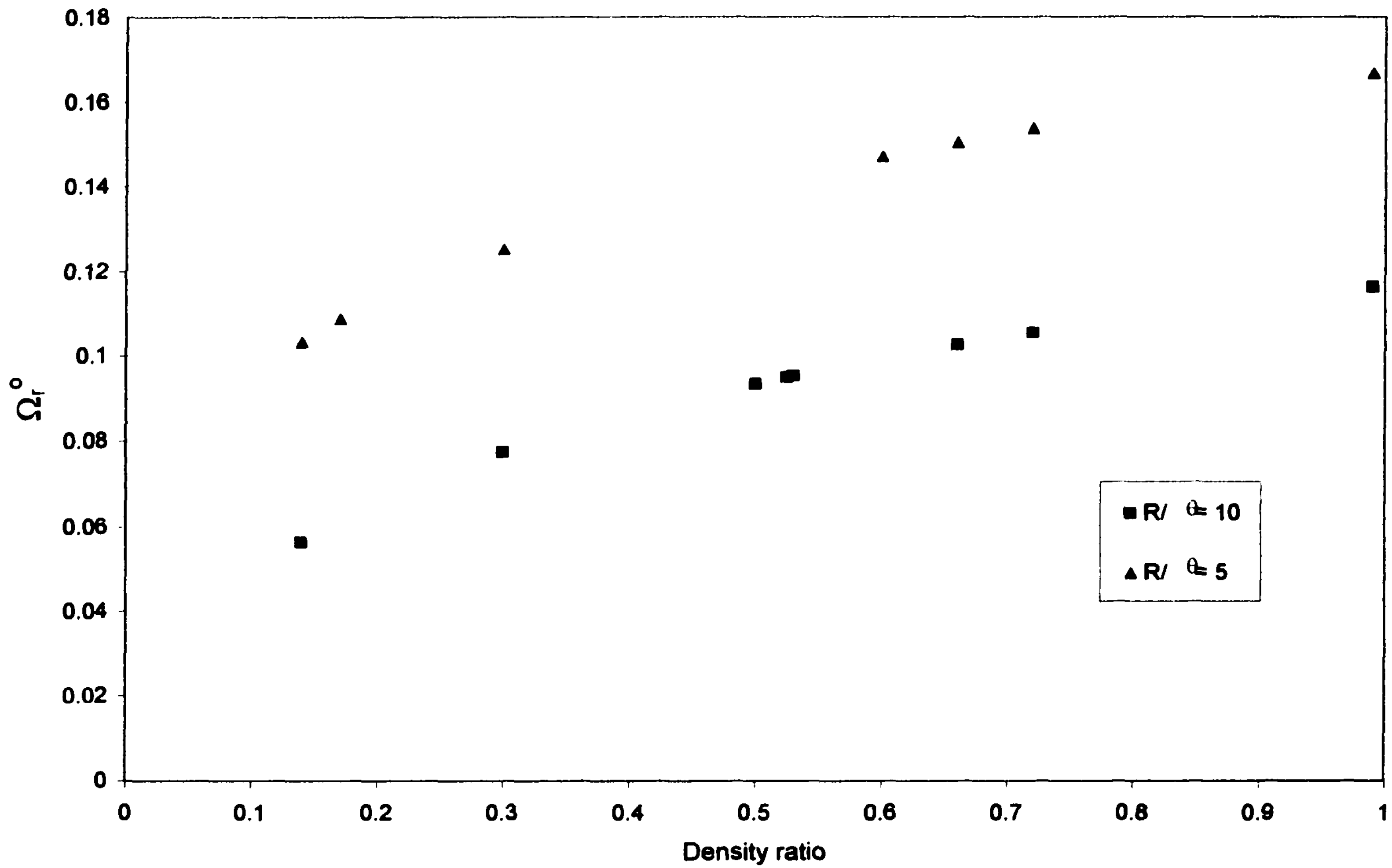

Figure 4.14: Ω_r^o vs density ratio at Fr = infinity

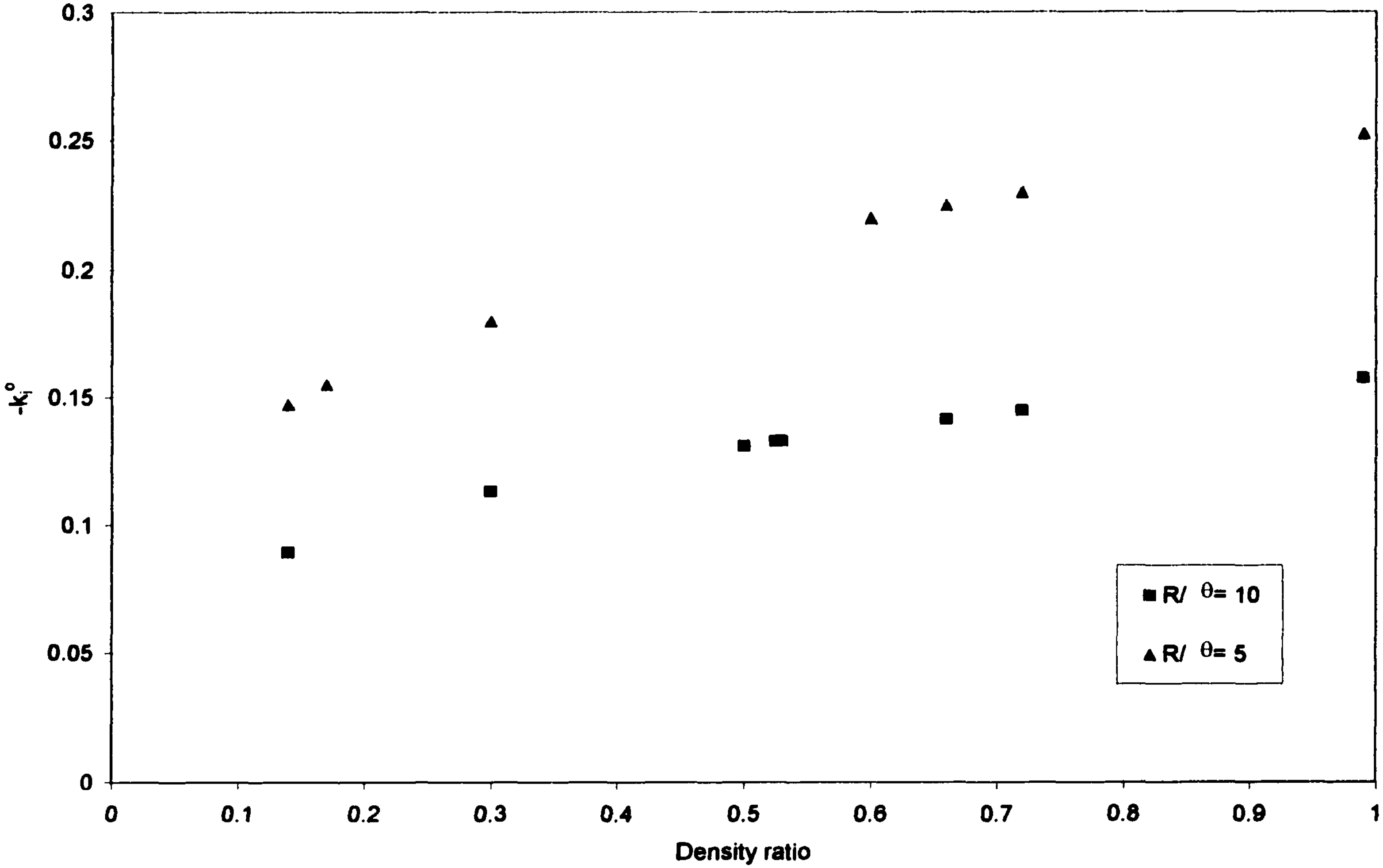

Figure 4.15: $-k_i^o$ vs density ratio at Fr = infinity

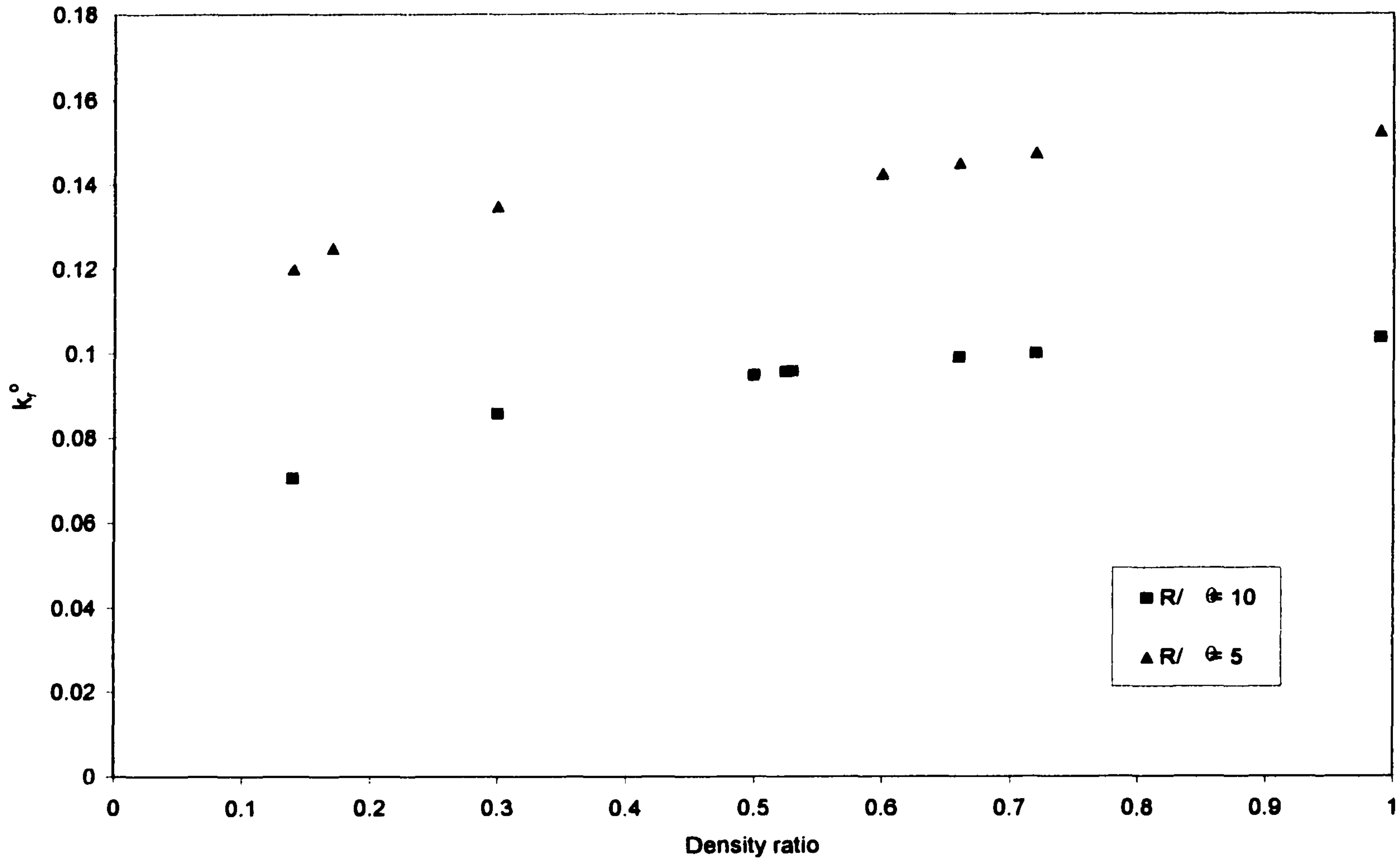

Figure 4.16: k_r^o vs Density ratio at Fr = infinity

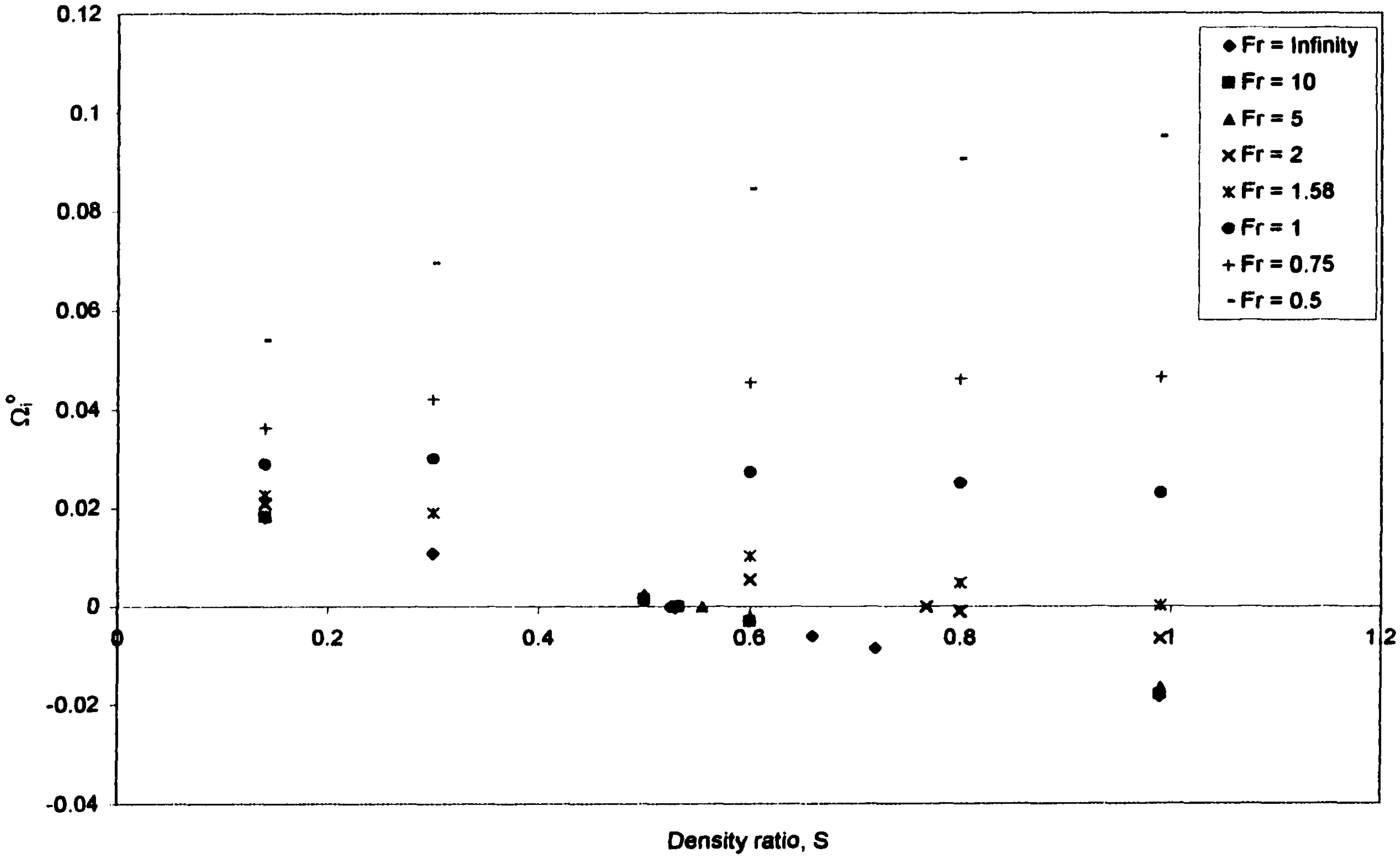

Figure 4.17: Ω_i^o vs density ratio at $R/\theta = 10$

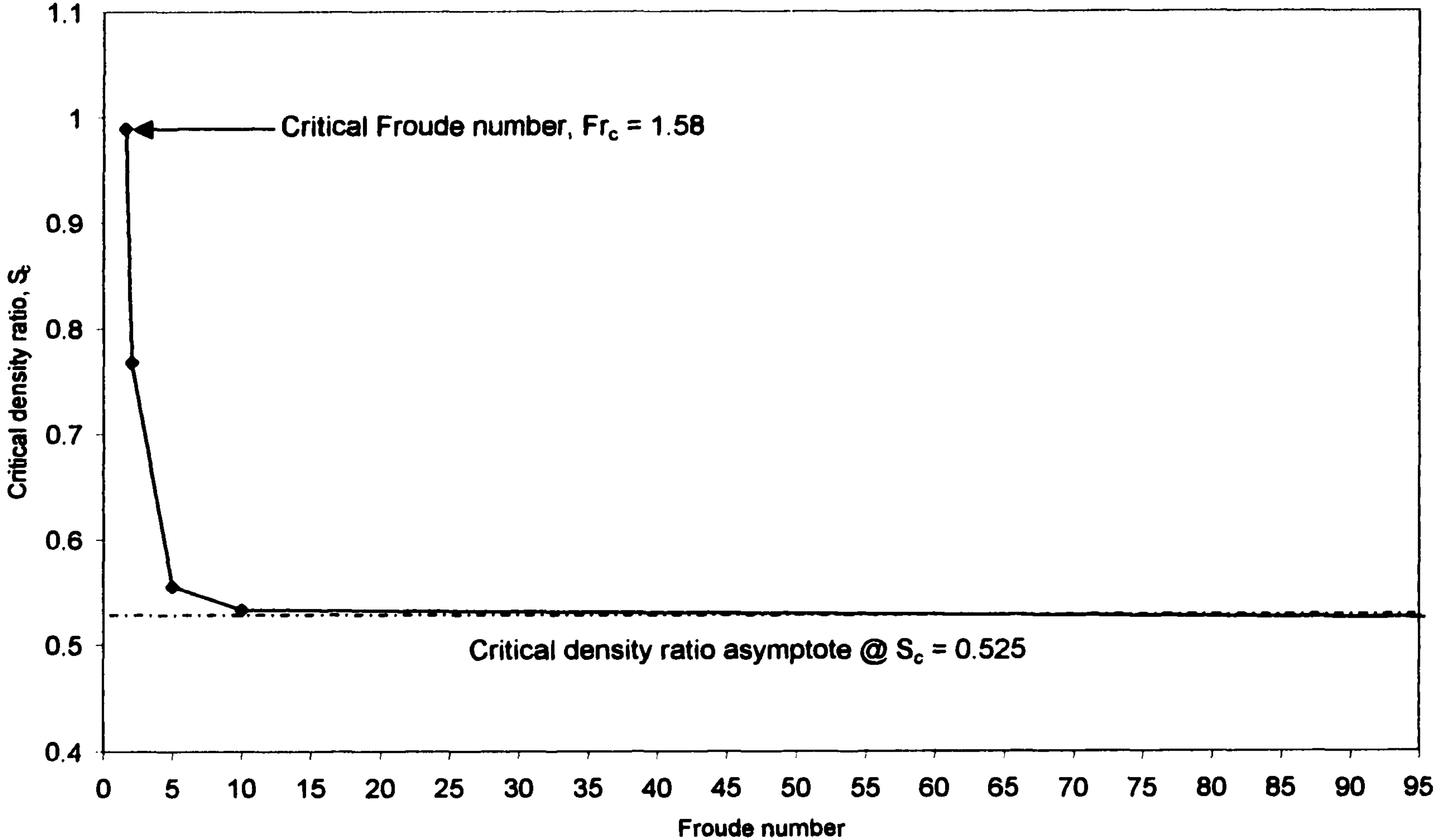

Figure 4.18: Critical density ratio, S_c vs Froude number at $R/\theta = 10$

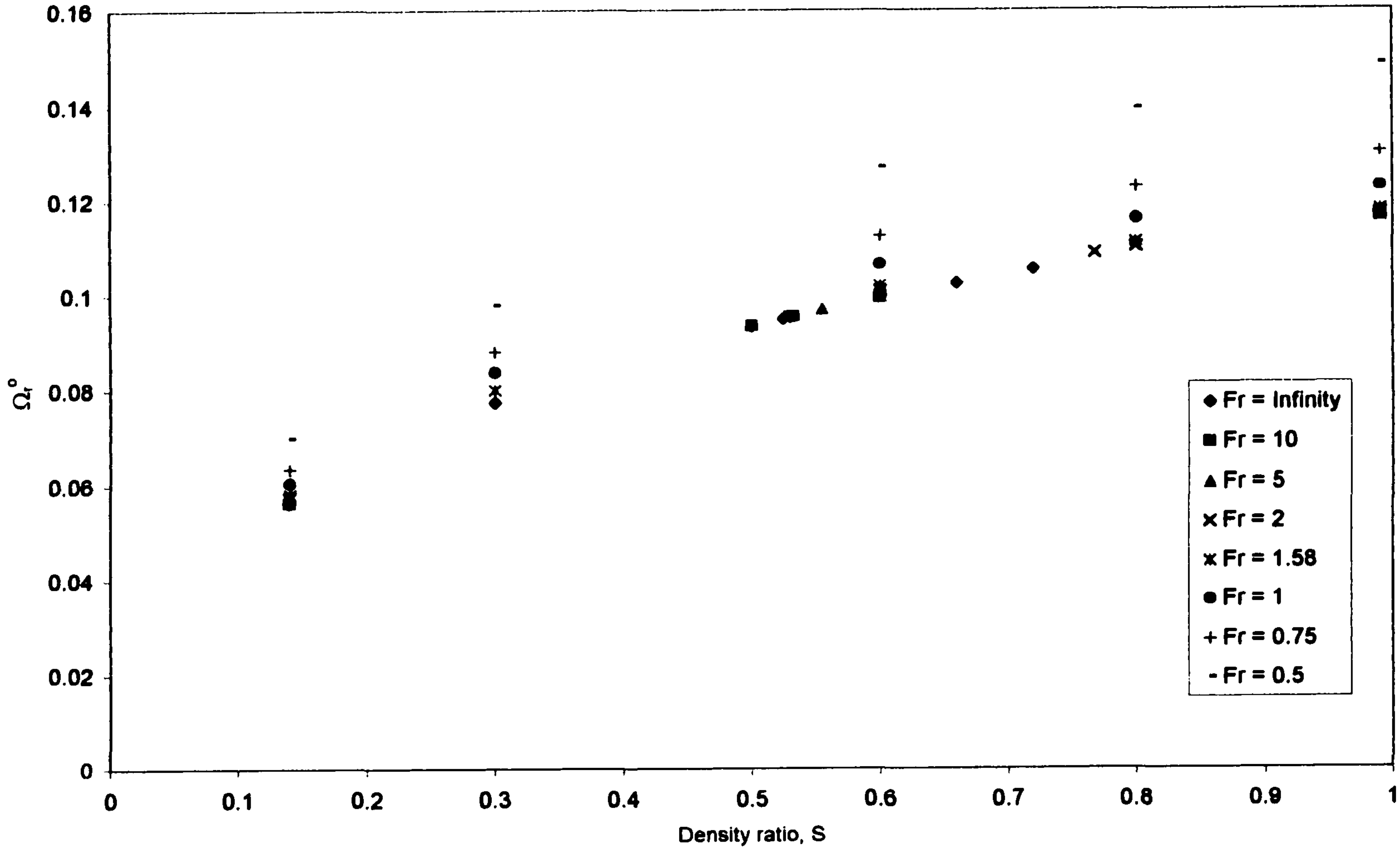

Figure 4.19: Ω_r^o vs density ratio at $R/\theta = 10$

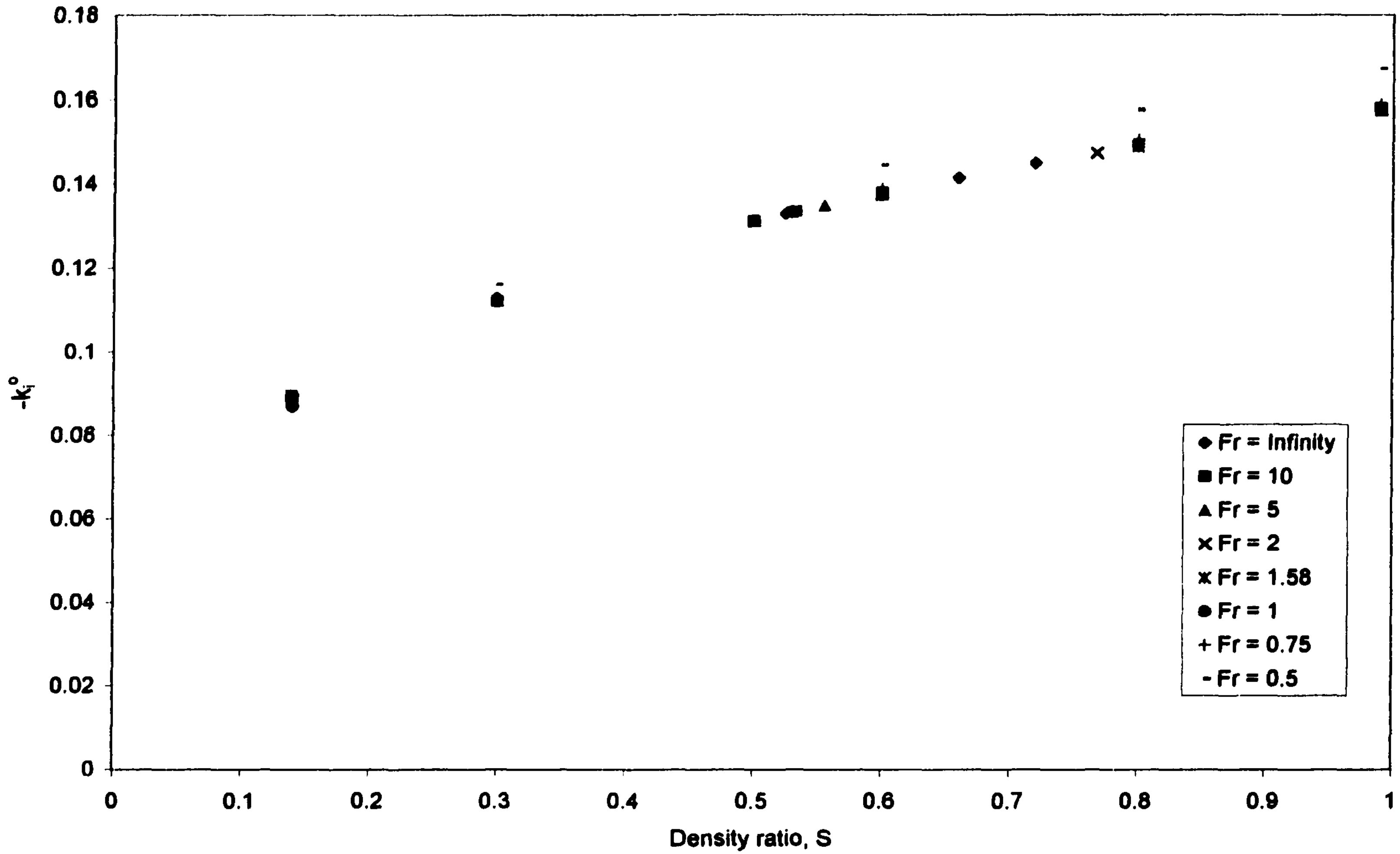

Figure 4.20: $-k_i^o$ vs density ratio at $R/\theta = 10$

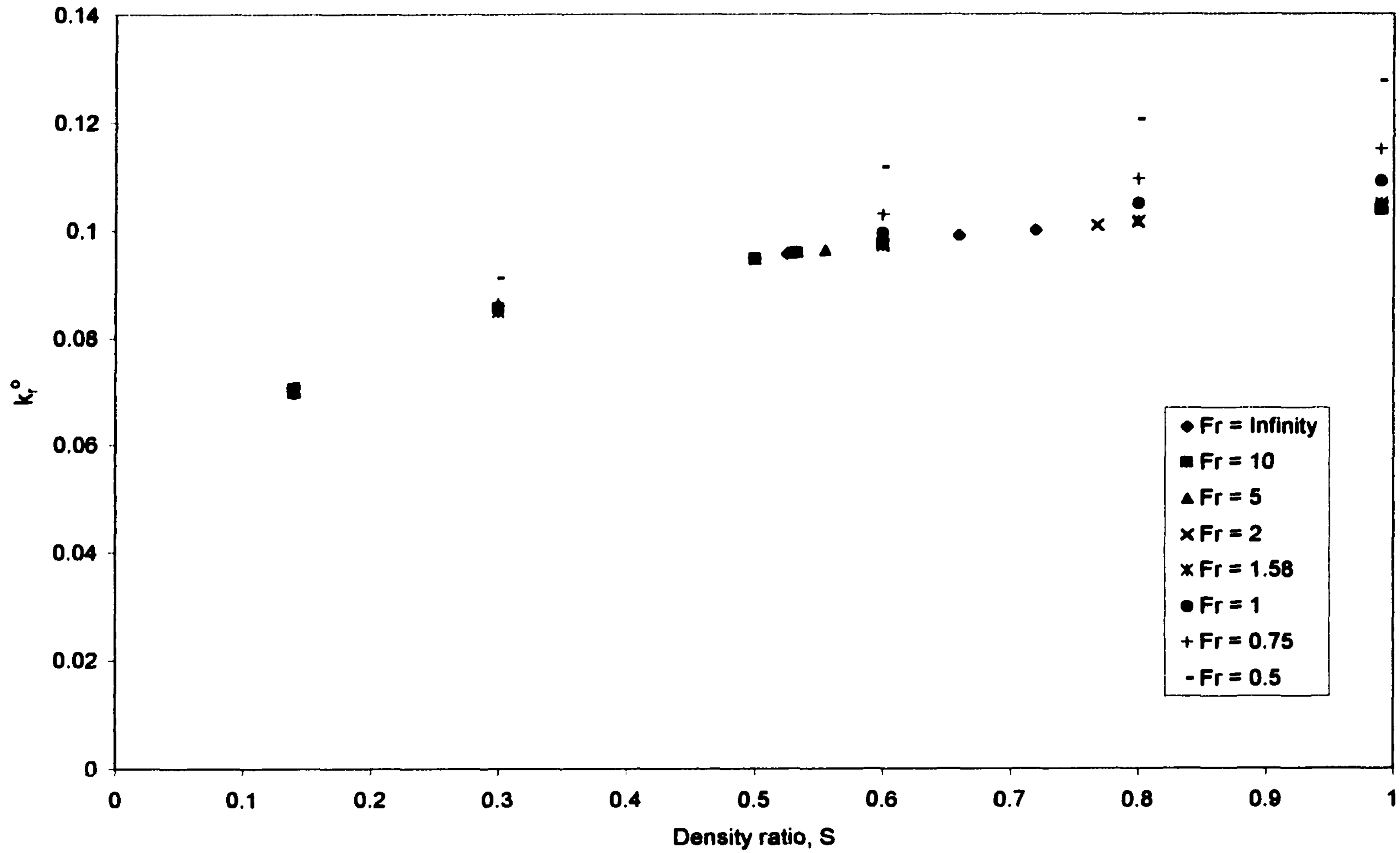

Figure 4.21: k_r^o vs Density ratio at $R/\theta = 10$

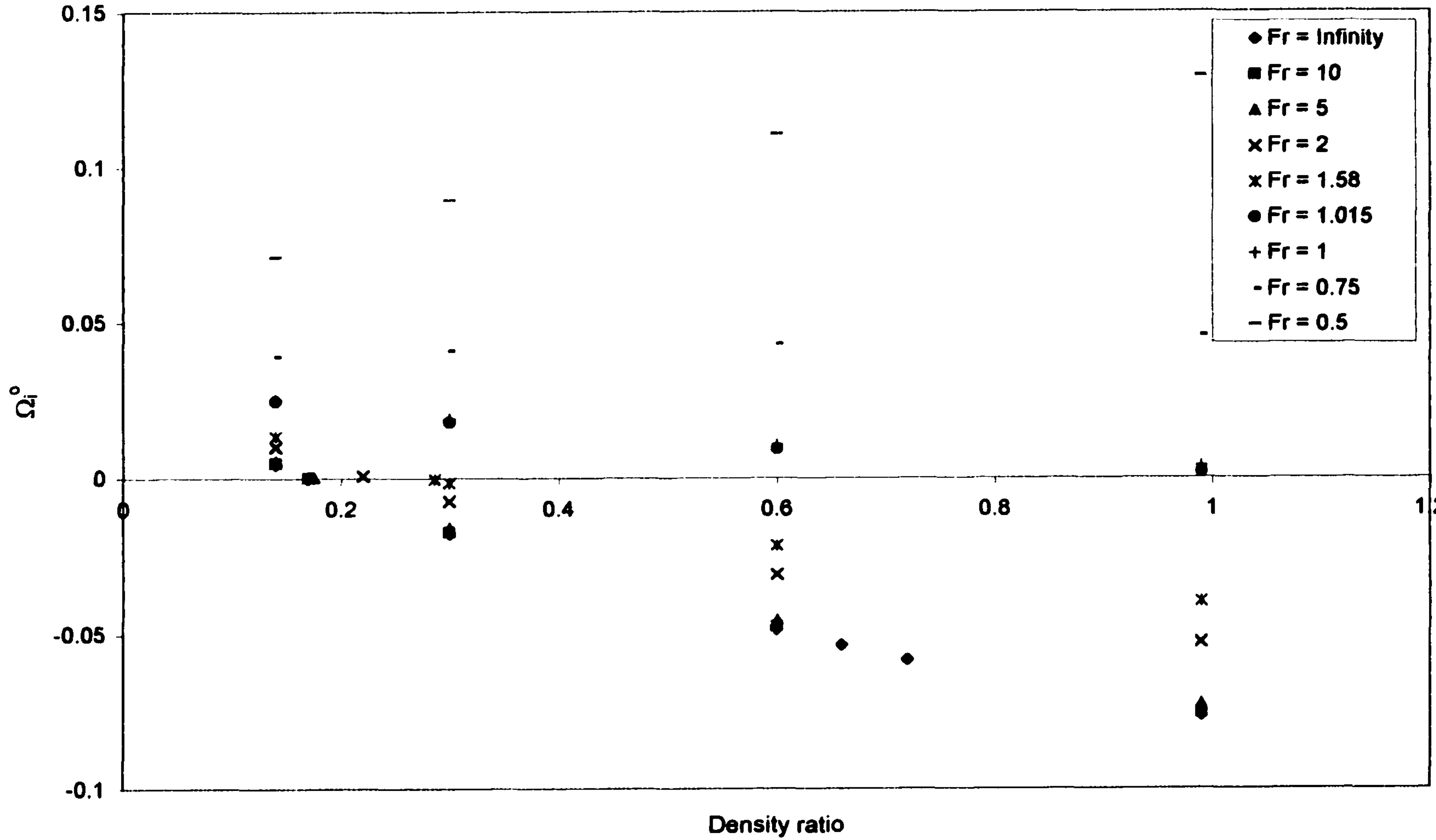

Figure 4.22: Ω_i^o vs density ratio at $R/\theta = 5$

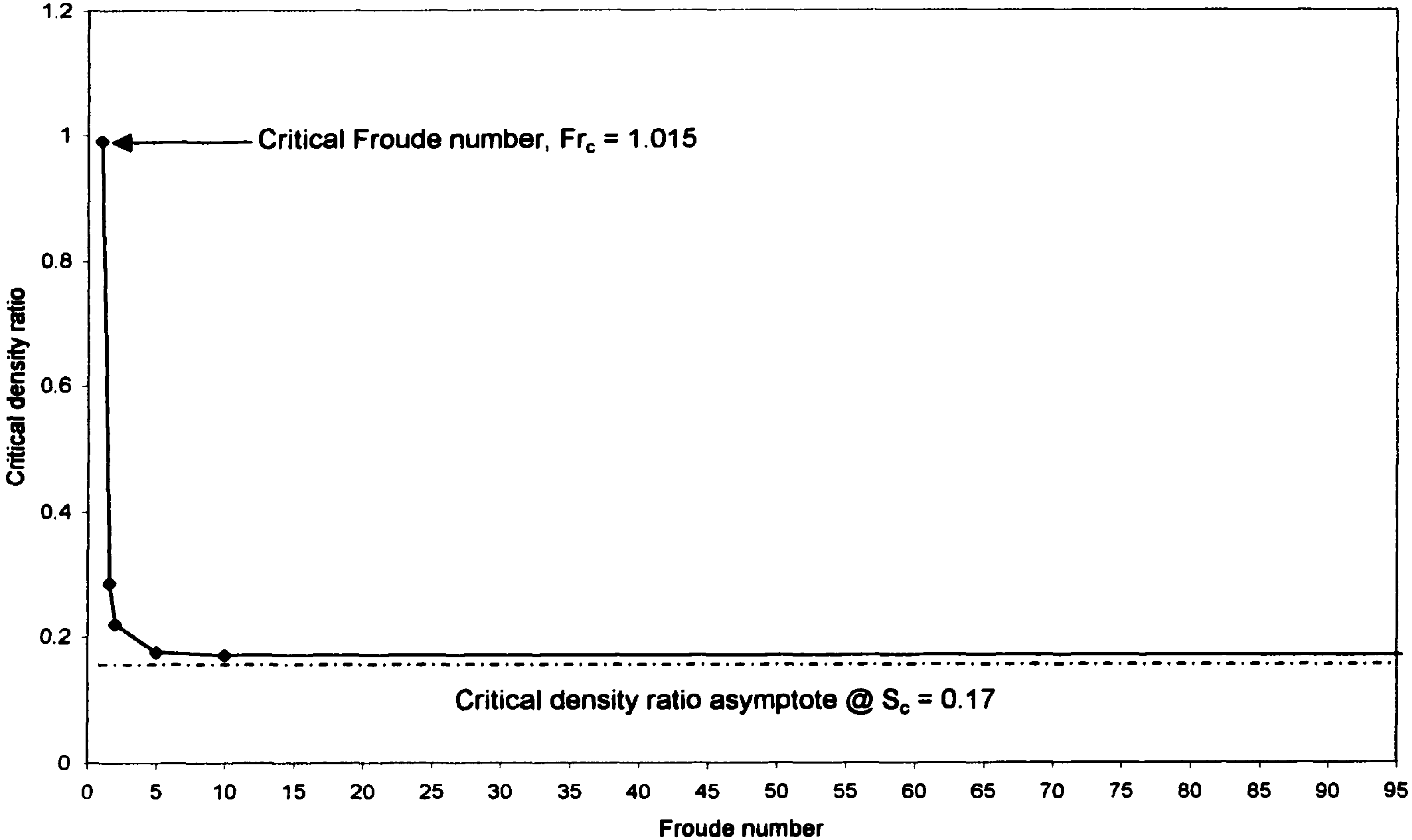

Figure 4.23: Critical density ratio, S_c vs Froude number, Fr at R/θ = 5

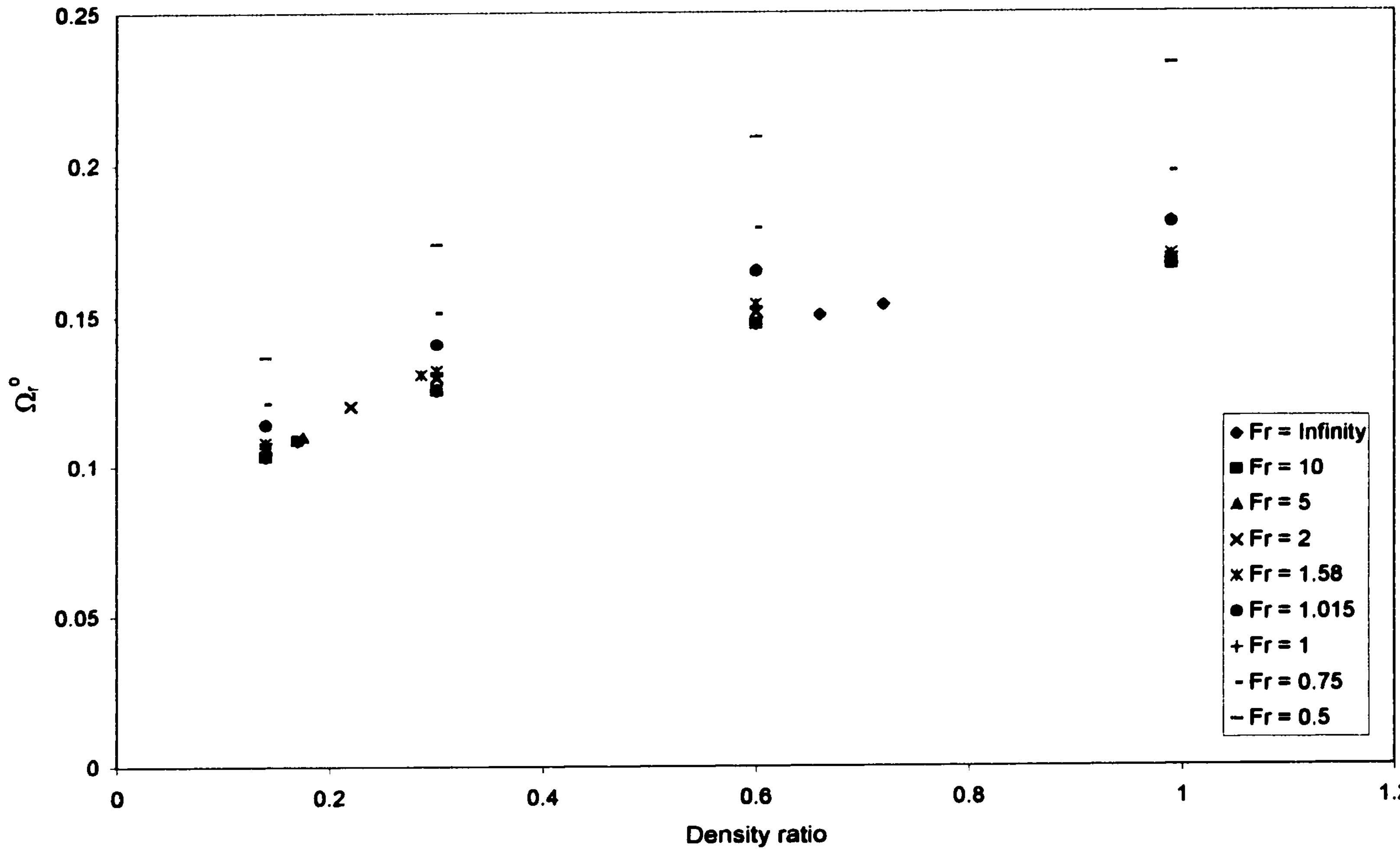

Figure 4.24: Ω_r^o vs density ratio at $R/\theta = 5$

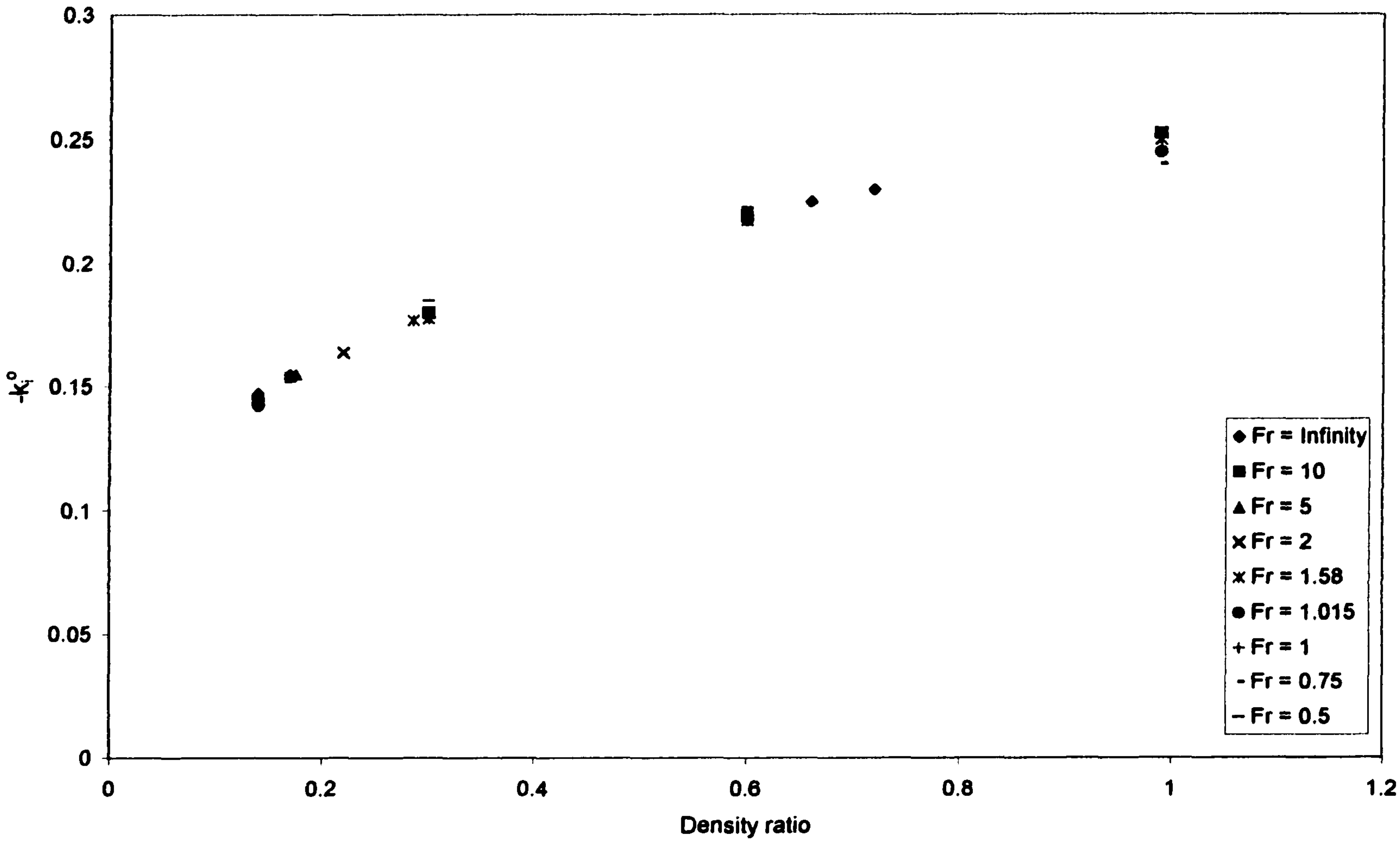

Figure 4.25: $-k_i^o$ vs density ratio at $R/\theta = 5$

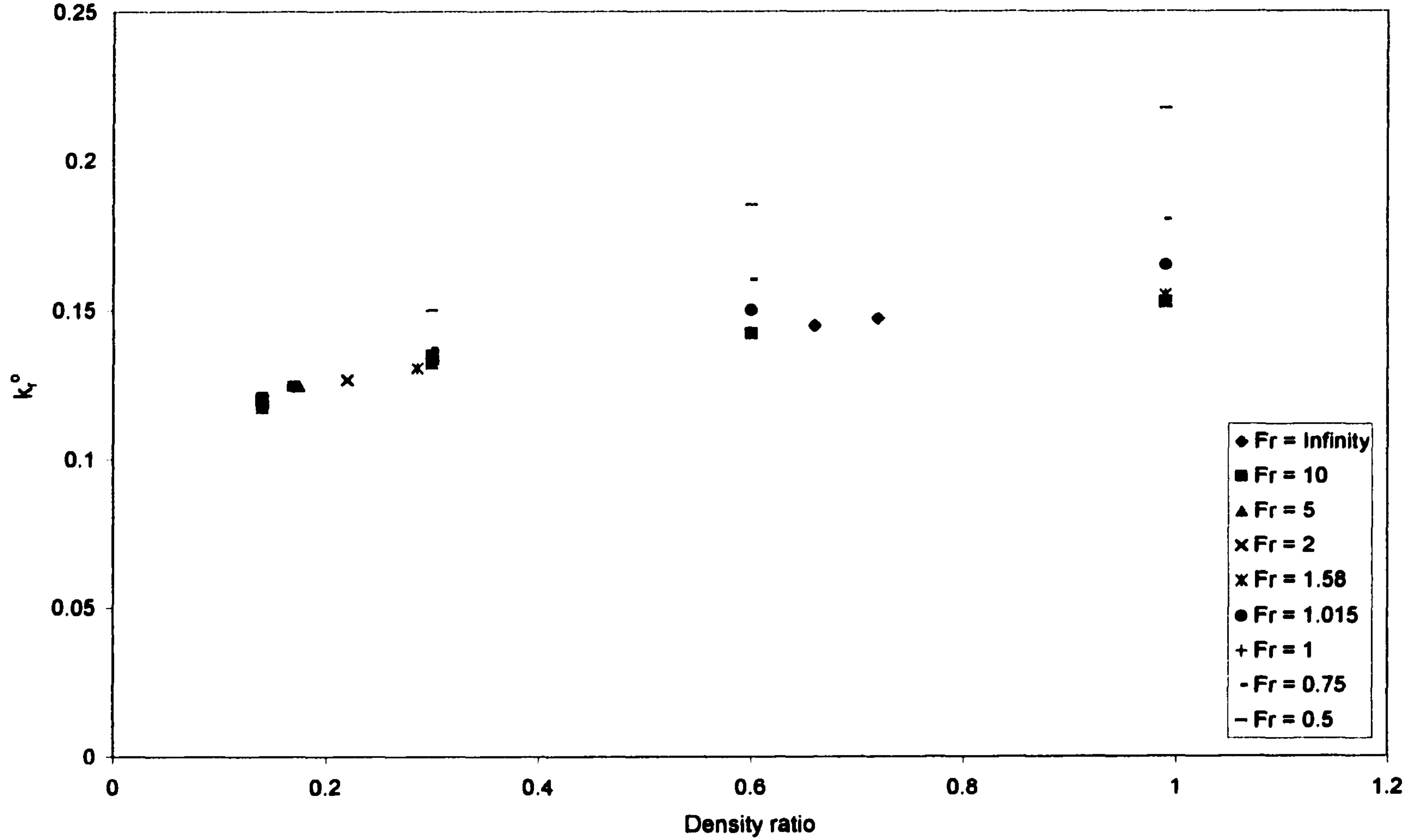

Figure 4.26: k_r^o vs Density ratio at $R/\theta = 5$

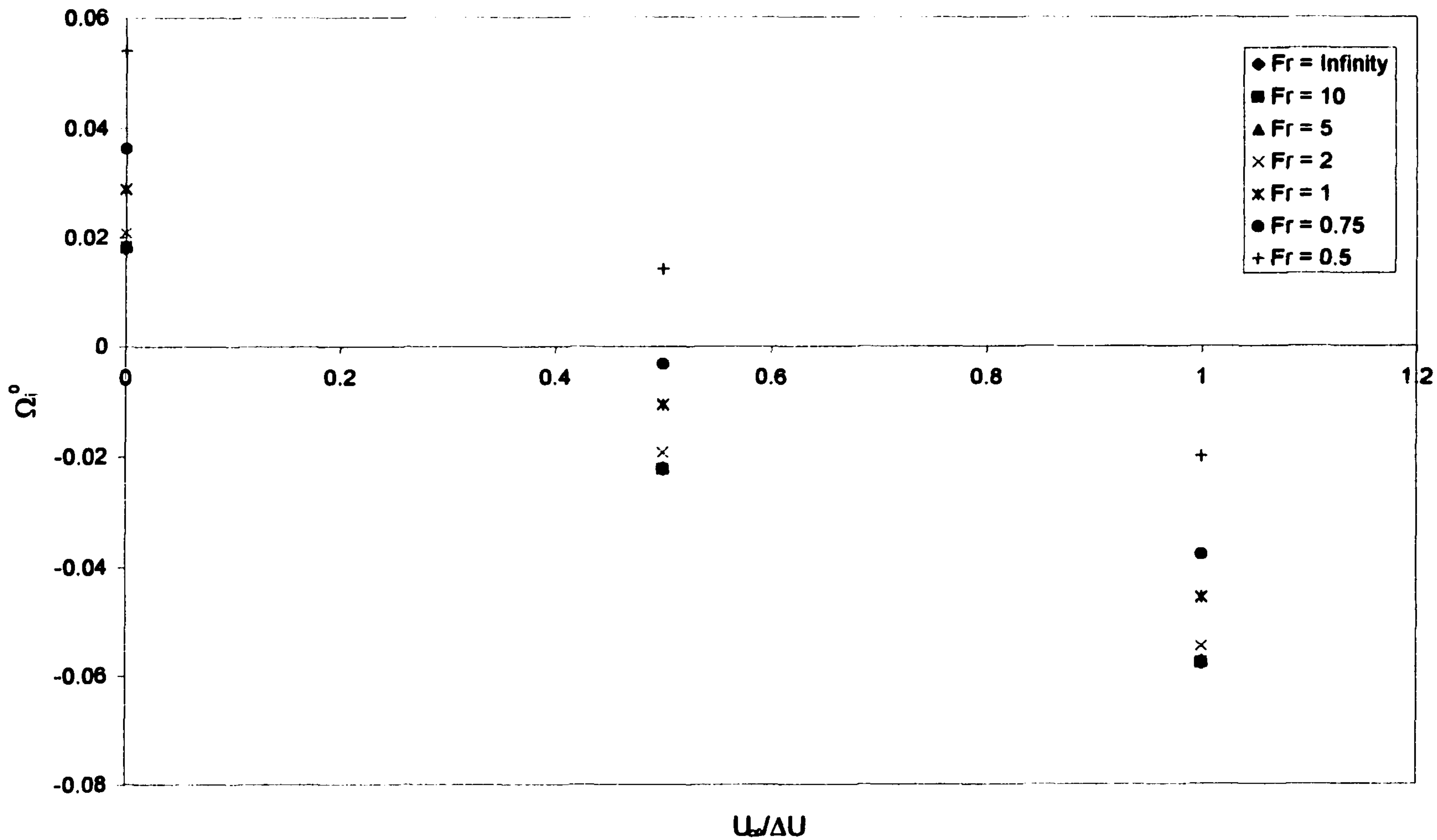

Figure 4.27: Ω_i^o vs co-flow velocity ratio, $U_\infty/\Delta U$ at $R/\theta = 10$

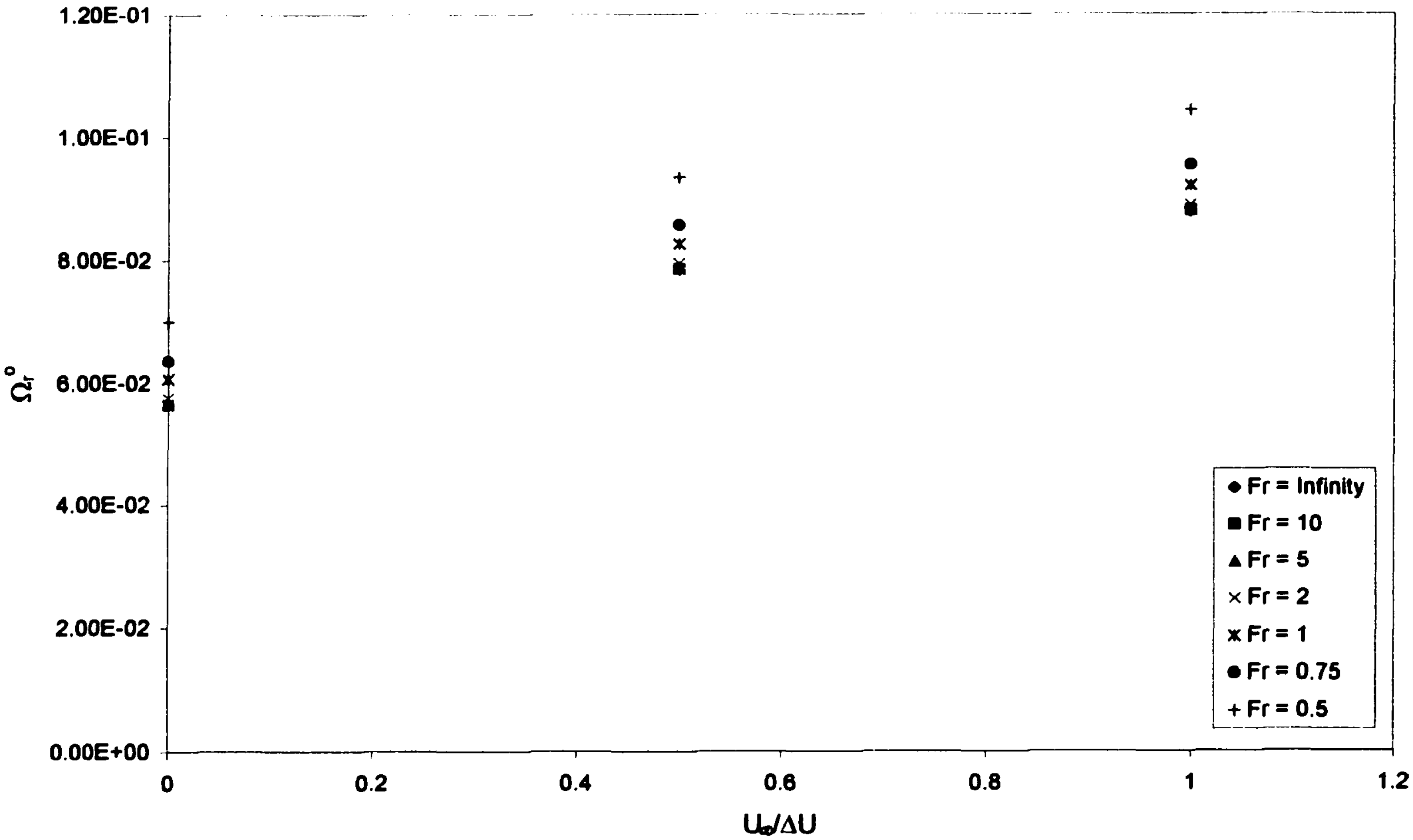

Figure 4.28: Ω_r^o vs co-flow velocity ratio, $U_\infty/\Delta U$ at $R/\theta = 10$

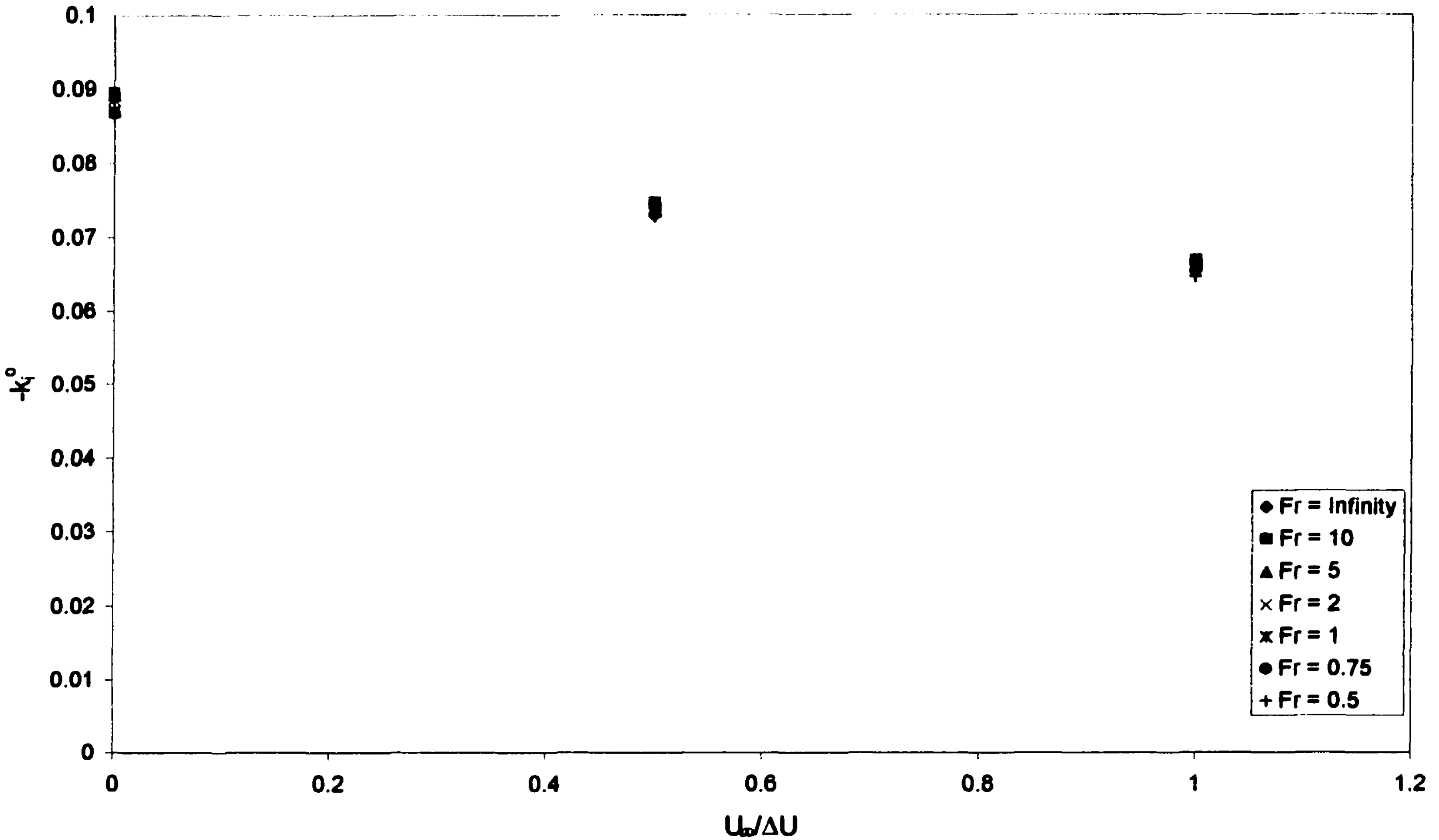

Figure 4.29: $-k_i^o$ vs co-flow velocity ratio, $U_\infty/\Delta U$ at $R/\theta = 10$

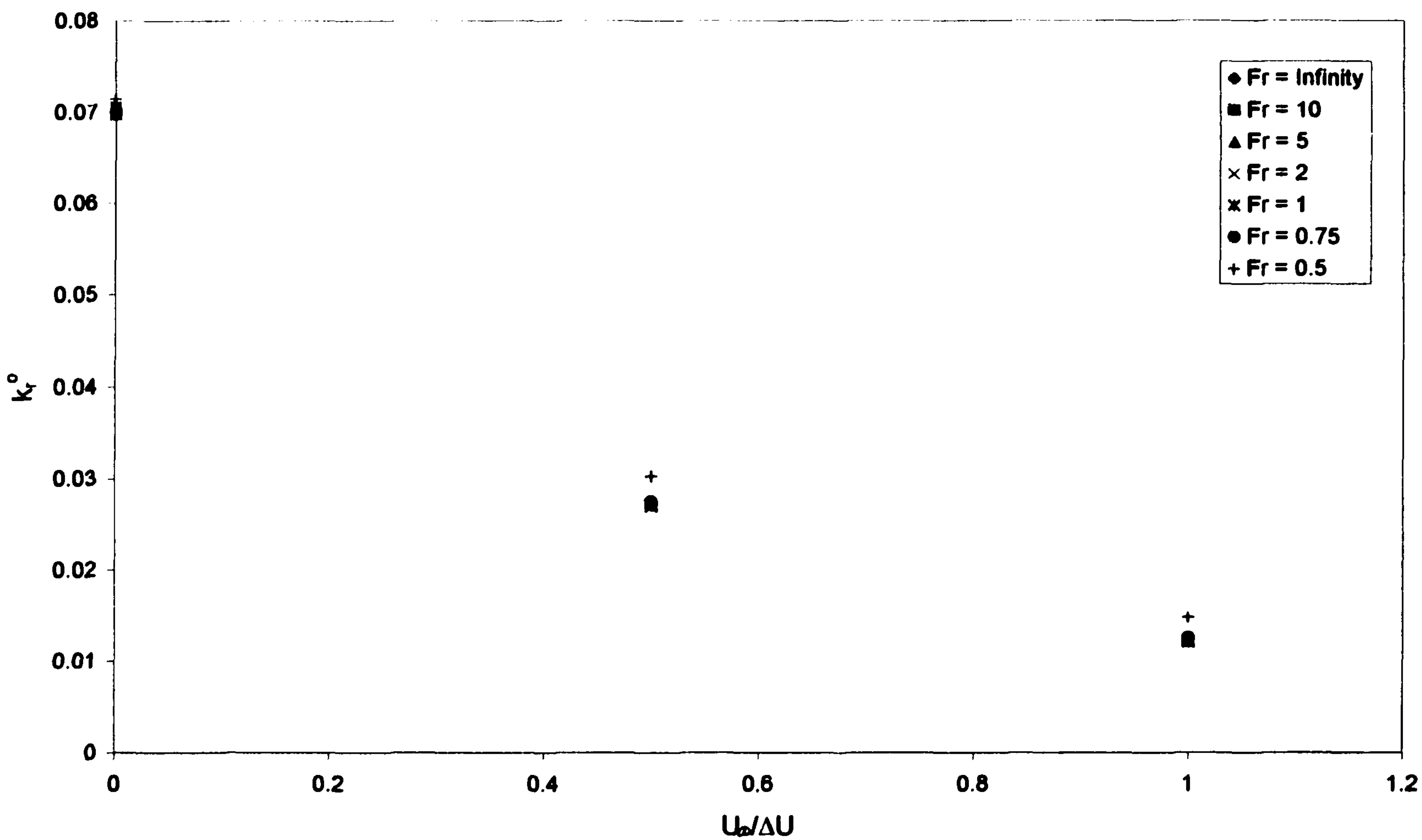

Figure 4.30: k_r^o vs co-flow velocity ratio, $U_\infty/\Delta U$ at $R/\theta = 10$

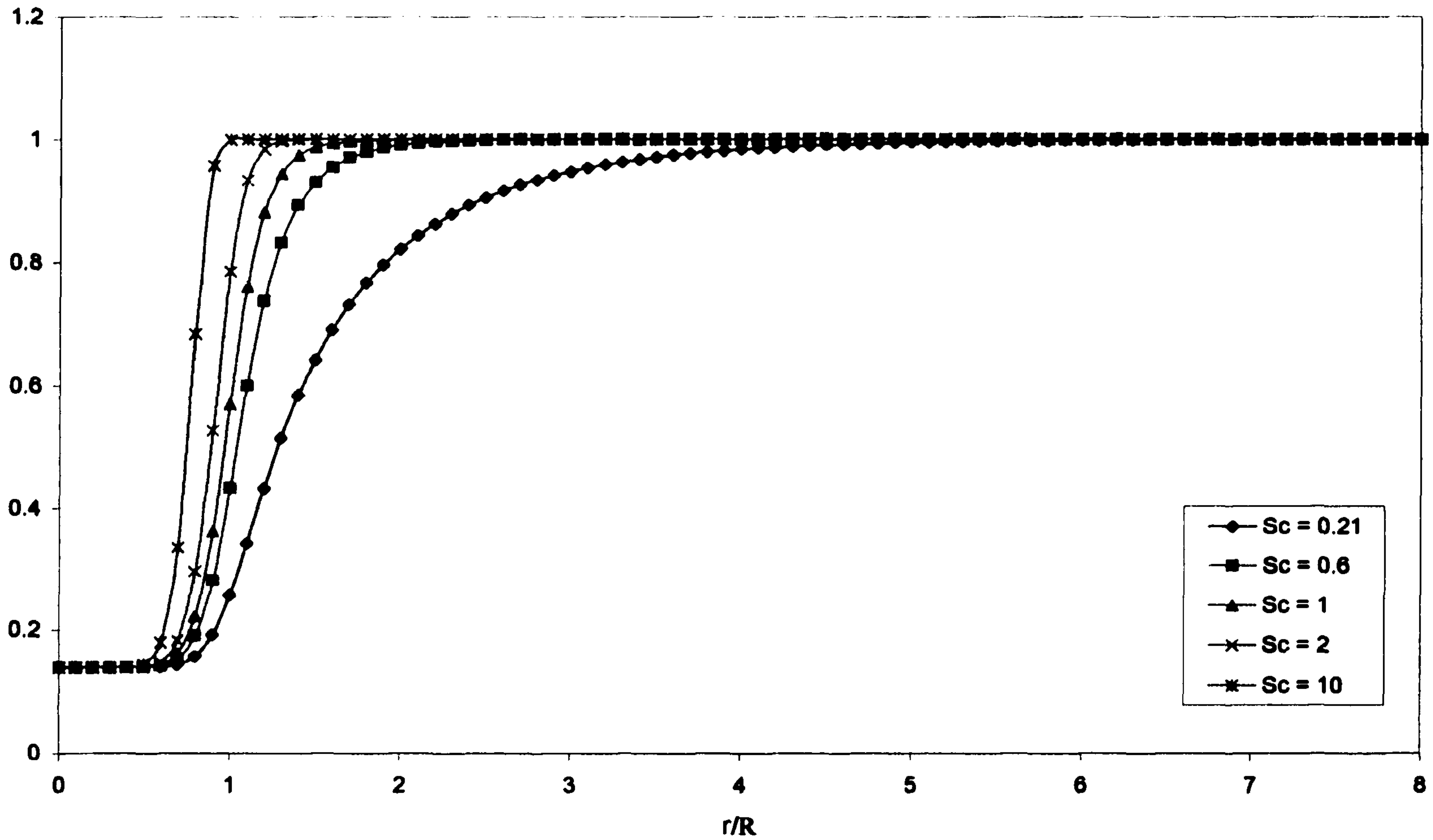

Figure 4.31: Density profile at various Schimdt numbers, Sc for $R/\theta = 10$ & $\rho_j/\rho = 0.14$

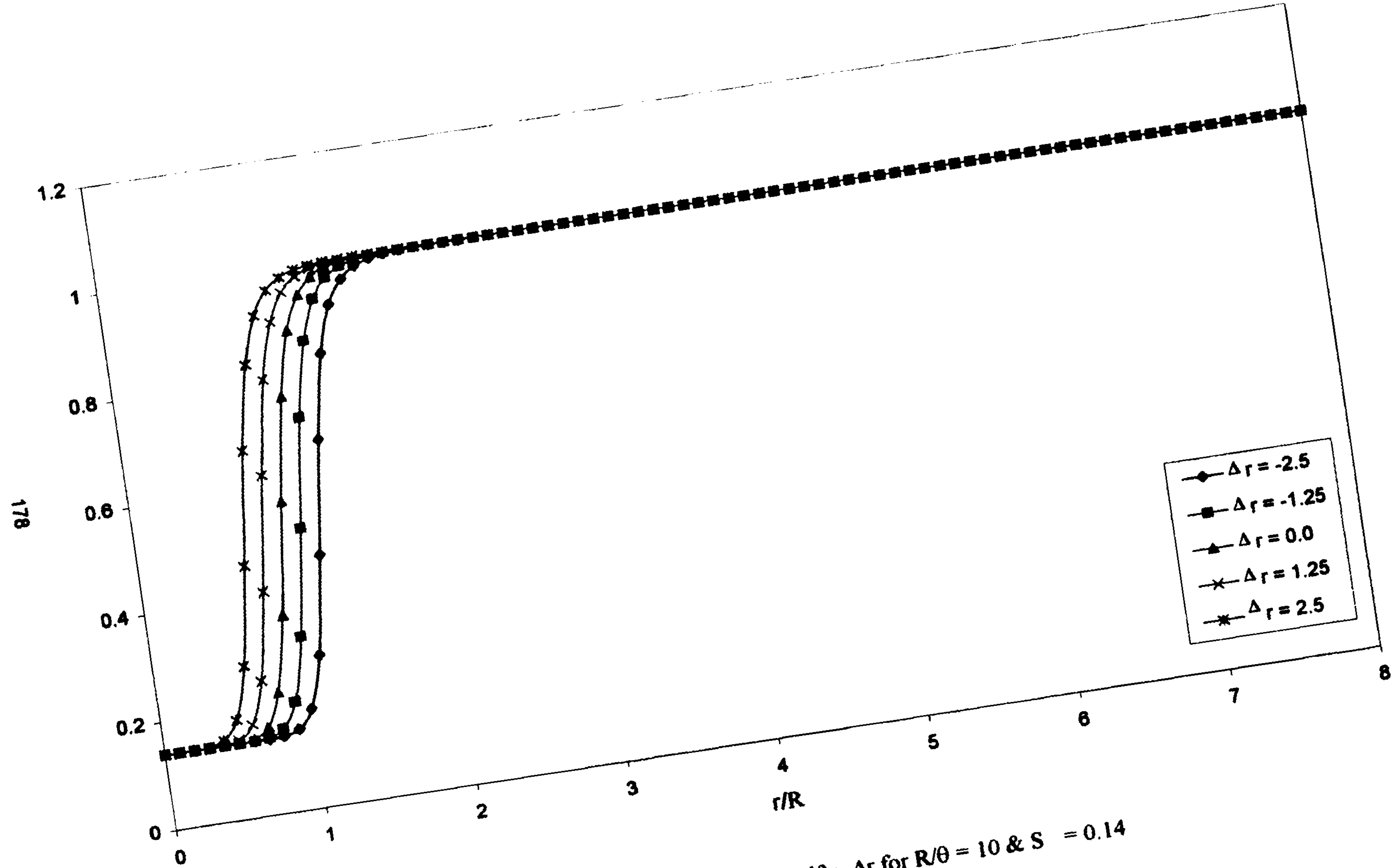

Figure 4.32: Density profile at various lateral shifts, Δr for R/θ = 10 & S = 0.14

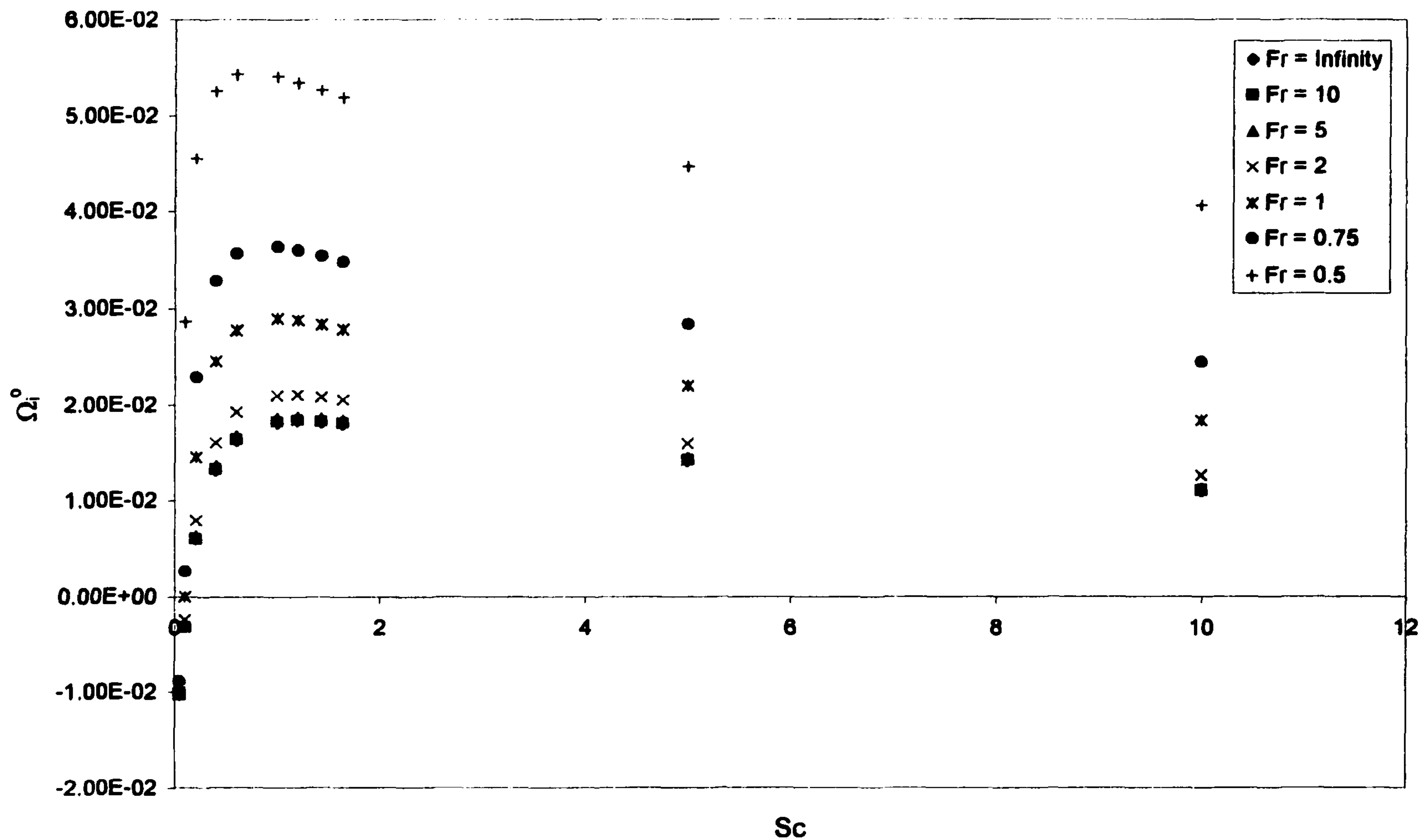

Figure 4.33: Ω_i^o vs Schmidt number, Sc at $R/\theta = 10$

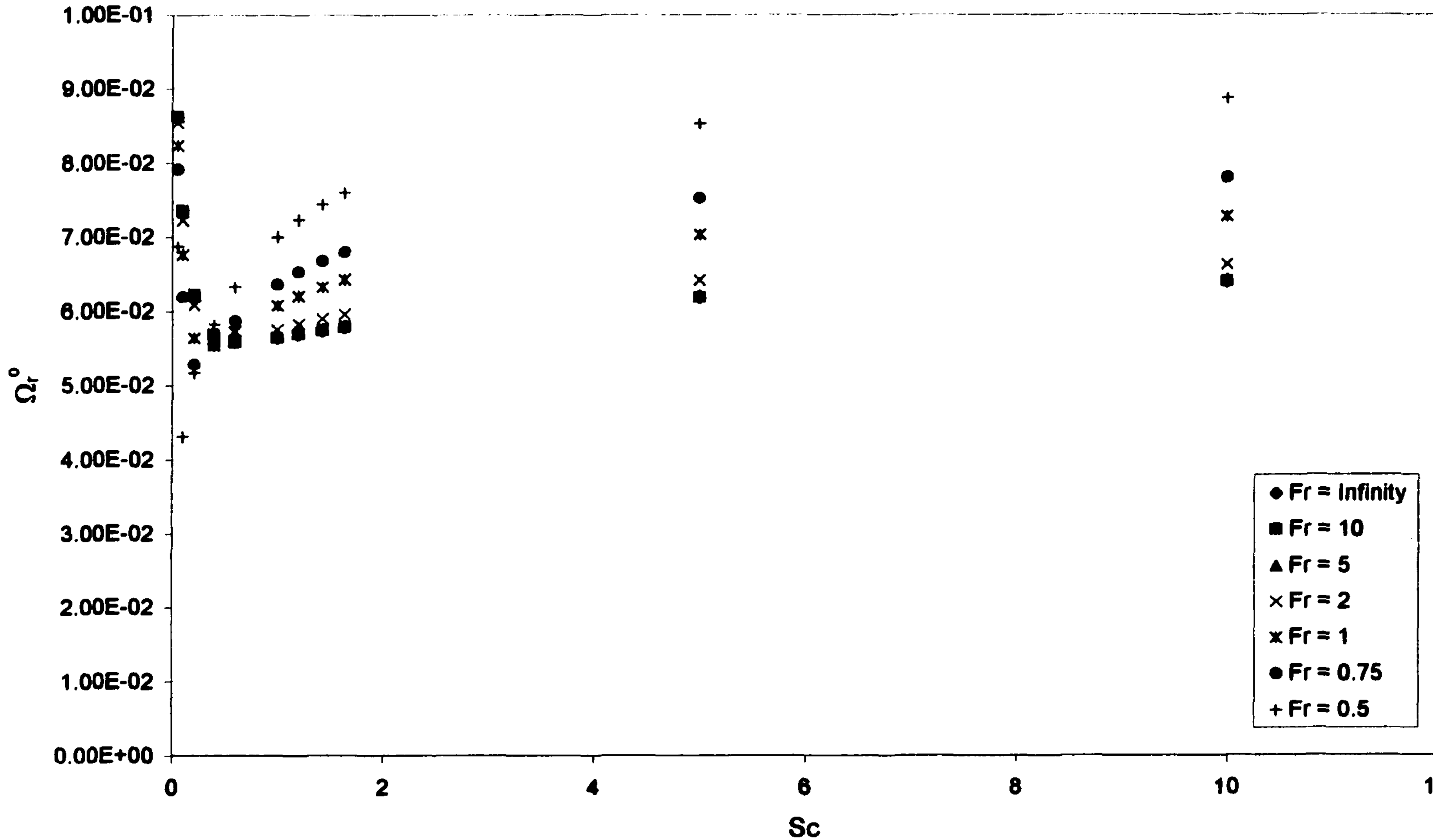

Figure 4.34: Ω_r^o vs Schmidt number, Sc at $R/\theta = 10$

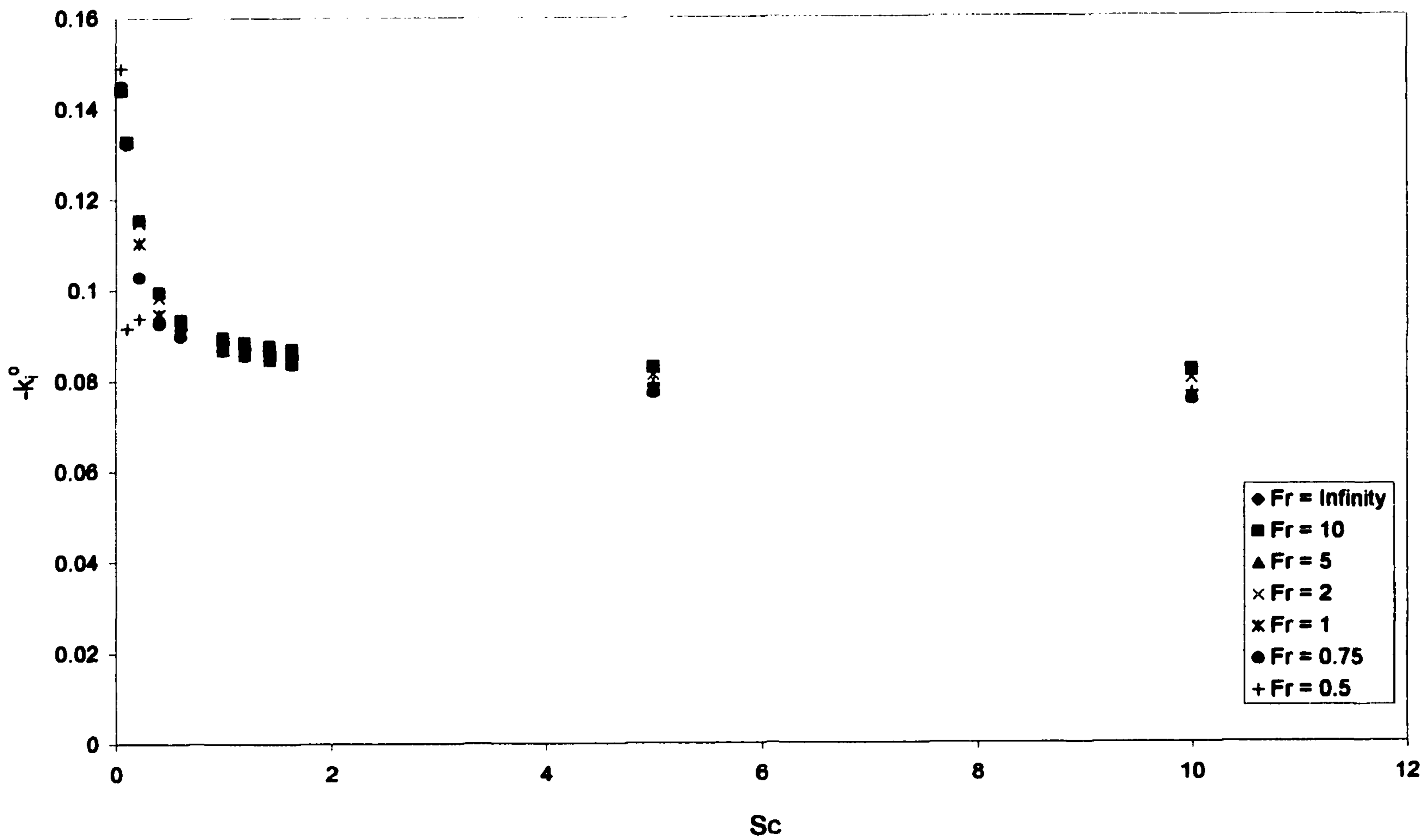

Figure 4.35: $-k_i^o$ vs Schmidt number, Sc at $R/\theta = 10$

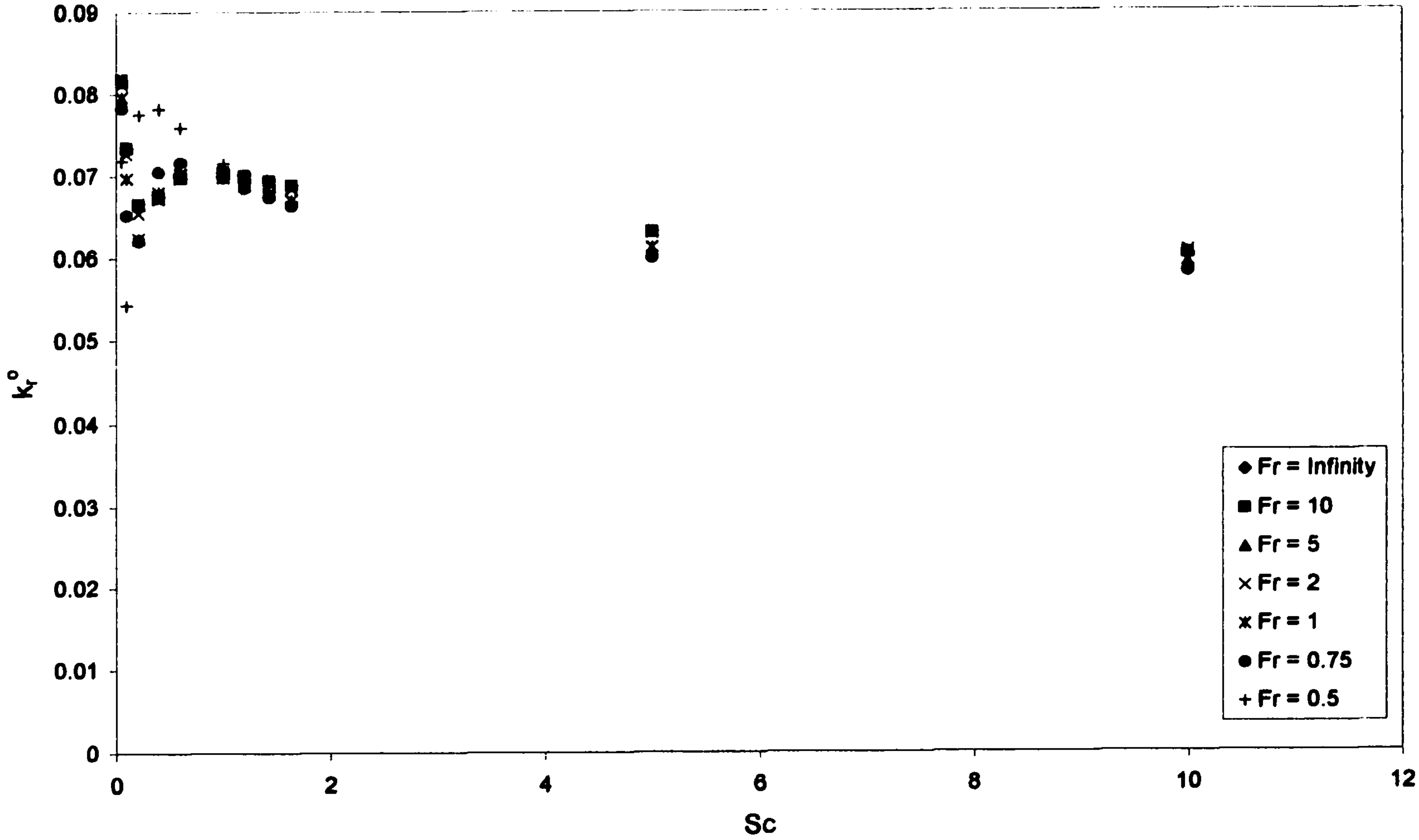

Figure 4.36: k_r^o vs Schmidt number, Sc at $R/\theta = 10$

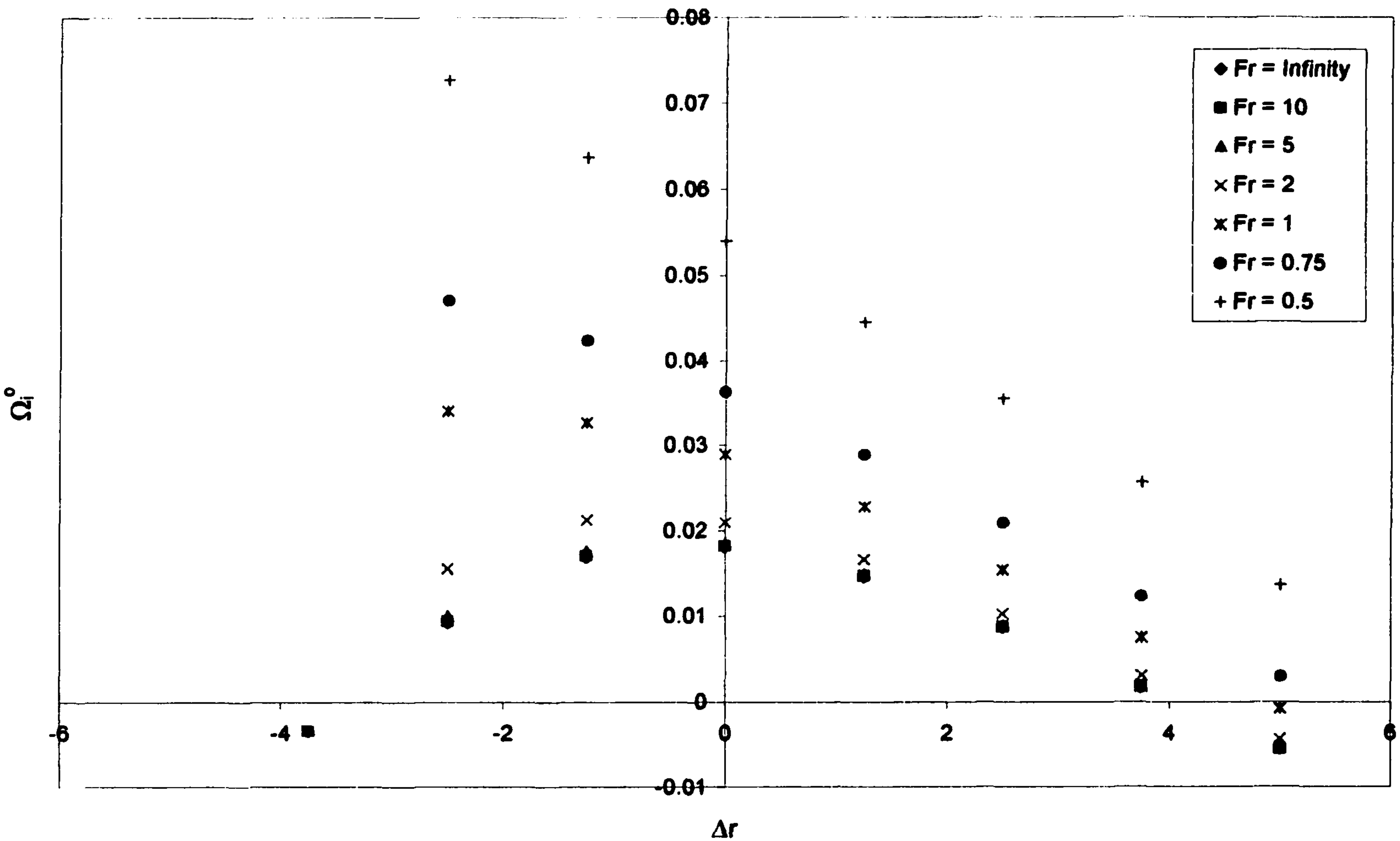

Figure 4.37: Ω_i^o vs Δr for S = 0.14 and Sc = 1 at $R/\theta = 10$

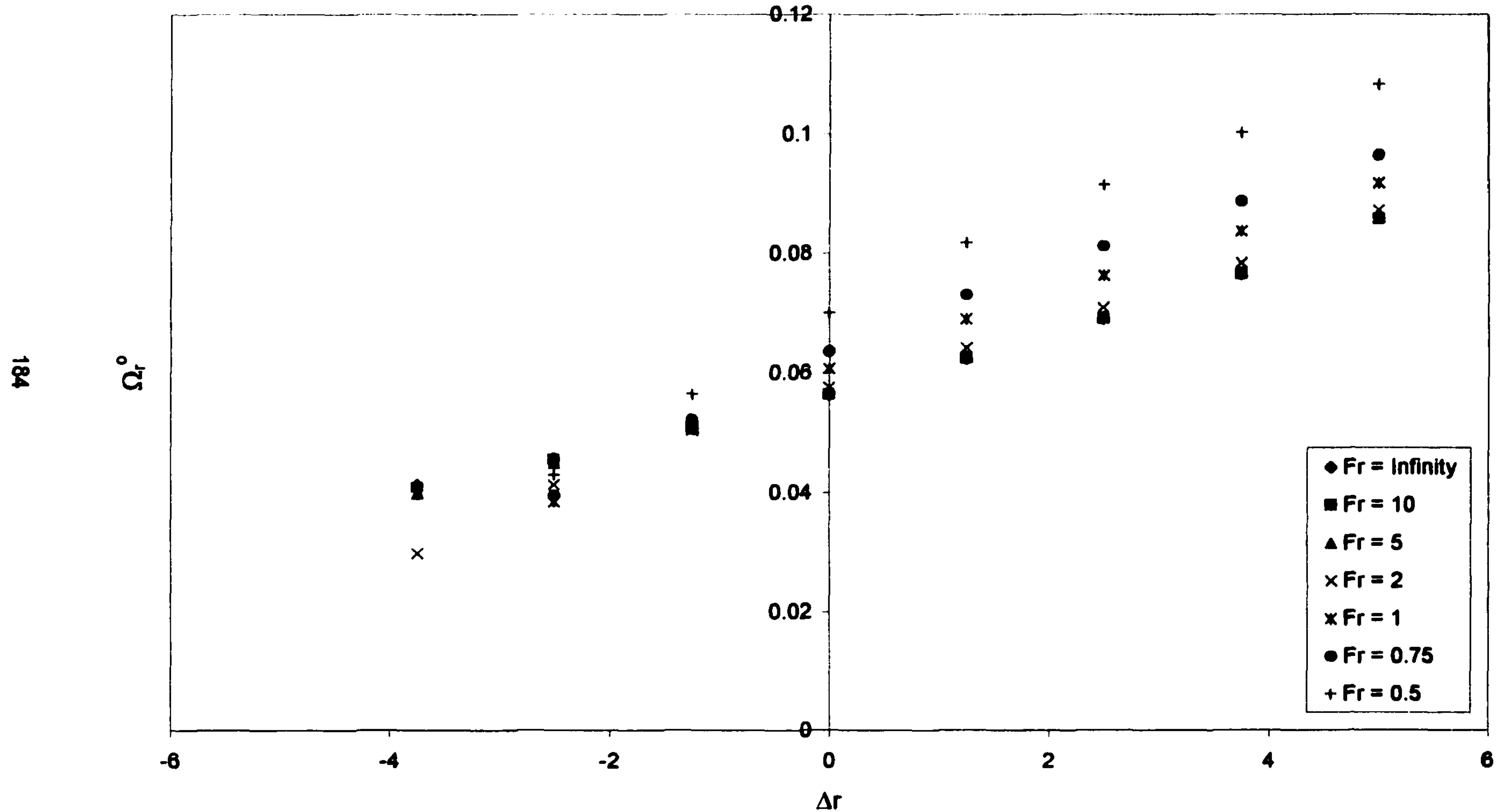

Figure 4.38: Ω_r^o vs Δr for S = 0.14 and Sc = 1 at R/θ = 10

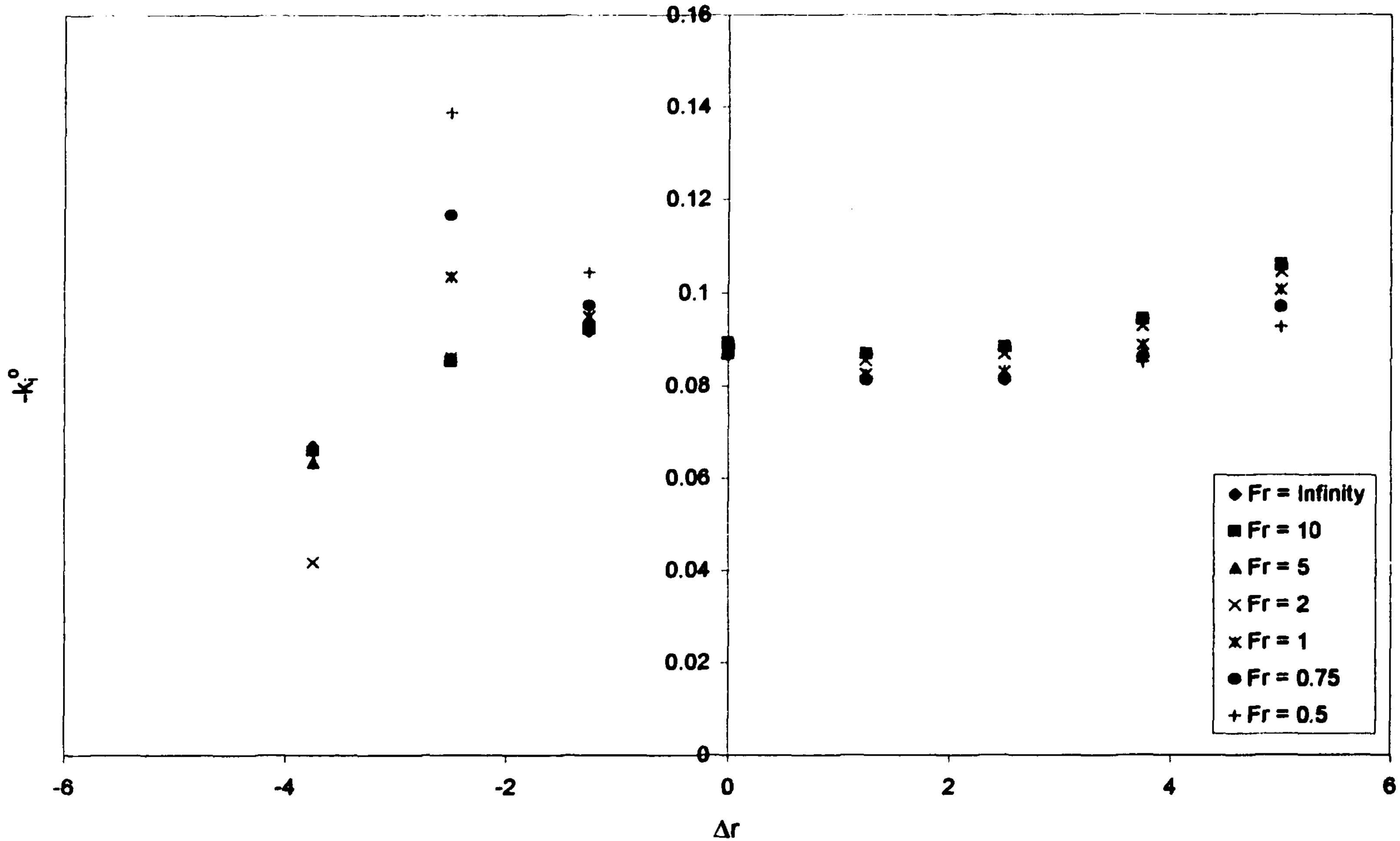

Figure 4.39: $-k_i^o$ vs Δr for $S = 0.14$ and $Sc = 1$ at $R/\theta = 10$

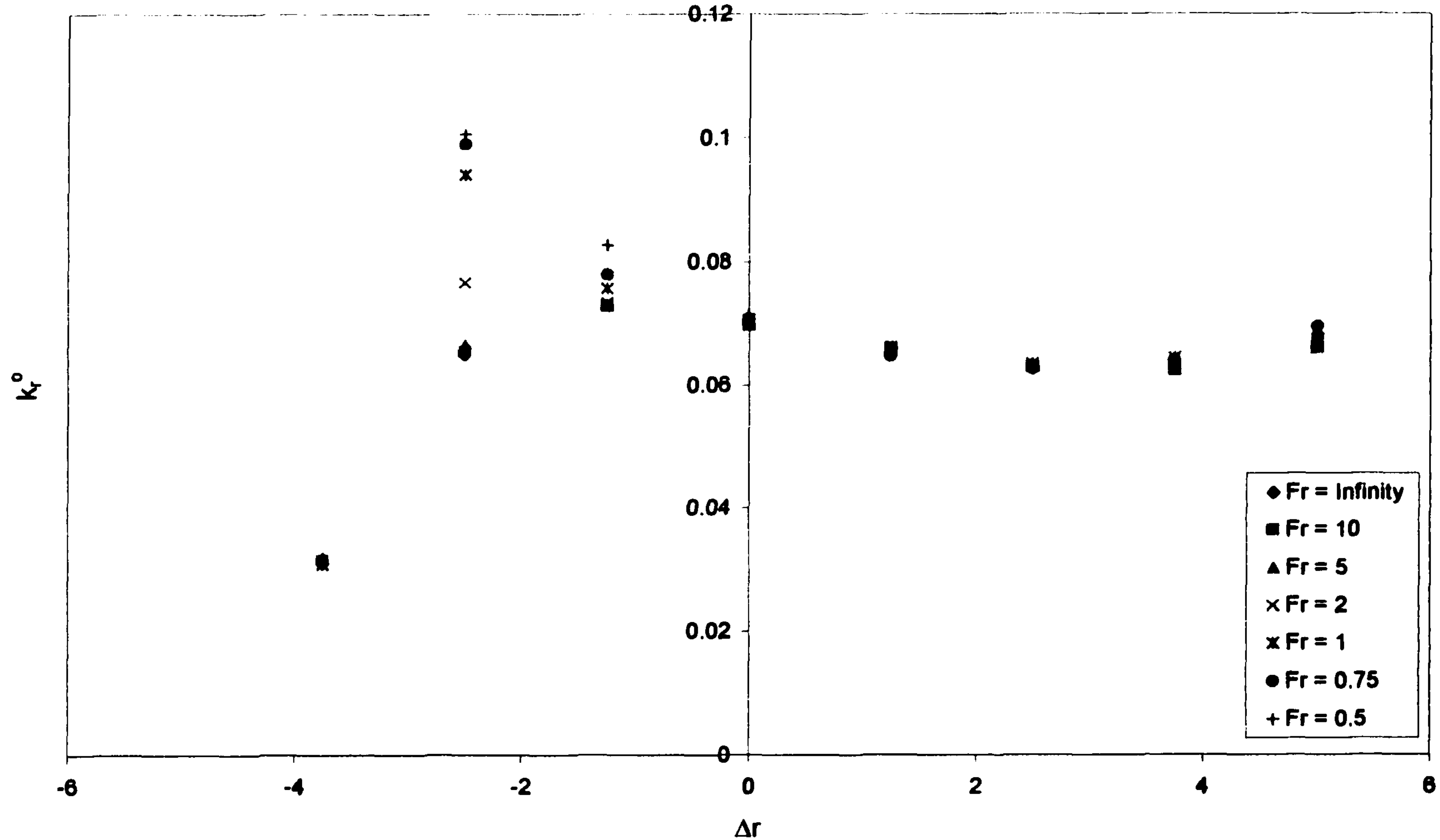

Figure 4.40: k_r^o vs Δr for S = 0.14 and Sc = 1 at R/θ = 10

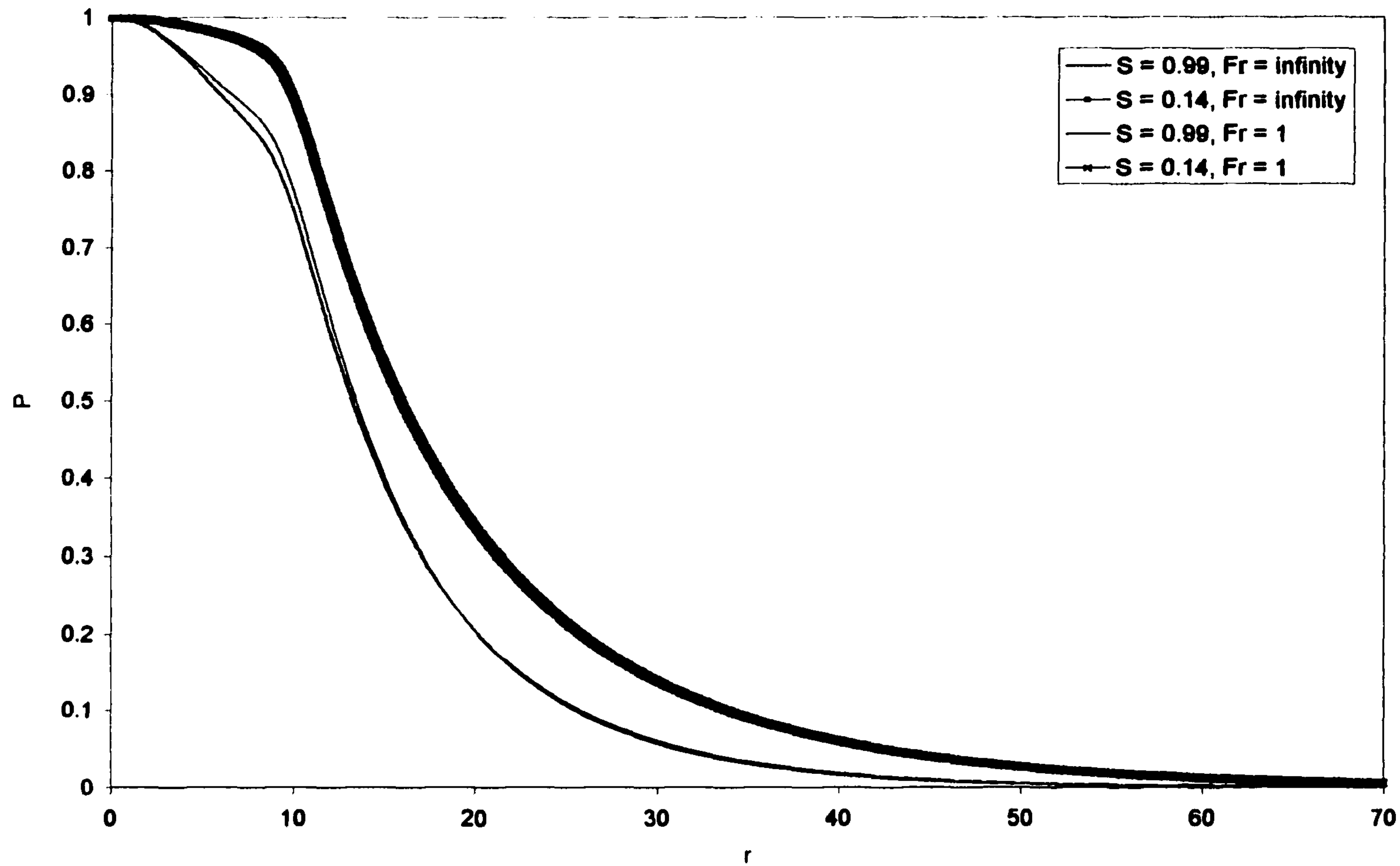

Figure 4.41: Absolute value of the amplitude of the pressure, P vs radial distance, r at R/θ = 10 from linear spatio-temporal stability analysis

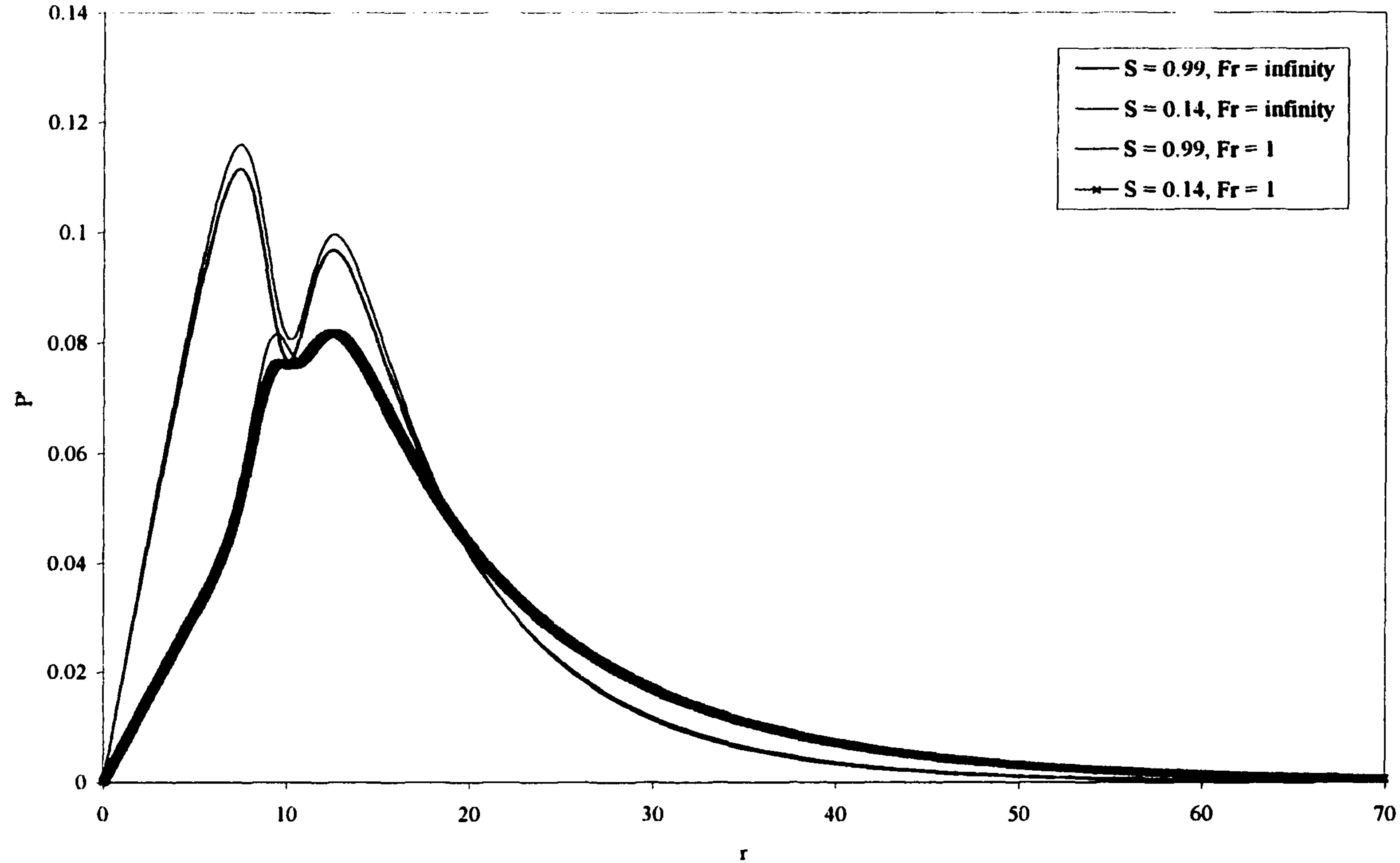

Figure 4.42: Absolute value of the amplitude of the pressure derivative, P' vs radial location, r at R/θ = 10 from linear spatio-temporal stability analysis

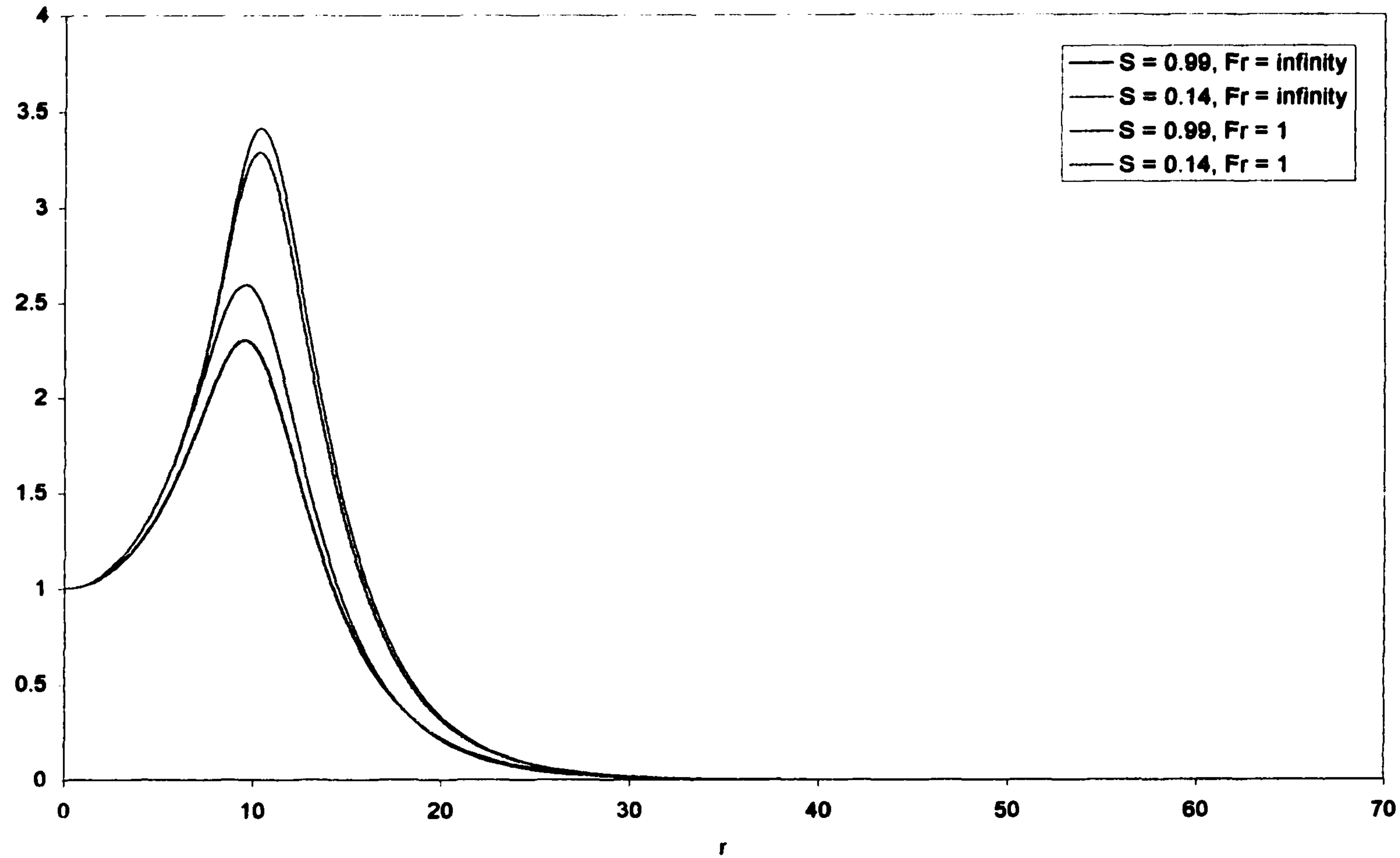

Figure 4.43: Absolute value of the amplitude of the pressure, P vs radial distance, r at R/θ = 10 from linear temporal stability analysis

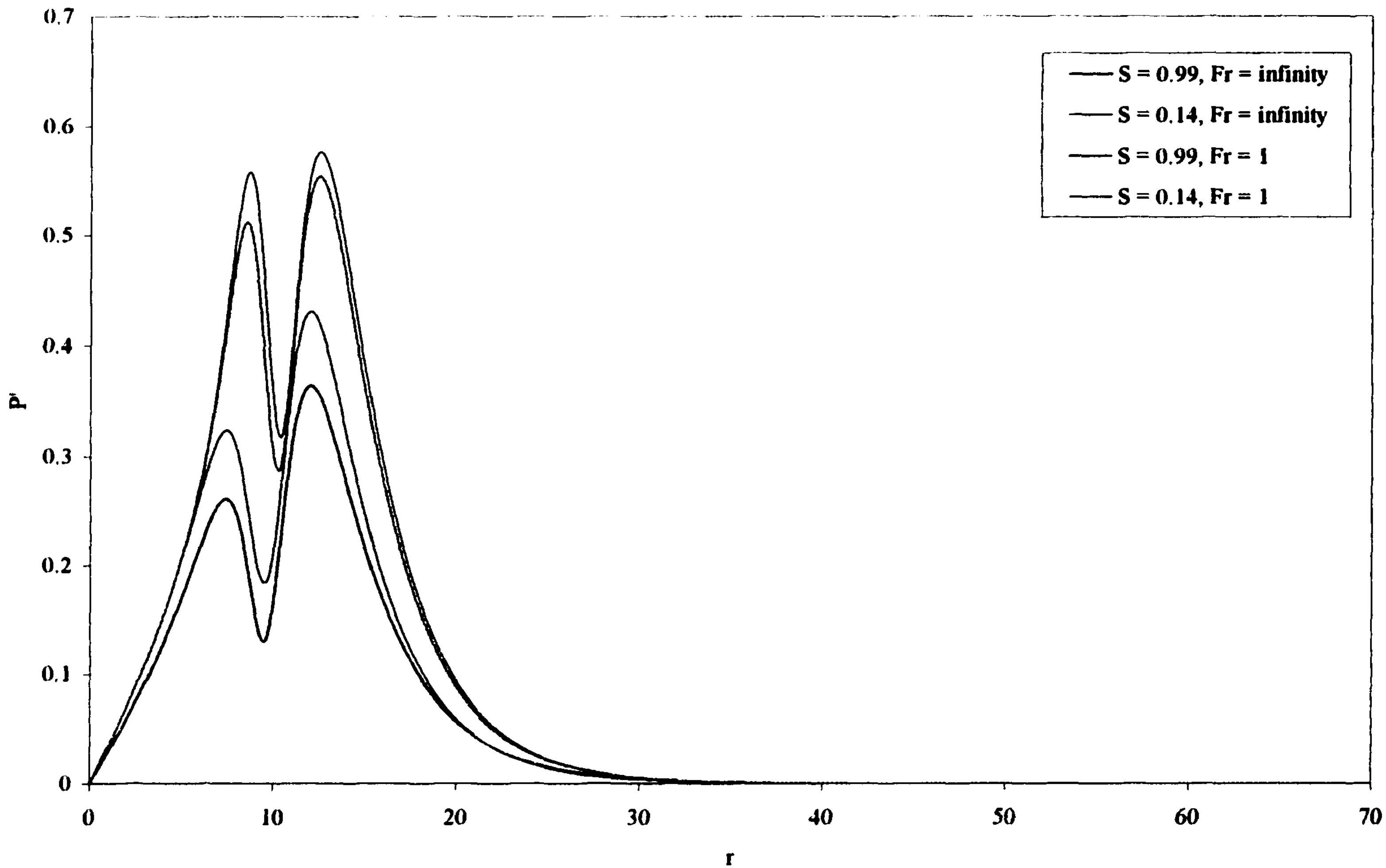

Figure 4.44: Absolute value of the amplitude of the Pressure derivative, P' vs radial location, r at R/θ = 10 from linear temporal stability analysis

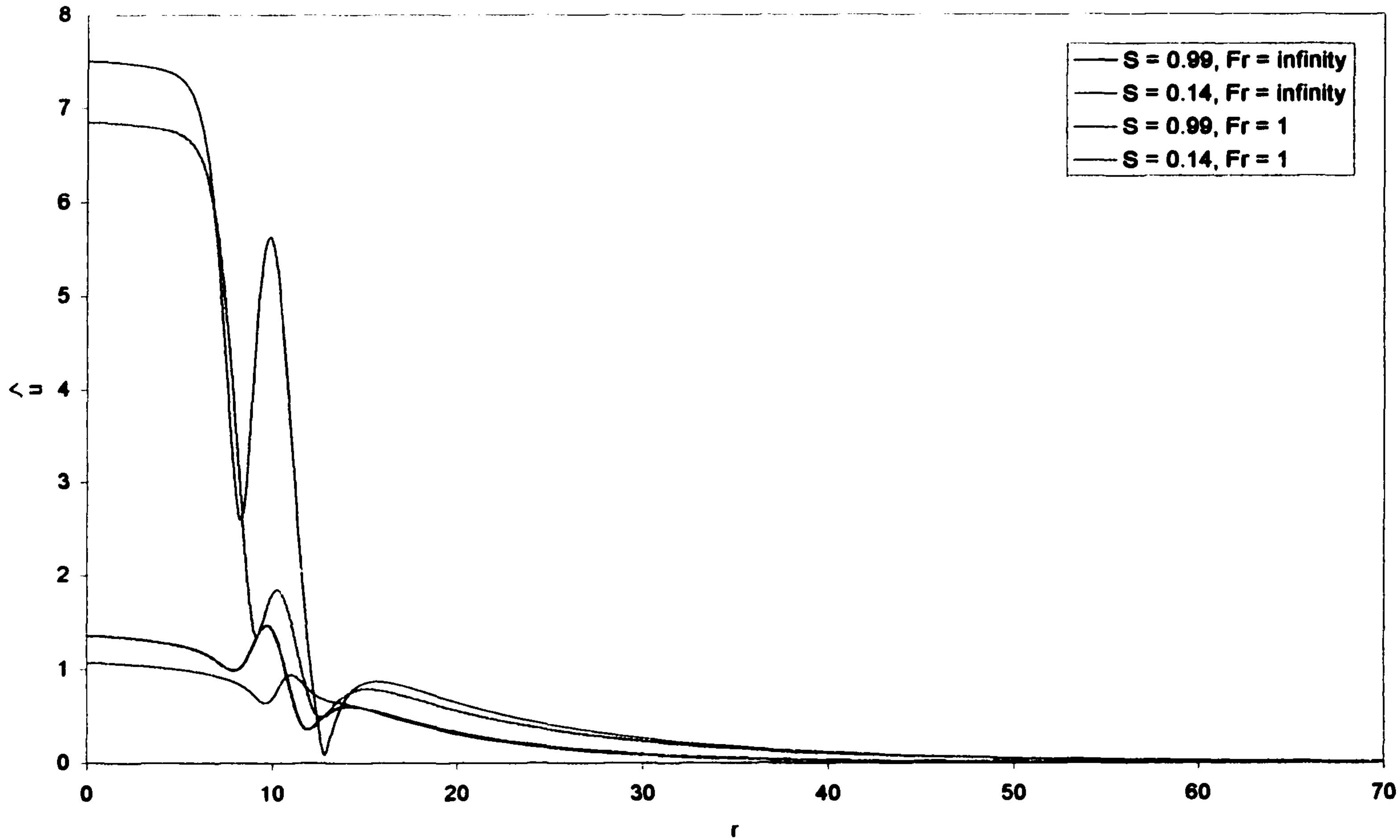

Figure 4.45: Absolute value of the amplitude of the axial velocity disturbance, $\hat{u}$ vs radial distance, r at R/θ = 10 from linear spatio-temporal stability analysis

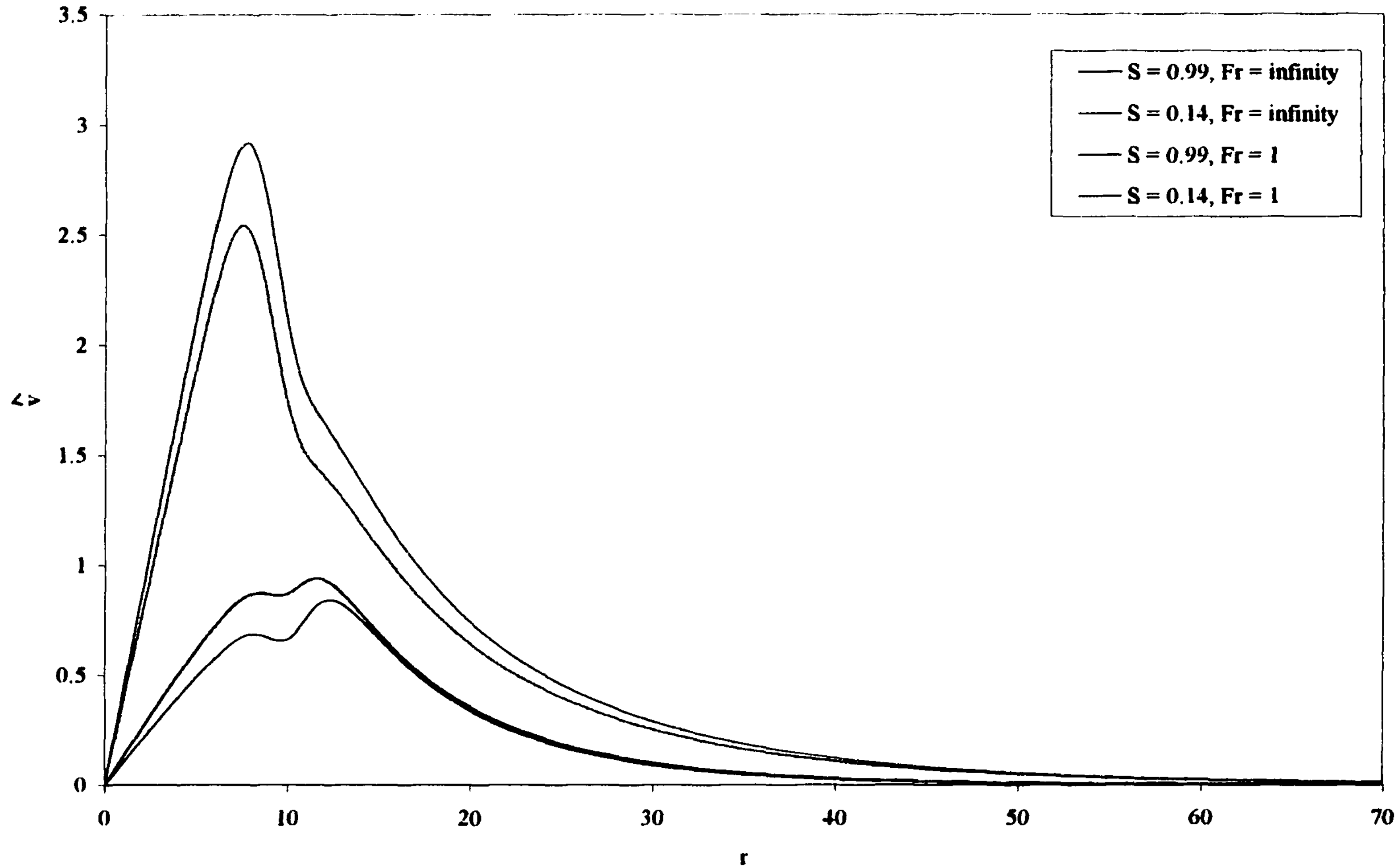

Figure 4.46: Absolute value of the amplitude of the radial velocity disturbance, $\hat{v}$ vs radial location, r at R/θ = 10 from linear spatio-temporal stability analysis

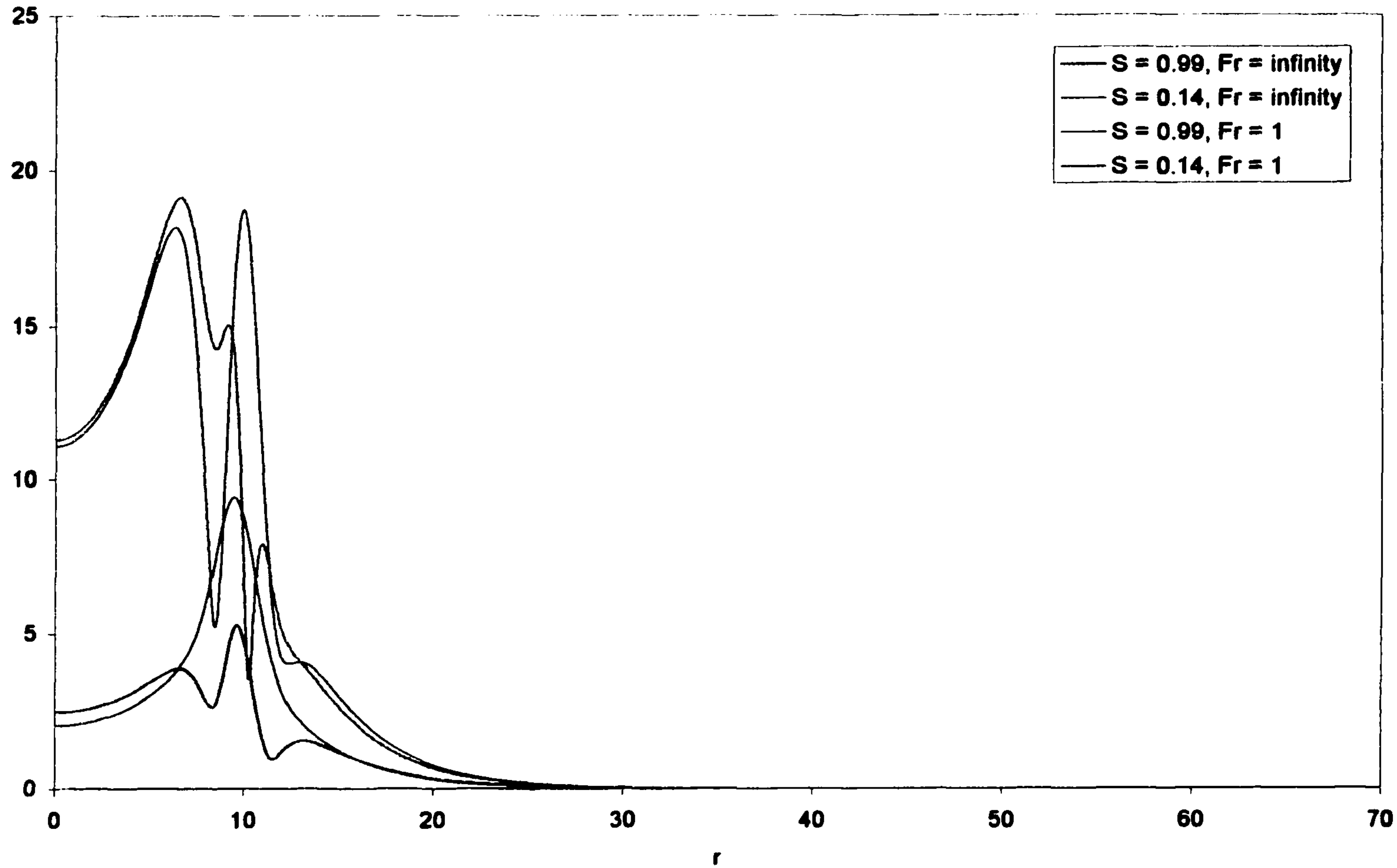

Figure 4.47: Absolute value of the amplitude of the axial velocity disturbance, û vs radial distance, r at R/θ = 10 from linear temporal stability analysis

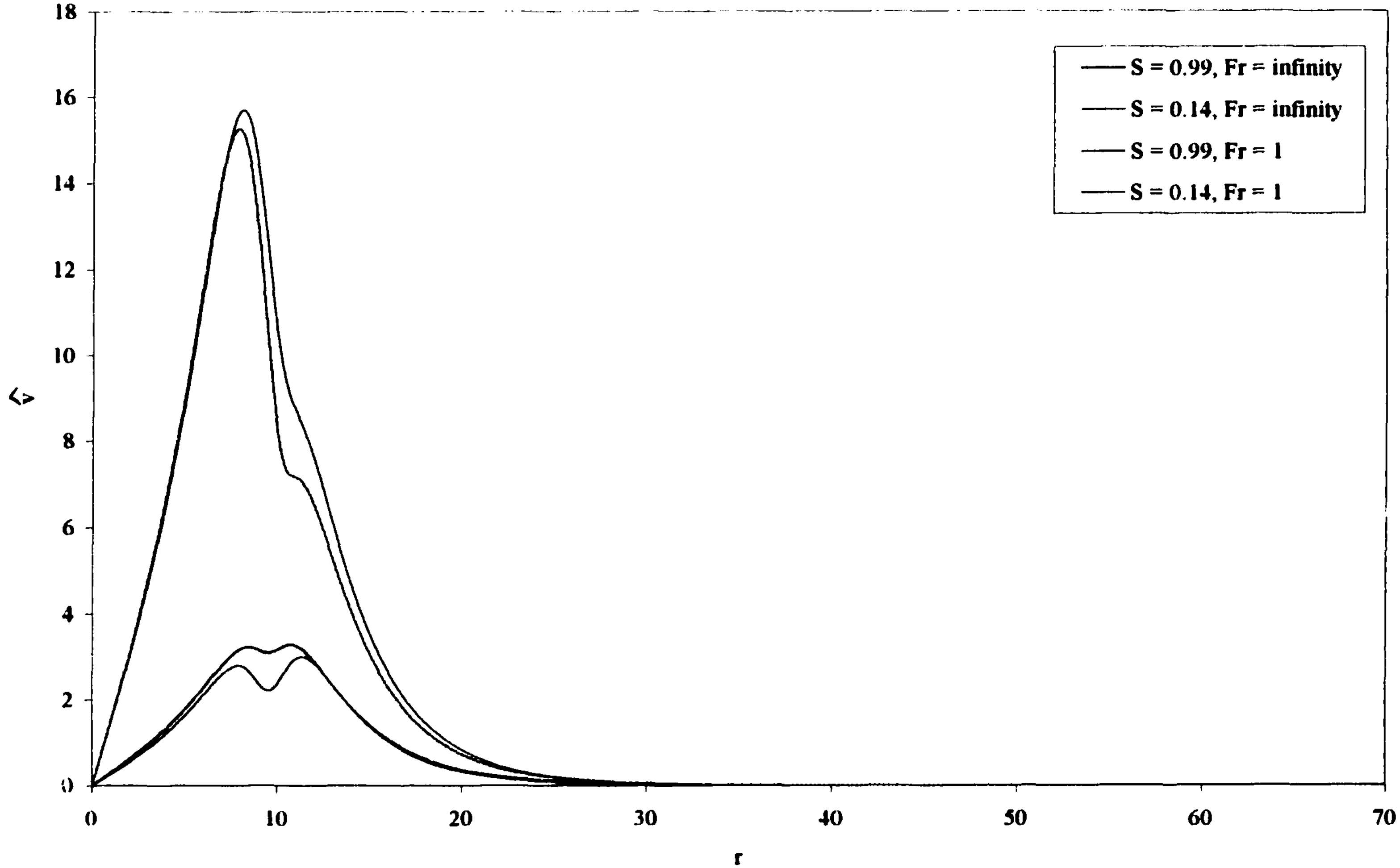

Figure 4.48: Absolute value of the amplitude of the radial velocity disturbance, $\hat{v}$ vs radial location, r at R/θ = 10 from linear temporal stability analysis

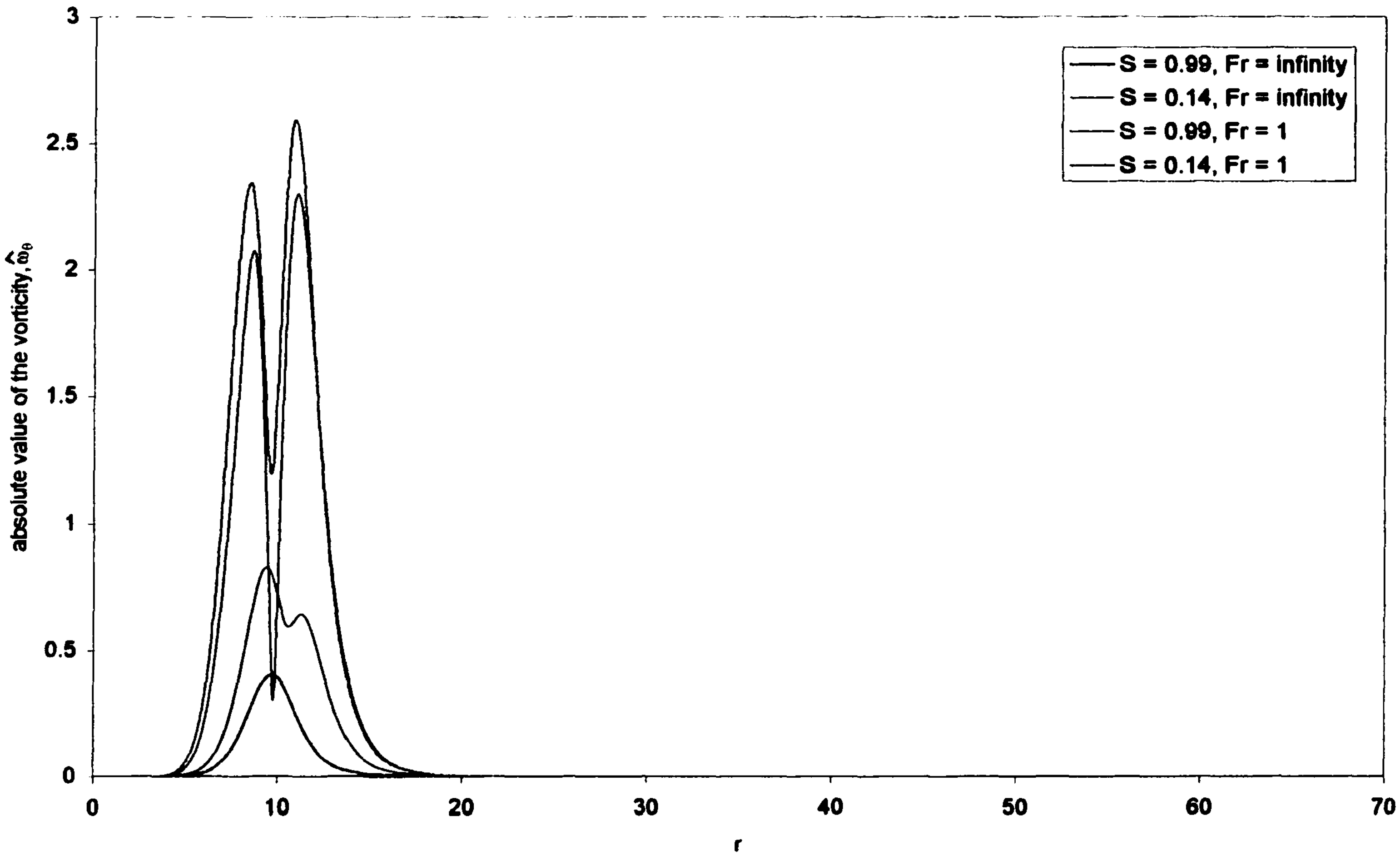

Figure 4.49: Absolute value of the vorticity, $\widehat{\omega}_\theta$ vs radial distance, r at R/θ = 10 from linear spatio-temporal stability analysis

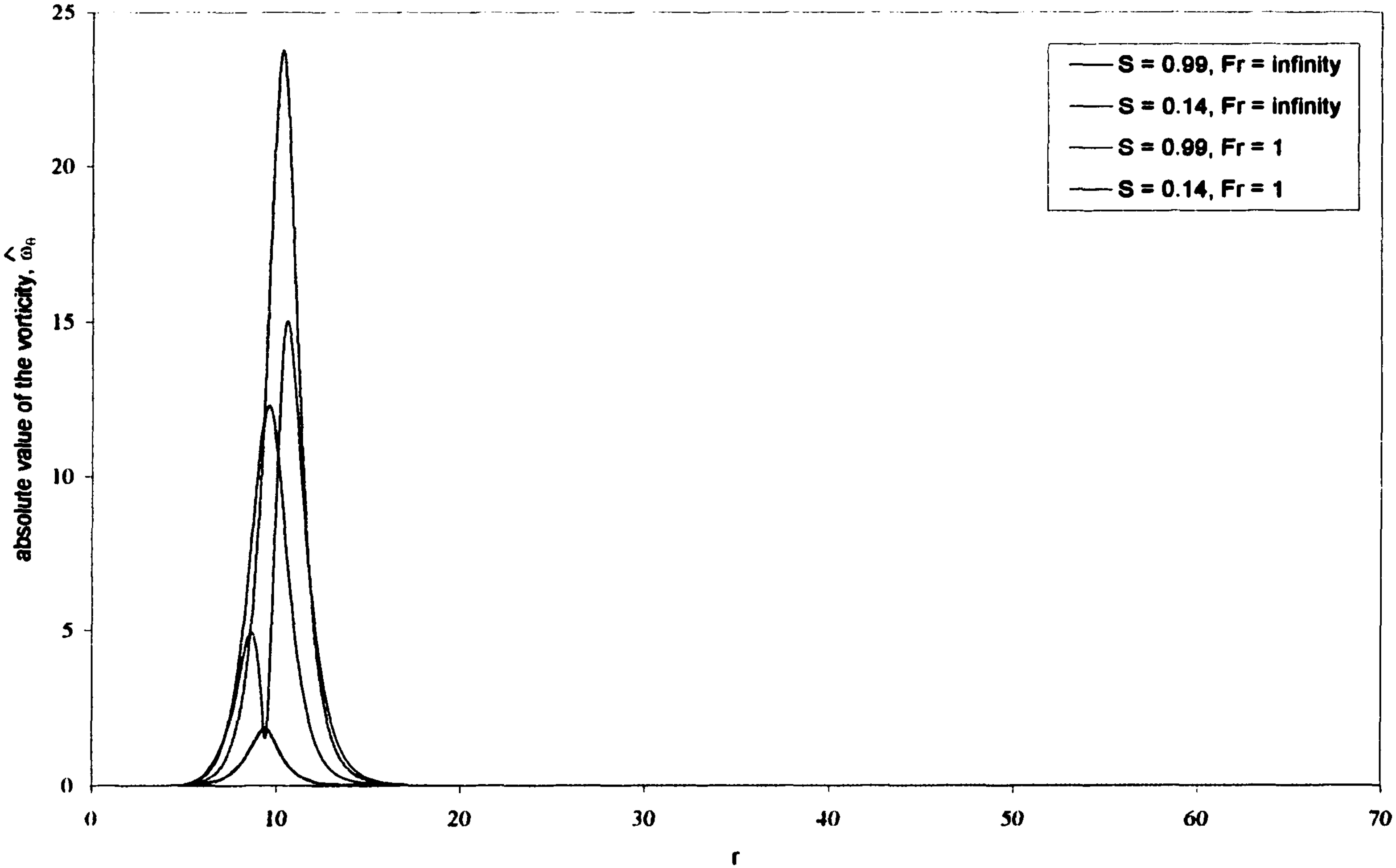

Figure 4.50: Absolute value of the vorticity, $\widehat{\omega}_\theta$ vs radial location, r at R/θ = 10 from linear temporal stability analysis

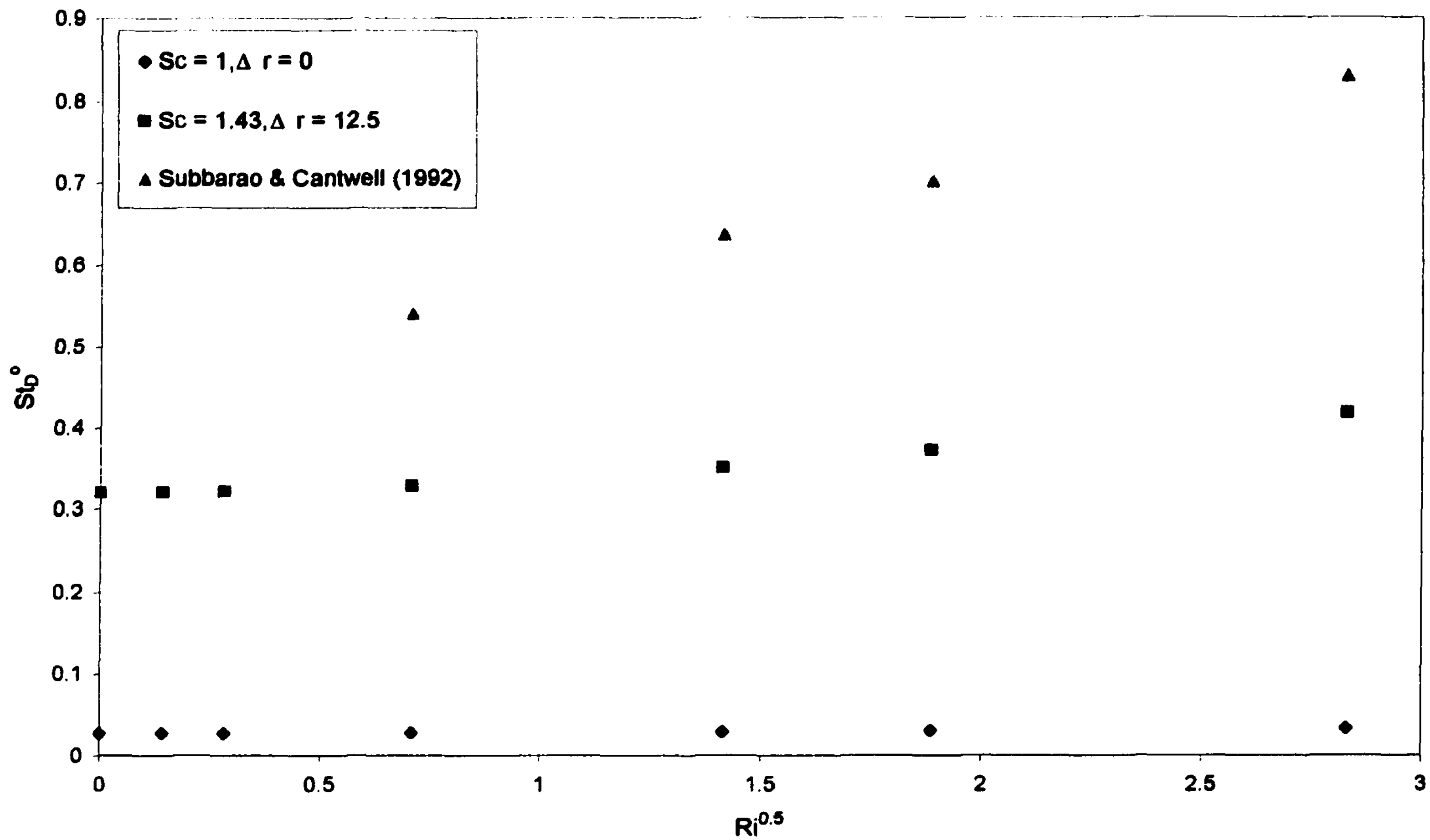

Figure 4.51: Comparison of absolute Strouhal number St_D^o vs square root of Richardson number for helium jet discharged into air and U /ΔU = 1 with Subbarao and Cantwell (1992)

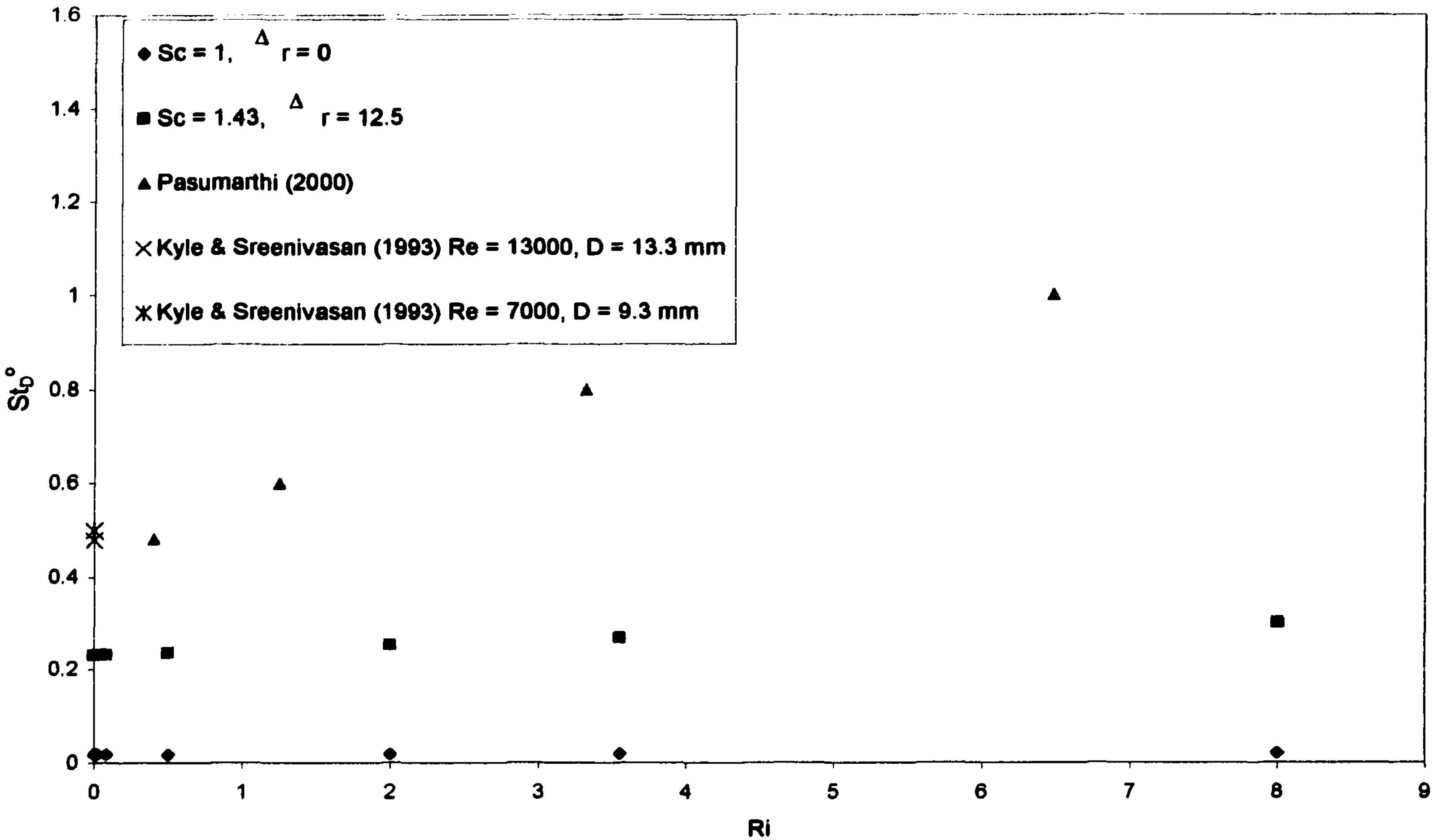

Figure 4.52: Comparison of absolute Strouhal number St_D^o vs Richardson number for helium jet discharged into air with Pasumarthi (2000) and Kyle & Sreenivasan (1993)

Chapter 5

Summary, Conclusions and Recommendations

5.1: Summary

In this study, the instability characteristics of a low-density round gas jet injected into a high-density ambient gas were investigated. A linear temporal stability analysis and a linear spatio-temporal stability analysis were performed to solve for eigenvalues of the pressure disturbance equation obtained from the simultaneous solution of the continuity equations and the equations of motion. The equation was solved numerically. First, the linear temporal stability analysis was carried out to determine the effects of buoyancy and density ratio on the evolution of the disturbances with time. The limits of the k-plane for the mesh-searching technique employed with the spatio-temporal stability analysis were also obtained from the results of the linear temporal analysis. Next, the effects of buoyancy and density ratio on the absolute instability of the jet were investigated using the linear spatio-temporal stability analysis. The results of Monkewitz and Sohn (1988) for hot round jets with negligible buoyancy effects were repeated to verify the accuracy of the solution technique. The results of the spatio-temporal stability analysis were compared with experiments conducted by Subbarao and Cantwell (1992) and Pasumarthi (2000). The effects of Schmidt number and the lateral distance between the velocity and density profiles were also evaluated. Experiments were also carried out to qualitatively compare the differences of an absolutely unstable helium jet injected into air and a constant-density air jet that was not absolutely unstable.

5.2: Conclusions

The following conclusions were made in investigating the absolute instability characteristics of a low-density round gas jet injected into a high-density ambient gas:

1. Reducing the density ratio steepens the density gradient in the shear layer causing additional disturbance. At a Froude number value of Fr = ∞, as the density ratio reduces, the low-density jet injected into a high-density gas medium becomes absolutely unstable at a critical density ratio of 0.525 and 0.17 at axial locations corresponding to R/θ = 10 and 5 respectively. Below this critical density ratio, reducing the density ratio further causes the jet to become more absolutely unstable. Mention must be made of the results from helium-jet-in-air (S = 0.14) experiments conducted by Tze-Wing Yep of the Microgravity Combustion Lab at the NASA Microgravity drop tower. The results showed the helium jet to be convectively unstable in the microgravity environment which suggests that gravity must be present for absolute instability of low-density jets. Thus, the absolute instability reported in this study, and previous studies, at Fr = ∞, may be due to the density and velocity profiles used not matching those in Tze-Wing Yep's microgravity experiments. As of the time of this report Tze-

Wing Yep's work was being prepared for the publication of his M.S. thesis.

2. As the Froude number decreases to account for increasing effect of buoyancy, the critical density ratio of the jet increases. Thus, reducing the Froude number has the effect of causing the jet to become absolutely unstable at higher density ratios.

3. A new nondimensional number $G=\dfrac{g}{\left(U_j^2/\theta\right)}=\dfrac{1}{Fr^2\dfrac{R}{\theta}\left(\dfrac{\rho_\infty}{\rho_j}-1\right)}$ that compares the acceleration of the large-scale structures of the jet due to buoyancy to that due to inertial forces was identified. The "G number" shed some light on the effect of buoyancy on the jet at low Froude numbers. At low Froude numbers, buoyancy causes the jet instabilities to increase exponentially which accounts for the abrupt breakdown of the jet large-scale structures observed in experiments at low Froude numbers.

4. There is a critical Froude number below which the jet is absolutely unstable at all density ratios less than unity. This critical Froude number also demarcates the jet flow into the momentum-driven regime and the buoyancy-driven regime similar to the Strouhal number regimes observed by Subbarao and Cantwell (1992) in their experiments on helium jets discharged into co-flowing air (density ratio = 0.14).

5. Increasing the co-flow velocity reduces the shear layer thickness and thus the

energy available for the growth of the instabilities in the jet. Thus increasing co-flow velocity makes the jet less absolutely unstable.

6. The influence of Schmidt number on the jet stability is complex. For large changes from a Schmidt number of unity the jet becomes less absolutely unstable. On the other hand, for small changes within the neighborhood of Sc = 1, the jet becomes more or less absolutely unstable depending on the Fr.
7. The effect of the lateral shift between the velocity and density profiles on the absolute instability of the jet depends on the relative locations of the density and velocity profiles and also on the Froude number. At Froude numbers greater than two, increasing the lateral shift between the velocity and density profiles causes the jet to be less absolutely unstable. At lower Froude number values decreasing the relative radial location (negative lateral shift) of the density profile with respect to the velocity profile causes the jet to be more absolutely unstable.
8. The Strouhal number results of the spatio-temporal stability analysis were compared with the experimental data of Subbarao and Cantwell (1992), and Pasumarthi (2000). The results from the spatio-temporal analysis considering effects of Schmidt number and the lateral shift in the density and velocity profiles agreed well with the experimental findings. Thus, it appears that linear stability analysis may be effectively used to predict the absolute instability characteristics of low-density gas jets injected into high-density gases.

9. From the experiments carried out it appears that due to the more energetic disturbances there is intense mixing and spreading in the near-injector region of the absolutely unstable helium jet unlike in the air jet that was not absolutely unstable. Also, periodic pulsations of the absolutely unstable jet due to the development of the vortex structures were observed.

5.3: Recommendations

Some recommendations for further research are:

1. Experiments to verify the critical Froude number should be carried out.
2. The effects of different mean velocity profiles on the jet instability need to be studied.
3. Within the shear layer the kinematic viscosity varies radial from that of the injected medium to that of the ambient gas. Thus, it is necessary to investigate the effect of the varying Schmidt number (ν/D_b) in the jet shear layer.
4. The numerical investigations need to be carried out to large values of co-flow to determine limiting trends of the co-flow on the instabilities of the jet.
5. The numerical investigations need to be carried out for other types of shear flow such as wakes and mixing layers.
6. Effects of swirl must be taken into account for practical applications. Numerical investigations need to be carried out to determine the effect of the swirl component on the flow instabilities.

References

Al-Ammar, (1999) "Scalar Measurements and Analysis of Hydrogen Gas-Jet Diffusion Flames in Normal and Microgravity," *PhD Dissertation*, School of Aerospace and Mechanical Engineering, University of Oklahoma, Norman, OK.

Agarwal, J. K. and Johnson, E. M., (1981) "Generating Aerosol for Laser Velocimeter Seeding," *TSI Quarterly*, Vol. III, No. 3.

Ahmed, S. A., Nejad, A. S., and Al-Garni, A. Z. (1995) "A Comprehensive Study of the Effects of LDV Velocity Bias in the Near Field of a Turbulent Free Jet," *Canadian Aeronautics and Space Journal*, Vol. 41, pp. 179-184.

Armstrong, R. R., Michalke, A., and Fuchs, H. V. (1977) "Coherent Structures in Jet Turbulence and Noise," *A.I.A.A. Journal*, Vol. 15, pp. 1011-1017.

Batchelor, G. K. and Gill, A. E. (1962) "Analysis of the Stability of Axisymmetric Jets," *Journal of Fluid Mechanics*, Vol. 14, pp. 529-551.

Bers, A., (1975) "Linear Waves and Instabilities," *Plasma Physics*, edited by C. DeWitt and J. Peyraud, Gordon and Breach, New York, pp. 117-213.

Bers, A., (1983) "Space-time Evolution of Plasma Instabilities," *Handbook of Plasma Physics*, Vol. I, pp. 452-517.

Briggs, R. J., (1964) *Electron Stream Interaction with Plasmas*, MIT Press, Cambridge, Massachusetts.

Buckmaster, J. and Peters, N., (1986) "The Infinite Candle and its Stability – A Paradigm for Flickering Diffusion Flames," *Twenty-First Symposium (International) on Combustion*, pp. 1829-1836.

Cetegen, B. M. and Kasper, K. D., (1996) "Experiments on the Oscillatory Behavior of Buoyant Plumes of Helium and Helium-Air Mixtures," *Physics of Fluids*, Vol. 8, No 11, pp. 2974-2984.

Cetegen, B. M., (1997-1) "Behavior of Naturally Unstable and Periodically Forced Axisymmetric Buoyant Plumes of Helium and Helium-Air Mixtures," *Physics of Fluids*, Vol. 9, No 12, pp. 3742-3752.

Cetegen, B. M., (1997-2) "Measurements of Instantaneous Velocity Field of a Non-Reacting Pulsating Buoyant Plume by Particle Image Velocimetry," *Combustion Science and Technology*, Vol. 123, pp. 377-387.

Cetegen, B. M., Dong, Y. and Soteriou, M. C.., (1998) "Experiments on Stability and Oscillatory Behavior of Planar Buoyant Plumes," *Physics of Fluids*, Vol. 10, No 7, pp. 1658-1665.

Cetegen, B. M. and Dong, Y. (2000) "Experiments on the Instability modes of Buoyant Diffusion Flames and Effects of Ambient Atmosphere on the Instabilities," *Experiments in Fluids*, Vol. 28, pp. 546-558.

Chen, L. D., Seaba, J. P., Roquemore, W. M., and Goss, L. P. (1988) "Buoyant Diffusion FLames," *Twenty-Second Symposium (International) on Combustion*, The Combustion Institute, pp. 677-684.

Cohen, J. and Wygnanski, I. (1987) "The Evolution of the Instabilities in the Axisymmetric Jet. Part 2. The Flow Resulting from the Interaction between Two Waves," *Journal of Fluid Mechanics*, Vol. 176, pp. 221.

Crighton, D. G. and Gaster, M. (1976) "Stability of Slowly Diverging Jet Flow" *Journal of Fluid Mechanics*, Vol. 77, pp. 397-413.

Crow, S. C., (1972) "Acoustic Gain of a Turbulent Jet," *Paper IE6, Annual Meeting of the Division of Fluid Dynamics of the American Physics Society, Boulder, CO, Nov. 20-22, 1972.*

Crowe, S. C. and Champagne, F. H. (1971) "Orderly Structure in Jet Turbulence," *Journal of Fluid Mechanics*, Vol. 48, pp. 547-591.

Chan, N. Y.-H. (1998) "Velocity Measurements in a Particle-Laden Round Jet Using Discriminator Laser Doppler Velocimetry," *MS Thesis*, University of Oklahoma.

Ffowcs-Williams, J. E. and Kempton, A. J., (1978) "The Noise from the Large-Scale Structure of a Jet," *Journal of Fluid Mechanics*, Vol. 84, Pt. 4, pp. 673-694.

Gaster, M., Kit, E., and Wygnanski, I. (1985) "Large-scale Structures in a Forced Turbulent Mixing Layer," *Journal of Fluid Mechanics*, Vol. 150, pp. 23.

Geankoplis, C. J., (1972) "Mass Transport Phenomena," *Holt, Rinehart and Winston*.

Gebhart, B. (1993) "Heat Conduction and Mass Diffusion," *McGraw-Hill*, New York.

Hamins, A., Yang, J. C. and Kashiwagi, T., (1992) "An Experimental Investigation of the Pulsation Frequency of Flames," *Twenty-Fourth Symposium (International) on Combustion/The Combustion Institute*, pp. 1695-1702.

Huerre, P. and Monkewitz, P. A., (1985) "Absolute and Convective Instabilities in Free Shear Layers," *Journal of Fluid Mechanics*, Vol. 159, pp. 151-168.

Huerre, P. and Monkewitz, P. A., (1990) "Local and Global Instabilities in Spatially Developing Flows," *Annual Review of Fluid Mechanics*, Vol. 22, pp. 473-537.

Jendoubi, S. and Strykowski, (1994) "Absolute and Convective Instability of Axisymmetric Jets with External Flow," *Physics of Fluids*, Vol. 6, No. 9, pp. 3000-3009.

Kyle, D. M. and Sreenivasan, K. R., (1993) "The Instability and Breakdown of a Round Variable-Density Jet," *Journal of Fluid Mechanics*, Vol. 249, pp. 619-664.

Li, X. and Shen, J. (1996) "Breakup of Cylinderical Liquid Jets in Co-Flowing Gas Streams," *ASME*, pp. 22-31.

Michalke, A. (1984) "Survey on Jet Instability Theory," *Progress in Aerospace Sciences*, Vol. 21, pp. 159-199.

Michalke, A. and Hermann, G. (1982) "On the Inviscid Instability of a Circular Jet with External Flow," *Journal of Fluid Mechanics*, Vol. 114, pp. 343-359.

Mollo-Christensen, E. (1967) "Jet Noise and Shear Flow Instability seen from an Experimenter's Viewpoint," Trans. A.S.M.E. E, *Journal of Applied Mechanics*, Vol. 89, pp. 1-7.

Monkewitz, P. A., Bechert, D. W., Barsikow, B. and Lehmann, B. (1990) "Self-excited Oscillations and Mixing in a Heated Round Jet," *Journal of Fluid Mechanics*, Vol. 213, pp. 611-639.

Monkewitz, P. A. and Sohn, K. D. (1988) "Absolute Instability in Hot Jets," *AIAA Journal*, Vol. 26, pp. 911-916.

Moore, C. J., (1977) "The Role of Shear-Layer Instability Waves in Jet Exhaust Noise," *Journal of Fluid Mechanics*, Vol. 80, Pt. 2, pp. 321-367.

Parthasarathy, R. N., (1985) "A Theoretical and Experimental Study of Turbulent Condensing Bubbly Jets," *MS Thesis*, Pennsylvania State University, University Park.

Pasumarthi, K. S., (2000) "Full Field Scalar Measurements in a Pulsating Helium Jet Using Rainbow Schlieren Deflectometry," *MS Thesis*, University of Oklahoma, Norman, Oklahoma.

Raynal, L., Harion, J.-L., Favre-Marinet, M. and Binder, G. (1996) "The Oscillatory Instability of Plane Variable-Density Jets," *Physics of Fluids*, Vol. 8, No. 4, pp. 993-1006.

Richards, C. D., Breuel, B. D., Clark, R. P. and Troutt, T. R., (1996) "Concentration Measurements in a Self-Excited Jet," *Experiments in Fluids*, Vol. 21, pp. 103-109.

Schlichting, H. (1979) "Boundary Layer Theory," 7th edition, *McGraw-Hill*, New York.

Sreenivasan, K. R., Raghu, S., and Kyle, D. (1989) "Absolute Instability in Variable Density Round Jets," *Experiments in Fluids*, Vol. 7, pp. 309-317.

Stromberg, J. L., McLaughlin, D. K., and Troutt, T. R. (1980) "Flow Field and Acoustic Properties of a Mach Number 0.9 Jet at Low Reynolds Number," *Journal of Sound Vibration*, Vol. 72, pp. 159-176.

Subbarao, E. R. and Cantwell, B. J., (1992) "Investigation of a Co-Flowing Buoyant Jet: Experiments on the Effects of Reynolds Number and Richardson Number," *Journal of Fluid Mechanics*, Vol. 245, pp. 69-90.

TSI, Incorporated, (2000-1) "Model 9306 Six-Jet Atomizer Instruction Manual," *TSI, Incorporated*.

TSI, Incorporated, (2000-2) "Model IFA 655 Digital Burst Correlator Instruction Manual," *TSI, Incorporated*.

Wheeler, A. J. and Ganji, A. R. (1996) "Introduction to Engineering Experimentation," *Prentice Hall, New Jersey*.

Yu, M.-H. (1990) "Local and Global Instability of Heated 2-D Jets and Wakes," *PhD Dissertation*, University of California.

Yu, M.-H. and Monkewitz, P. A. (1990) "The Effect of NonUniform Density on the Absolute Instability of Two-Dimensional Inertial Jets and Wakes," *Physics of Fluids A*, Vol. 2, No. 7, pp. 1175-1181.

Appendix A

Contour plots

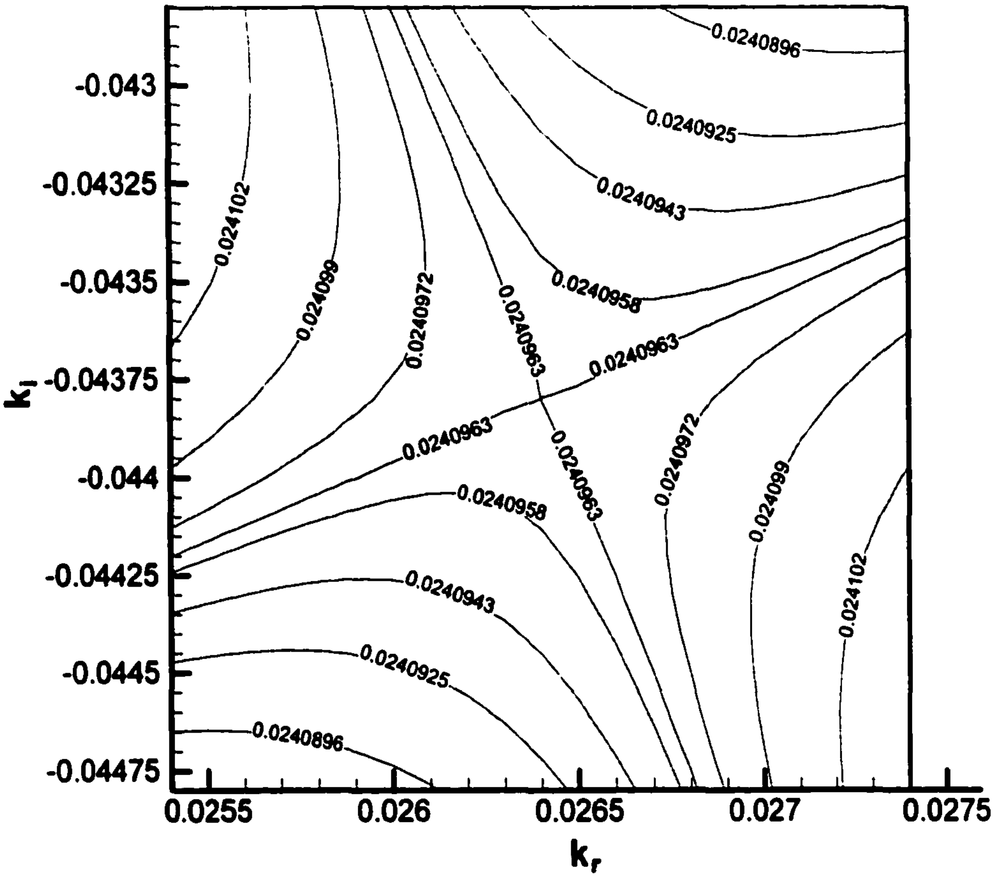

Figure A1: Contour plot of Ω_r for $R/\theta = 25$, $Fr = \infty$, $\rho_j/\rho_\infty = 0.14$ in the k-plane illustrating the pinch point formation

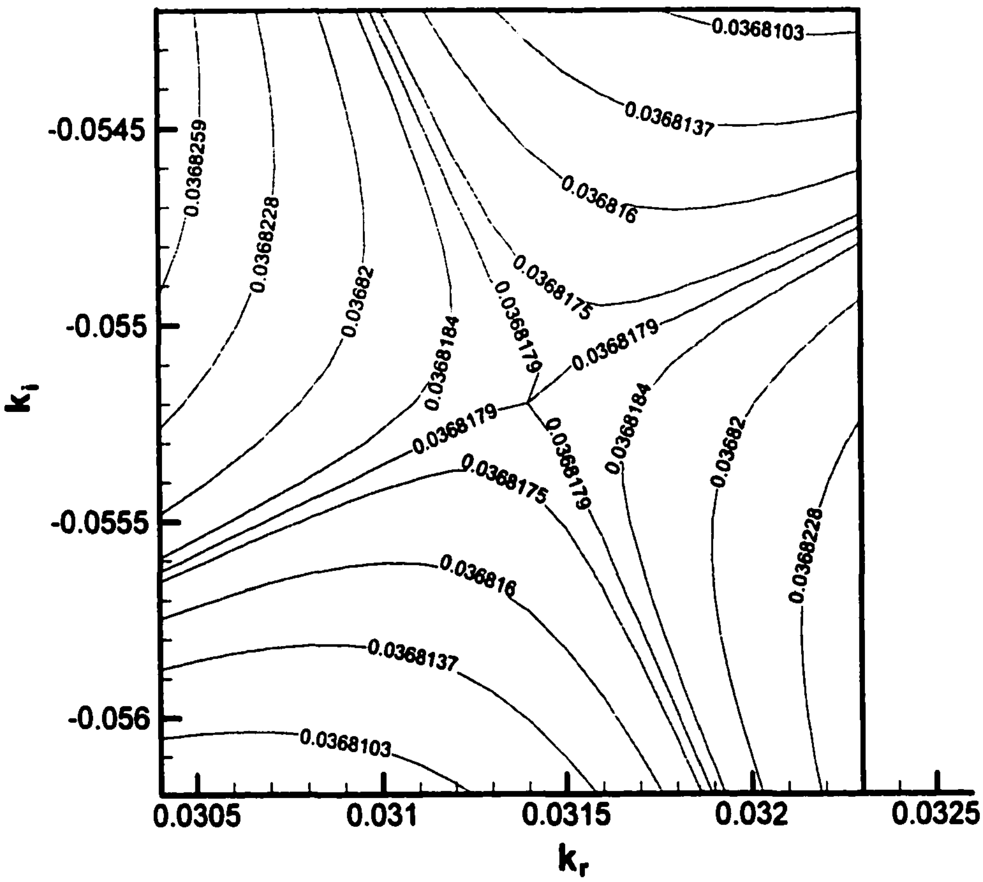

Figure A2: Contour plot of Ω_r for $R/\theta = 25$, $Fr = \infty$, $\rho_j/\rho_\infty = 0.3$ in the k-plane illustrating the pinch point formation

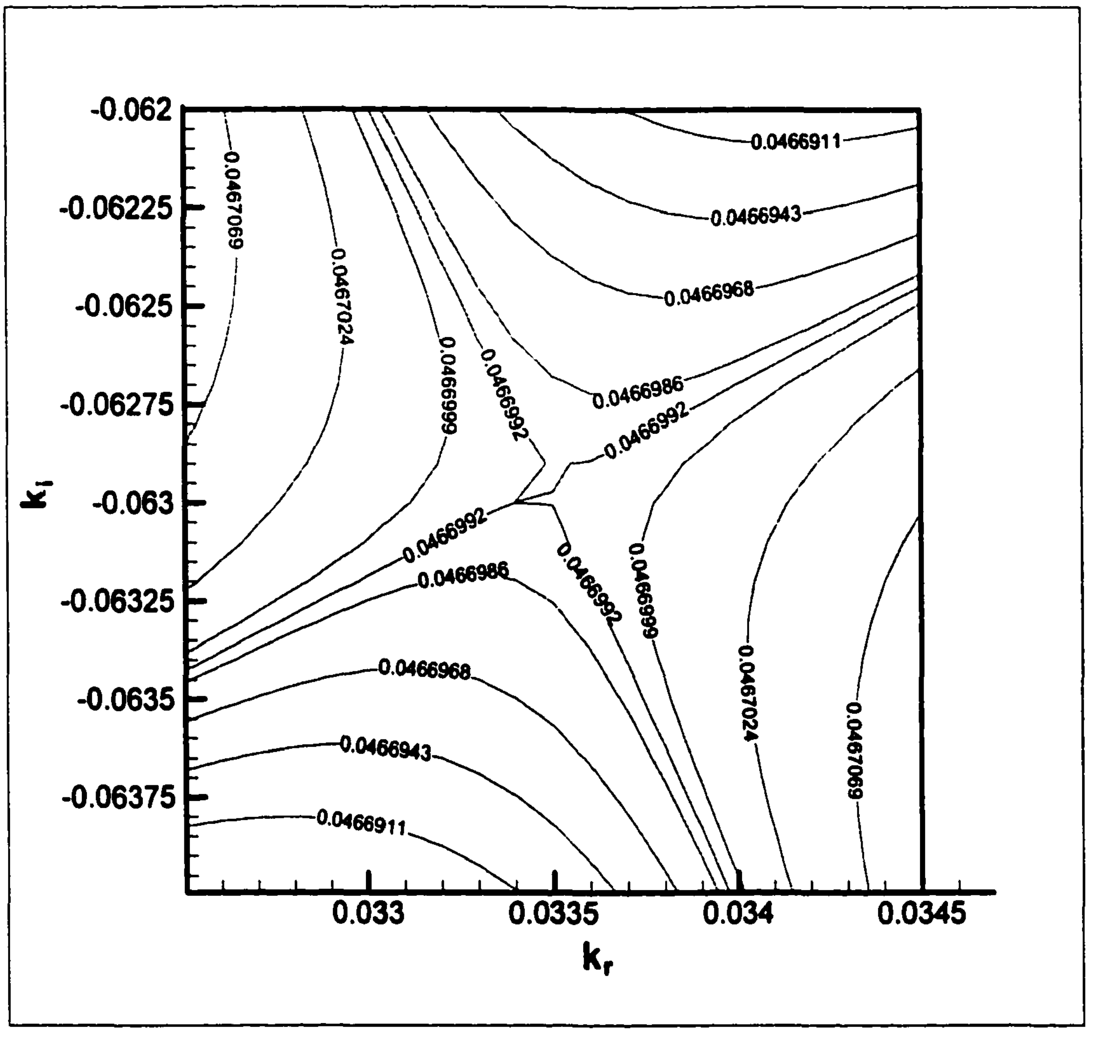

Figure A3: Contour plot of Ω_r for $R/\theta = 25$, $Fr = \infty$, $\rho_j/\rho_\infty = 0.5$ in the k-plane illustrating the pinch point formation

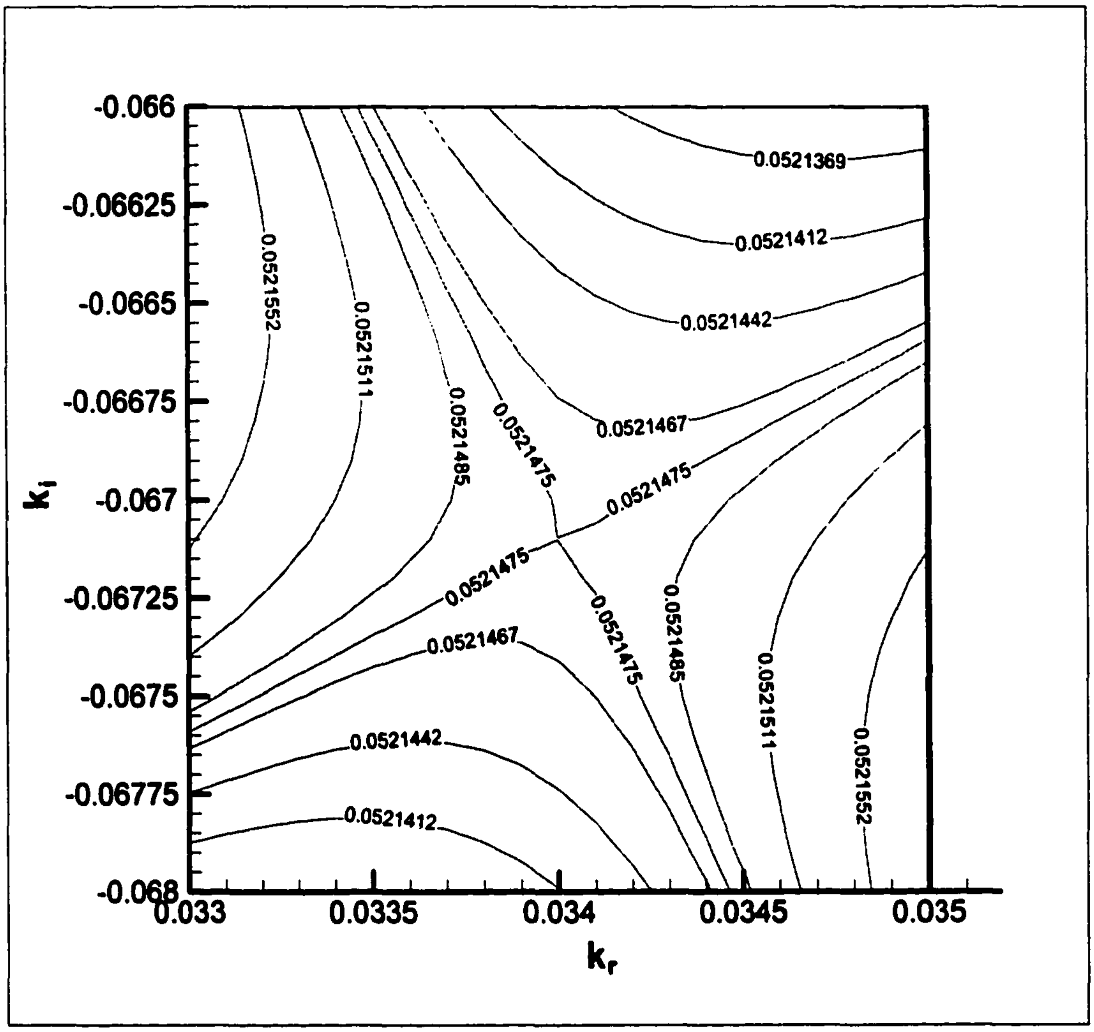

Figure A4: Contour plot of Ω_r for $R/\theta = 25$, $Fr = \infty$, $\rho_j/\rho_\infty = 0.66$ in the k-plane illustrating the pinch point formation

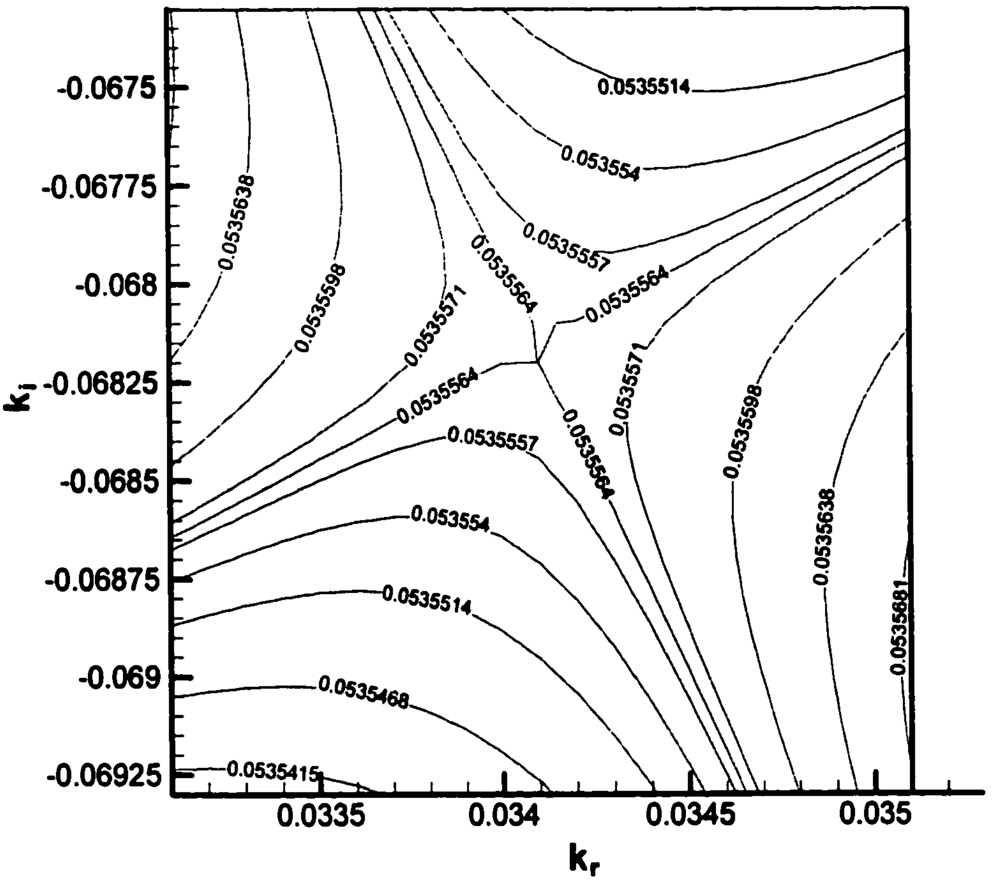

Figure A5: Contour plot of Ω_r for $R/\theta = 25$, $Fr = \infty$, $\rho_j/\rho_\infty = 0.71$ in the k-plane illustrating the pinch point formation

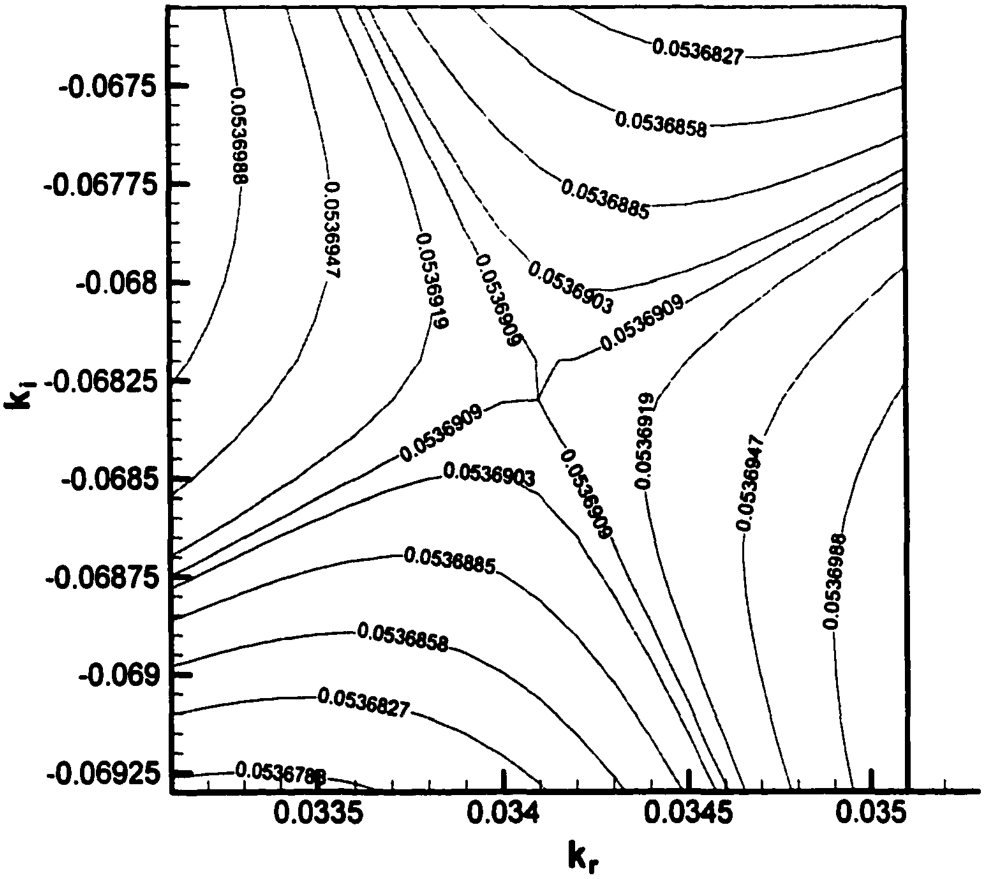

Figure A6: Contour plot of Ω_r for $R/\theta = 25$, $Fr = \infty$, $\rho_j/\rho_\infty = 0.715$ in the k-plane illustrating the pinch point formation

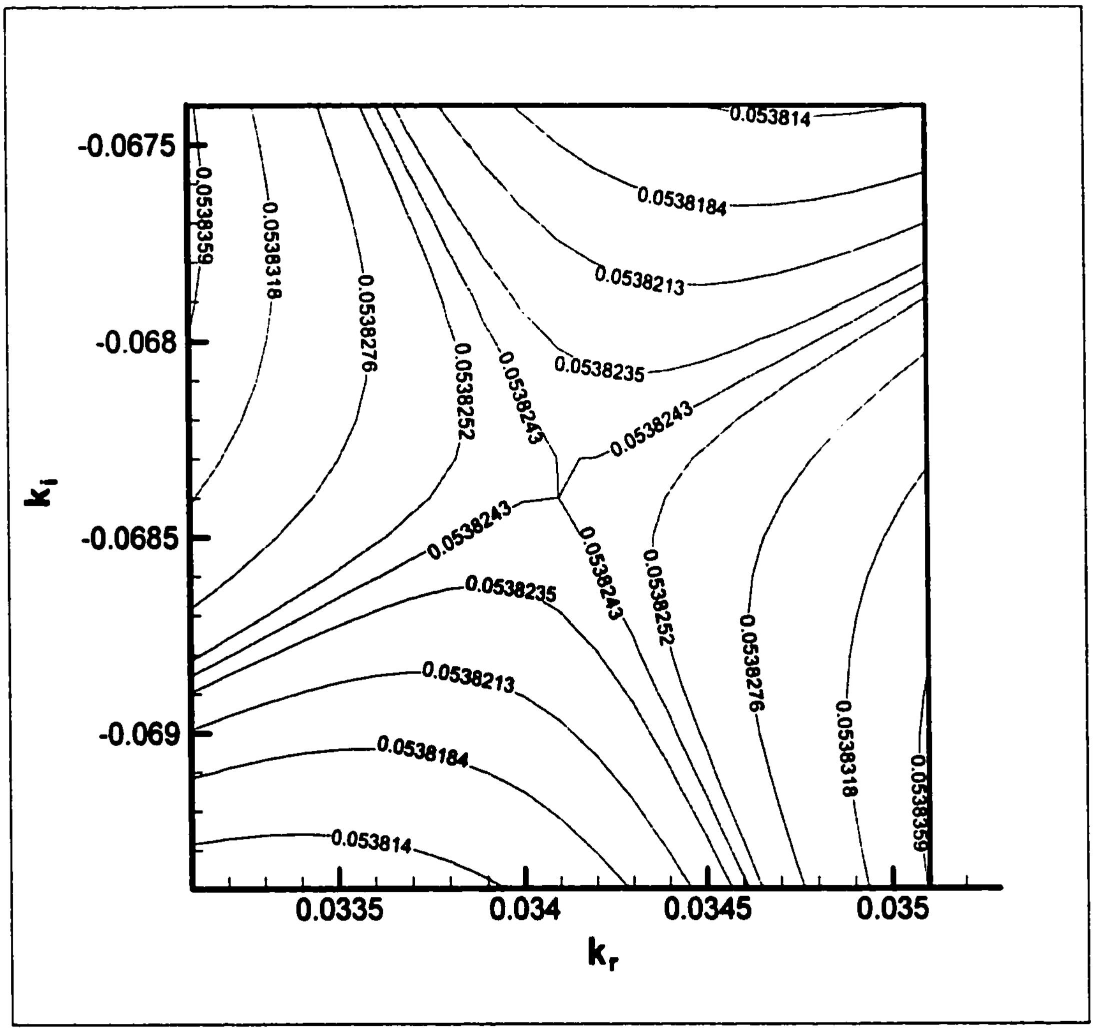

Figure A7: Contour plot of Ω_r for $R/\theta = 25$, $Fr = \infty$, $\rho_j/\rho_\infty = 0.72$ in the k-plane illustrating the pinch point formation

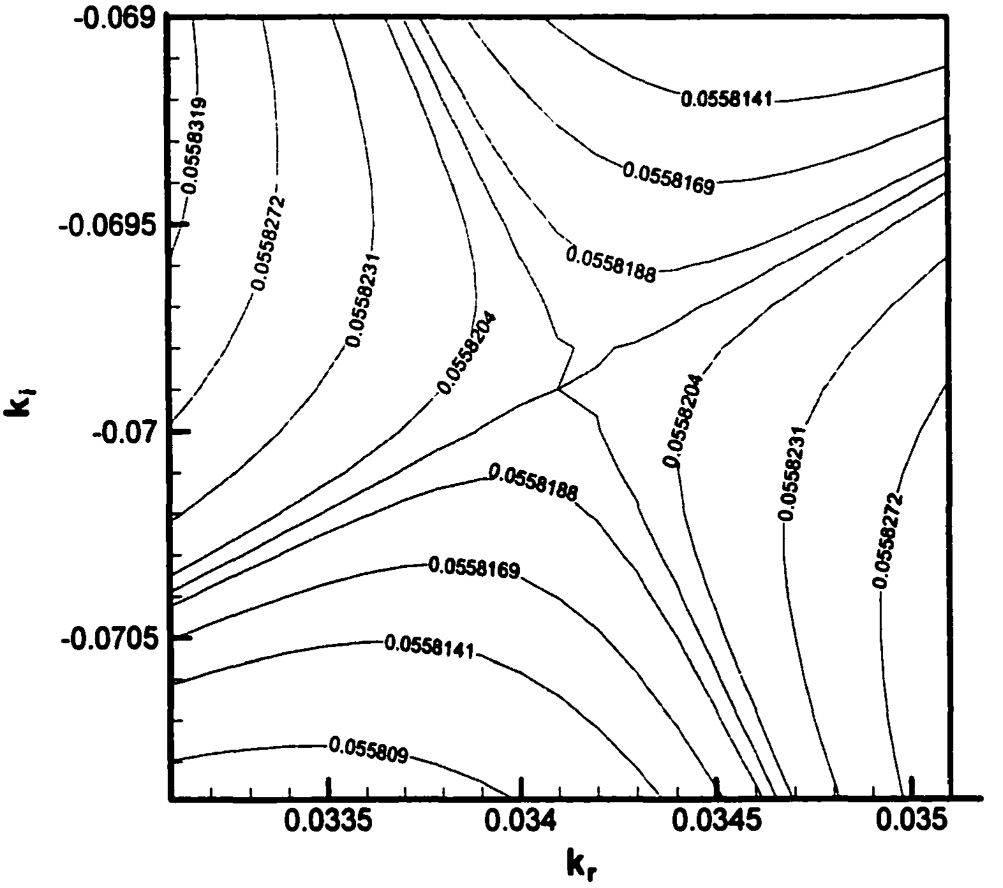

Figure A8: Contour plot of Ω_r for $R/\theta = 25$, $Fr = \infty$, $\rho_j/\rho_\infty = 0.8$ in the k-plane illustrating the pinch point formation

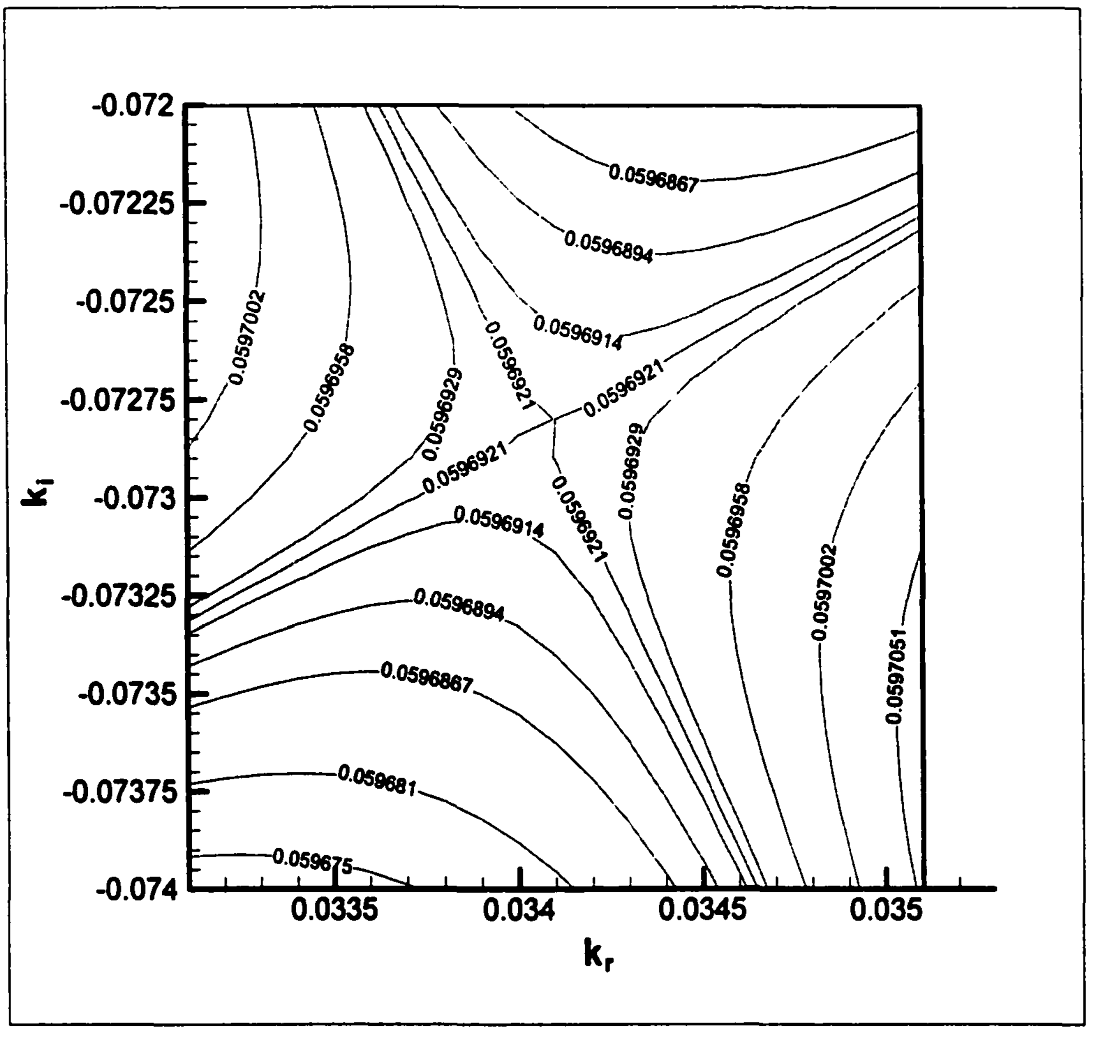

Figure A9: Contour plot of Ω_r for $R/\theta = 25$, $Fr = \infty$, $\rho_j/\rho_\infty = 0.99$ in the k-plane illustrating the pinch point formation

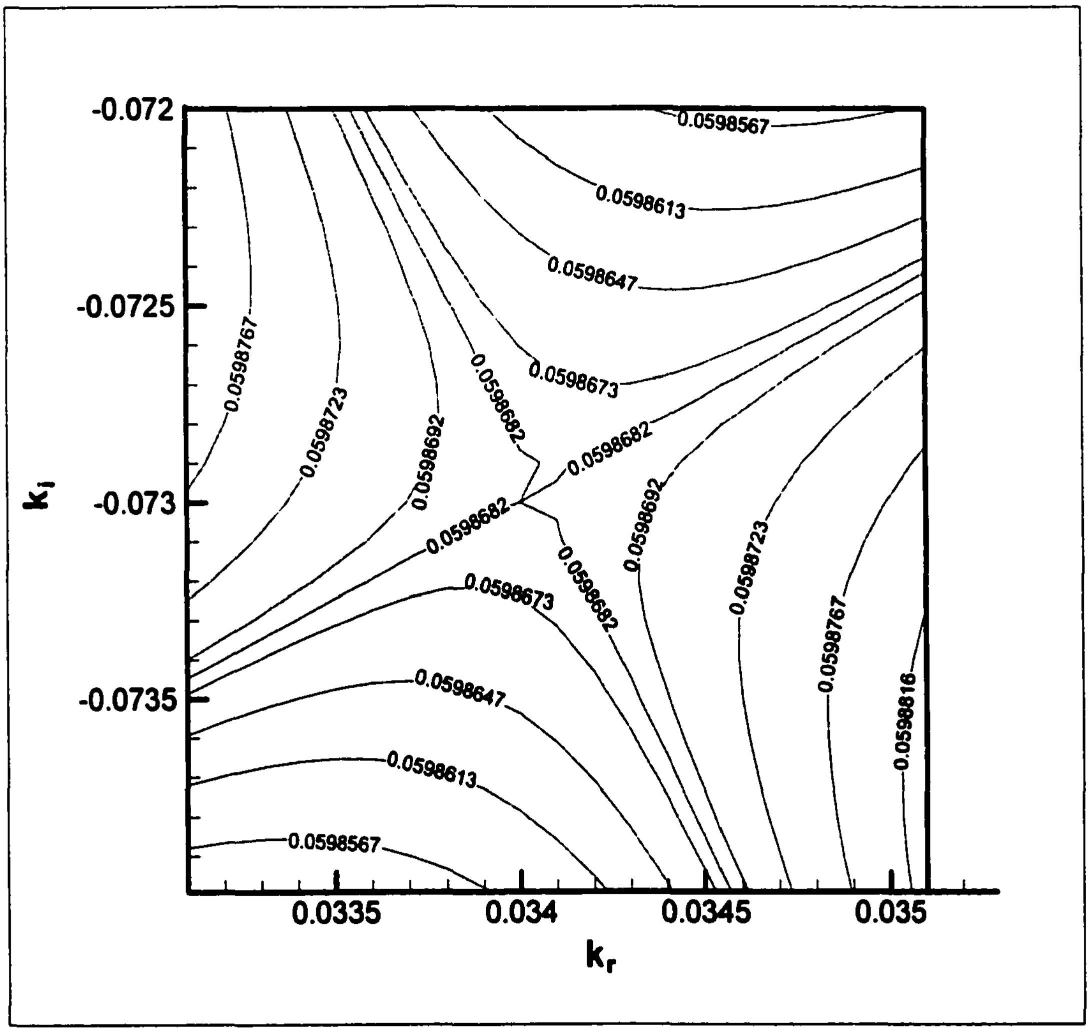

Figure A10: Contour plot of Ω_r for $R/\theta = 25$, $Fr = \infty$, $\rho_j/\rho_\infty = 1$ (constant density jet) in the k-plane illustrating the pinch point formation

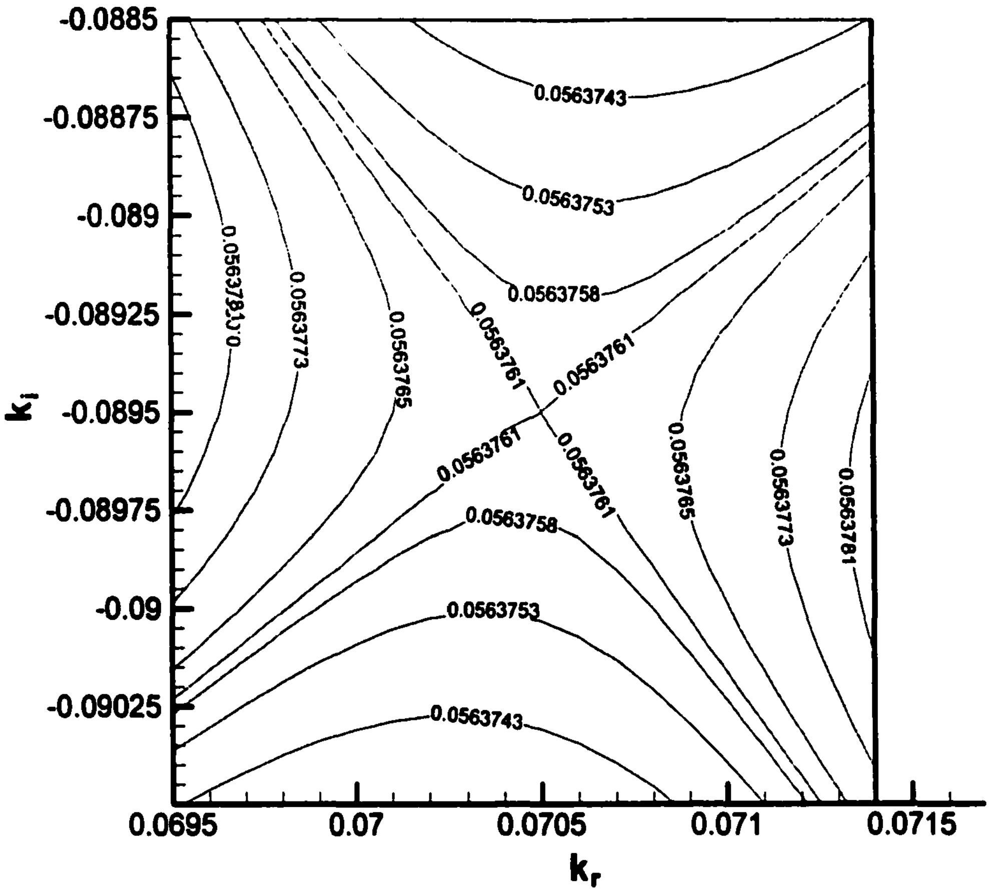

Figure A11: Contour plot of Ω_r for $R/\theta = 10$, $Fr = \infty$, $\rho_j/\rho_\infty = 0.14$ in the k-plane illustrating the pinch point formation

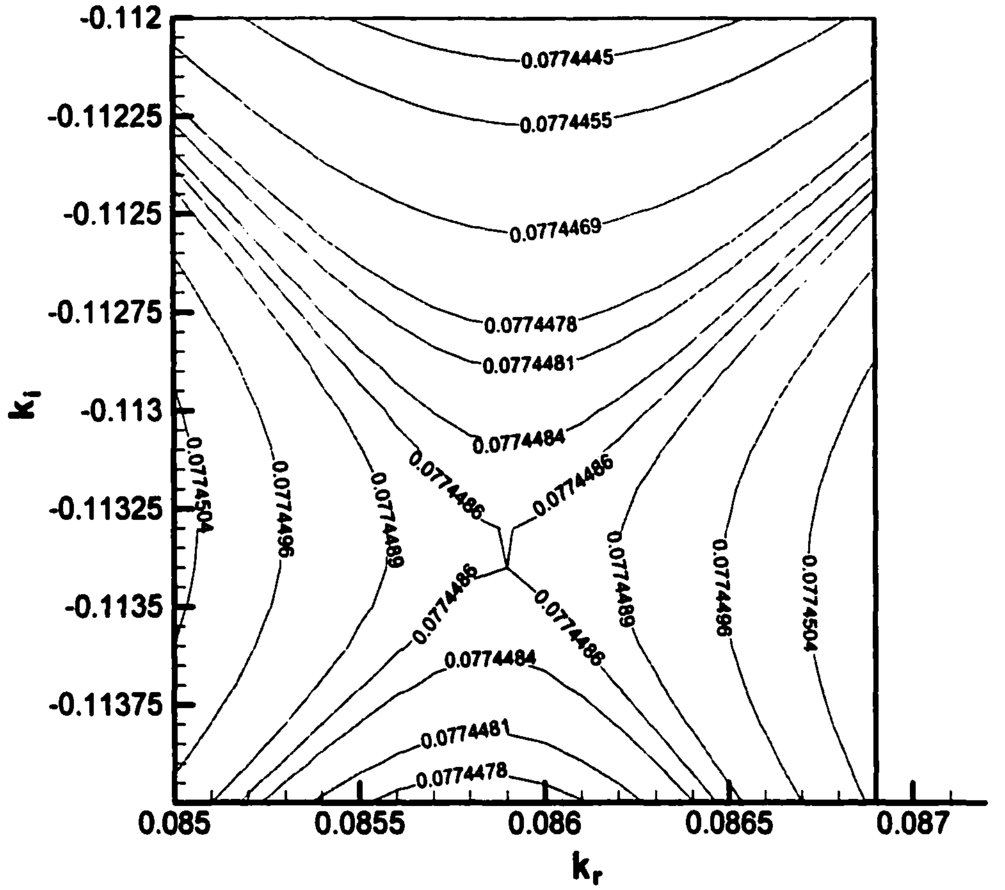

Figure A12: Contour plot of Ω_r for $R/\theta = 10$, $Fr = \infty$, $\rho_j/\rho_\infty = 0.3$ in the k-plane illustrating the pinch point formation

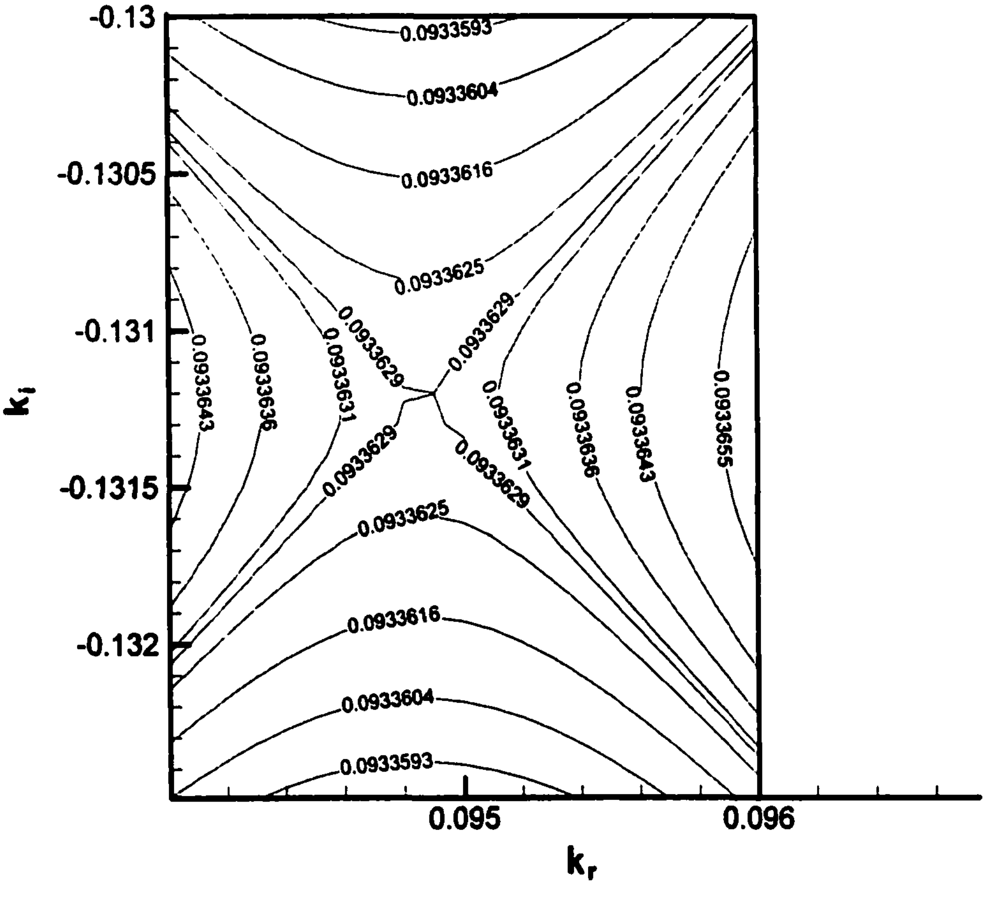

Figure A13: Contour plot of Ω_r for $R/\theta = 10$, $Fr = \infty$, $\rho_j/\rho_\infty = 0.5$ in the k-plane illustrating the pinch point formation

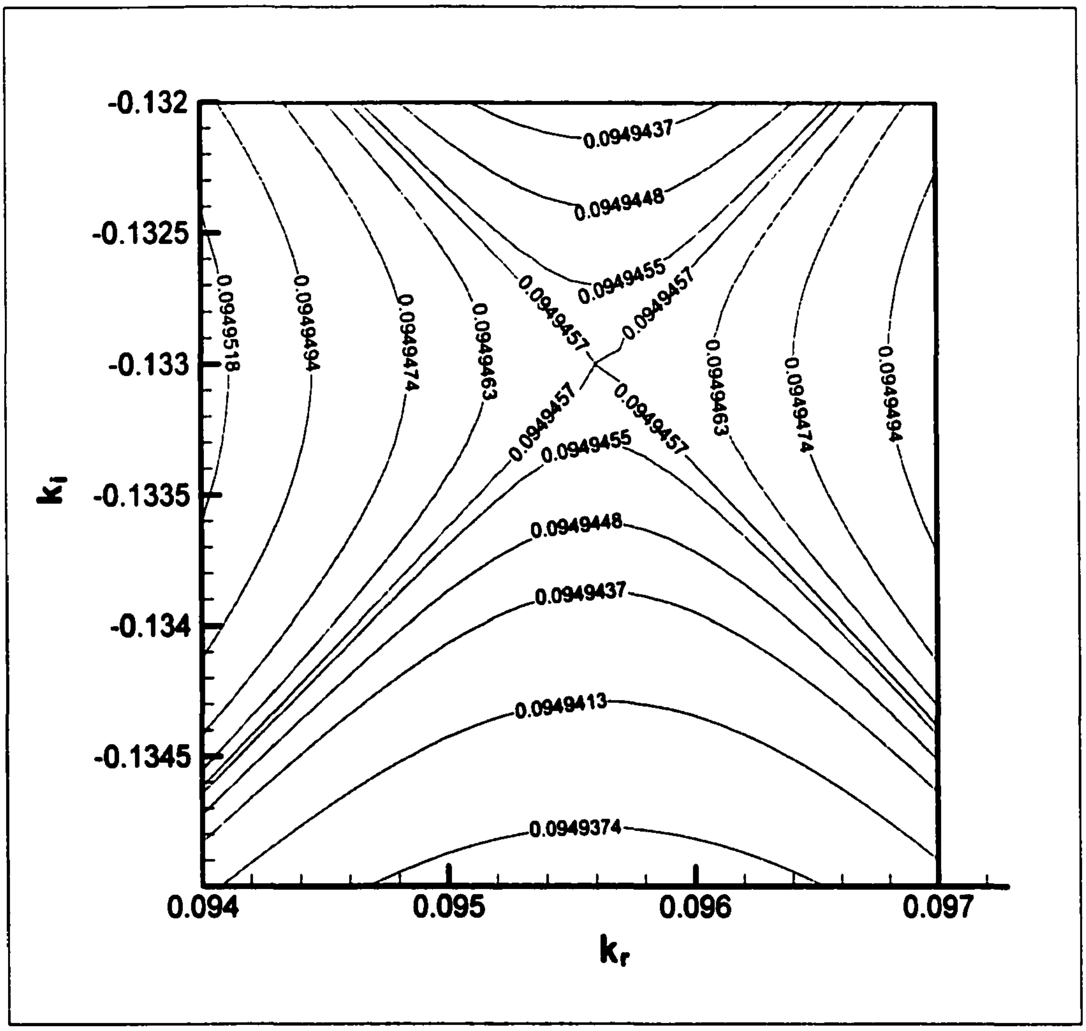

Figure A14: Contour plot of Ω_r for $R/\theta = 10$, $Fr = \infty$, $\rho_j/\rho_\infty = 0.525$ in the k-plane illustrating the pinch point formation

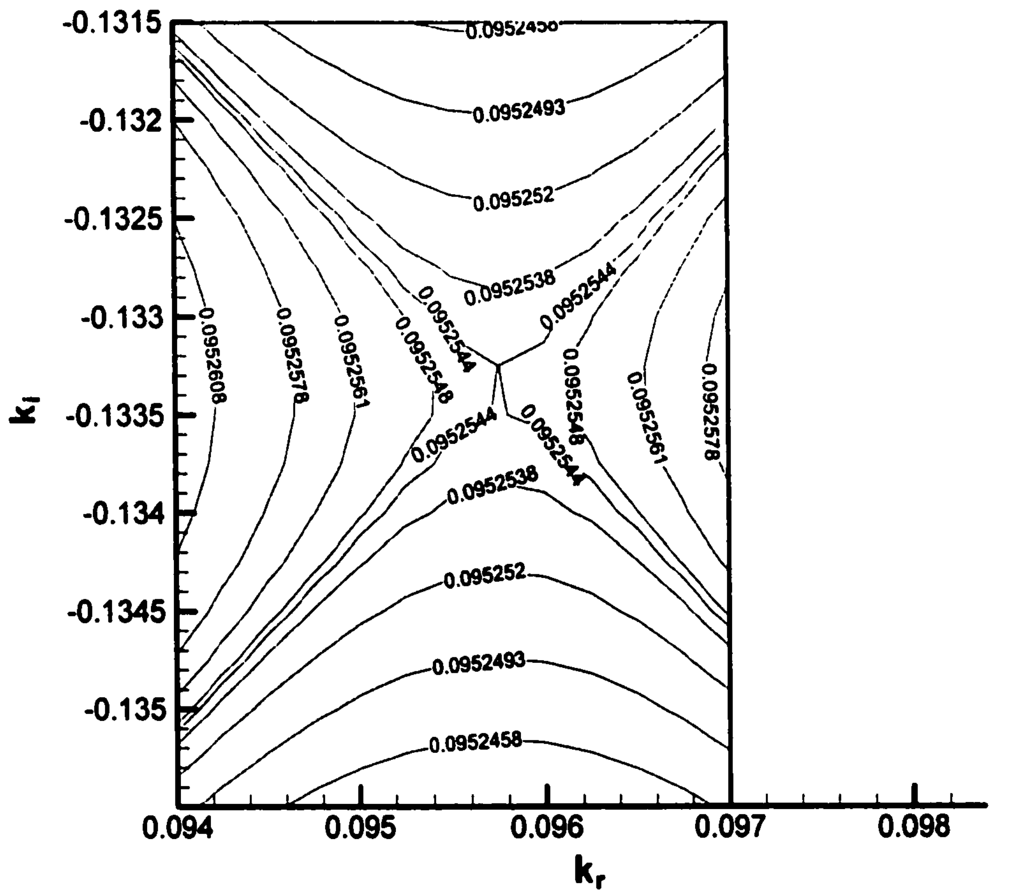

Figure A15: Contour plot of Ω_i for $R/\theta = 10$, $Fr = \infty$, $\rho_j/\rho_\infty = 0.53$ in the k-plane illustrating the pinch point formation

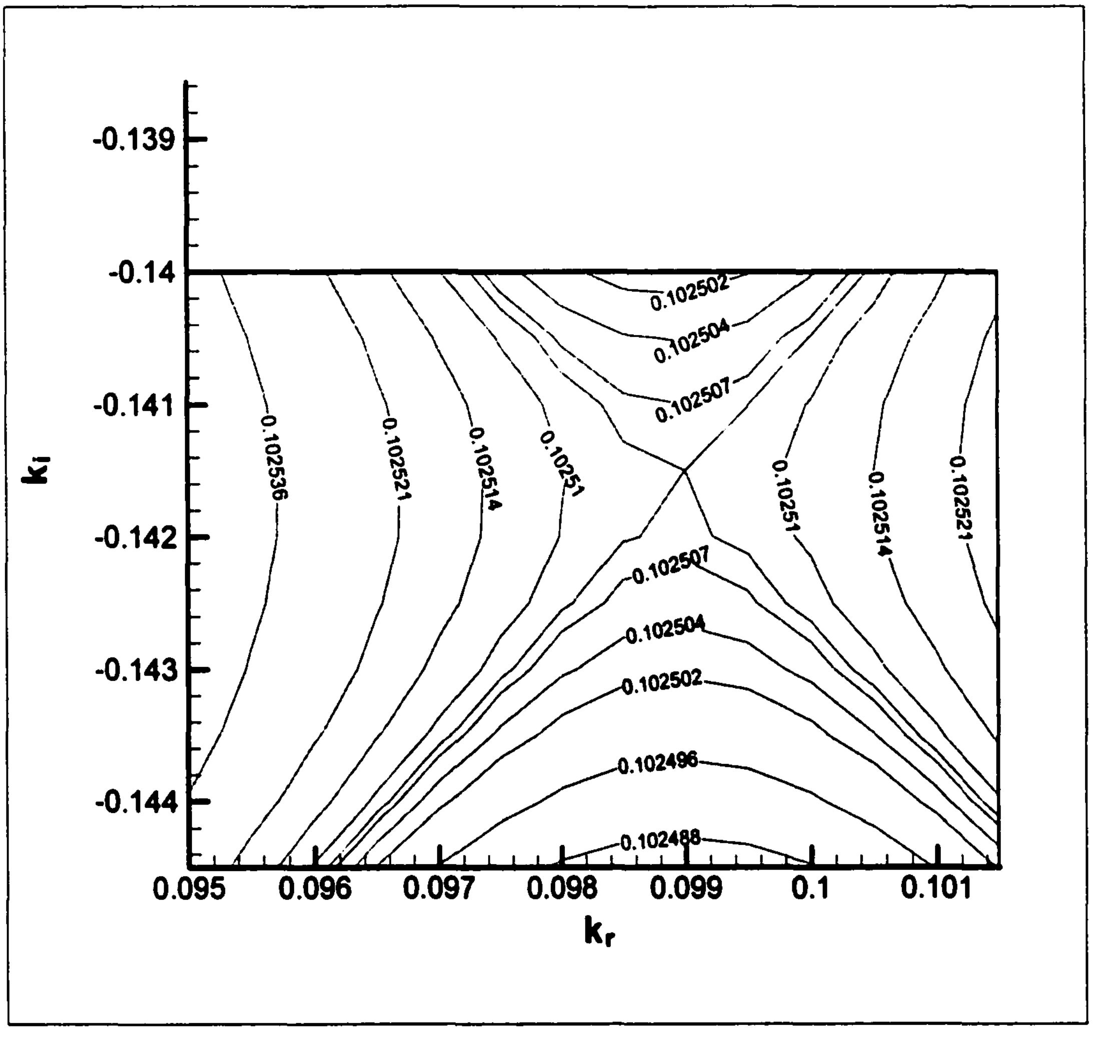

Figure A16: Contour plot of Ω_r for $R/\theta = 10$, $Fr = \infty$, $\rho_j/\rho_\infty = 0.66$ in the k-plane illustrating the pinch point formation

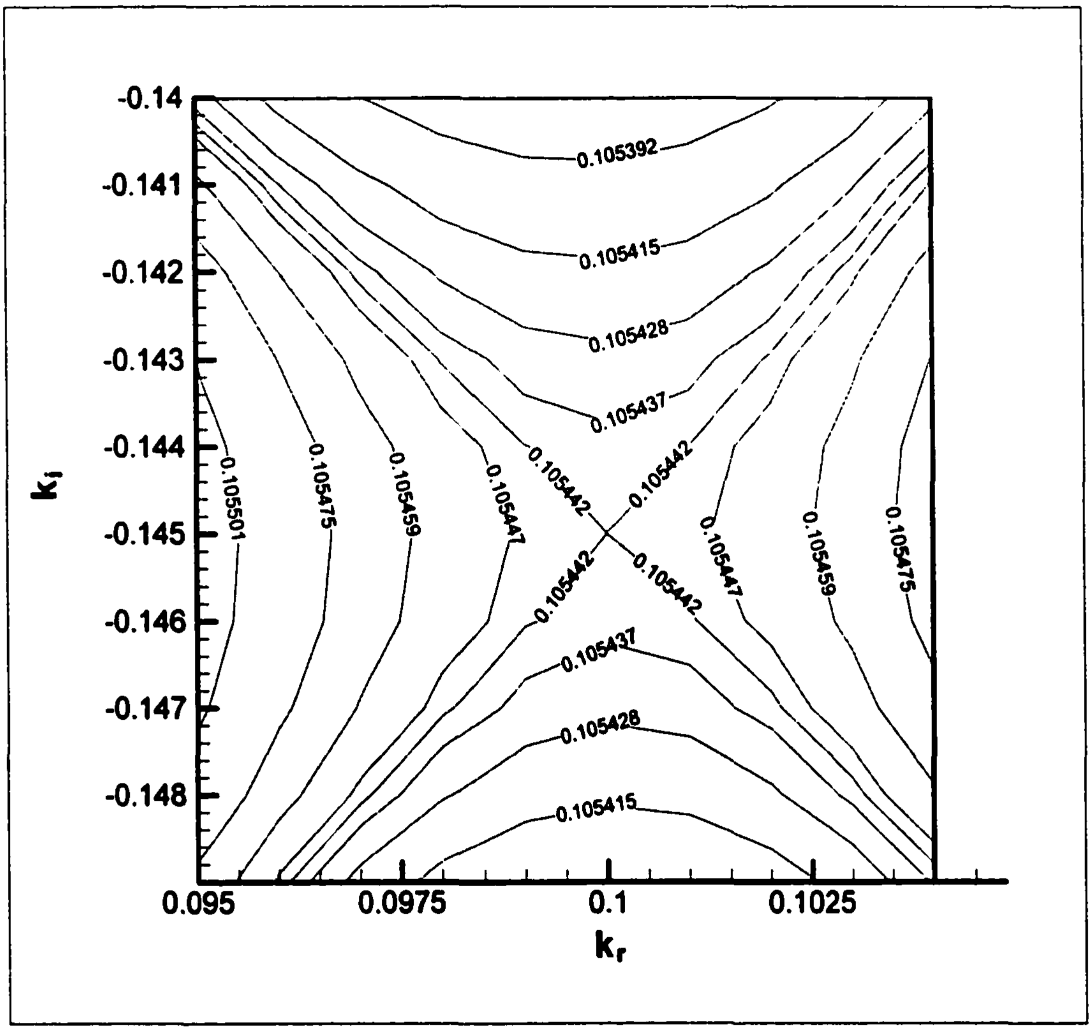

Figure A17: Contour plot of Ω_r for $R/\theta = 10$, $Fr = \infty$, $\rho_j/\rho_\infty = 0.72$ in the k-plane illustrating the pinch point formation

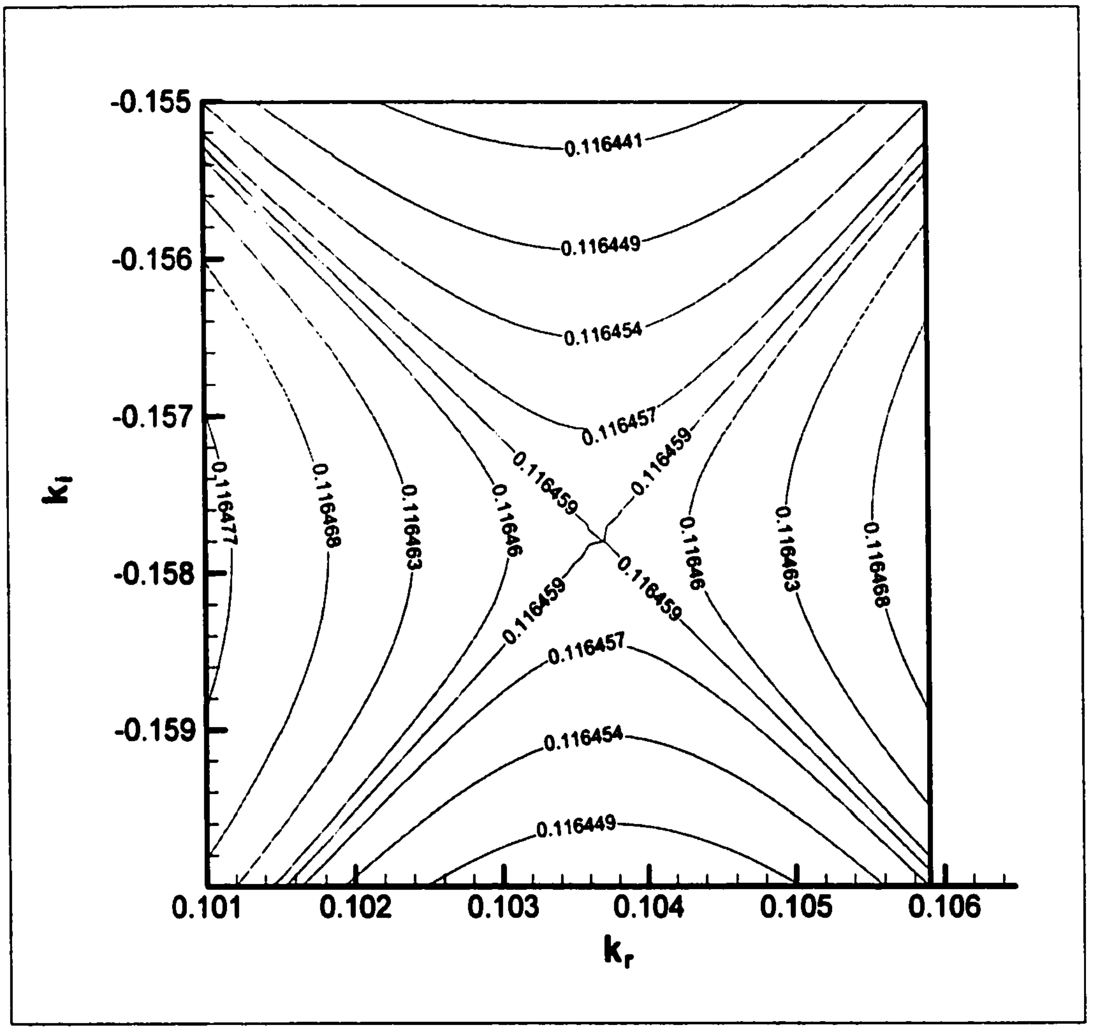

Figure A18: Contour plot of Ω_r for $R/\theta = 10$, $Fr = \infty$, $\rho_j/\rho_\infty = 0.99$ in the k-plane illustrating the pinch point formation

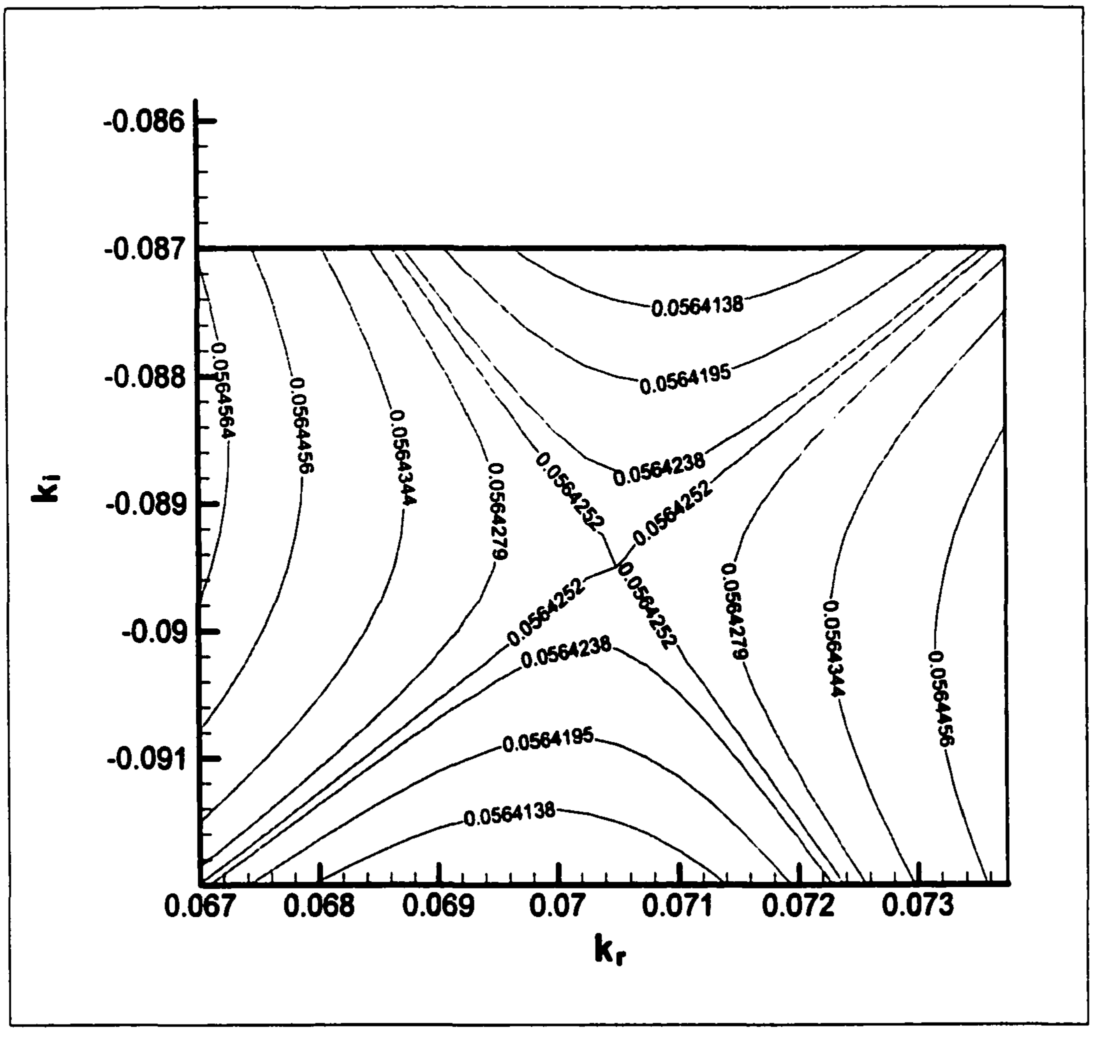

Figure A19: Contour plot of Ω_r for $R/\theta = 10$, $Fr = 10$, $\rho_j/\rho_\infty = 0.14$ in the k-plane illustrating the pinch point formation

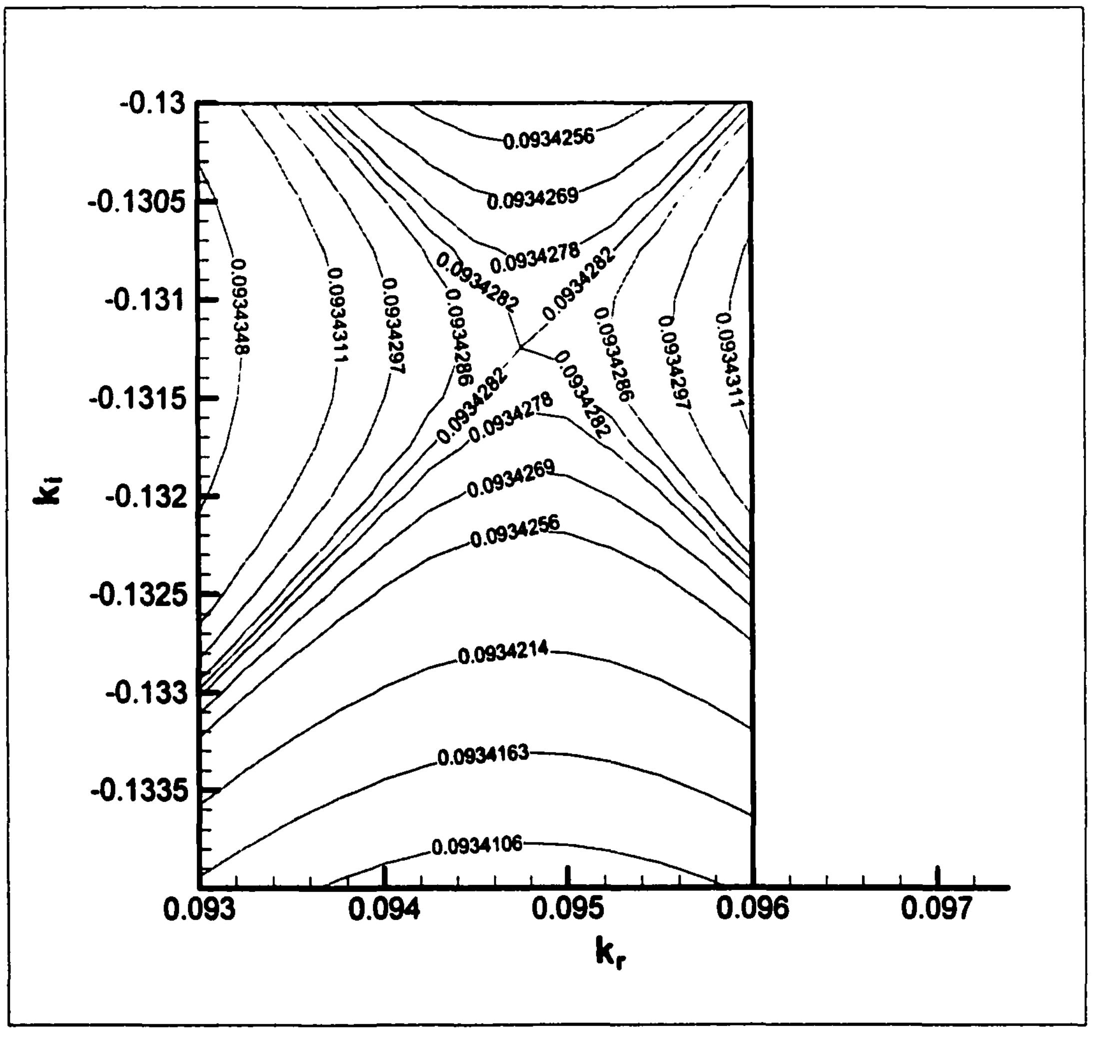

Figure A20: Contour plot of Ω_r for $R/\theta = 10$, $Fr = 10$, $\rho_j/\rho_\infty = 0.5$ in the k-plane illustrating the pinch point formation

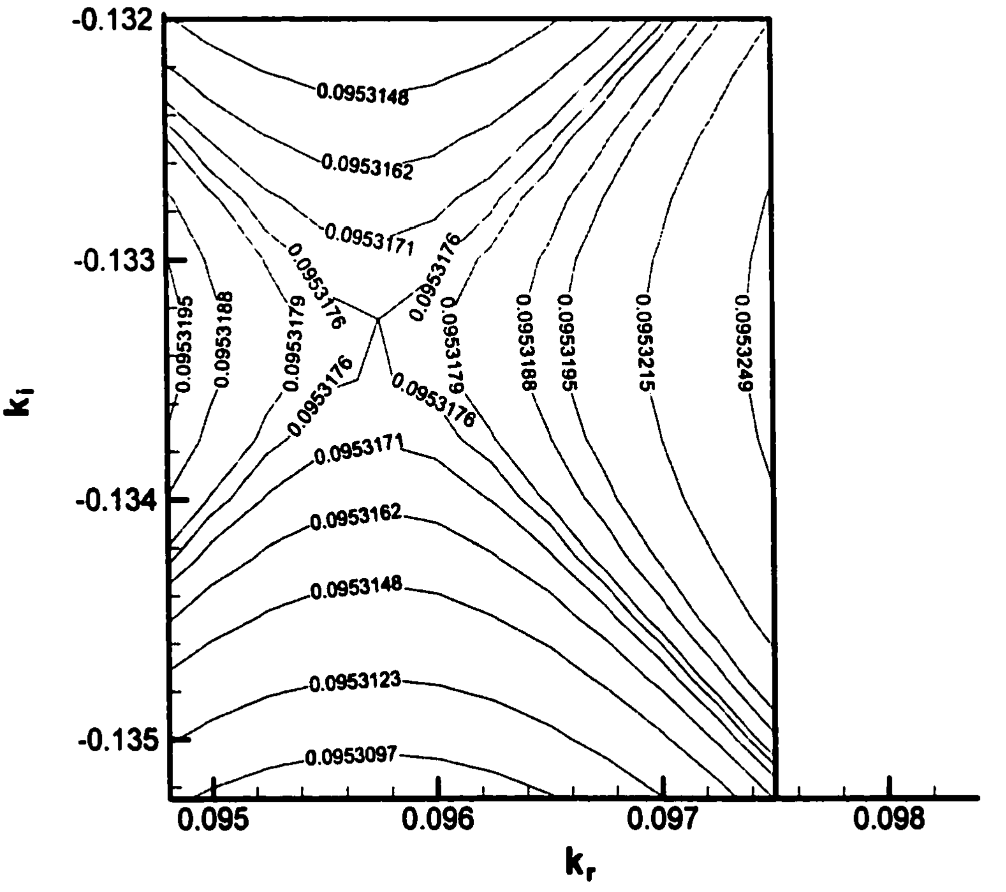

Figure A21: Contour plot of Ω_r for $R/\theta = 10$, $Fr = 10$, $\rho_j/\rho_\infty = 0.53$ in the k-plane illustrating the pinch point formation

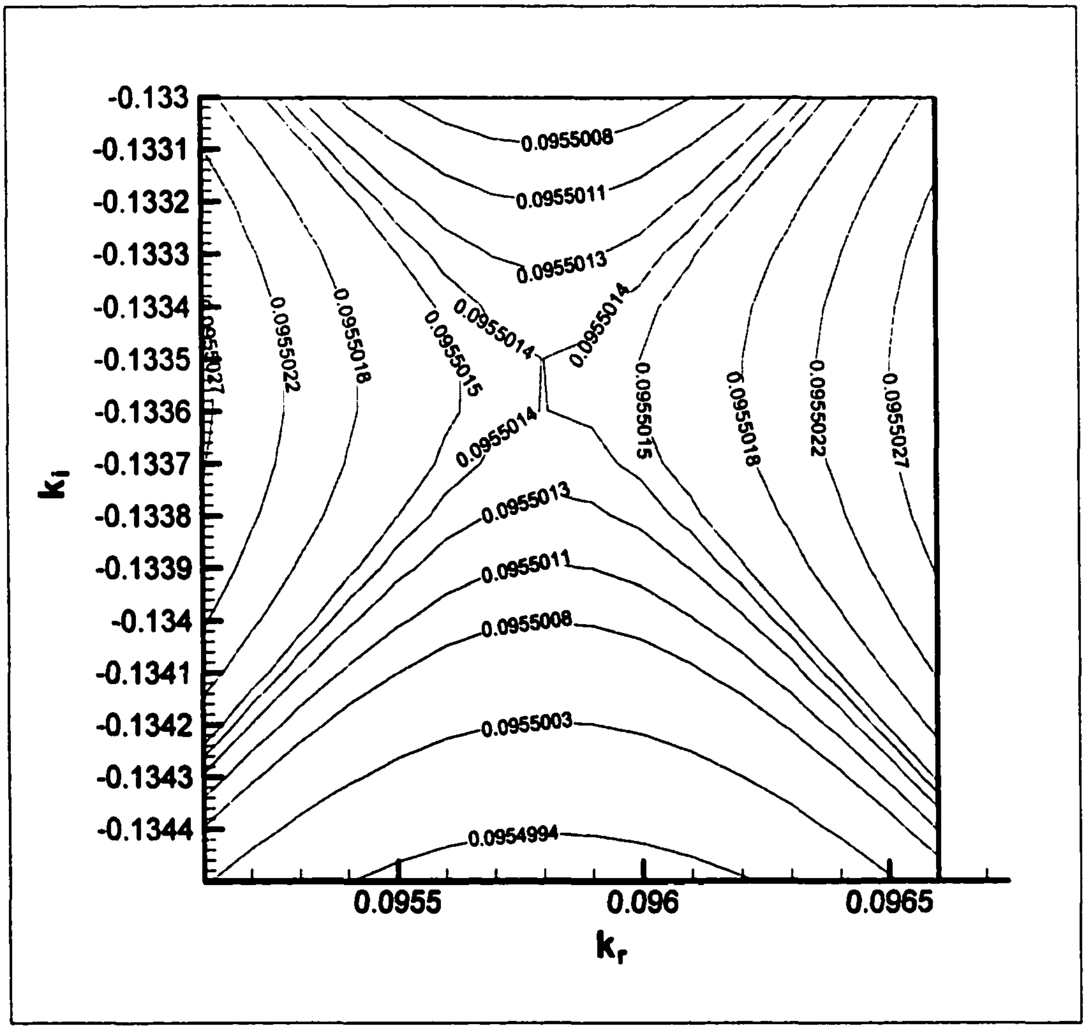

Figure A22: Contour plot of Ω_r for $R/\theta = 10$, $Fr = 10$, $\rho_j/\rho_\infty = 0.533$ in the k-plane illustrating the pinch point formation

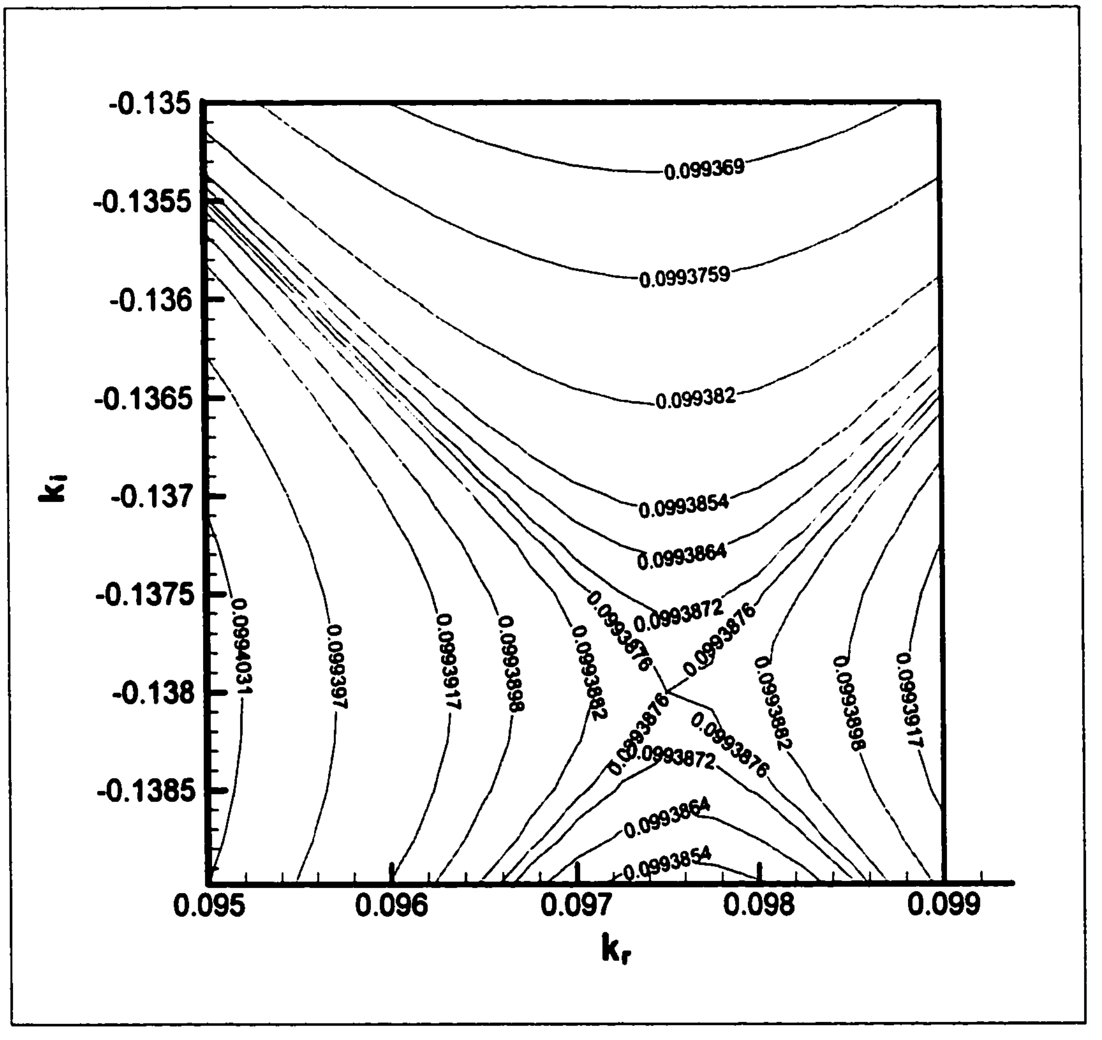

Figure A23: Contour plot of Ω_r for $R/\theta = 10$, $Fr = 10$, $\rho_j/\rho_\infty = 0.6$ in the k-plane illustrating the pinch point formation

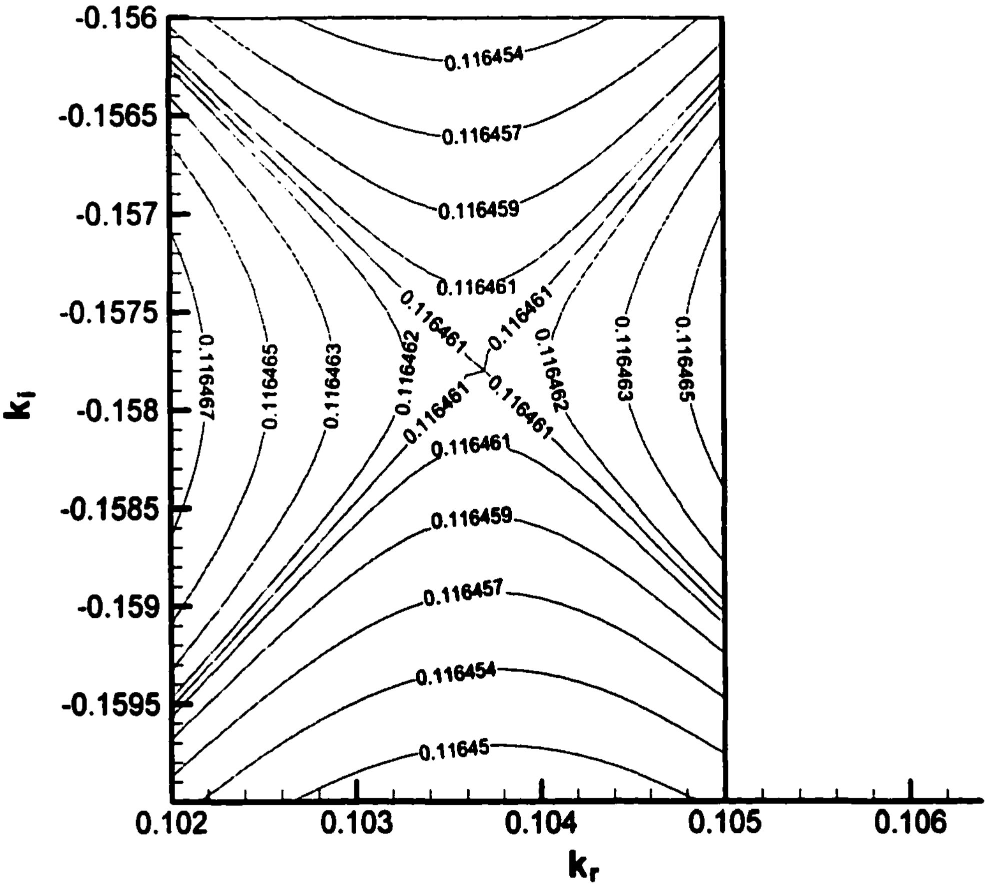

Figure A24: Contour plot of Ω_r for $R/\theta = 10$, $Fr = 10$, $\rho_j/\rho_\infty = 0.99$ in the k-plane illustrating the pinch point formation

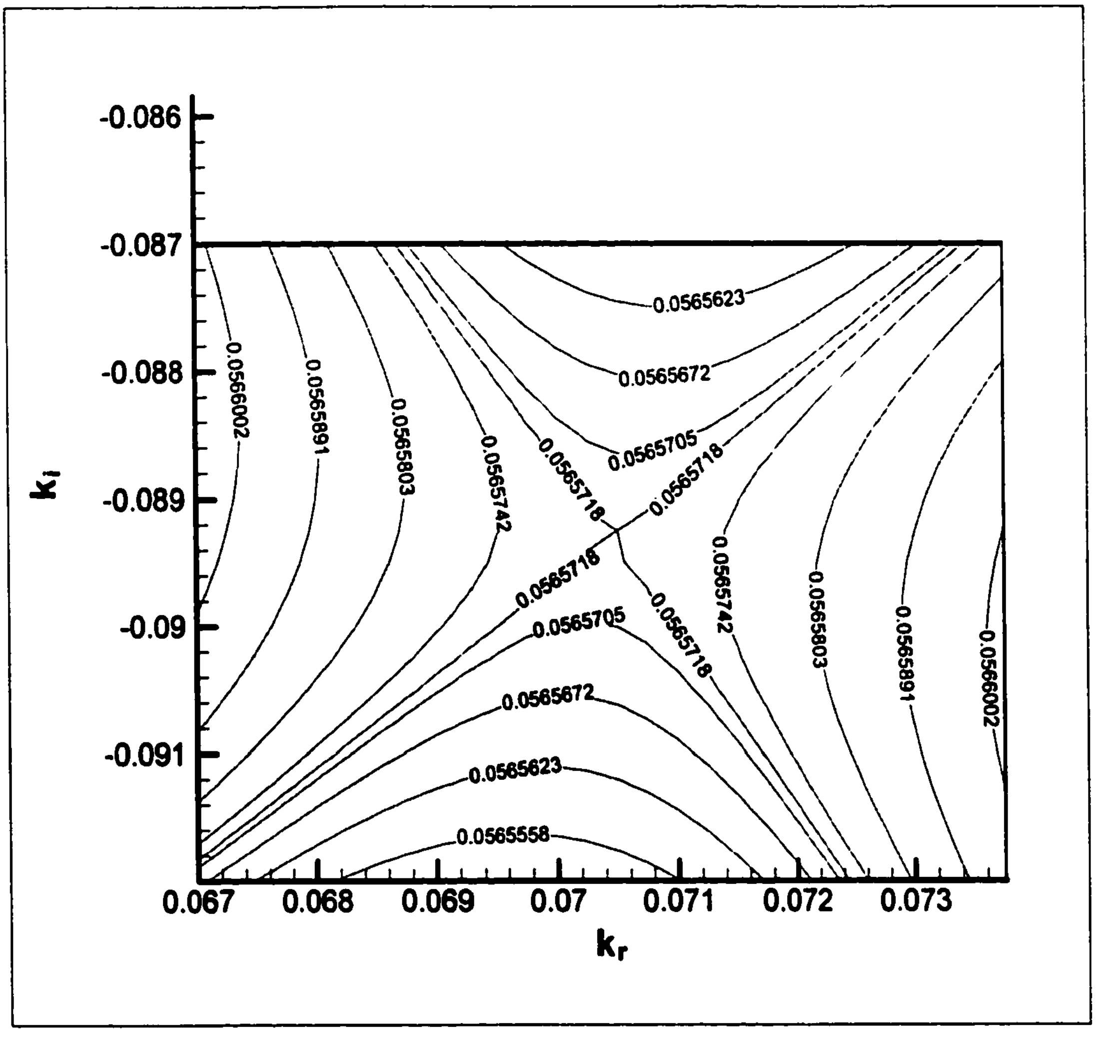

Figure A25: Contour plot of Ω_r for $R/\theta = 10$, $Fr = 5$, $\rho_j/\rho_\infty = 0.14$ in the k-plane illustrating the pinch point formation

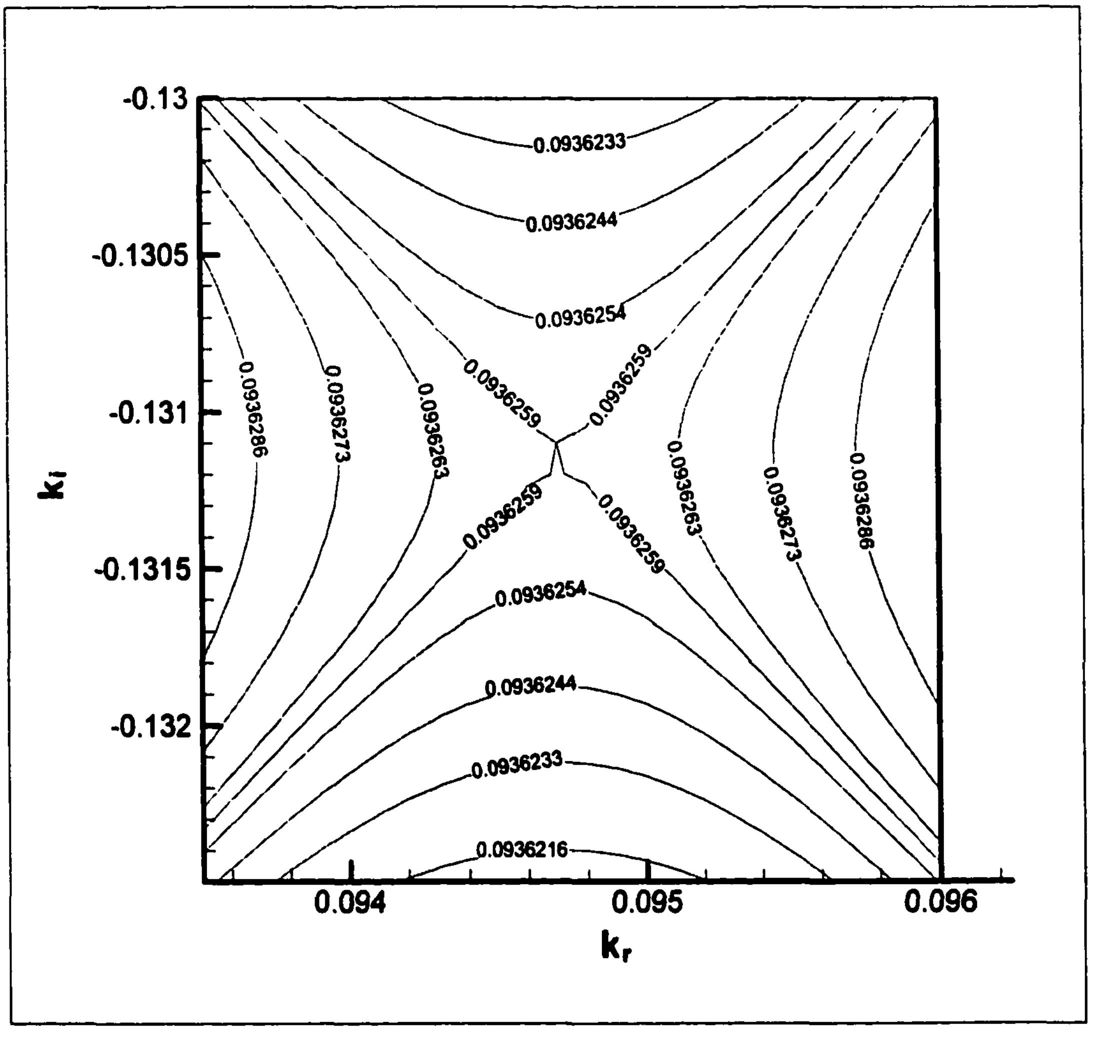

Figure A26: Contour plot of Ω_r for $R/\theta = 10$, $Fr = 5$, $\rho_j/\rho_\infty = 0.5$ in the k-plane illustrating the pinch point formation

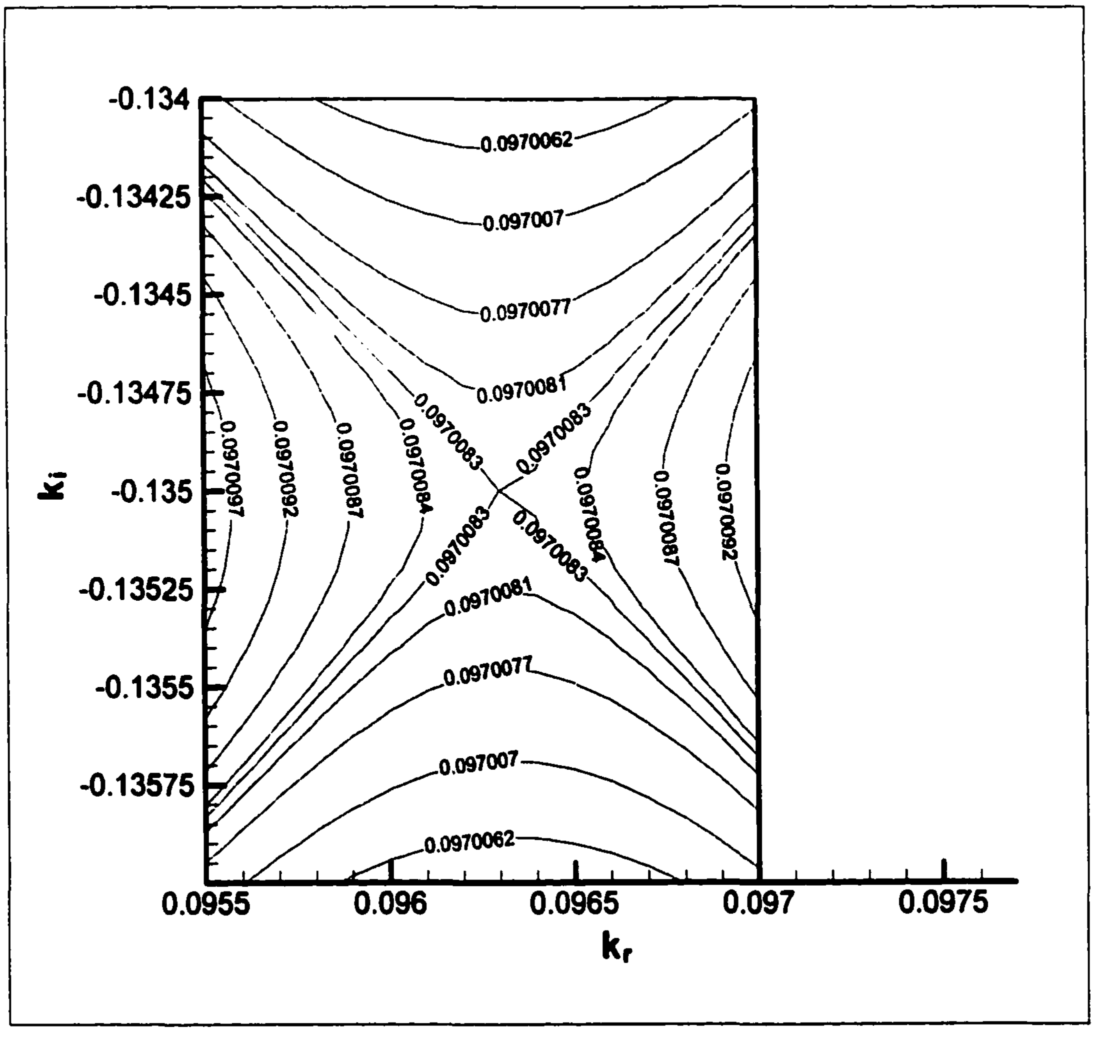

Figure A27: Contour plot of Ω_r for $R/\theta = 10$, $Fr = 5$, $\rho_j/\rho_\infty = 0.555$ in the k-plane illustrating the pinch point formation

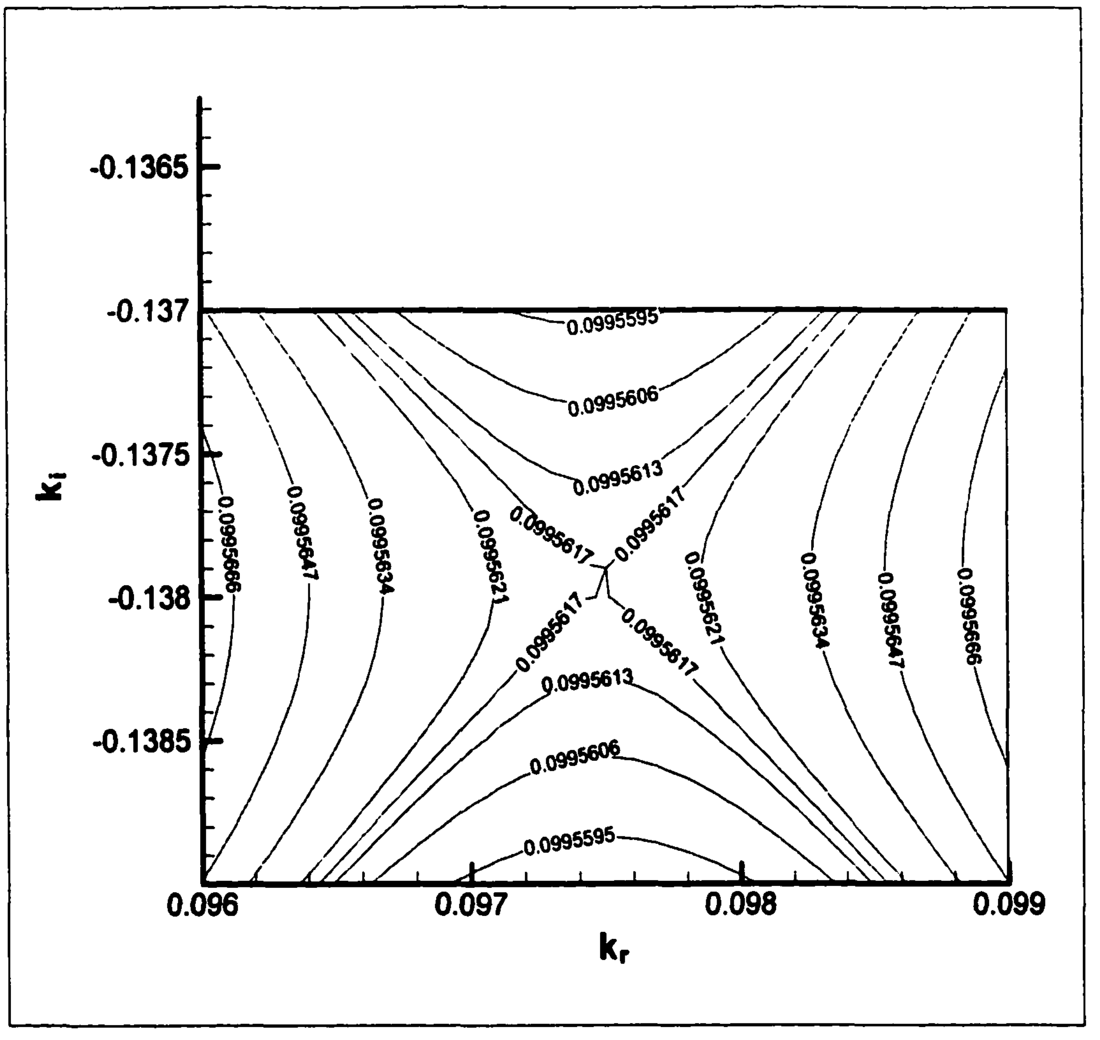

Figure A28: Contour plot of Ω_r for $R/\theta = 10$, $Fr = 5$, $\rho_j/\rho_\infty = 0.6$ in the k-plane illustrating the pinch point formation

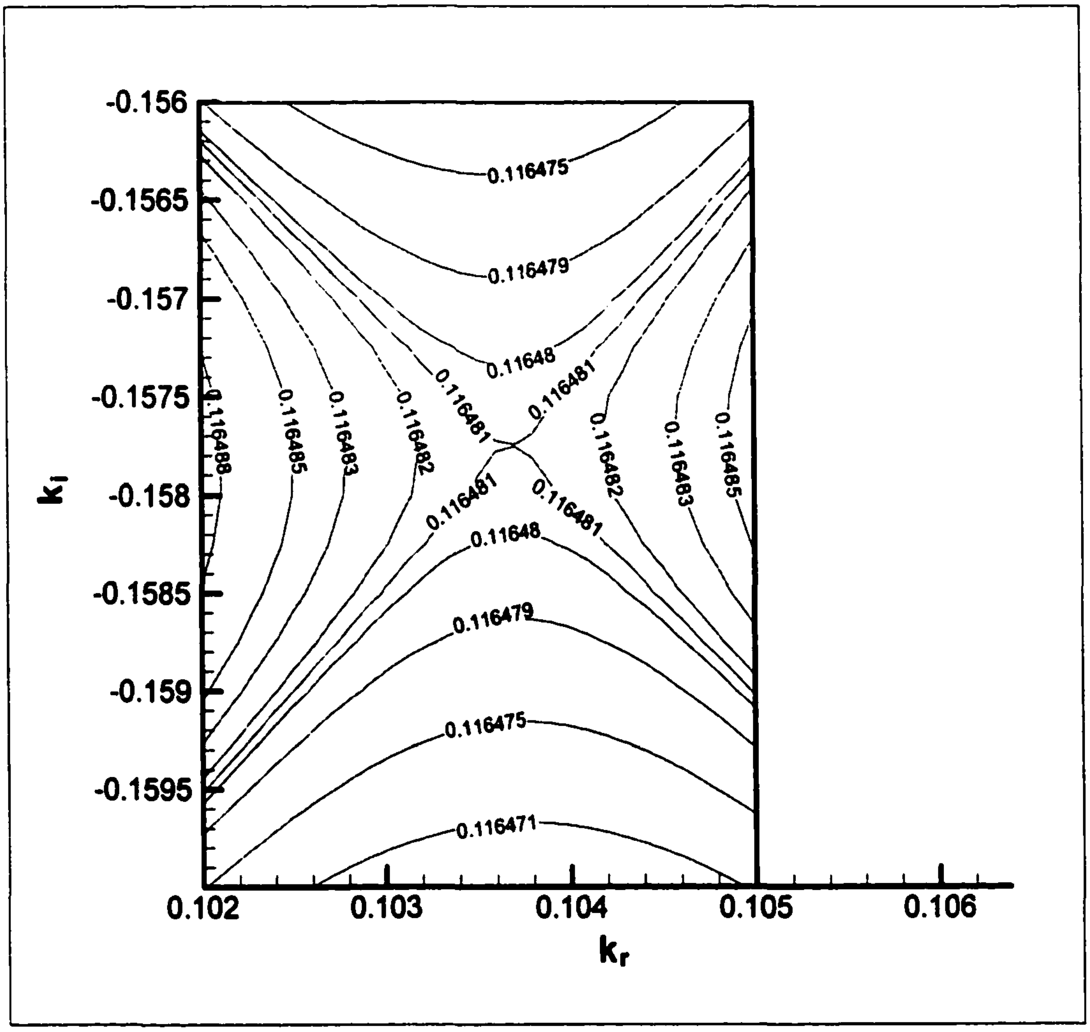

Figure A29: Contour plot of Ω_r for $R/\theta = 10$, $Fr = 5$, $\rho_j/\rho_\infty = 0.99$ in the k-plane illustrating the pinch point formation

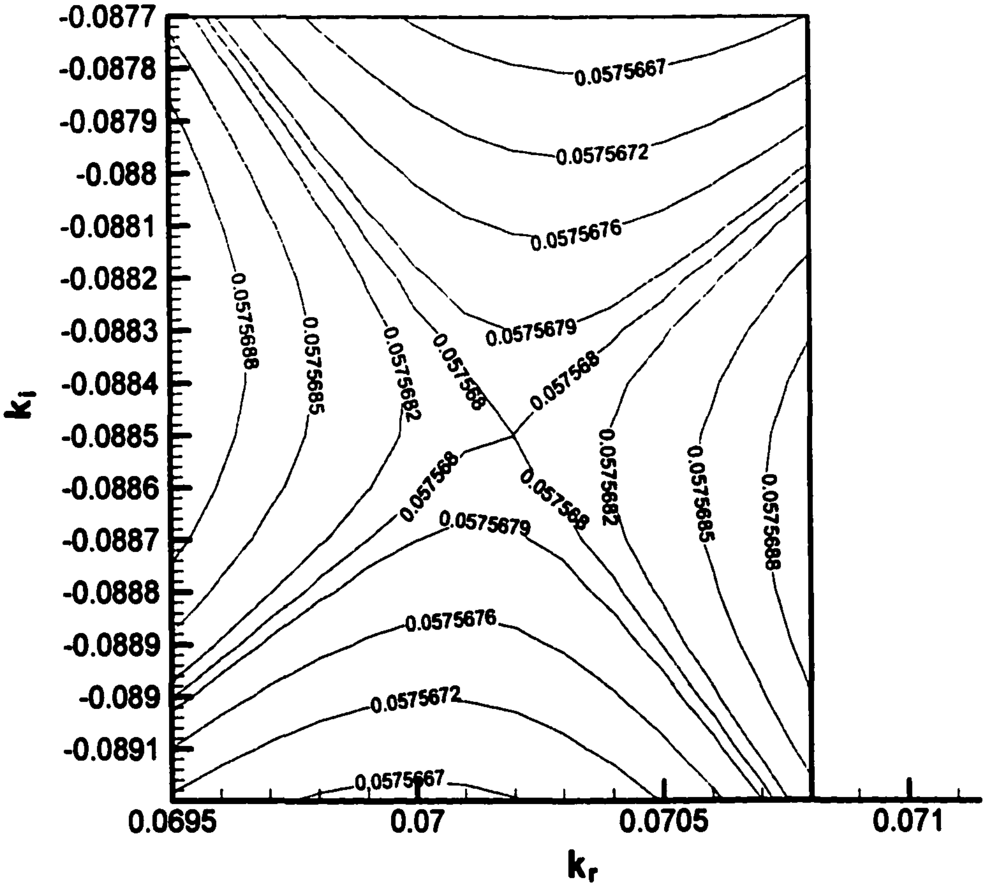

Figure A30: Contour plot of Ω_r for $R/\theta = 10$, $Fr = 2$, $\rho_j/\rho_\infty = 0.14$ in the k-plane illustrating the pinch point formation

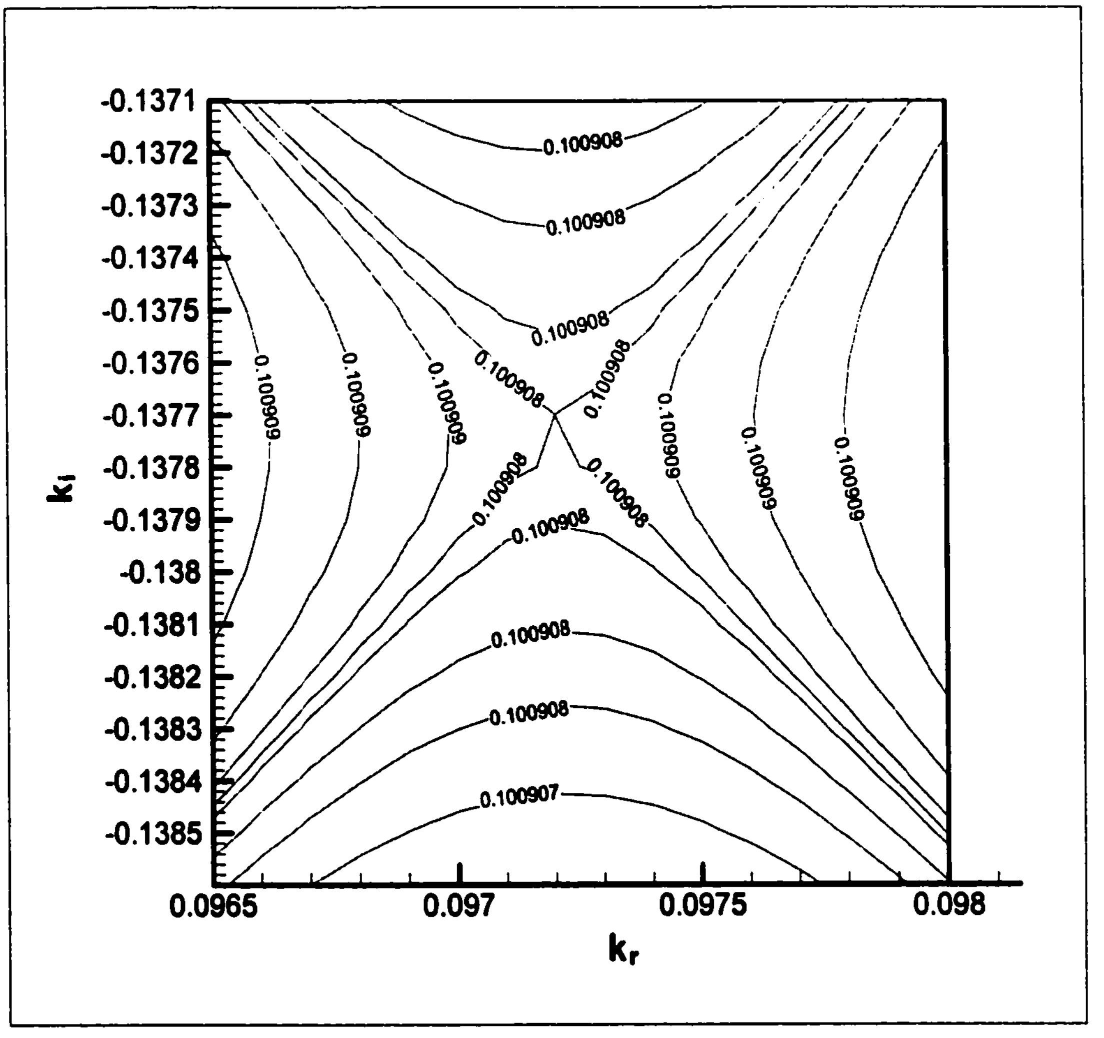

Figure A31: Contour plot of Ω_r for $R/\theta = 10$, $Fr = 2$, $\rho_j/\rho_\infty = 0.6$ in the k-plane illustrating the pinch point formation

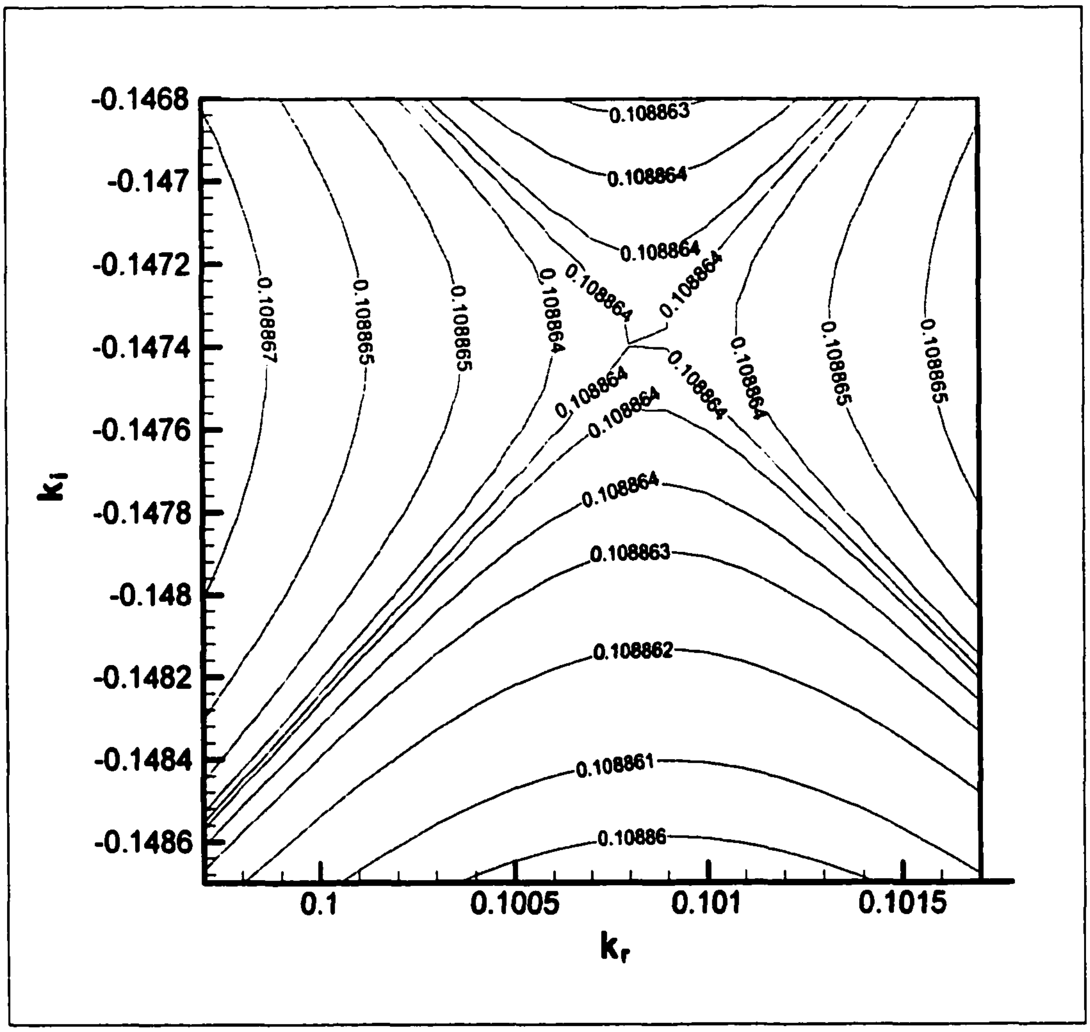

Figure A32: Contour plot of Ω_r for $R/\theta = 10$, $Fr = 2$, $\rho_j/\rho_\infty = 0.768$ in the k-plane illustrating the pinch point formation

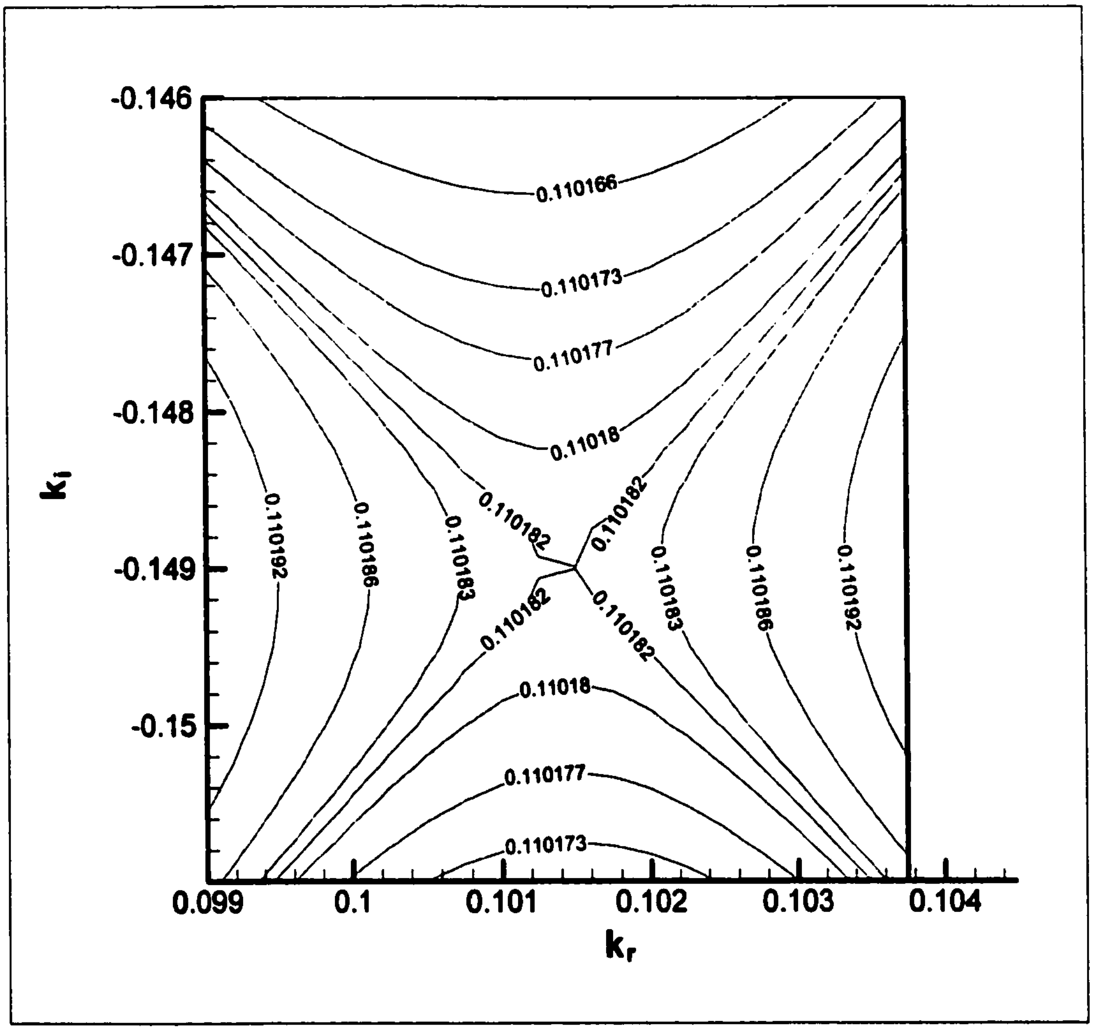

Figure A33: Contour plot of Ω_r for $R/\theta = 10$, $Fr = 2$, $\rho_j/\rho_\infty = 0.8$ in the k-plane illustrating the pinch point formation

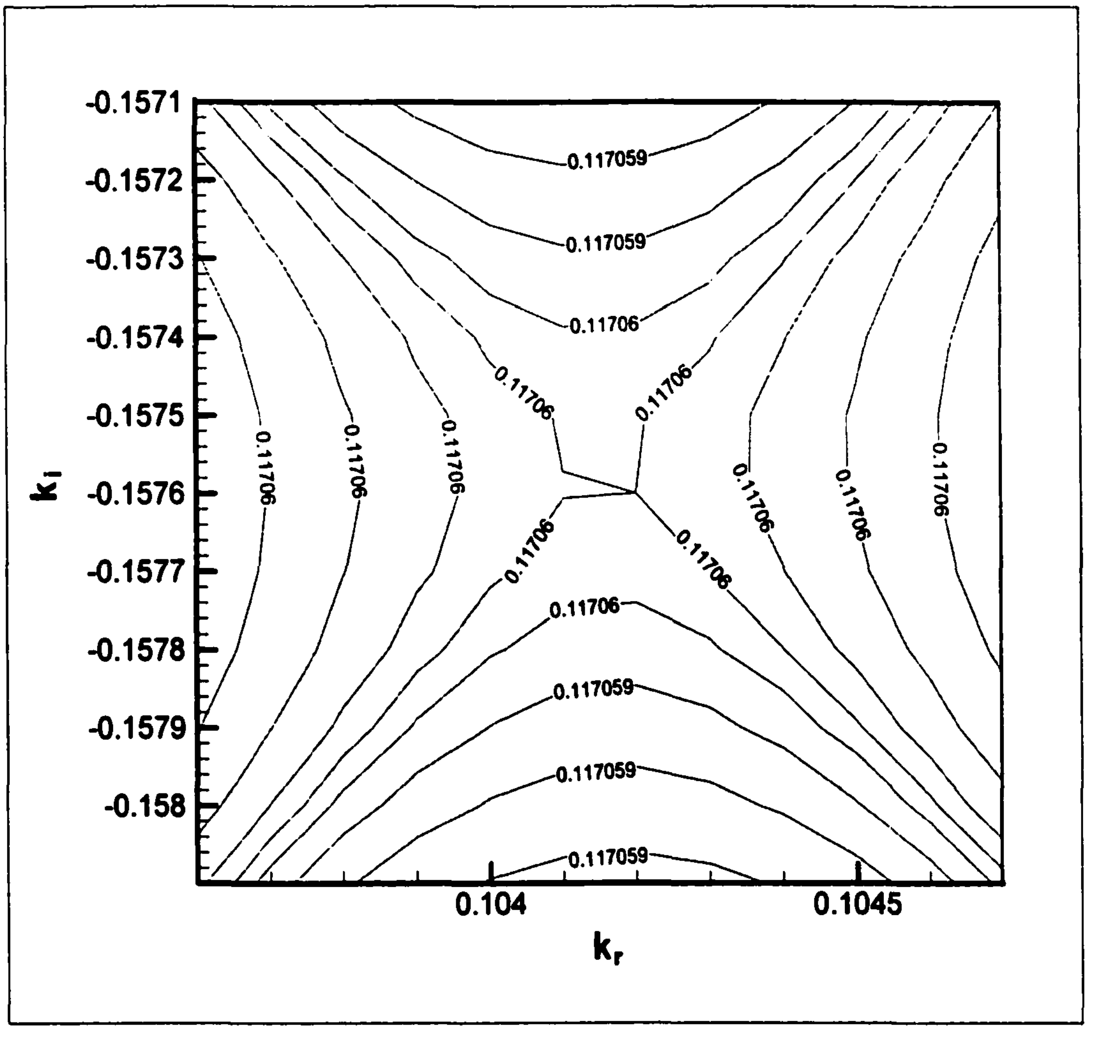

Figure A34: Contour plot of Ω_r for $R/\theta = 10$, $Fr = 2$, $\rho_j/\rho_\infty = 0.99$ in the k-plane illustrating the pinch point formation

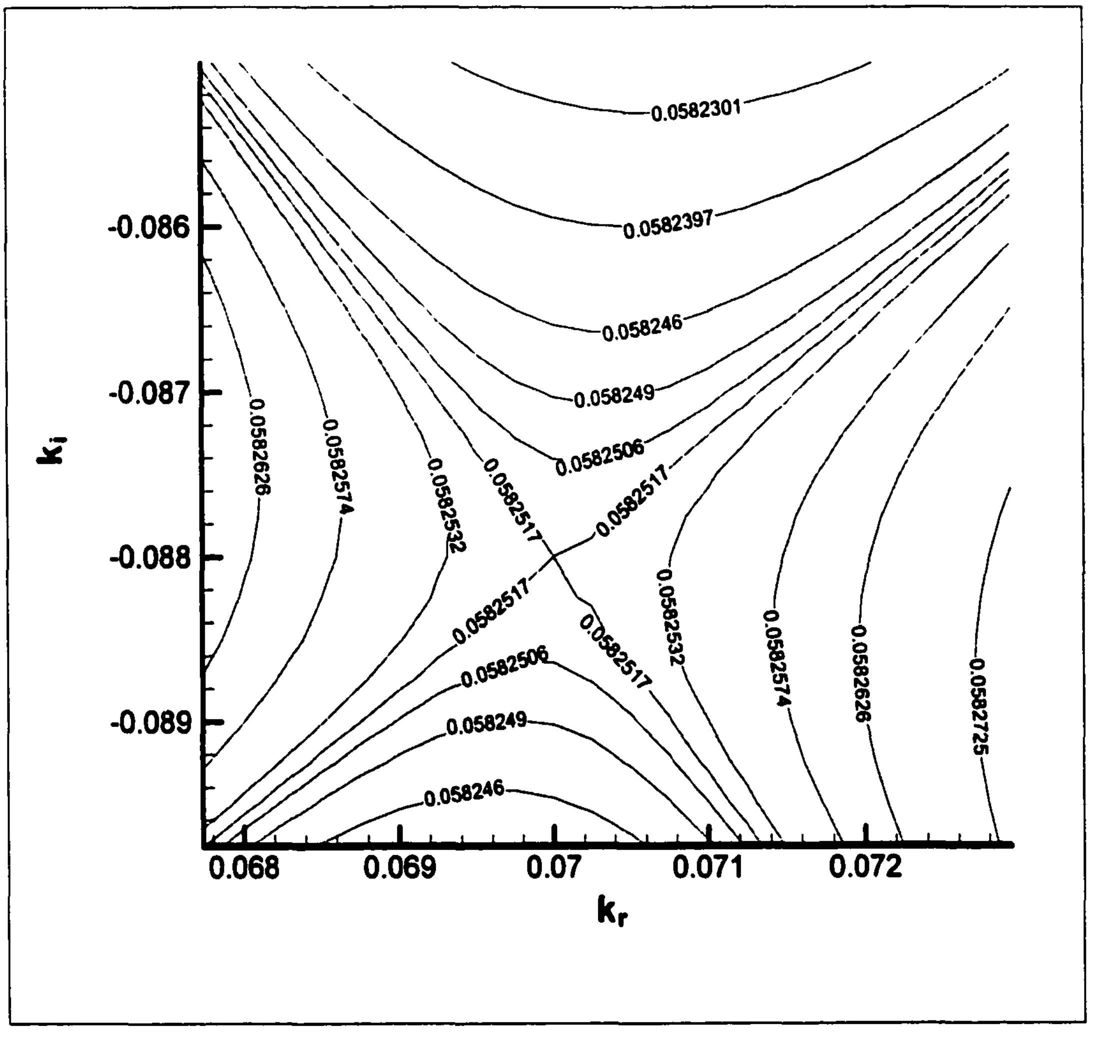

Figure A35: Contour plot of Ω_r for $R/\theta = 10$, $Fr = 1.58$, $\rho_j/\rho_\infty = 0.14$ in the k-plane illustrating the pinch point formation

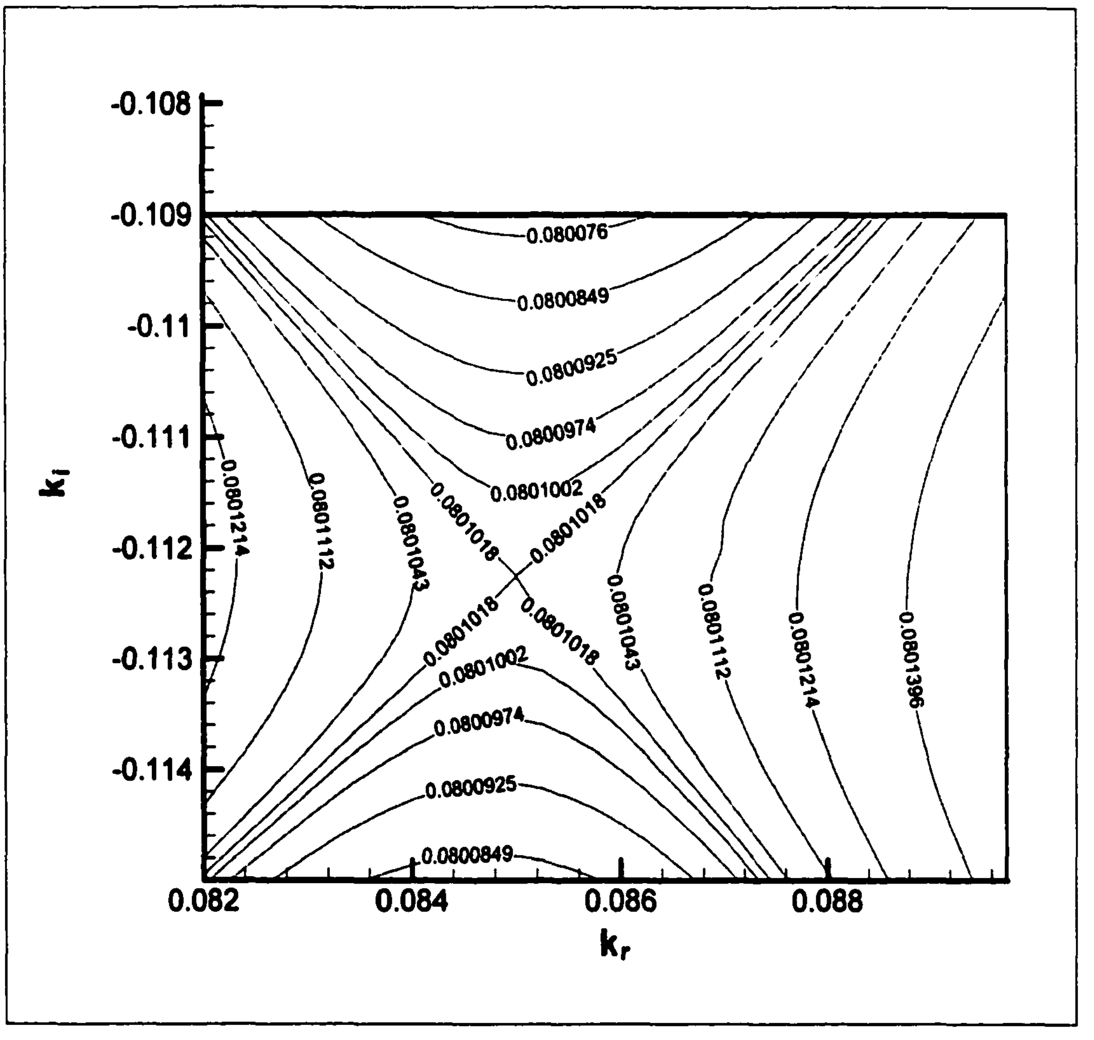

Figure A36: Contour plot of Ω_r for $R/\theta = 10$, $Fr = 1.58$, $\rho_j/\rho_\infty = 0.3$ in the k-plane illustrating the pinch point formation

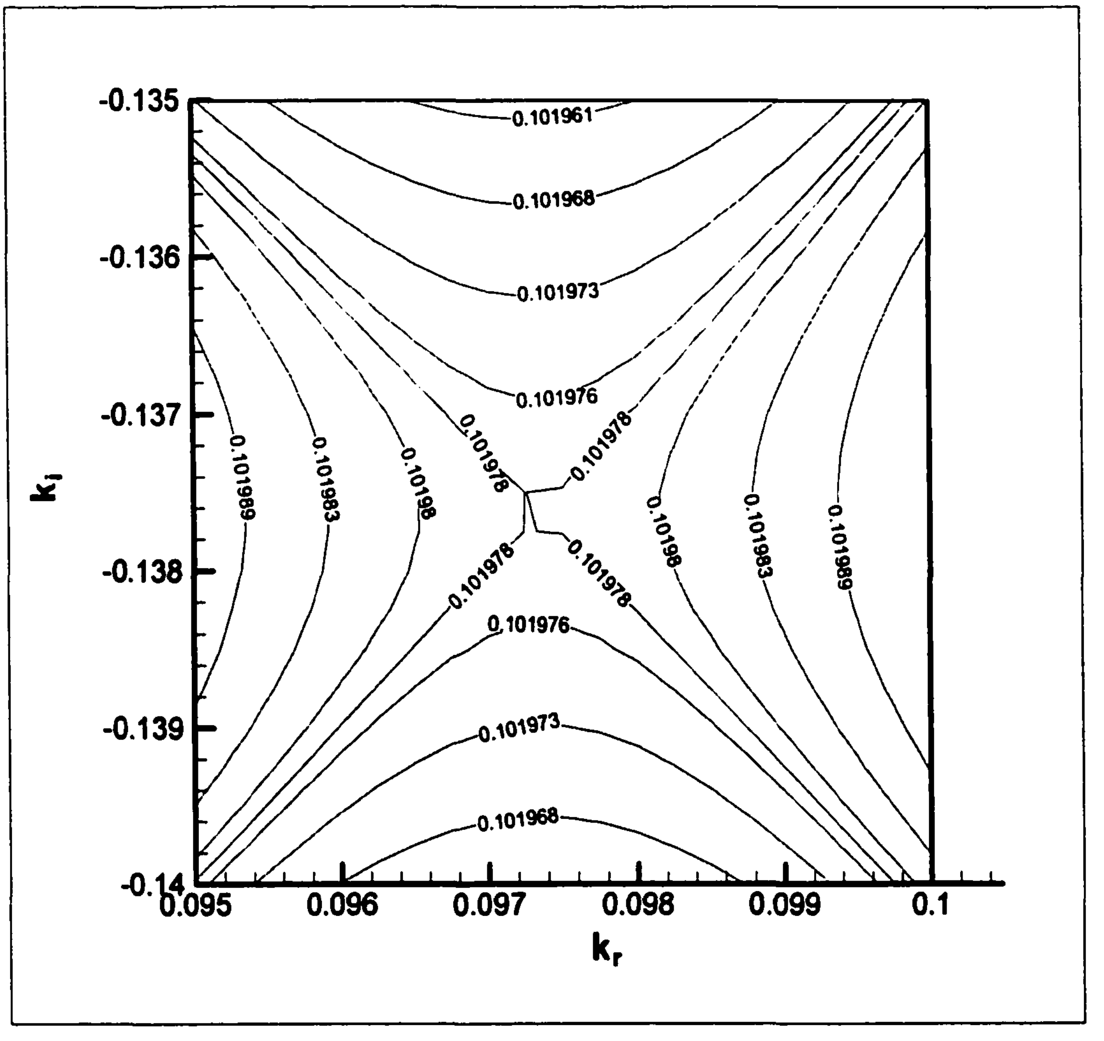

Figure A37: Contour plot of Ω_r for $R/\theta = 10$, $Fr = 1.58$, $\rho_j/\rho_\infty = 0.6$ in the k-plane illustrating the pinch point formation

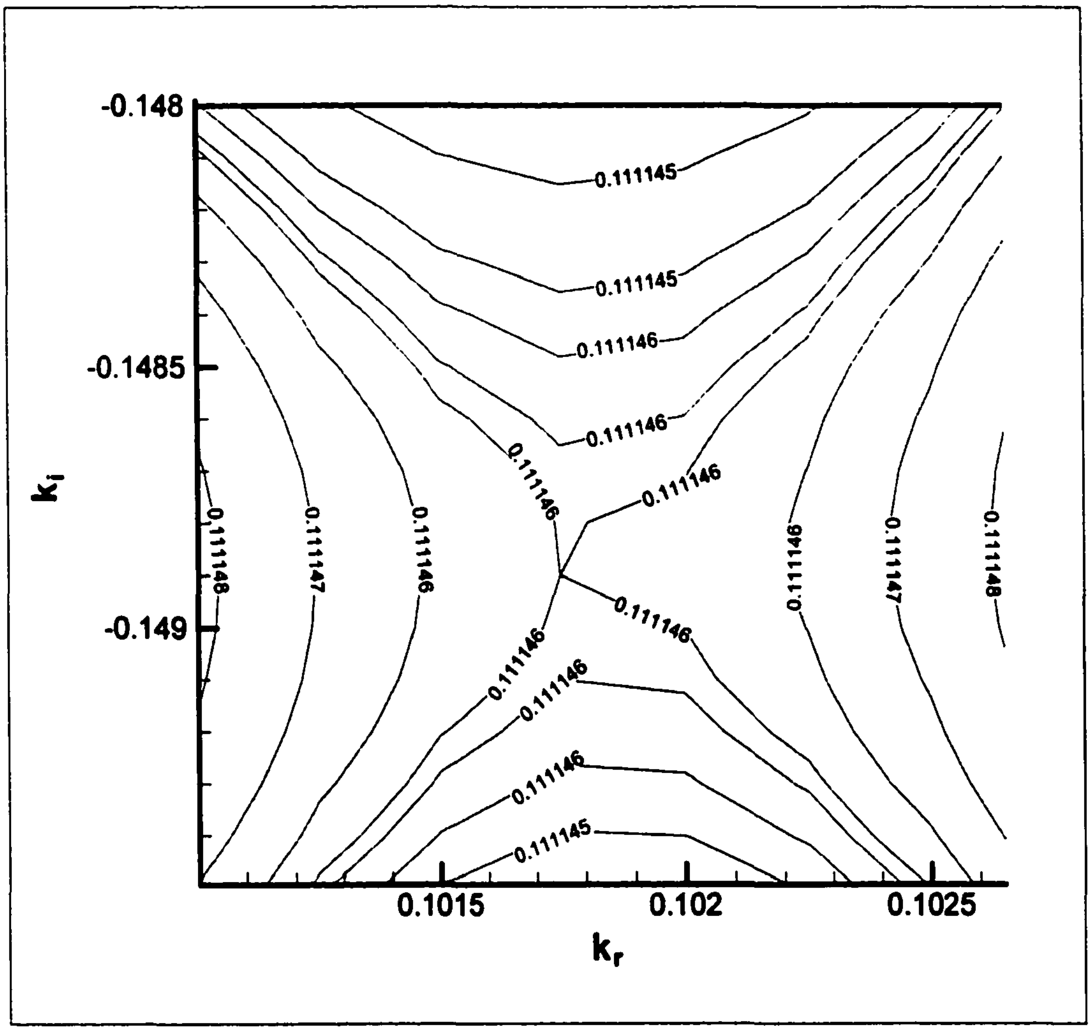

Figure A38: Contour plot of Ω_r for $R/\theta = 10$, $Fr = 1.58$, $\rho_j/\rho_\infty = 0.8$ in the k-plane illustrating the pinch point formation

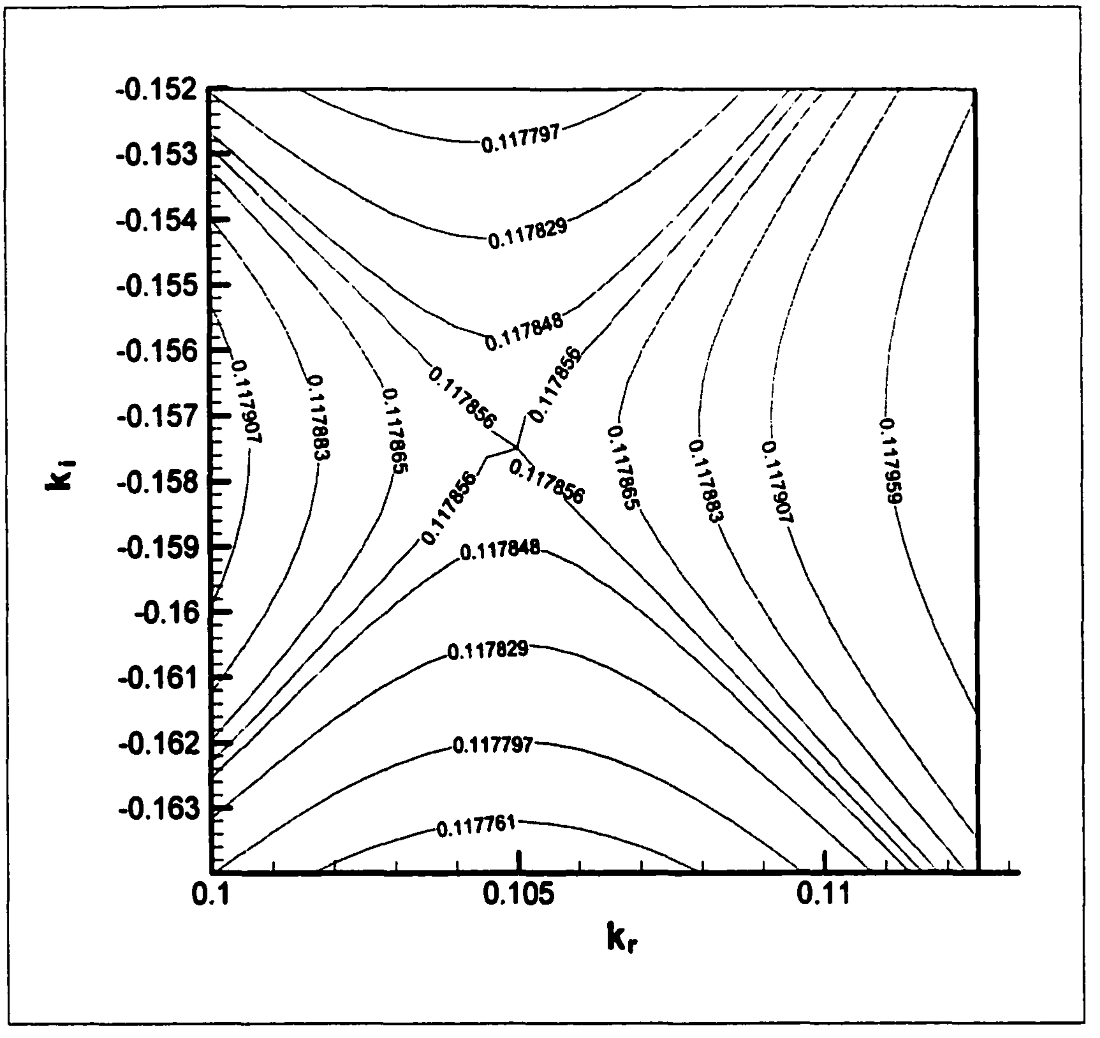

Figure A39: Contour plot of Ω_r for $R/\theta = 10$, $Fr = 1.58$, $\rho_j/\rho_\infty = 0.99$ in the k-plane illustrating the pinch point formation

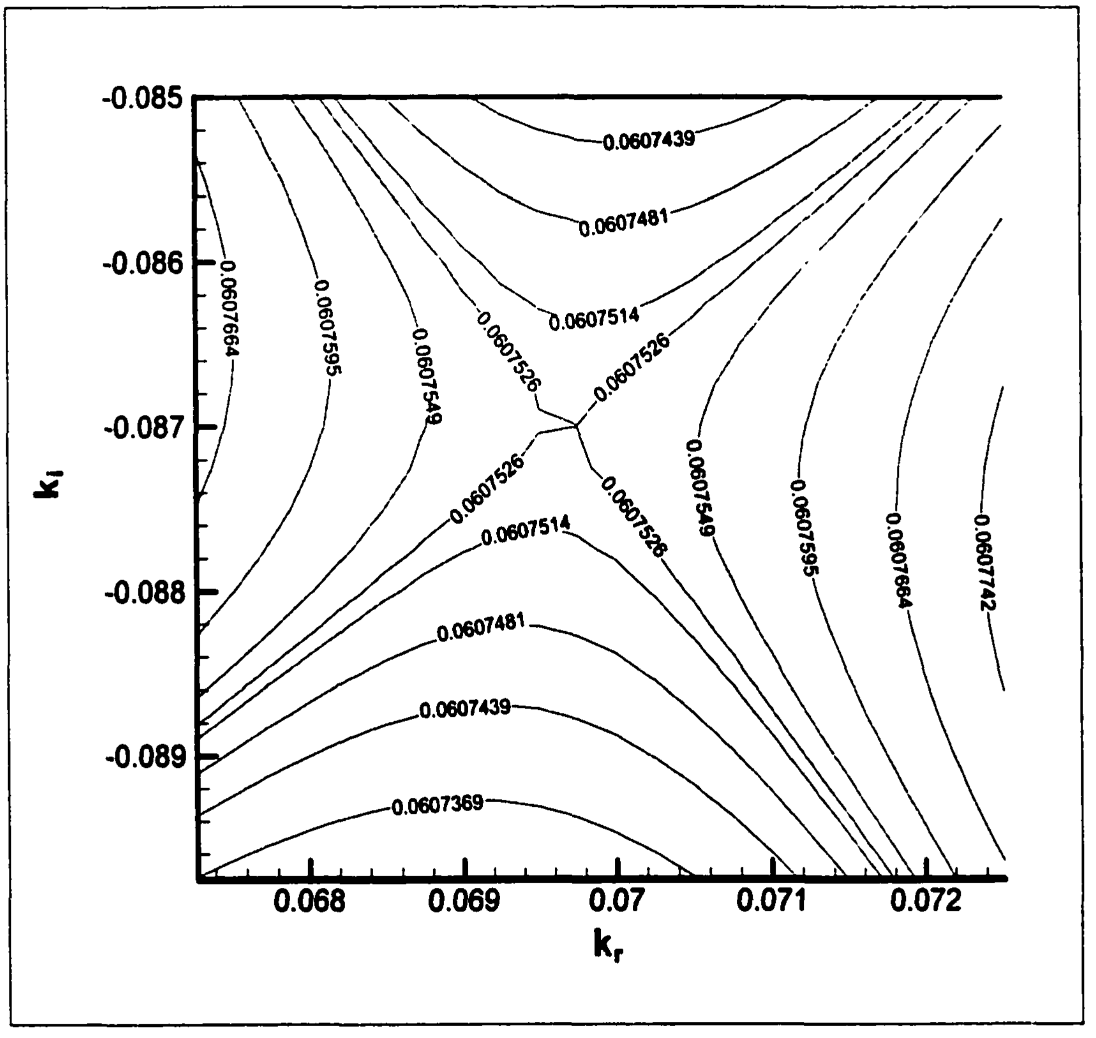

Figure A40: Contour plot of Ω_r for $R/\theta = 10$, $Fr = 1$, $\rho_j/\rho_\infty = 0.14$ in the k-plane illustrating the pinch point formation

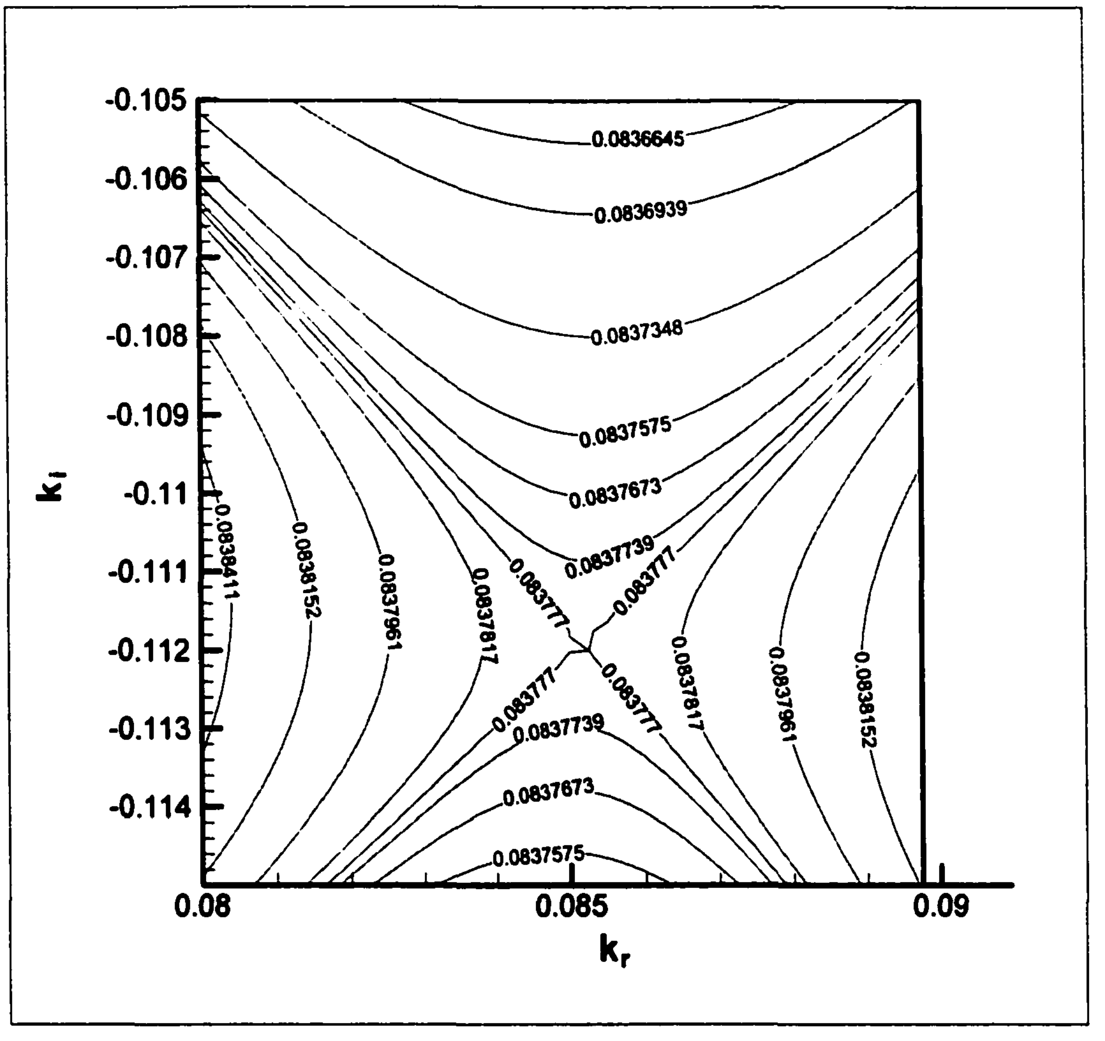

Figure A41: Contour plot of Ω_r for $R/\theta = 10$, $Fr = 1$, $\rho_j/\rho_\infty = 0.3$ in the k-plane illustrating the pinch point formation

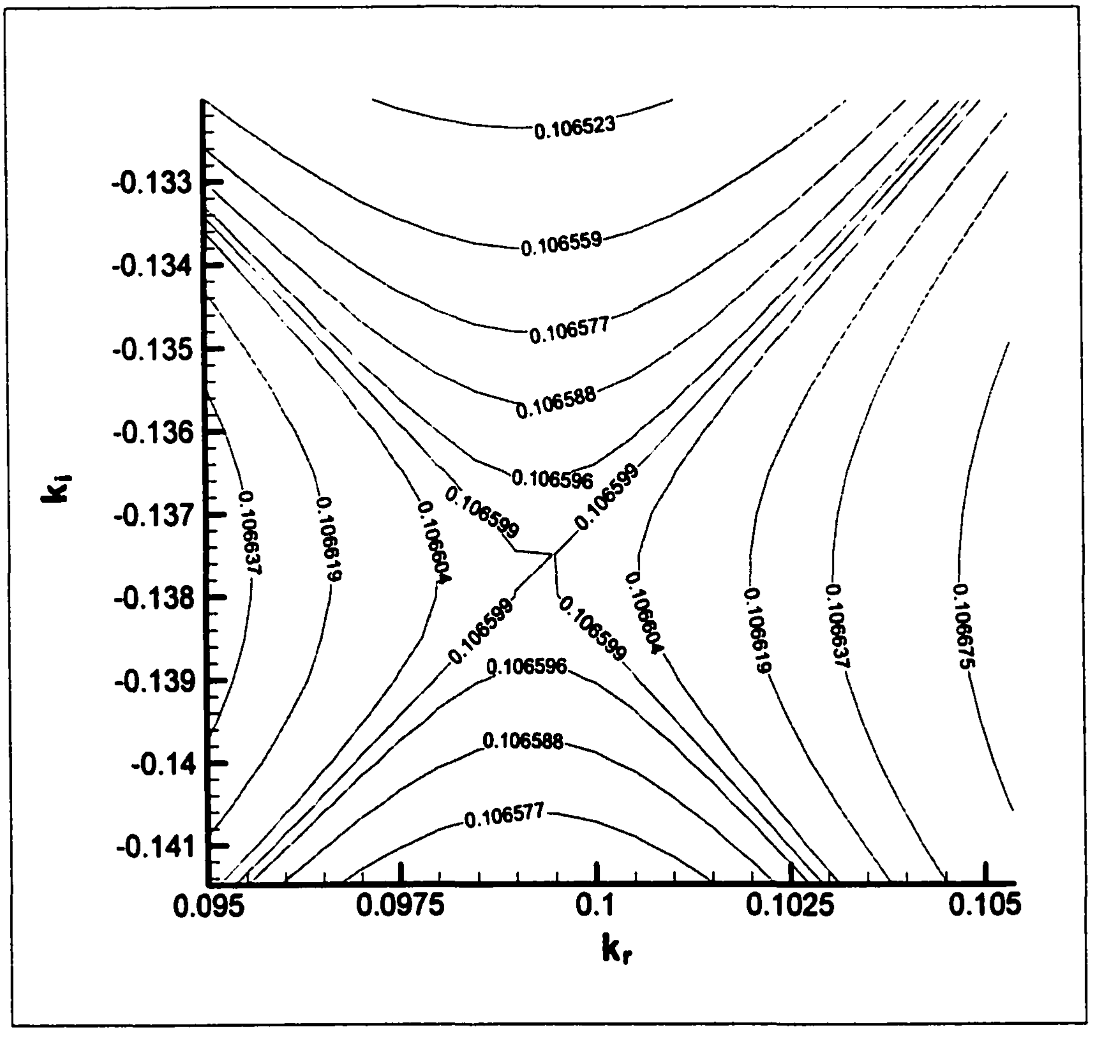

Figure A42: Contour plot of Ω_r for $R/\theta = 10$, $Fr = 1$, $\rho_j/\rho_\infty = 0.6$ in the k-plane illustrating the pinch point formation

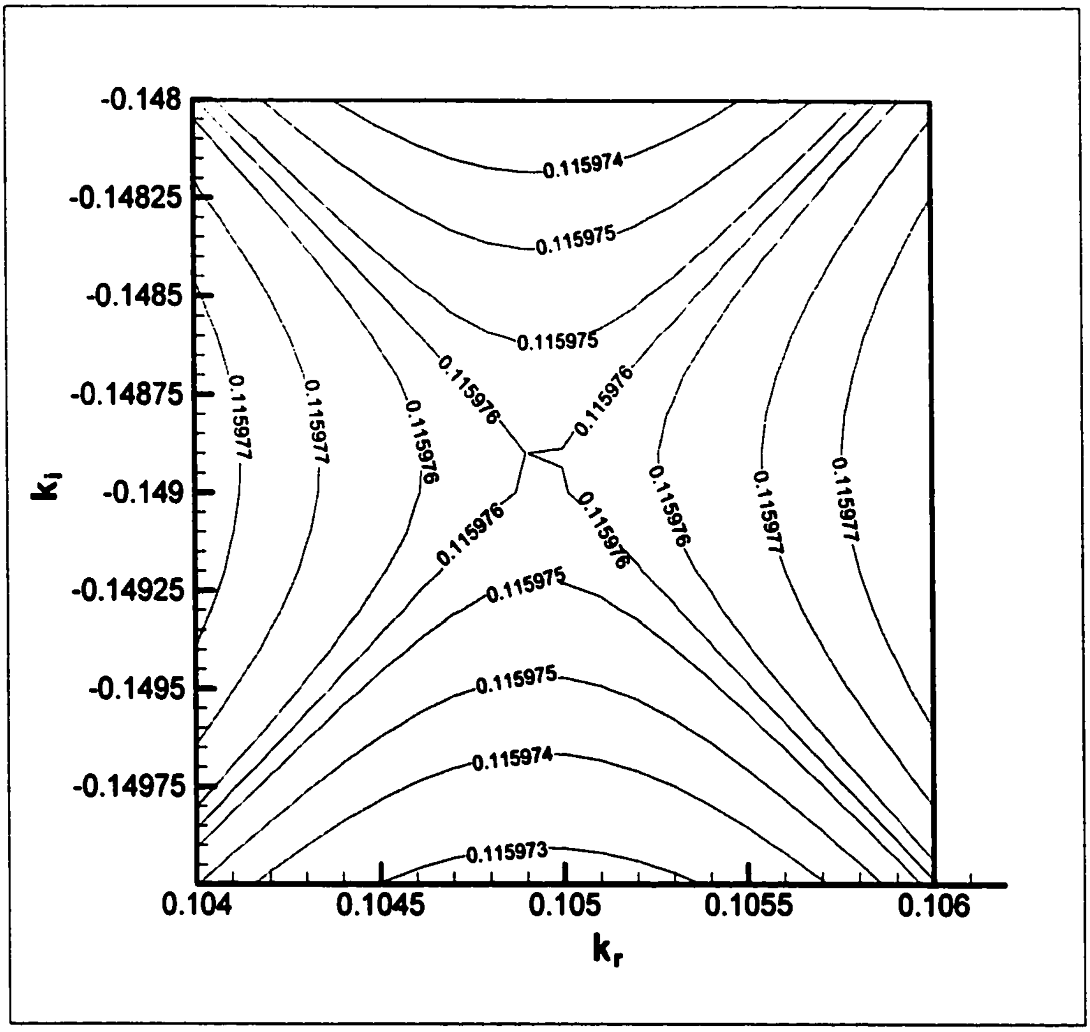

Figure A43: Contour plot of Ω_r for $R/\theta = 10$, $Fr = 1$, $\rho_j/\rho_\infty = 0.8$ in the k-plane illustrating the pinch point formation

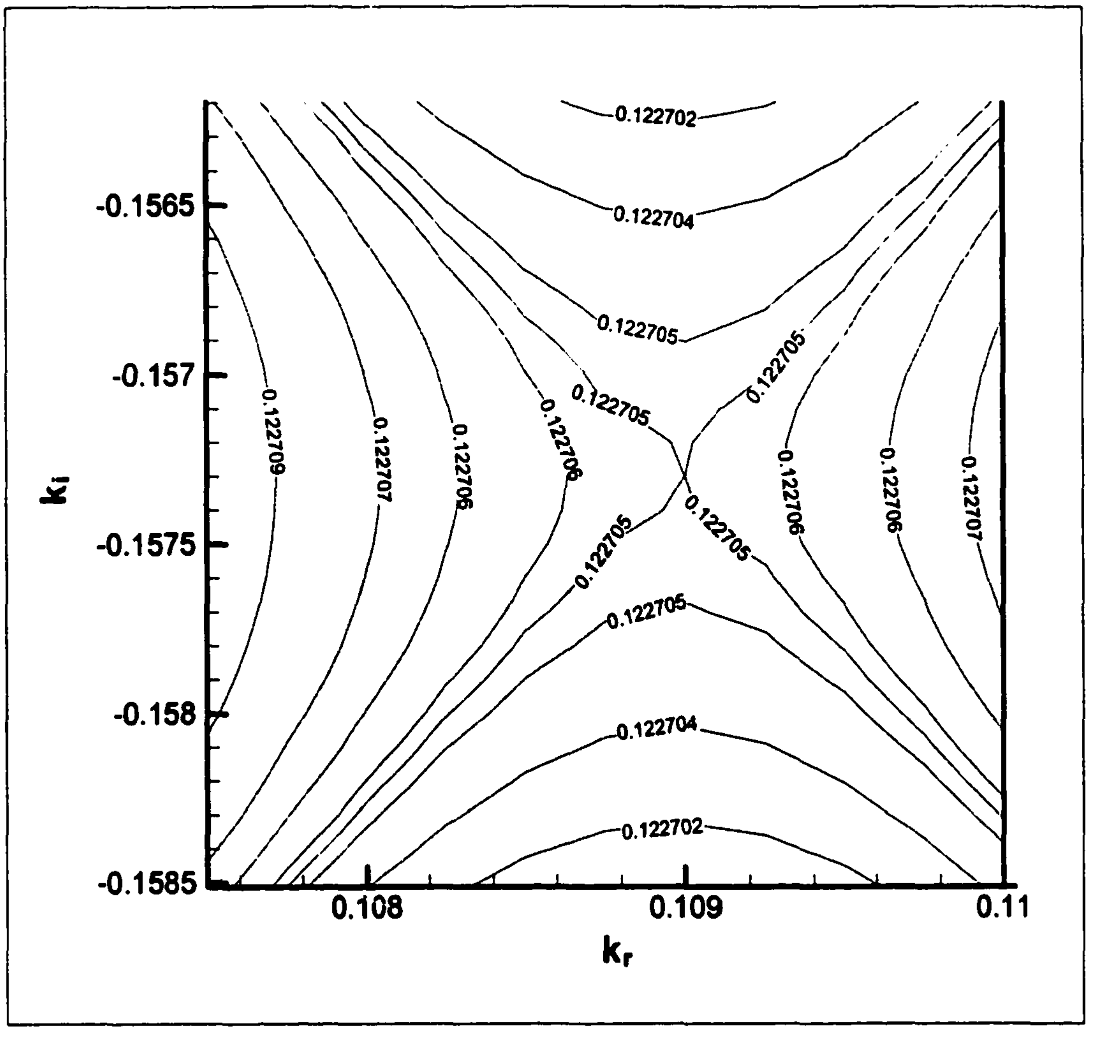

Figure A44: Contour plot of Ω_r for $R/\theta = 10$, $Fr = 1$, $\rho_j/\rho_\infty = 0.99$ in the k-plane illustrating the pinch point formation

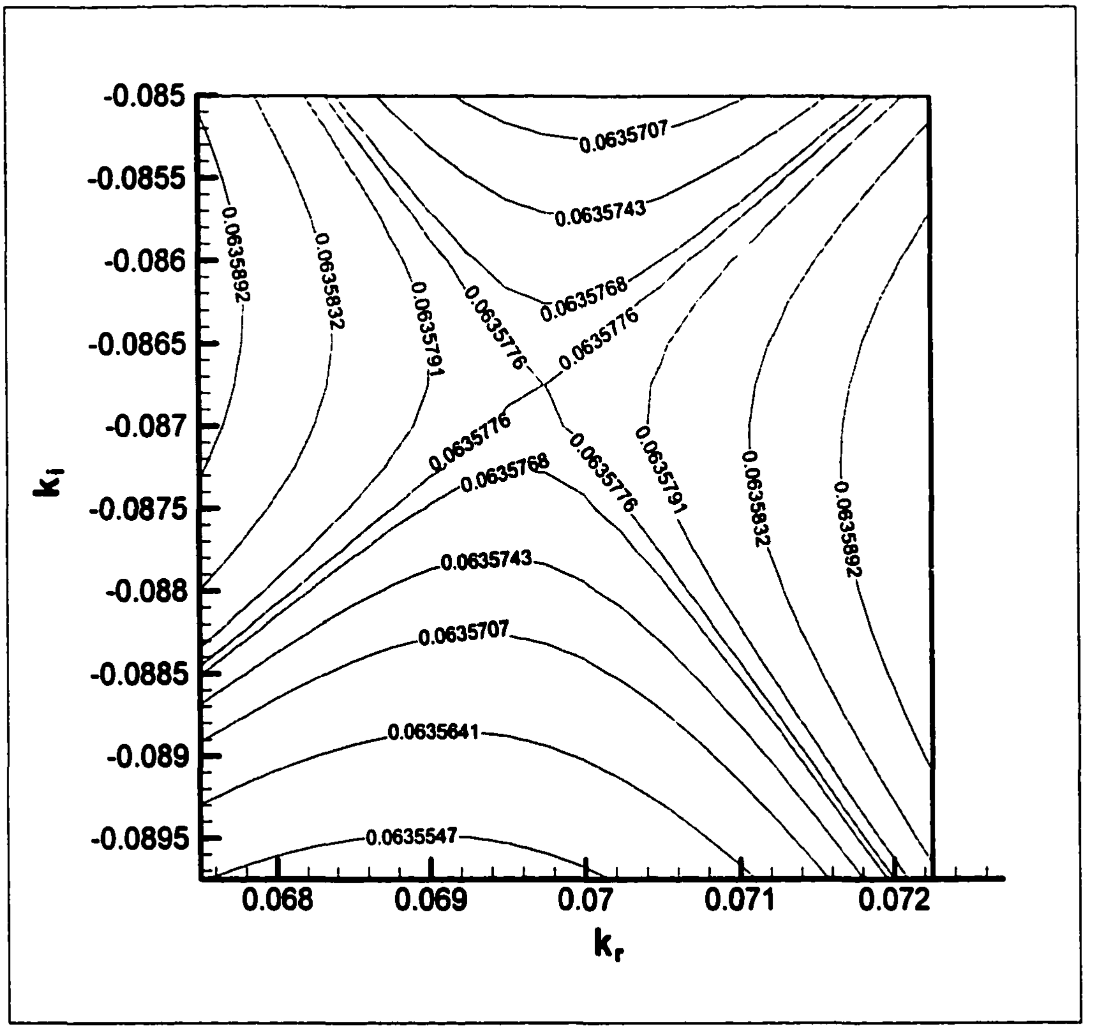

Figure A45: Contour plot of Ω_r for $R/\theta = 10$, $Fr = 0.75$, $\rho_j/\rho_\infty = 0.14$ in the k-plane illustrating the pinch point formation

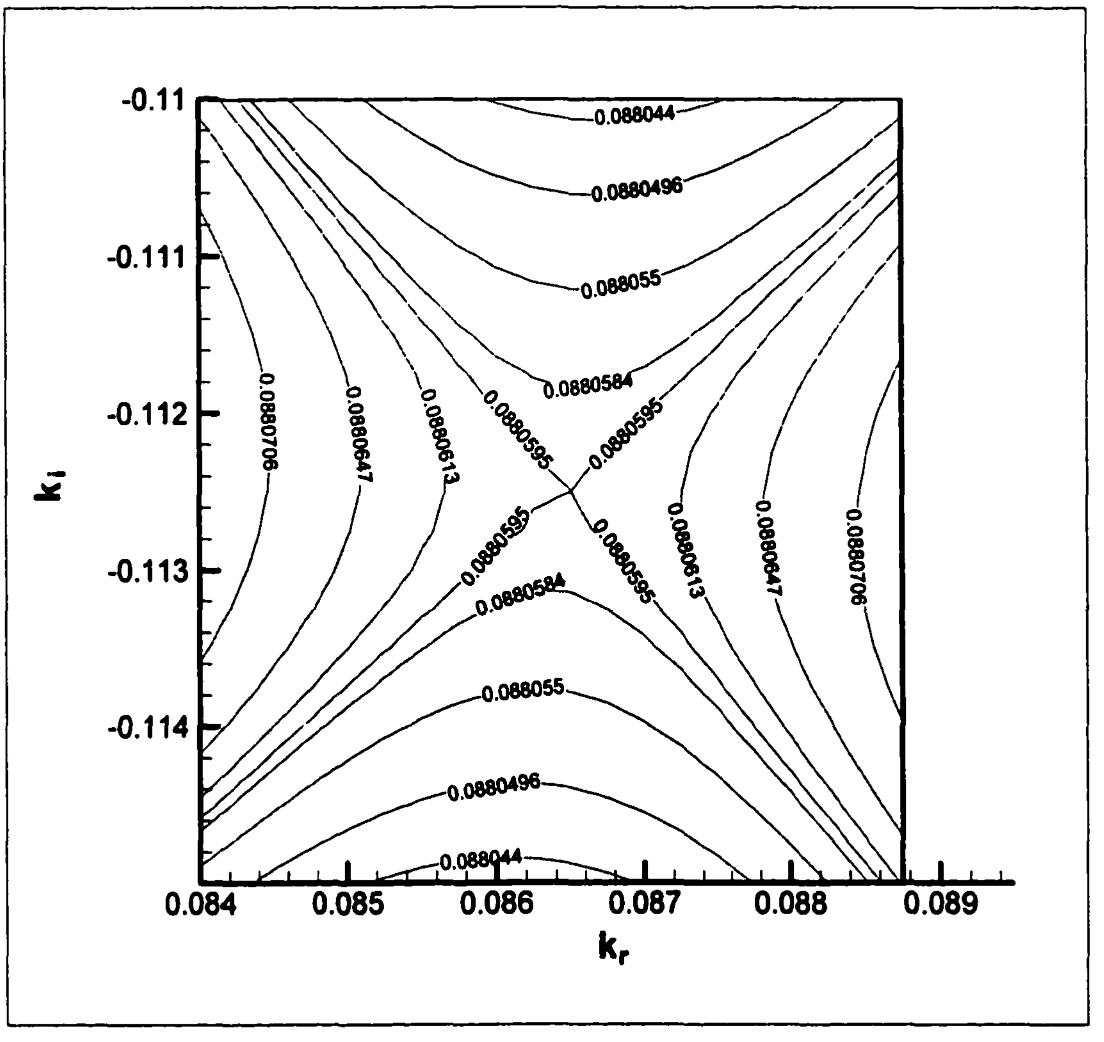

Figure A46: Contour plot of Ω_r for $R/\theta = 10$, $Fr = 0.75$, $\rho_j/\rho_\infty = 0.3$ in the k-plane illustrating the pinch point formation

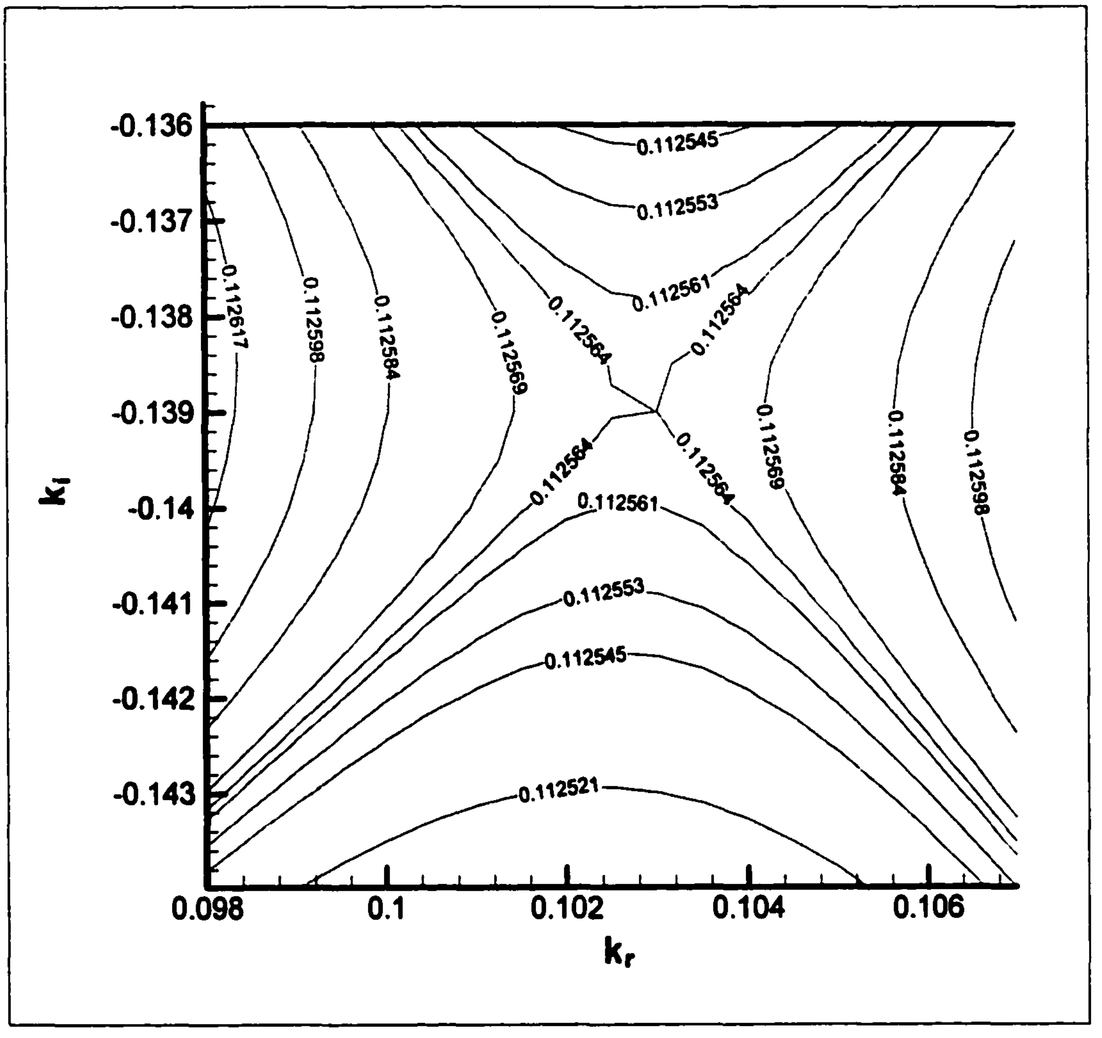

Figure A47: Contour plot of Ω_r for $R/\theta = 10$, $Fr = 0.75$, $\rho_j/\rho_\infty = 0.6$ in the k-plane illustrating the pinch point formation

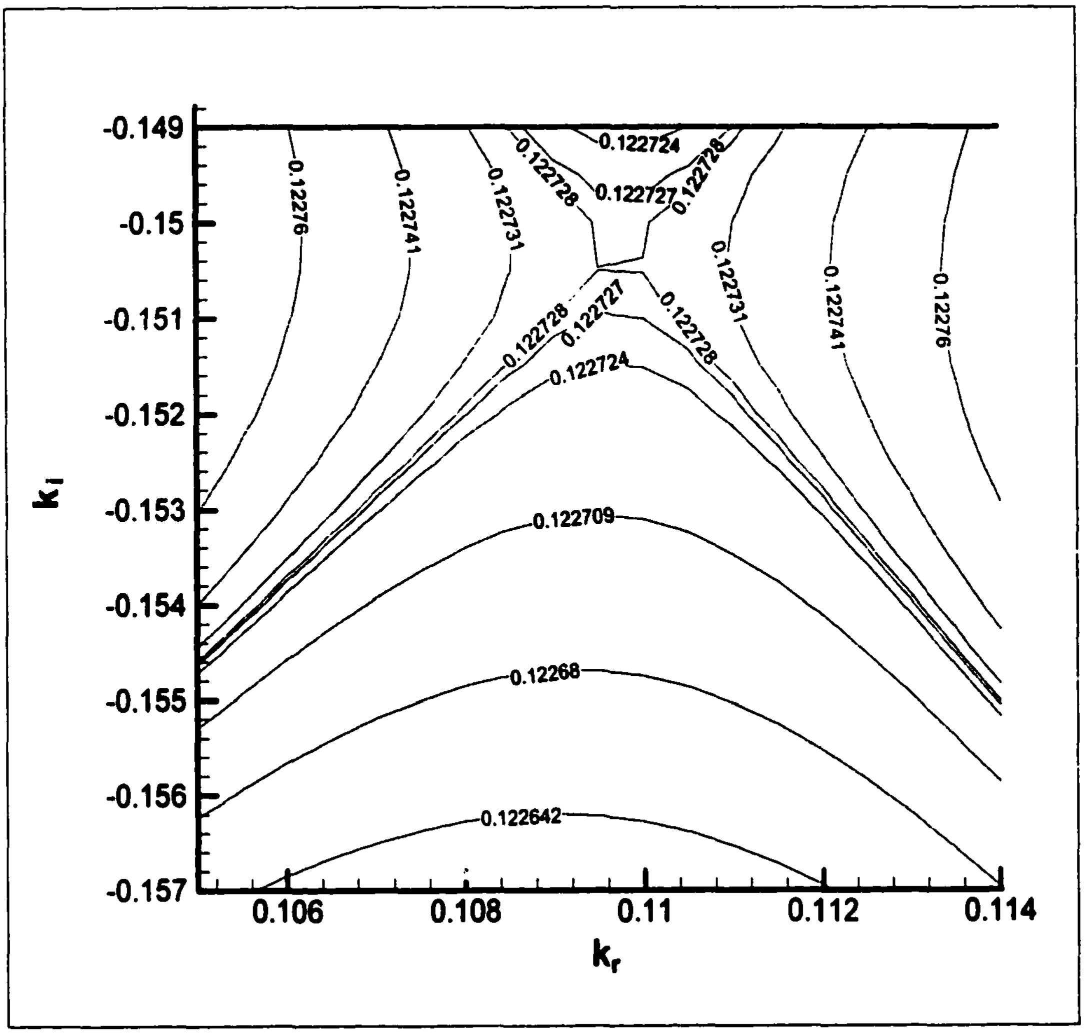

Figure A48: Contour plot of Ω_r for $R/\theta = 10$, $Fr = 0.75$, $\rho_j/\rho_\infty = 0.8$ in the k-plane illustrating the pinch point formation

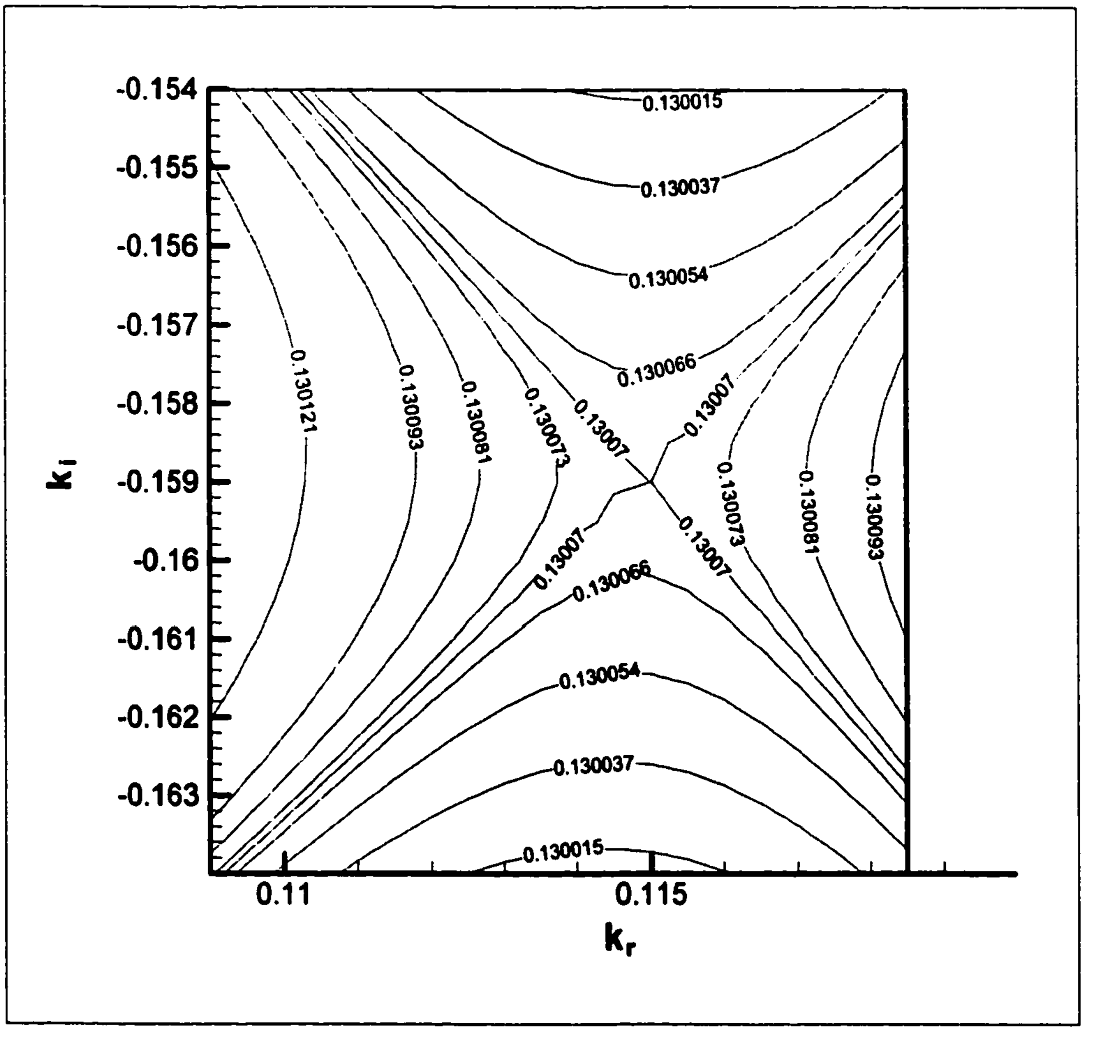

Figure A49: Contour plot of Ω_r for $R/\theta = 10$, $Fr = 0.75$, $\rho_j/\rho_\infty = 0.99$ in the k-plane illustrating the pinch point formation

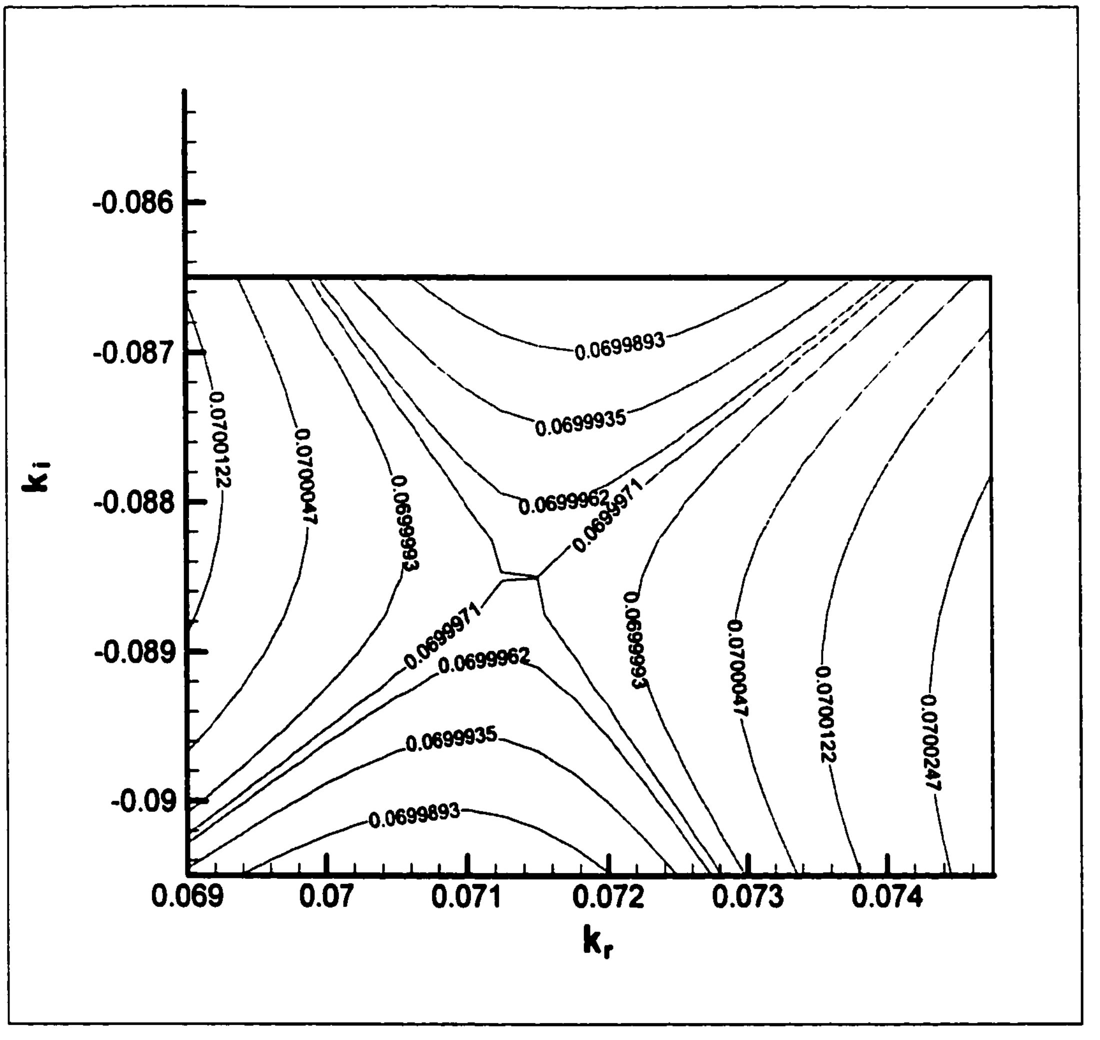

Figure A50: Contour plot of Ω_r for $R/\theta = 10$, $Fr = 0.5$, $\rho_j/\rho_\infty = 0.14$ in the k-plane illustrating the pinch point formation

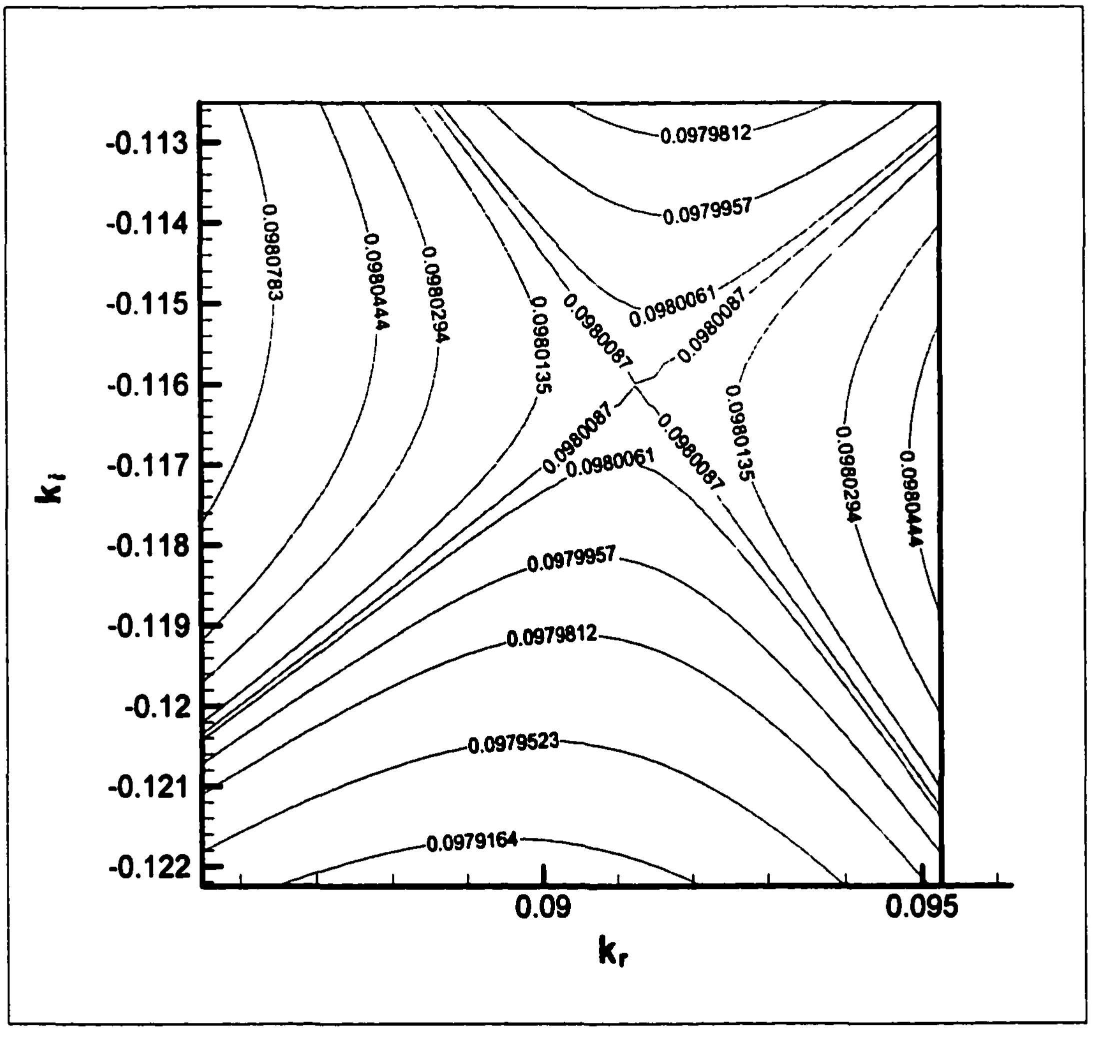

Figure A51: Contour plot of Ω_r for $R/\theta = 10$, $Fr = 0.5$, $\rho_j/\rho_\infty = 0.3$ in the k-plane illustrating the pinch point formation

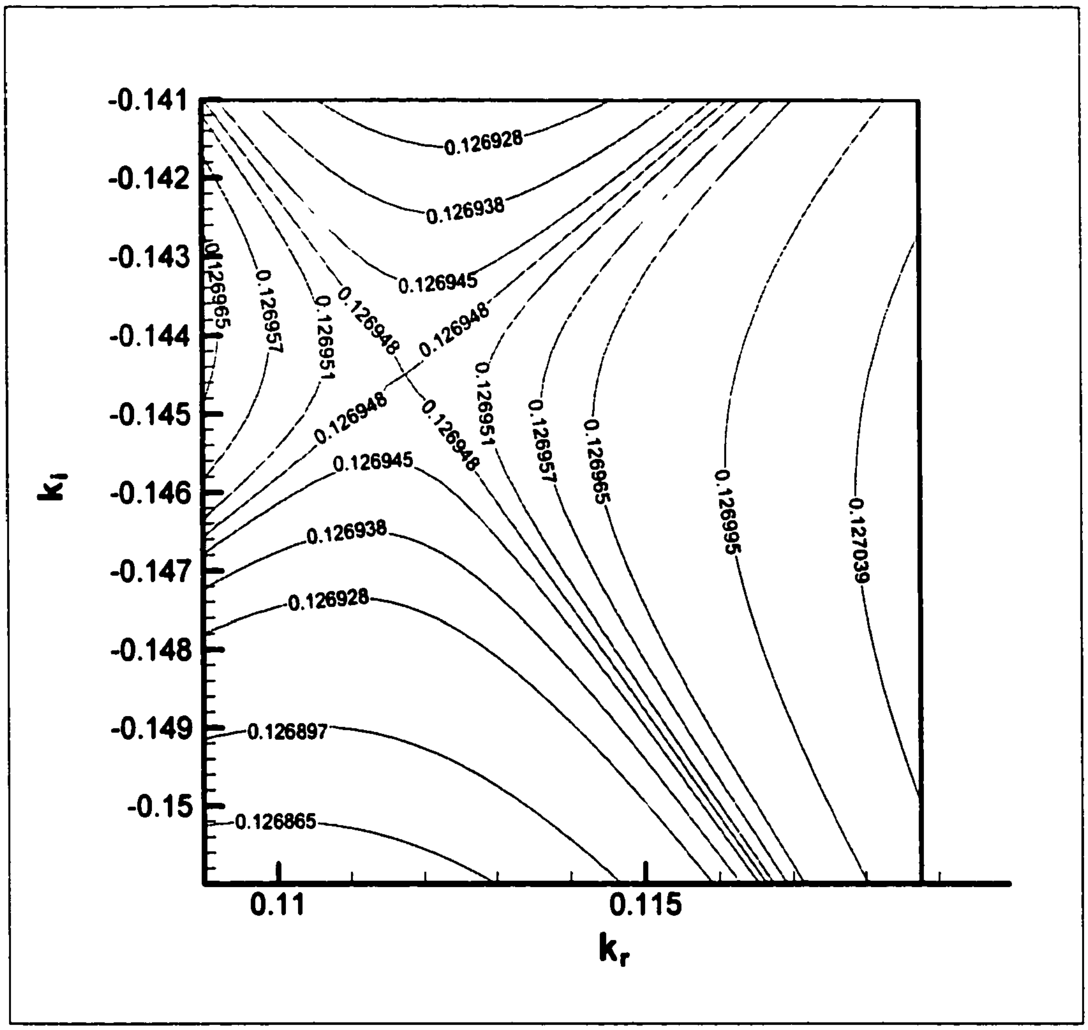

Figure A52: Contour plot of Ω_r for $R/\theta = 10$, $Fr = 0.5$, $\rho_j/\rho_\infty = 0.6$ in the k-plane illustrating the pinch point formation

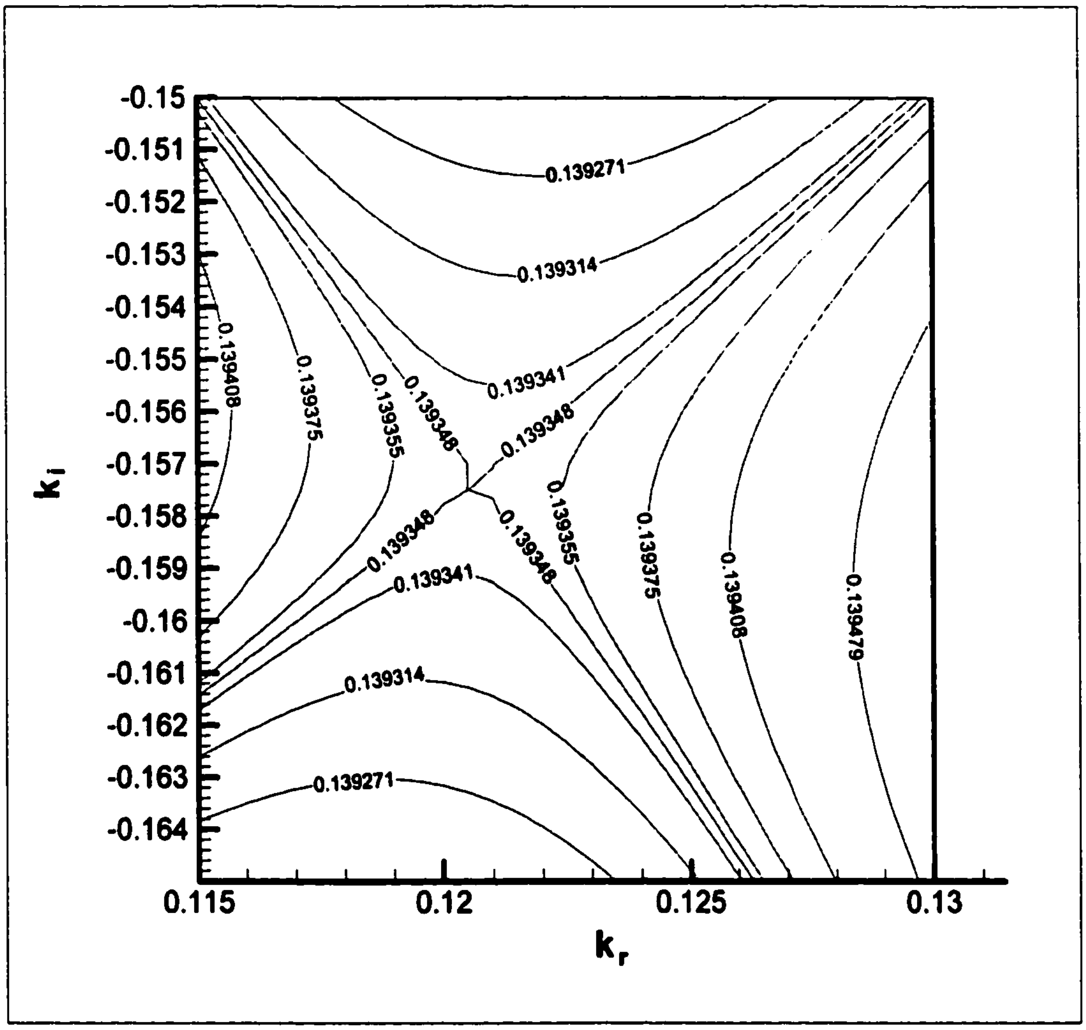

Figure A53: Contour plot of Ω_r for $R/\theta = 10$, $Fr = 0.5$, $\rho_j/\rho_\infty = 0.8$ in the k-plane illustrating the pinch point formation

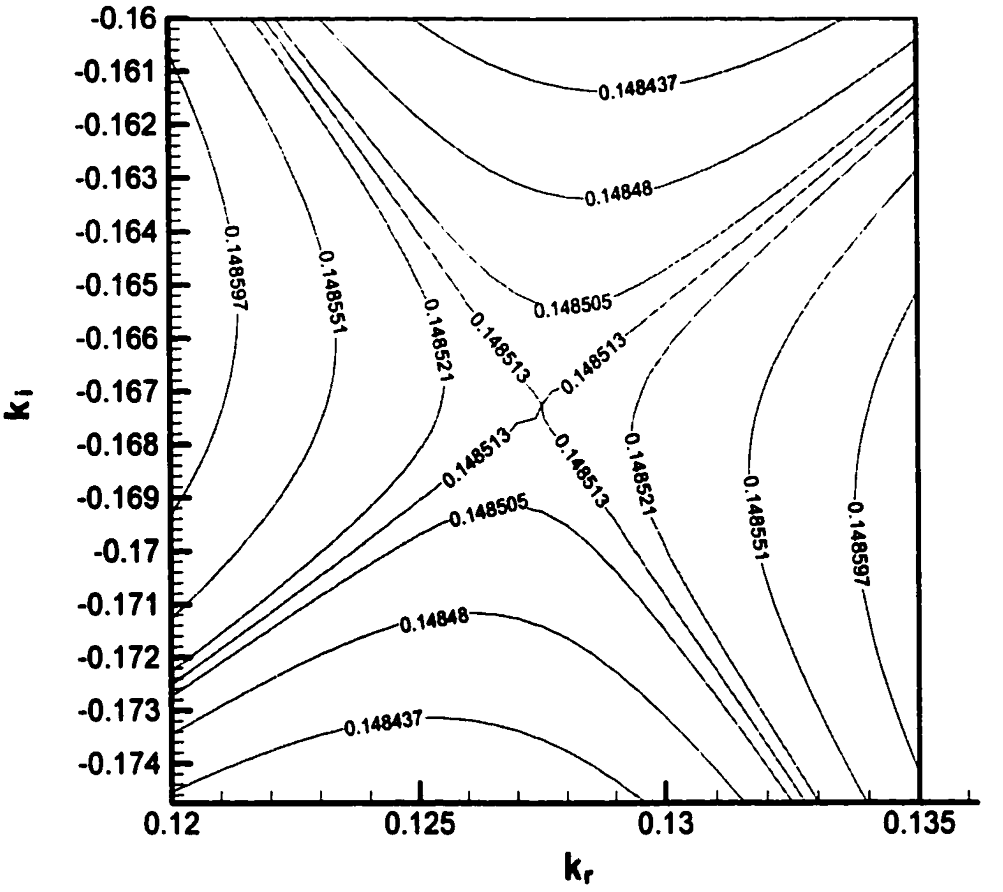

Figure A54: Contour plot of Ω_r for $R/\theta = 10$, $Fr = 0.5$, $\rho_j/\rho_\infty = 0.99$ in the k-plane illustrating the pinch point formation

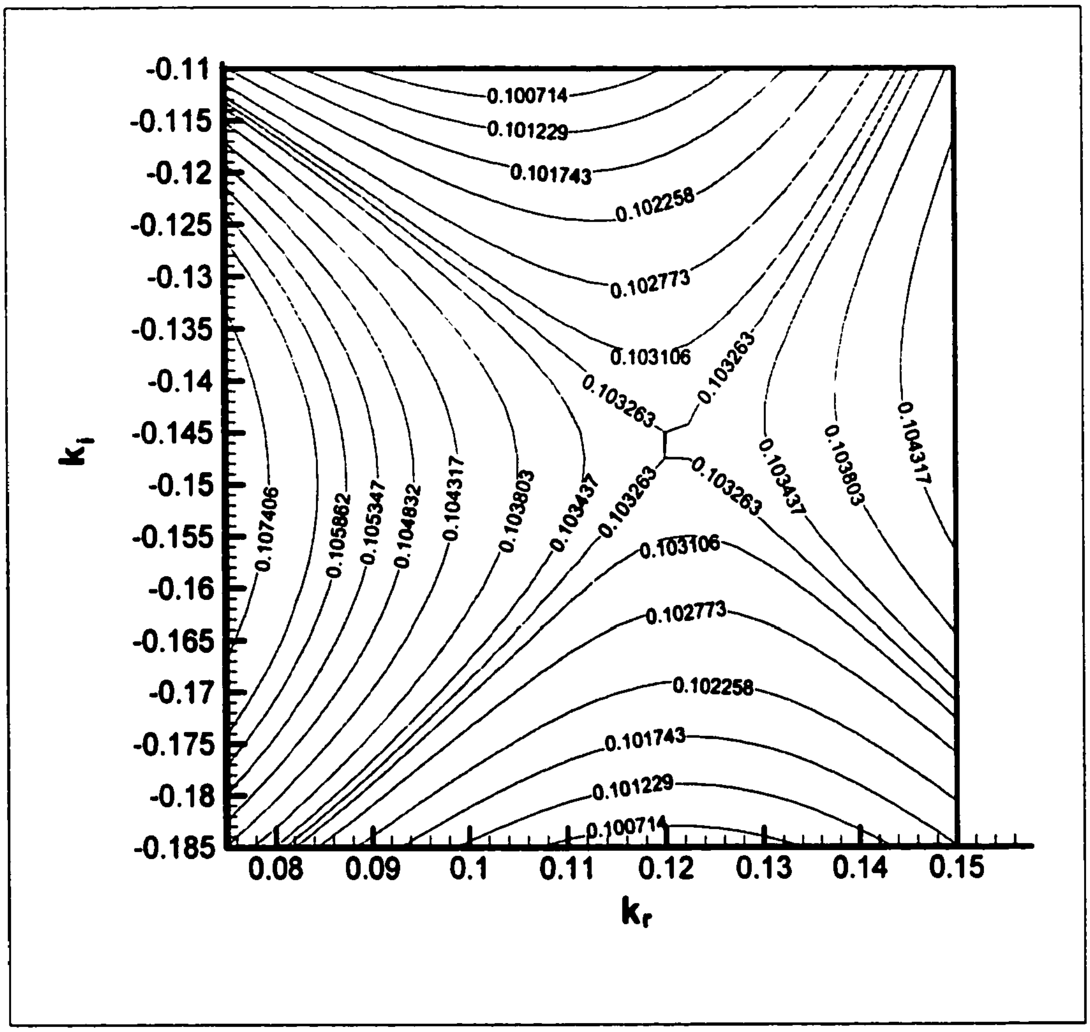

Figure A55: Contour plot of Ω_r for $R/\theta = 5$, $Fr = \infty$, $\rho_j/\rho_\infty = 0.14$ in the k-plane illustrating the pinch point formation

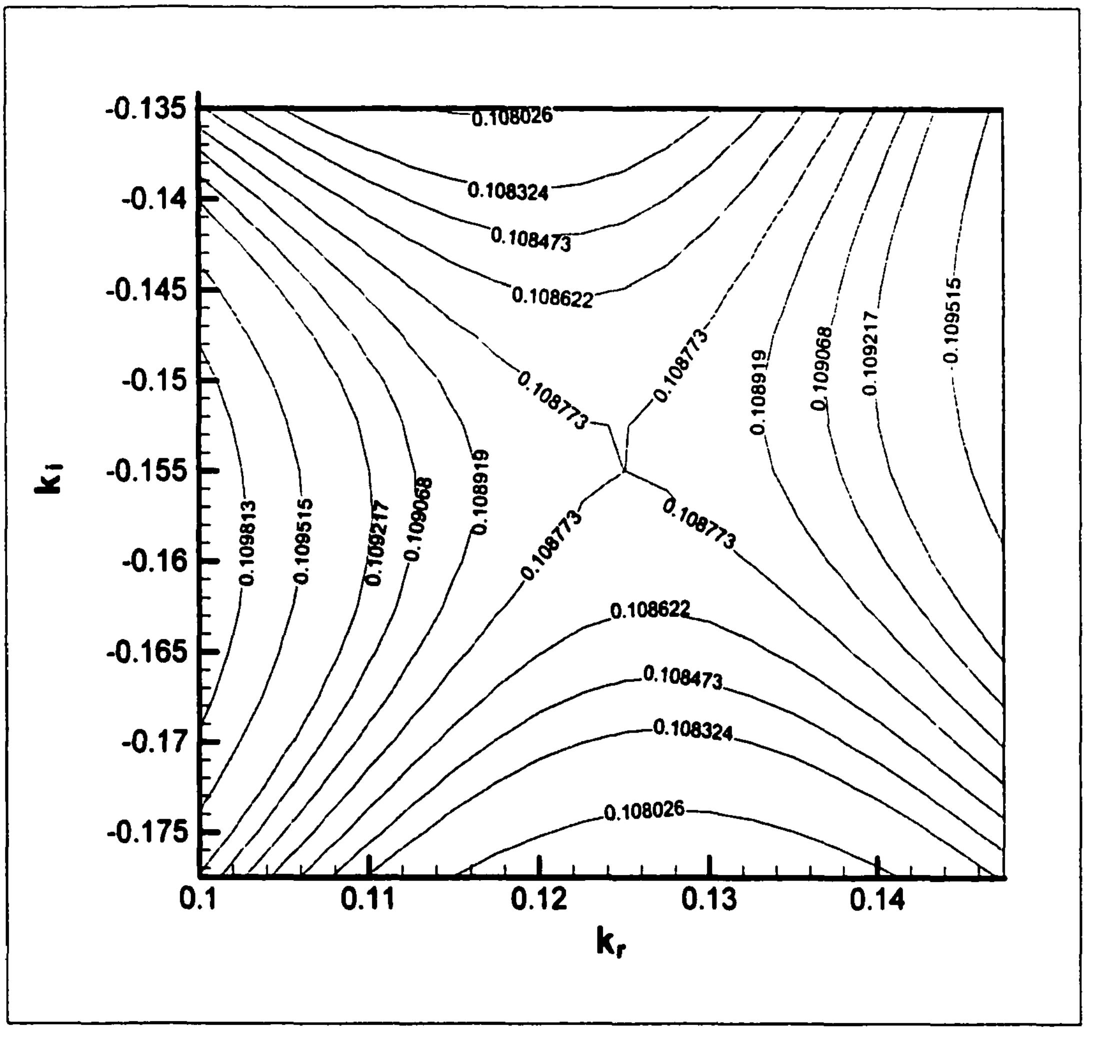

Figure A56: Contour plot of Ω_r for $R/\theta = 5$, $Fr = \infty$, $\rho_j/\rho_\infty = 0.17$ in the k-plane illustrating the pinch point formation

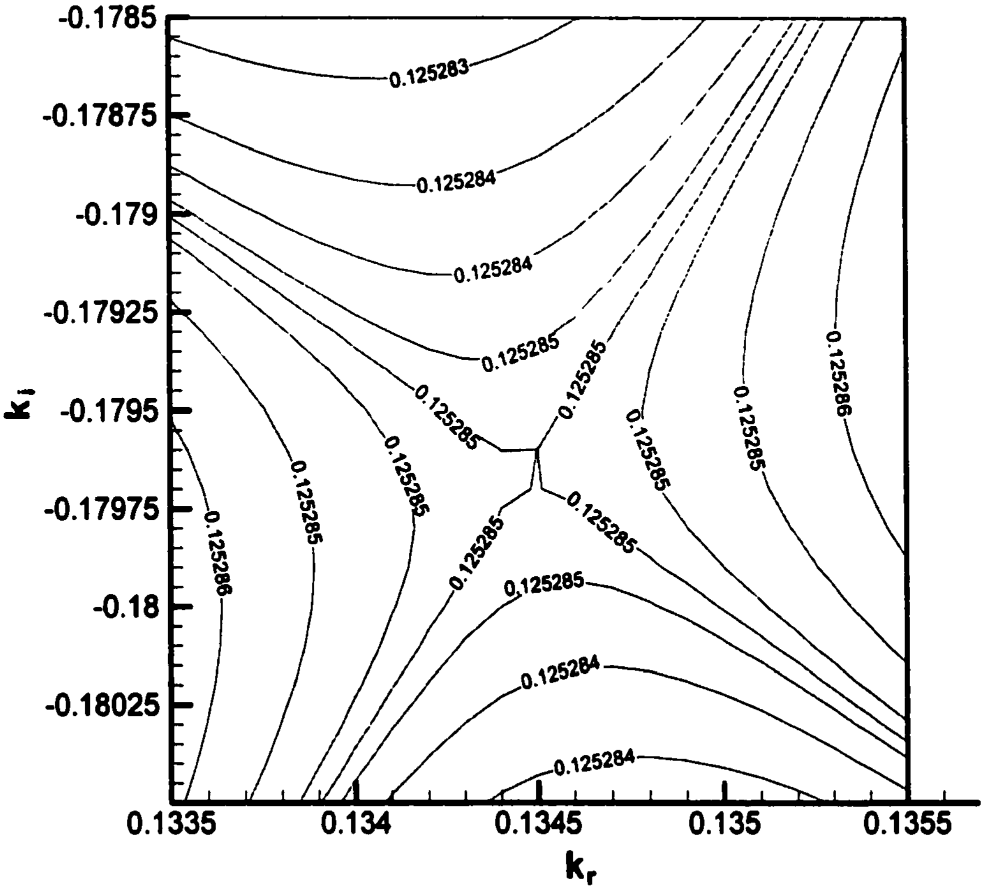

Figure A57: Contour plot of Ω_r for $R/\theta = 5$, $Fr = \infty$, $\rho_j/\rho_\infty = 0.3$ in the k-plane illustrating the pinch point formation

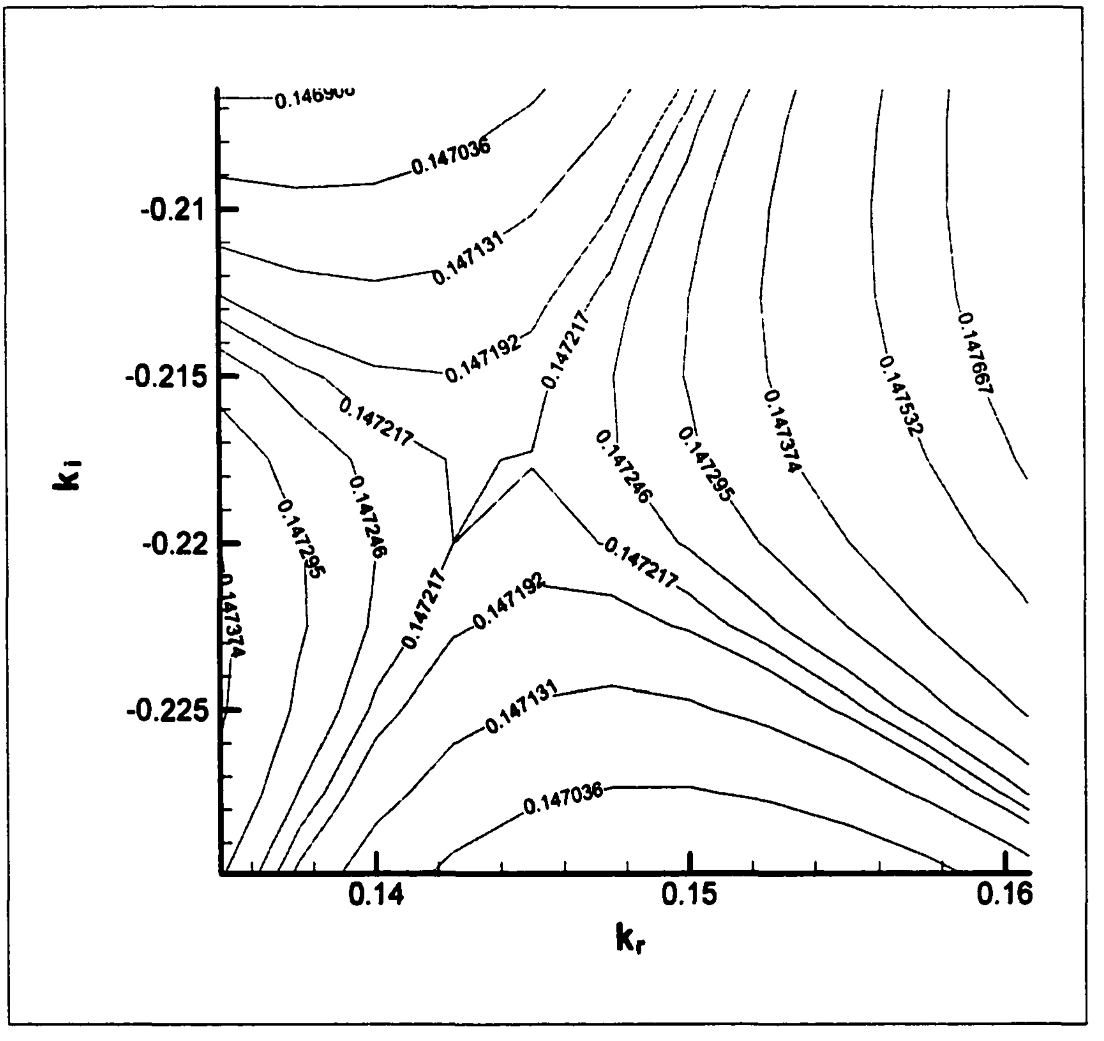

Figure A58: Contour plot of Ω_r for $R/\theta = 5$, $Fr = \infty$, $\rho_j/\rho_\infty = 0.6$ in the k-plane illustrating the pinch point formation

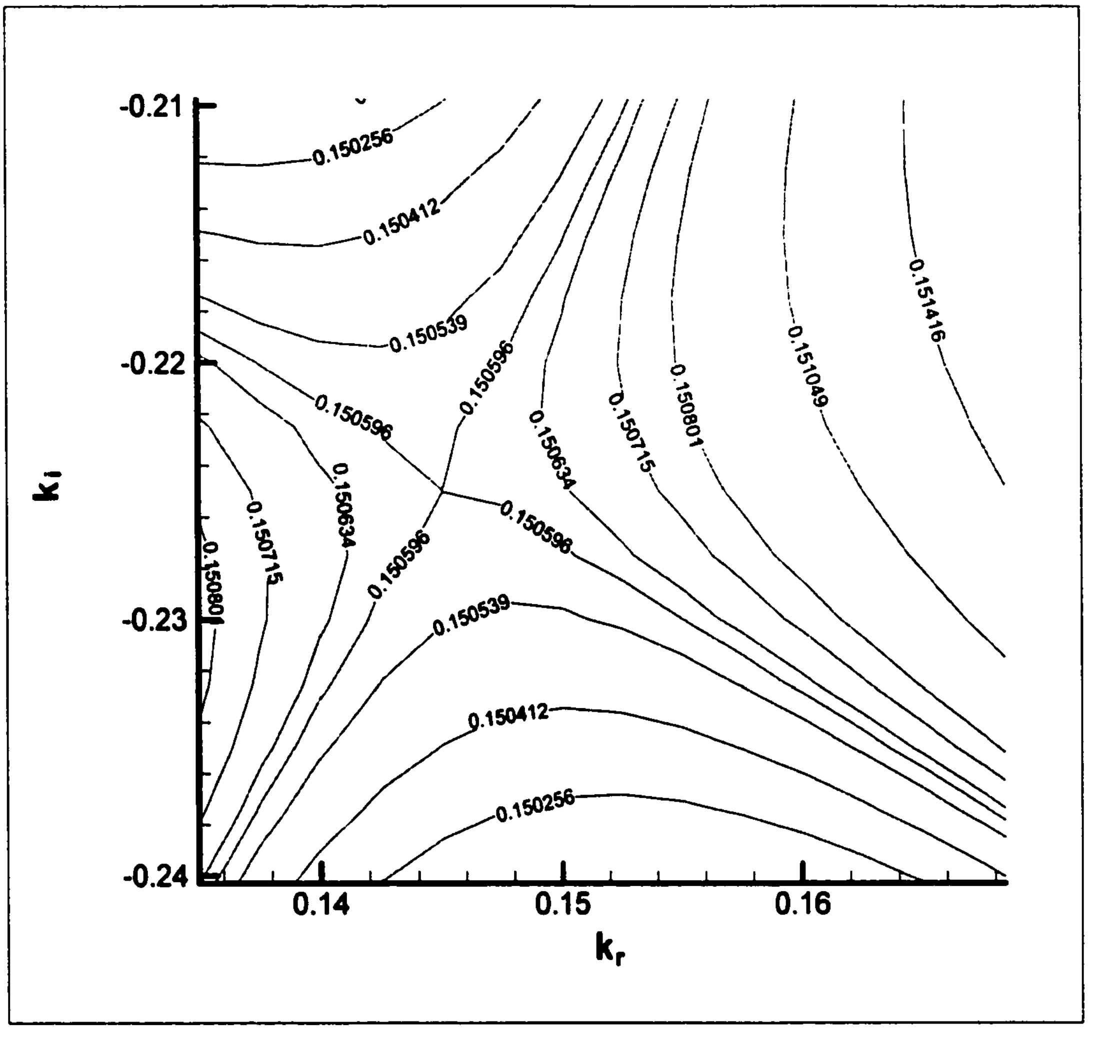

Figure A59: Contour plot of Ω_r for $R/\theta = 5$, $Fr = \infty$, $\rho_j/\rho_\infty = 0.66$ in the k-plane illustrating the pinch point formation

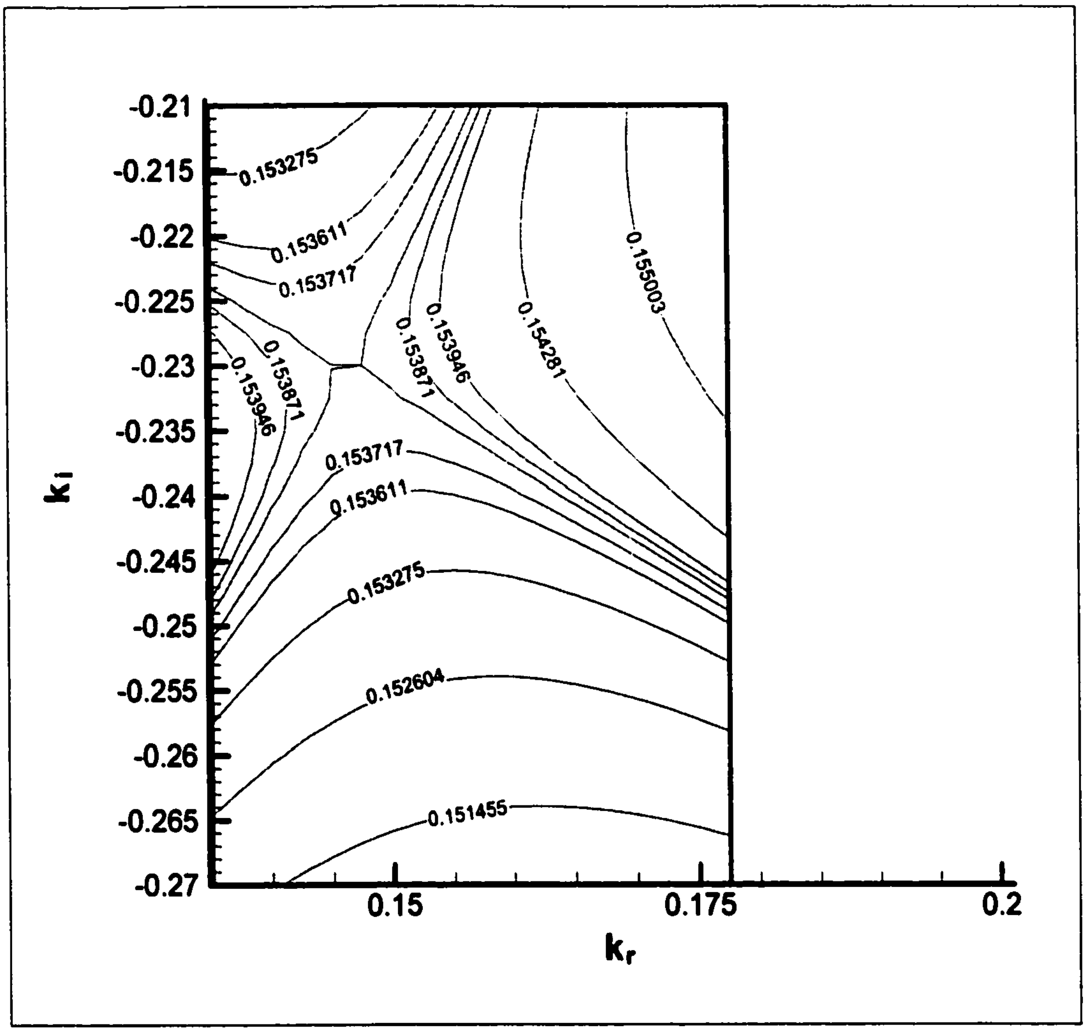

Figure A60: Contour plot of Ω_r for $R/\theta = 5$, $Fr = \infty$, $\rho_j/\rho_\infty = 0.72$ in the k-plane illustrating the pinch point formation

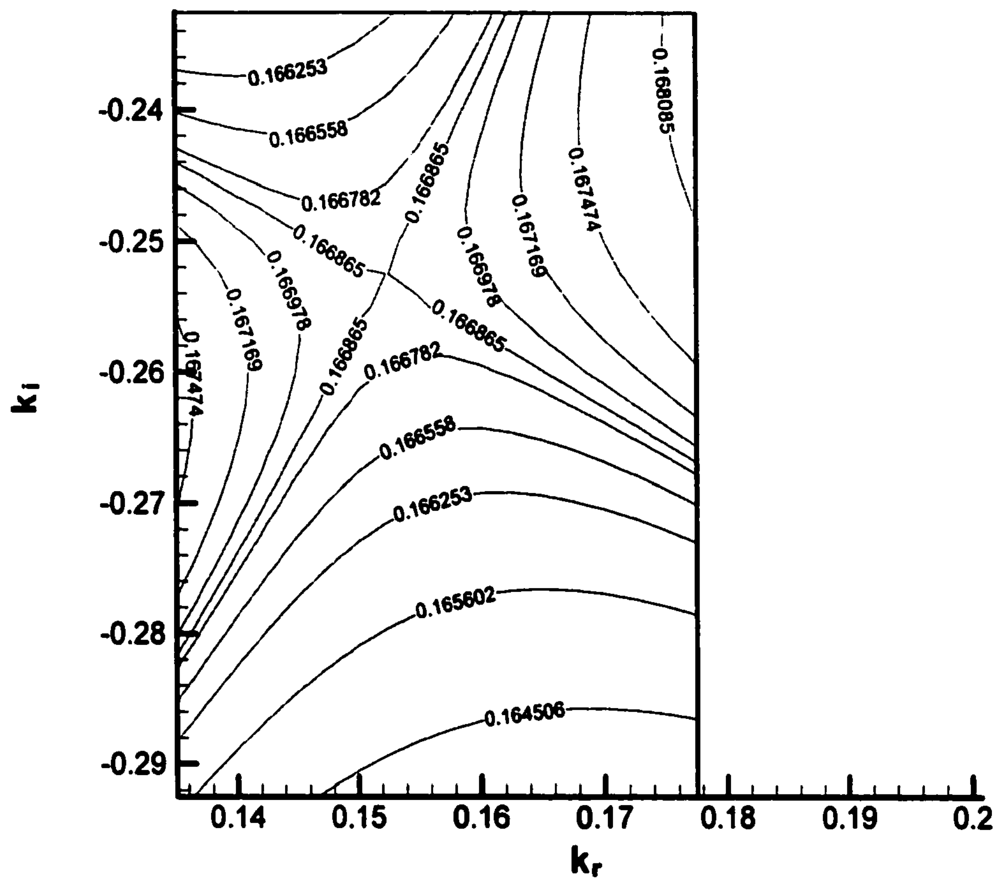

Figure A61: Contour plot of Ω_r for $R/\theta = 5$, $Fr = \infty$, $\rho_j/\rho_\infty = 0.99$ in the k-plane illustrating the pinch point formation

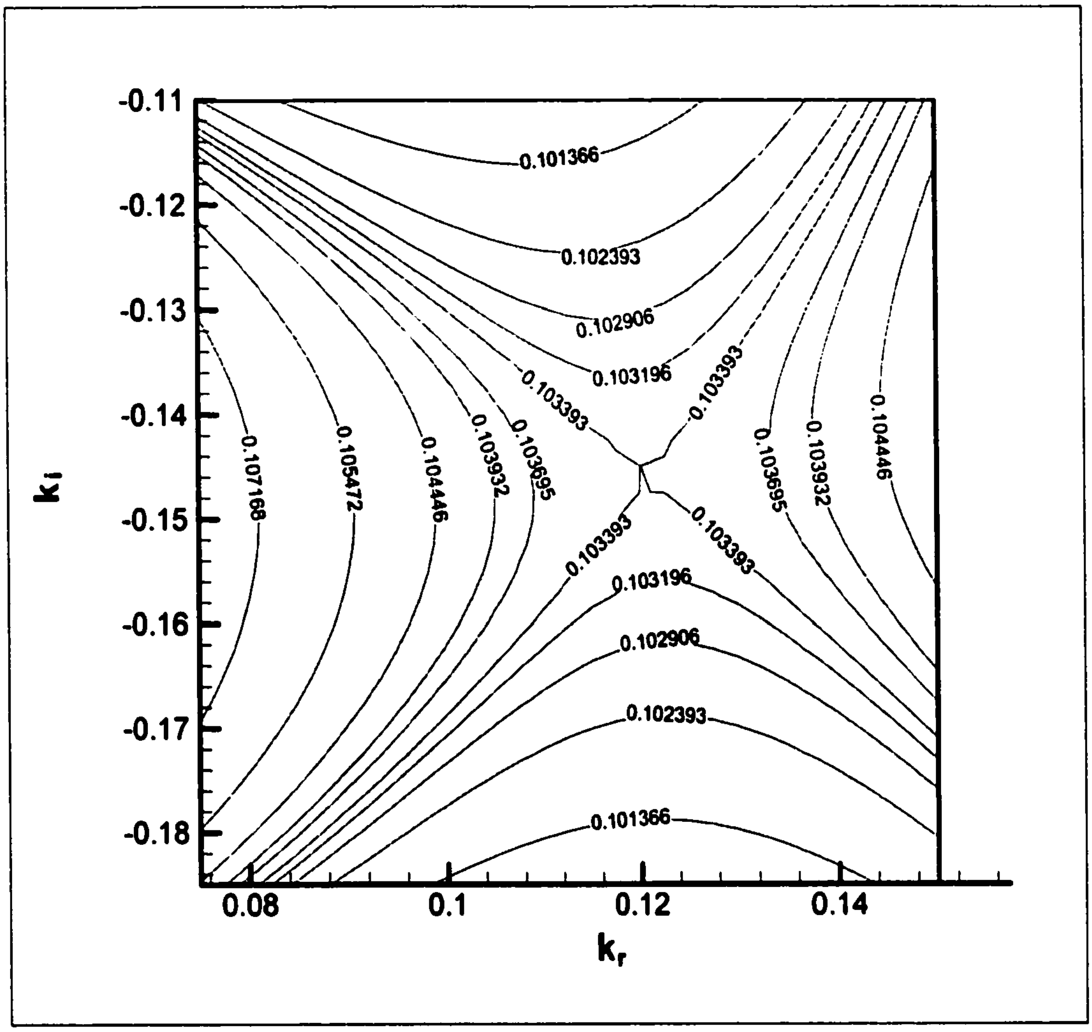

Figure A62: Contour plot of Ω_r for $R/\theta = 5$, $Fr = 10$, $\rho_j/\rho_\infty = 0.14$ in the k-plane illustrating the pinch point formation

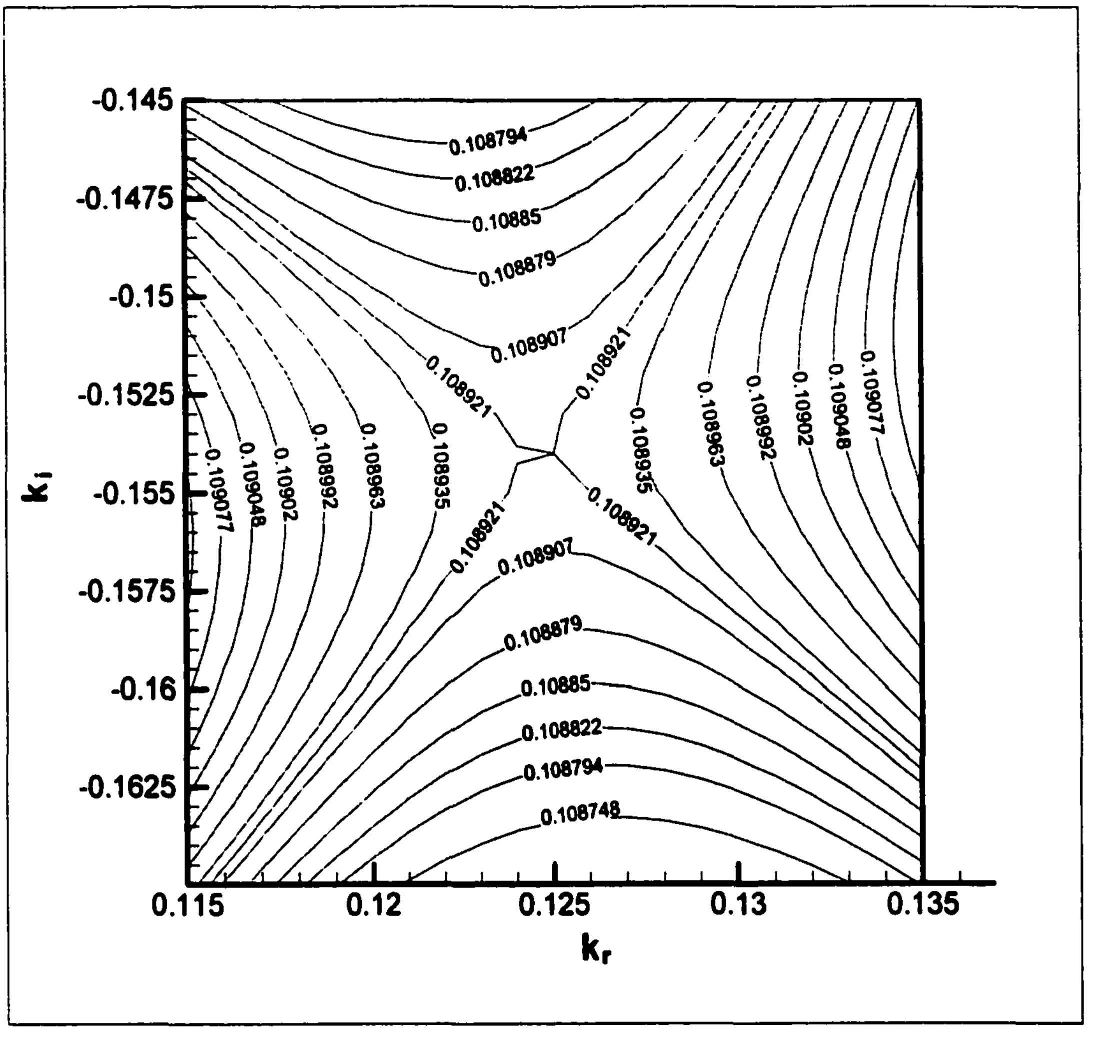

Figure A63: Contour plot of Ω_r for $R/\theta = 5$, $Fr = 10$, $\rho_j/\rho_\infty = 0.17$ in the k-plane illustrating the pinch point formation

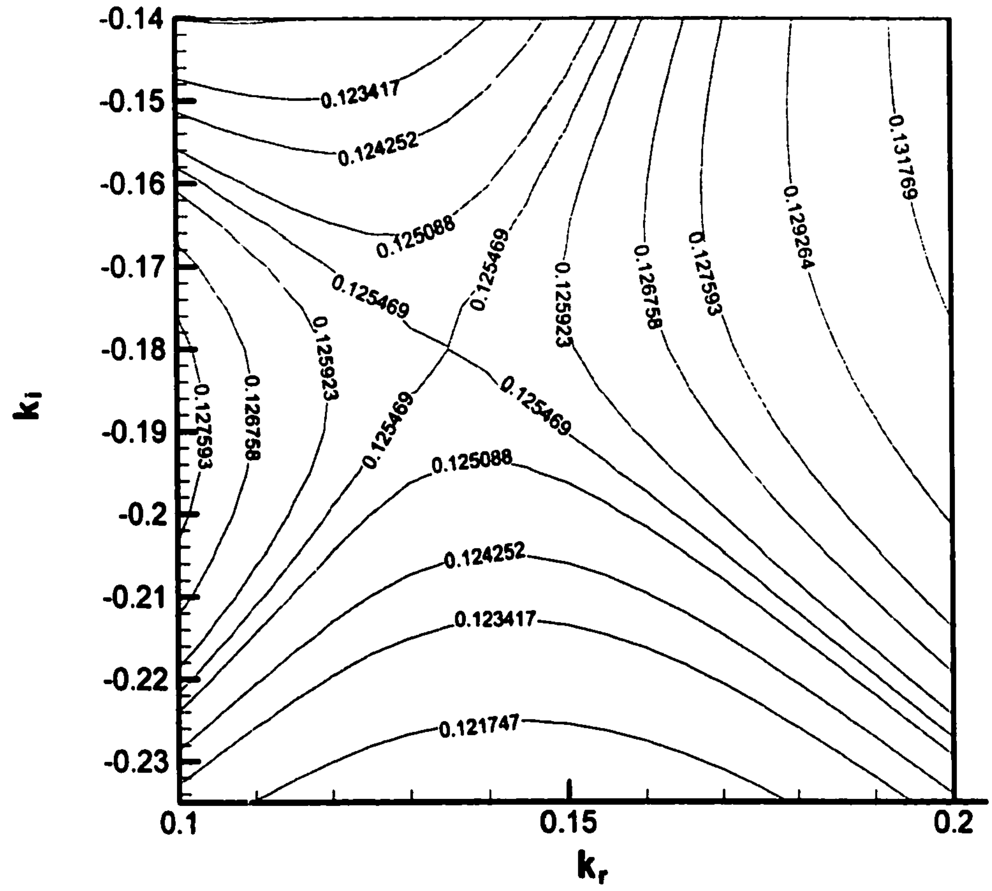

Figure A64: Contour plot of Ω_r for $R/\theta = 5$, $Fr = 10$, $\rho_j/\rho_\infty = 0.3$ in the k-plane illustrating the pinch point formation

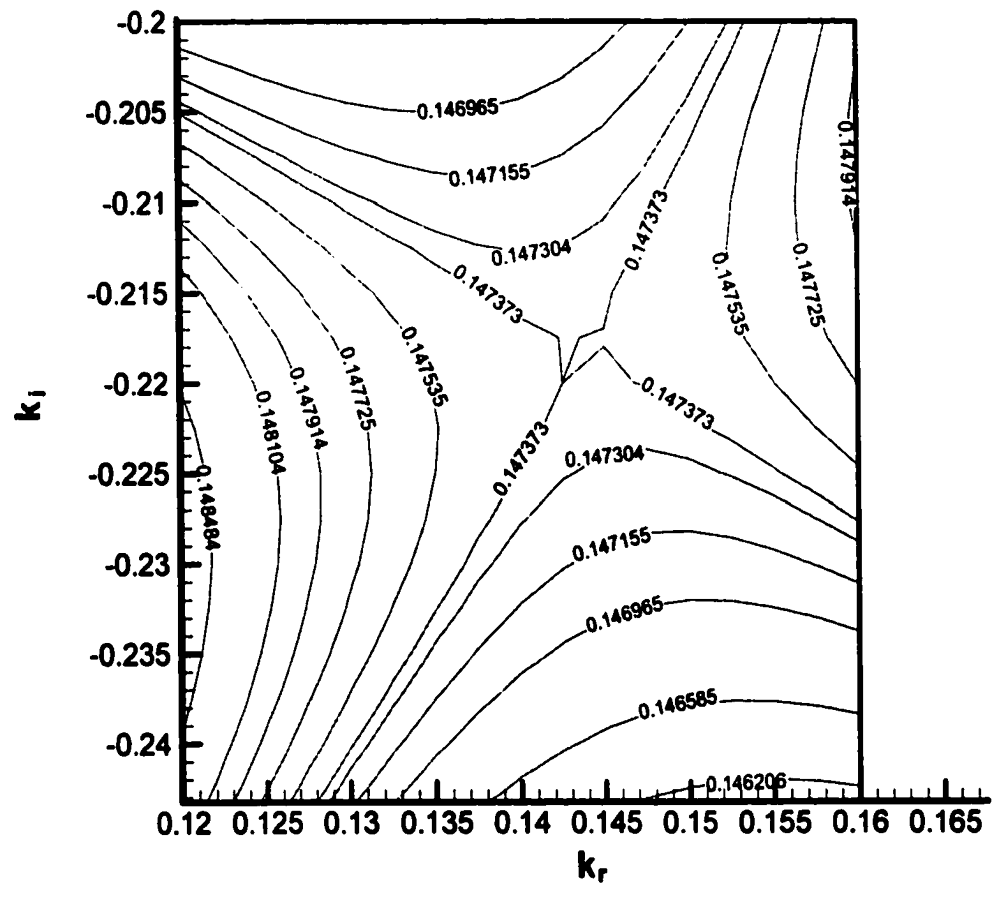

Figure A65: Contour plot of Ω_r for $R/\theta = 5$, $Fr = 10$, $\rho_j/\rho_\infty = 0.6$ in the k-plane illustrating the pinch point formation

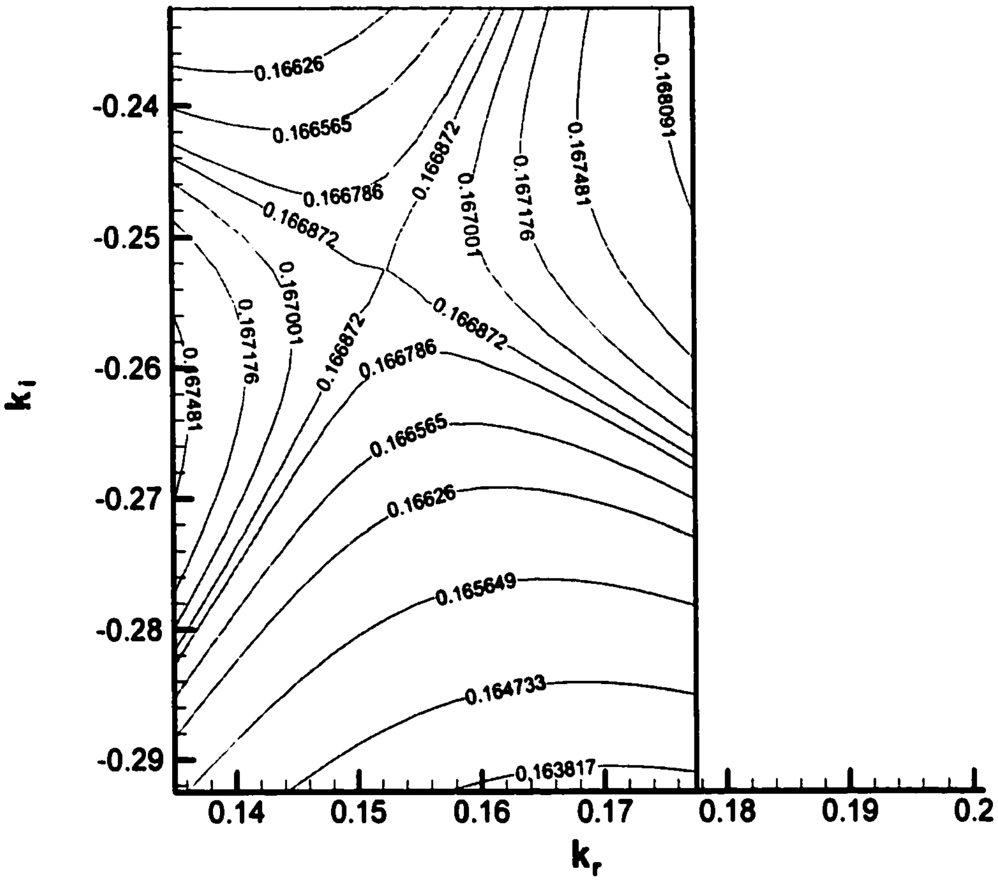

Figure A66: Contour plot of Ω_r for $R/\theta = 5$, $Fr = 10$, $\rho_j/\rho_\infty = 0.99$ in the k-plane illustrating the pinch point formation

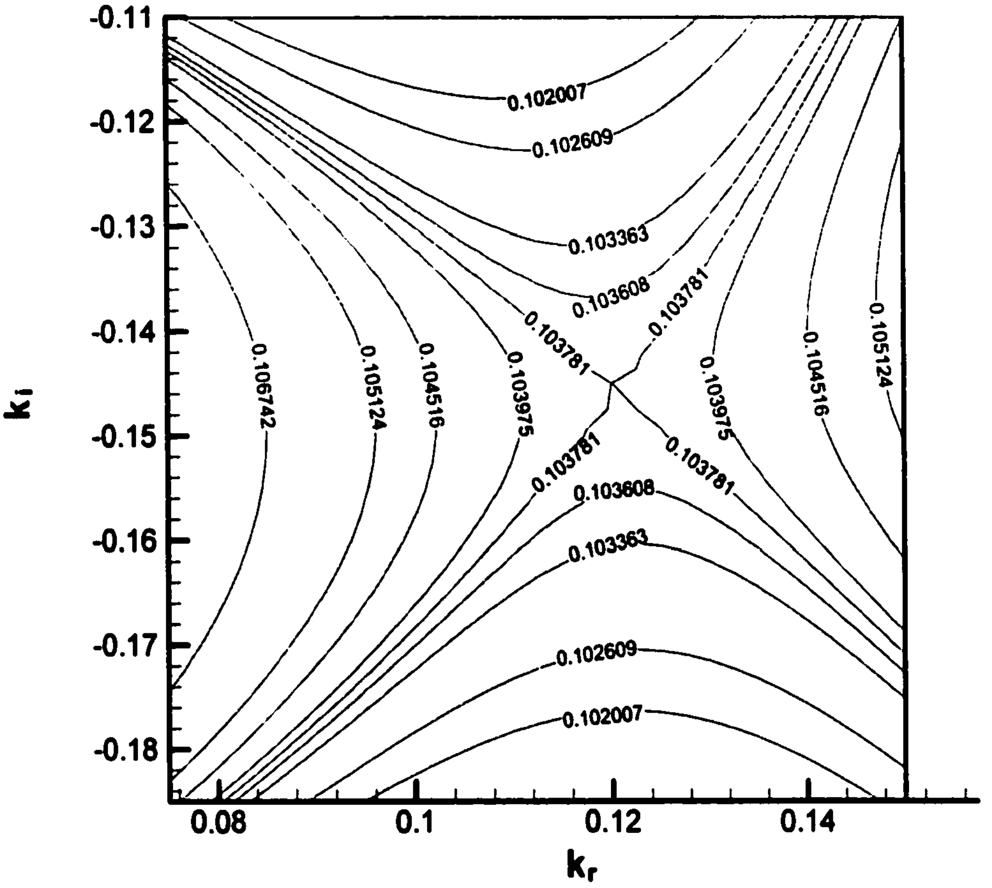

Figure A67: Contour plot of Ω_r for $R/\theta = 5$, $Fr = 5$, $\rho_j/\rho_\infty = 0.14$ in the k-plane illustrating the pinch point formation

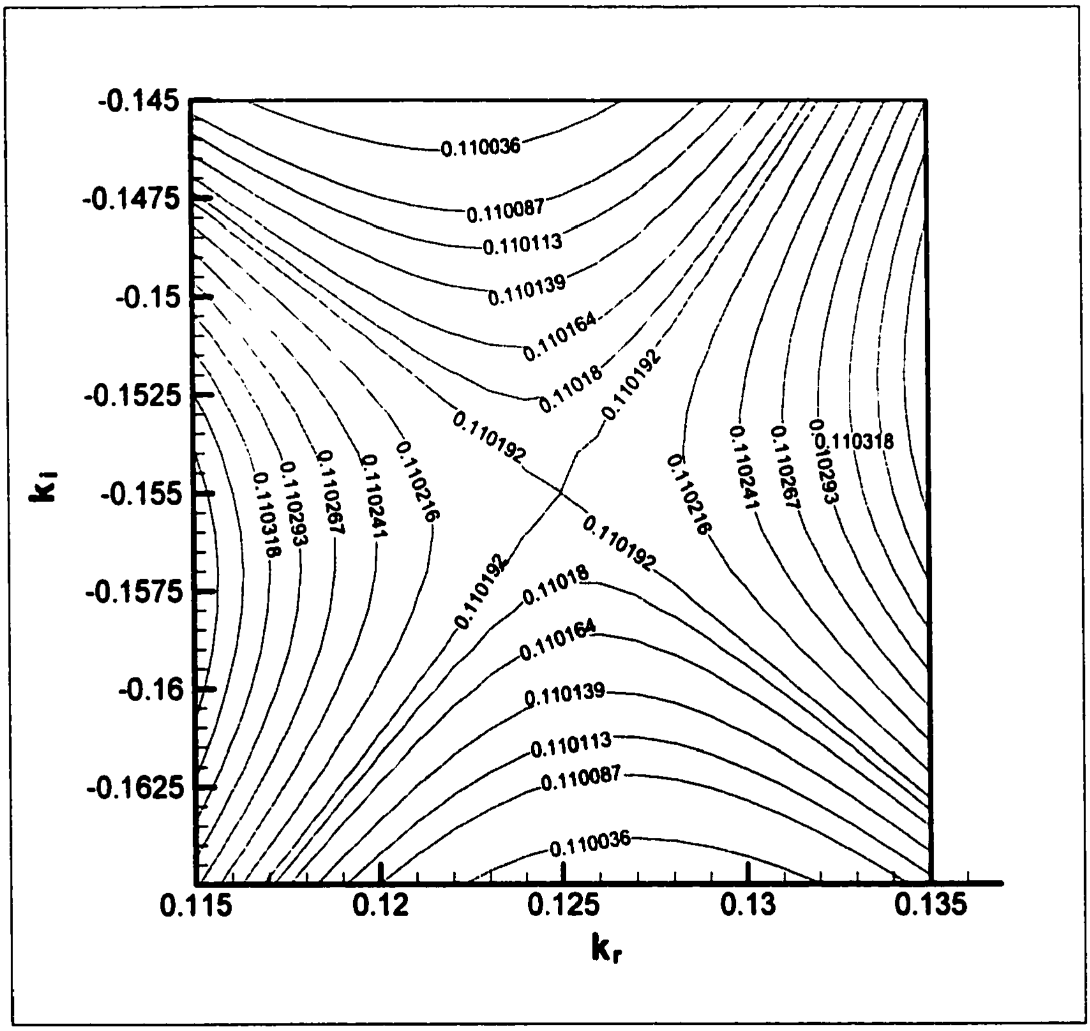

Figure A68: Contour plot of Ω_r for $R/\theta = 5$, $Fr = 5$, $\rho_j/\rho_\infty = 0.175$ in the k-plane illustrating the pinch point formation

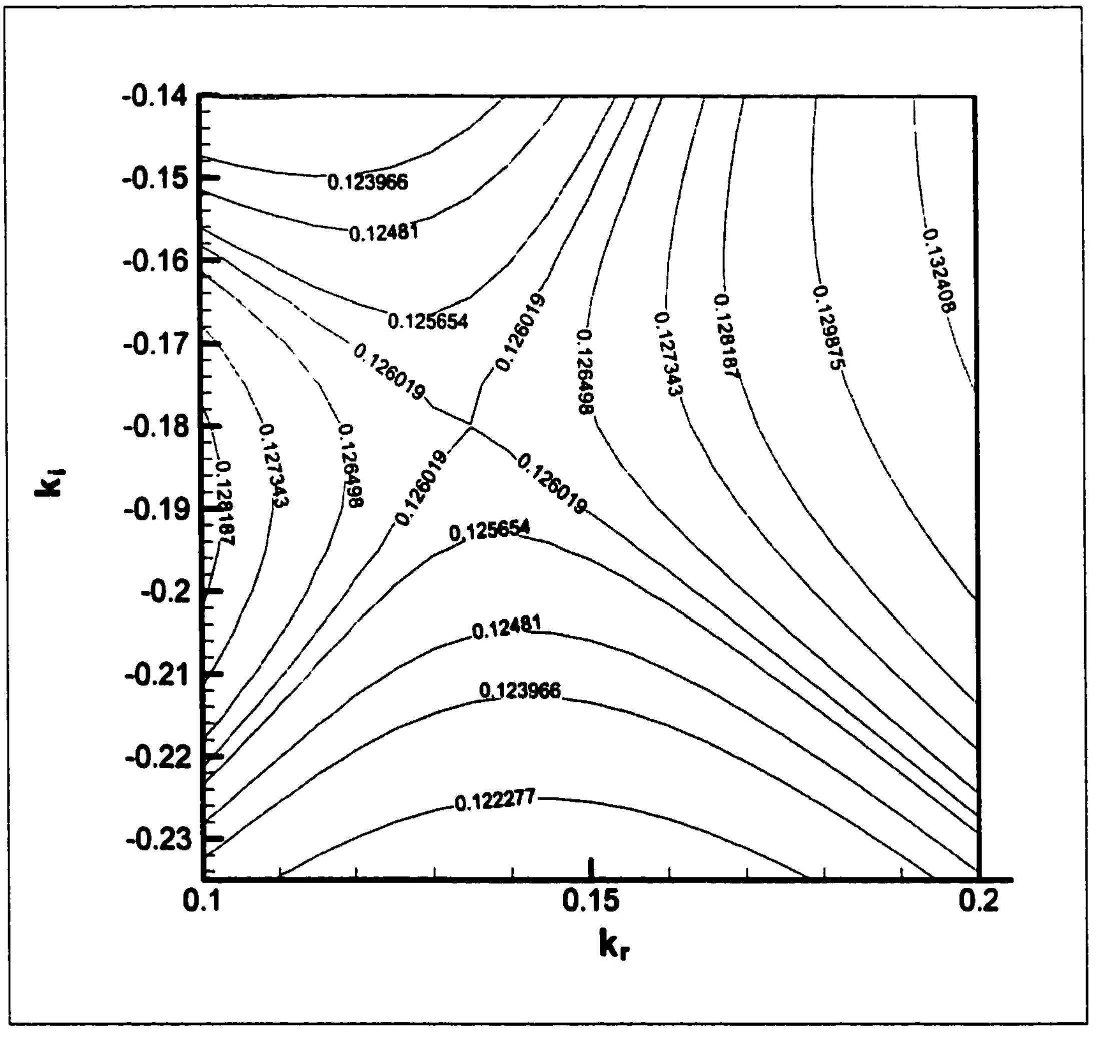

Figure A69: Contour plot of Ω_r for $R/\theta = 5$, $Fr = 5$, $\rho_j/\rho_\infty = 0.3$ in the k-plane illustrating the pinch point formation

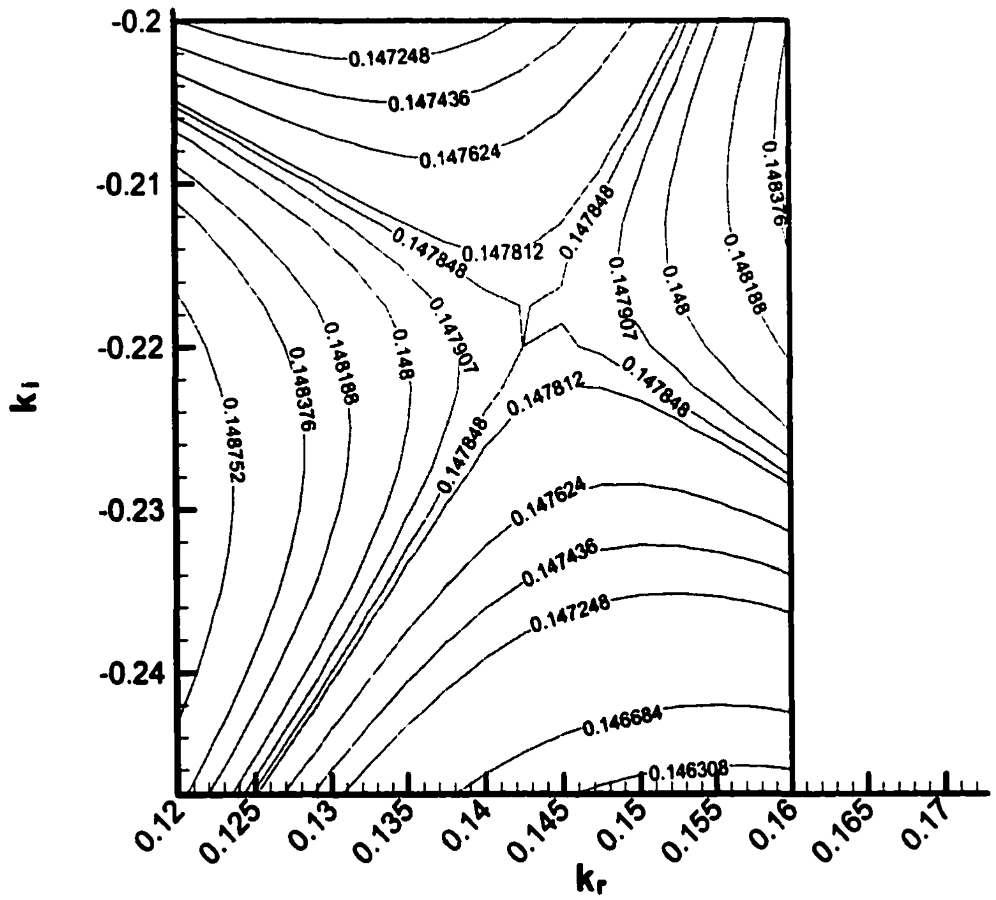

Figure A70: Contour plot of Ω_r for $R/\theta = 5$, $Fr = 5$, $\rho_j/\rho_\infty = 0.6$ in the k-plane illustrating the pinch point formation

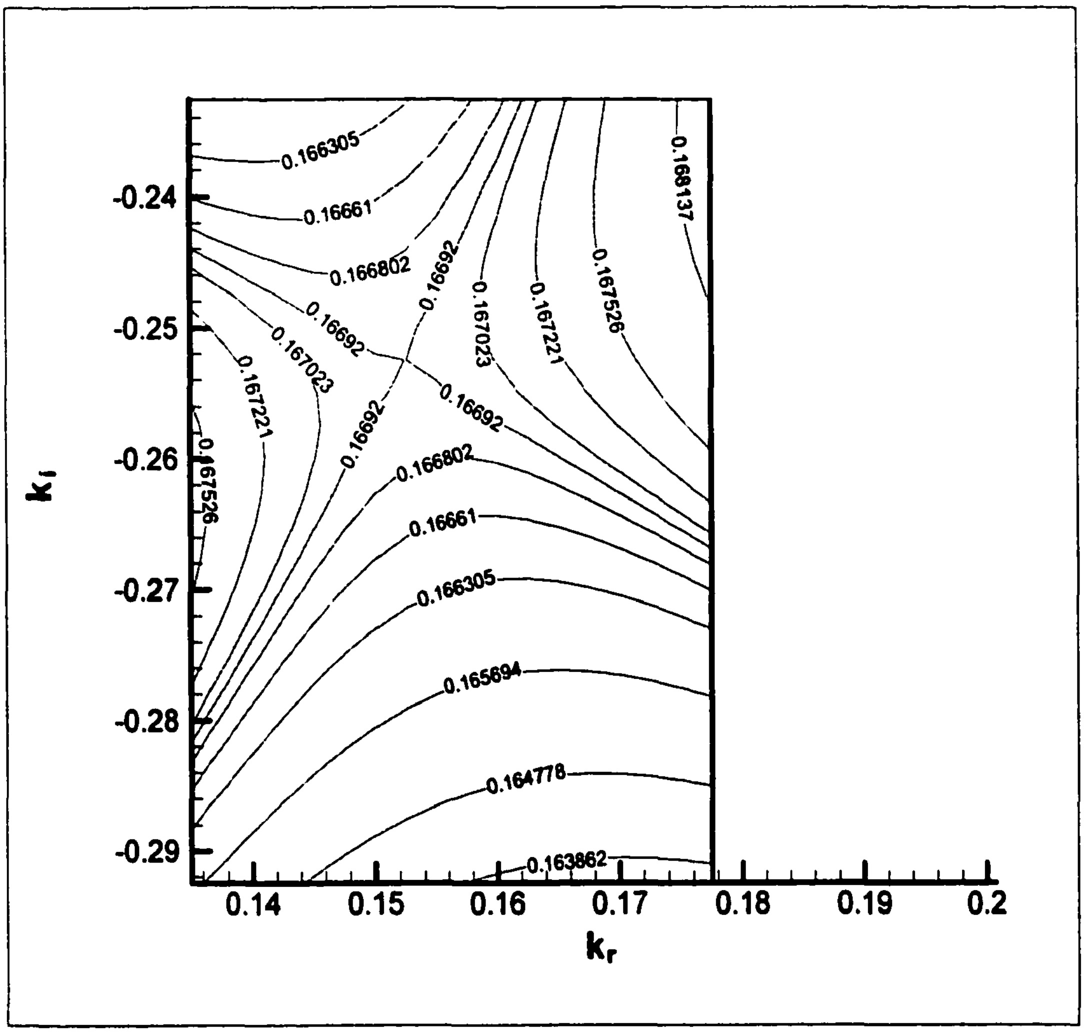

Figure A71: Contour plot of Ω_r for $R/\theta = 5$, $Fr = 5$, $\rho_j/\rho_\infty = 0.99$ in the k-plane illustrating the pinch point formation

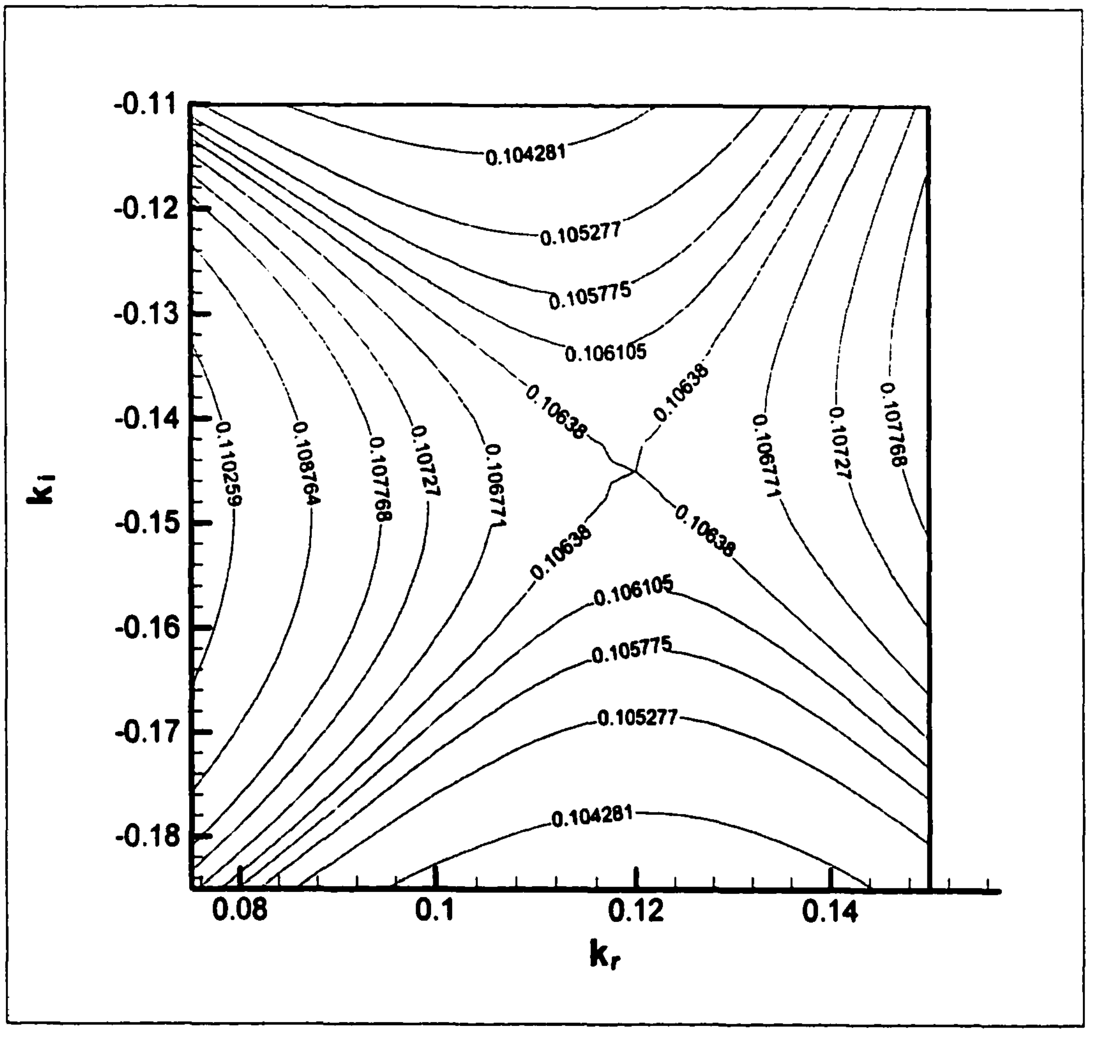

Figure A72: Contour plot of Ω_r for $R/\theta = 5$, $Fr = 2$, $\rho_j/\rho_\infty = 0.14$ in the k-plane illustrating the pinch point formation

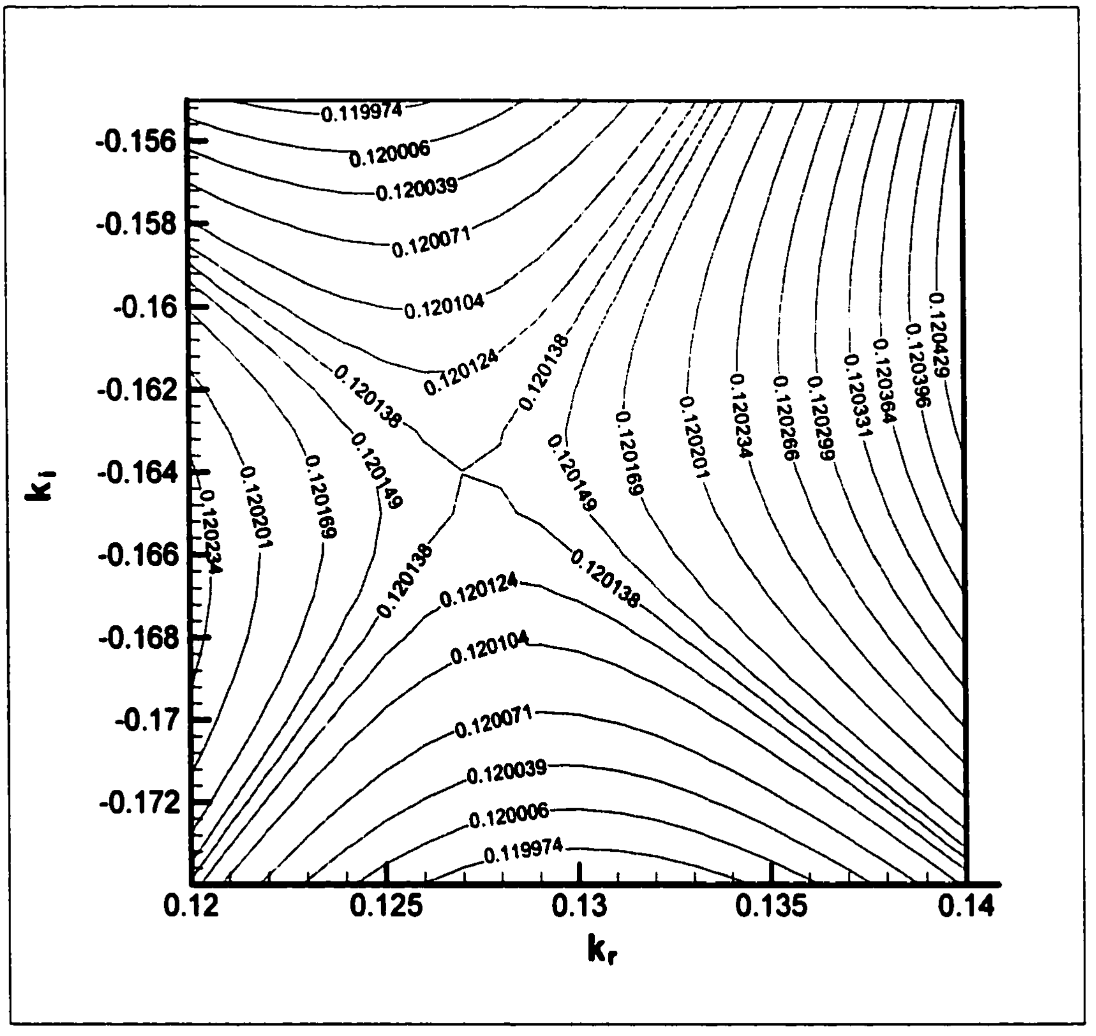

Figure A73: Contour plot of Ω_r for $R/\theta = 5$, $Fr = 2$, $\rho_j/\rho_\infty = 0.22$ in the k-plane illustrating the pinch point formation

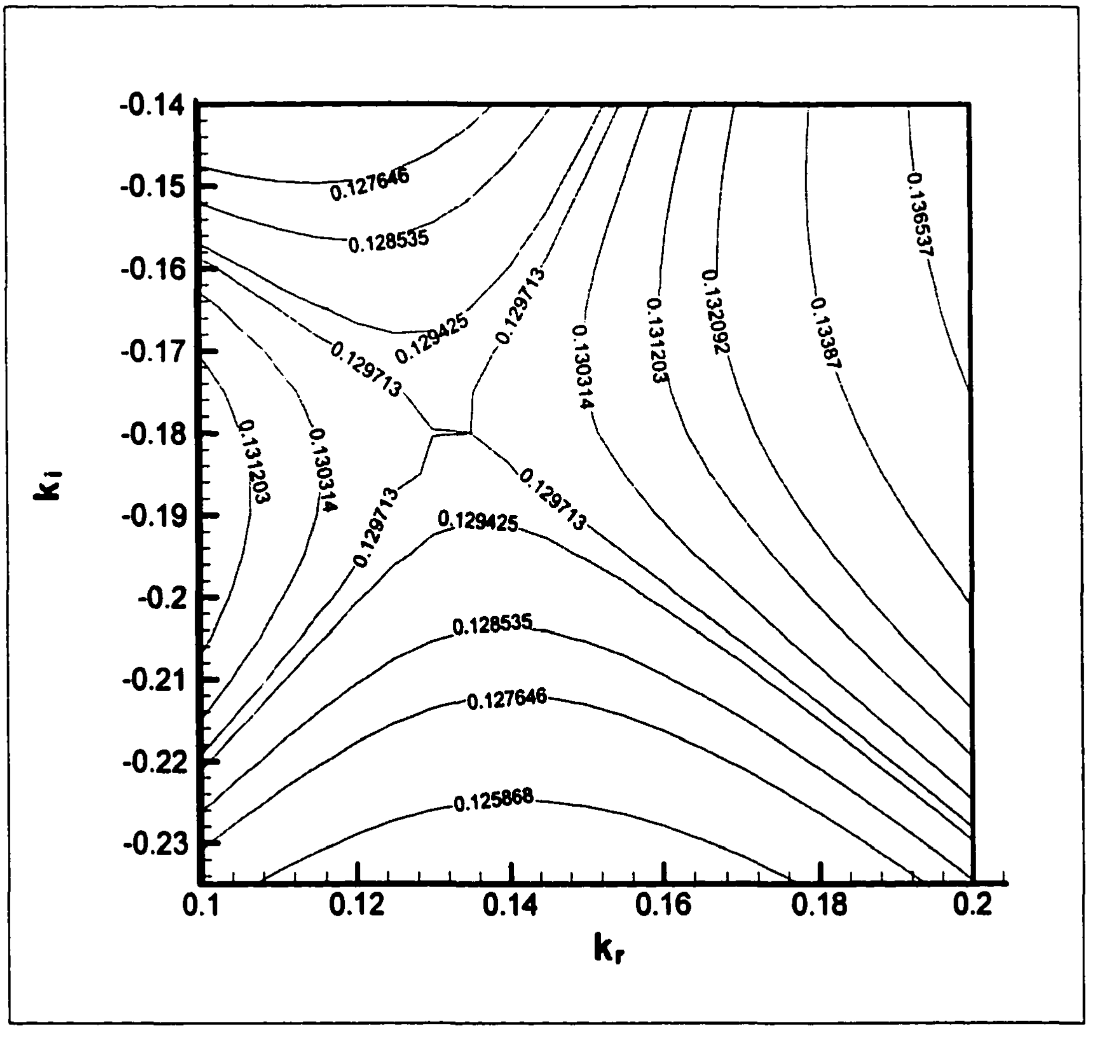

Figure A74: Contour plot of Ω_r for $R/\theta = 5$, $Fr = 2$, $\rho_j/\rho_\infty = 0.3$ in the k-plane illustrating the pinch point formation

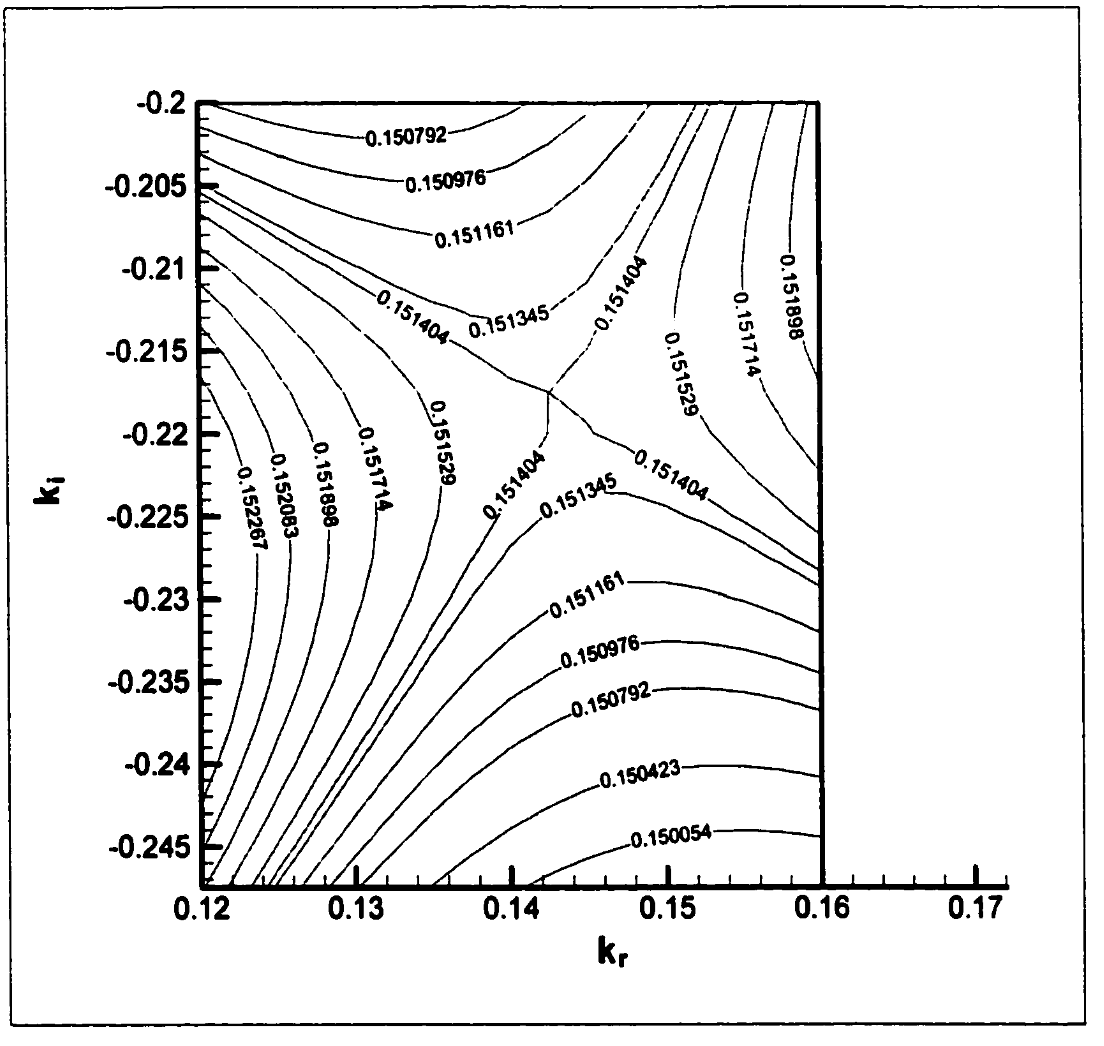

Figure A75: Contour plot of Ω_r for $R/\theta = 5$, $Fr = 2$, $\rho_j/\rho_\infty = 0.6$ in the k-plane illustrating the pinch point formation

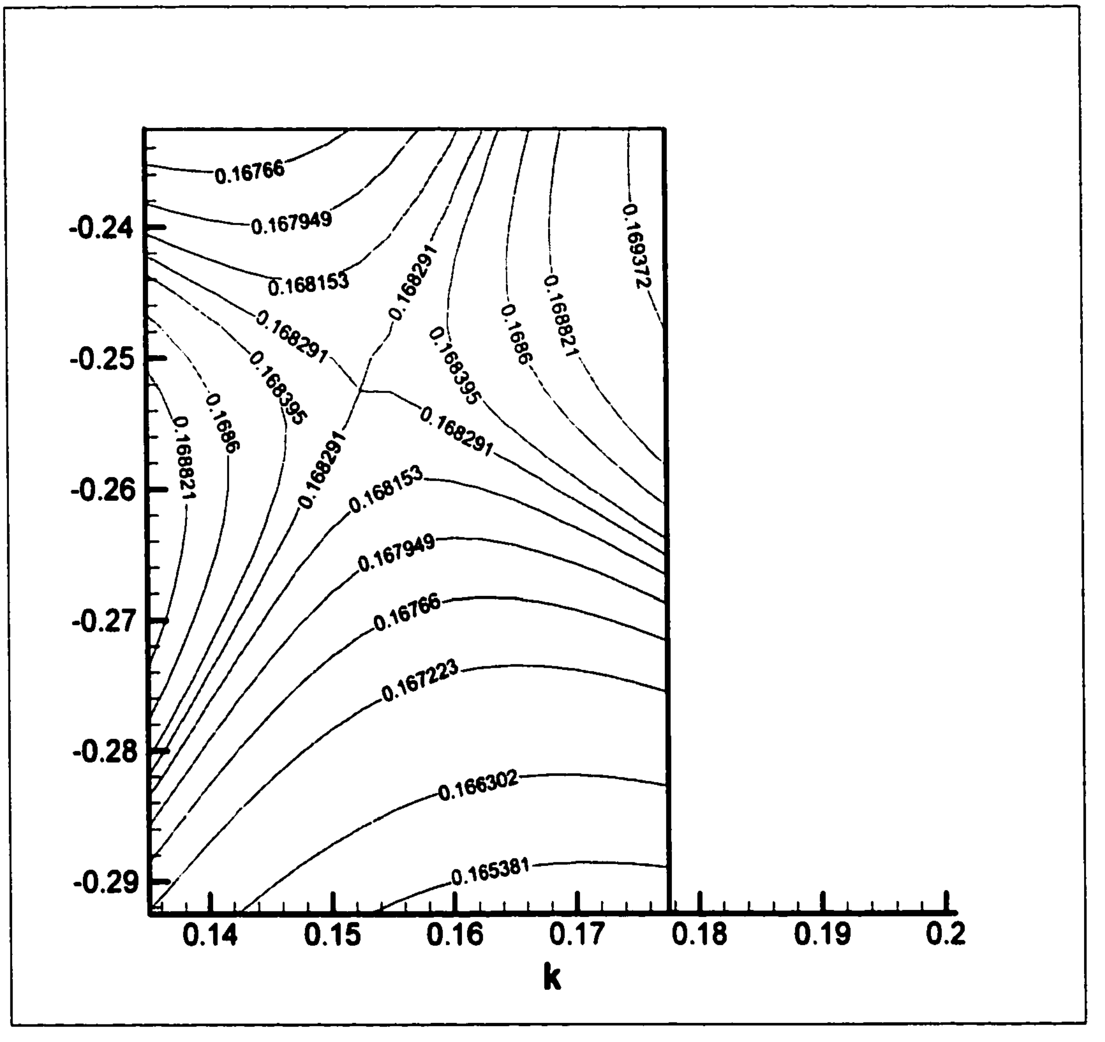

Figure A76: Contour plot of Ω_r for $R/\theta = 5$, $Fr = 2$, $\rho_j/\rho_\infty = 0.99$ in the k-plane illustrating the pinch point formation

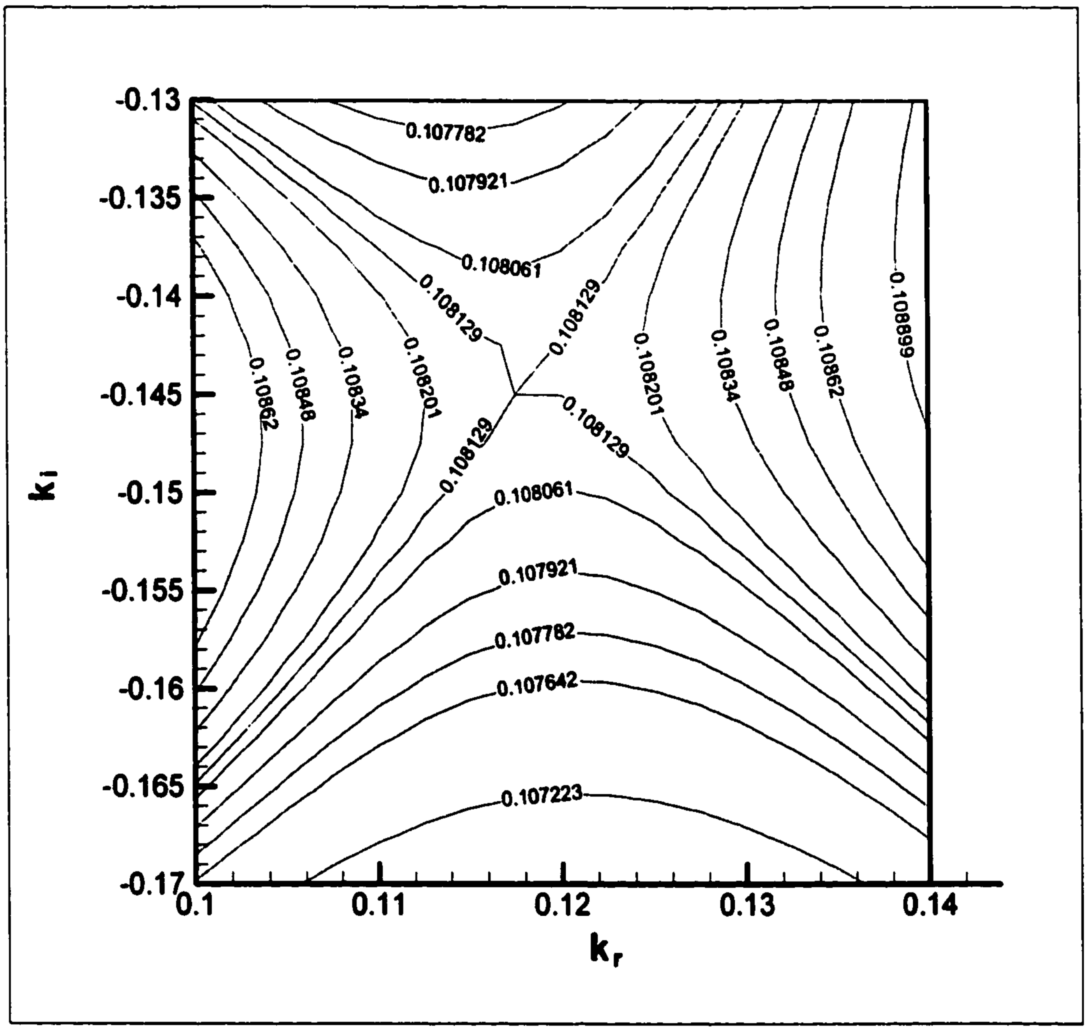

Figure A77: Contour plot of Ω_r for $R/\theta = 5$, $Fr = 1.58$, $\rho_j/\rho_\infty = 0.14$ in the k-plane illustrating the pinch point formation

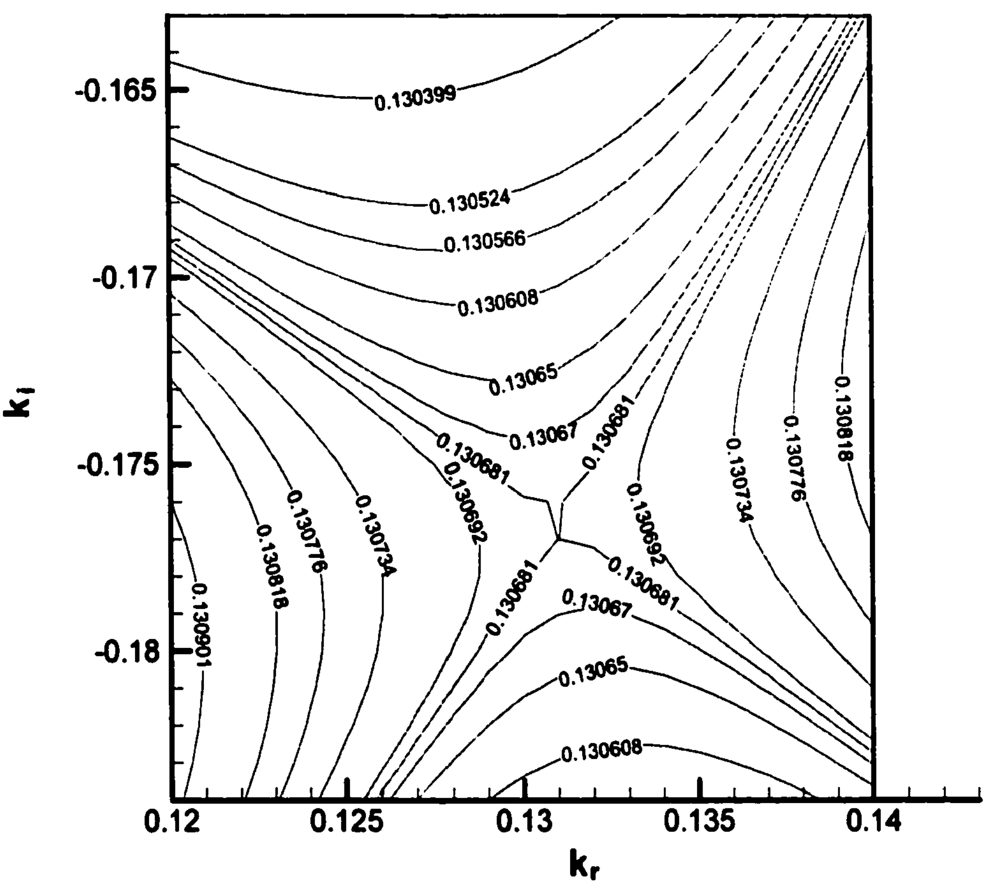

Figure A78: Contour plot of Ω_r for $R/\theta = 5$, $Fr = 1.58$, $\rho_j/\rho_\infty = 0.286$ in the k-plane illustrating the pinch point formation

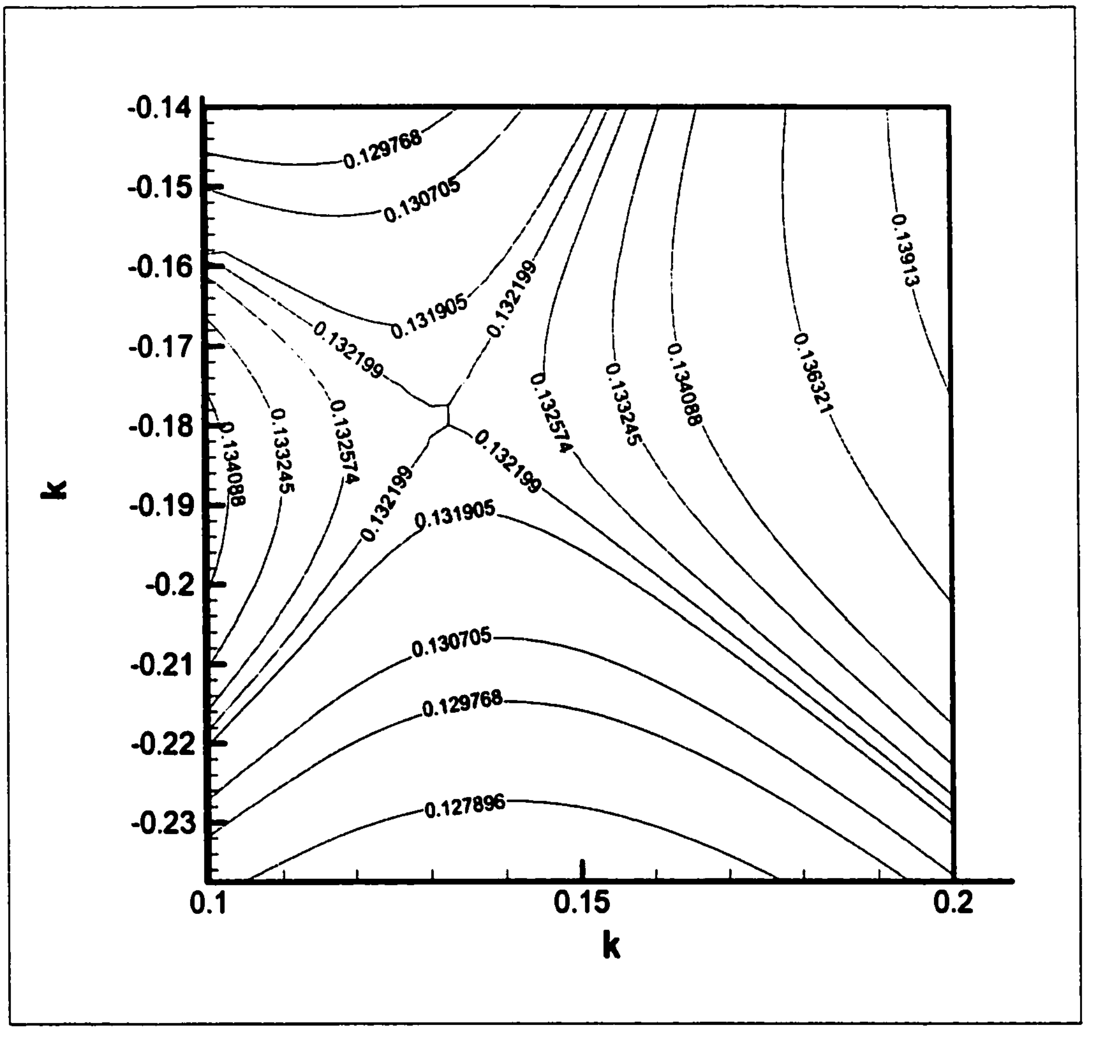

Figure A79: Contour plot of Ω_r for $R/\theta = 5$, $Fr = 1.58$, $\rho_j/\rho_\infty = 0.3$ in the k-plane illustrating the pinch point formation

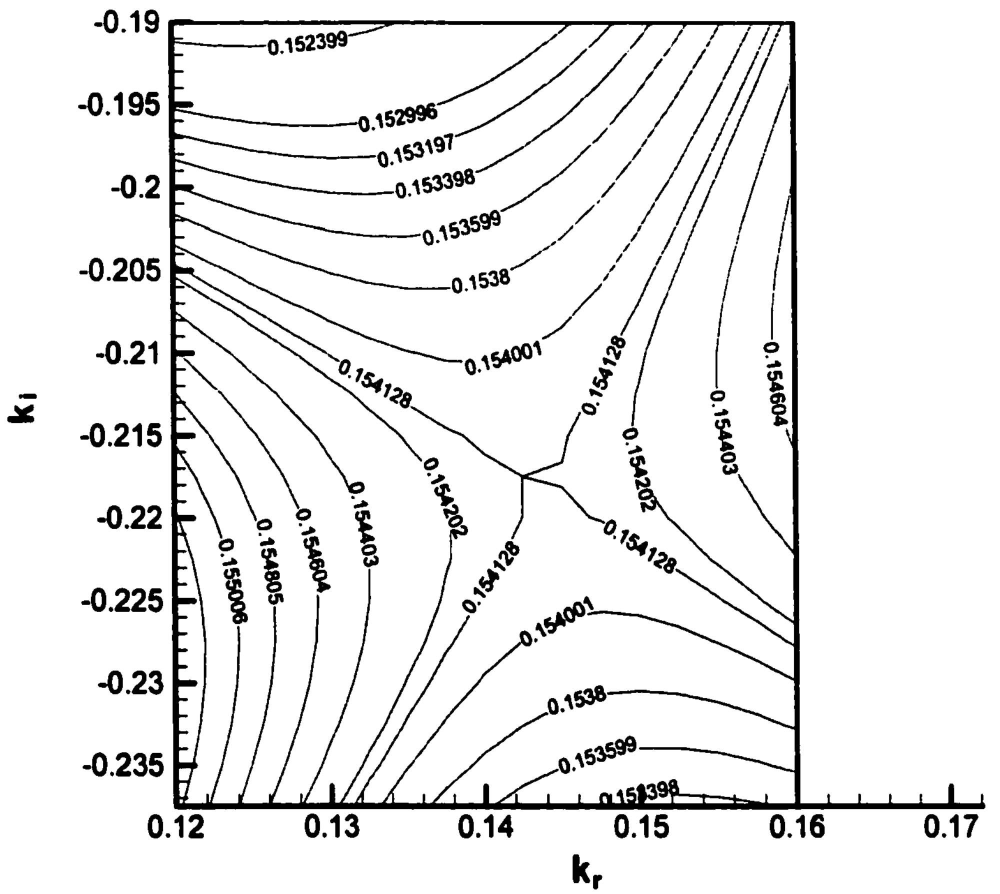

Figure A80: Contour plot of Ω_r for $R/\theta = 5$, $Fr = 1.58$, $\rho_j/\rho_\infty = 0.6$ in the k-plane illustrating the pinch point formation

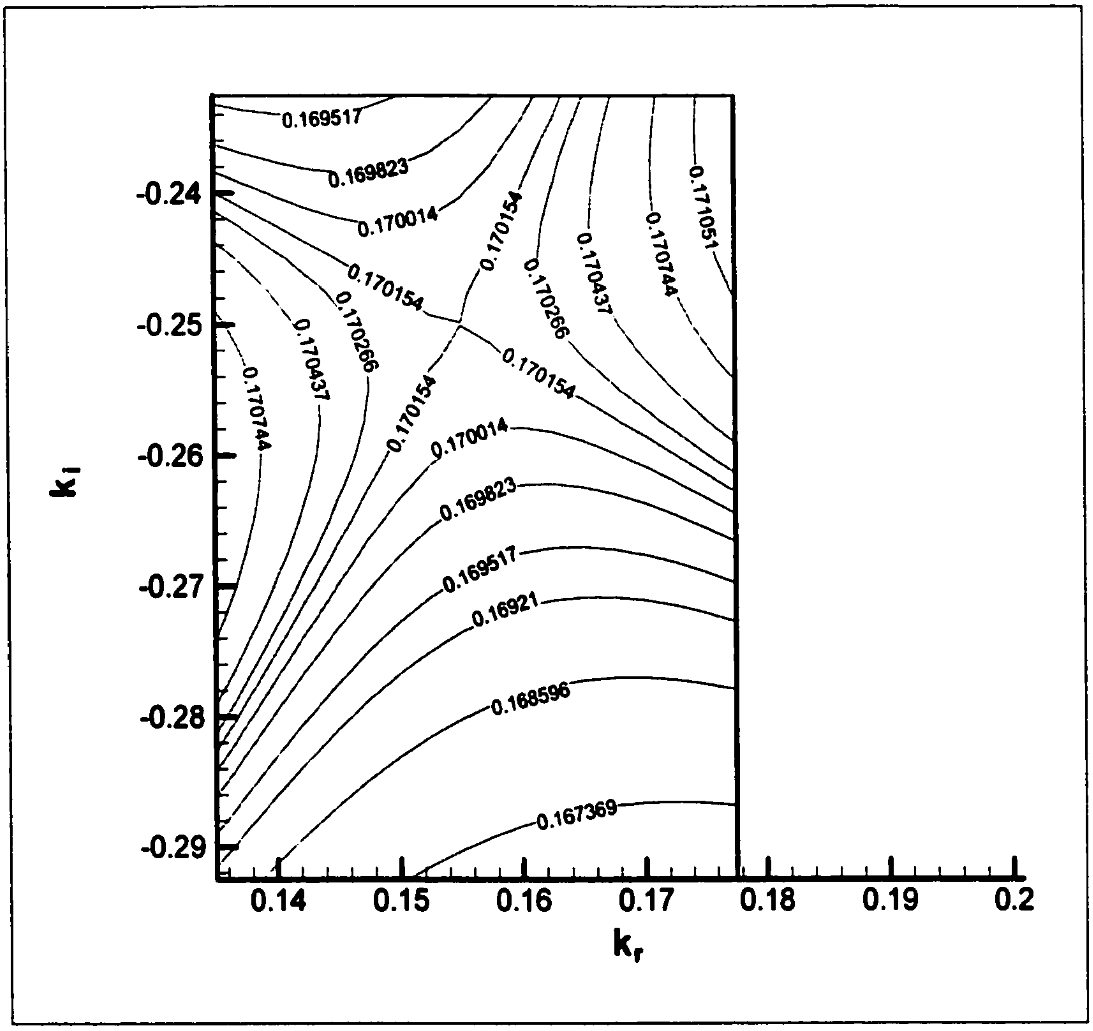

Figure A81: Contour plot of Ω_r for $R/\theta = 5$, $Fr = 1.58$, $\rho_j/\rho_\infty = 0.99$ in the k-plane illustrating the pinch point formation

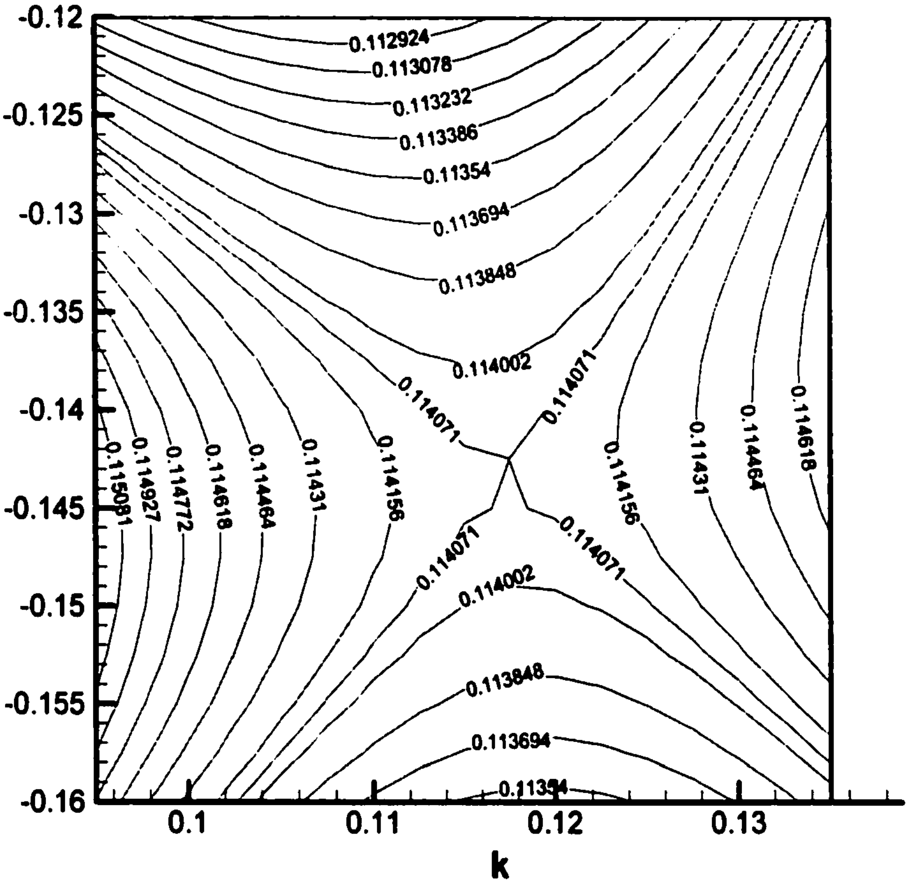

Figure A82: Contour plot of Ω_r for $R/\theta = 5$, $Fr = 1.015$, $\rho_j/\rho_\infty = 0.14$ in the k-plane illustrating the pinch point formation

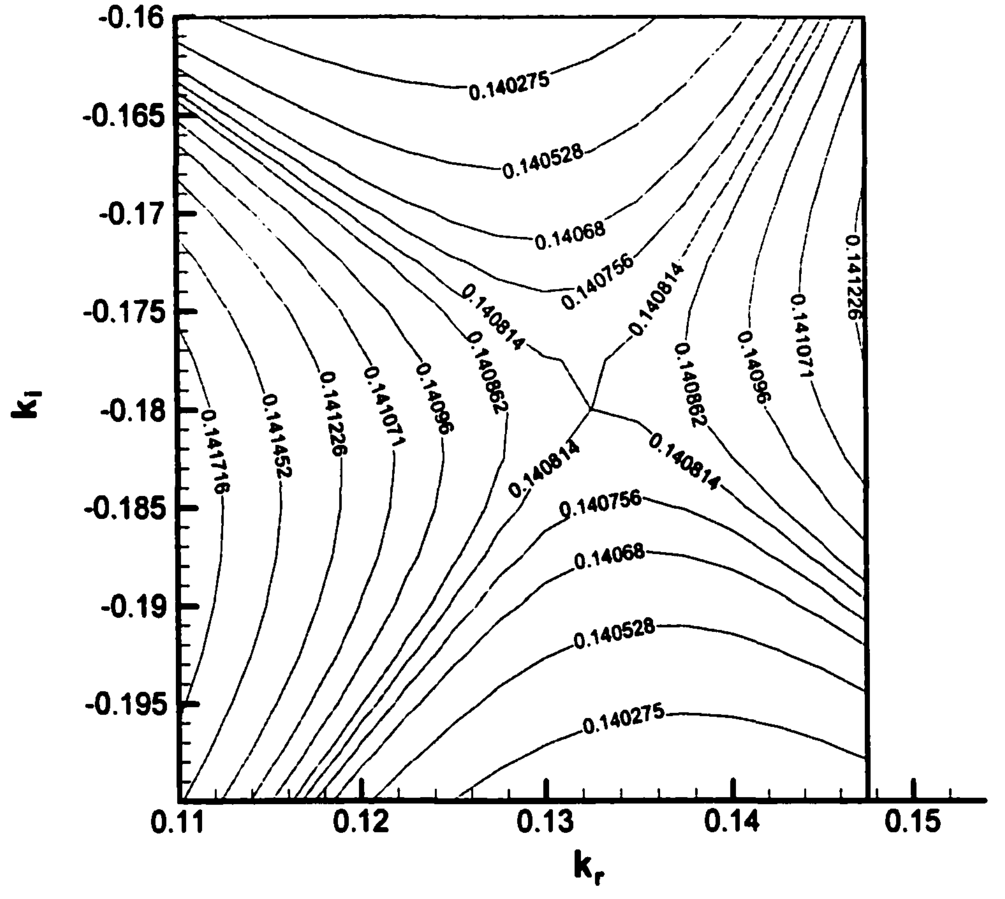

Figure A83: Contour plot of Ω_r for $R/\theta = 5$, $Fr = 1.015$, $\rho_j/\rho_\infty = 0.3$ in the k-plane illustrating the pinch point formation

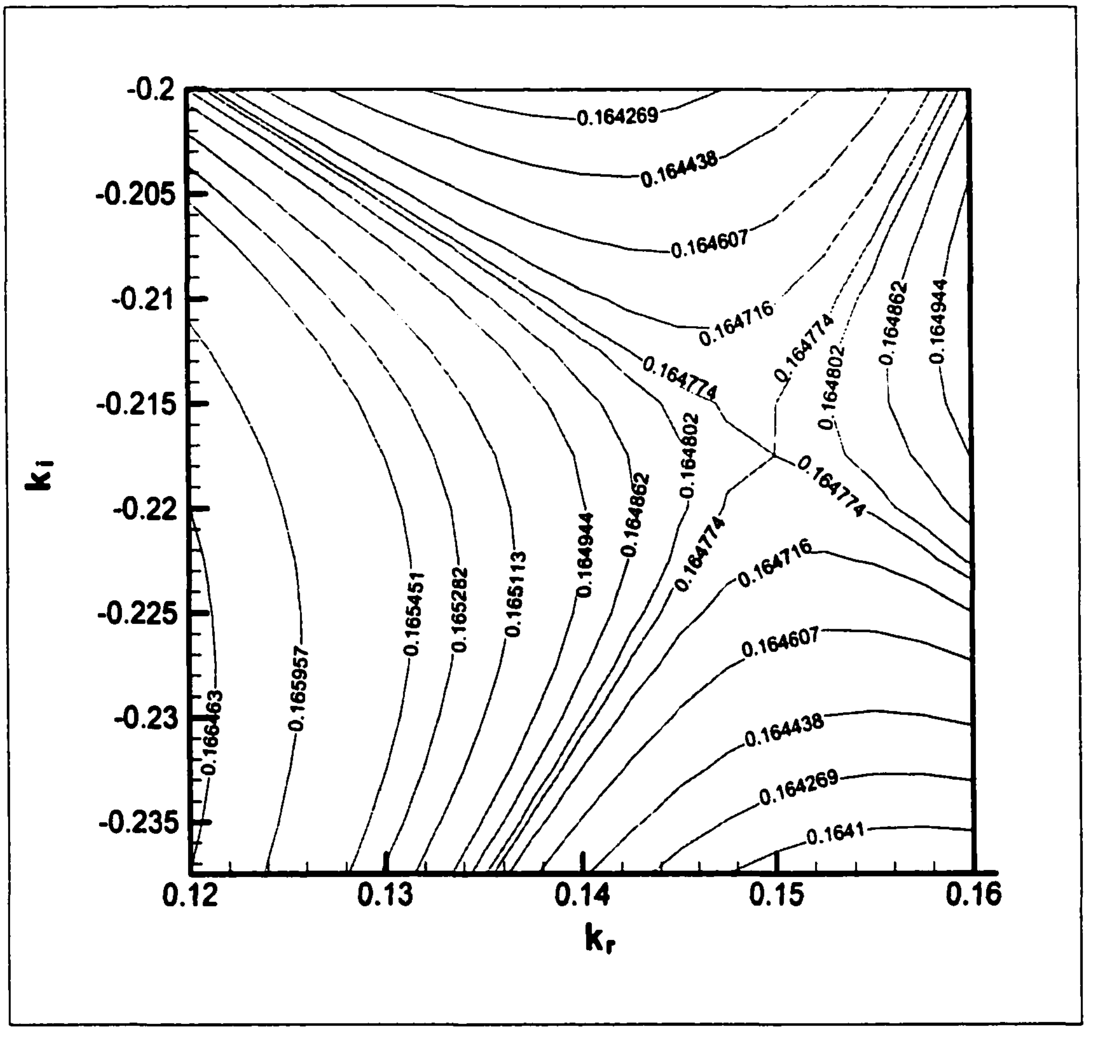

Figure A84: Contour plot of Ω_r for $R/\theta = 5$, $Fr = 1.015$, $\rho_j/\rho_\infty = 0.6$ in the k-plane illustrating the pinch point formation

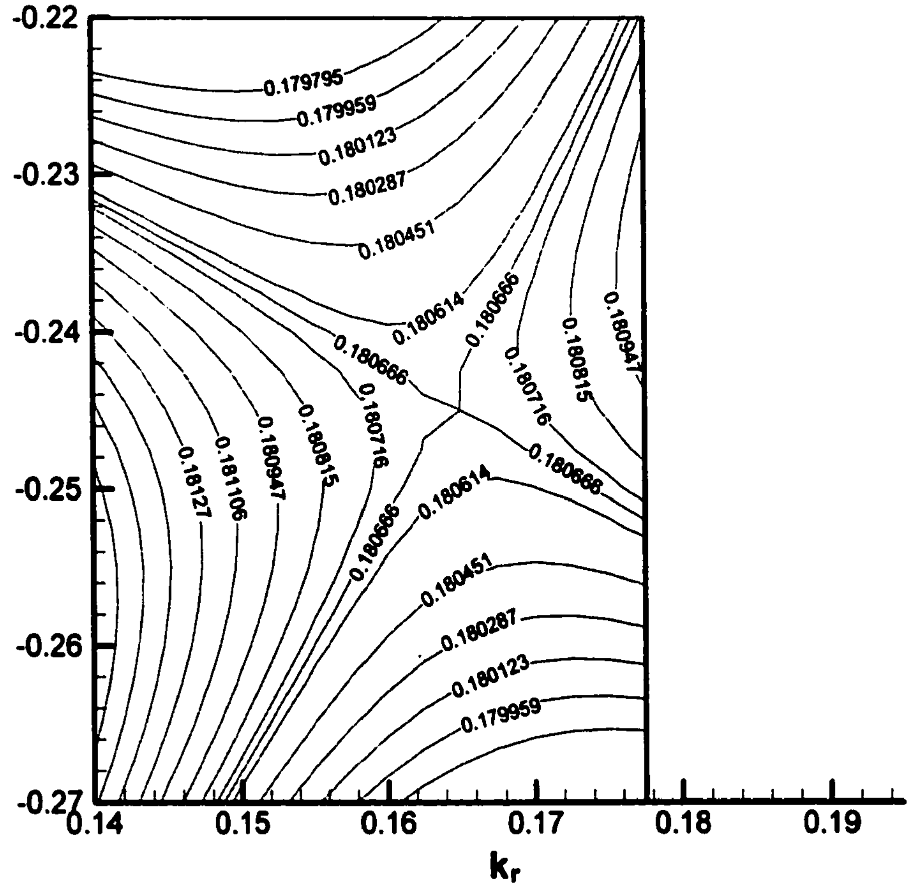

Figure A85: Contour plot of Ω_r for $R/\theta = 5$, $Fr = 1.015$, $\rho_j/\rho_\infty = 0.99$ in the k-plane illustrating the pinch point formation

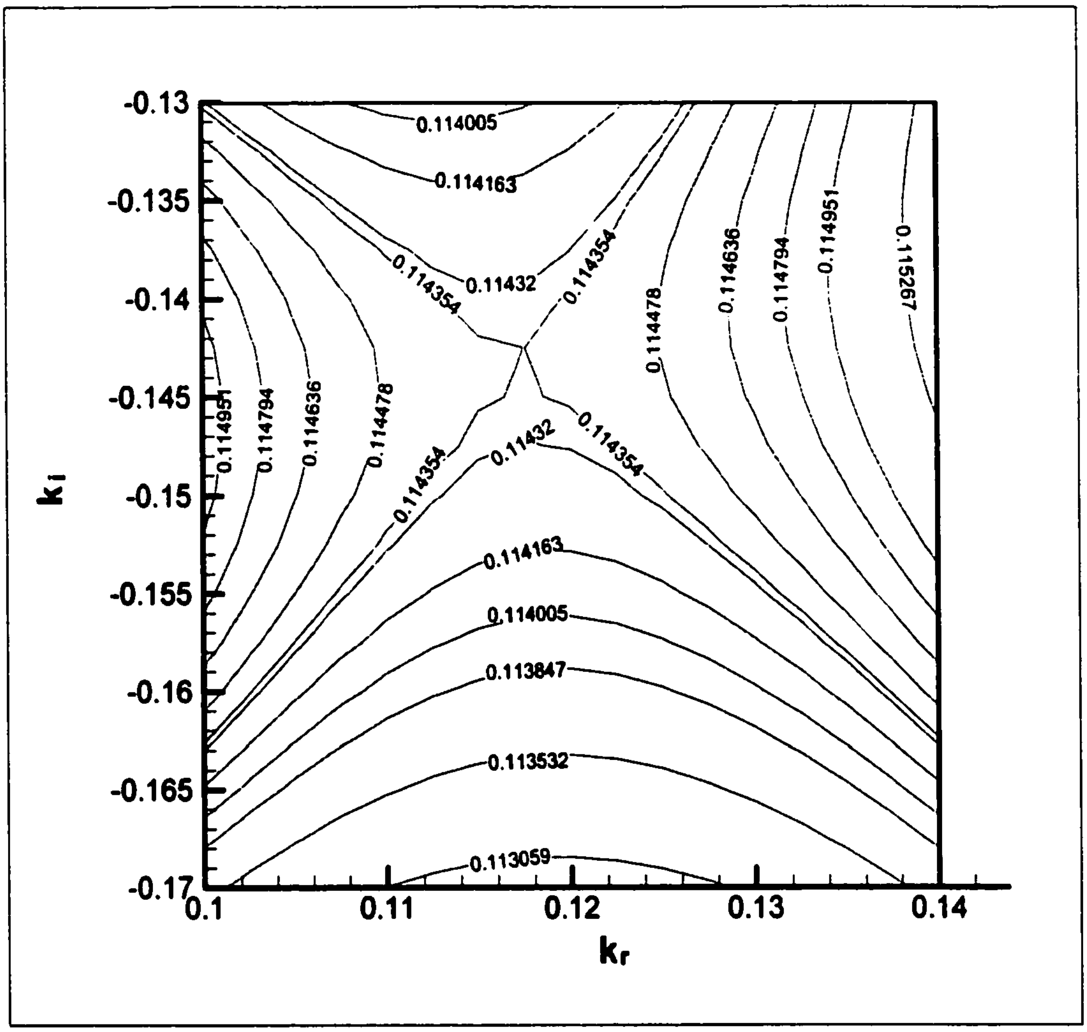

Figure A86: Contour plot of Ω_r for $R/\theta = 5$, $Fr = 1$, $\rho_j/\rho_\infty = 0.14$ in the k-plane illustrating the pinch point formation

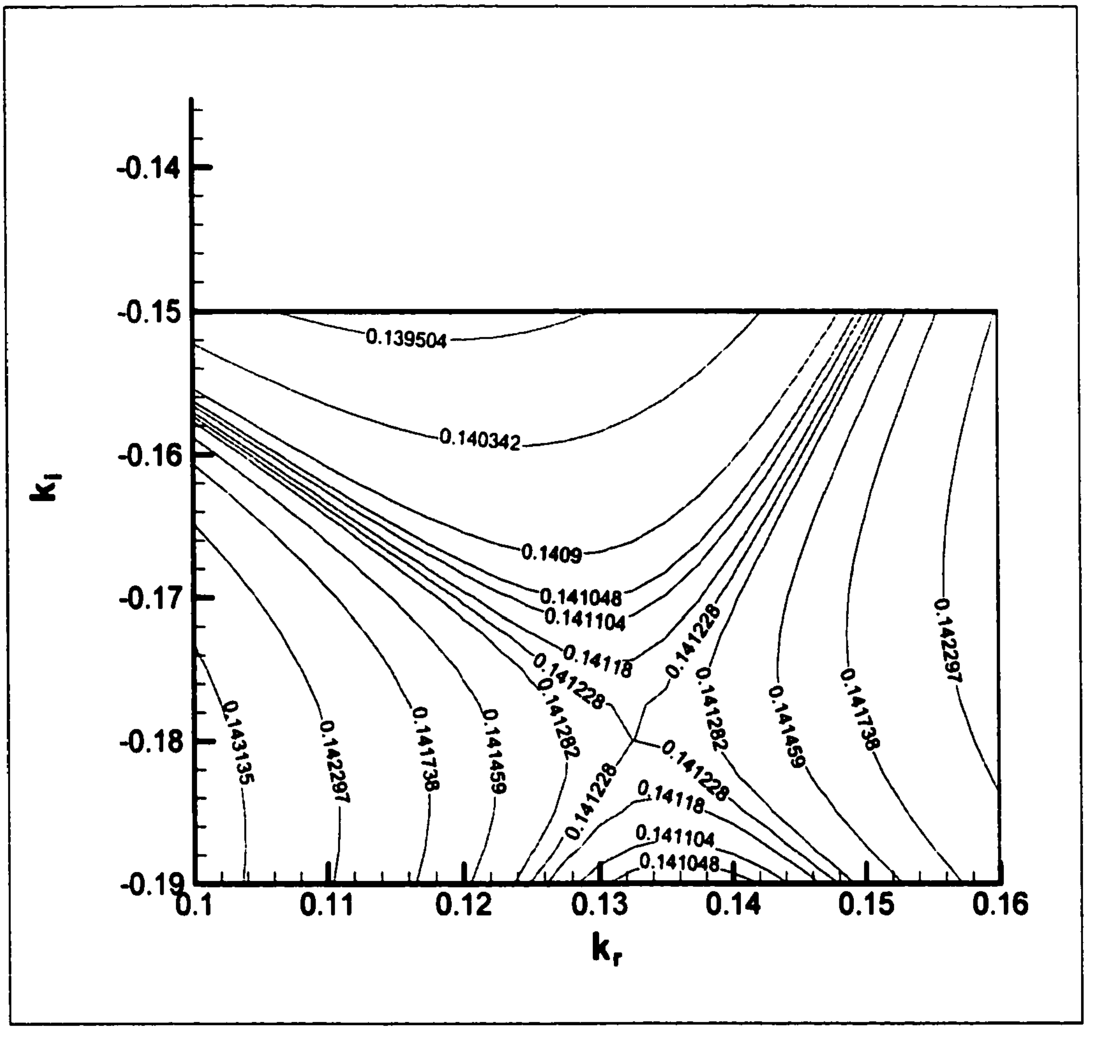

Figure A87: Contour plot of Ω_r for $R/\theta = 5$, $Fr = 1$, $\rho_j/\rho_\infty = 0.3$ in the k-plane illustrating the pinch point formation

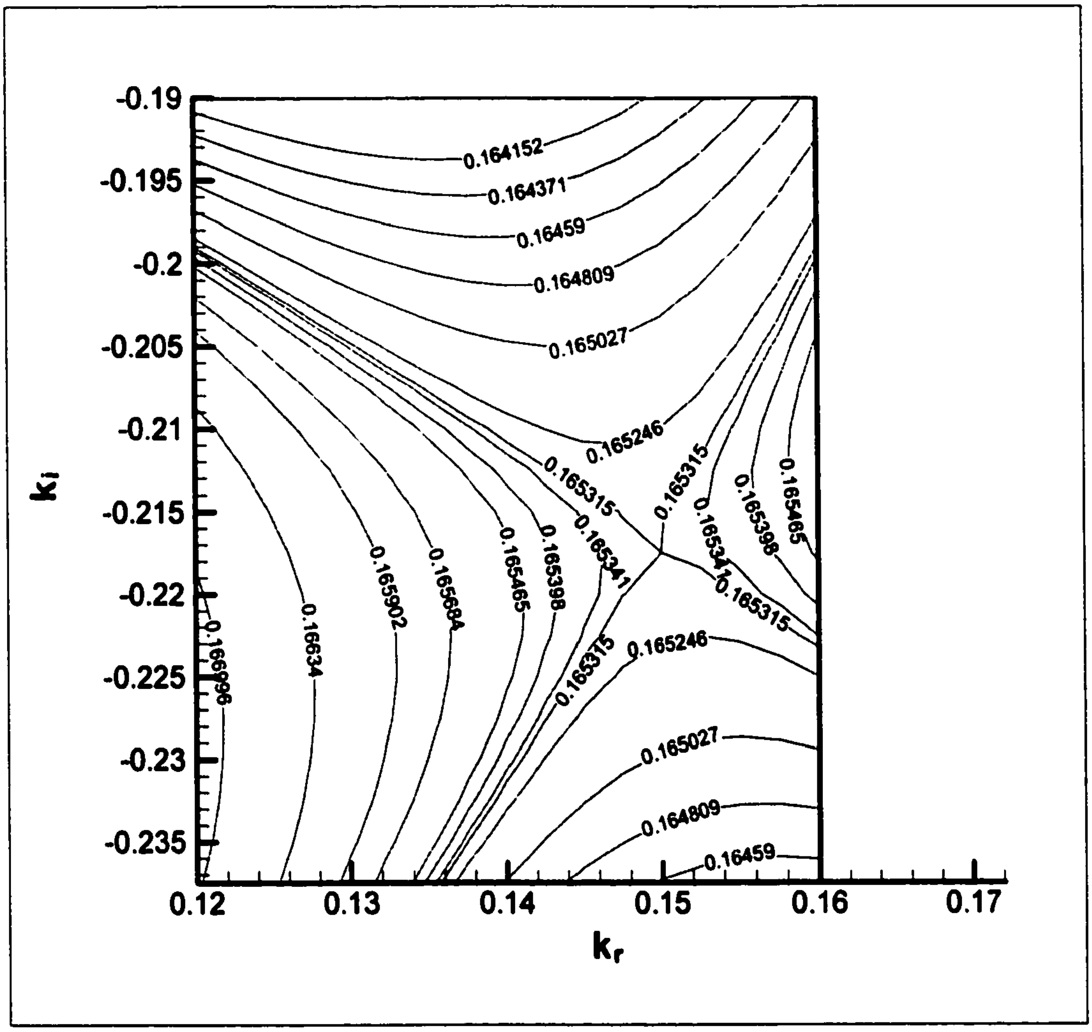

Figure A88: Contour plot of Ω_r for $R/\theta = 5$, $Fr = 1$, $\rho_j/\rho_\infty = 0.6$ in the k-plane illustrating the pinch point formation

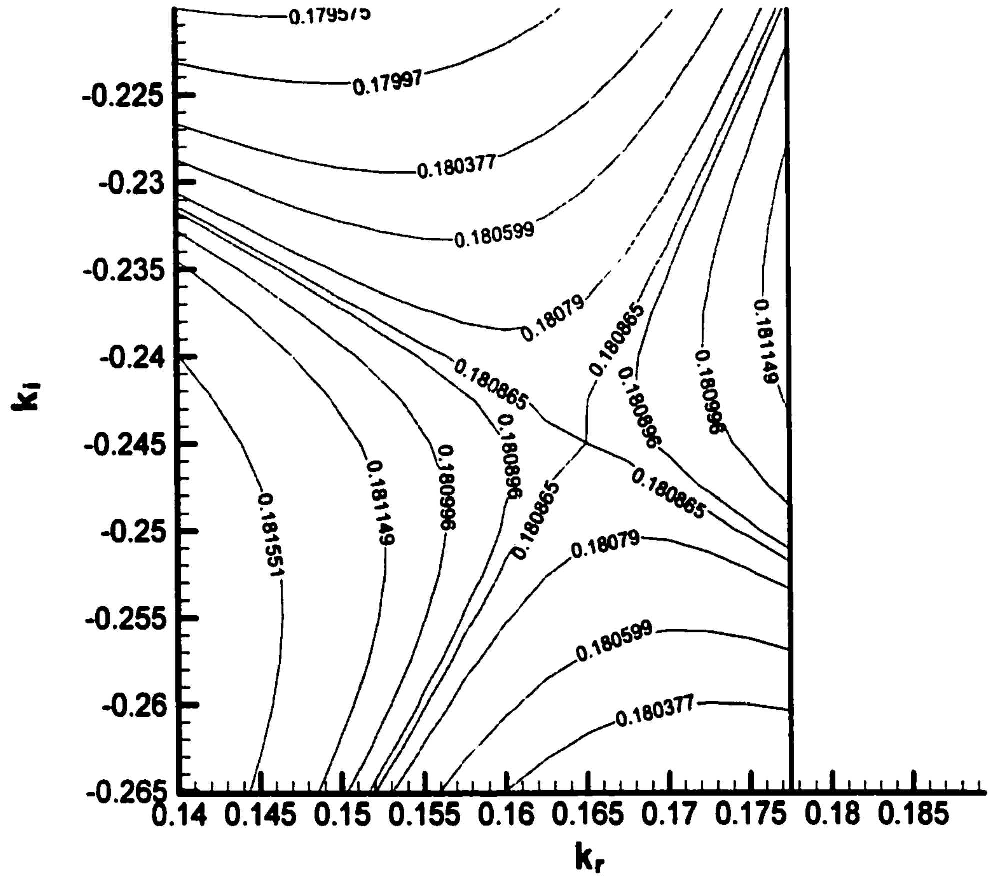

Figure A89: Contour plot of Ω_r for $R/\theta = 5$, $Fr = 1$, $\rho_j/\rho_\infty = 0.99$ in the k-plane illustrating the pinch point formation

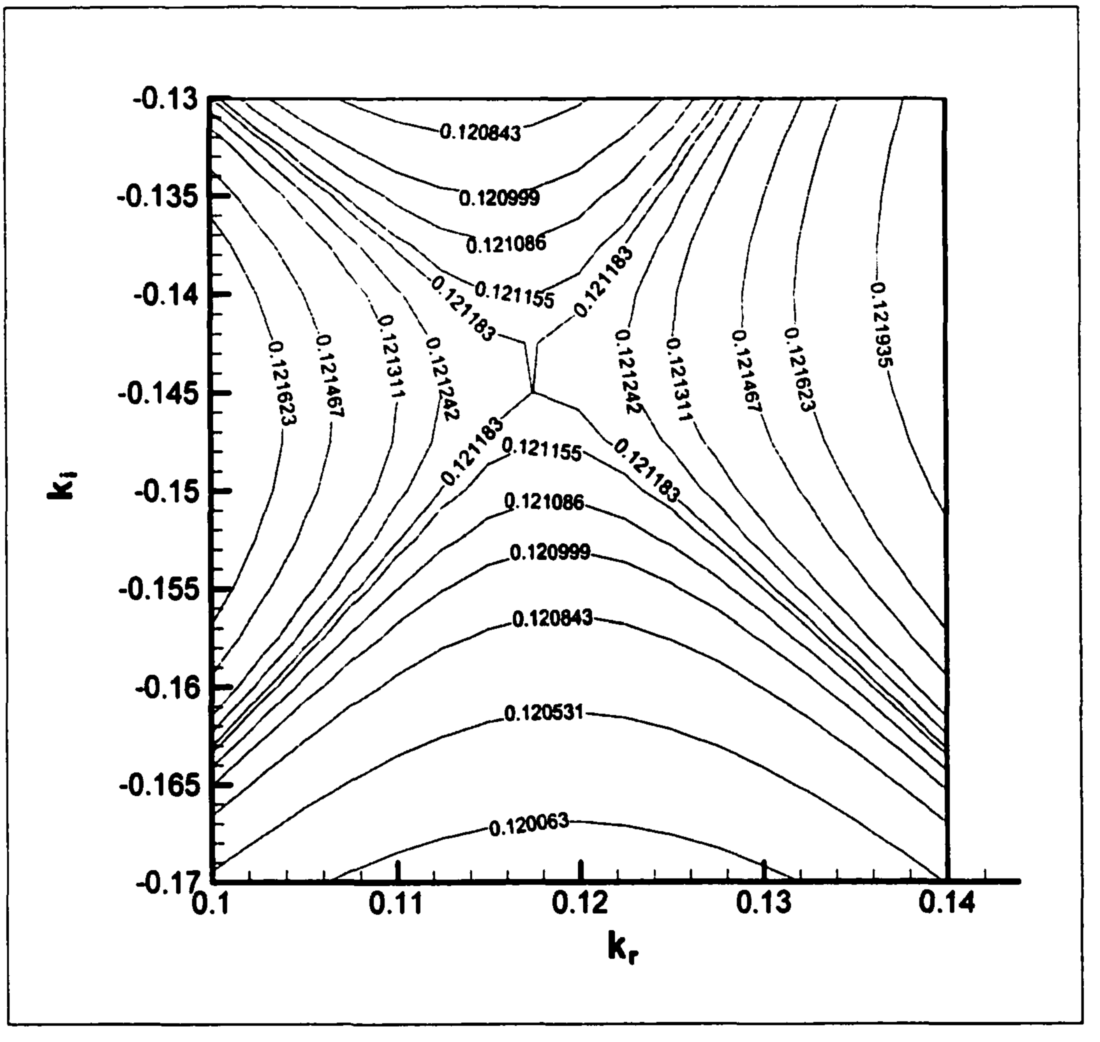

Figure A90: Contour plot of Ω_r for $R/\theta = 5$, $Fr = 0.75$, $\rho_j/\rho_\infty = 0.14$ in the k-plane illustrating the pinch point formation

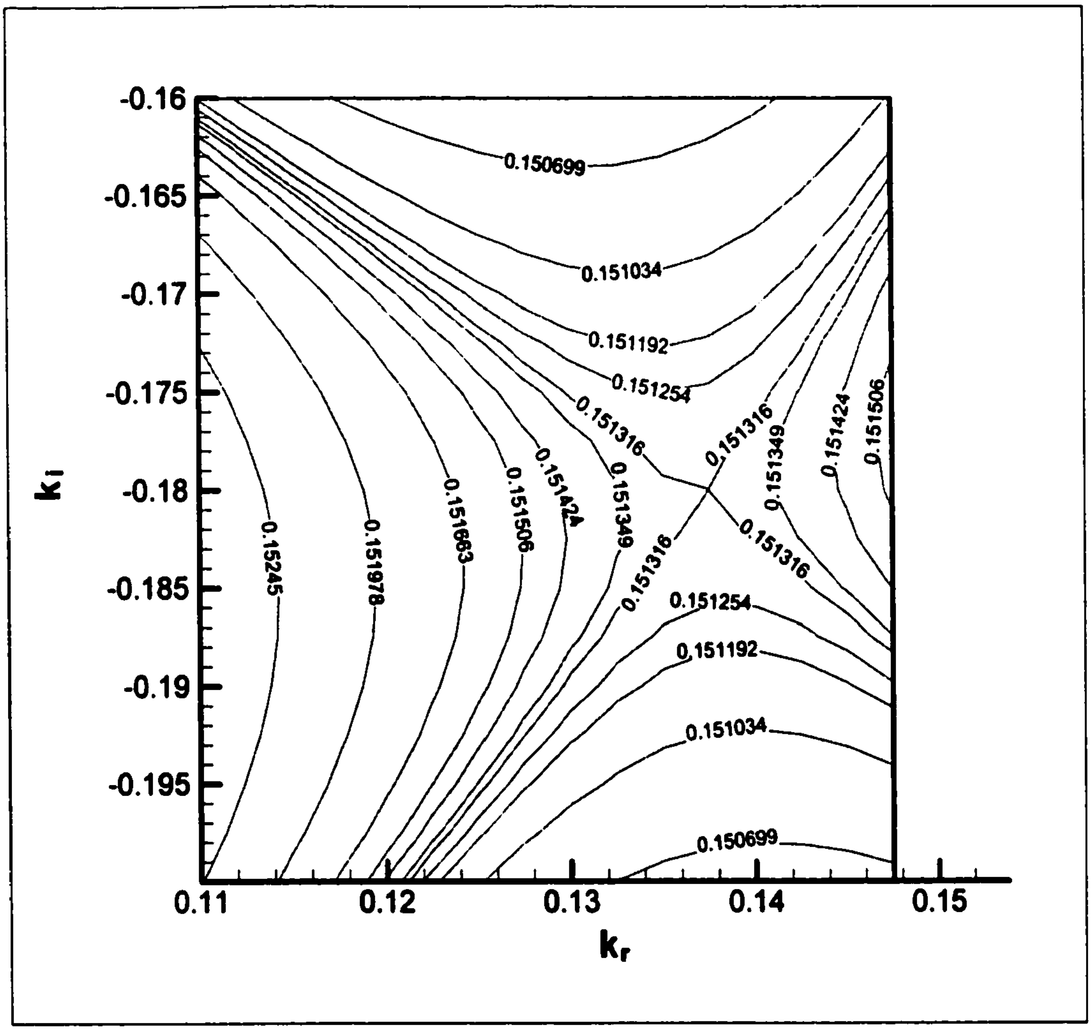

Figure A91: Contour plot of Ω_r for $R/\theta = 5$, $Fr = 0.75$, $\rho_j/\rho_\infty = 0.3$ in the k-plane illustrating the pinch point formation

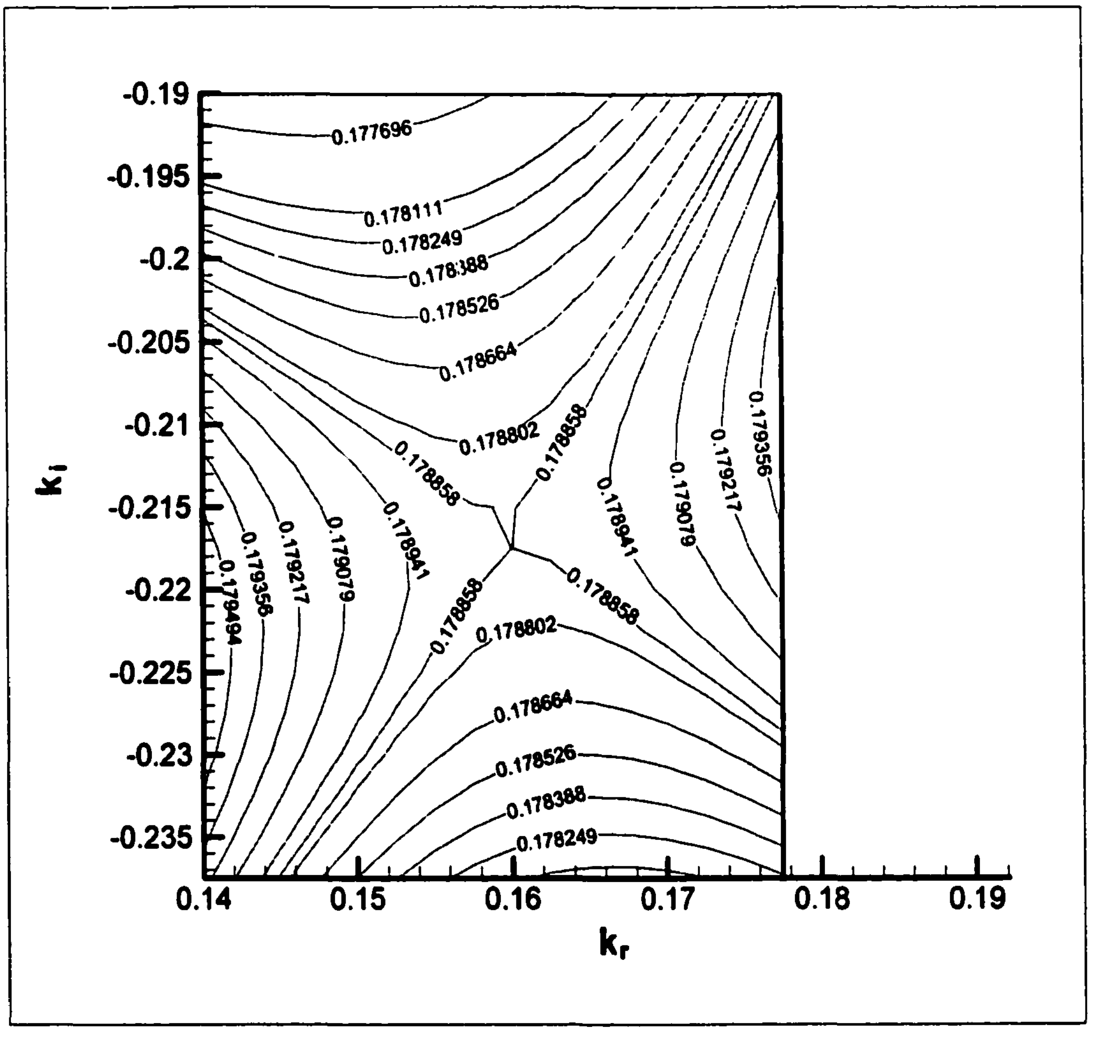

Figure A92: Contour plot of Ω_r for $R/\theta = 5$, $Fr = 0.75$, $\rho_j/\rho_\infty = 0.6$ in the k-plane illustrating the pinch point formation

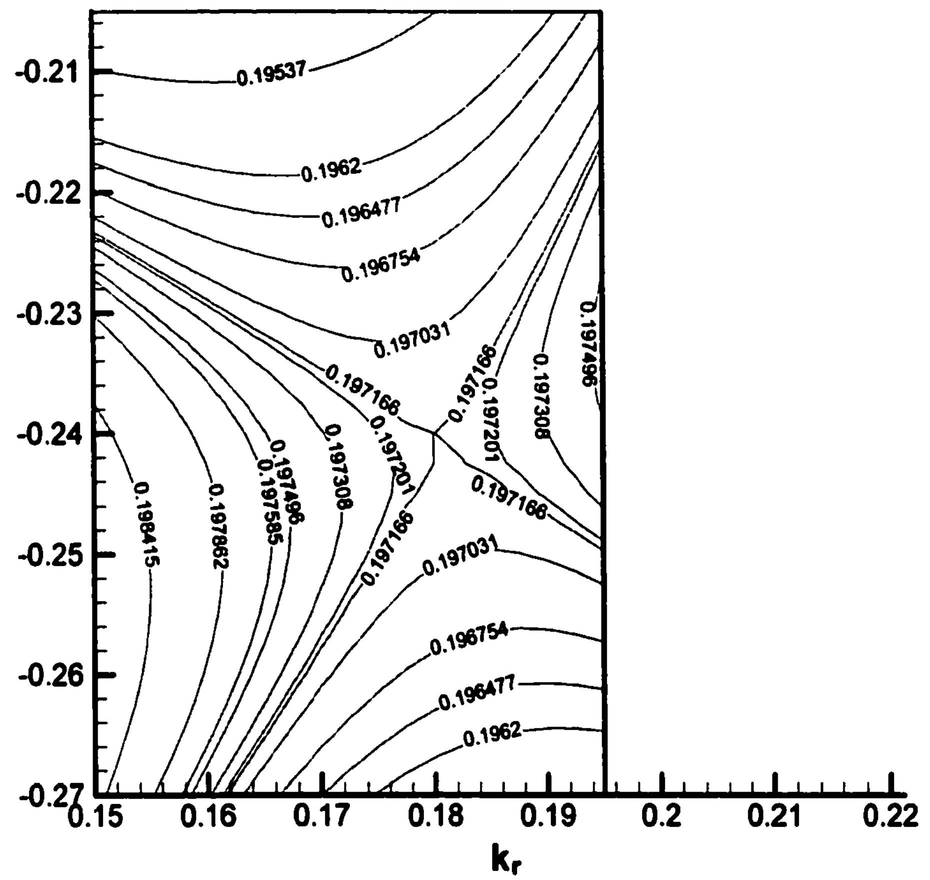

Figure A93: Contour plot of Ω_r for $R/\theta = 5$, $Fr = 0.75$, $\rho_j/\rho_\infty = 0.99$ in the k-plane illustrating the pinch point formation

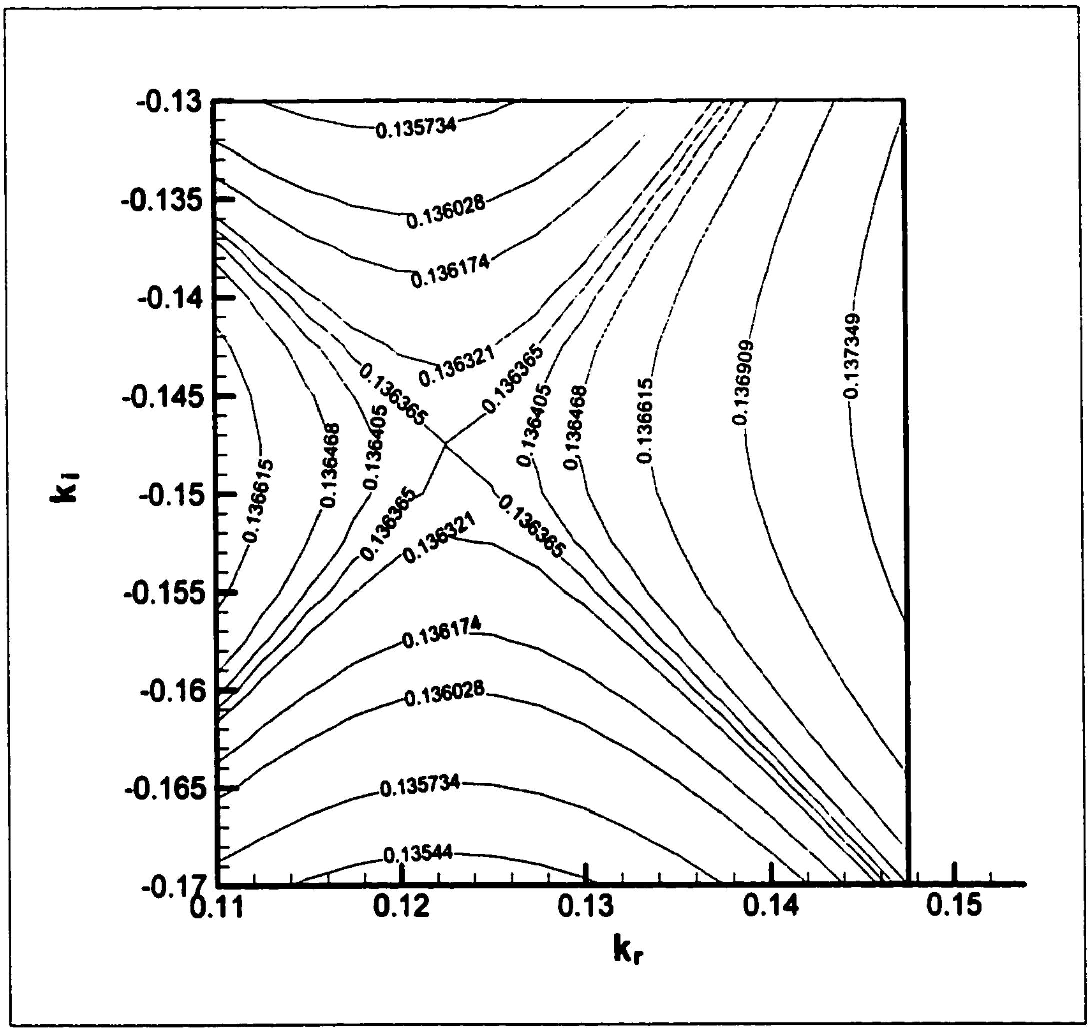

Figure A94: Contour plot of Ω_r for $R/\theta = 5$, $Fr = 0.5$, $\rho_j/\rho_\infty = 0.14$ in the k-plane illustrating the pinch point formation

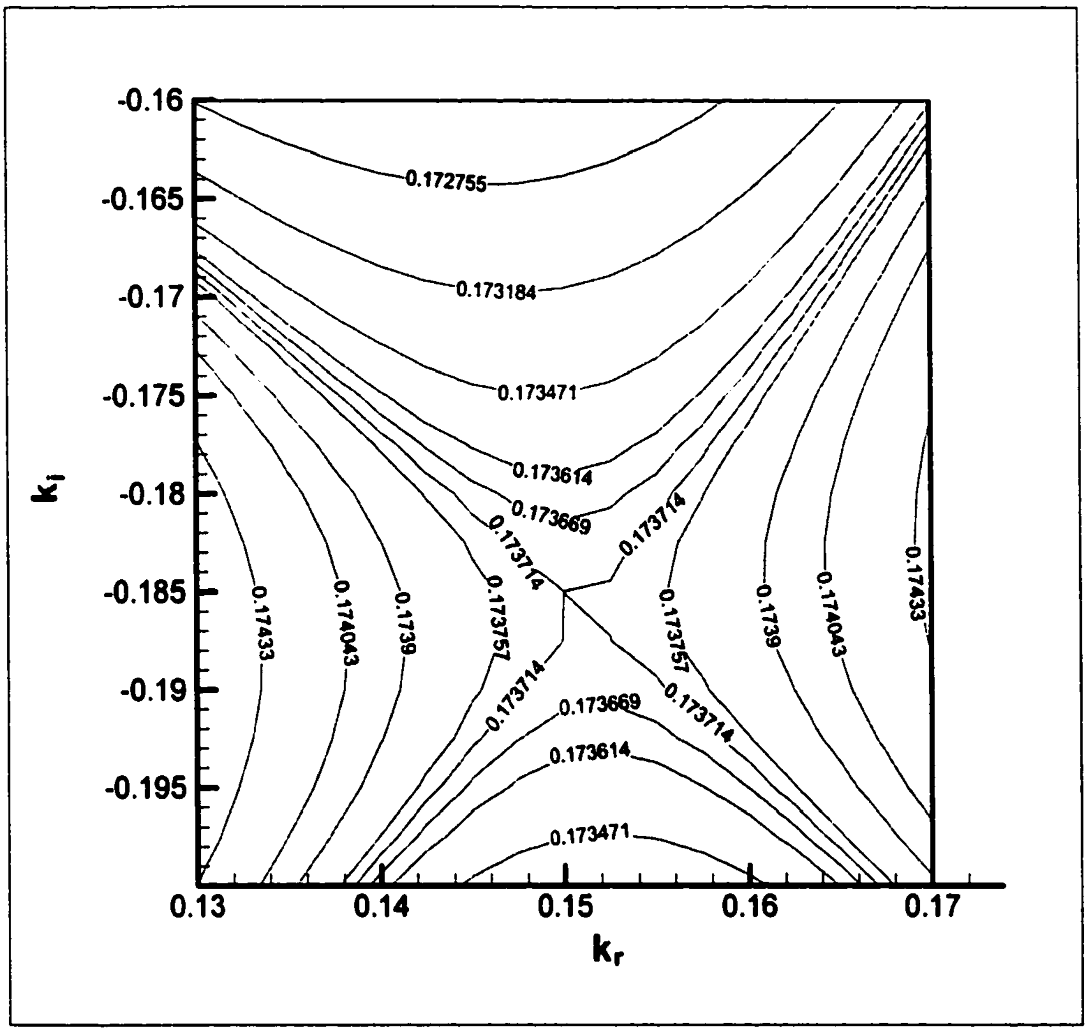

Figure A95: Contour plot of Ω_r for $R/\theta = 5$, $Fr = 0.5$, $\rho_j/\rho_\infty = 0.3$ in the k-plane illustrating the pinch point formation

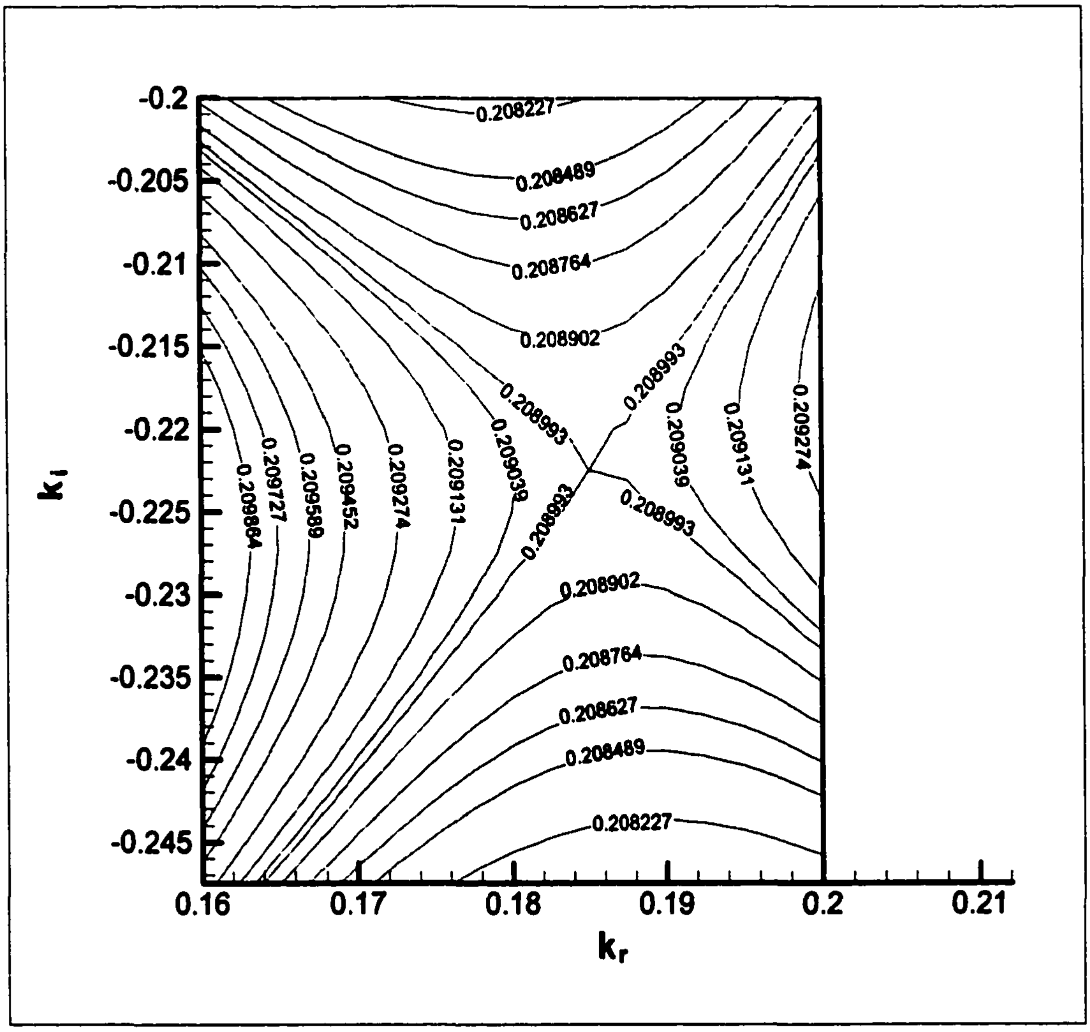

Figure A96: Contour plot of Ω_r for $R/\theta = 5$, $Fr = 0.5$, $\rho_j/\rho_\infty = 0.6$ in the k-plane illustrating the pinch point formation

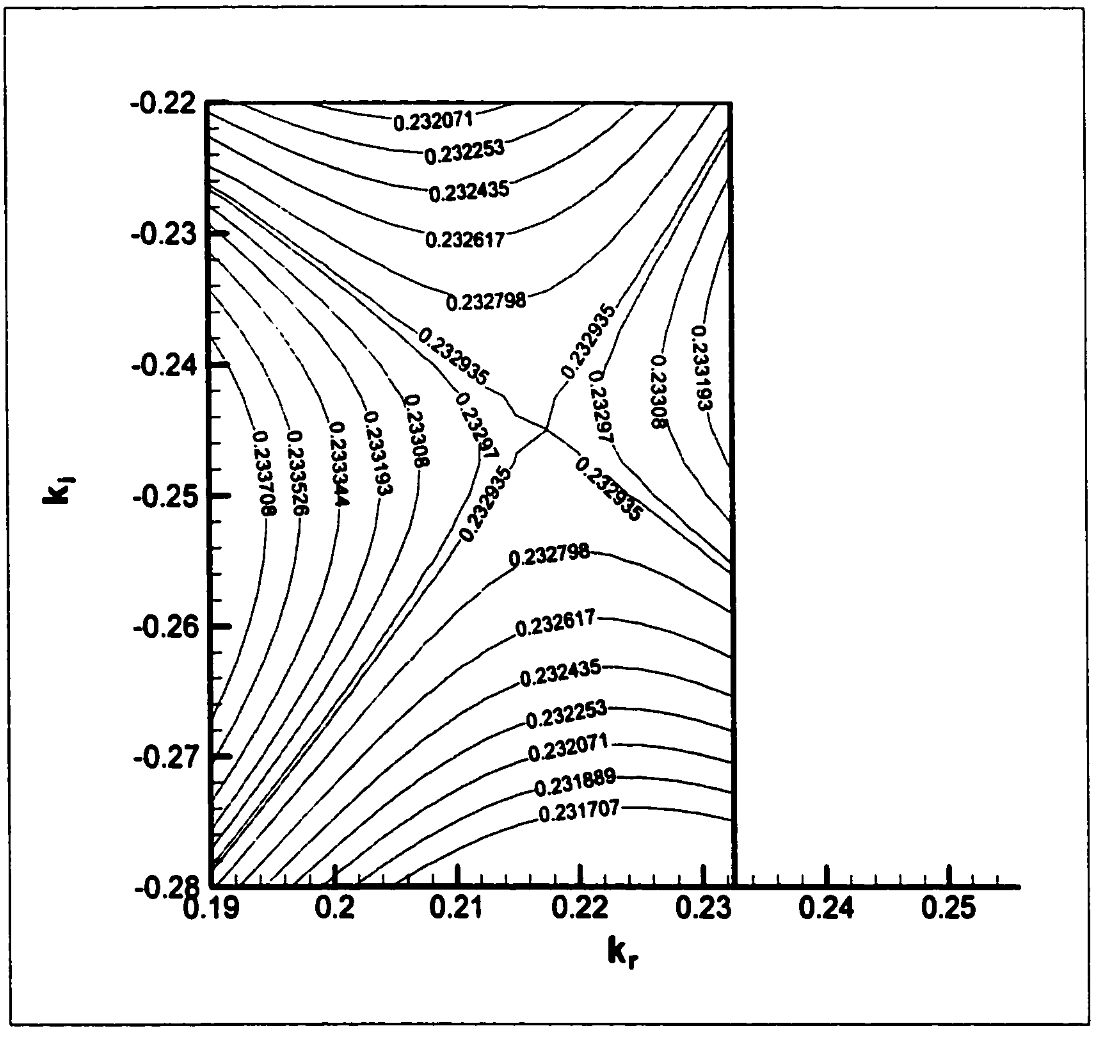

Figure A97: Contour plot of Ω_r for $R/\theta = 5$, $Fr = 0.5$, $\rho_j/\rho_\infty = 0.99$ in the k-plane illustrating the pinch point formation

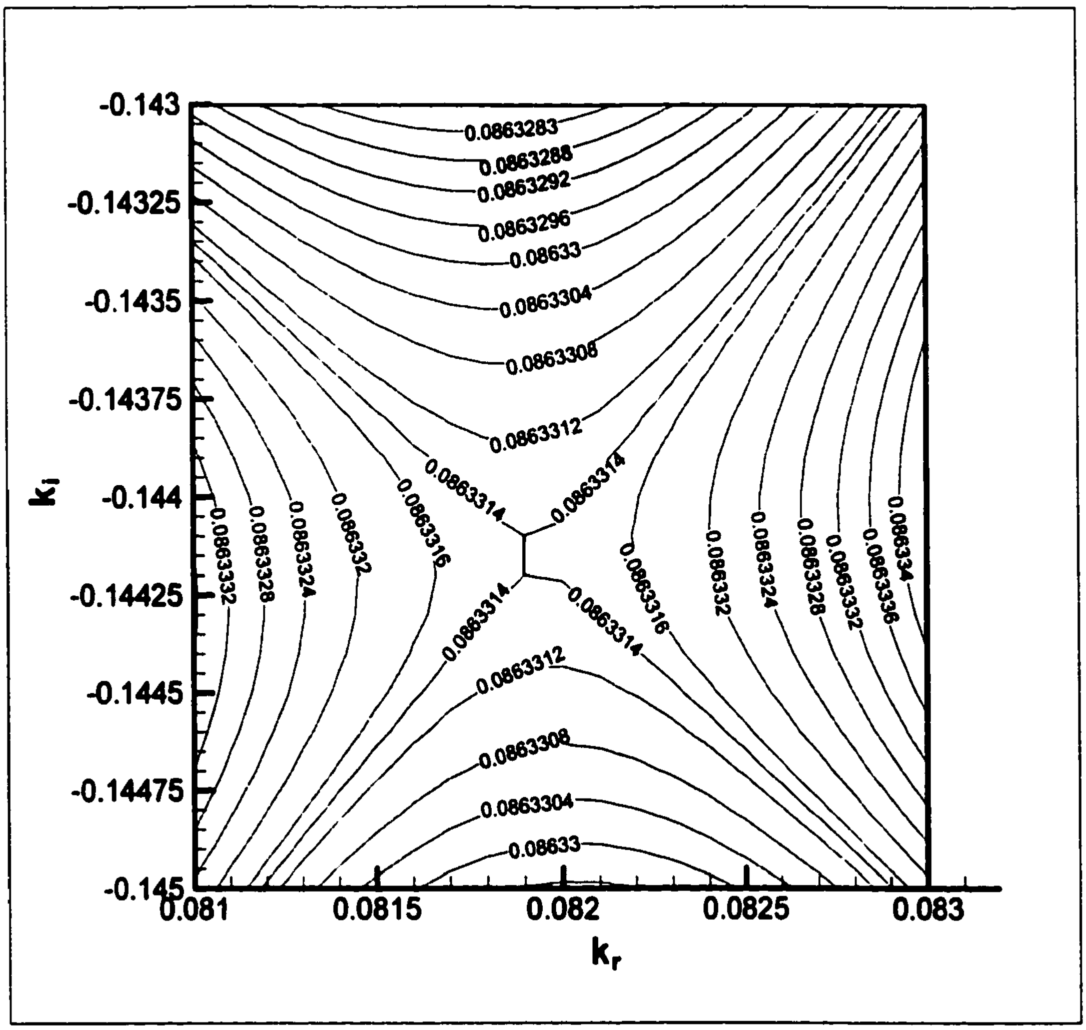

Figure A98: Contour plot of Ω_r for $R/\theta = 10$, $Fr = \infty$, $\rho_j/\rho_\infty = 0.14$, $Sc = 0.05$, and $\Delta r = 0$ in the k-plane illustrating the pinch point formation

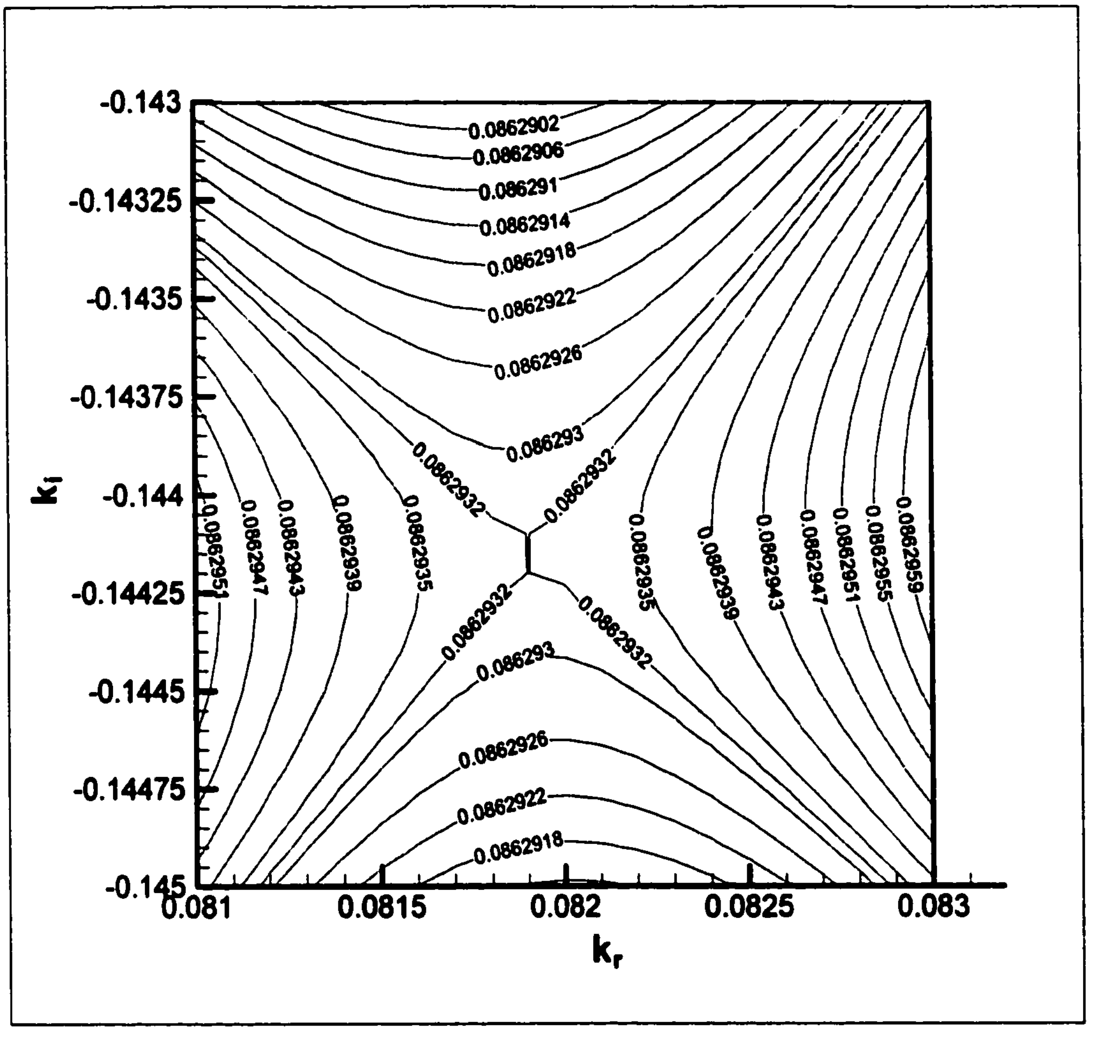

Figure A99: Contour plot of Ω_r for $R/\theta = 10$, $Fr = 10$, $\rho_j/\rho_\infty = 0.14$, $Sc = 0.05$, and $\Delta r = 0$ in the k-plane illustrating the pinch point formation

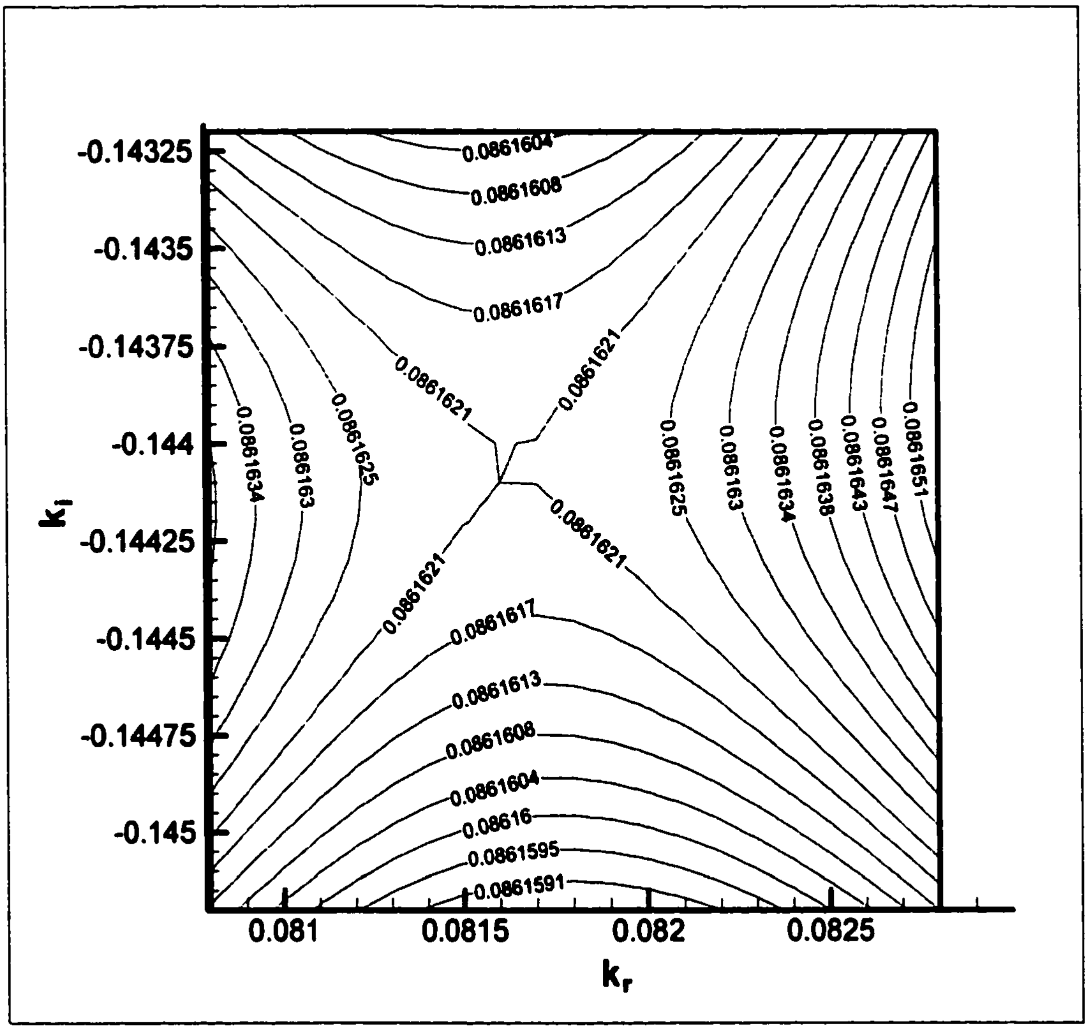

Figure A100: Contour plot of Ω_r for $R/\theta = 10$, $Fr = 5$, $\rho_j/\rho_\infty = 0.14$, $Sc = 0.05$, and $\Delta r = 0$ in the k-plane illustrating the pinch point formation

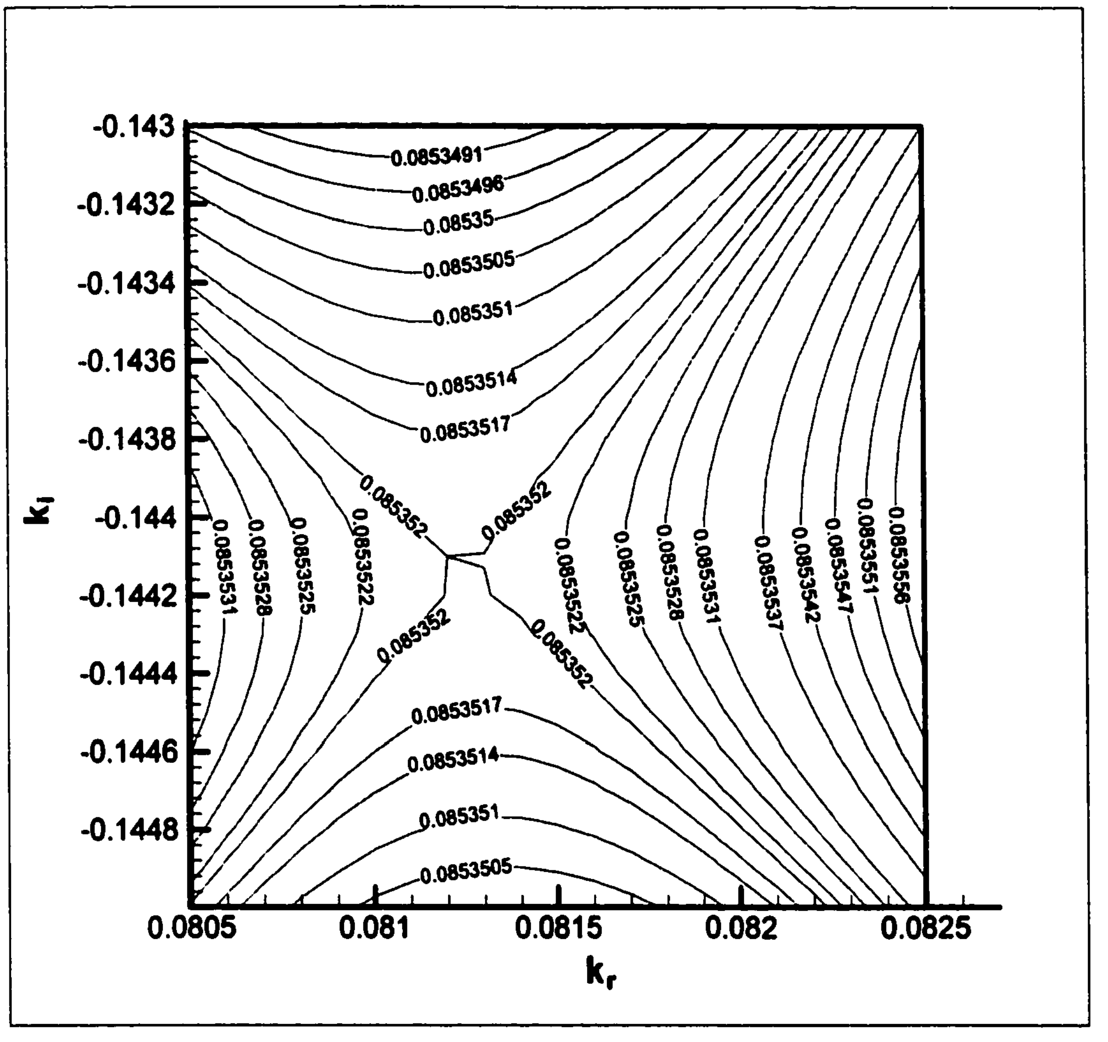

Figure 101: Contour plot of Ω_r for $R/\theta = 10$, $Fr = 2$, $\rho_j/\rho_\infty = 0.14$, $Sc = 0.05$, and $\Delta r = 0$ in the k-plane illustrating the pinch point formation

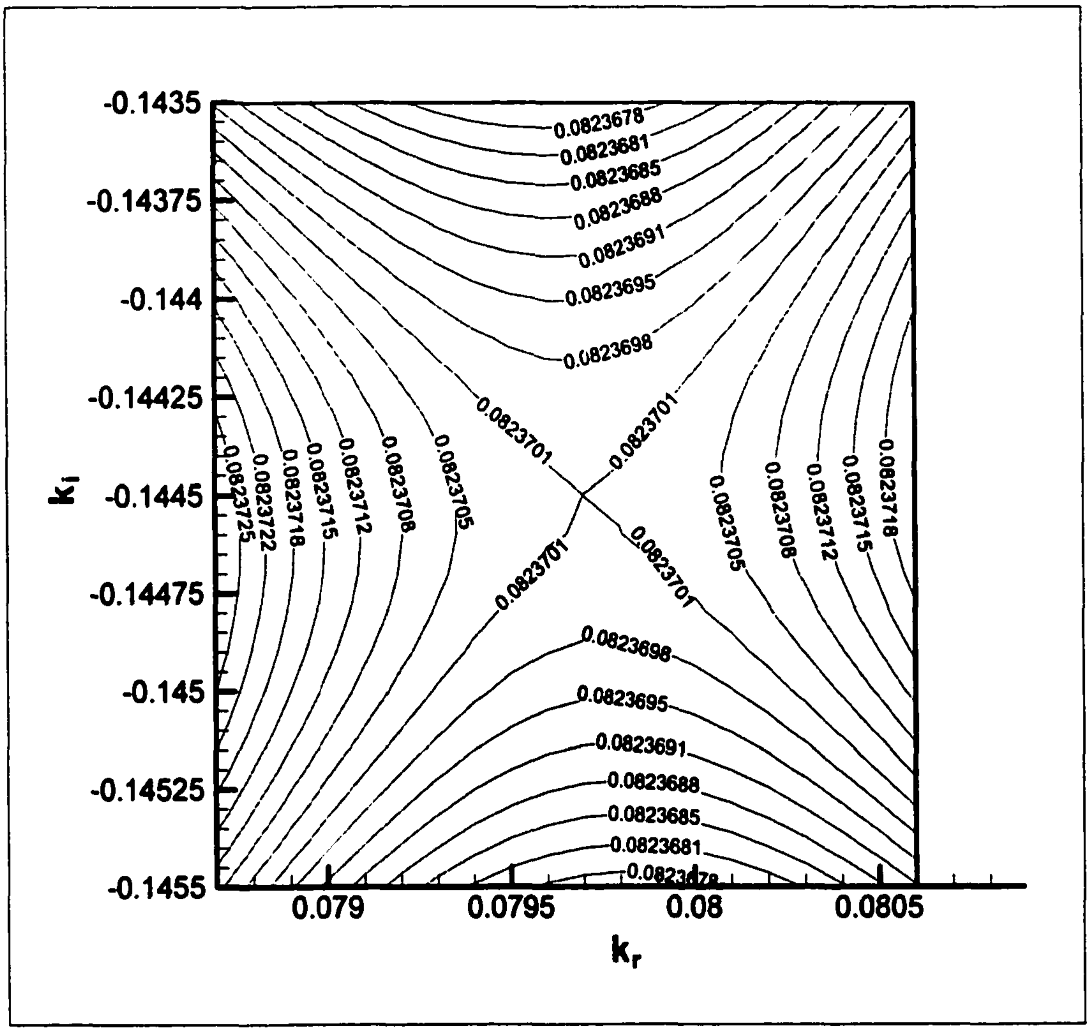

Figure A102: Contour plot of Ω_r for $R/\theta = 10$, $Fr = 1$, $\rho_j/\rho_\infty = 0.14$, $Sc = 0.05$, and $\Delta r = 0$ in the k-plane illustrating the pinch point formation

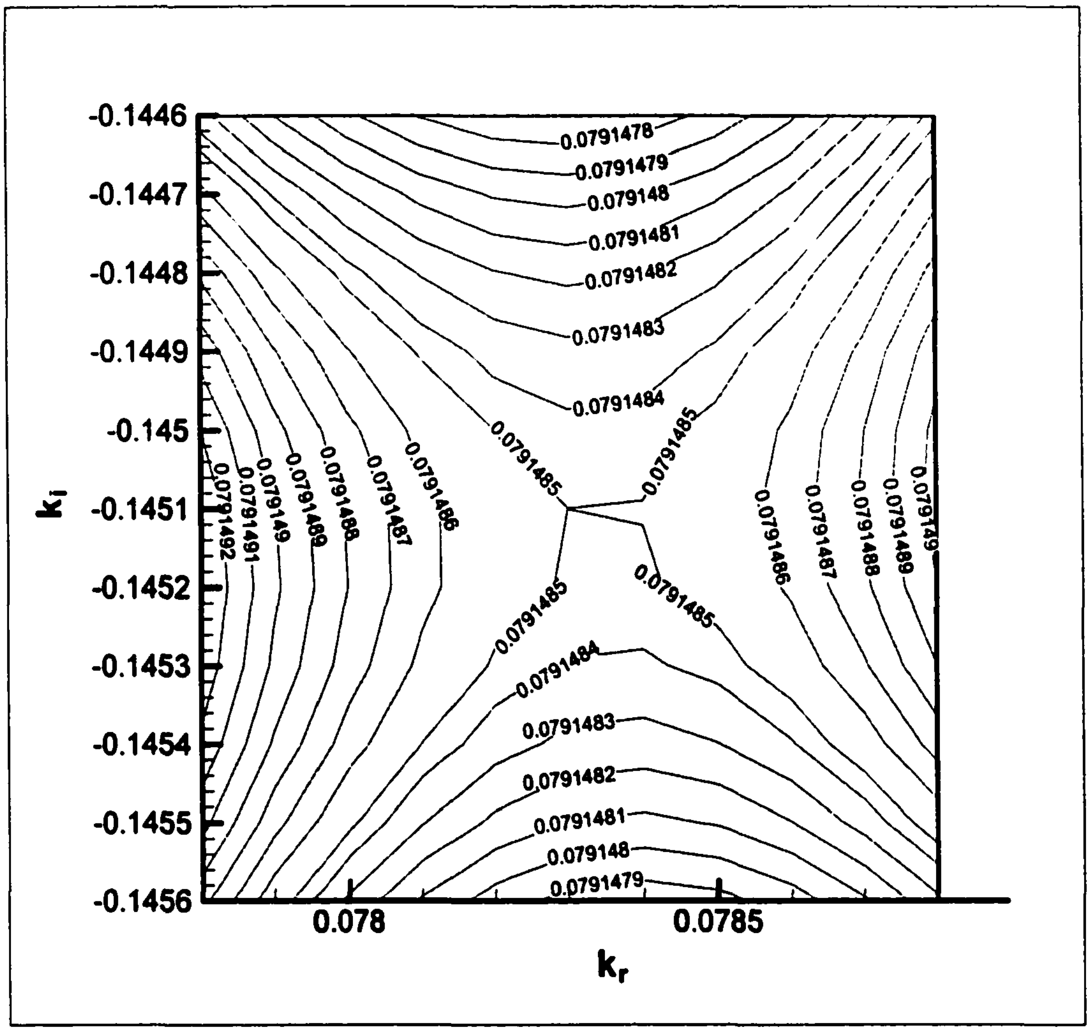

Figure A103: Contour plot of Ω_r for $R/\theta = 10$, $Fr = 0.75$, $\rho_j/\rho_\infty = 0.14$, $Sc = 0.05$, and $\Delta r = 0$ in the k-plane illustrating the pinch point formation

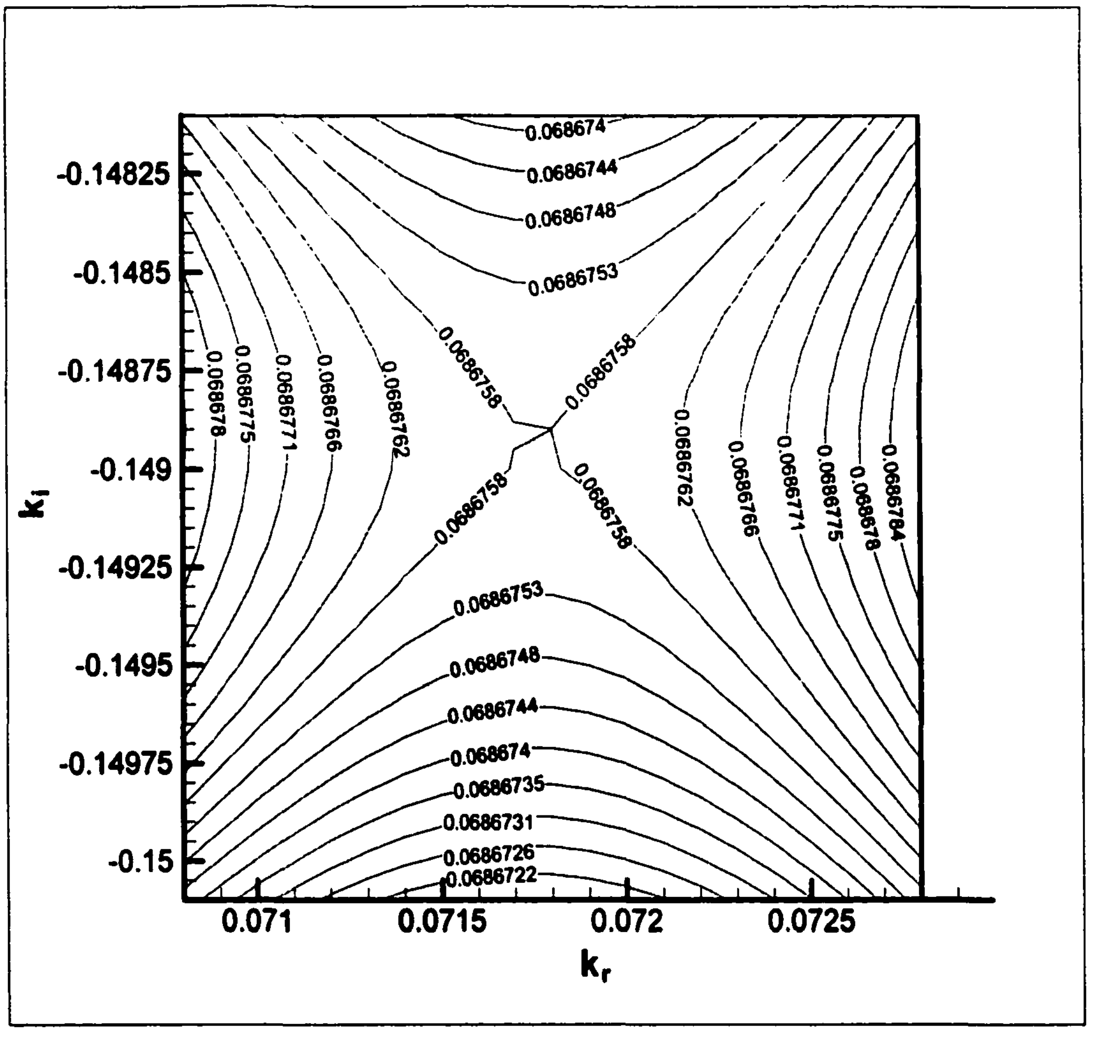

Figure A104: Contour plot of Ω_r for $R/\theta = 10$, $Fr = 0.5$, $\rho_j/\rho_\infty = 0.14$, $Sc = 0.05$, and $\Delta r = 0$ in the k-plane illustrating the pinch point formation

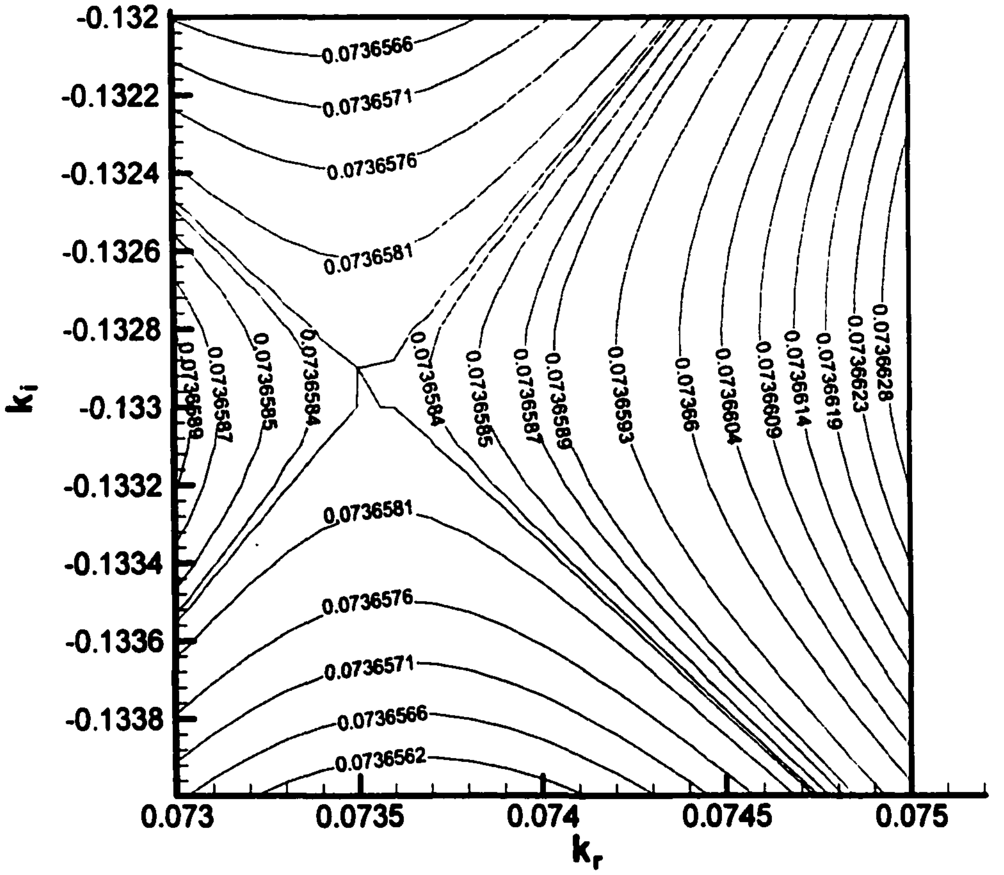

Figure A105: Contour plot of Ω_r for $R/\theta = 10$, $Fr = \infty$, $\rho_j/\rho_\infty = 0.14$, $Sc = 0.1$, and $\Delta r = 0$ in the k-plane illustrating the pinch point formation

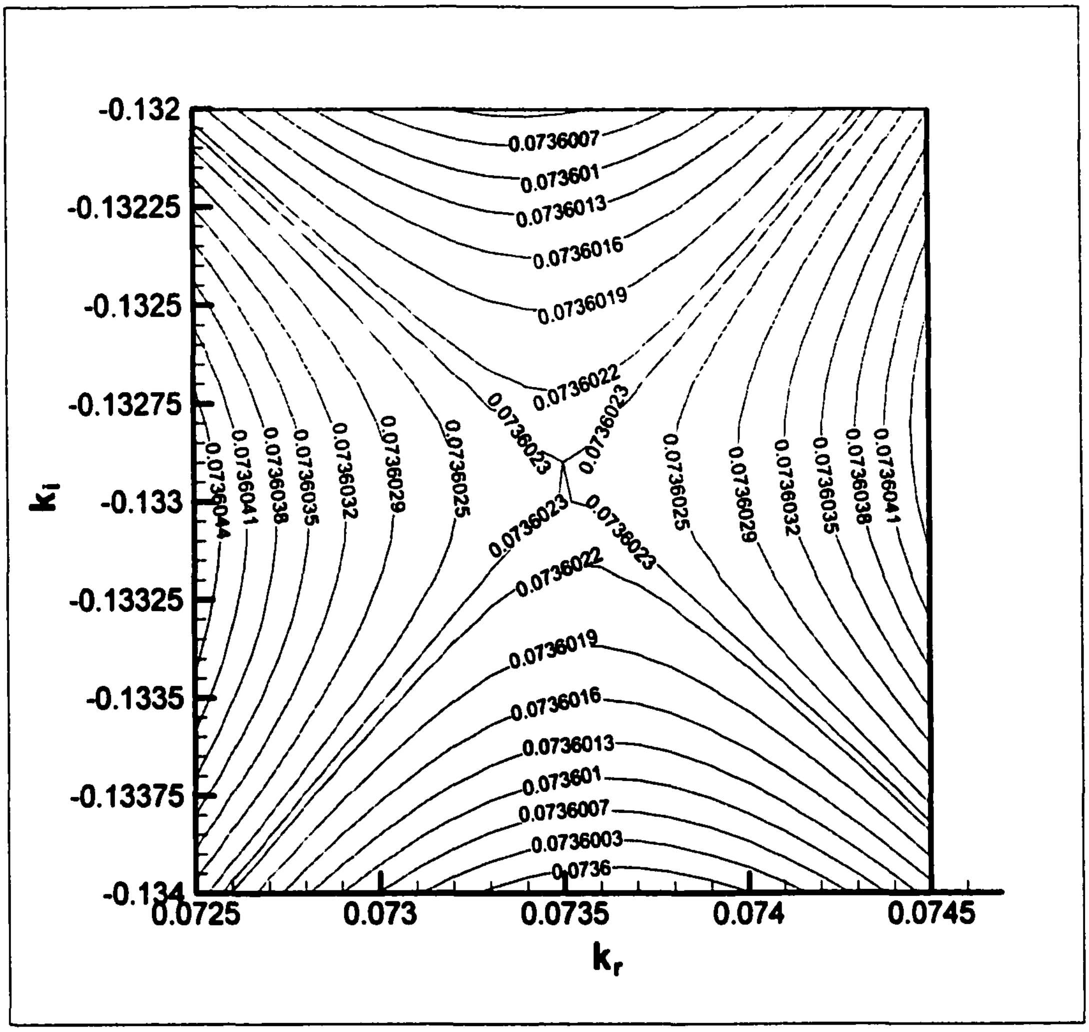

Figure A106: Contour plot of Ω_r for $R/\theta = 10$, $Fr = 10$, $\rho_j/\rho_\infty = 0.14$, $Sc = 0.1$, and $\Delta r = 0$ in the k-plane illustrating the pinch point formation

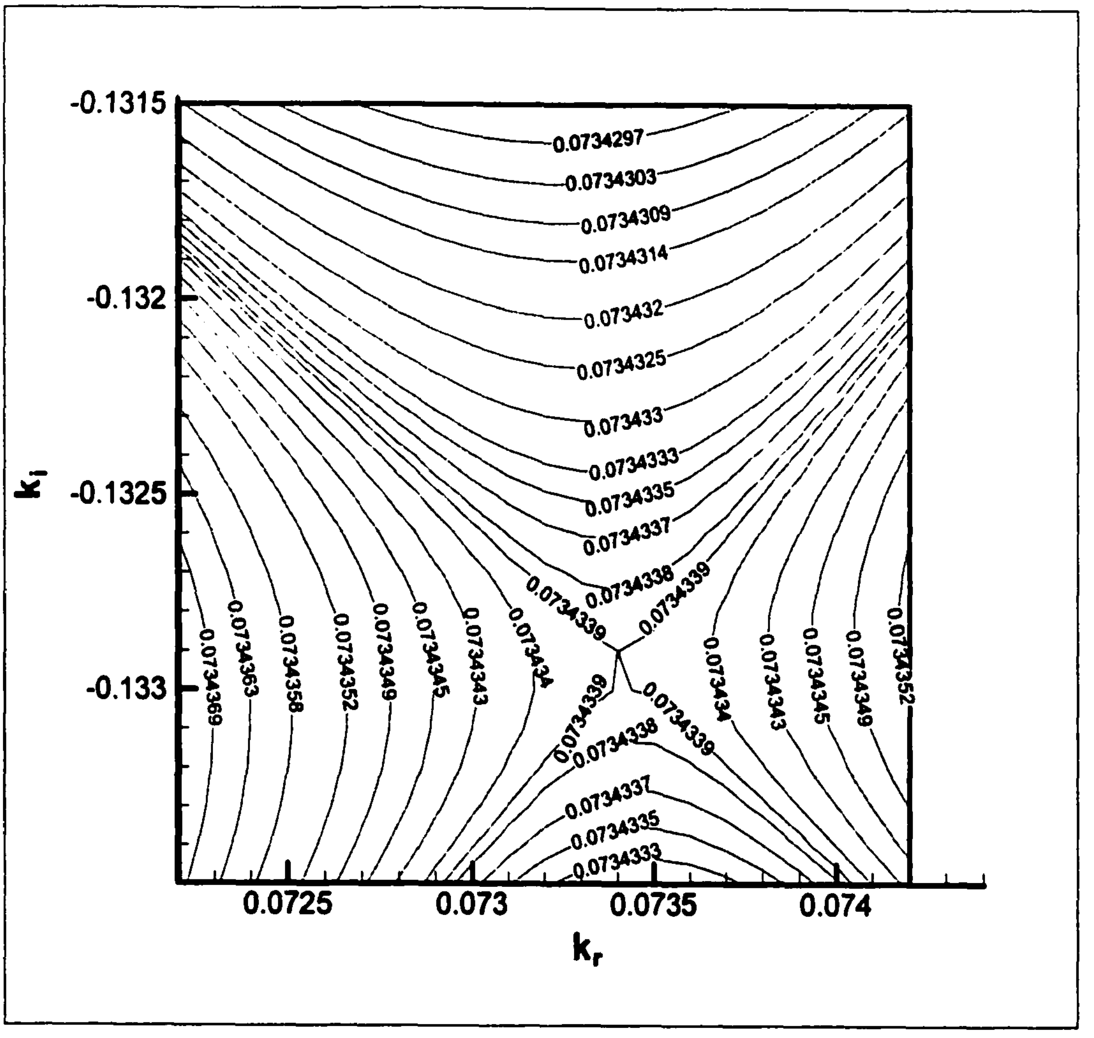

Figure A107: Contour plot of Ω_r for $R/\theta = 10$, $Fr = 5$, $\rho_j/\rho_\infty = 0.14$, $Sc = 0.1$, and $\Delta r = 0$ in the k-plane illustrating the pinch point formation

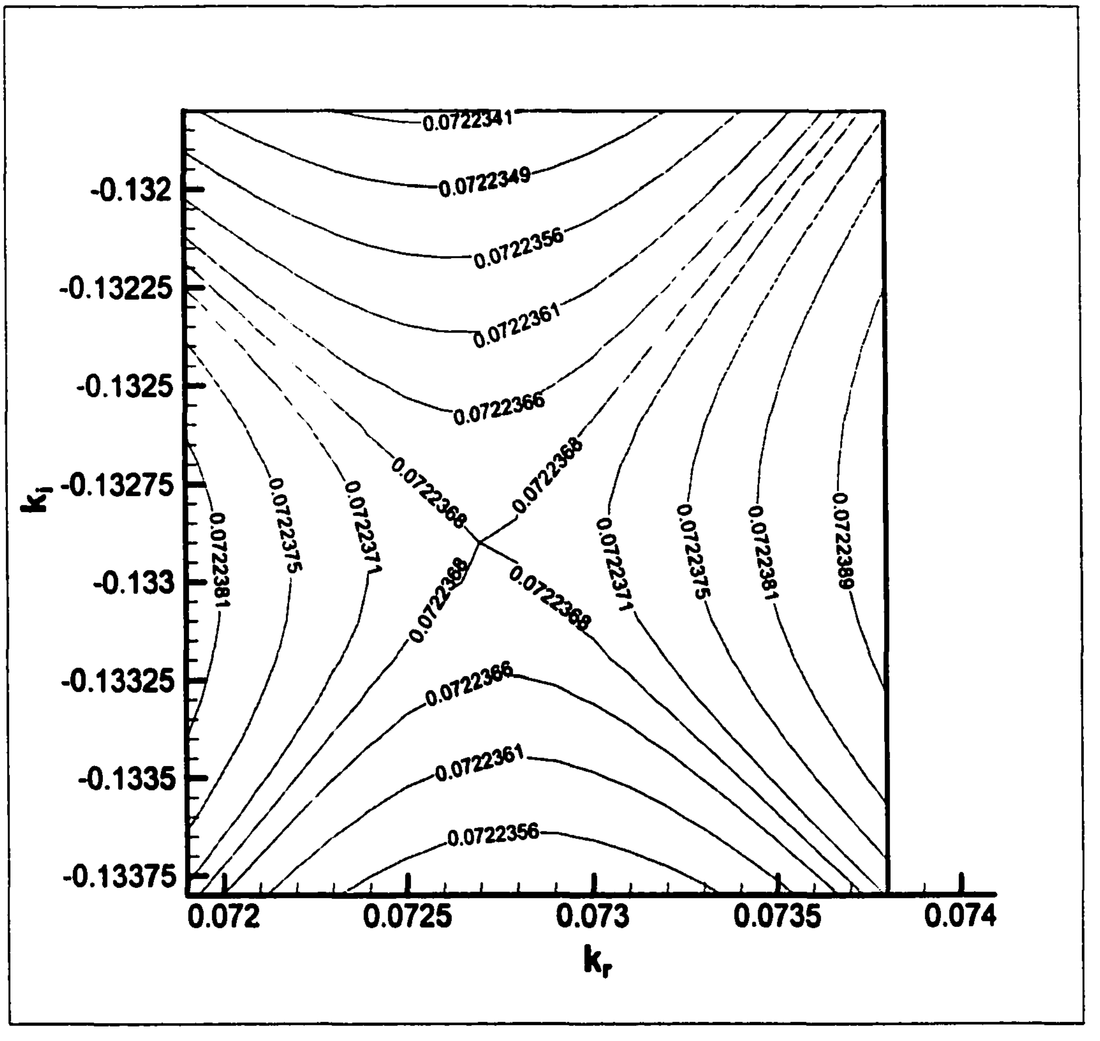

Figure A108: Contour plot of Ω_r for $R/\theta = 10$, $Fr = 2$, $\rho_j/\rho_\infty = 0.14$, $Sc = 0.1$, and $\Delta r = 0$ in the k-plane illustrating the pinch point formation

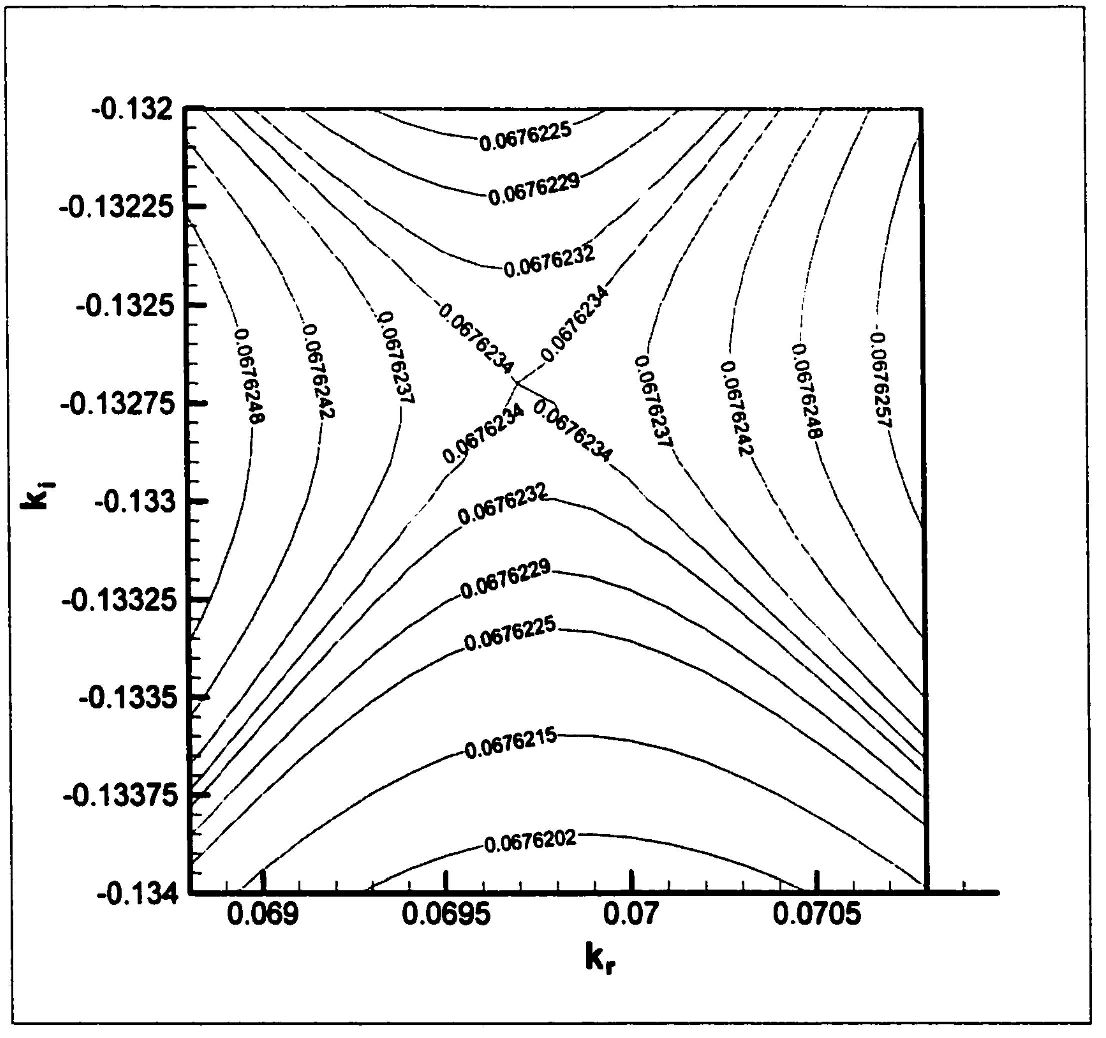

Figure A109: Contour plot of Ω_r for $R/\theta = 10$, $Fr = 1$, $\rho_j/\rho_\infty = 0.14$, $Sc = 0.1$, and $\Delta r = 0$ in the k-plane illustrating the pinch point formation

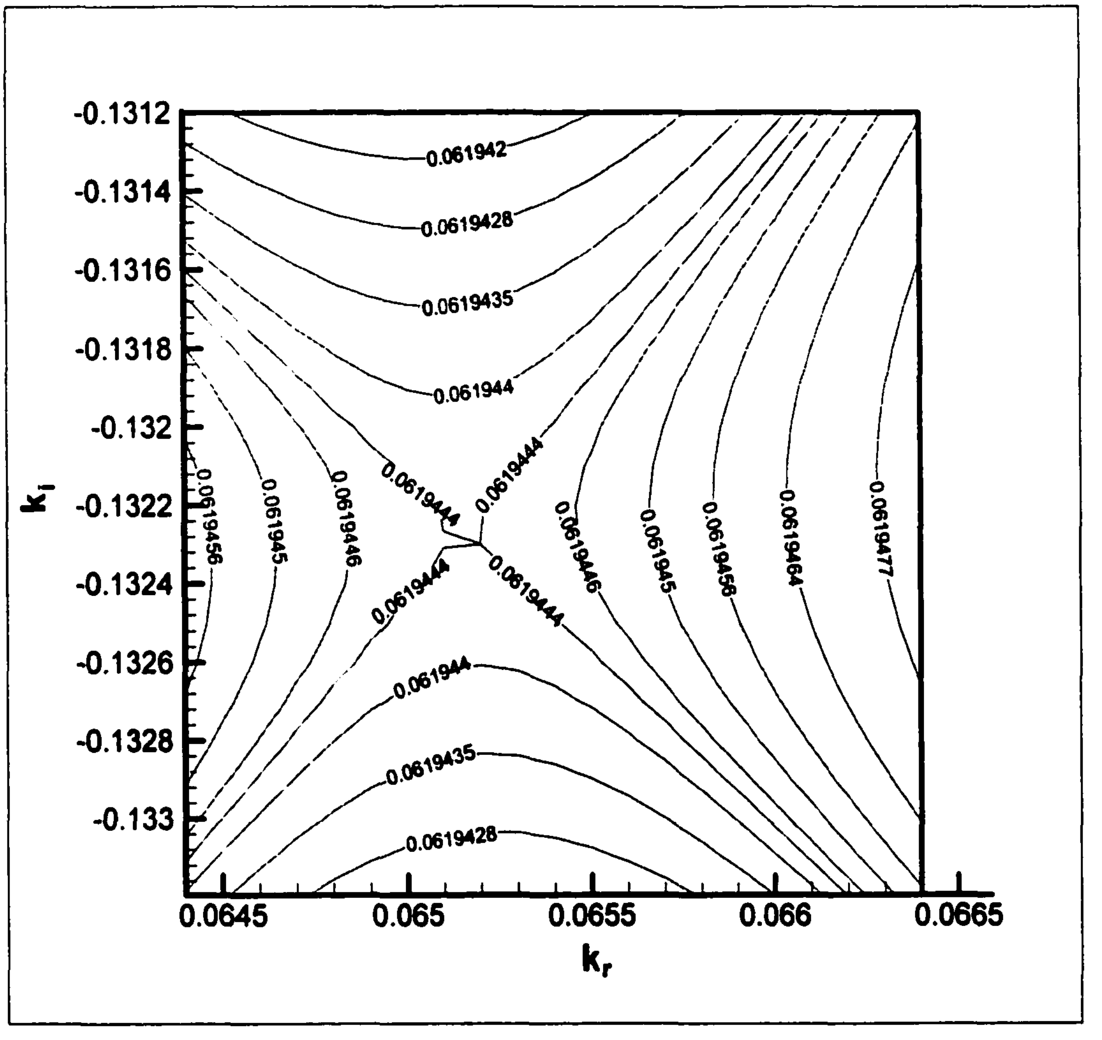

Figure A110: Contour plot of Ω_r for $R/\theta = 10$, $Fr = 0.75$, $\rho_j/\rho_\infty = 0.14$, $Sc = 0.1$, and $\Delta r = 0$ in the k-plane illustrating the pinch point formation

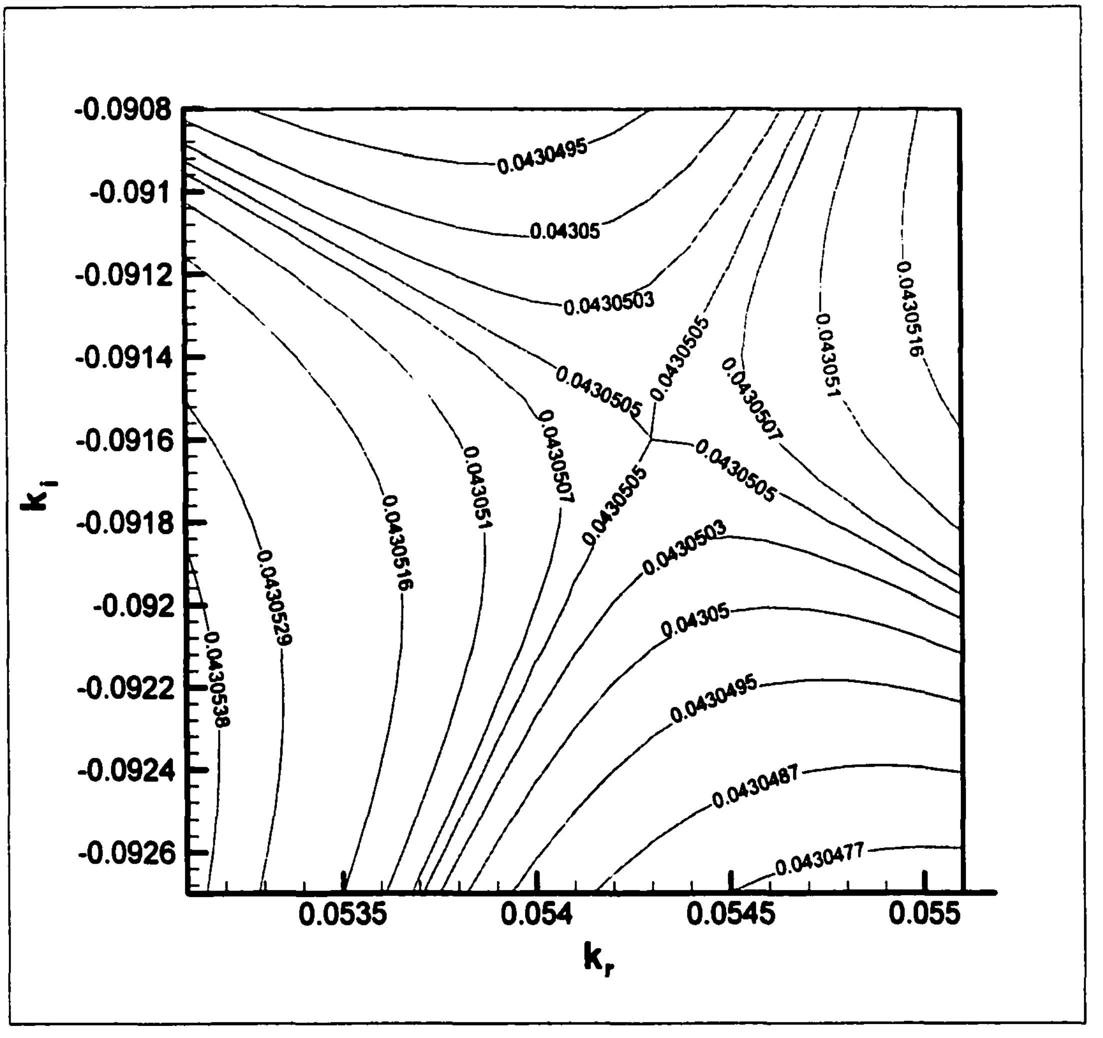

Figure A111: Contour plot of Ω_r for $R/\theta = 10$, $Fr = 0.5$, $\rho_j/\rho_\infty = 0.14$, $Sc = 0.1$, and $\Delta r = 0$ in the k-plane illustrating the pinch point formation

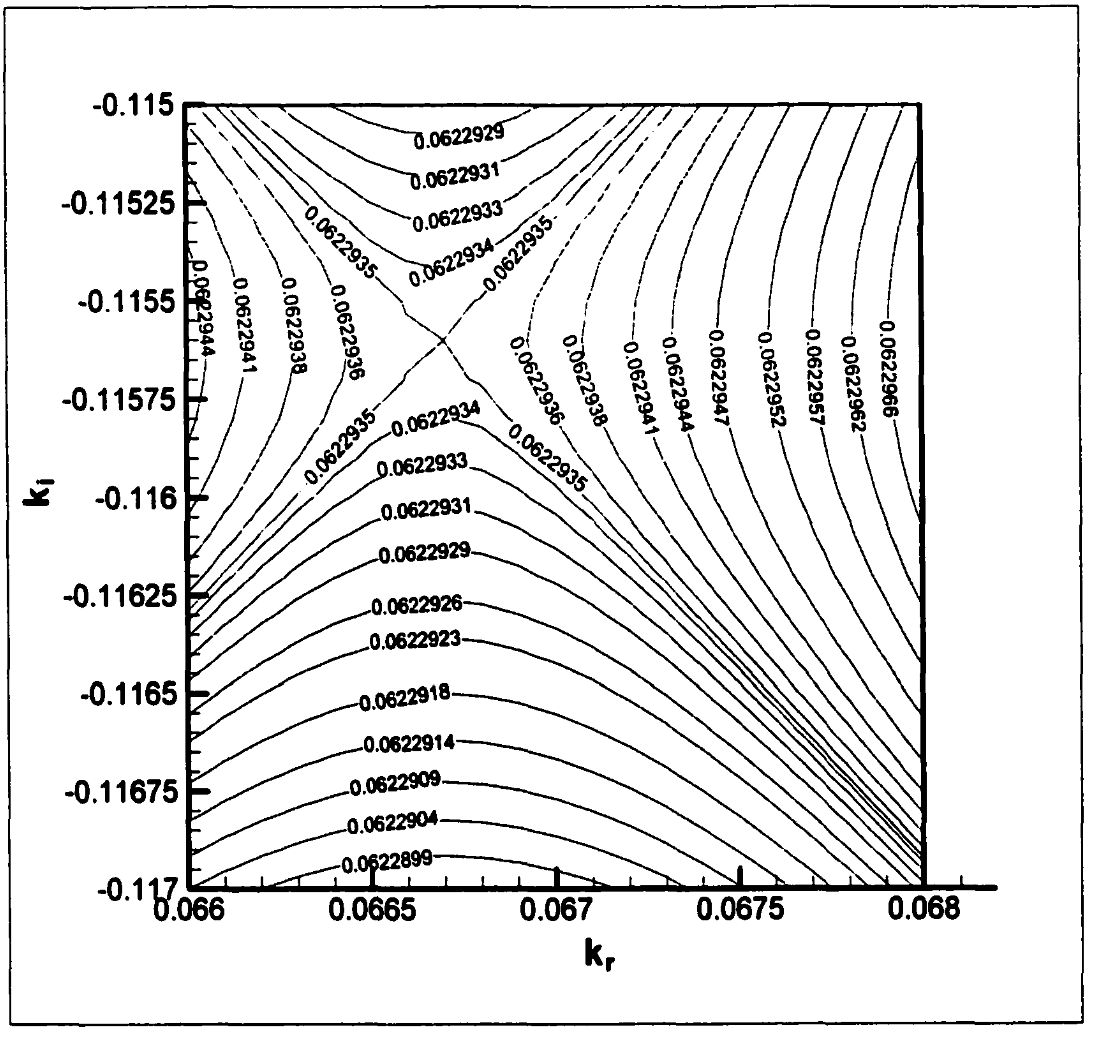

Figure A112: Contour plot of Ω_r for $R/\theta = 10$, $Fr = \infty$, $\rho_j/\rho_\infty = 0.14$, $Sc = 0.21$, and $\Delta r = 0$ in the k-plane illustrating the pinch point formation

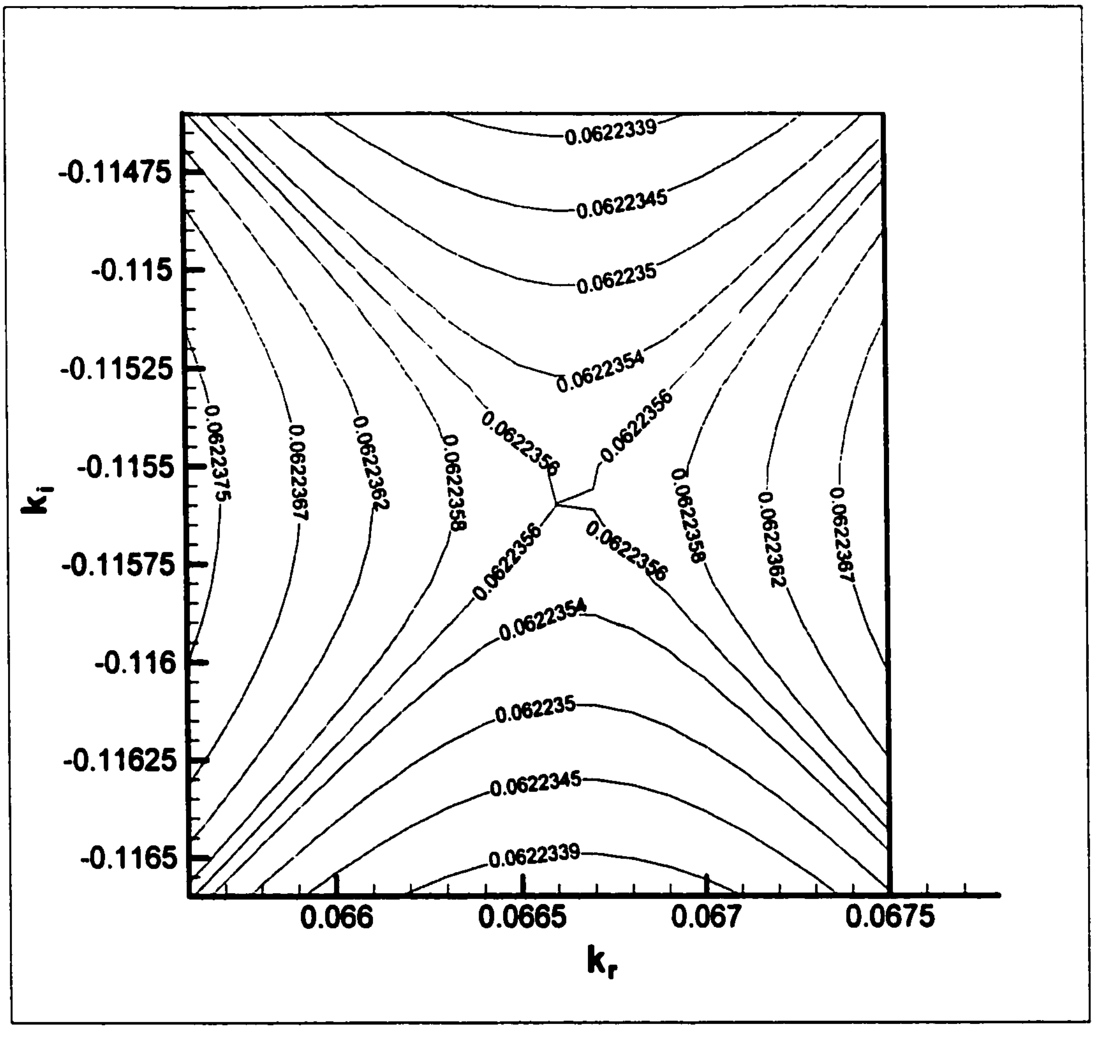

Figure A113: Contour plot of Ω_r for $R/\theta = 10$, $Fr = 10$, $\rho_j/\rho_\infty = 0.14$, $Sc = 0.21$, and $\Delta r = 0$ in the k-plane illustrating the pinch point formation

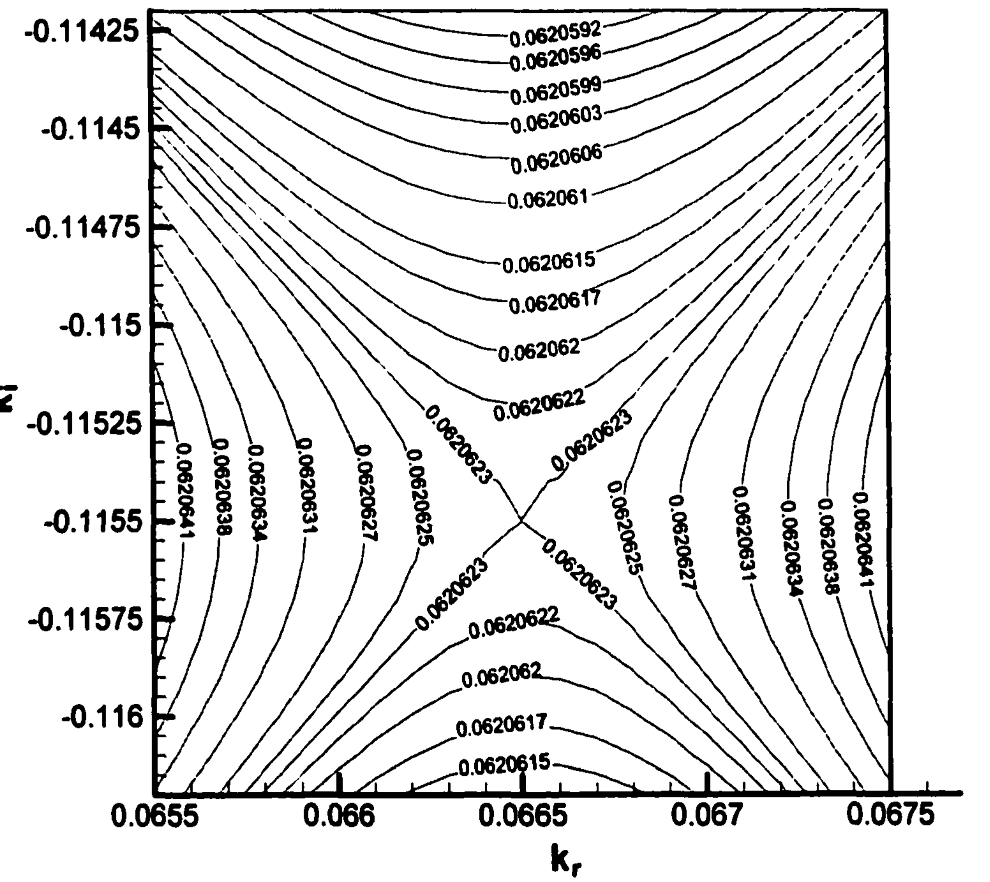

Figure A114: Contour plot of Ω_r for $R/\theta = 10$, $Fr = 5$, $\rho_j/\rho_\infty = 0.14$, $Sc = 0.21$, and $\Delta r = 0$ in the k-plane illustrating the pinch point formation

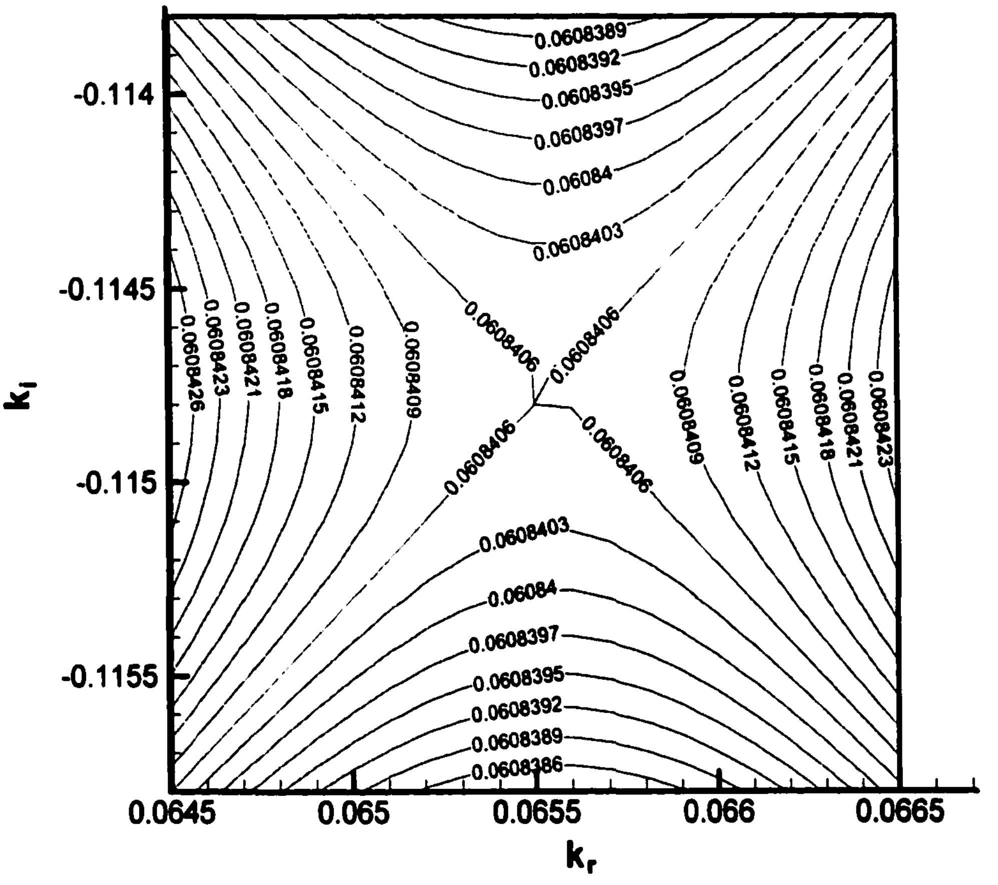

Figure A115: Contour plot of Ω_r for $R/\theta = 10$, $Fr = 2$, $\rho_j/\rho_\infty = 0.14$, $Sc = 0.21$, and $\Delta r = 0$ in the k-plane illustrating the pinch point formation

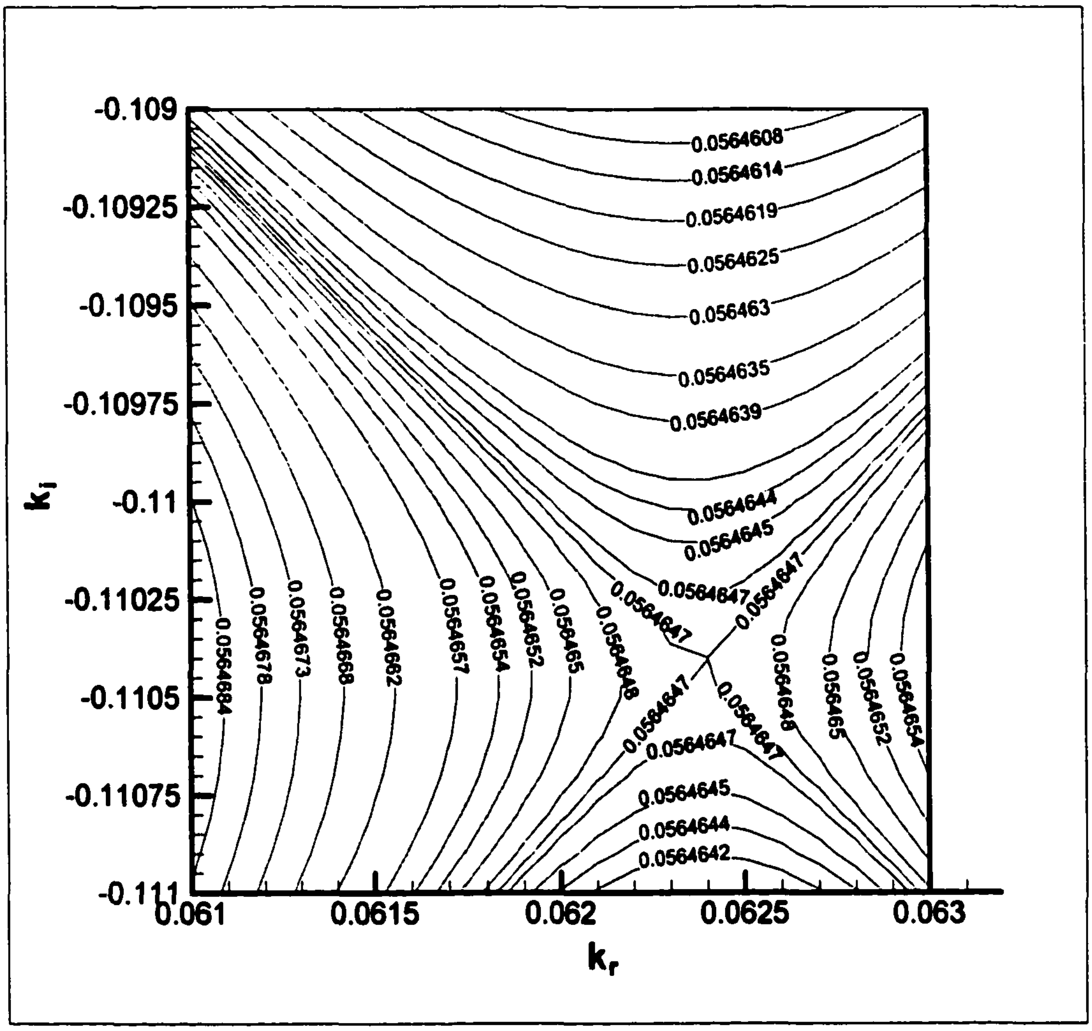

Figure A116: Contour plot of Ω_r for $R/\theta = 10$, $Fr = 1$, $\rho_j/\rho_\infty = 0.14$, $Sc = 0.21$, and $\Delta r = 0$ in the k-plane illustrating the pinch point formation

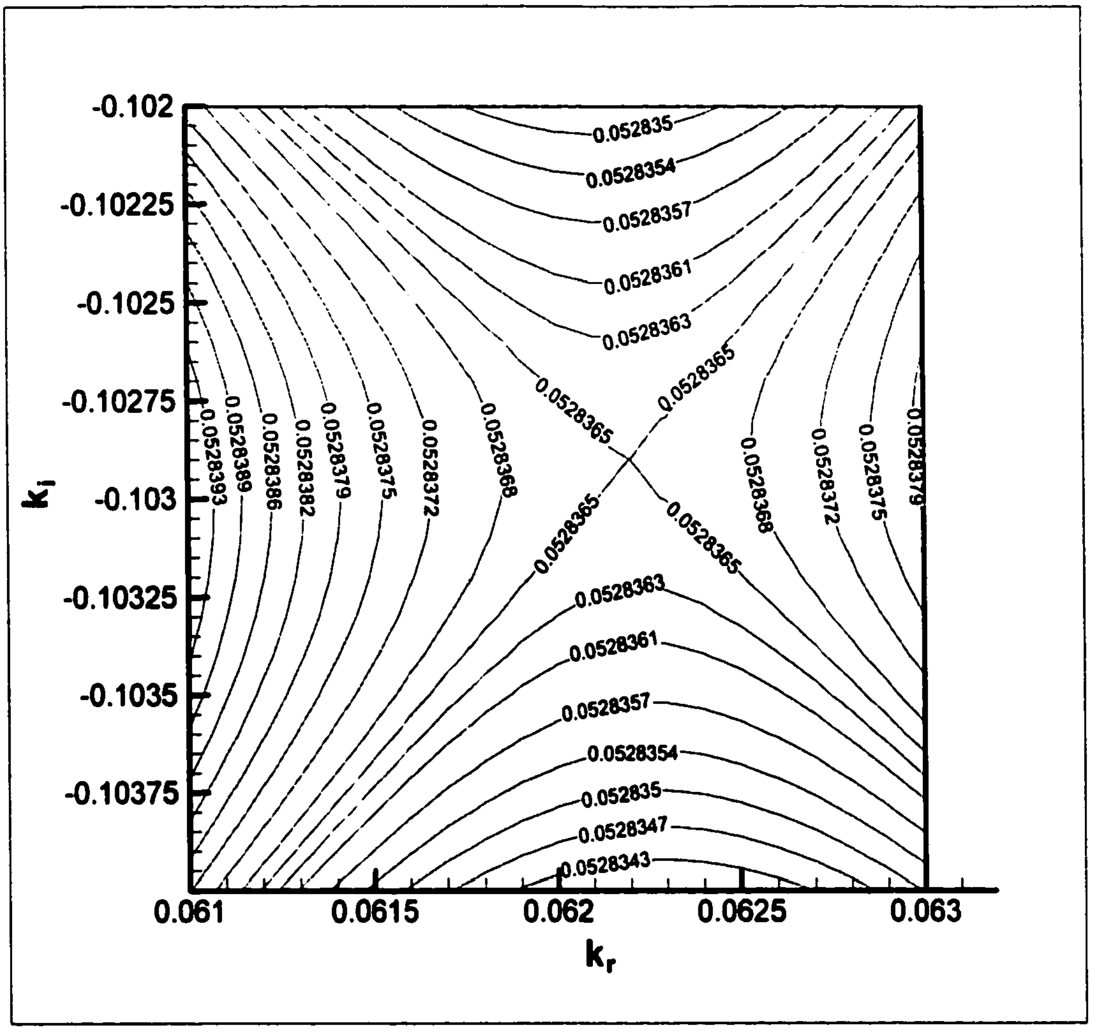

Figure A117: Contour plot of Ω_r for $R/\theta = 10$, $Fr = 0.75$, $\rho_j/\rho_\infty = 0.14$, $Sc = 0.21$, and $\Delta r = 0$ in the k-plane illustrating the pinch point formation

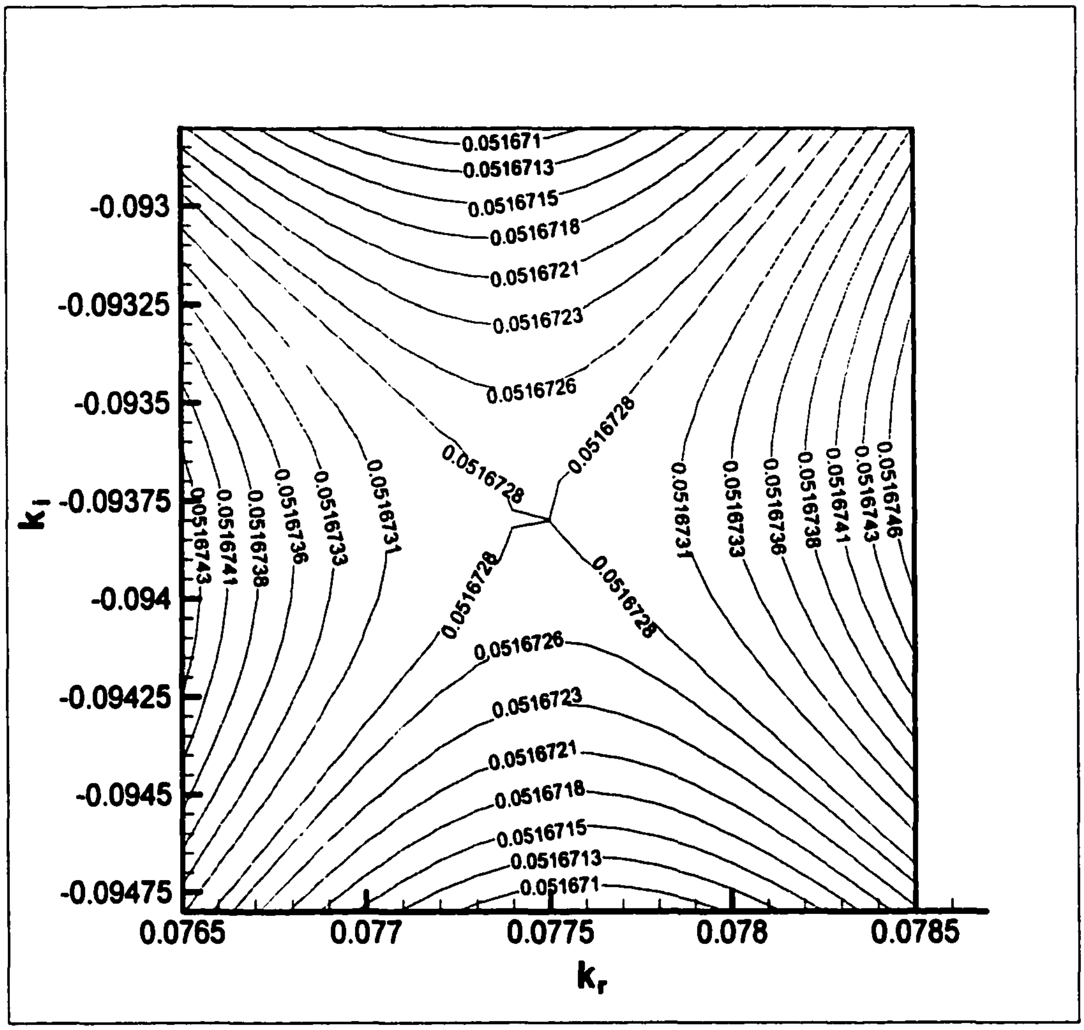

Figure A118: Contour plot of Ω_r for $R/\theta = 10$, $Fr = 0.5$, $\rho_j/\rho_\infty = 0.14$, $Sc = 0.21$, and $\Delta r = 0$ in the k-plane illustrating the pinch point formation

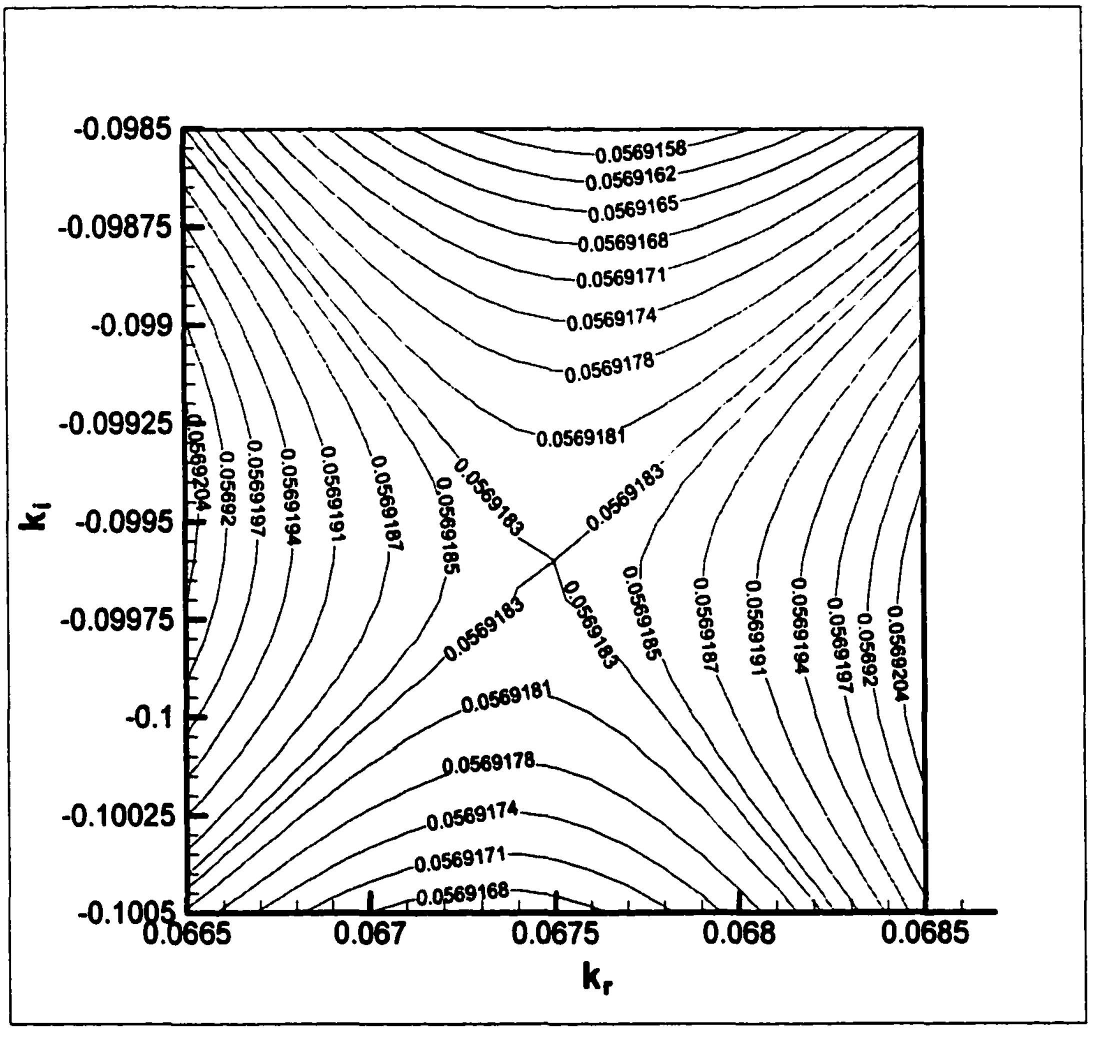

Figure A119: Contour plot of Ω_r for $R/\theta = 10$, $Fr = \infty$, $\rho_j/\rho_\infty = 0.14$, $Sc = 0.4$, and $\Delta r = 0$ in the k-plane illustrating the pinch point formation

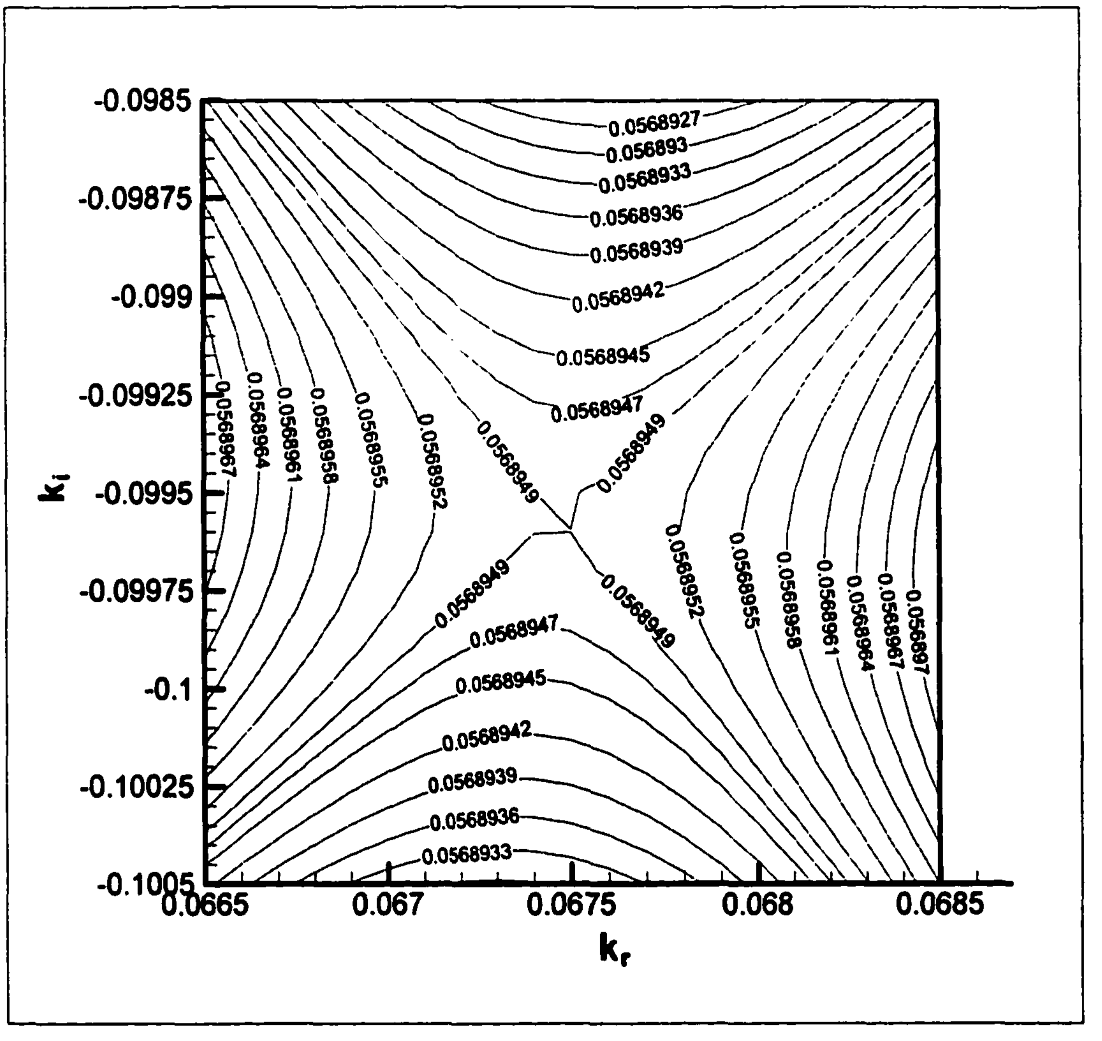

Figure A120: Contour plot of Ω_r for $R/\theta = 10$, $Fr = 10$, $\rho_j/\rho_\infty = 0.14$, $Sc = 0.4$, and $\Delta r = 0$ in the k-plane illustrating the pinch point formation

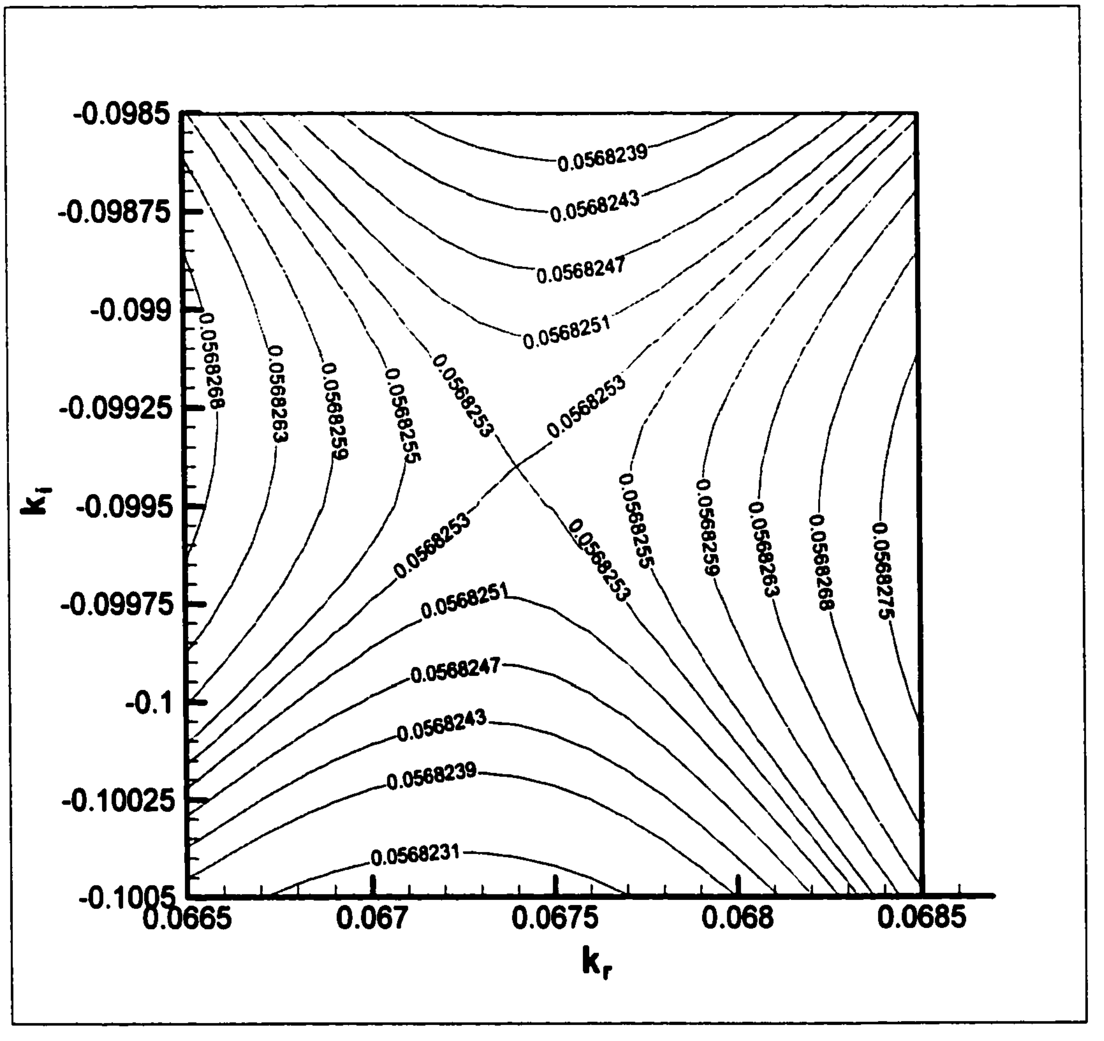

Figure A121: Contour plot of Ω_r for $R/\theta = 10$, $Fr = 5$, $\rho_j/\rho_\infty = 0.14$, $Sc = 0.4$, and $\Delta r = 0$ in the k-plane illustrating the pinch point formation

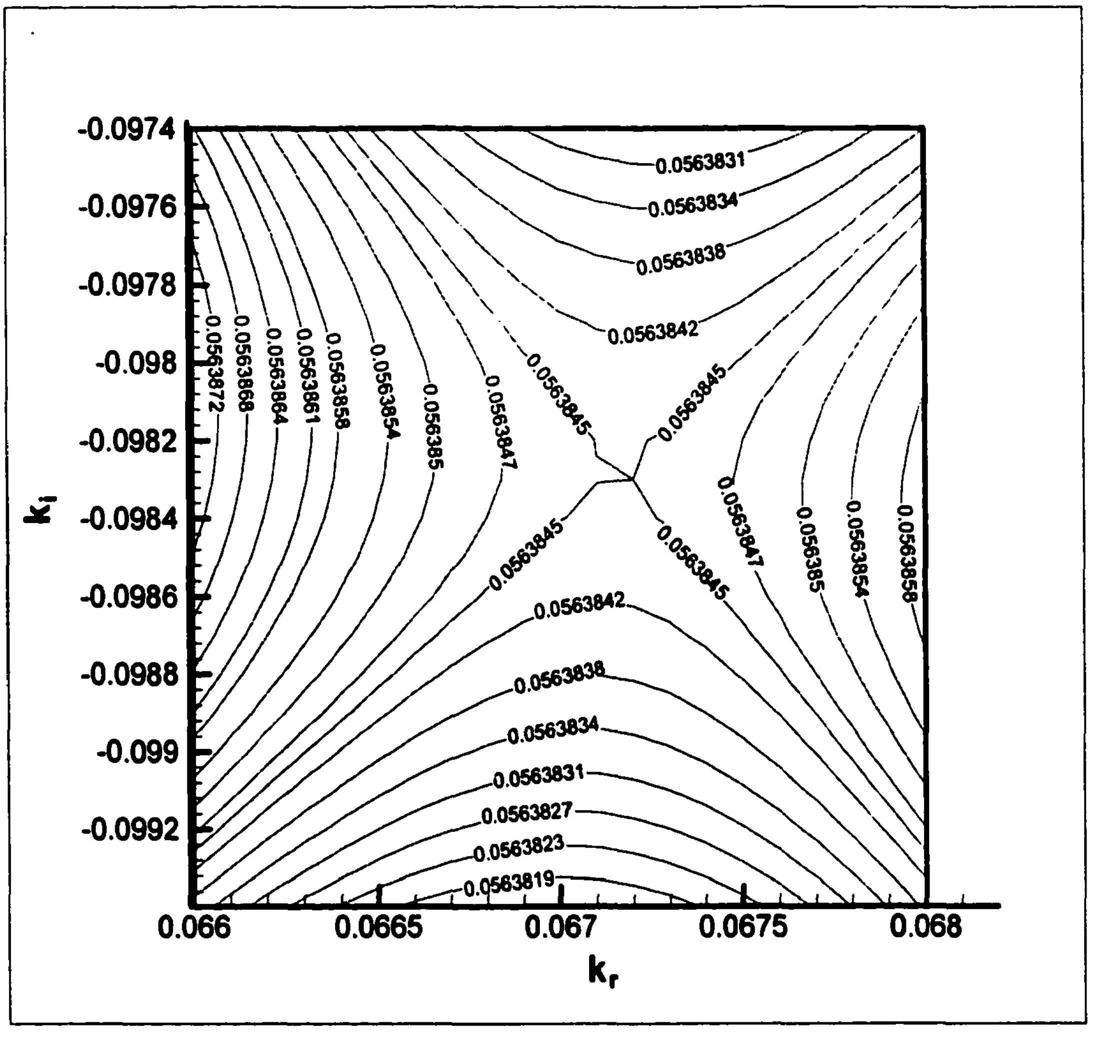

Figure A122: Contour plot of Ω_r for $R/\theta = 10$, $Fr = 2$, $\rho_j/\rho_\infty = 0.14$, $Sc = 0.4$, and $\Delta r = 0$ in the k-plane illustrating the pinch point formation

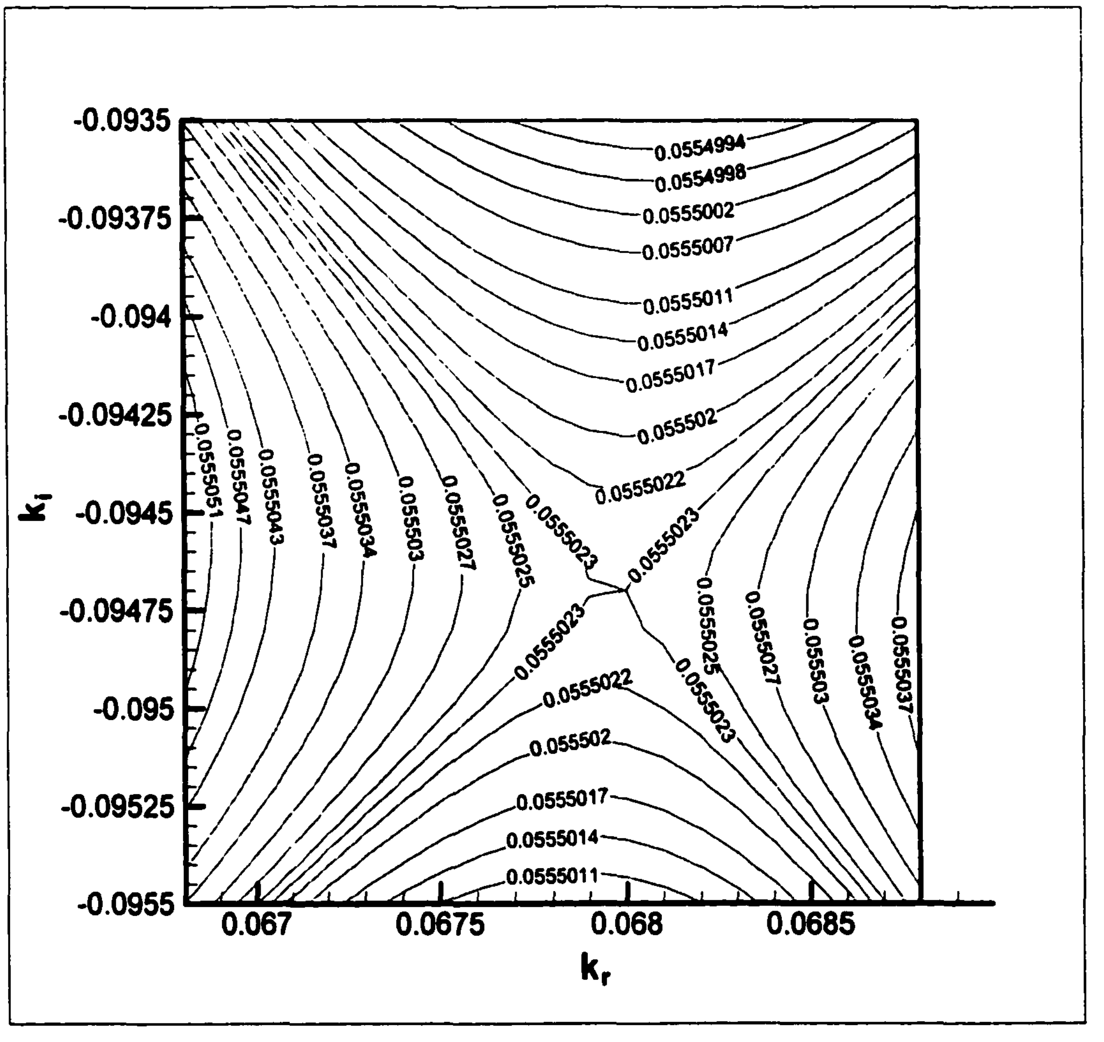

Figure A123: Contour plot of Ω_r for $R/\theta = 10$, $Fr = 1$, $\rho_j/\rho_\infty = 0.14$, $Sc = 0.4$, and $\Delta r = 0$ in the k-plane illustrating the pinch point formation

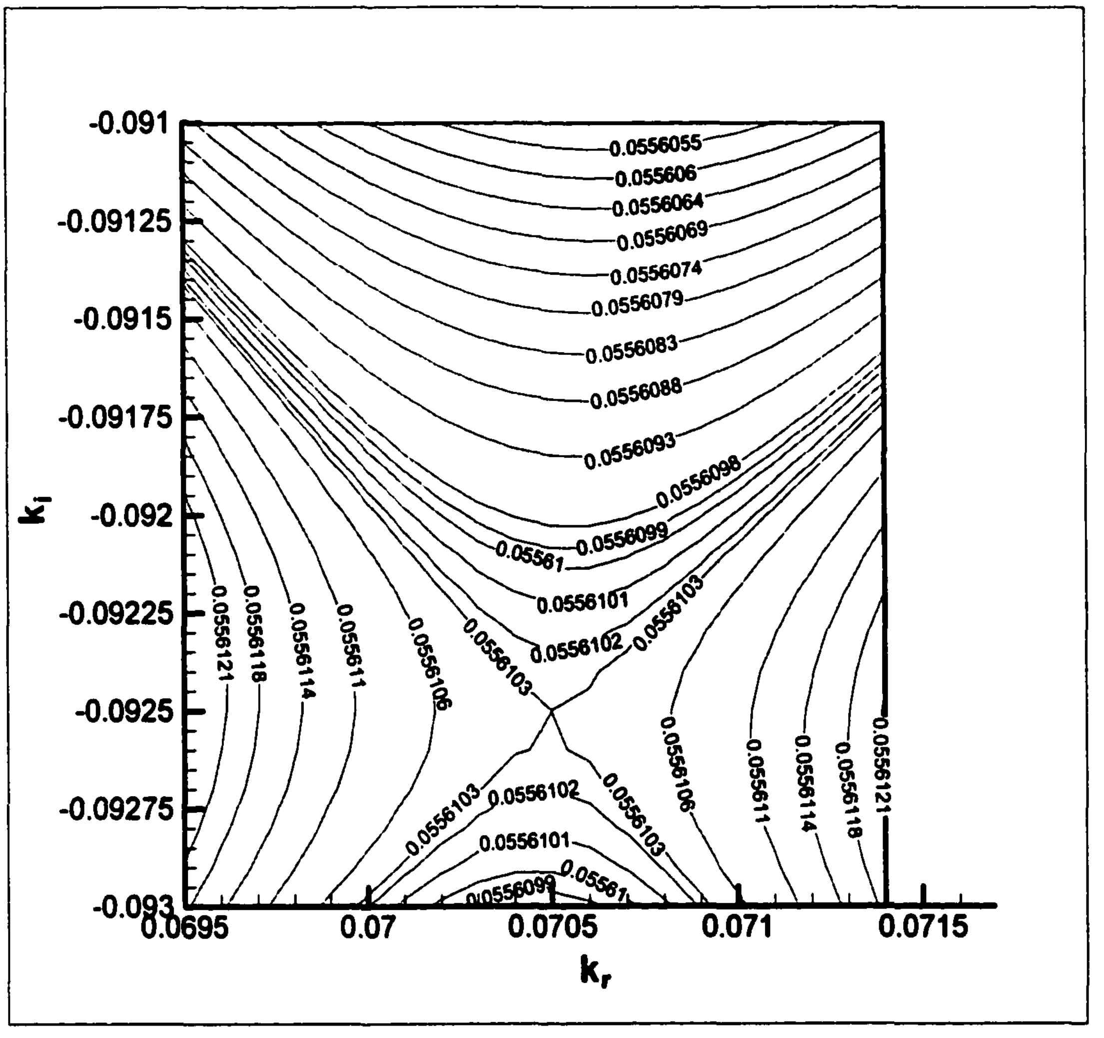

Figure A124: Contour plot of Ω_r for $R/\theta = 10$, $Fr = 0.75$, $\rho_j/\rho_\infty = 0.14$, $Sc = 0.4$, and $\Delta r = 0$ in the k-plane illustrating the pinch point formation

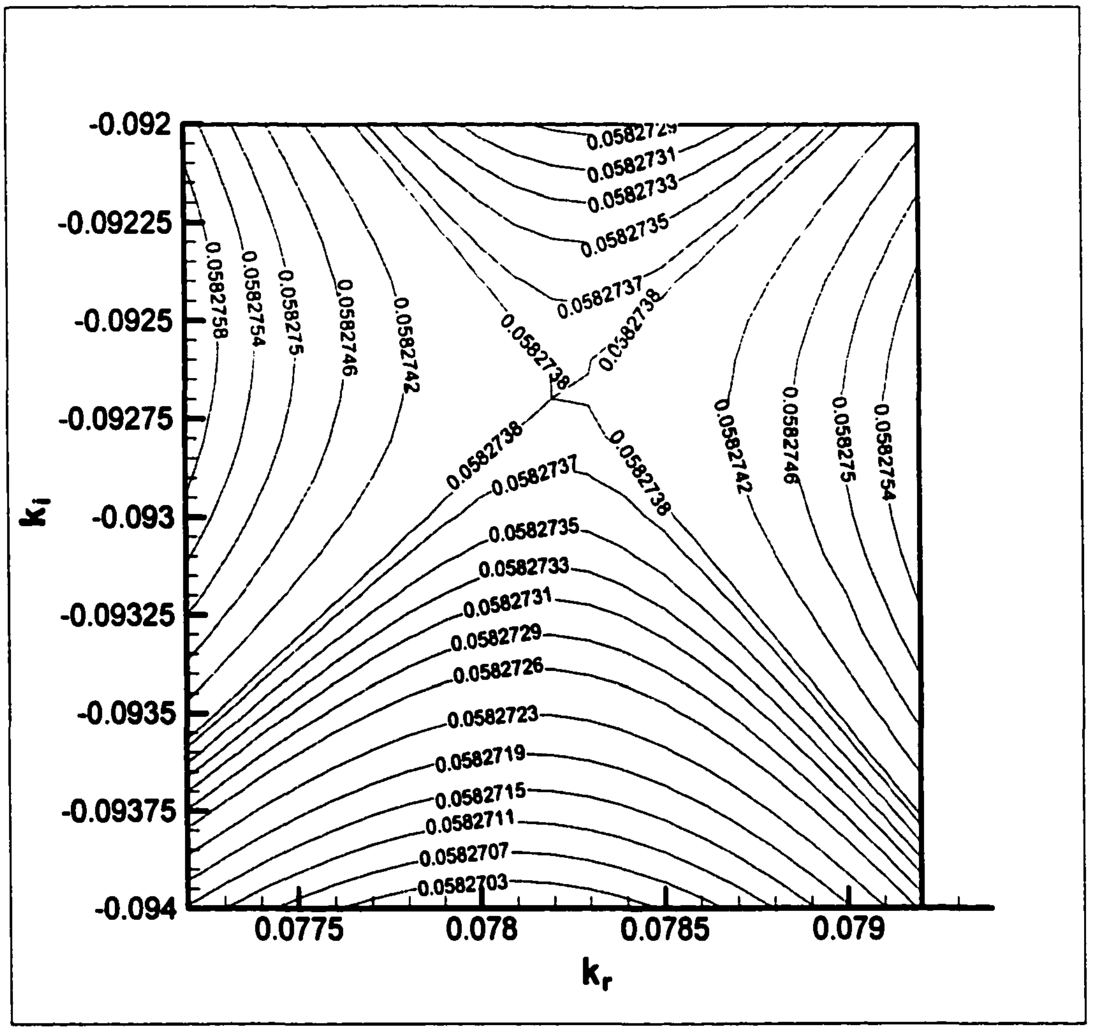

Figure A125: Contour plot of Ω_r for $R/\theta = 10$, $Fr = 0.5$, $\rho_j/\rho_\infty = 0.14$, $Sc = 0.4$, and $\Delta r = 0$ in the k-plane illustrating the pinch point formation

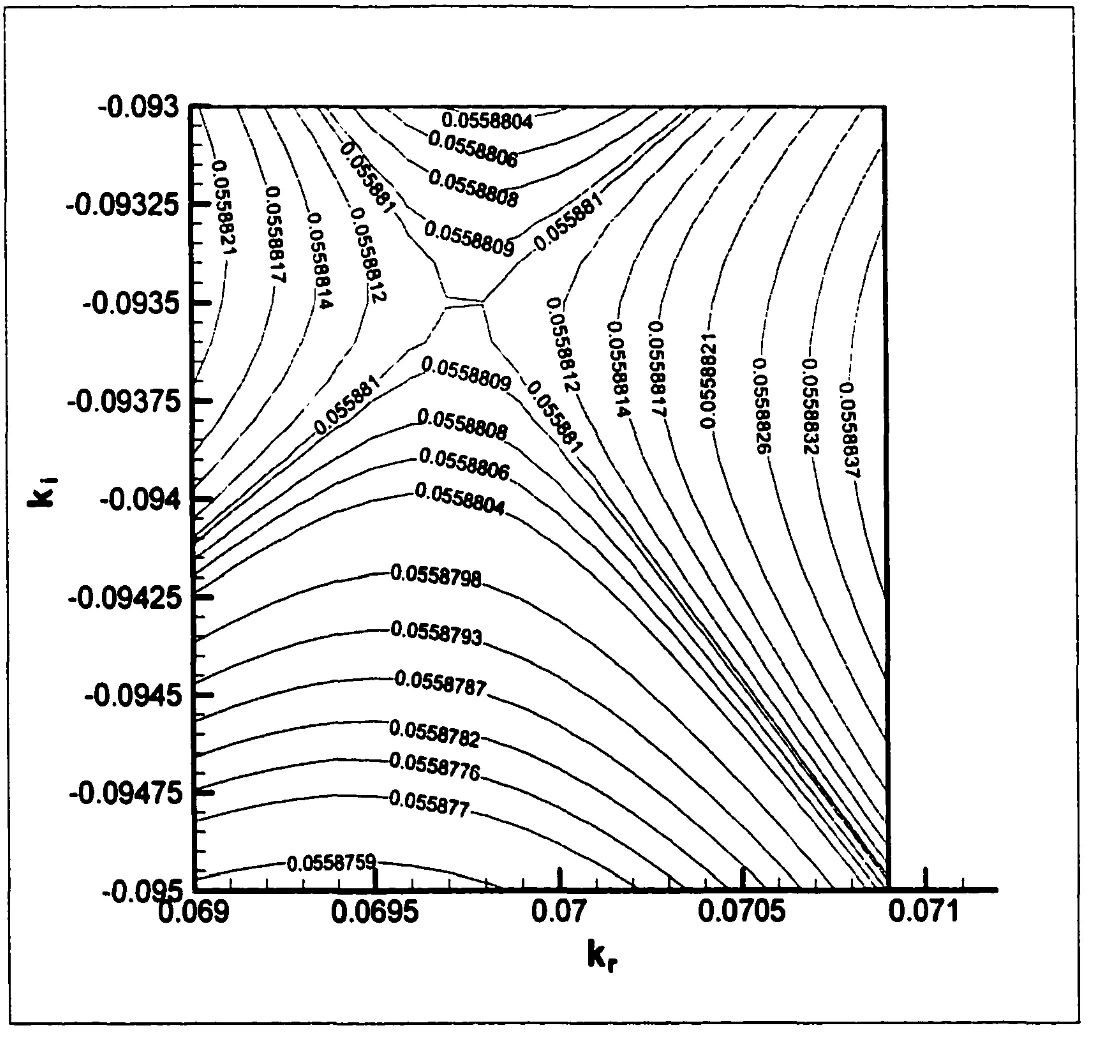

Figure A126: Contour plot of Ω_r for $R/\theta = 10$, $Fr = \infty$, $\rho_j/\rho_\infty = 0.14$, $Sc = 0.6$, and $\Delta r = 0$ in the k-plane illustrating the pinch point formation

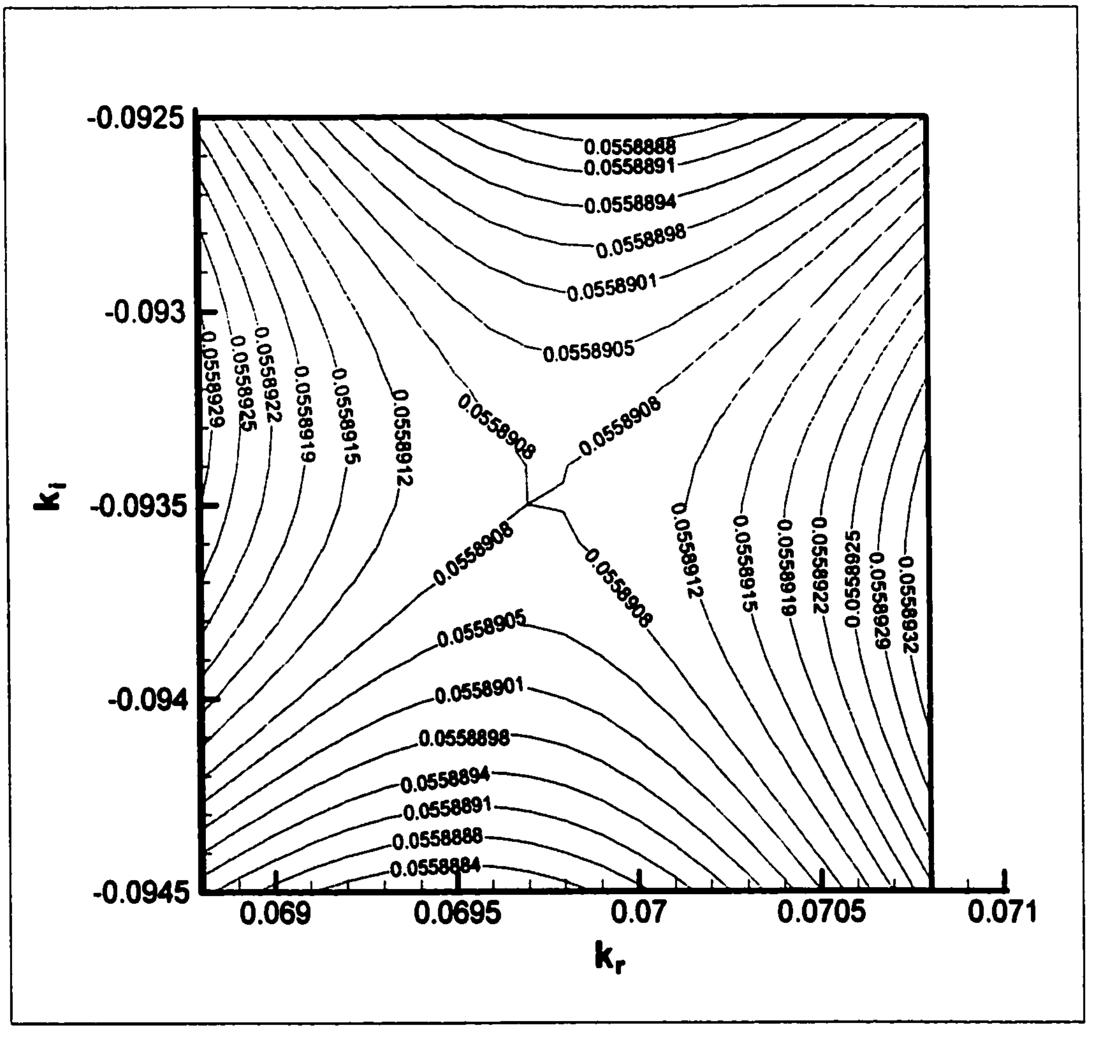

Figure A127: Contour plot of Ω_r for $R/\theta = 10$, $Fr = 10$, $\rho_j/\rho_\infty = 0.14$, $Sc = 0.6$, and $\Delta r = 0$ in the k-plane illustrating the pinch point formation

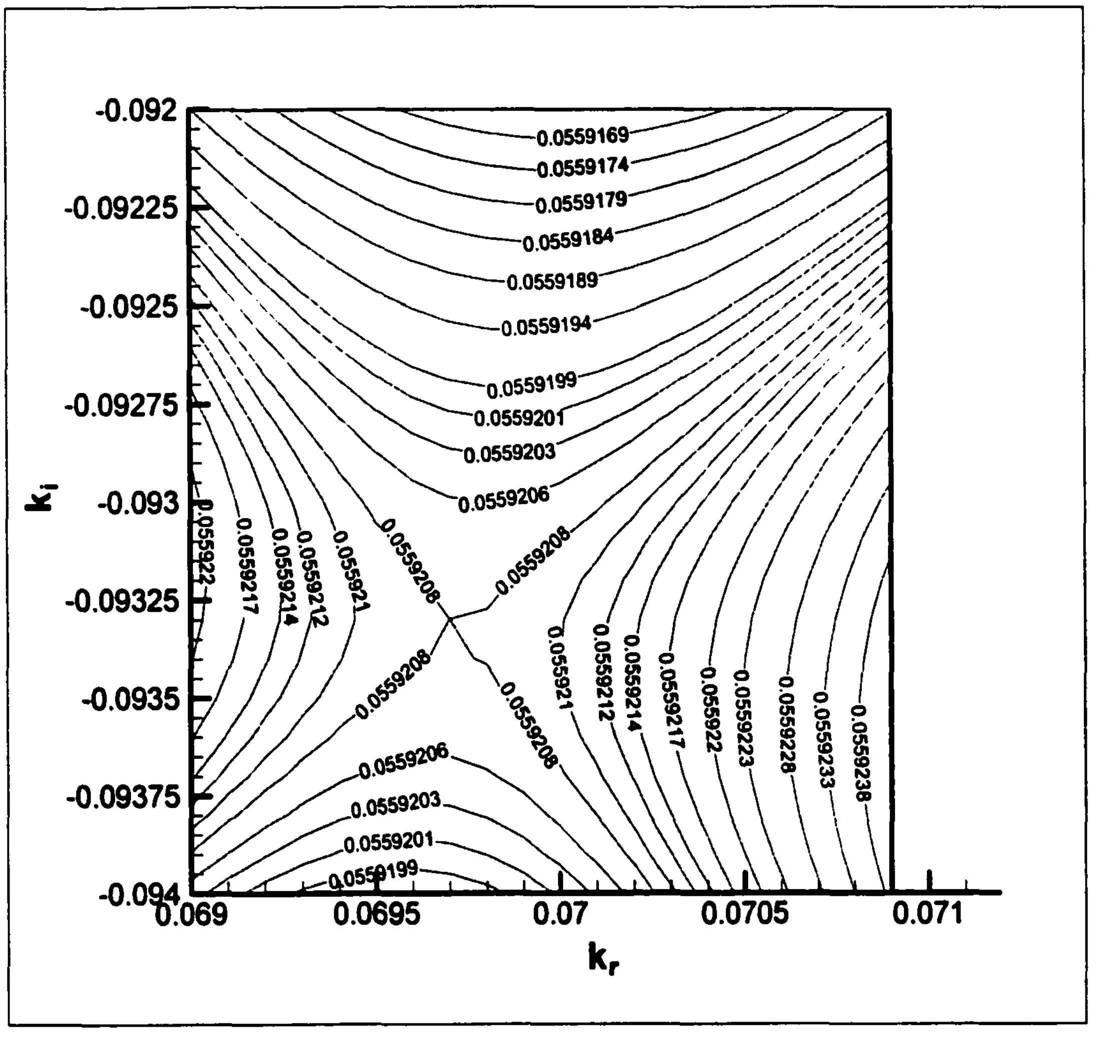

Figure A128: Contour plot of Ω_r for $R/\theta = 10$, $Fr = 5$, $\rho_j/\rho_\infty = 0.14$, $Sc = 0.6$, and $\Delta r = 0$ in the k-plane illustrating the pinch point formation

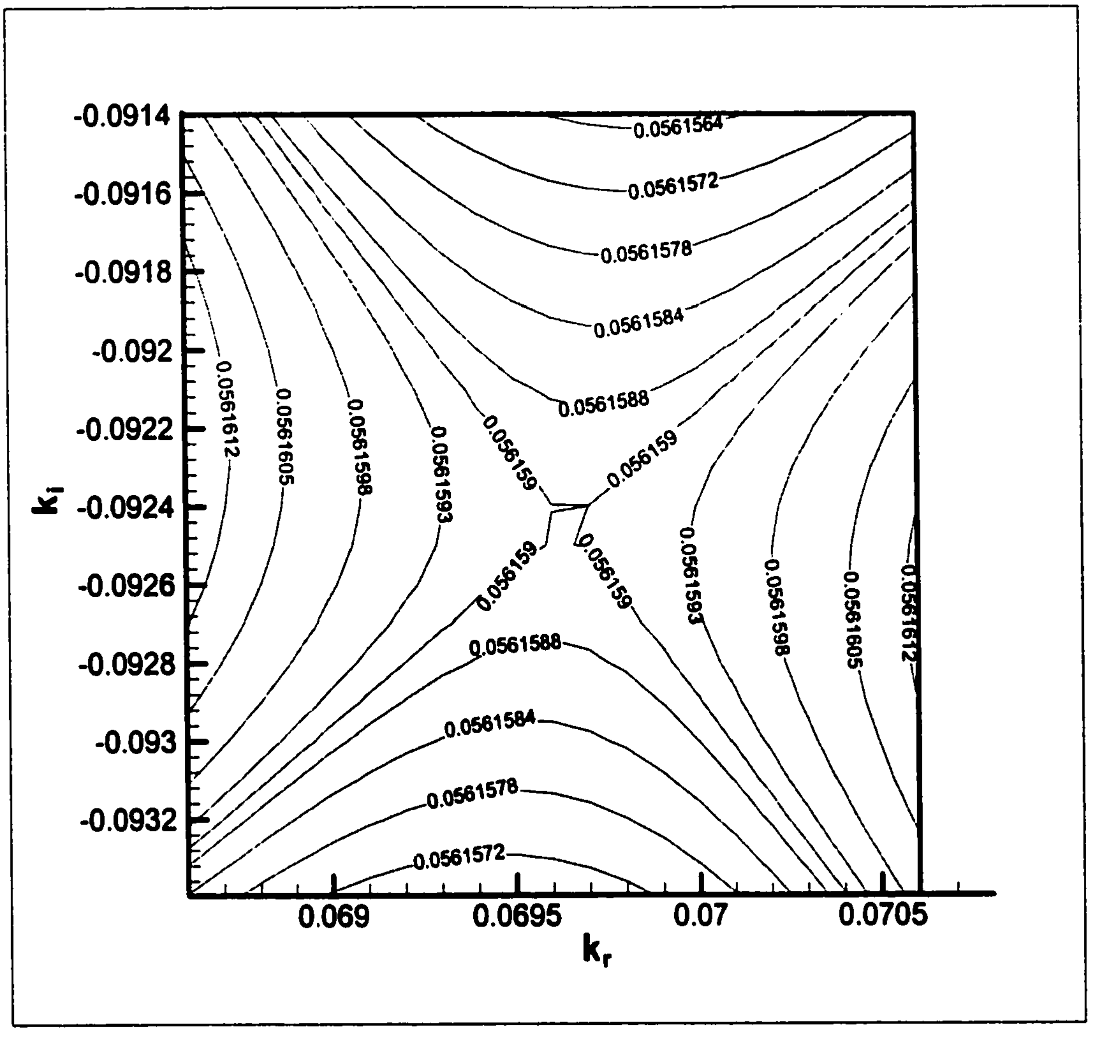

Figure A129: Contour plot of Ω_r for $R/\theta = 10$, $Fr = 2$, $\rho_j/\rho_\infty = 0.14$, $Sc = 0.6$, and $\Delta r = 0$ in the k-plane illustrating the pinch point formation

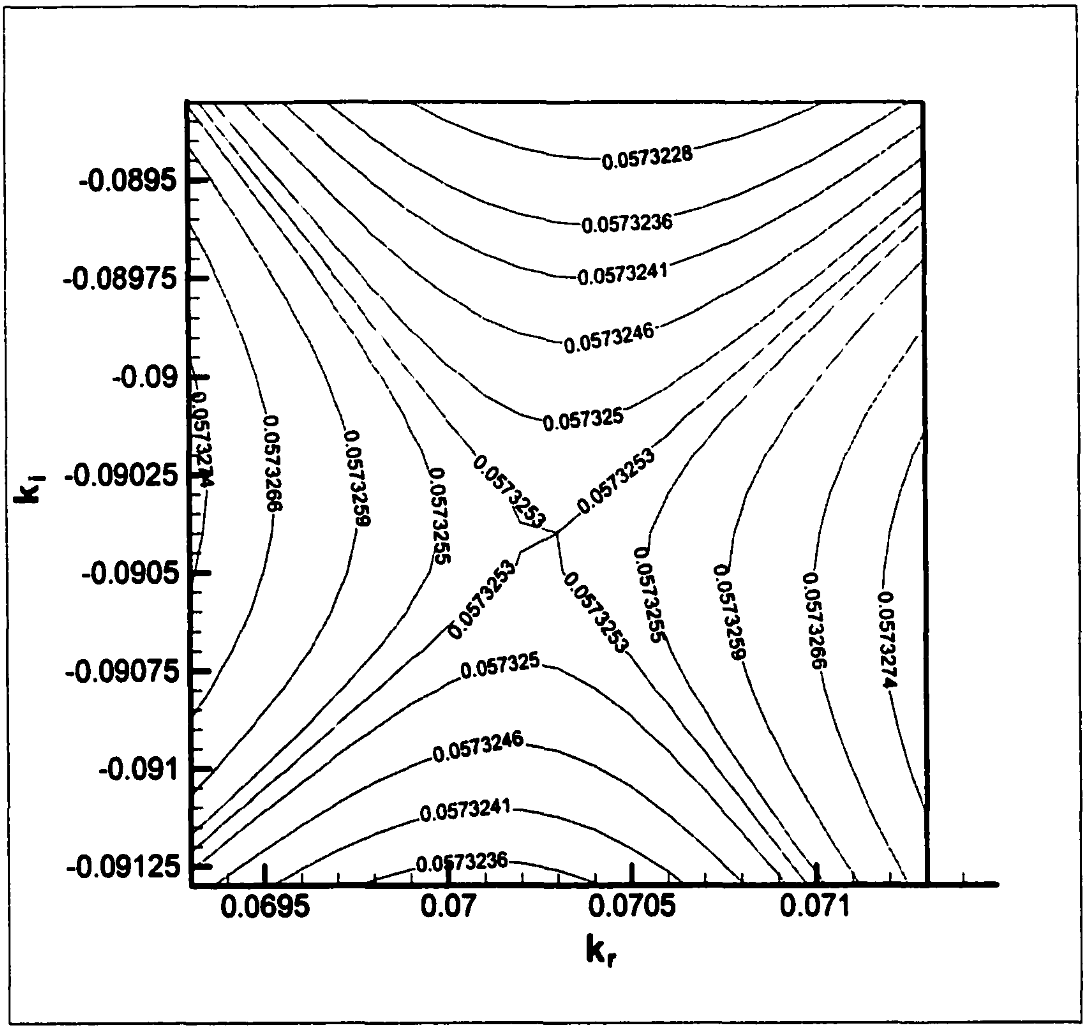

Figure A130: Contour plot of Ω_r for $R/\theta = 10$, $Fr = 1$, $\rho_j/\rho_\infty = 0.14$, $Sc = 0.6$, and $\Delta r = 0$ in the k-plane illustrating the pinch point formation

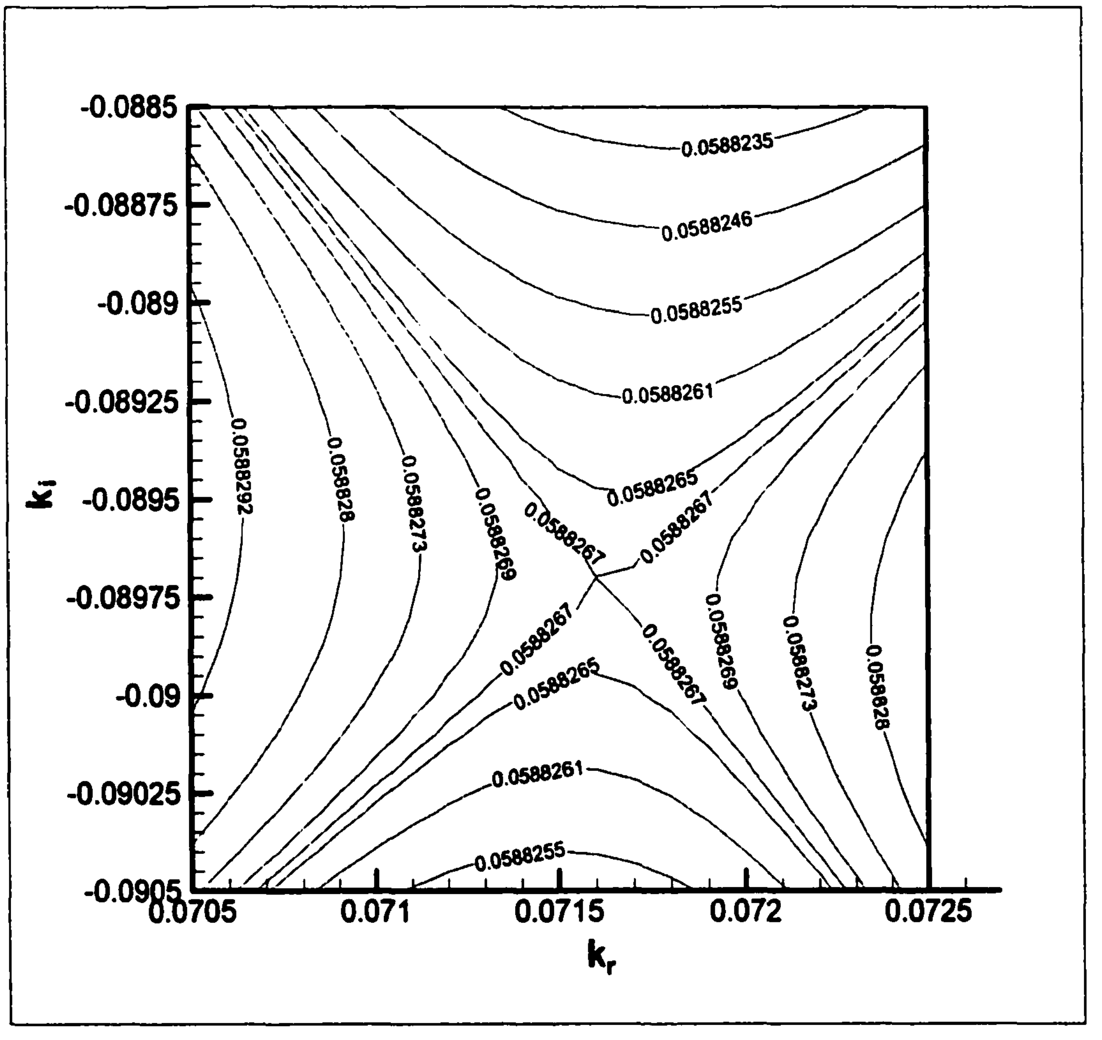

Figure A131: Contour plot of Ω_r for $R/\theta = 10$, $Fr = 0.75$, $\rho_j/\rho_\infty = 0.14$, $Sc = 0.6$, and $\Delta r = 0$ in the k-plane illustrating the pinch point formation

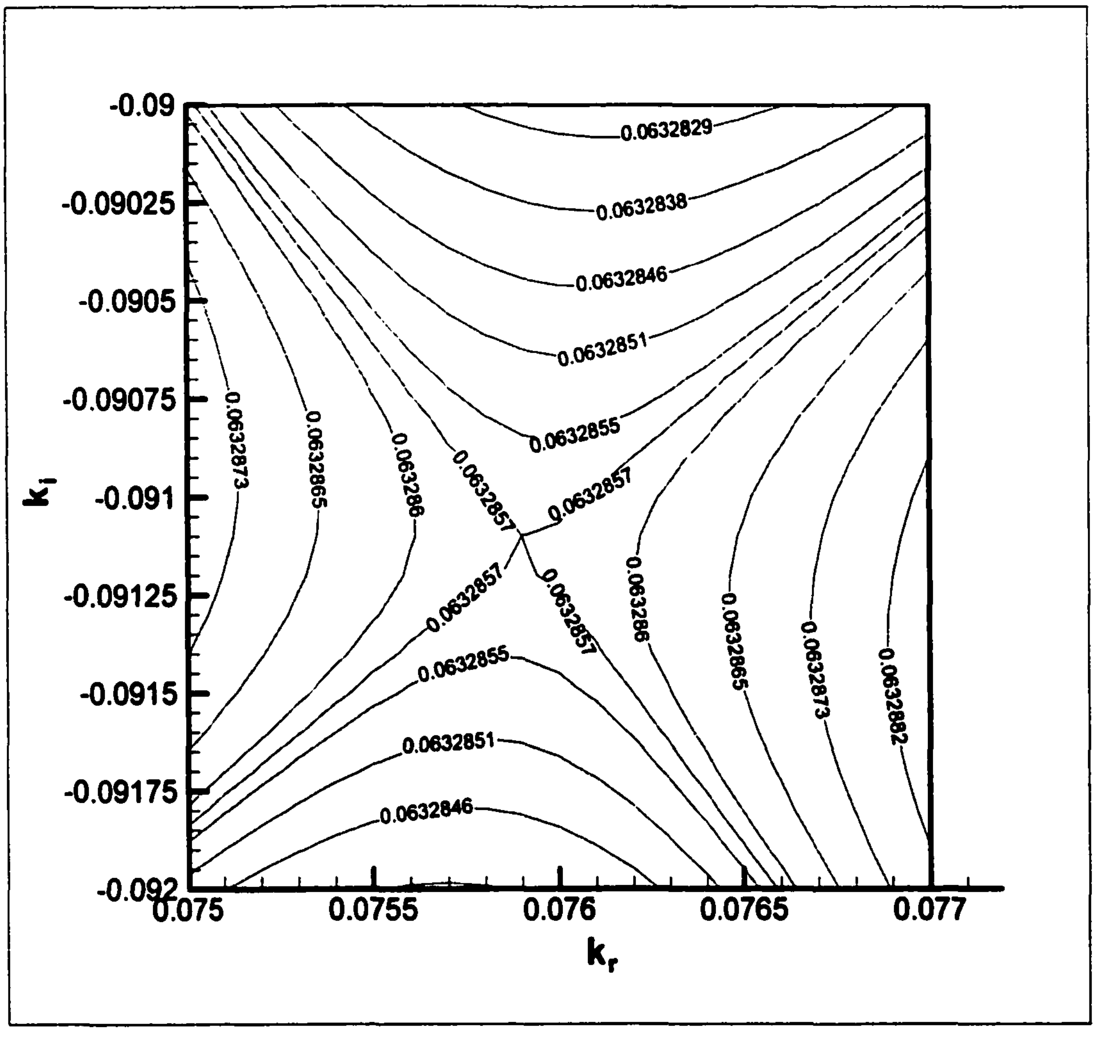

Figure A132: Contour plot of Ω_r for $R/\theta = 10$, $Fr = 0.5$, $\rho_j/\rho_\infty = 0.14$, $Sc = 0.6$, and $\Delta r = 0$ in the k-plane illustrating the pinch point formation

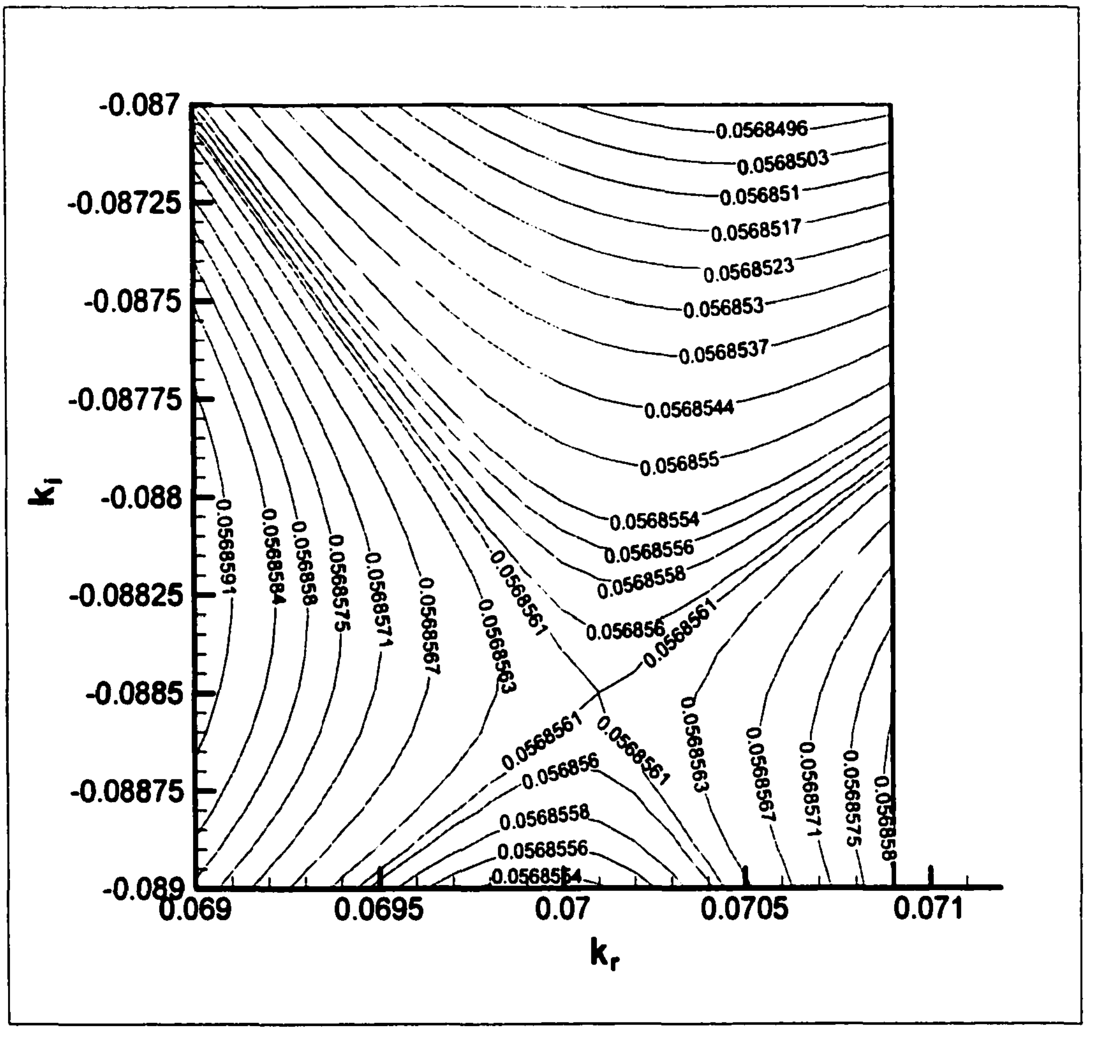

Figure A133: Contour plot of Ω_r for $R/\theta = 10$, $Fr = \infty$, $\rho_j/\rho_\infty = 0.14$, $Sc = 1.2$, and $\Delta r = 0$ in the k-plane illustrating the pinch point formation

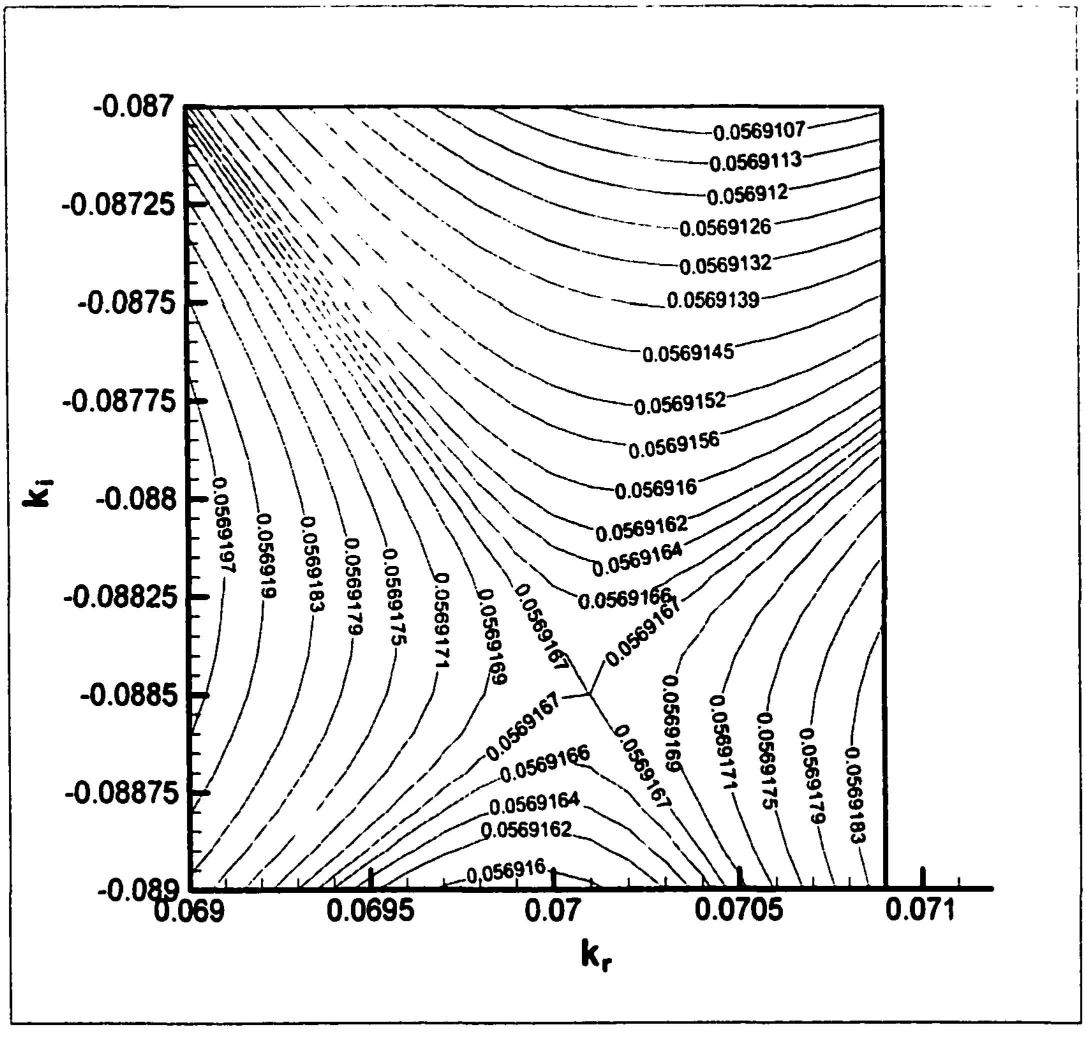

Figure A134: Contour plot of Ω_r for $R/\theta = 10$, $Fr = 10$, $\rho_j/\rho_\infty = 0.14$, $Sc = 1.2$, and $\Delta r = 0$ in the k-plane illustrating the pinch point formation

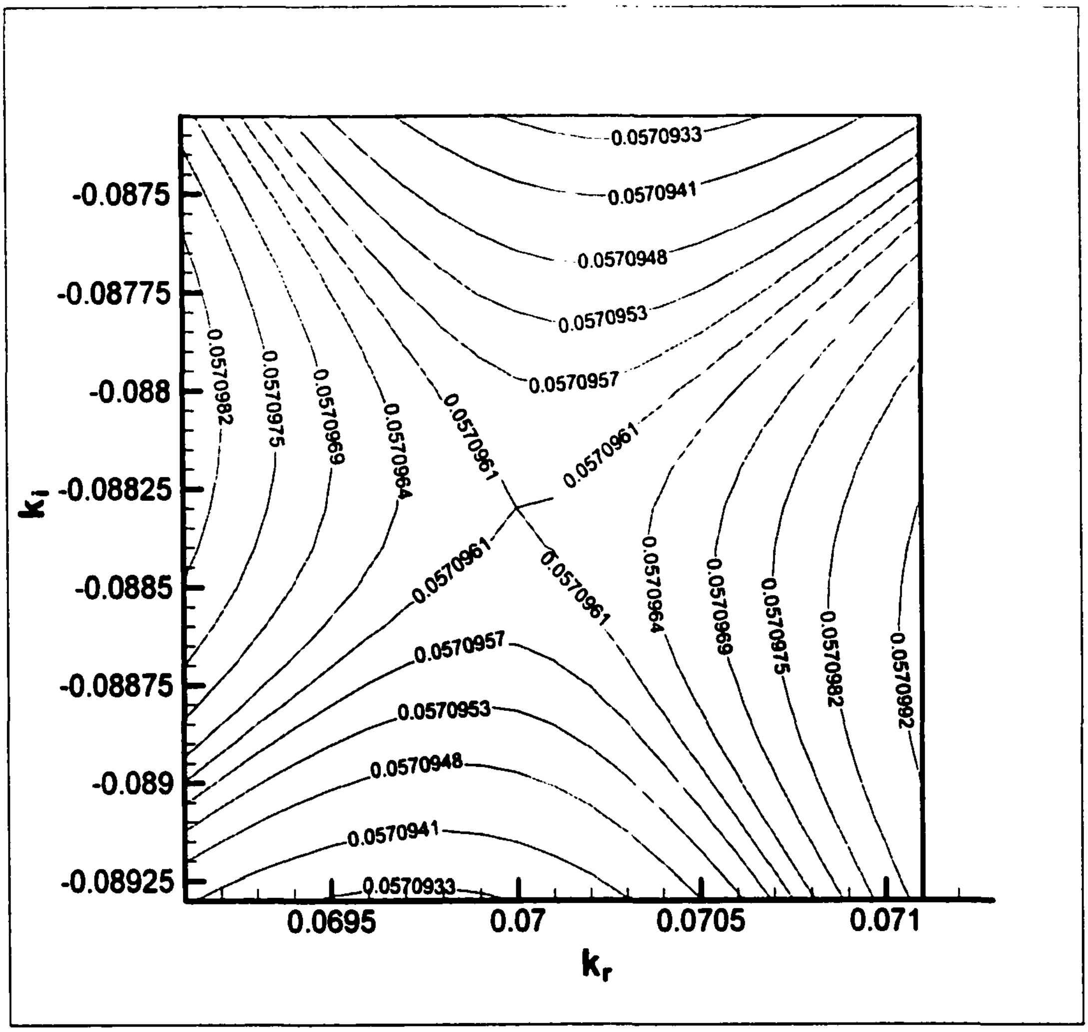

Figure A135: Contour plot of Ω_r for $R/\theta = 10$, $Fr = 5$, $\rho_j/\rho_\infty = 0.14$, $Sc = 1.2$, and $\Delta r = 0$ in the k-plane illustrating the pinch point formation

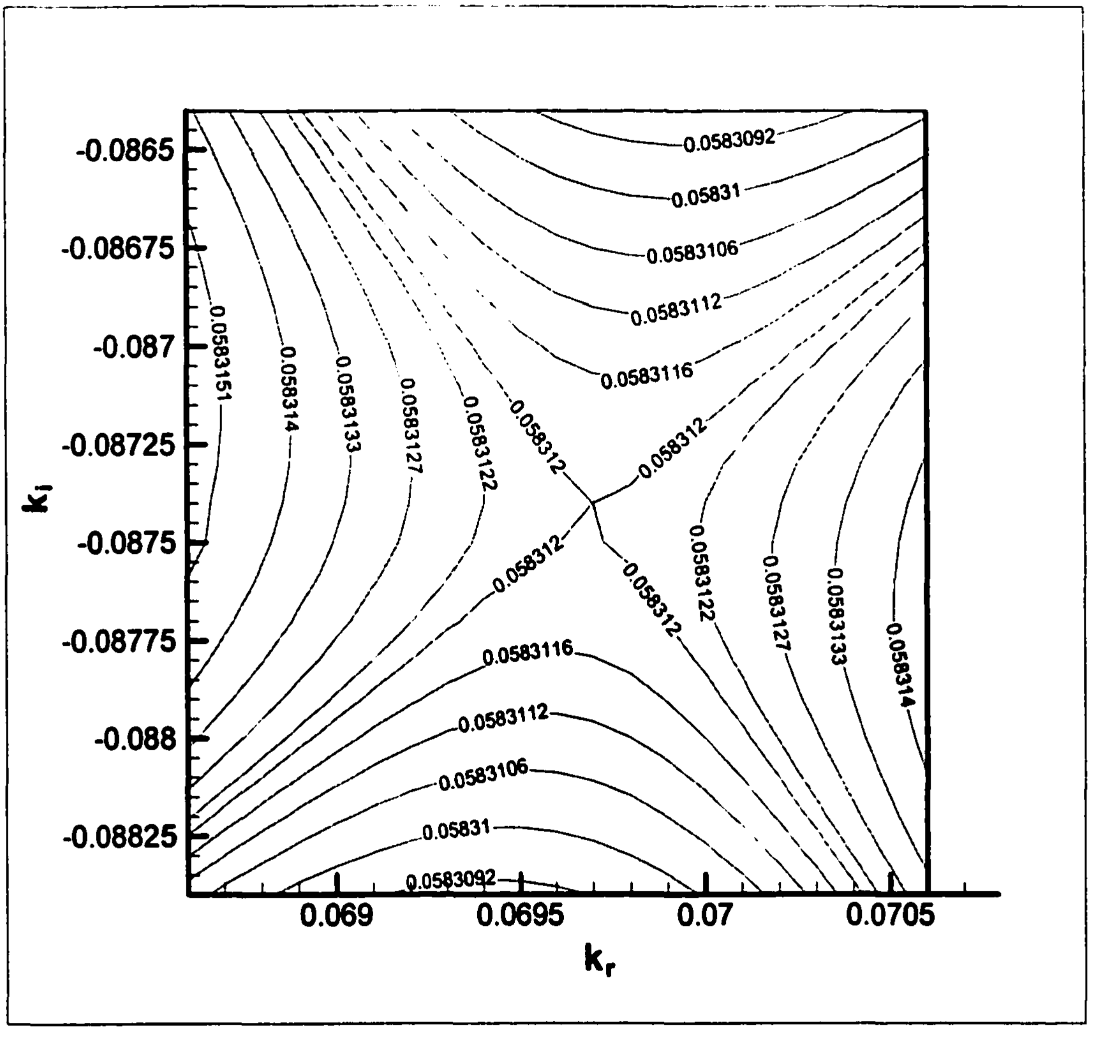

Figure A136: Contour plot of Ω_r for $R/\theta = 10$, $Fr = 2$, $\rho_j/\rho_\infty = 0.14$, $Sc = 1.2$, and $\Delta r = 0$ in the k-plane illustrating the pinch point formation

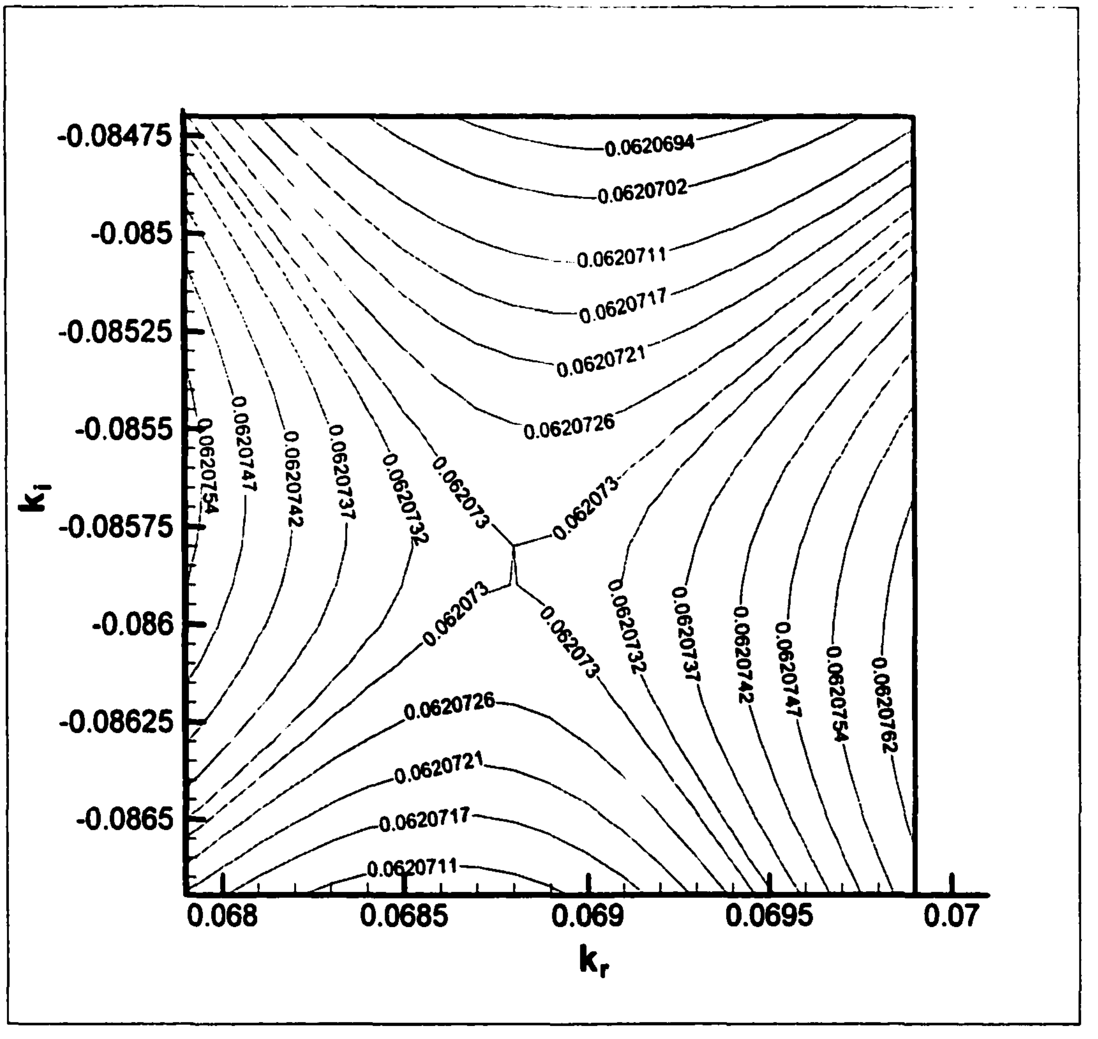

Figure A137: Contour plot of Ω_r for $R/\theta = 10$, $Fr = 1$, $\rho_j/\rho_\infty = 0.14$, $Sc = 1.2$, and $\Delta r = 0$ in the k-plane illustrating the pinch point formation

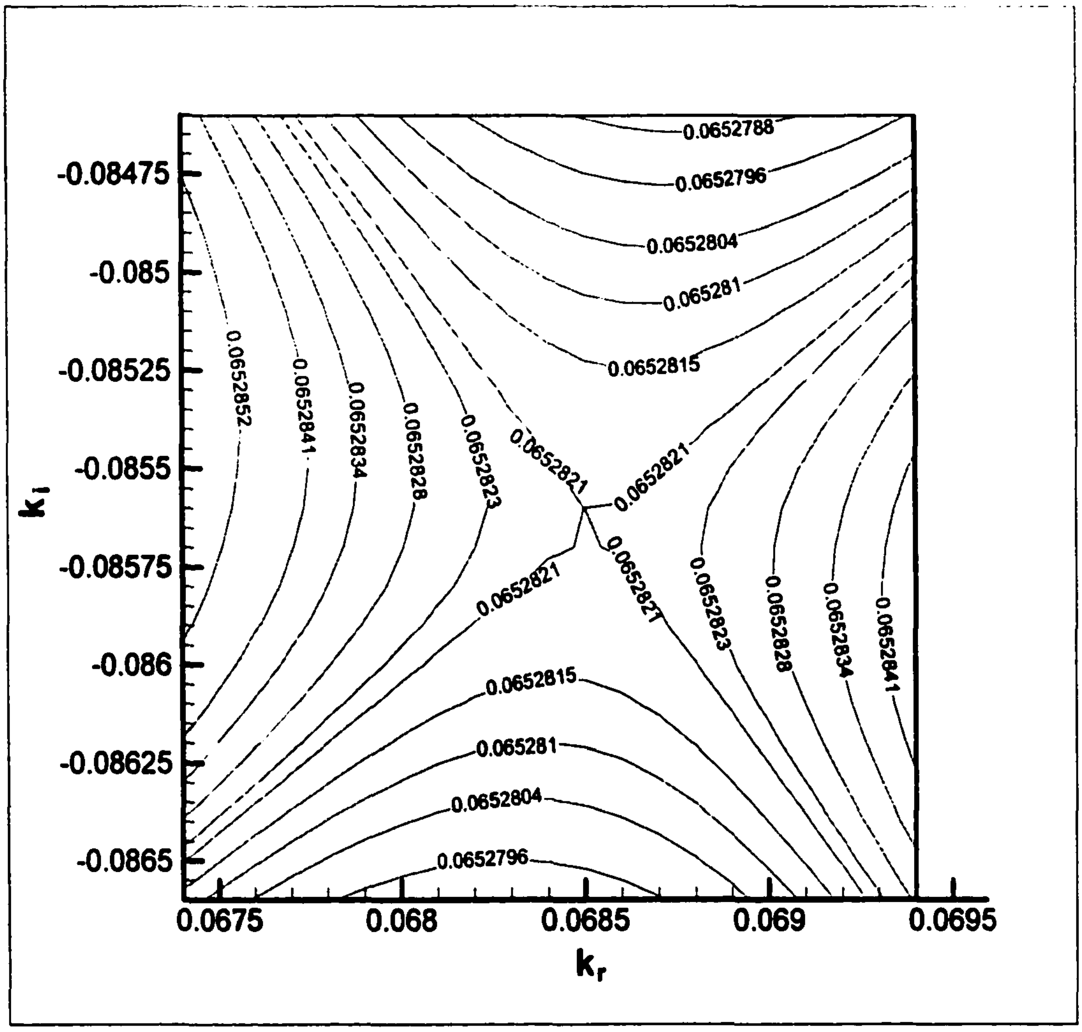

Figure A138: Contour plot of Ω_r for $R/\theta = 10$, $Fr = 0.75$, $\rho_j/\rho_\infty = 0.14$, $Sc = 1.2$, and $\Delta r = 0$ in the k-plane illustrating the pinch point formation

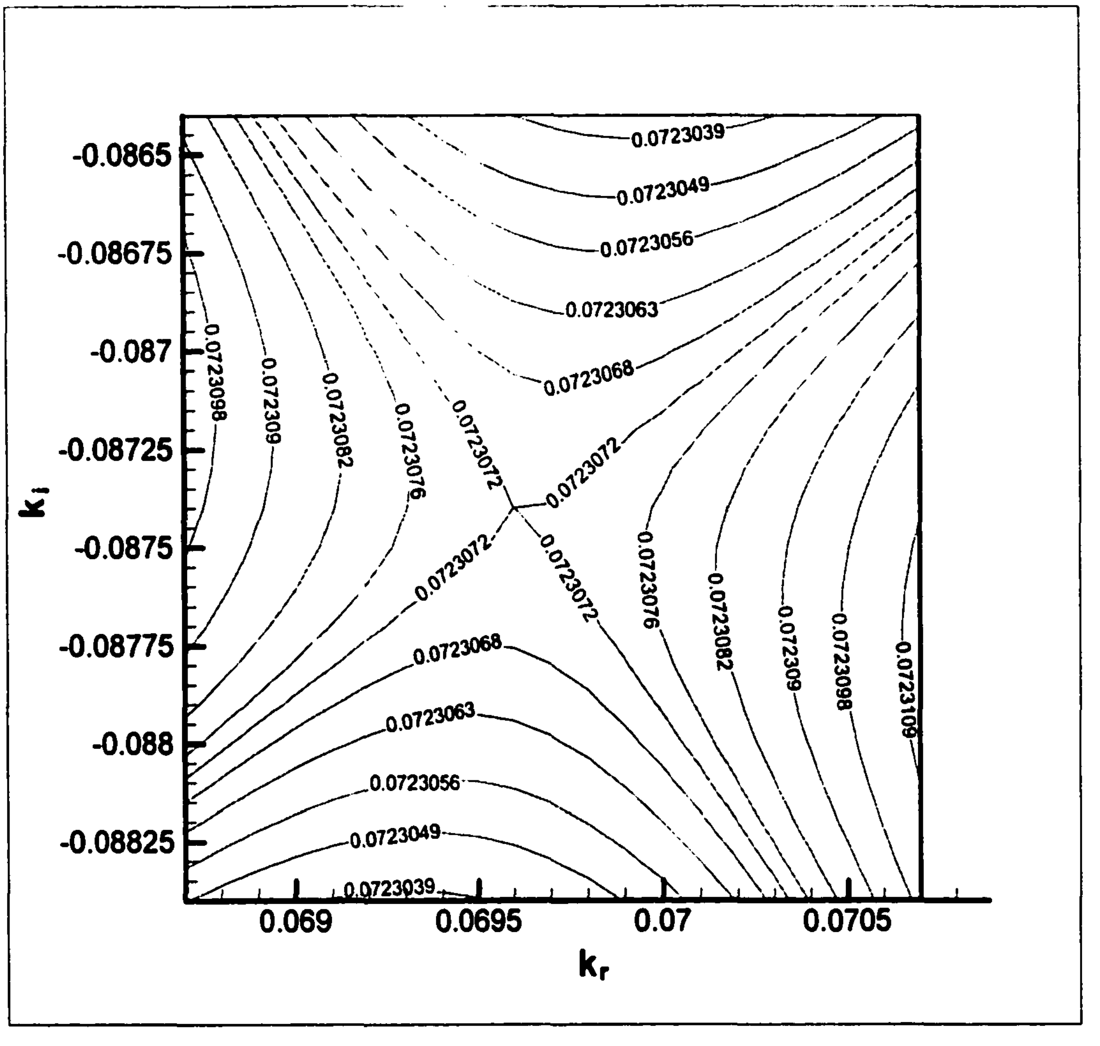

Figure A139: Contour plot of Ω_r for $R/\theta = 10$, $Fr = 0.5$, $\rho_j/\rho_\infty = 0.14$, $Sc = 1.2$, and $\Delta r = 0$ in the k-plane illustrating the pinch point formation

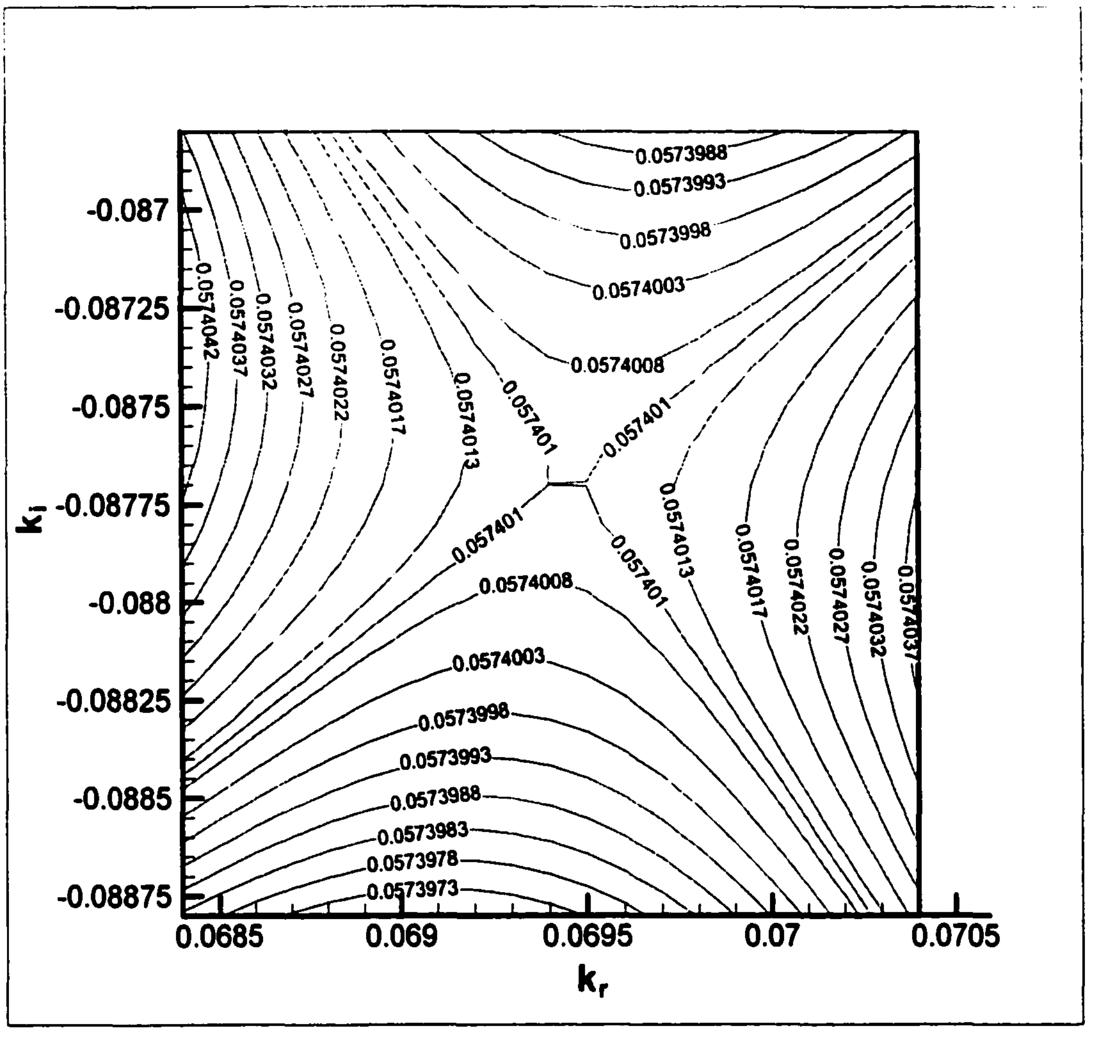

Figure A140: Contour plot of Ω_r for $R/\theta = 10$, $Fr = \infty$, $\rho_j/\rho_\infty = 0.14$, $Sc = 1.43$, and $\Delta r = 0$ in the k-plane illustrating the pinch point formation

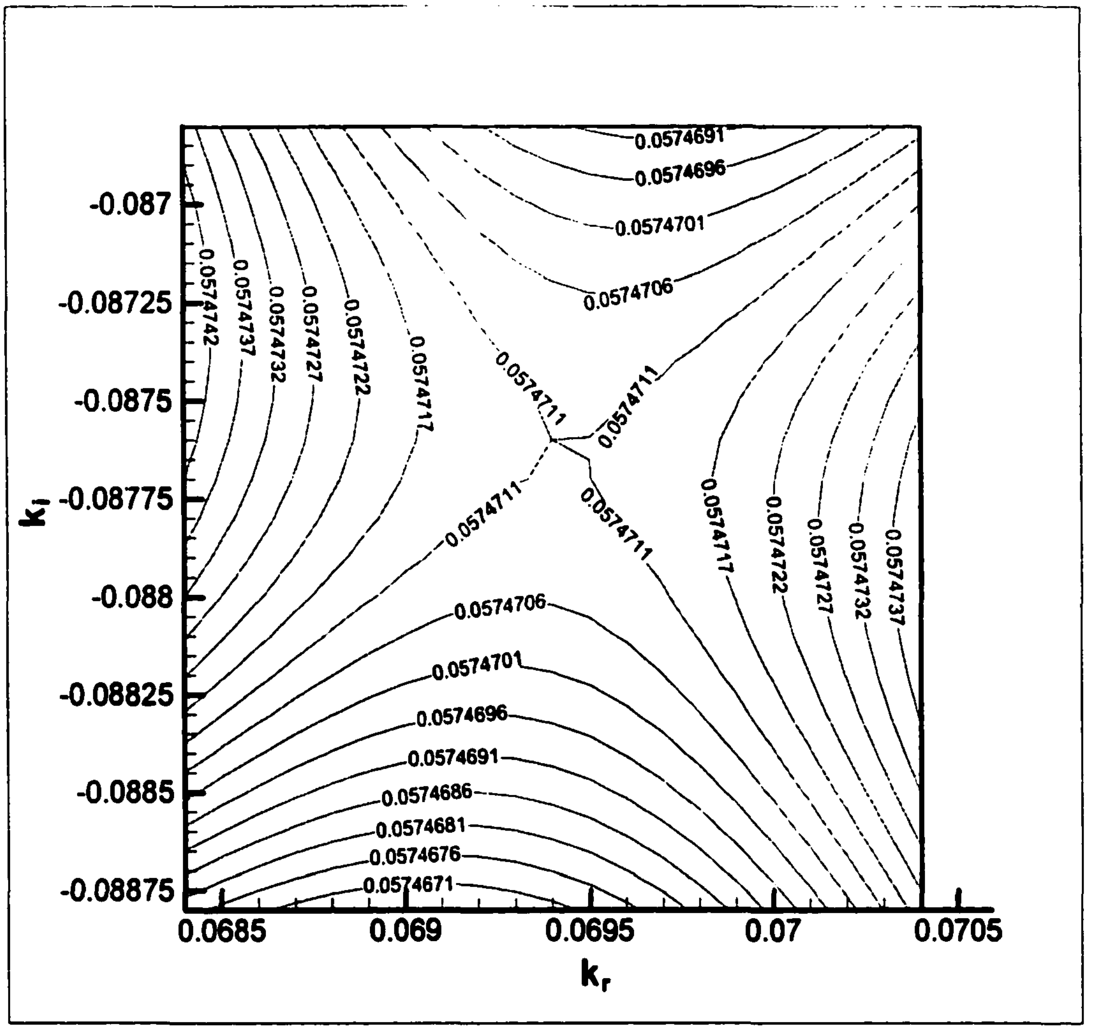

Figure A141: Contour plot of Ω_r for $R/\theta = 10$, $Fr = 10$, $\rho_j/\rho_\infty = 0.14$, $Sc = 1.43$, and $\Delta r = 0$ in the k-plane illustrating the pinch point formation

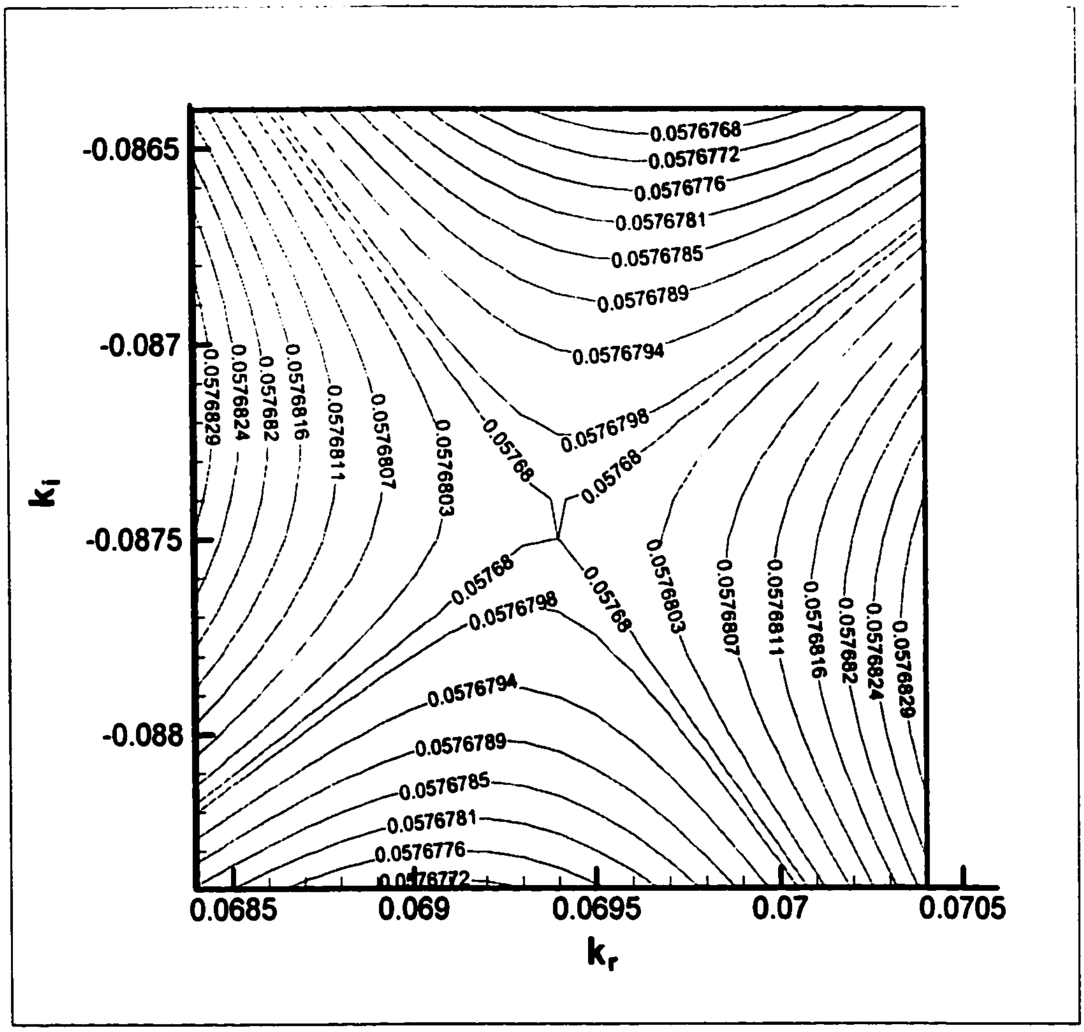

Figure A142: Contour plot of Ω_r for $R/\theta = 10$, $Fr = 5$, $\rho_j/\rho_\infty = 0.14$, $Sc = 1.43$, and $\Delta r = 0$ in the k-plane illustrating the pinch point formation

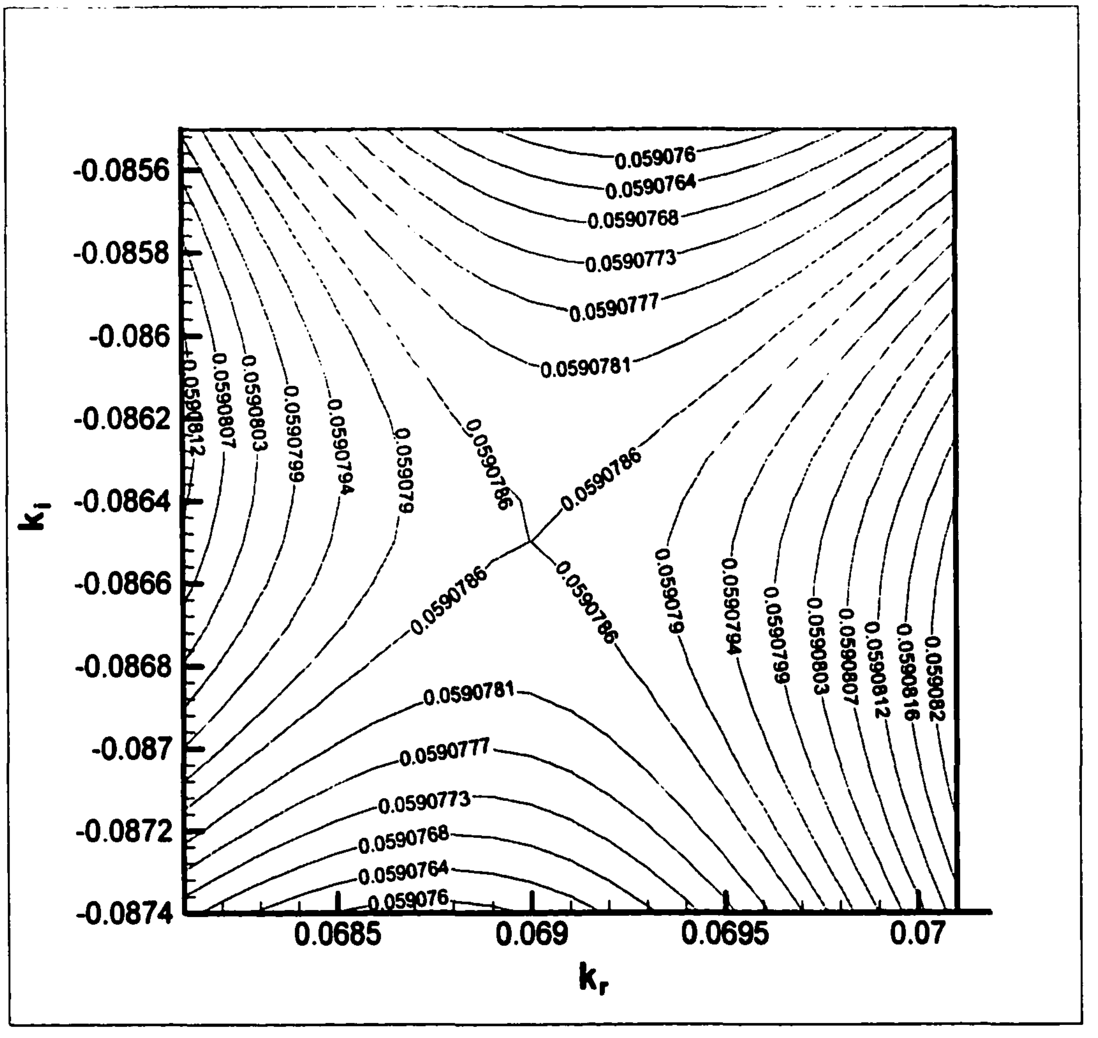

Figure A143: Contour plot of Ω_r for $R/\theta = 10$, $Fr = 2$, $\rho_j/\rho_\infty = 0.14$, $Sc = 1.43$, and $\Delta r = 0$ in the k-plane illustrating the pinch point formation

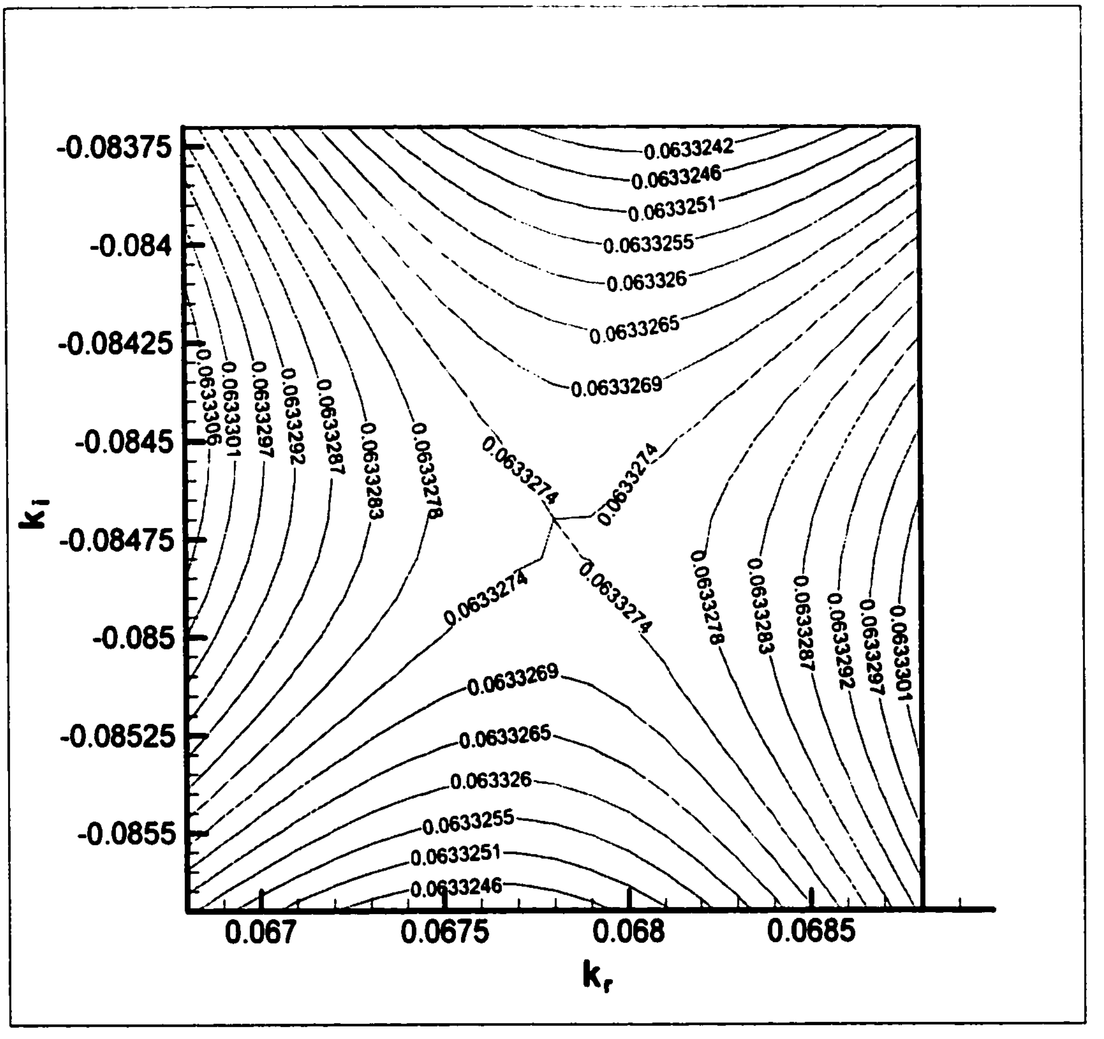

Figure A144: Contour plot of Ω_r for $R/\theta = 10$, $Fr = 1$, $\rho_j/\rho_\infty = 0.14$, $Sc = 1.43$, and $\Delta r = 0$ in the k-plane illustrating the pinch point formation

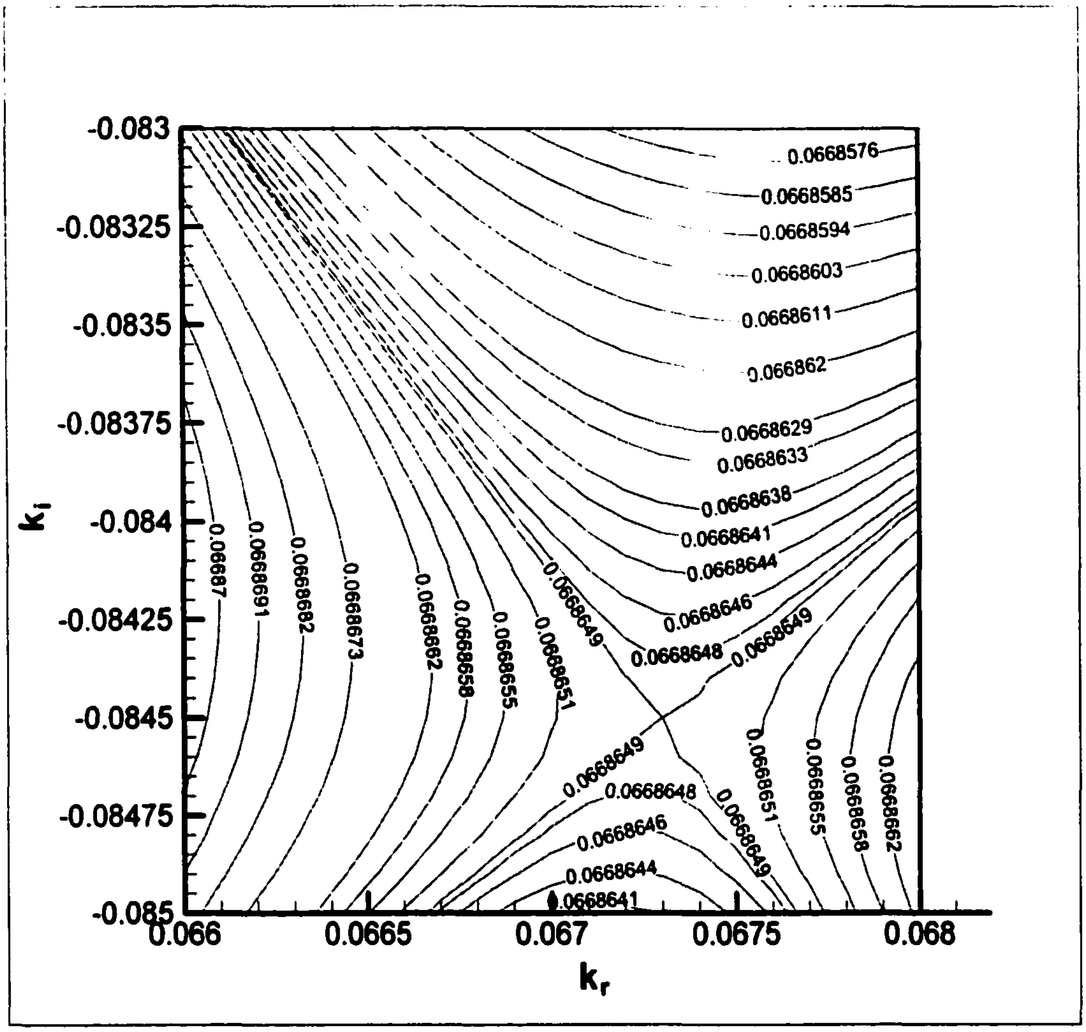

Figure A145: Contour plot of Ω_r for $R/\theta = 10$, $Fr = 0.75$, $\rho_j/\rho_\infty = 0.14$, $Sc = 1.43$, and $\Delta r = 0$ in the k-plane illustrating the pinch point formation

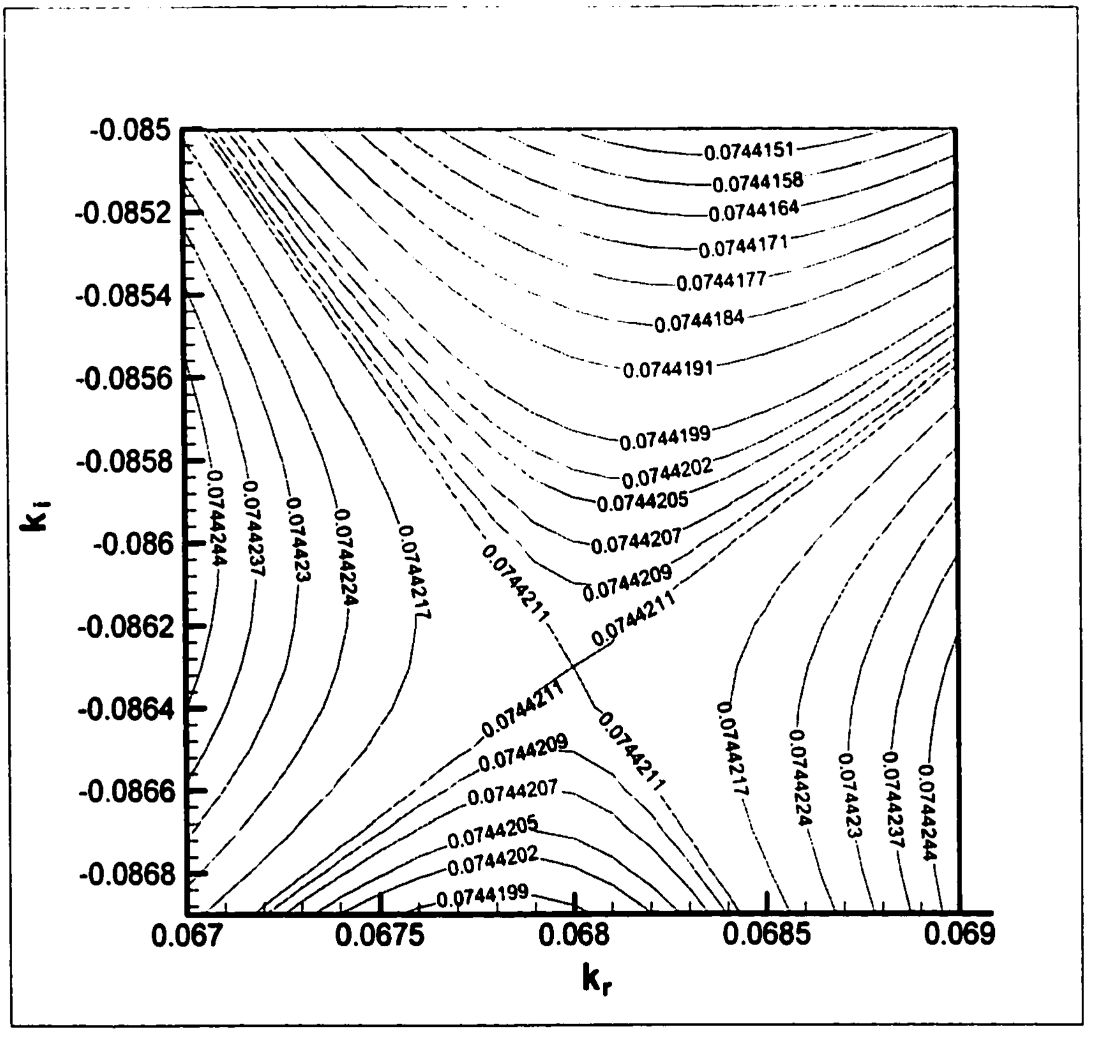

Figure A146: Contour plot of Ω_r for $R/\theta = 10$, $Fr = 0.5$, $\rho_j/\rho_\infty = 0.14$, $Sc = 1.43$, and $\Delta r = 0$ in the k-plane illustrating the pinch point formation

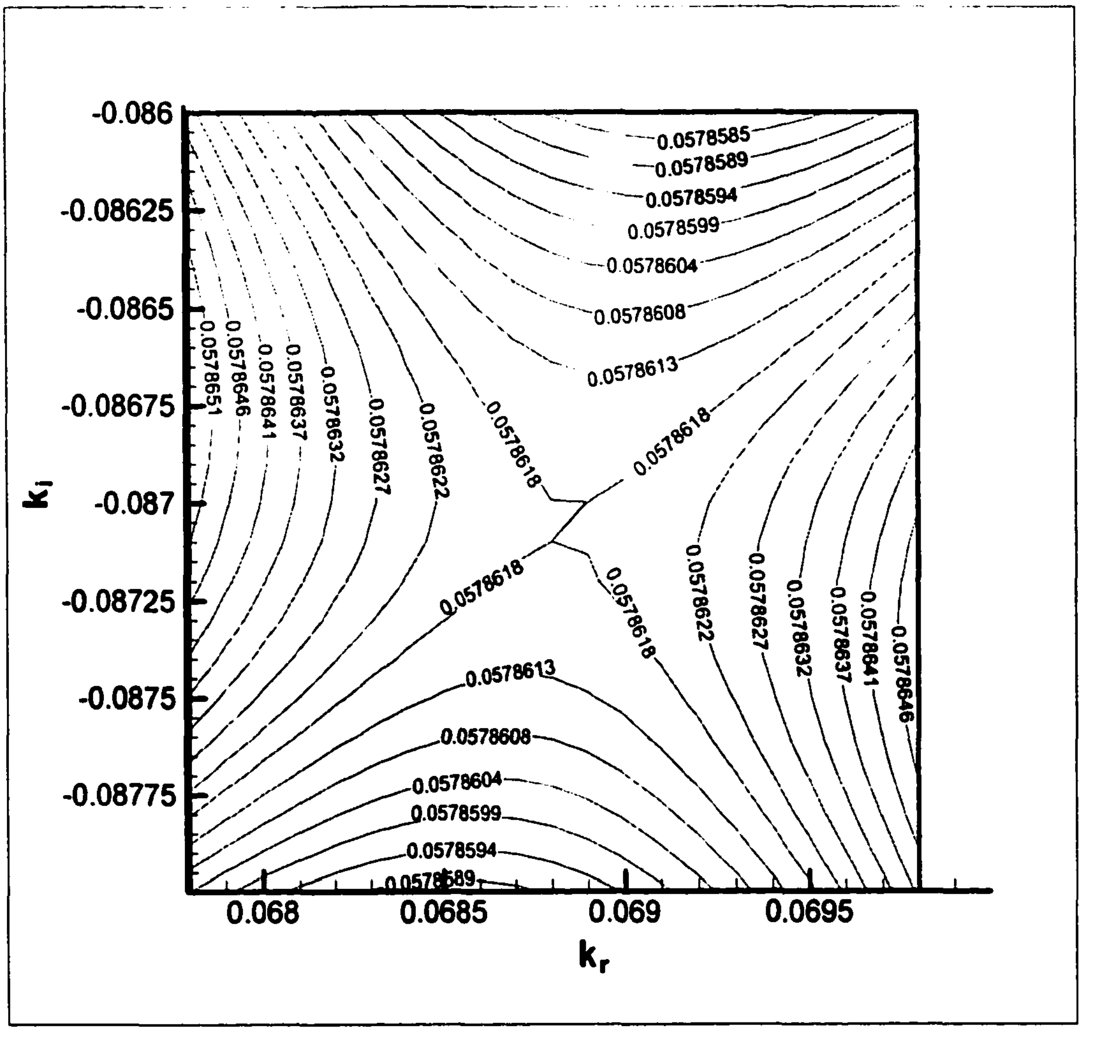

Figure A147: Contour plot of Ω_r for $R/\theta = 10$, $Fr = \infty$, $\rho_j/\rho_\infty = 0.14$, $Sc = 1.64$, and $\Delta r = 0$ in the k-plane illustrating the pinch point formation

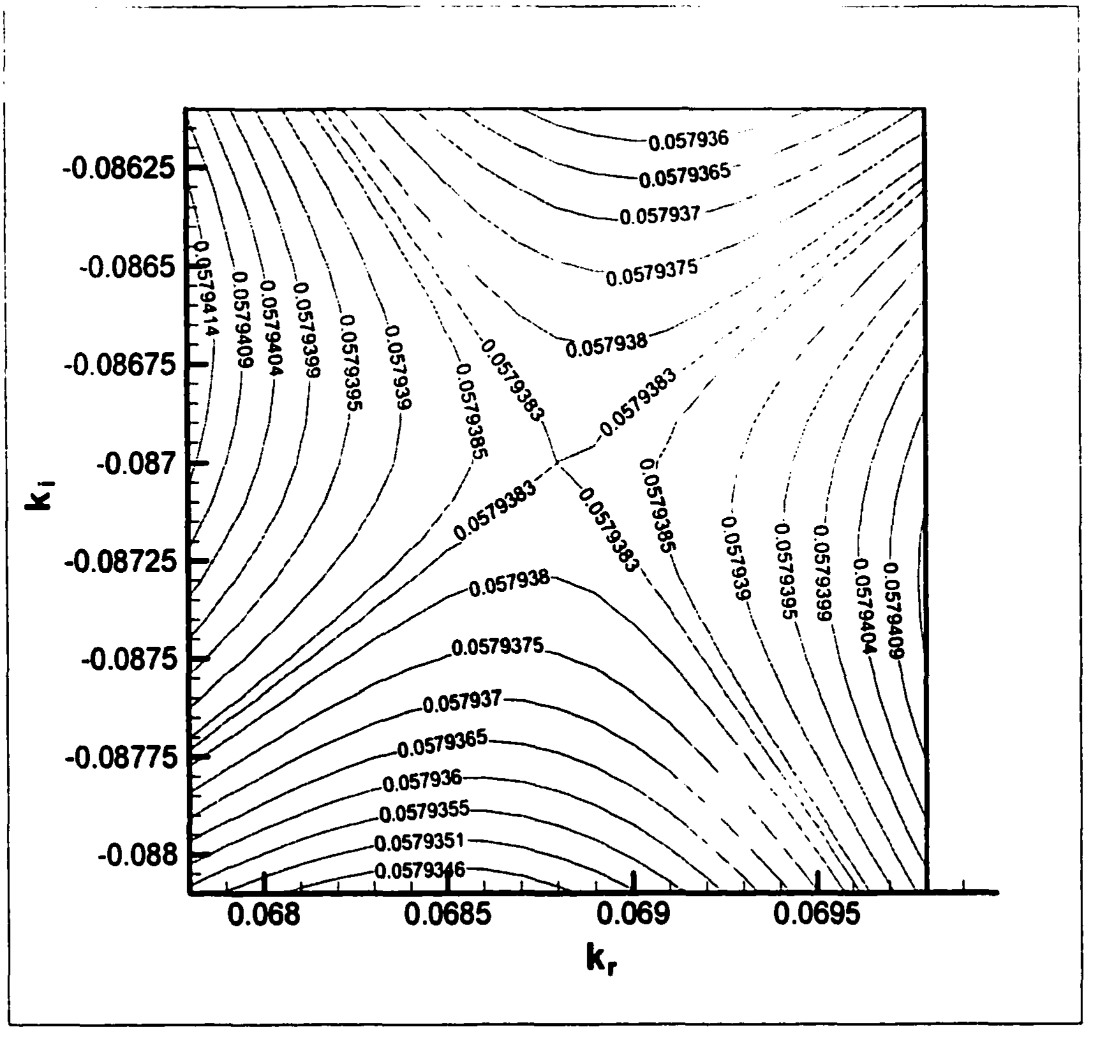

Figure A148: Contour plot of Ω_r for $R/\theta = 10$, $Fr = 10$, $\rho_j/\rho_\infty = 0.14$, $Sc = 1.64$, and $\Delta r = 0$ in the k-plane illustrating the pinch point formation

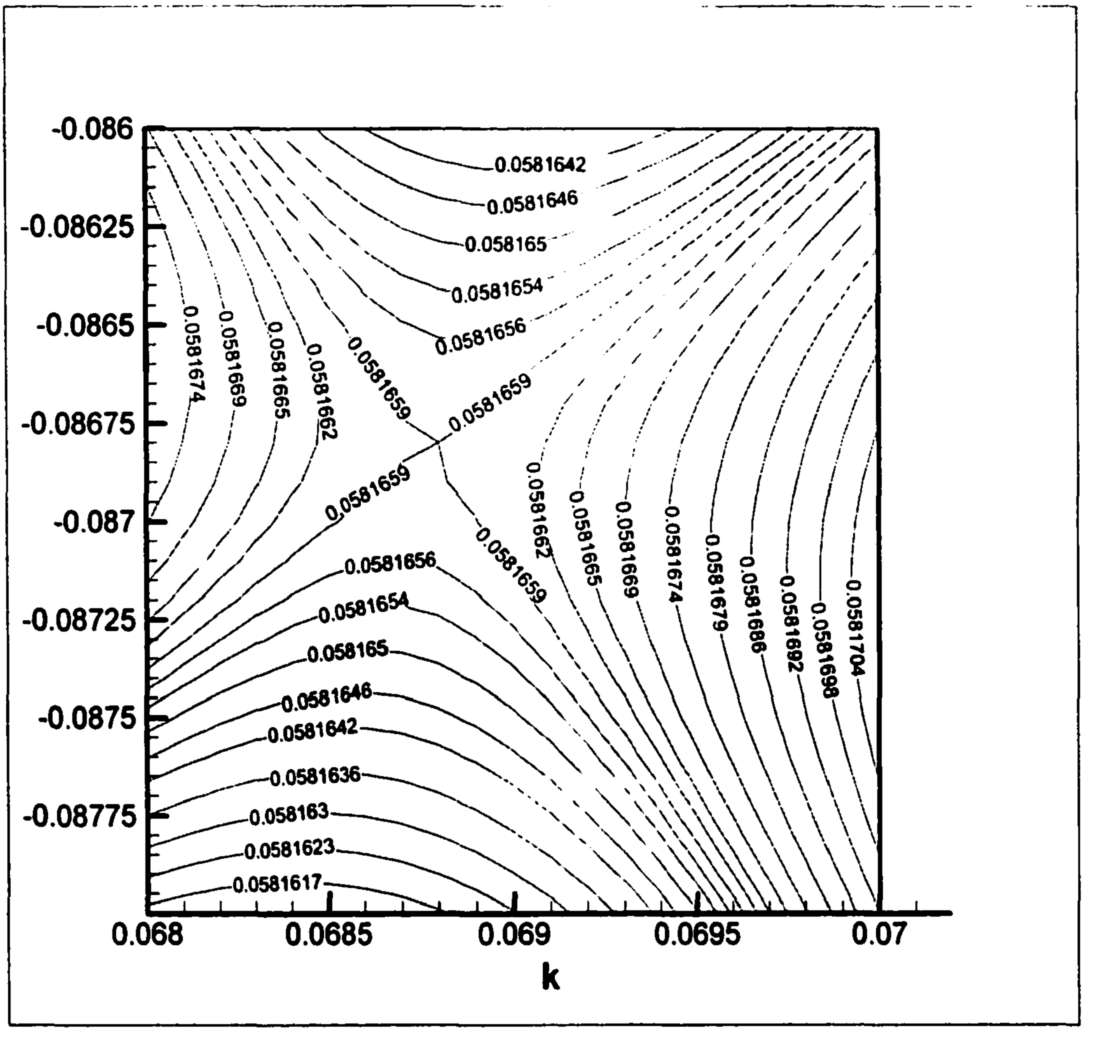

Figure A149: Contour plot of Ω_r for $R/\theta = 10$, $Fr = 5$, $\rho_j/\rho_\infty = 0.14$, $Sc = 1.64$, and $\Delta r = 0$ in the k-plane illustrating the pinch point formation

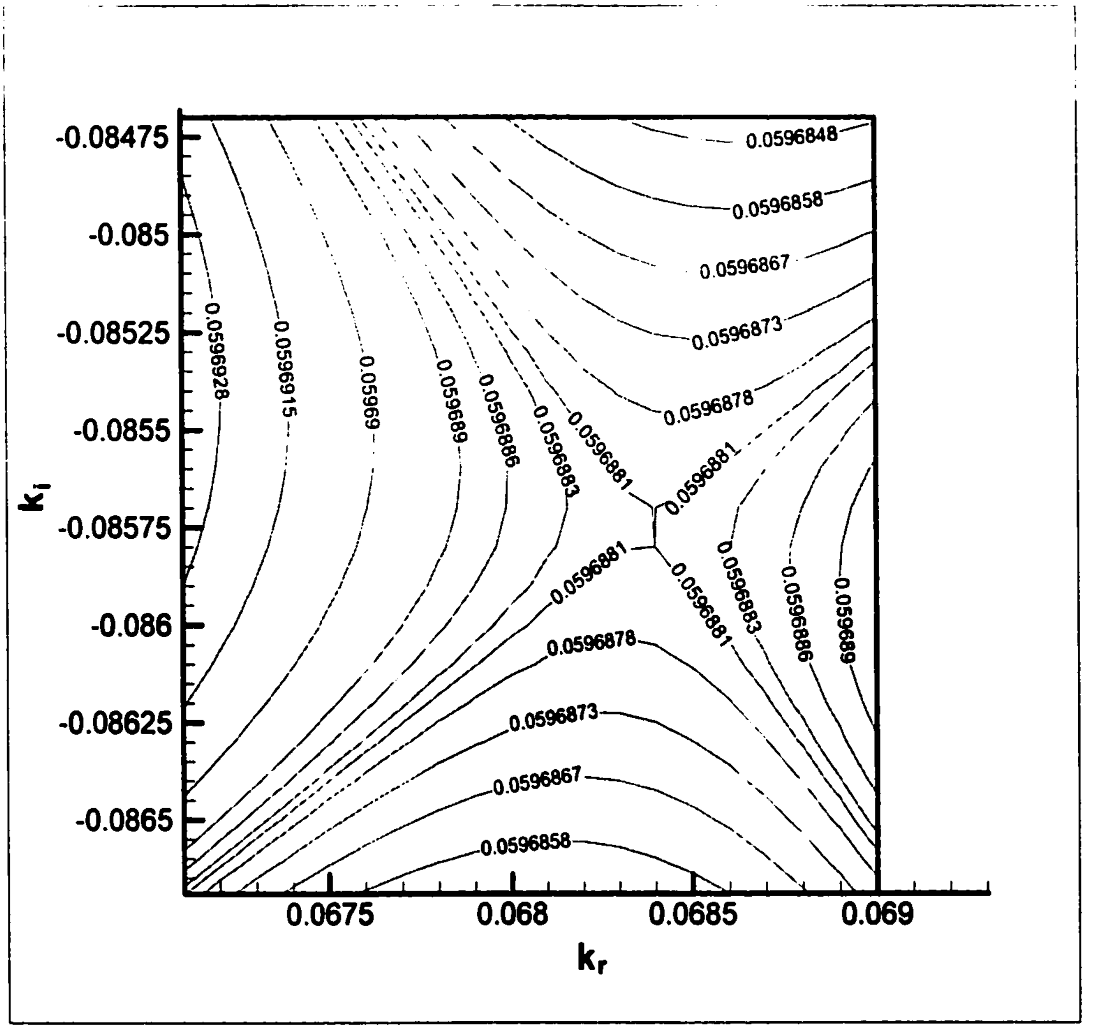

Figure A150: Contour plot of Ω_r for $R/\theta = 10$, $Fr = 2$, $\rho_j/\rho_\infty = 0.14$, $Sc = 1.64$, and $\Delta r = 0$ in the k-plane illustrating the pinch point formation

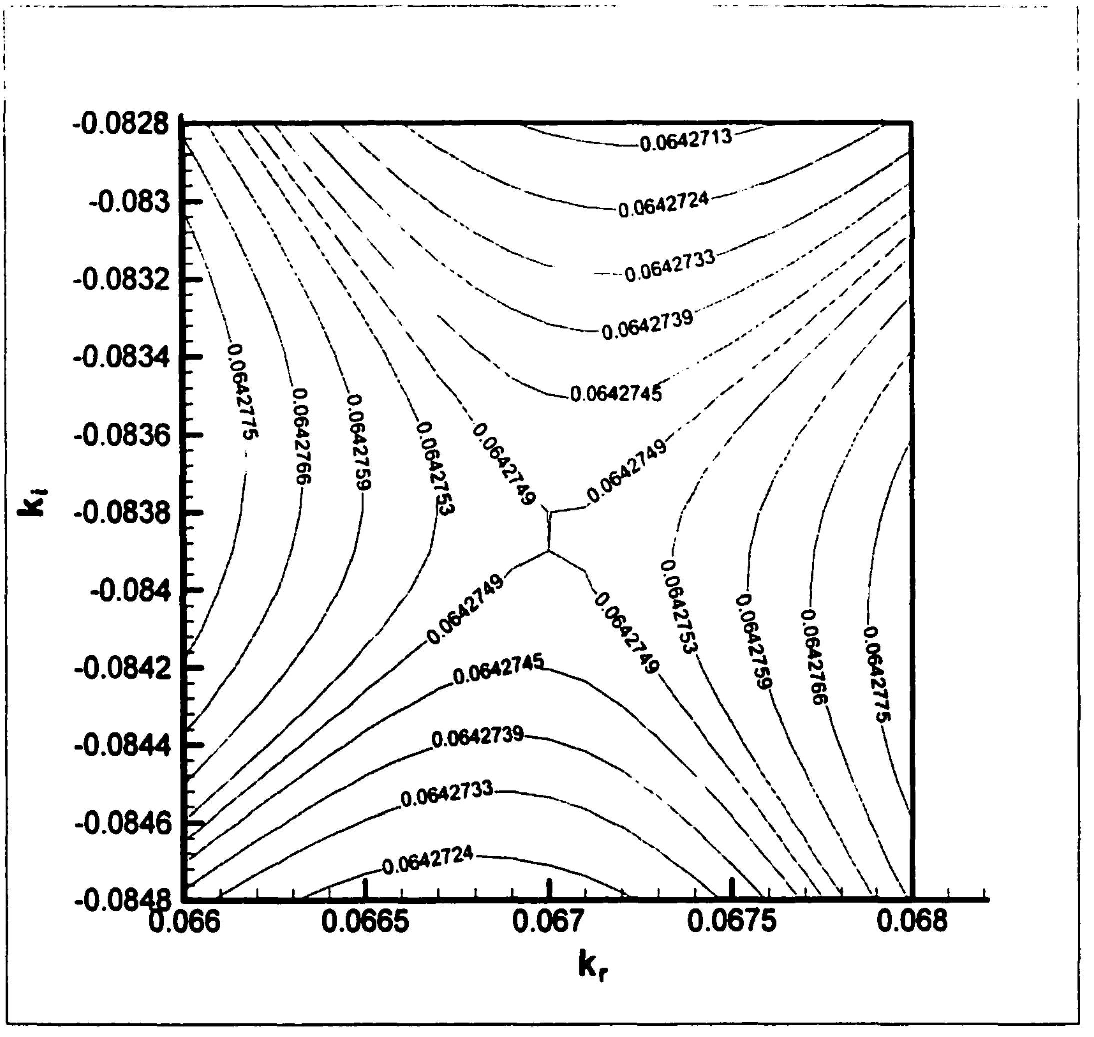

Figure A151: Contour plot of Ω_r for $R/\theta = 10$, $Fr = 1$, $\rho_j/\rho_\infty = 0.14$, $Sc = 1.64$, and $\Delta r = 0$ in the k-plane illustrating the pinch point formation

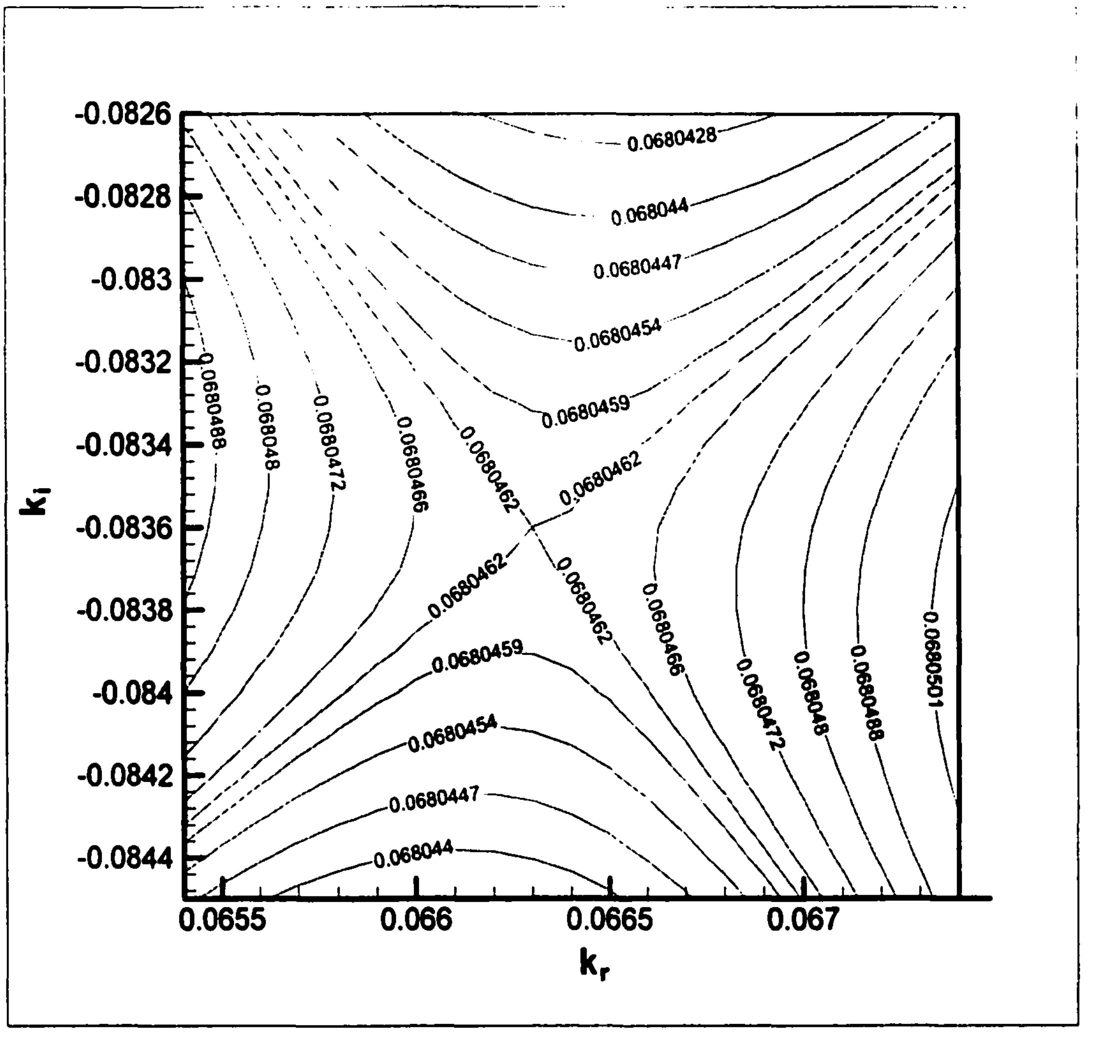

Figure A152: Contour plot of Ω_r for $R/\theta = 10$, $Fr = 0.75$, $\rho_j/\rho_\infty = 0.14$, $Sc = 1.64$, and $\Delta r = 0$ in the k-plane illustrating the pinch point formation

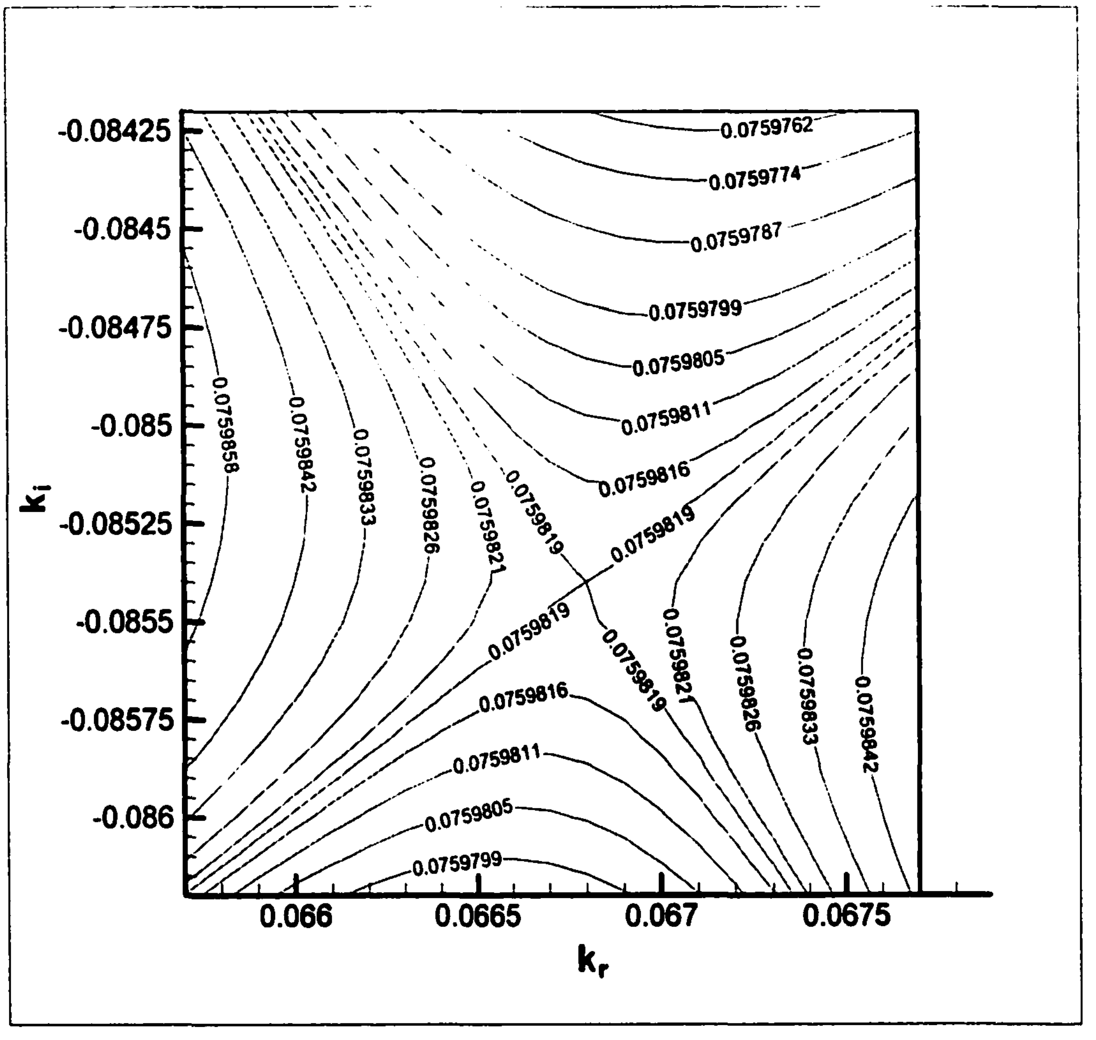

Figure A153: Contour plot of Ω_r for $R/\theta = 10$, $Fr = 0.5$, $\rho_j/\rho_\infty = 0.14$, $Sc = 1.64$, and $\Delta r = 0$ in the k-plane illustrating the pinch point formation

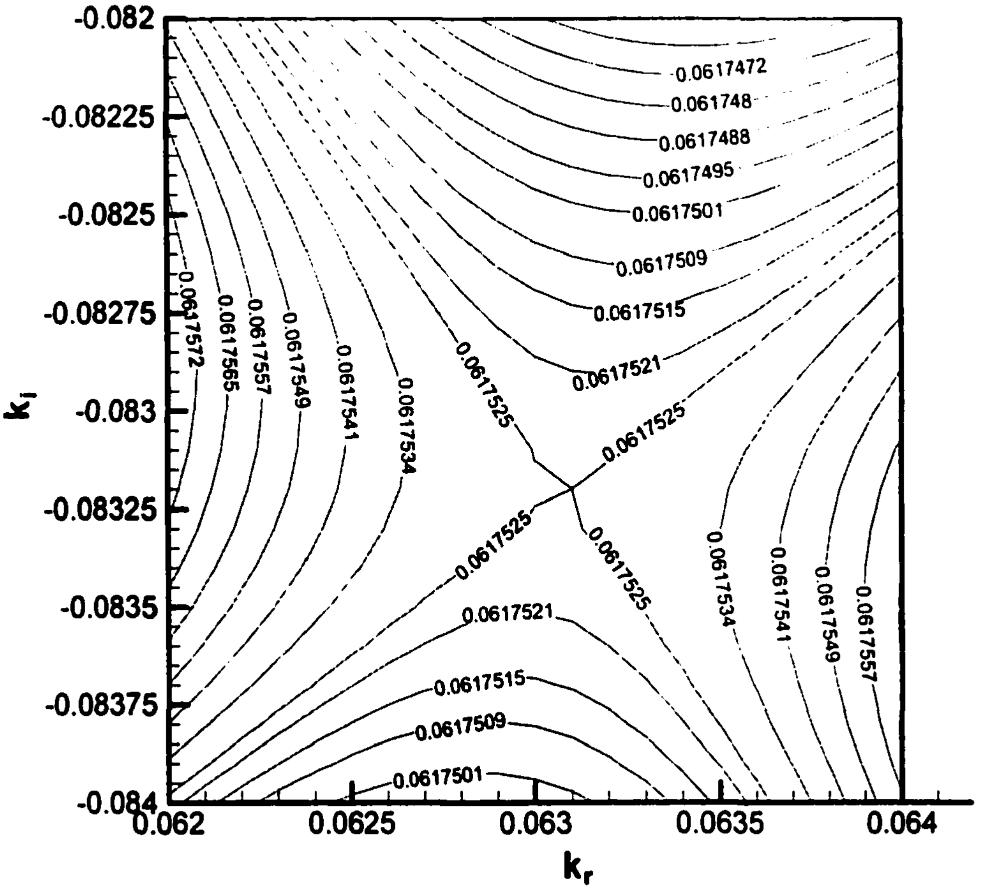

Figure A154: Contour plot of Ω_r for $R/\theta = 10$, $Fr = \infty$, $\rho_j/\rho_\infty = 0.14$, $Sc = 5$, and $\Delta r = 0$ in the k-plane illustrating the pinch point formation

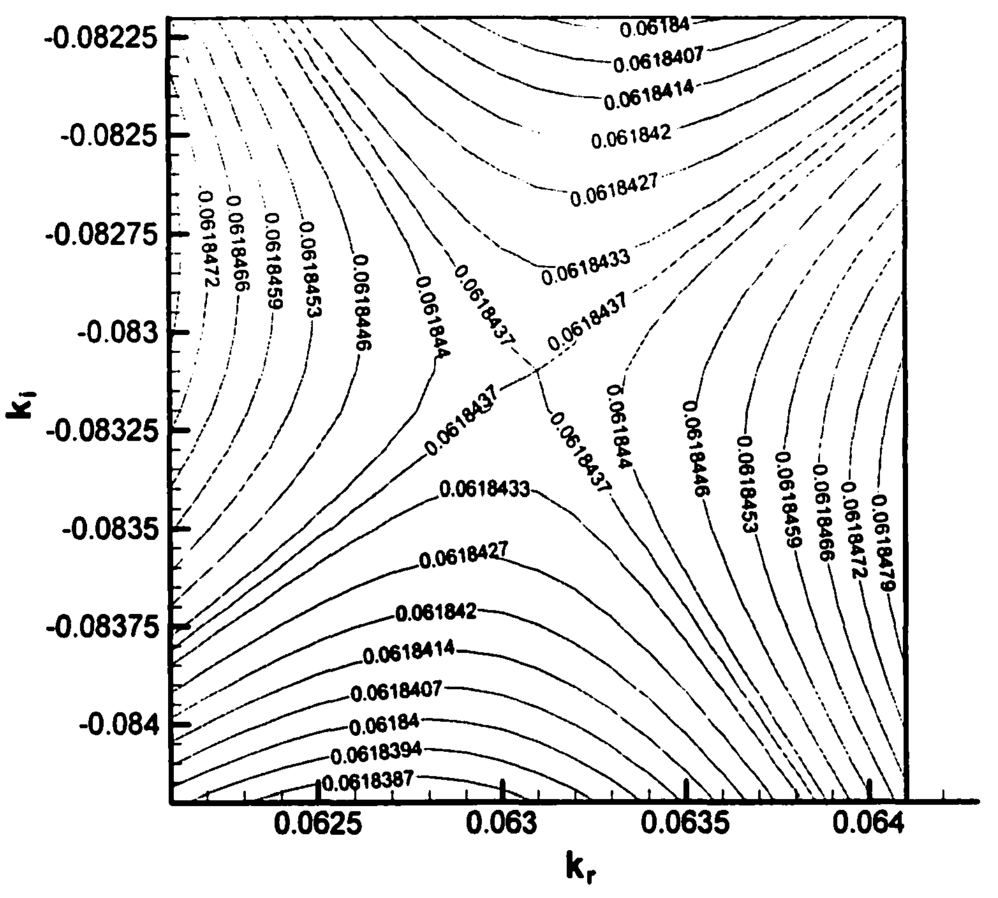

Figure A155: Contour plot of Ω_r for $R/\theta = 10$, $Fr = 10$, $\rho_j/\rho_\infty = 0.14$, $Sc = 5$, and $\Delta r = 0$ in the k-plane illustrating the pinch point formation

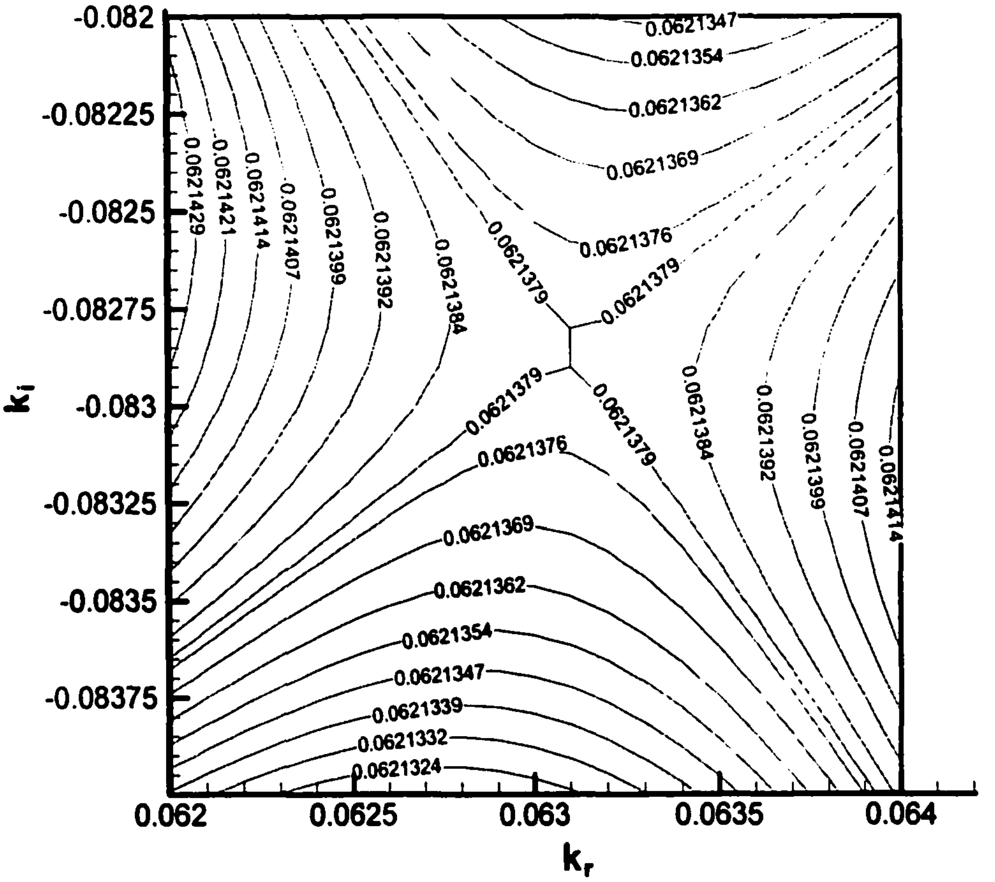

Figure A156: Contour plot of Ω_r for $R/\theta = 10$, $Fr = 5$, $\rho_j/\rho_\infty = 0.14$, $Sc = 5$, and $\Delta r = 0$ in the k-plane illustrating the pinch point formation

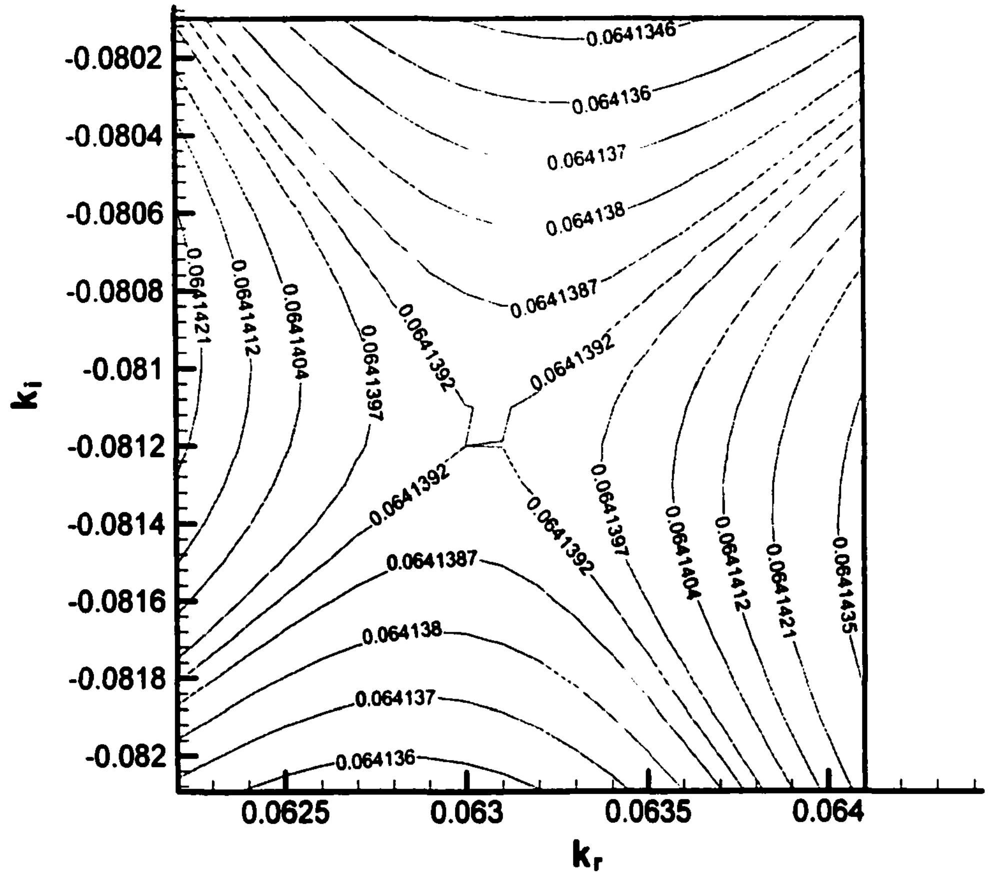

Figure A157: Contour plot of Ω_r for $R/\theta = 10$, $Fr = 2$, $\rho_j/\rho_\infty = 0.14$, $Sc = 5$, and $\Delta r = 0$ in the k-plane illustrating the pinch point formation

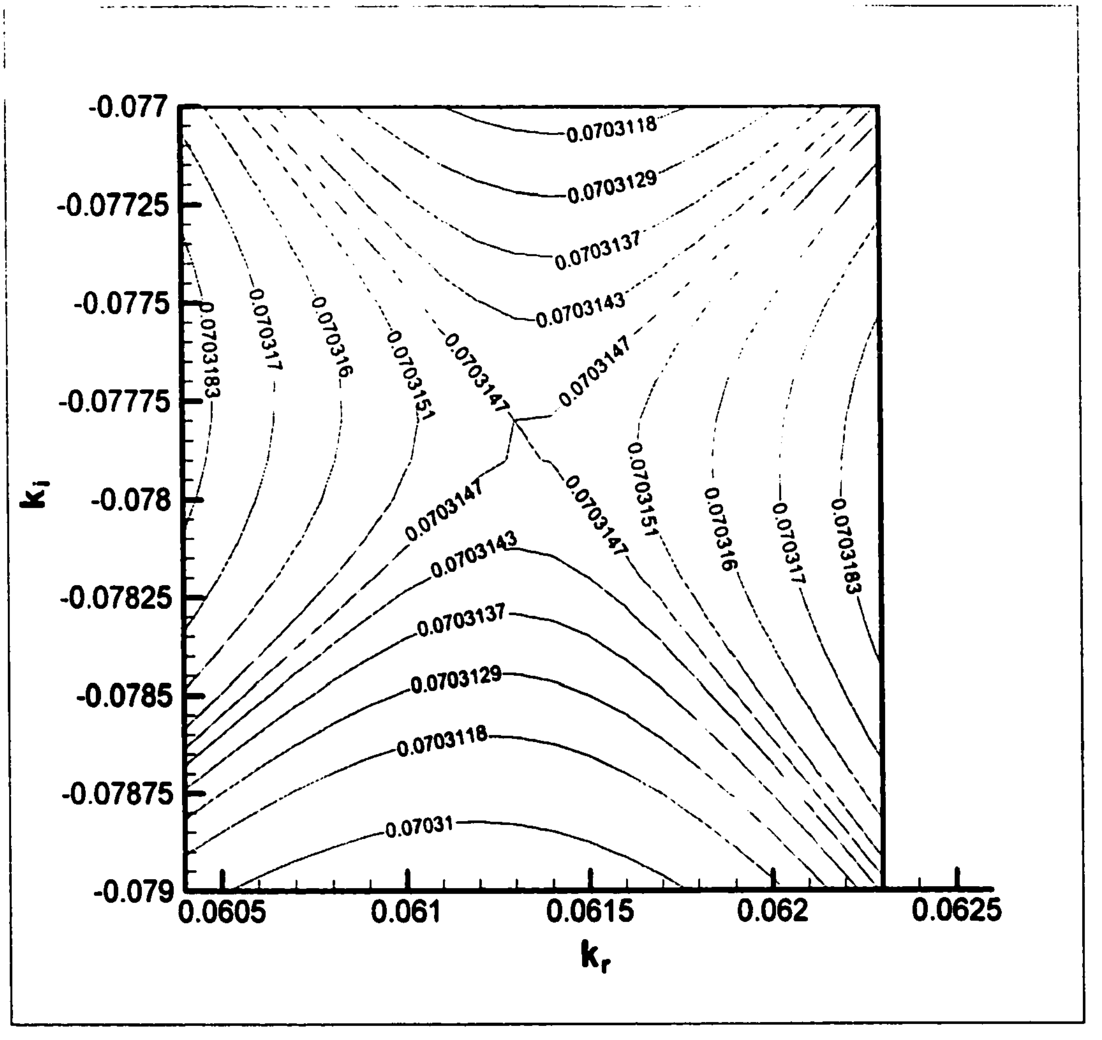

Figure A158: Contour plot of Ω_r for $R/\theta = 10$, $Fr = 1$, $\rho_j/\rho_\infty = 0.14$, $Sc = 5$, and $\Delta r = 0$ in the k-plane illustrating the pinch point formation

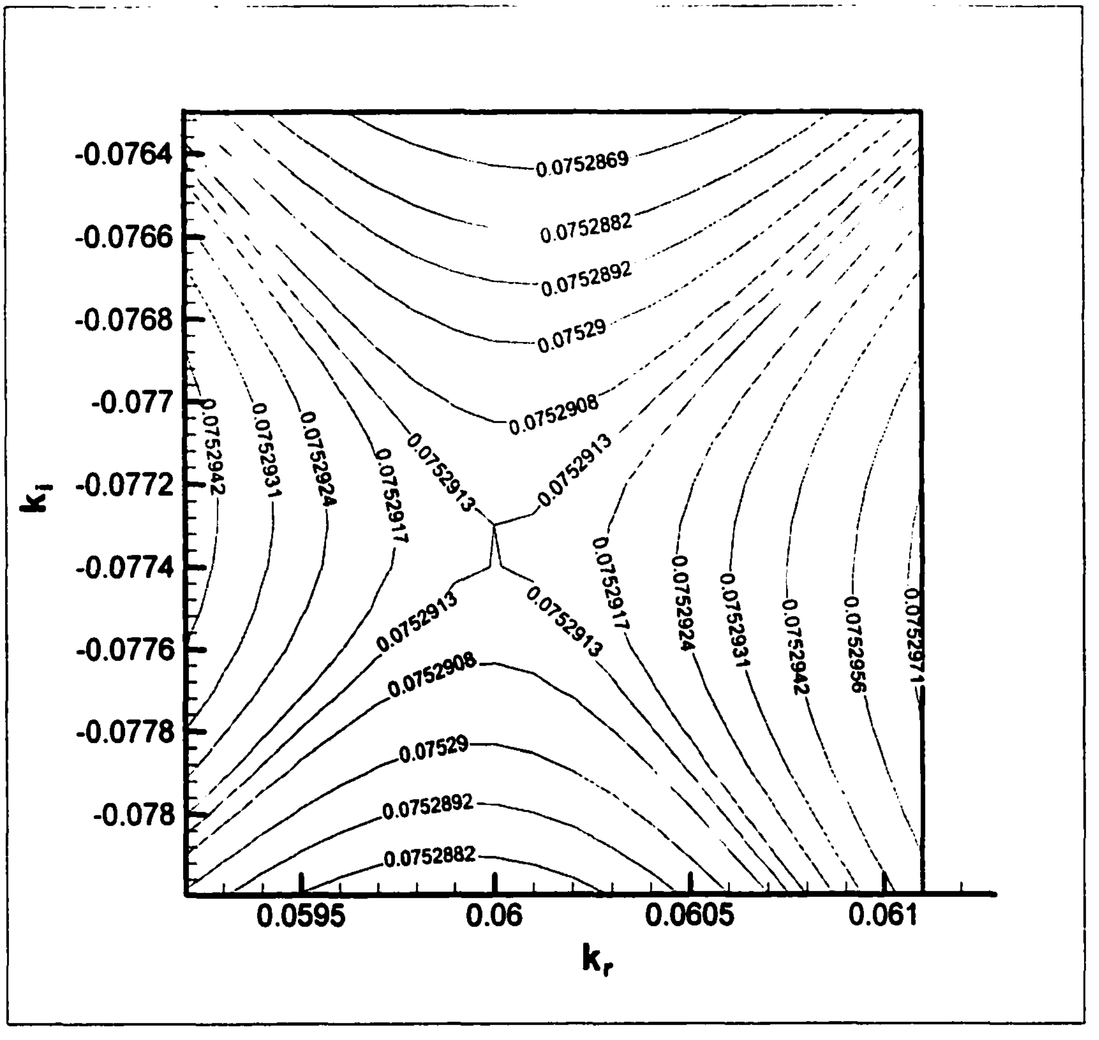

Figure A159: Contour plot of Ω_r for $R/\theta = 10$, $Fr = 0.75$, $\rho_j/\rho_\infty = 0.14$, $Sc = 5$, and $\Delta r = 0$ in the k-plane illustrating the pinch point formation

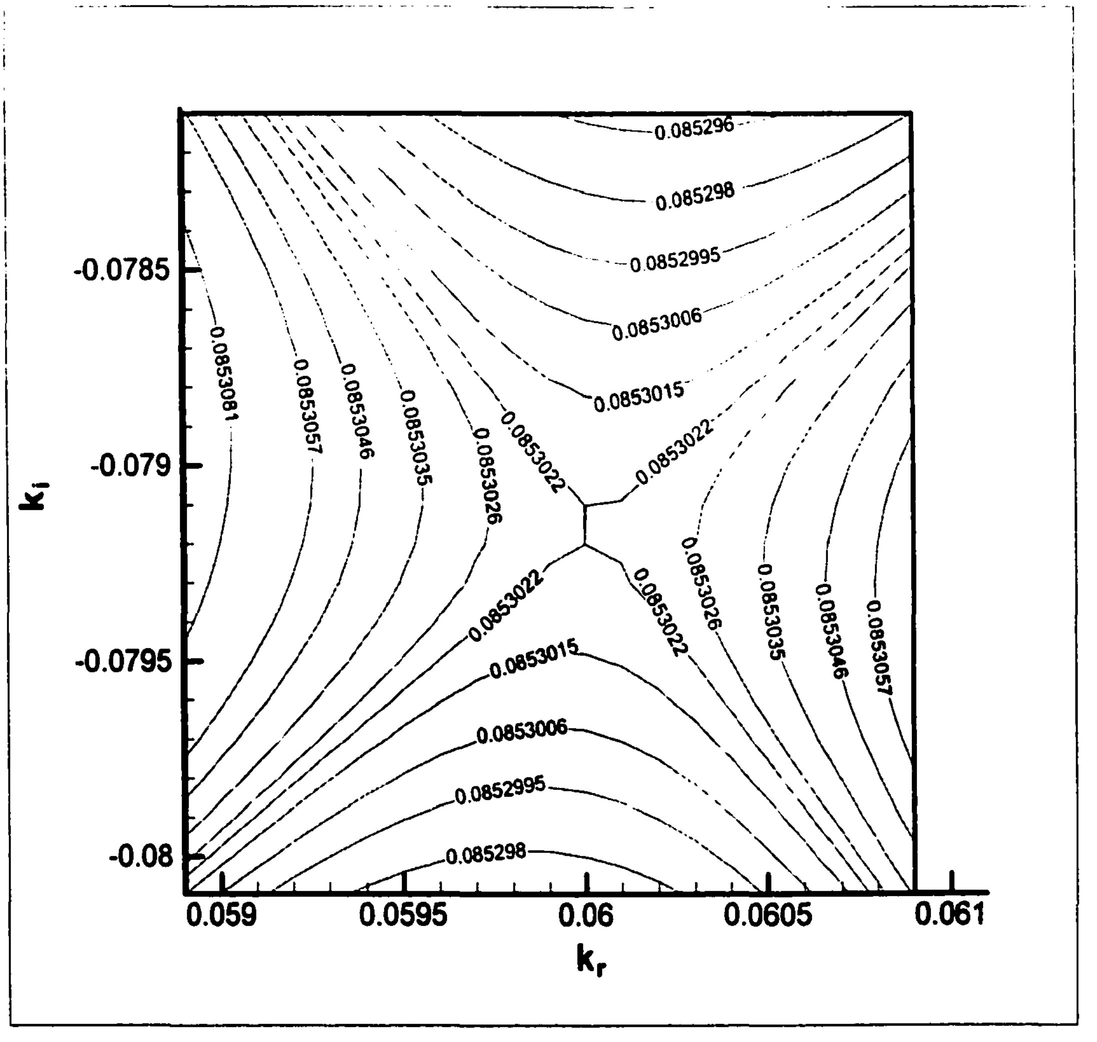

Figure A160: Contour plot of Ω_r for $R/\theta = 10$, $Fr = 0.5$, $\rho_j/\rho_\infty = 0.14$, $Sc = 5$, and $\Delta r = 0$ in the k-plane illustrating the pinch point formation

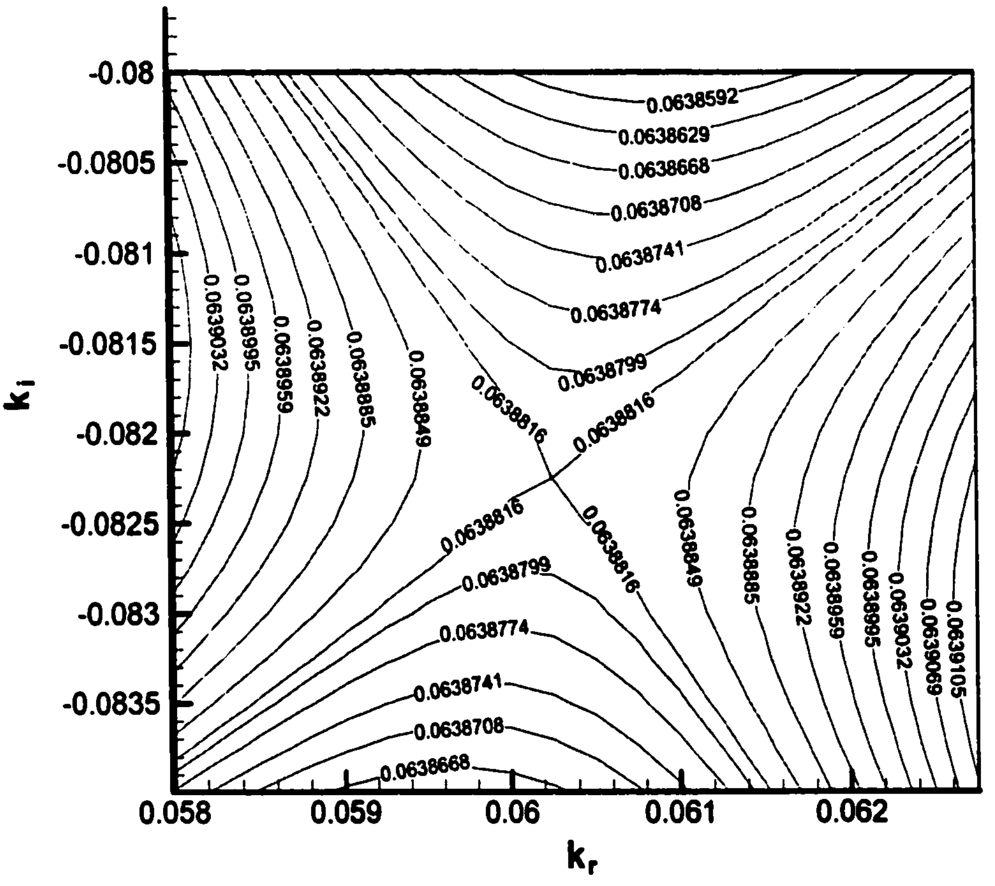

Figure A161: Contour plot of Ω_r for $R/\theta = 10$, $Fr = \infty$, $\rho_j/\rho_\infty = 0.14$, $Sc = 10$, and $\Delta r = 0$ in the k-plane illustrating the pinch point formation

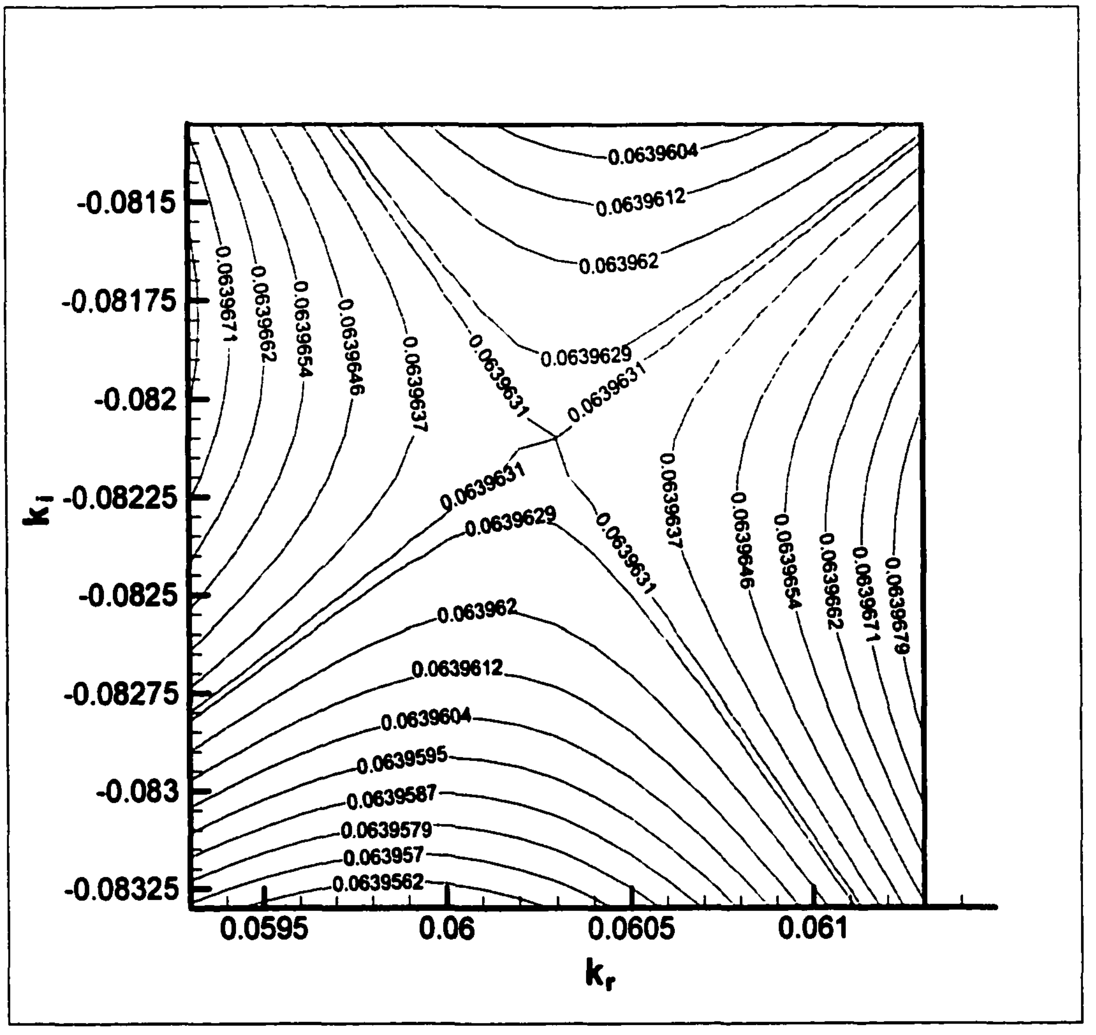

Figure A162: Contour plot of Ω_r for $R/\theta = 10$, $Fr = 10$, $\rho_j/\rho_\infty = 0.14$, $Sc = 10$, and $\Delta r = 0$ in the k-plane illustrating the pinch point formation

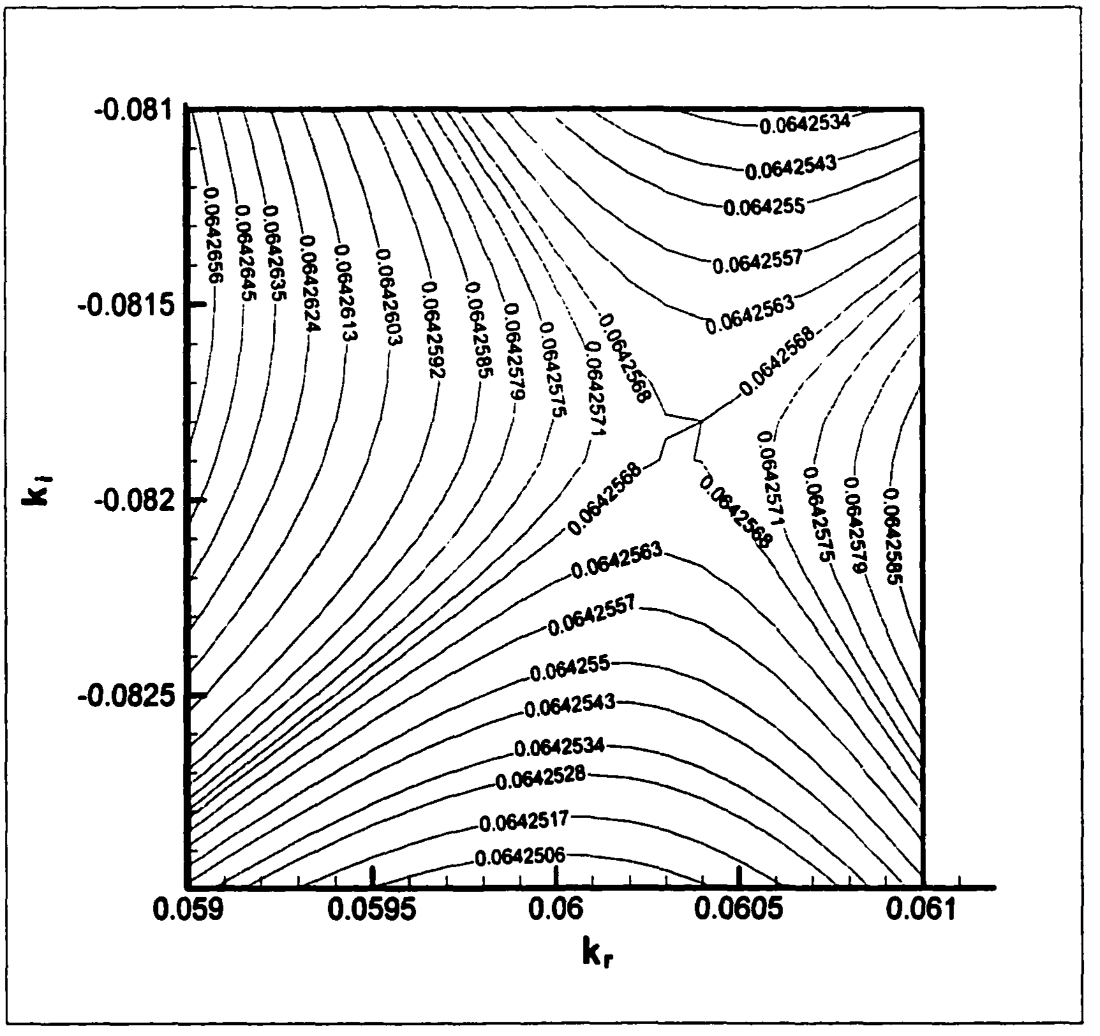

Figure A163: Contour plot of Ω_r for $R/\theta = 10$, $Fr = 5$, $\rho_j/\rho_\infty = 0.14$, $Sc = 10$, and $\Delta r = 0$ in the k-plane illustrating the pinch point formation

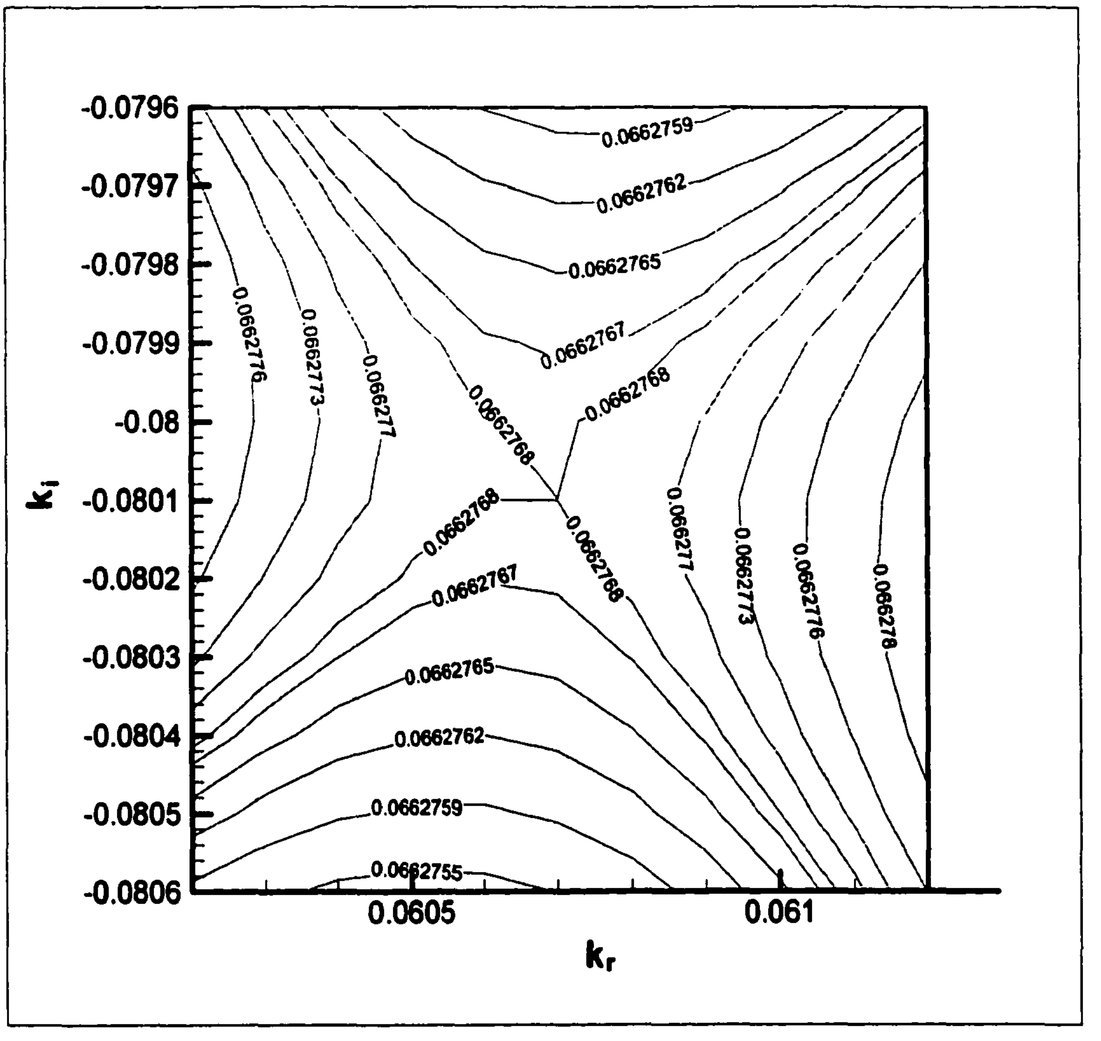

Figure A164: Contour plot of Ω_r for $R/\theta = 10$, $Fr = 2$, $\rho_j/\rho_\infty = 0.14$, $Sc = 10$, and $\Delta r = 0$ in the k-plane illustrating the pinch point formation

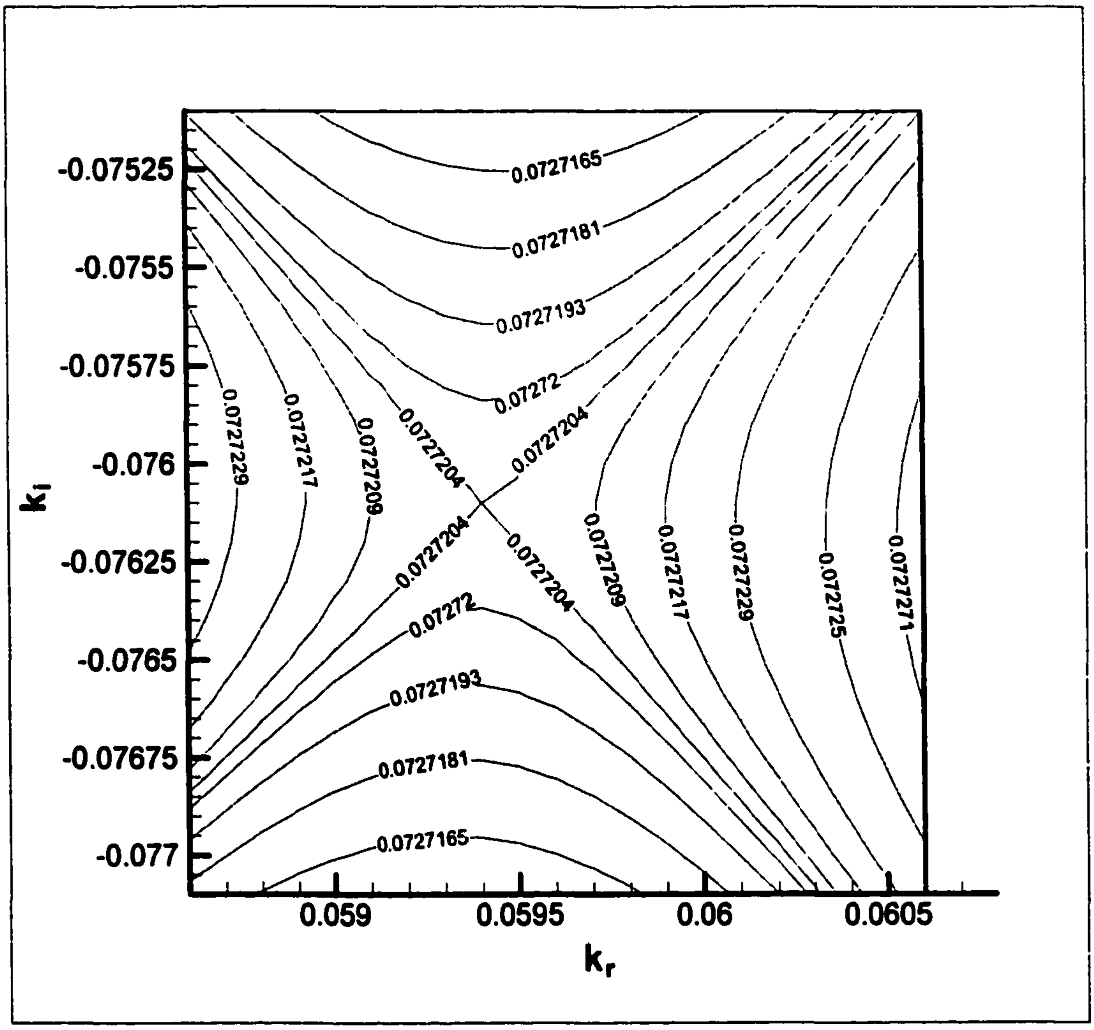

Figure A165: Contour plot of Ω_r for $R/\theta = 10$, $Fr = 1$, $\rho_j/\rho_\infty = 0.14$, $Sc = 10$, and $\Delta r = 0$ in the k-plane illustrating the pinch point formation

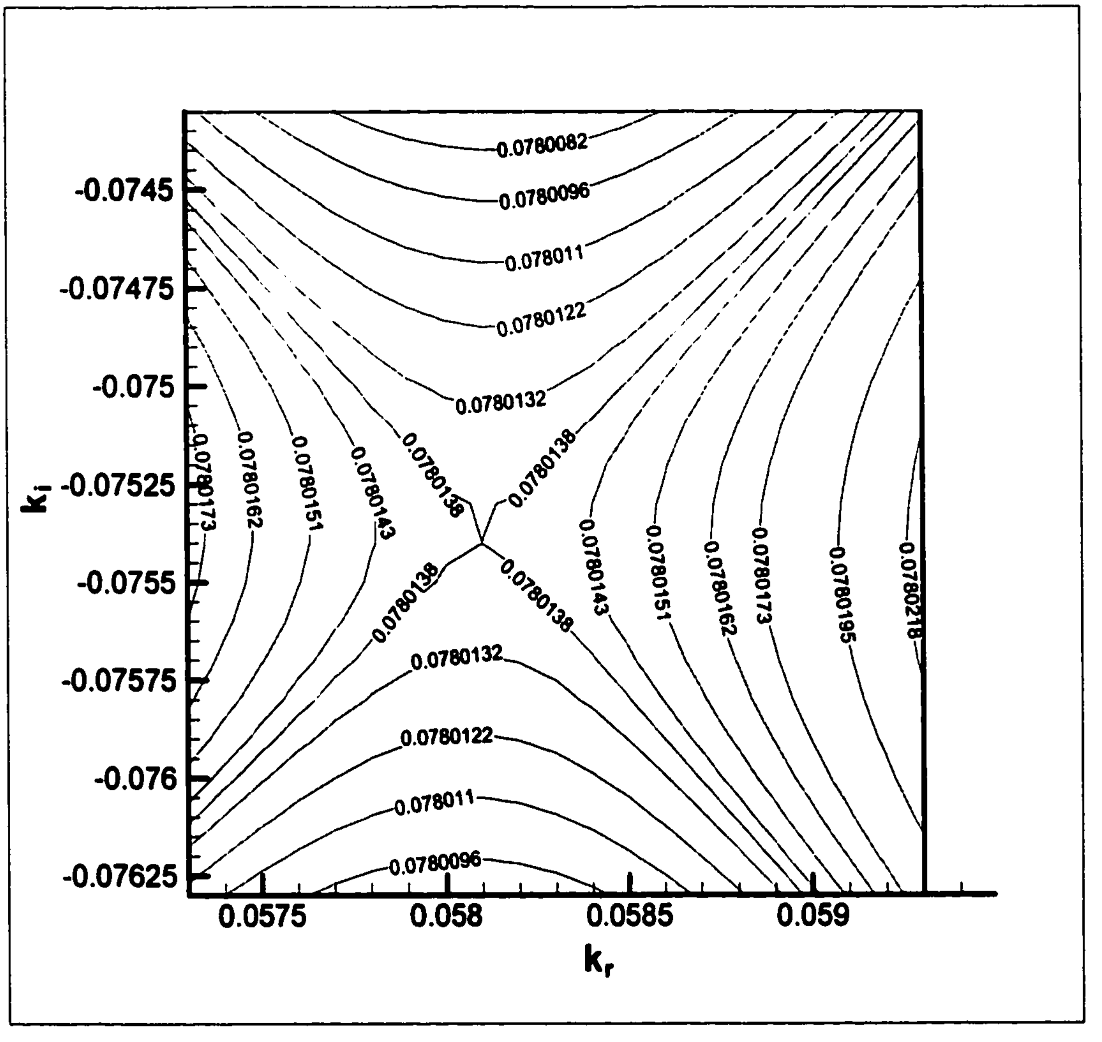

Figure A166: Contour plot of Ω_r for $R/\theta = 10$, $Fr = 0.75$, $\rho_j/\rho_\infty = 0.14$, $Sc = 10$, and $\Delta r = 0$ in the k-plane illustrating the pinch point formation

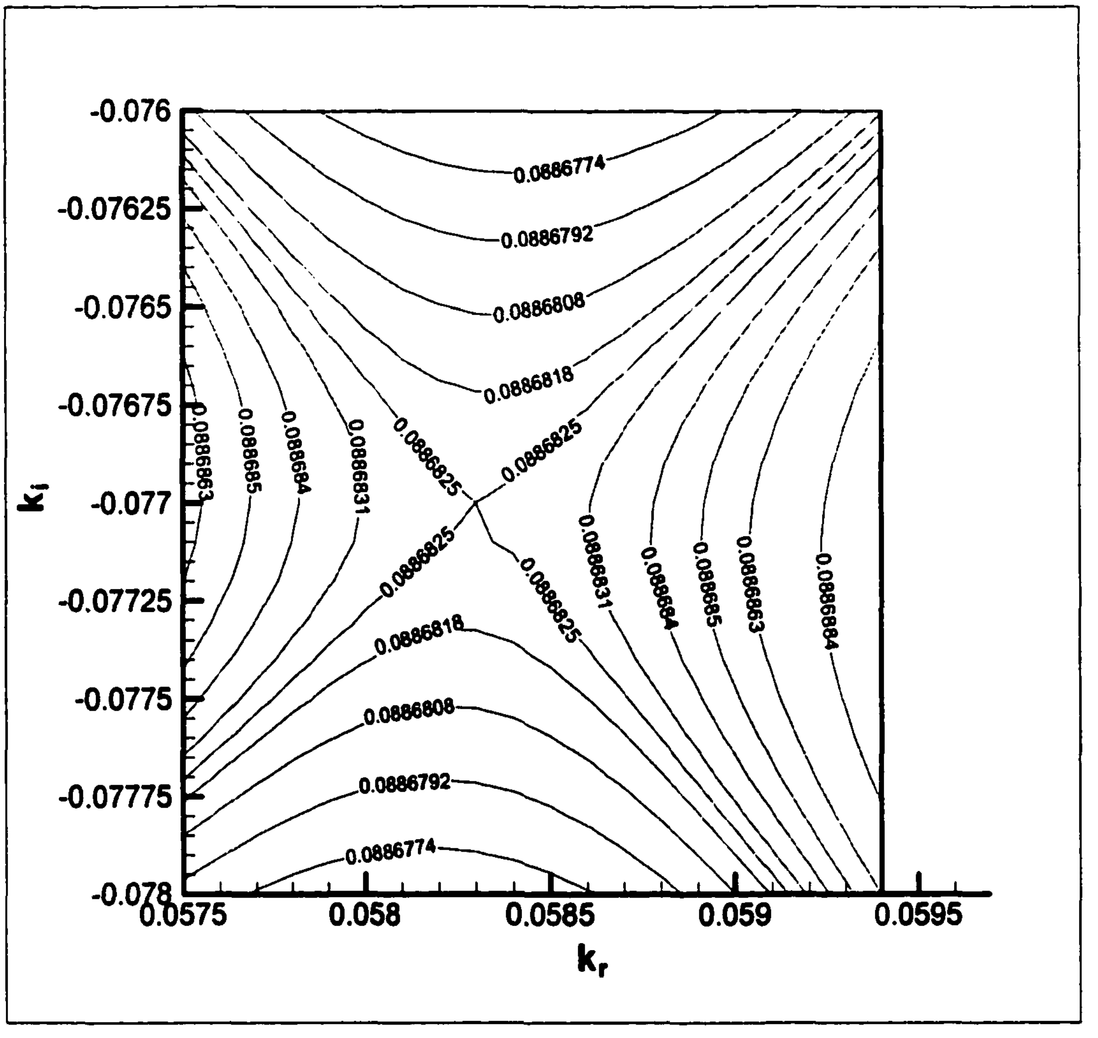

Figure A167: Contour plot of Ω_r for $R/\theta = 10$, $Fr = 0.5$, $\rho_j/\rho_\infty = 0.14$, $Sc = 10$, and $\Delta r = 0$ in the k-plane illustrating the pinch point formation

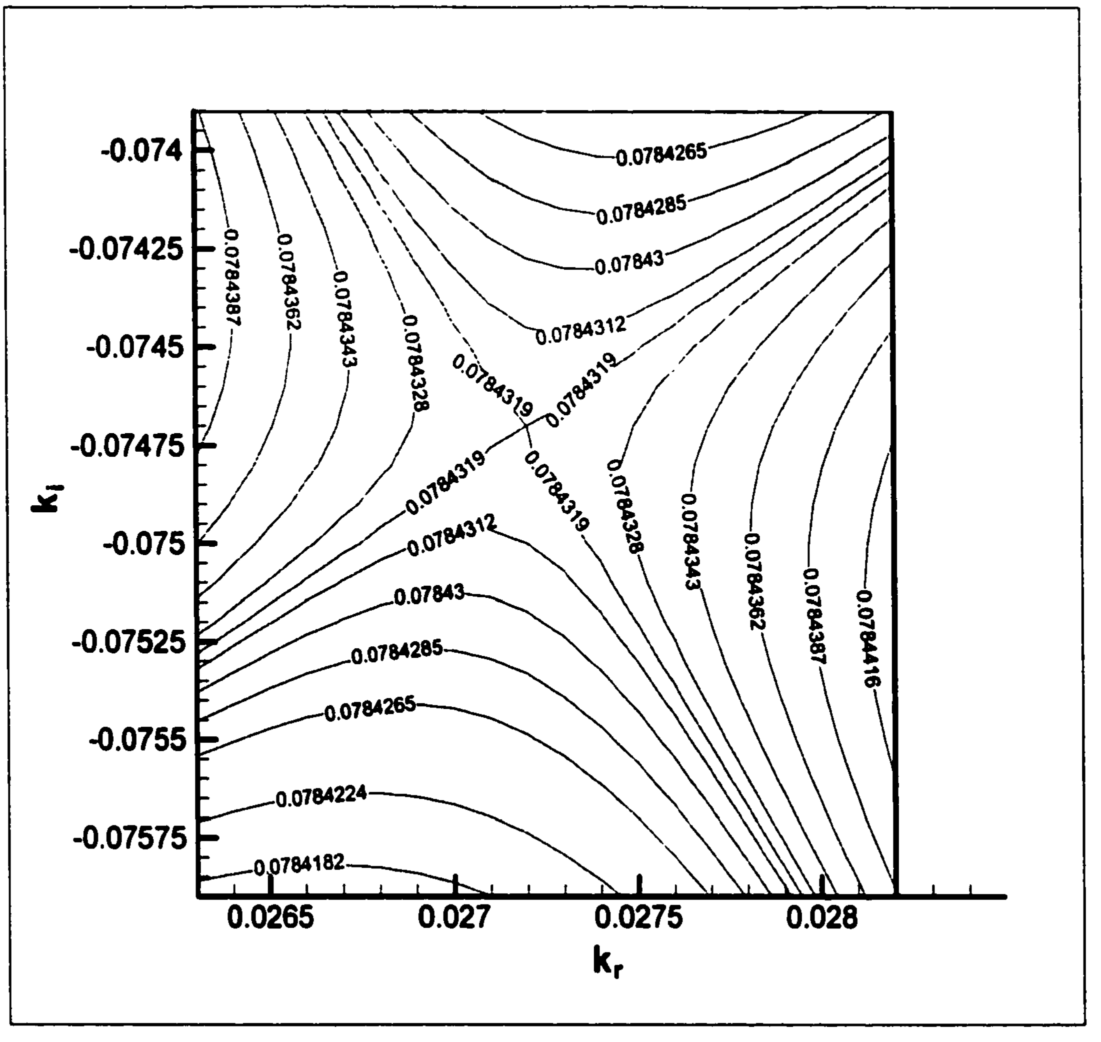

Figure A168: Contour plot of Ω_r for $R/\theta = 10$, $Fr = \infty$, $\rho_j/\rho_\infty = 0.14$, $Sc = 1$, and $\Delta r = 0$, $U_\infty/\Delta U = 0.5$ in the k-plane illustrating the pinch point formation

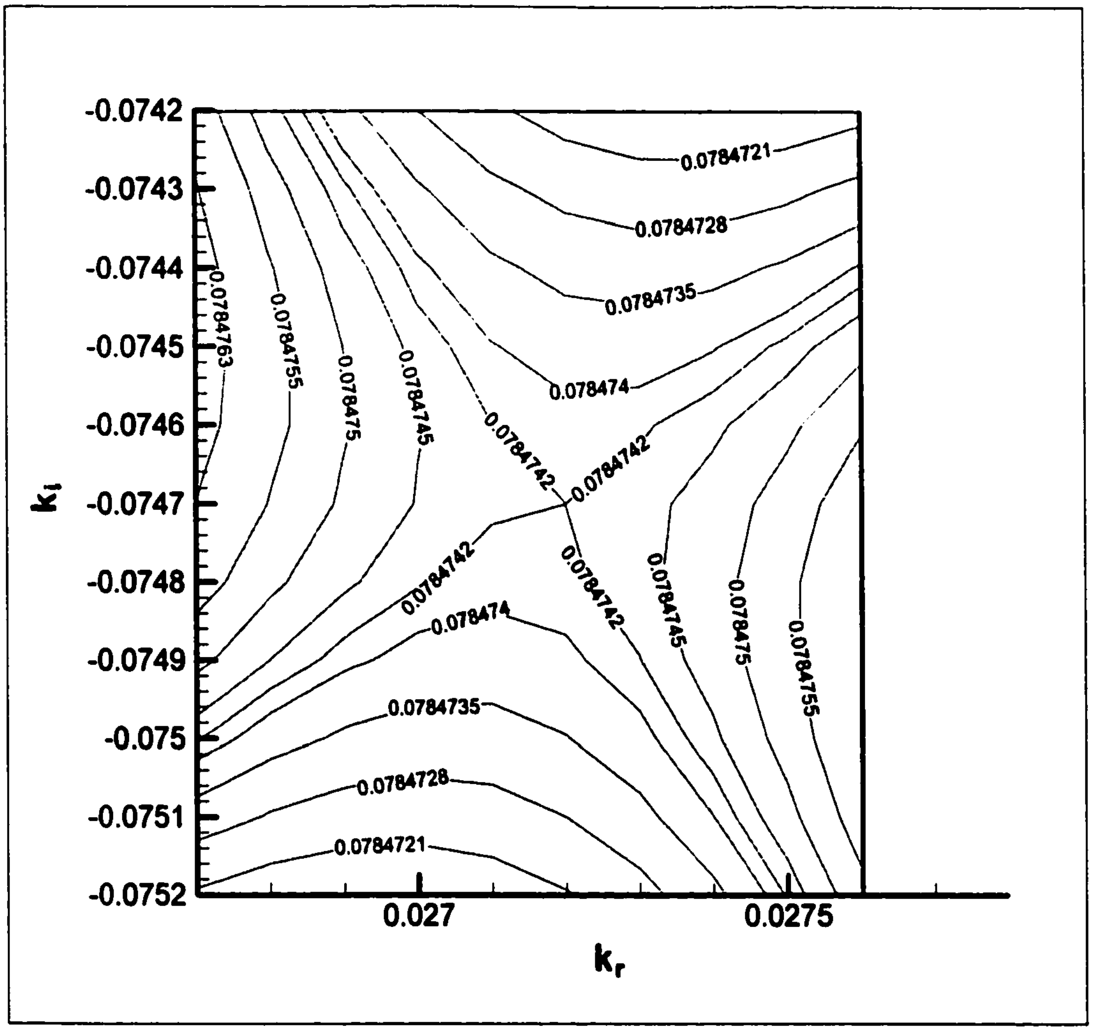

Figure A169: Contour plot of Ω_r for $R/\theta = 10$, $Fr = 10$, $\rho_j/\rho_\infty = 0.14$, $Sc = 1$, and $\Delta r = 0$, $U_\infty/\Delta U = 0.5$ in the k-plane illustrating the pinch point formation

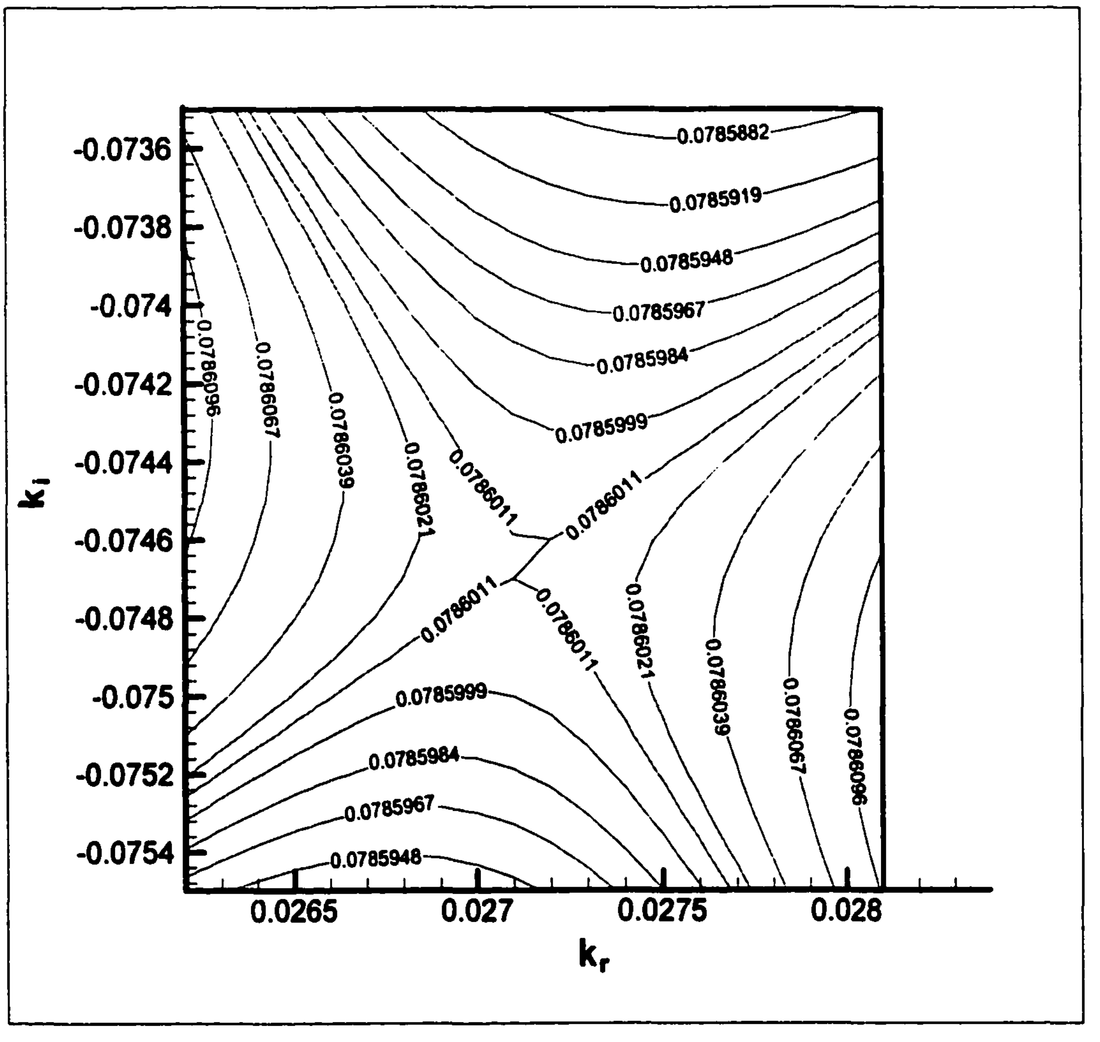

Figure A170: Contour plot of Ω_r for $R/\theta = 10$, $Fr = 5$, $\rho_j/\rho_\infty = 0.14$, $Sc = 1$, and $\Delta r = 0$, $U_\infty/\Delta U = 0.5$ in the k-plane illustrating the pinch point formation

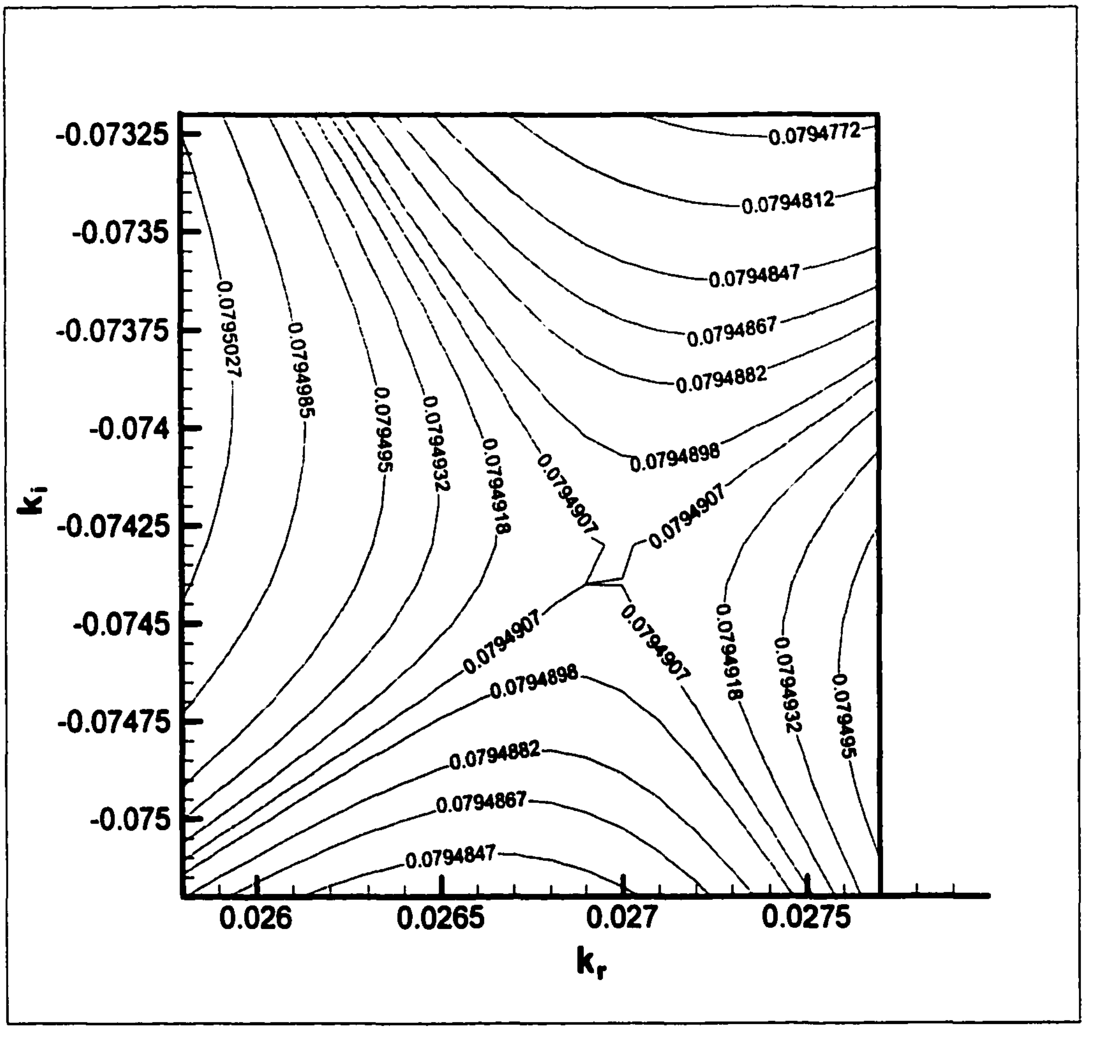

Figure A171: Contour plot of Ω_r for $R/\theta = 10$, $Fr = 2$, $\rho_j/\rho_\infty = 0.14$, $Sc = 1$, and $\Delta r = 0$, $U_\infty/\Delta U = 0.5$ in the k-plane illustrating the pinch point formation

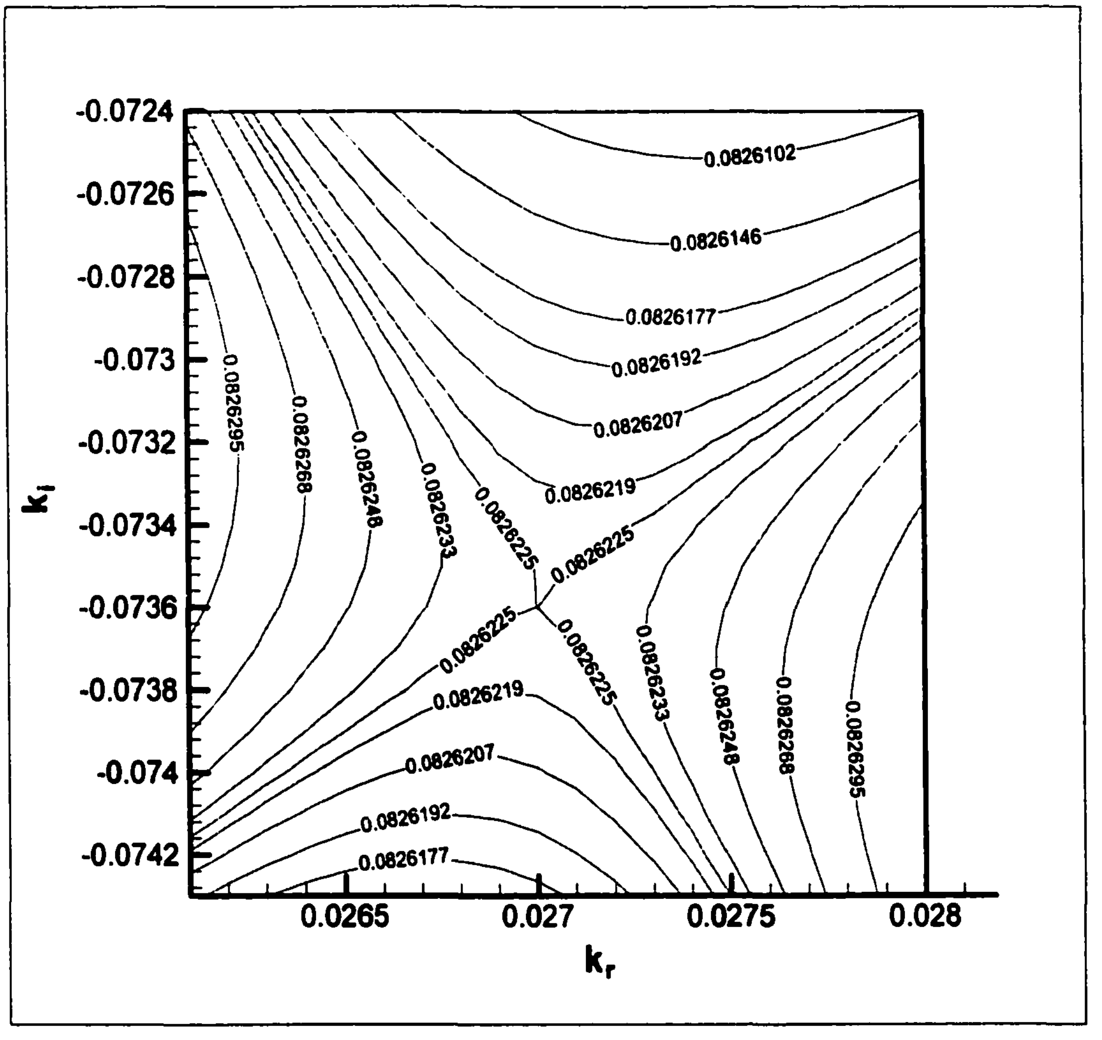

Figure A172: Contour plot of Ω_r for $R/\theta = 10$, $Fr = 1$, $\rho_j/\rho_\infty = 0.14$, $Sc = 1$, and $\Delta r = 0$, $U_\infty/\Delta U = 0.5$ in the k-plane illustrating the pinch point formation

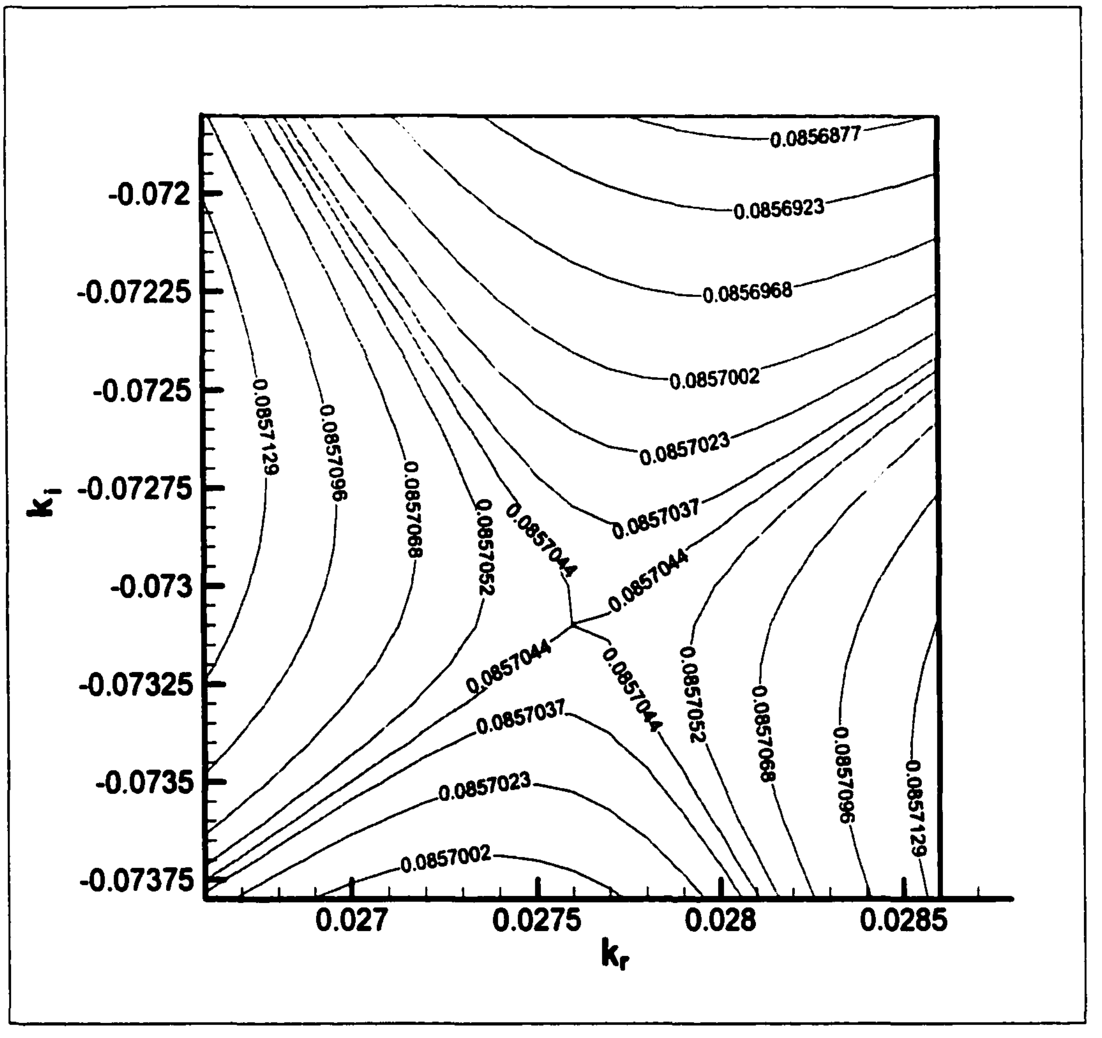

Figure A173: Contour plot of Ω_r for $R/\theta = 10$, $Fr = 0.75$, $\rho_j/\rho_\infty = 0.14$, $Sc = 1$, and $\Delta r = 0$, $U_\infty/\Delta U = 0.5$ in the k-plane illustrating the pinch point formation

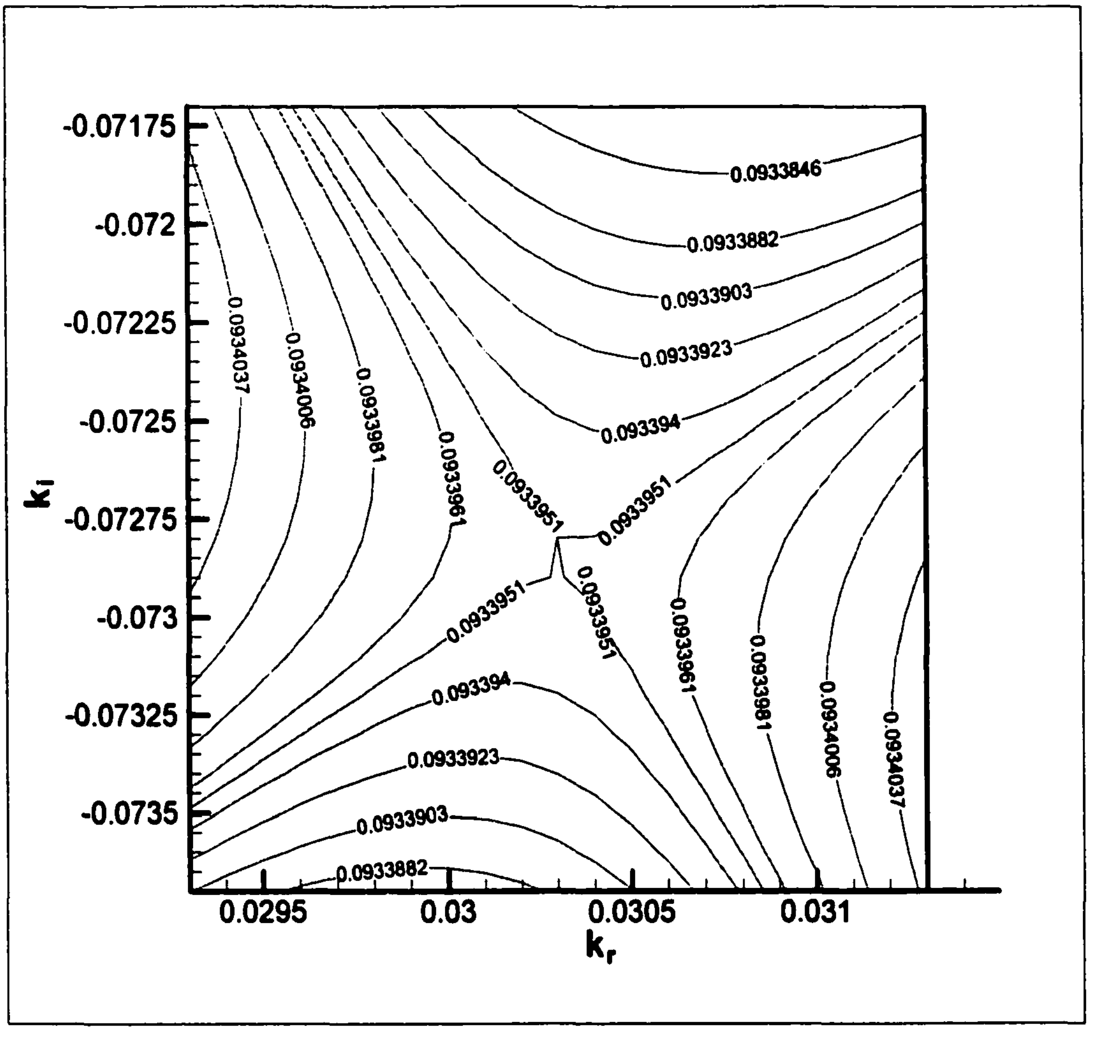

Figure A174: Contour plot of Ω_r for $R/\theta = 10$, $Fr = 0.5$, $\rho_j/\rho_\infty = 0.14$, $Sc = 1$, and $\Delta r = 0$, $U_\infty/\Delta U = 0.5$ in the k-plane illustrating the pinch point formation

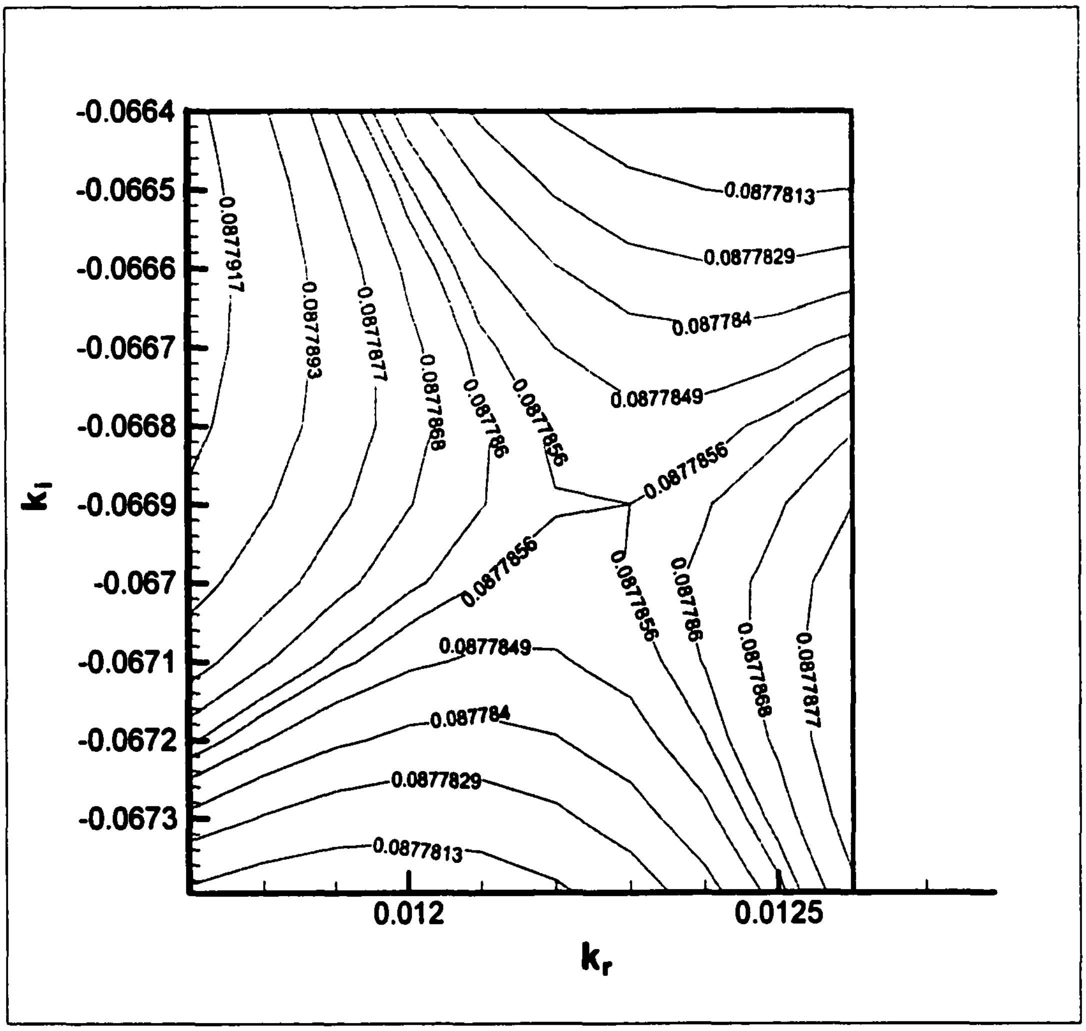

Figure A175: Contour plot of Ω_r for $R/\theta = 10$, $Fr = \infty$, $\rho_j/\rho_\infty = 0.14$, $Sc = 1$, and $\Delta r = 0$, $U_\infty/\Delta U = 1$ in the k-plane illustrating the pinch point formation

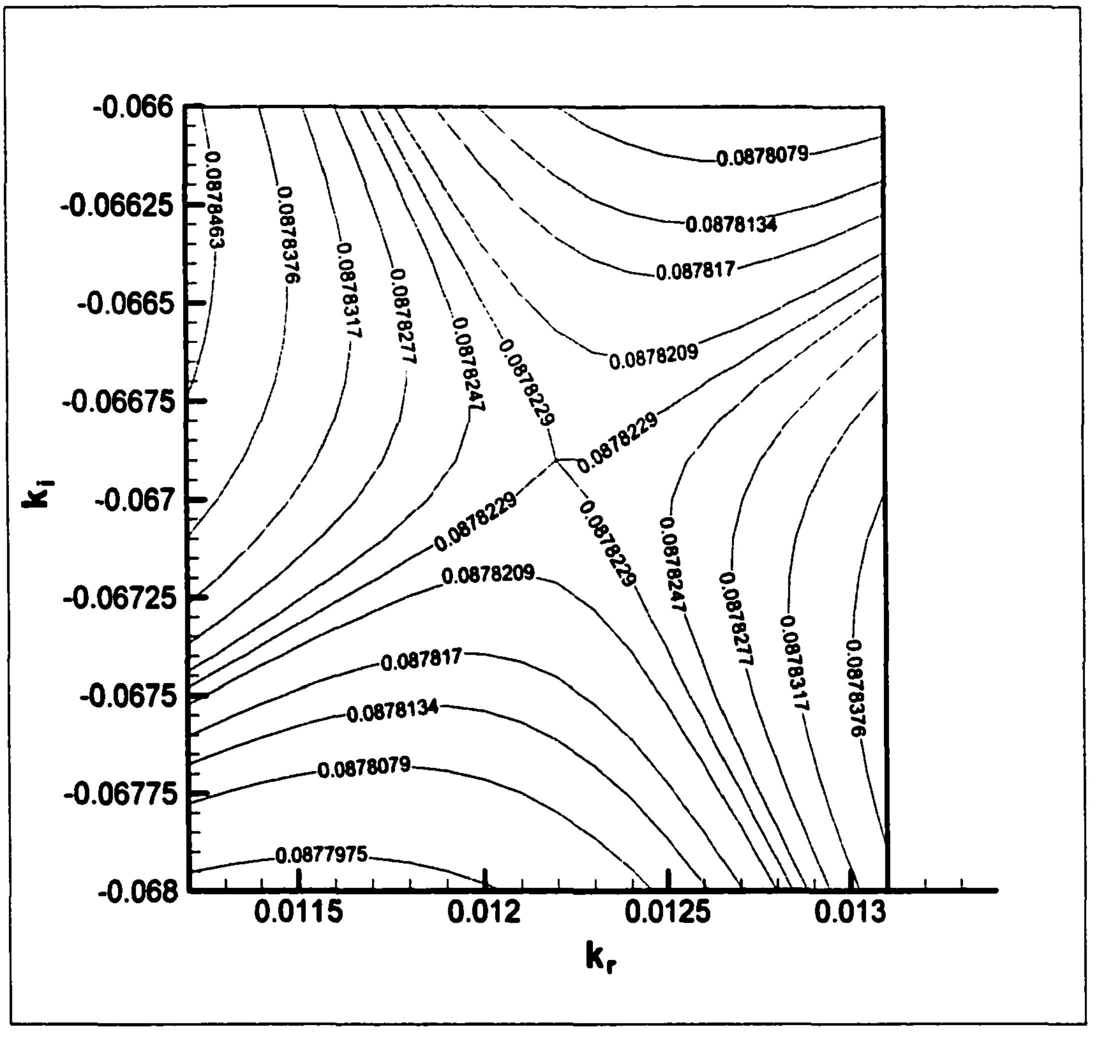

Figure A176: Contour plot of Ω_r for $R/\theta = 10$, $Fr = 10$, $\rho_j/\rho_\infty = 0.14$, $Sc = 1$, and $\Delta r = 0$, $U_\infty/\Delta U = 1$ in the k-plane illustrating the pinch point formation

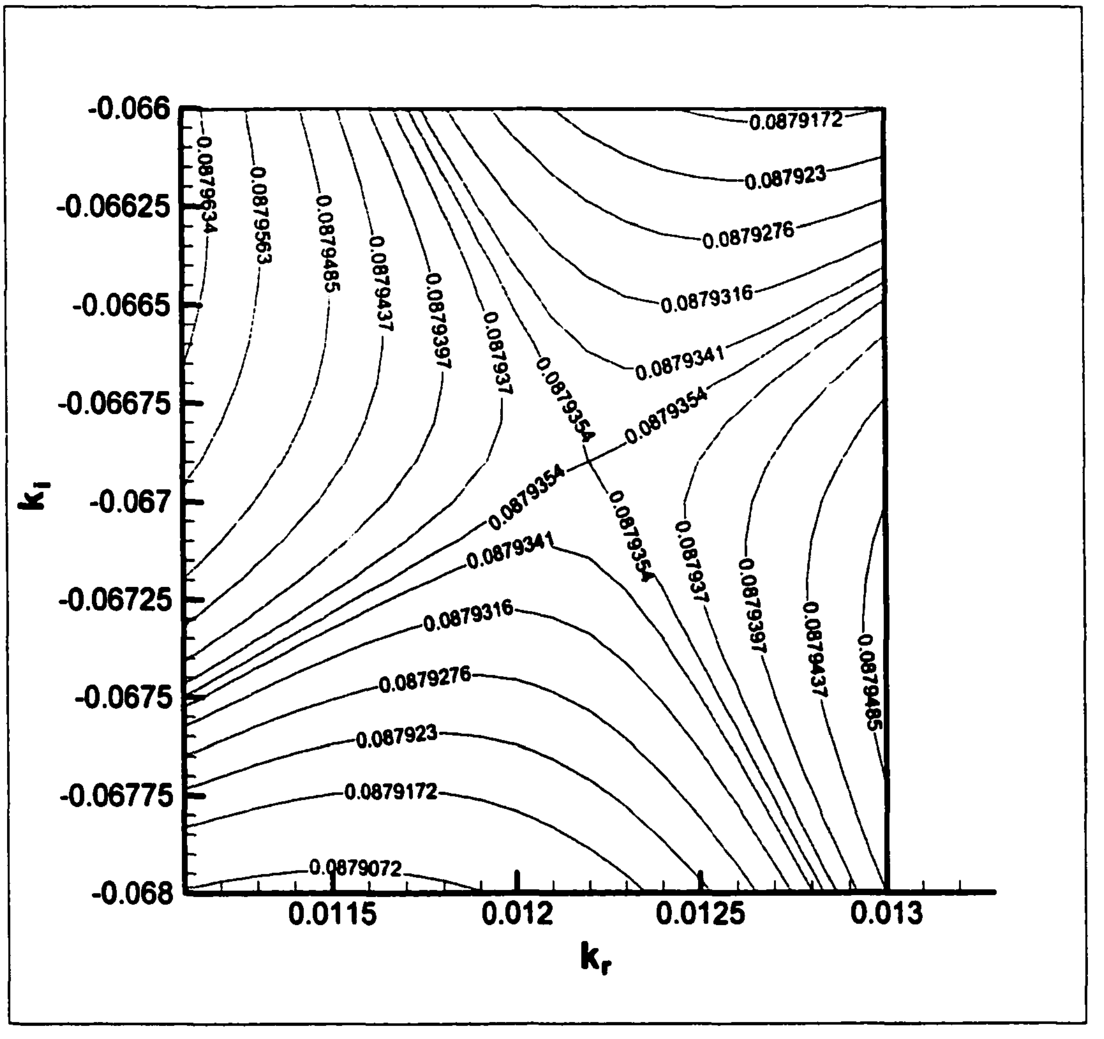

Figure A177: Contour plot of Ω_r for $R/\theta = 10$, $Fr = 5$, $\rho_j/\rho_\infty = 0.14$, $Sc = 1$, and $\Delta r = 0$, $U_\infty/\Delta U = 1$ in the k-plane illustrating the pinch point formation

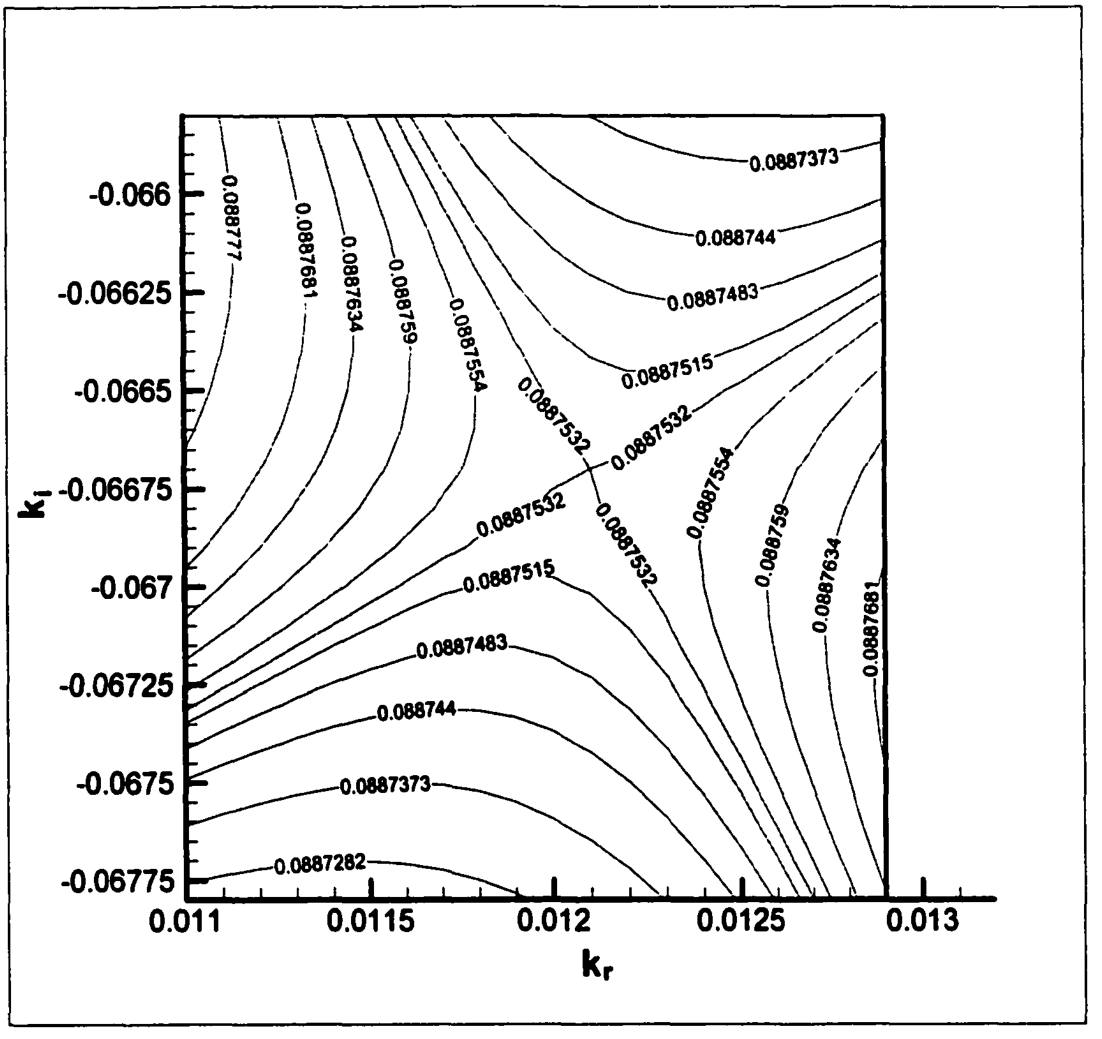

Figure A178: Contour plot of Ω_r for $R/\theta = 10$, $Fr = 2$, $\rho_j/\rho_\infty = 0.14$, $Sc = 1$, and $\Delta r = 0$, $U_\infty/\Delta U = 1$ in the k-plane illustrating the pinch point formation

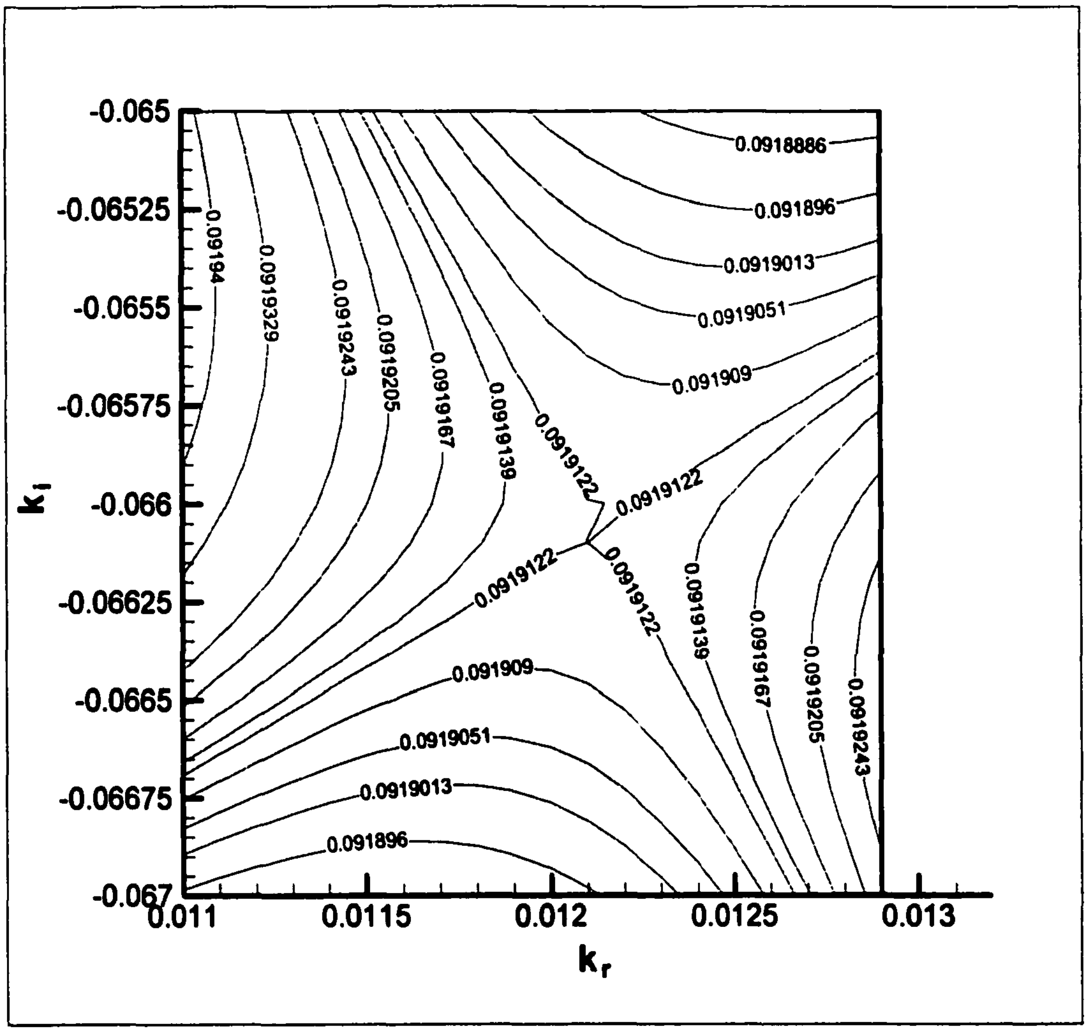

Figure A179: Contour plot of Ω_r for $R/\theta = 10$, $Fr = 1$, $\rho_j/\rho_\infty = 0.14$, $Sc = 1$, and $\Delta r = 0$, $U_\infty/\Delta U = 1$ in the k-plane illustrating the pinch point formation

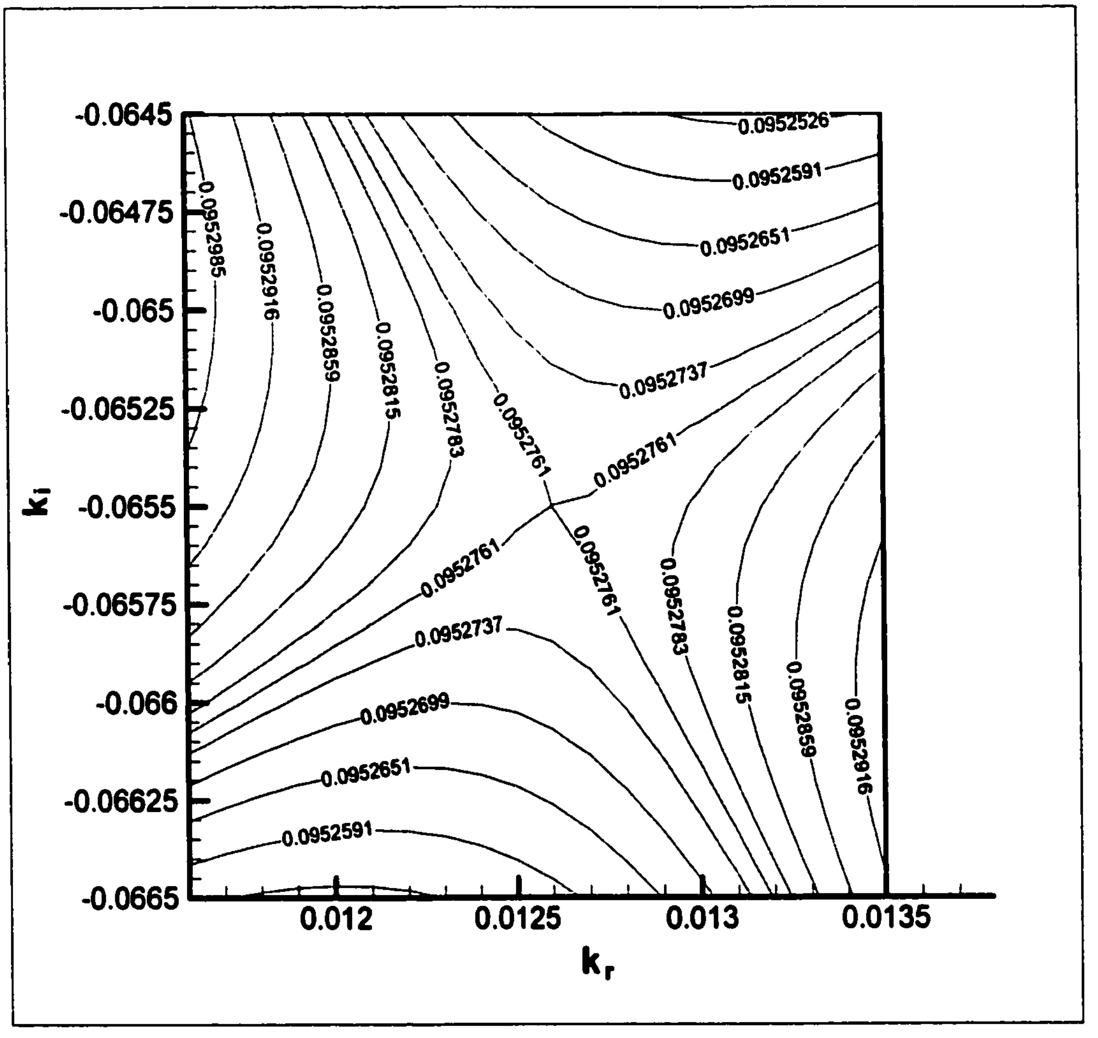

Figure A180: Contour plot of Ω_r for $R/\theta = 10$, $Fr = 0.75$, $\rho_j/\rho_\infty = 0.14$, $Sc = 1$, and $\Delta r = 0$, $U_\infty/\Delta U = 1$ in the k-plane illustrating the pinch point formation

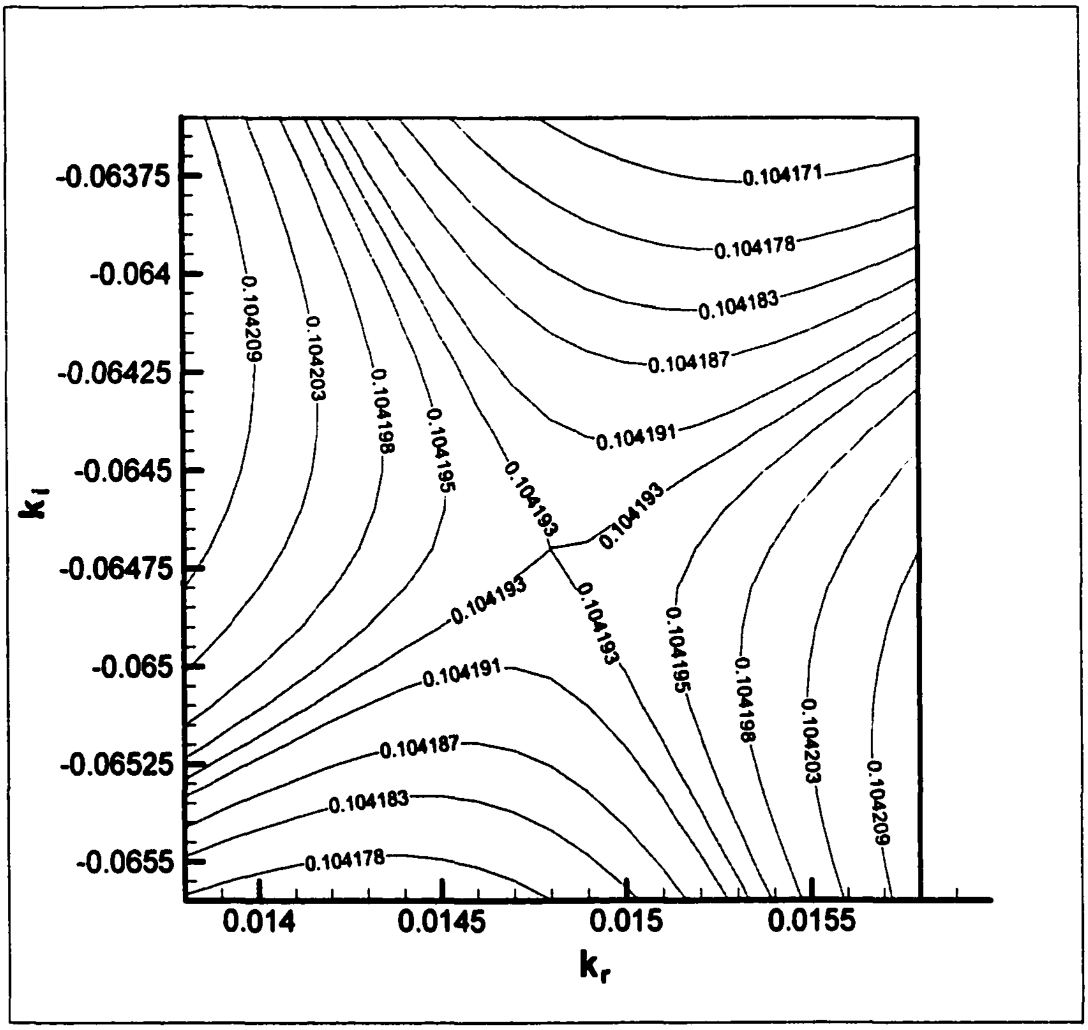

Figure A181: Contour plot of Ω_r for $R/\theta = 10$, $Fr = 0.5$, $\rho_j/\rho_\infty = 0.14$, $Sc = 1$, and $\Delta r = 0$, $U_\infty/\Delta U = 1$ in the k-plane illustrating the pinch point formation

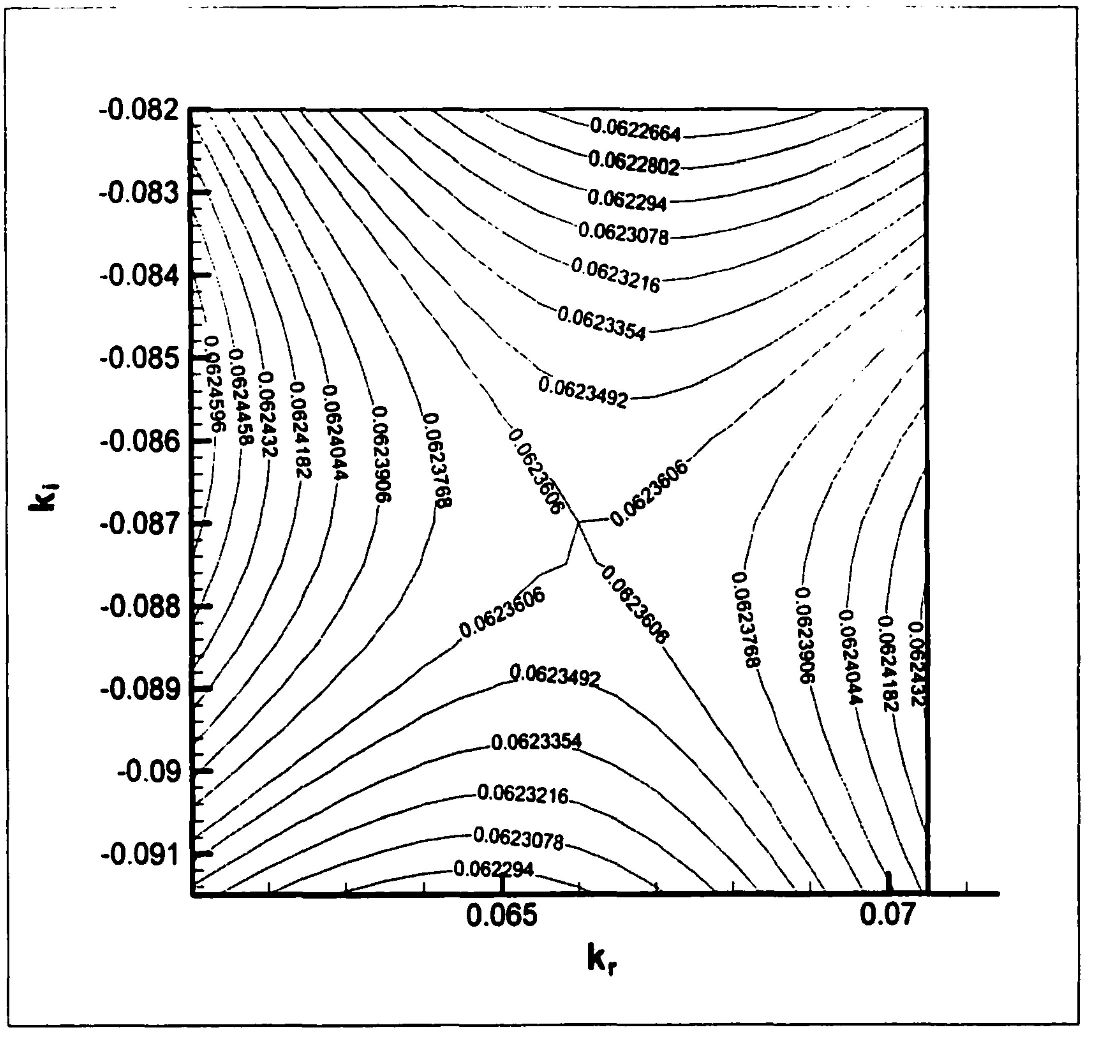

Figure A182: Contour plot of Ω_r for $R/\theta = 10$, $Fr = \infty$, $\rho_j/\rho_\infty = 0.14$, $Sc = 1$, and $\Delta r = 1.25$ in the k-plane illustrating the pinch point formation

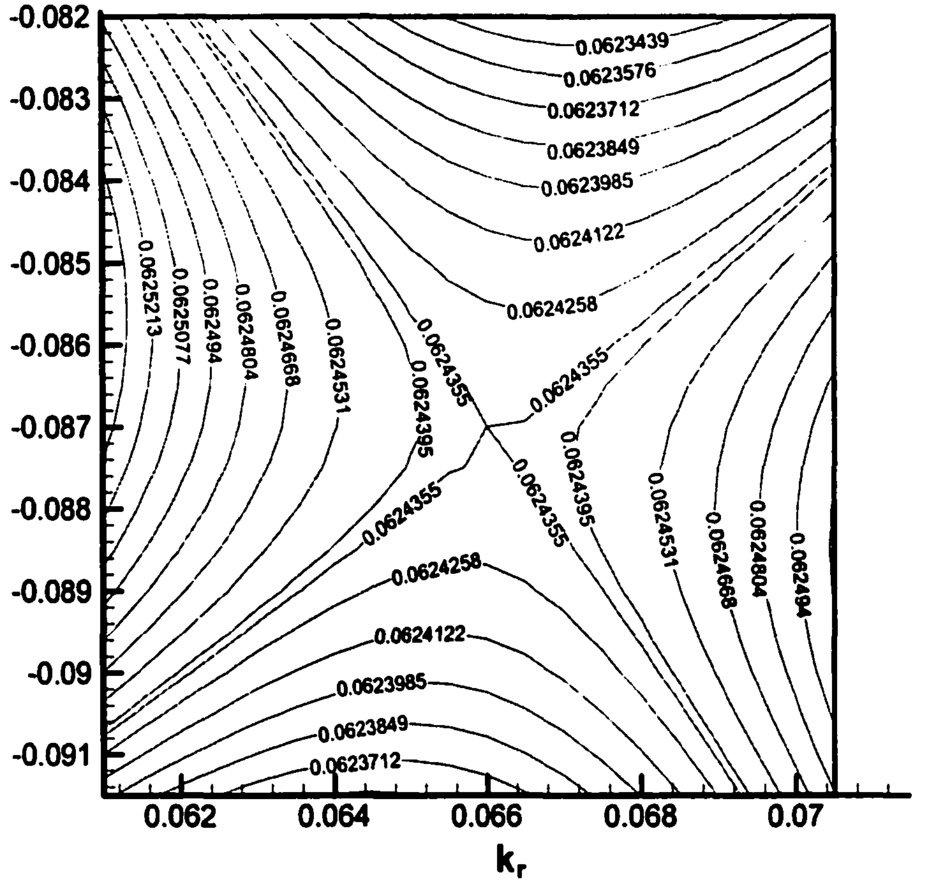

Figure A183: Contour plot of Ω_r for $R/\theta = 10$, $Fr = 10$, $\rho_j/\rho_\infty = 0.14$, $Sc = 1$, and $\Delta r = 1.25$ in the k-plane illustrating the pinch point formation

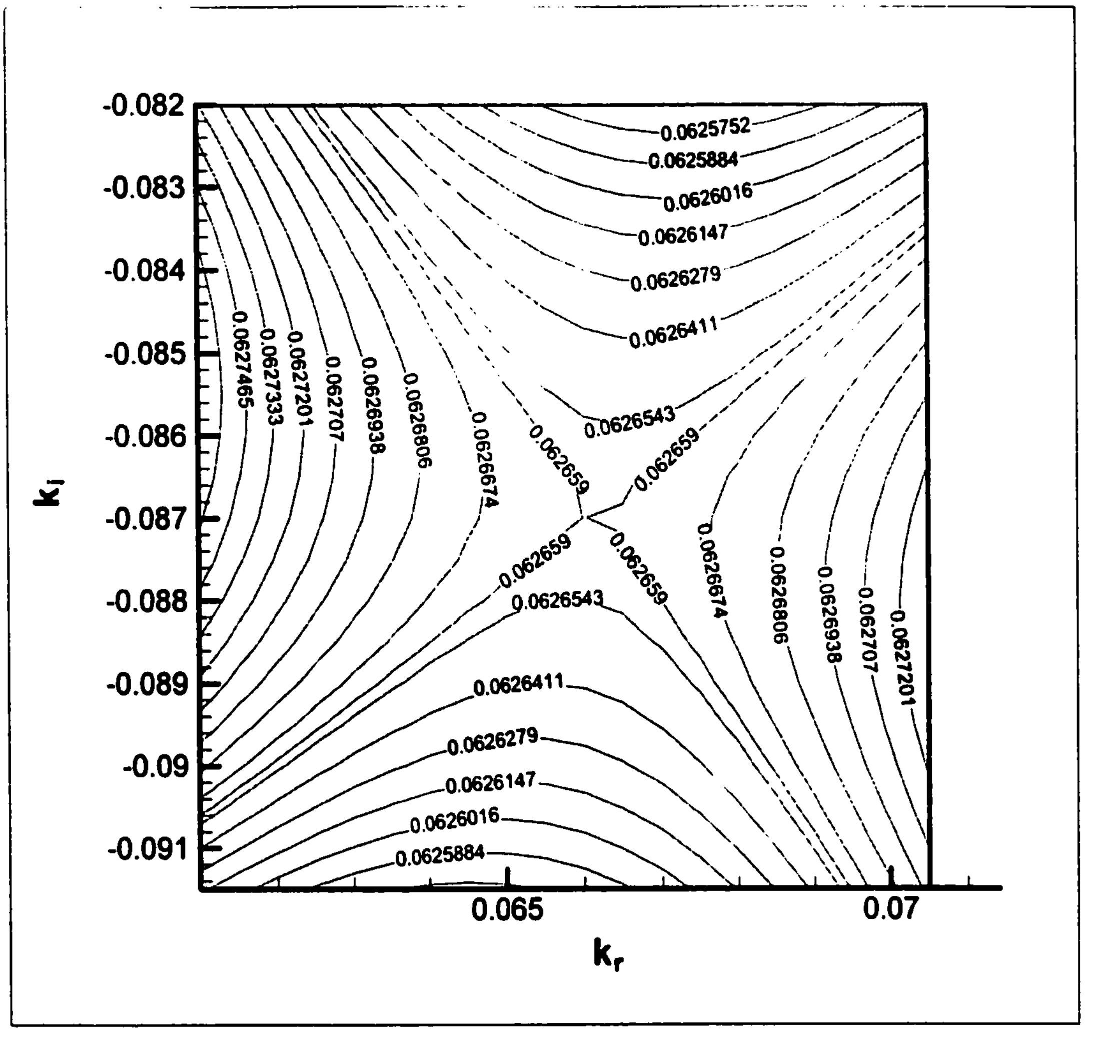

Figure A184: Contour plot of Ω_r for $R/\theta = 10$, $Fr = 5$, $\rho_j/\rho_\infty = 0.14$, $Sc = 1$, and $\Delta r = 1.25$ in the k-plane illustrating the pinch point formation

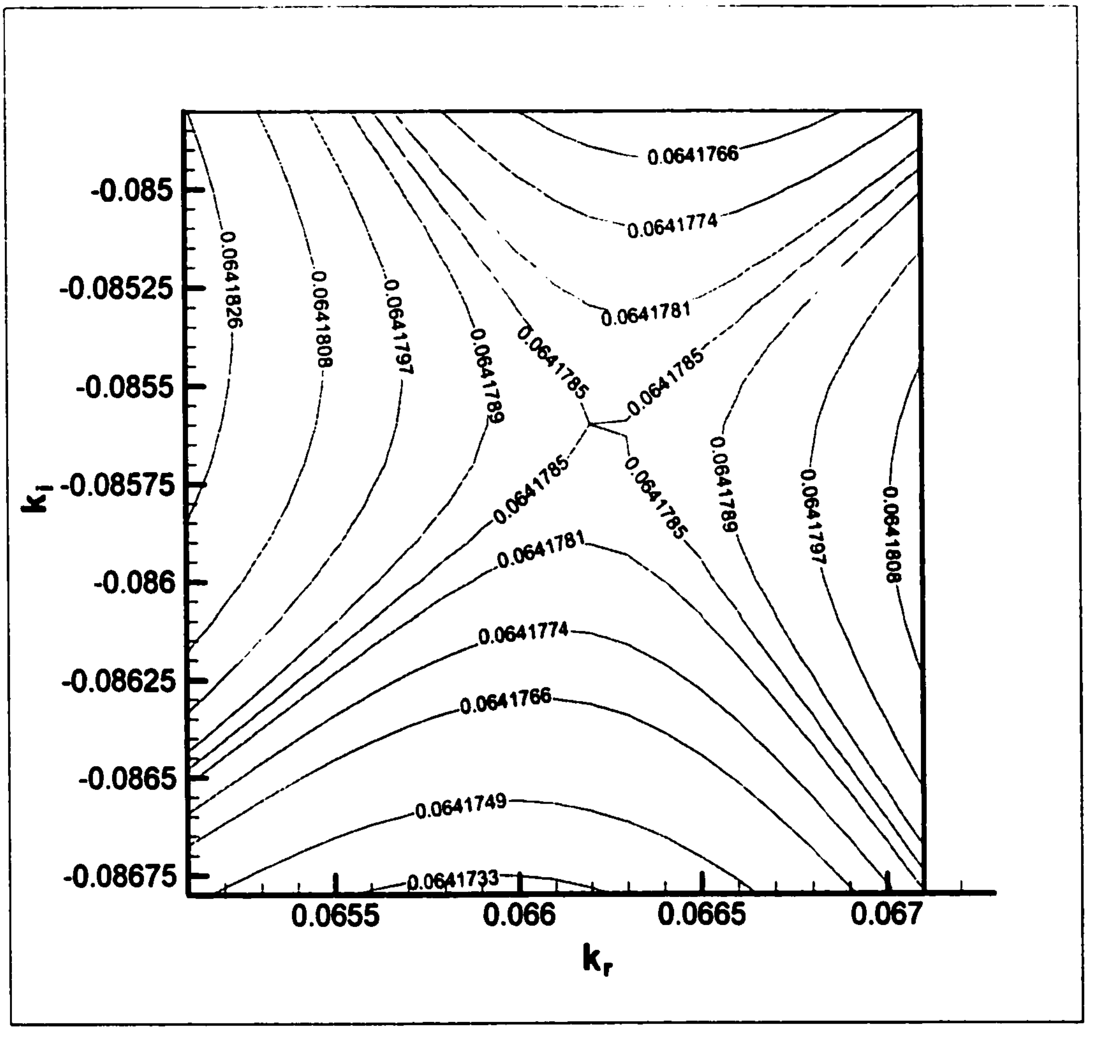

Figure A185: Contour plot of Ω_r for $R/\theta = 10$, $Fr = 2$, $\rho_j/\rho_\infty = 0.14$, $Sc = 1$, and $\Delta r = 1.25$ in the k-plane illustrating the pinch point formation

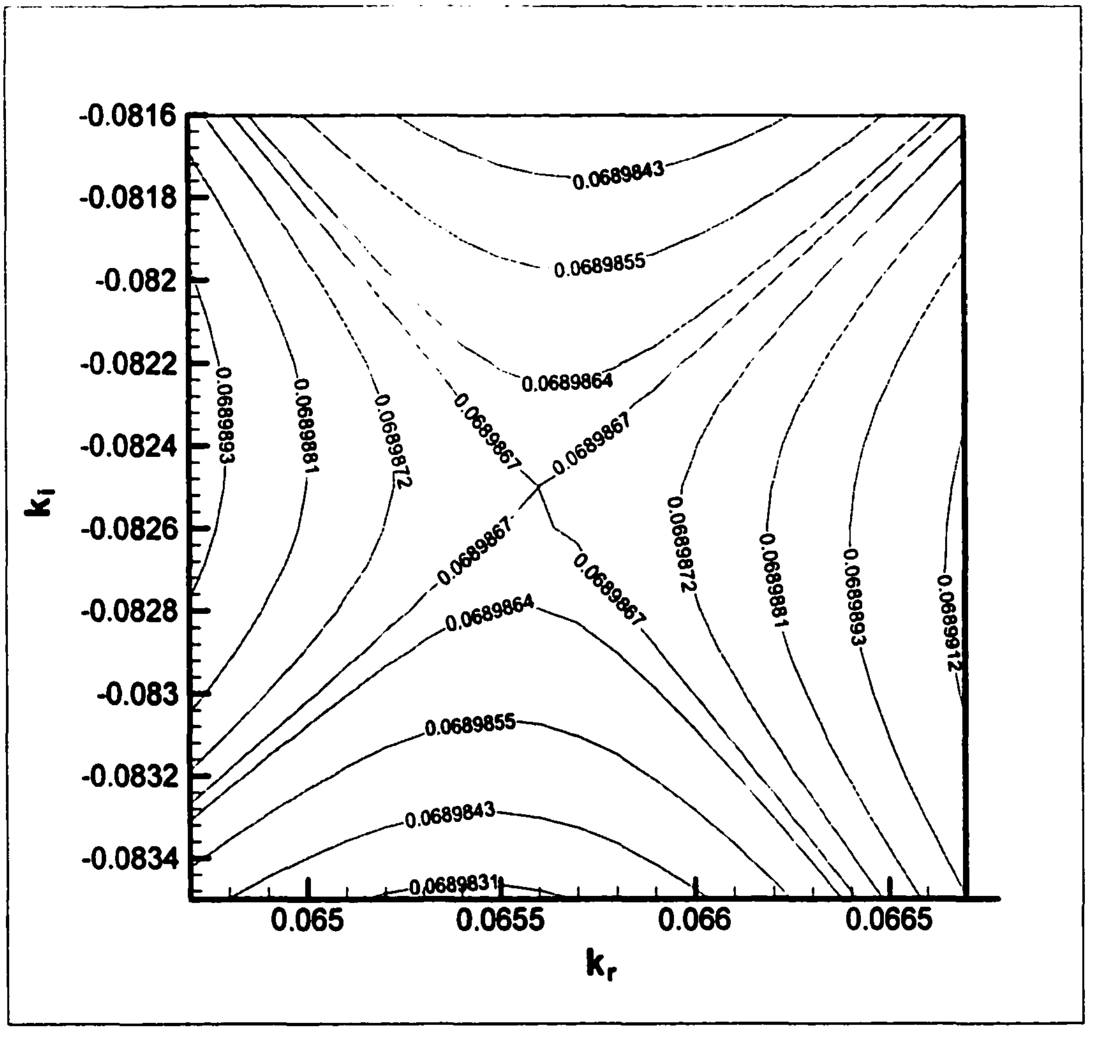

Figure A186: Contour plot of Ω_r for $R/\theta = 10$, $Fr = 1$, $\rho_j/\rho_\infty = 0.14$, $Sc = 1$, and $\Delta r = 1.25$ in the k-plane illustrating the pinch point formation

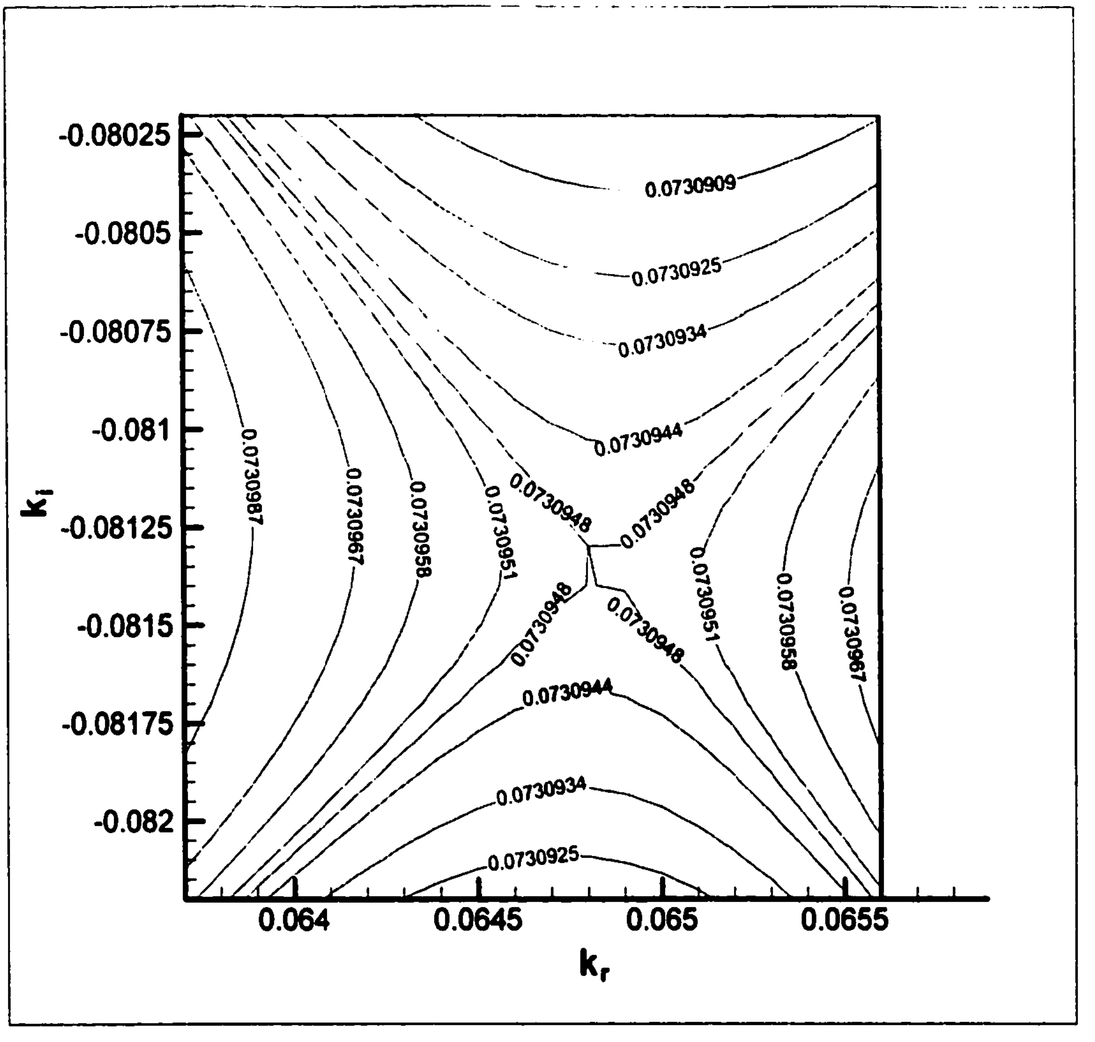

Figure A187: Contour plot of Ω_r for $R/\theta = 10$, $Fr = 0.75$, $\rho_j/\rho_\infty = 0.14$, $Sc = 1$, and $\Delta r = 1.25$ in the k-plane illustrating the pinch point formation

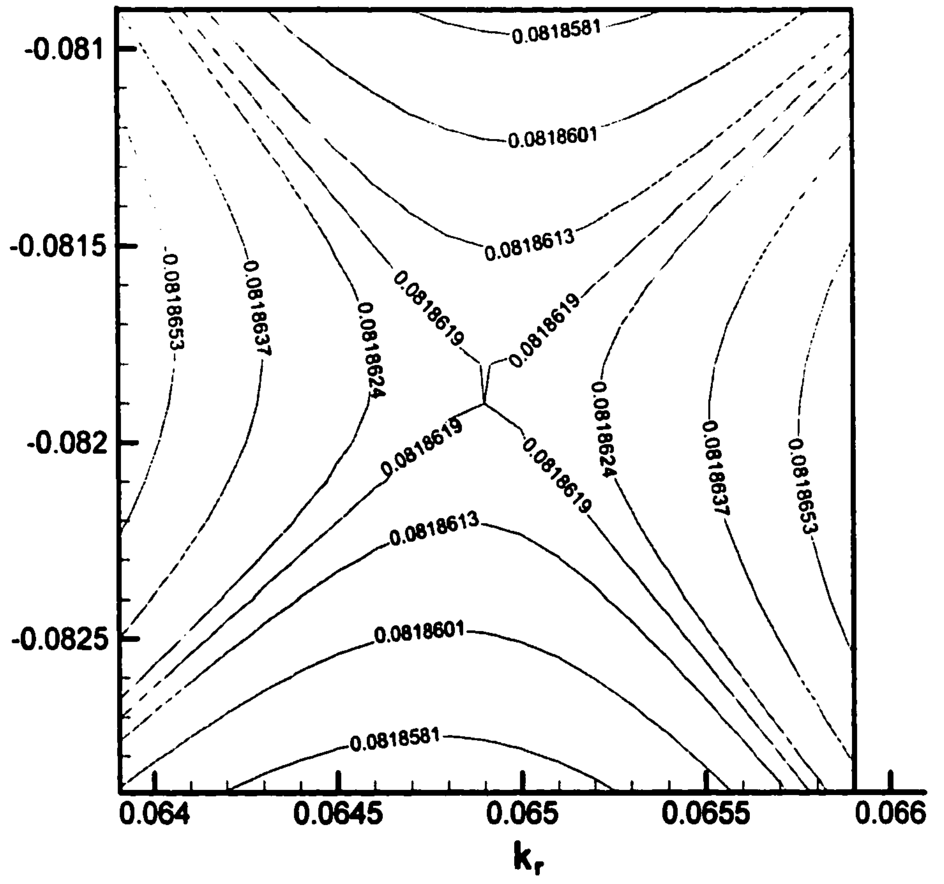

Figure A188: Contour plot of Ω_r for $R/\theta = 10$, $Fr = 0.5$, $\rho_j/\rho_\infty = 0.14$, $Sc = 1$, and $\Delta r = 1.25$ in the k-plane illustrating the pinch point formation

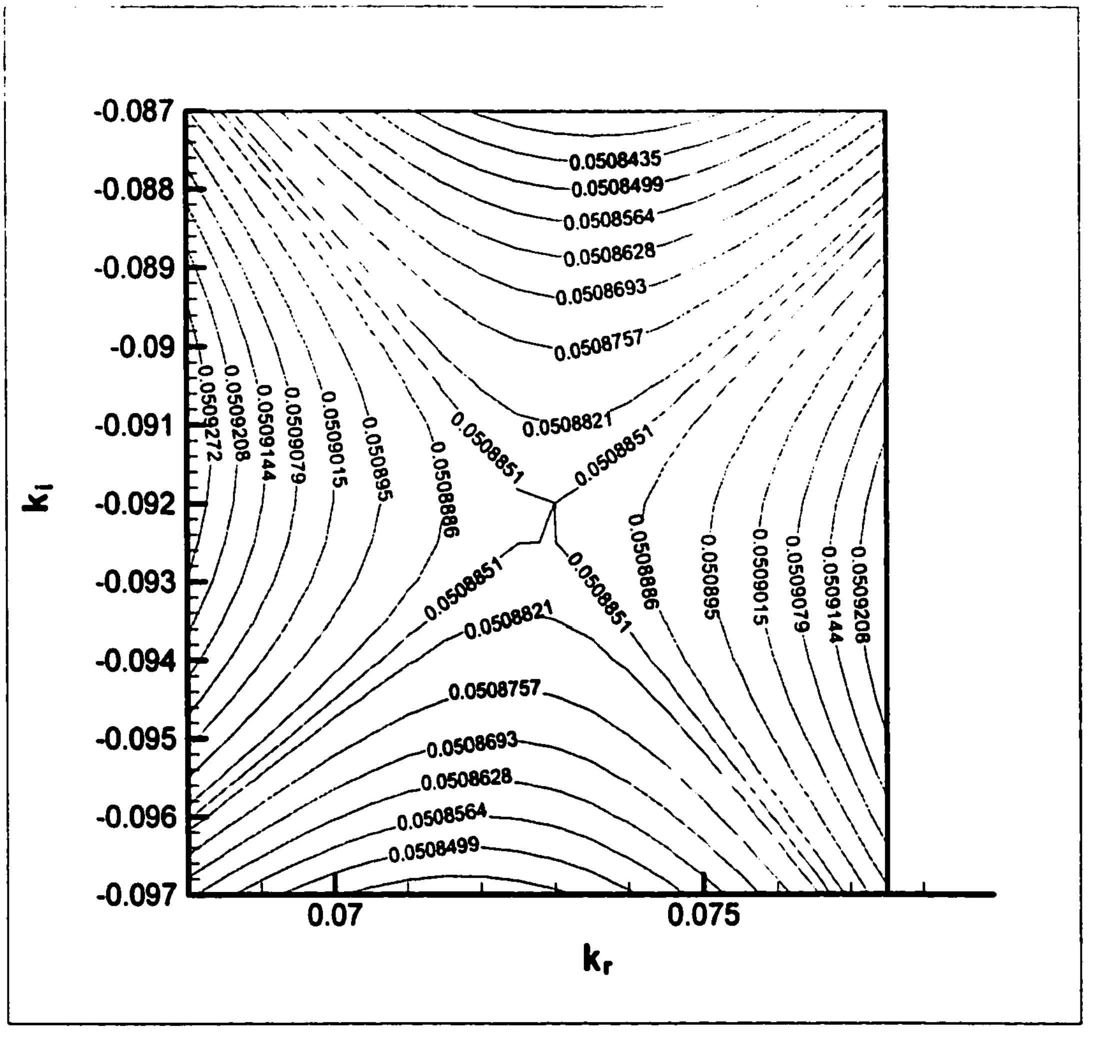

Figure A189: Contour plot of Ω_r for $R/\theta = 10$, $Fr = \infty$, $\rho_j/\rho_\infty = 0.14$, $Sc = 1$, and $\Delta r = -1.25$ in the k-plane illustrating the pinch point formation

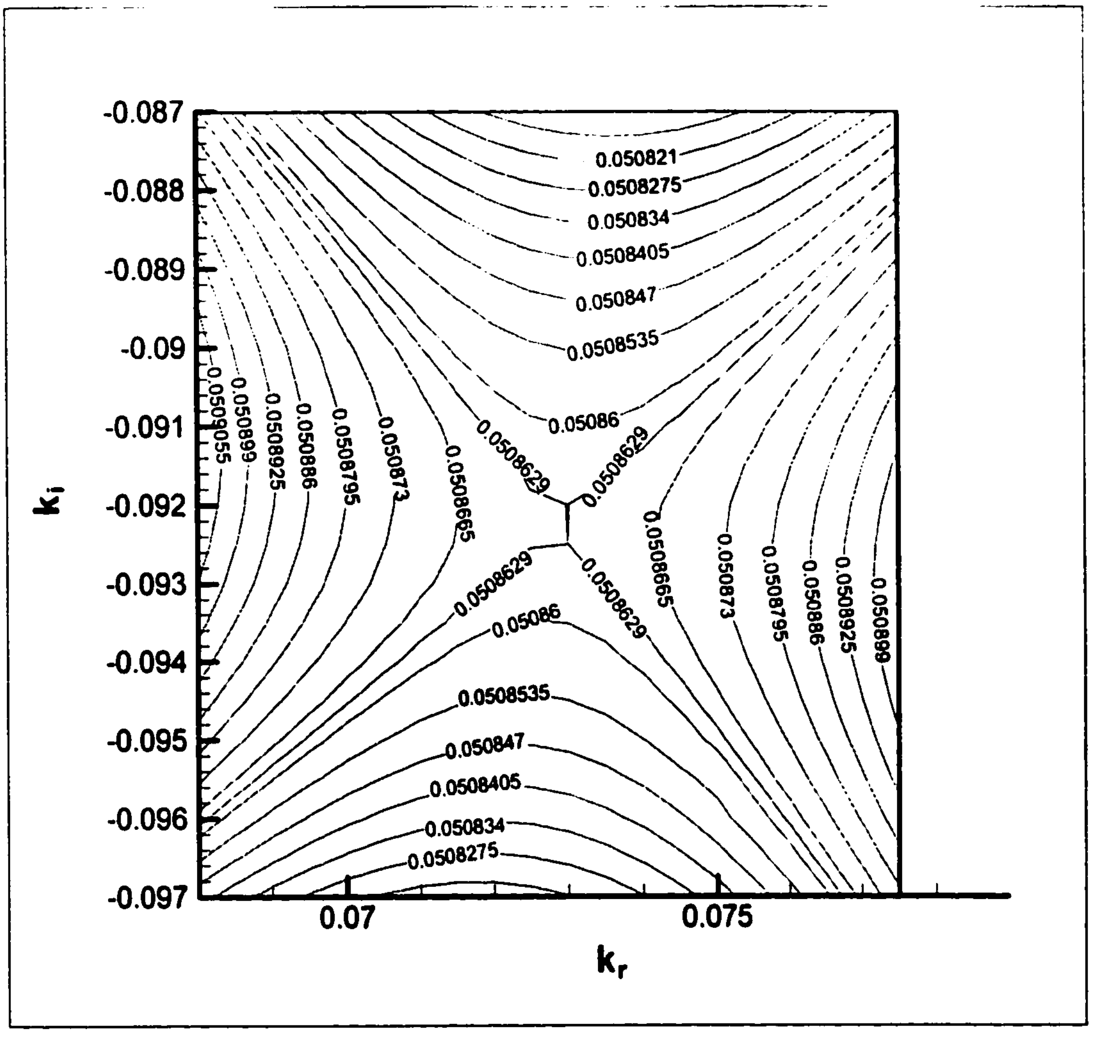

Figure A190: Contour plot of Ω_r for $R/\theta = 10$, $Fr = 10$, $\rho_j/\rho_\infty = 0.14$, $Sc = 1$, and $\Delta r = -1.25$ in the k-plane illustrating the pinch point formation

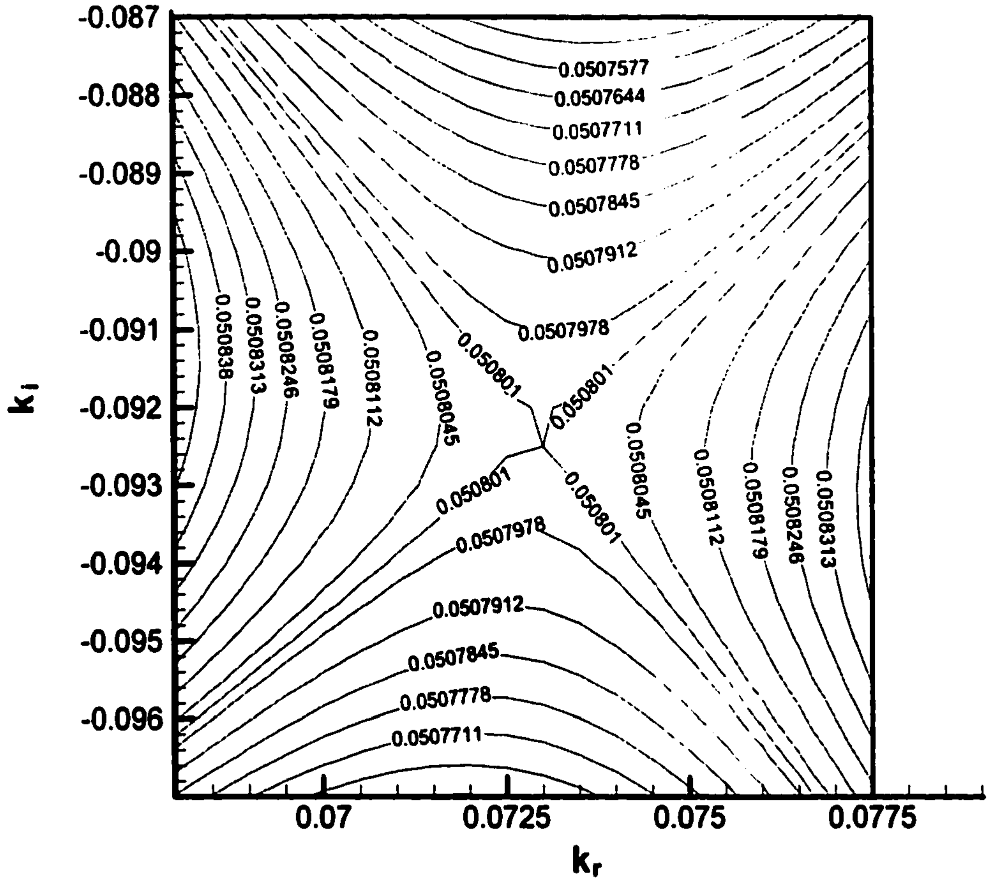

Figure A191: Contour plot of Ω_r for $R/\theta = 10$, $Fr = 5$, $\rho_j/\rho_\infty = 0.14$, $Sc = 1$, and $\Delta r = -1.25$ in the k-plane illustrating the pinch point formation

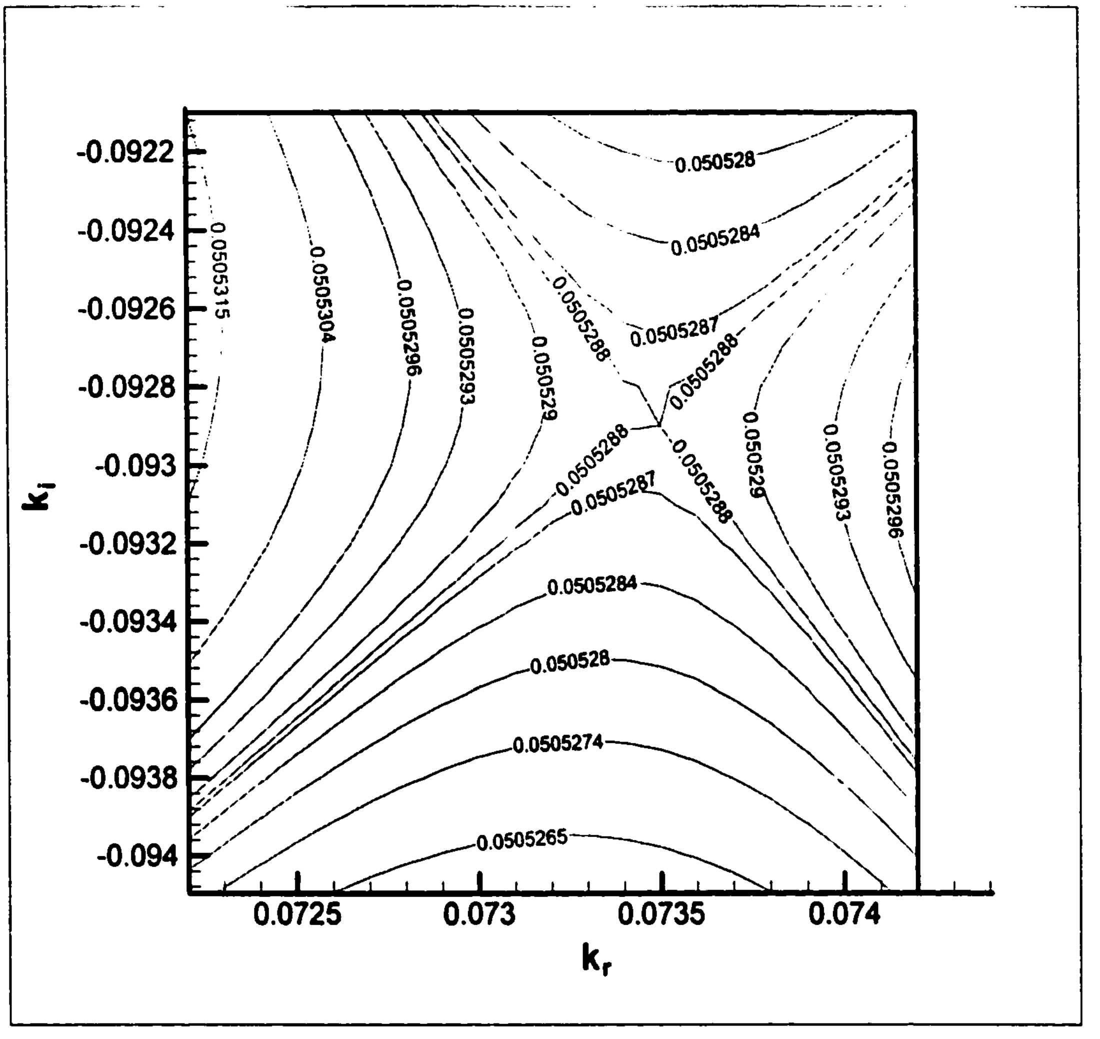

Figure A192: Contour plot of Ω_r for $R/\theta = 10$, $Fr = 2$, $\rho_j/\rho_\infty = 0.14$, $Sc = 1$, and $\Delta r = -1.25$ in the k-plane illustrating the pinch point formation

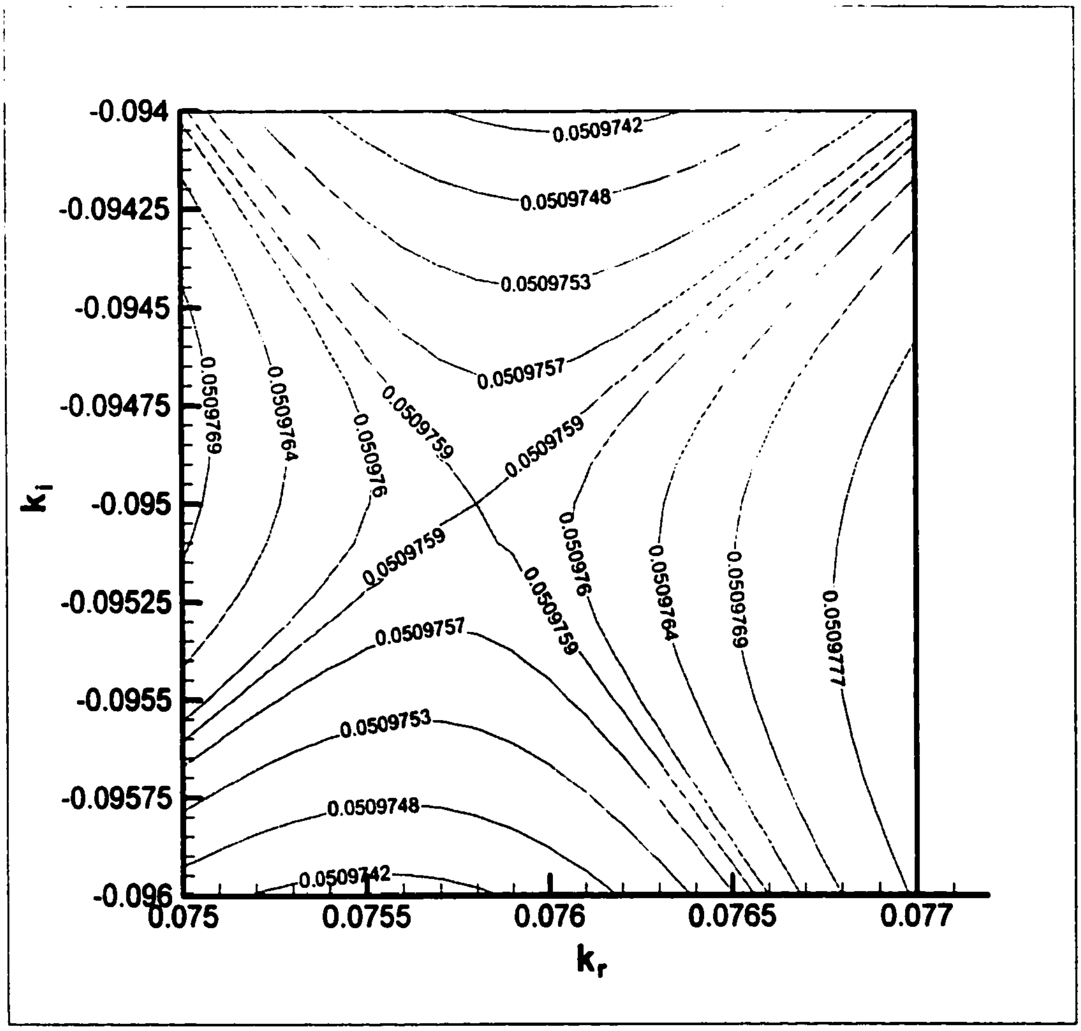

Figure A193: Contour plot of Ω_r for $R/\theta = 10$, $Fr = 1$, $\rho_j/\rho_\infty = 0.14$, $Sc = 1$, and $\Delta r = -1.25$ in the k-plane illustrating the pinch point formation

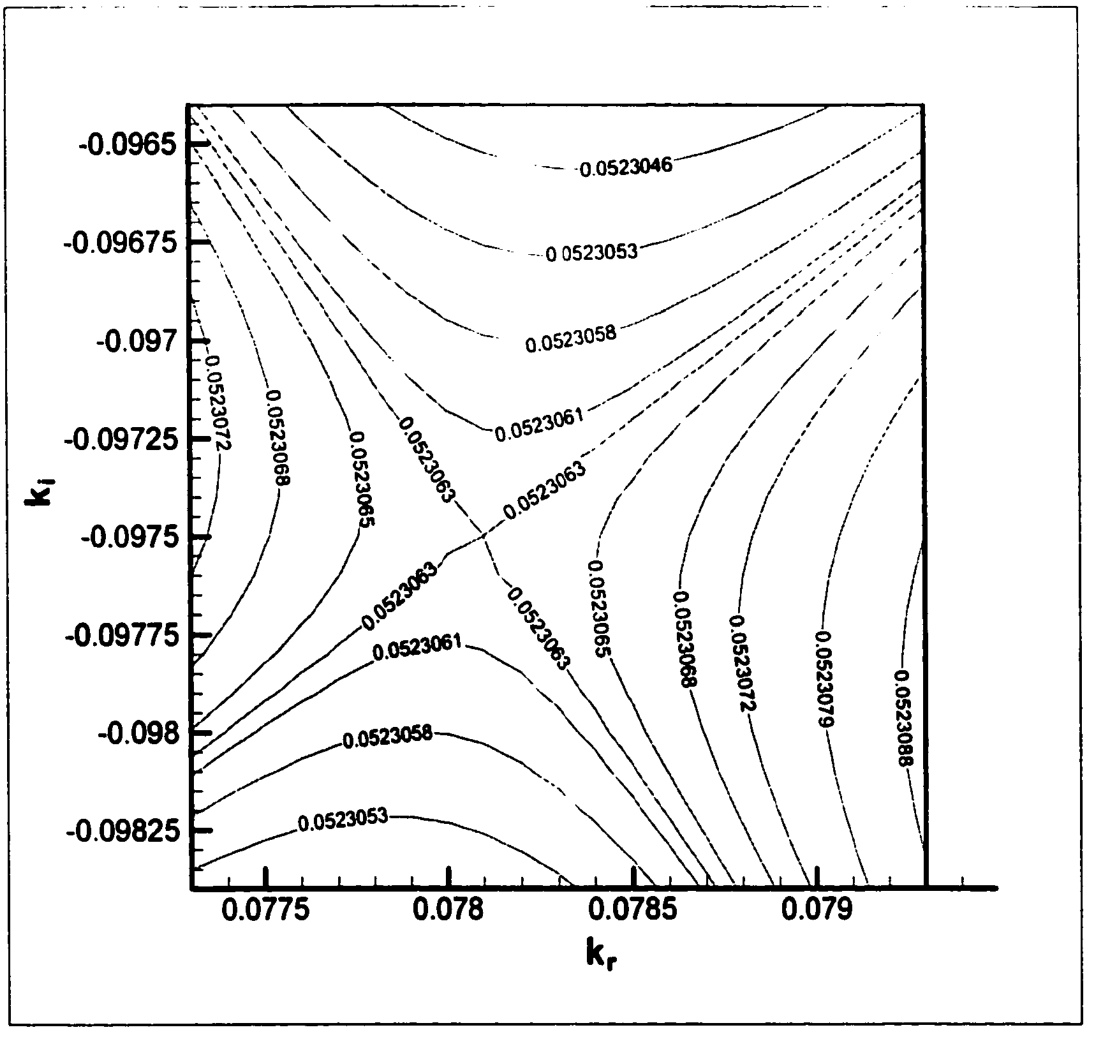

Figure A194: Contour plot of Ω_r for $R/\theta = 10$, $Fr = 0.75$, $\rho_j/\rho_\infty = 0.14$, $Sc = 1$, and $\Delta r = -1.25$ in the k-plane illustrating the pinch point formation

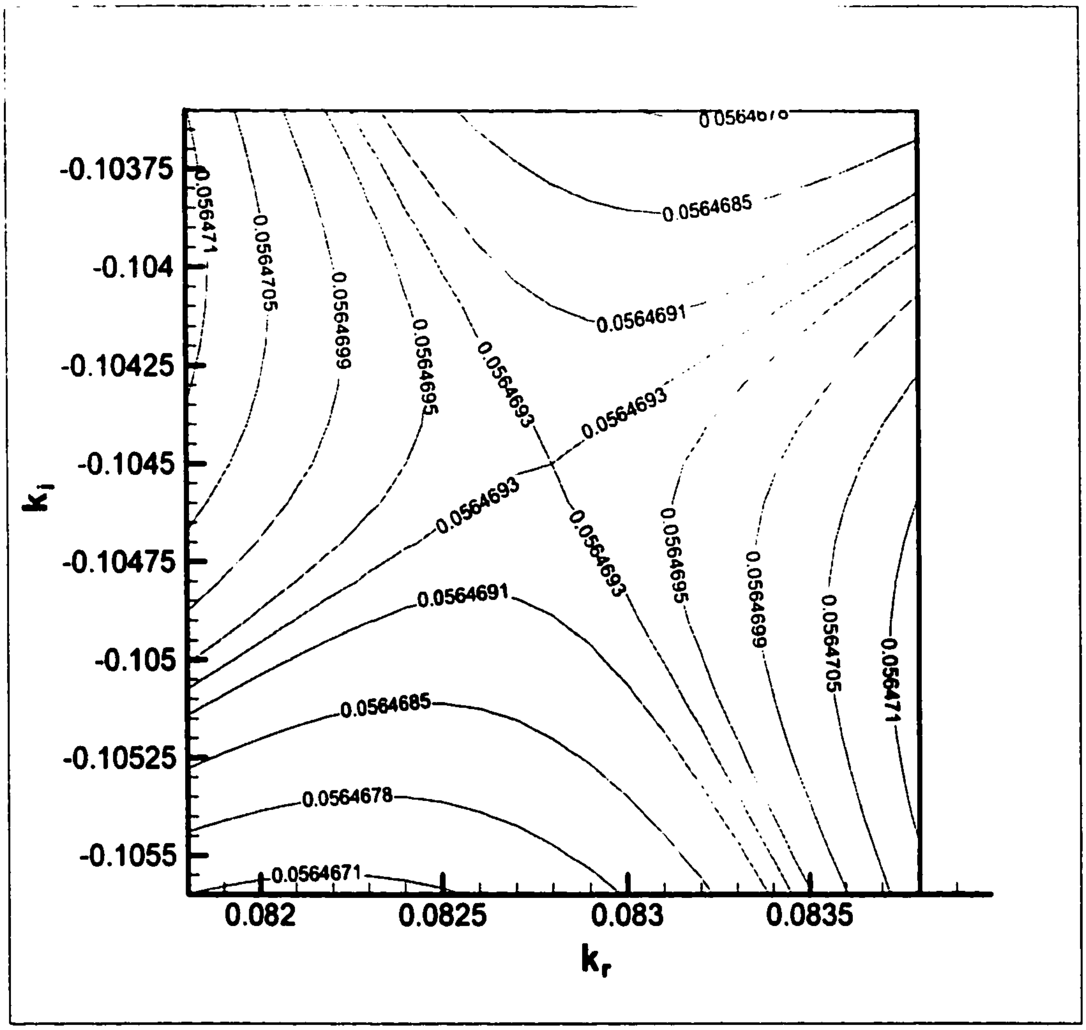

Figure A195: Contour plot of Ω_r for $R/\theta = 10$, $Fr = 0.5$, $\rho_j/\rho_\infty = 0.14$, $Sc = 1$, and $\Delta r = -1.25$ in the k-plane illustrating the pinch point formation

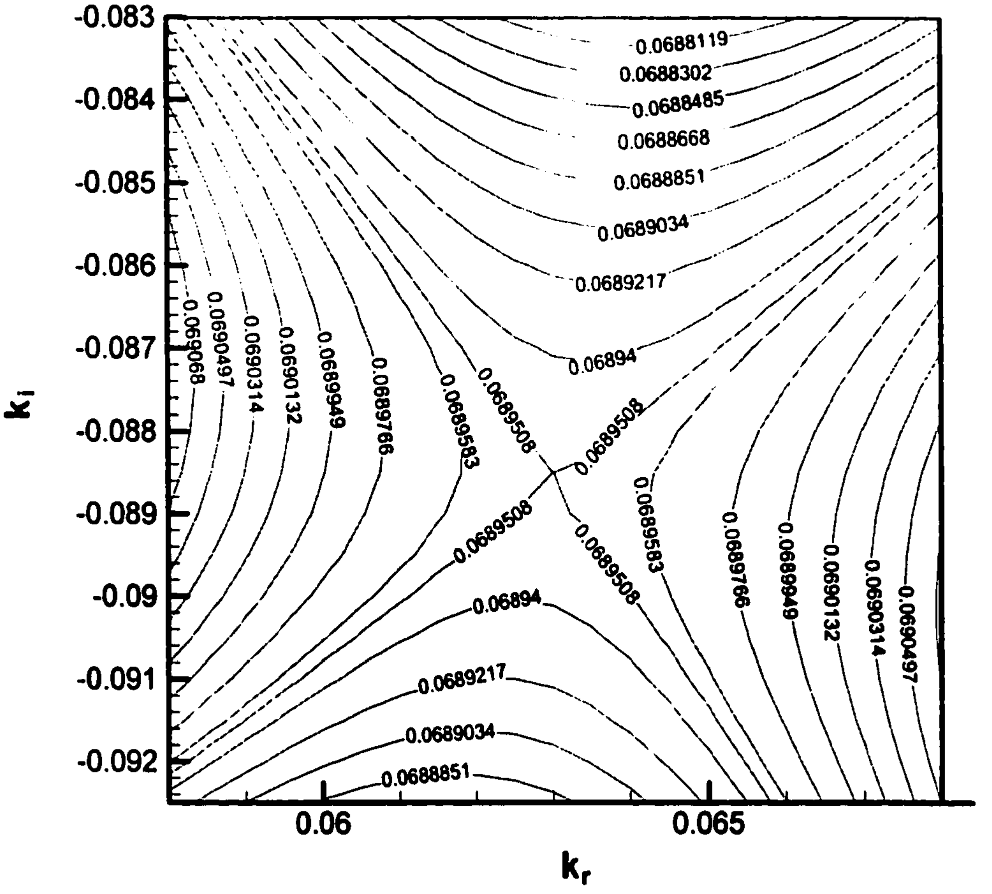

Figure A196: Contour plot of Ω_r for $R/\theta = 10$, $Fr = \infty$, $\rho_j/\rho_\infty = 0.14$, $Sc = 1$, and $\Delta r = 2.5$ in the k-plane illustrating the pinch point formation

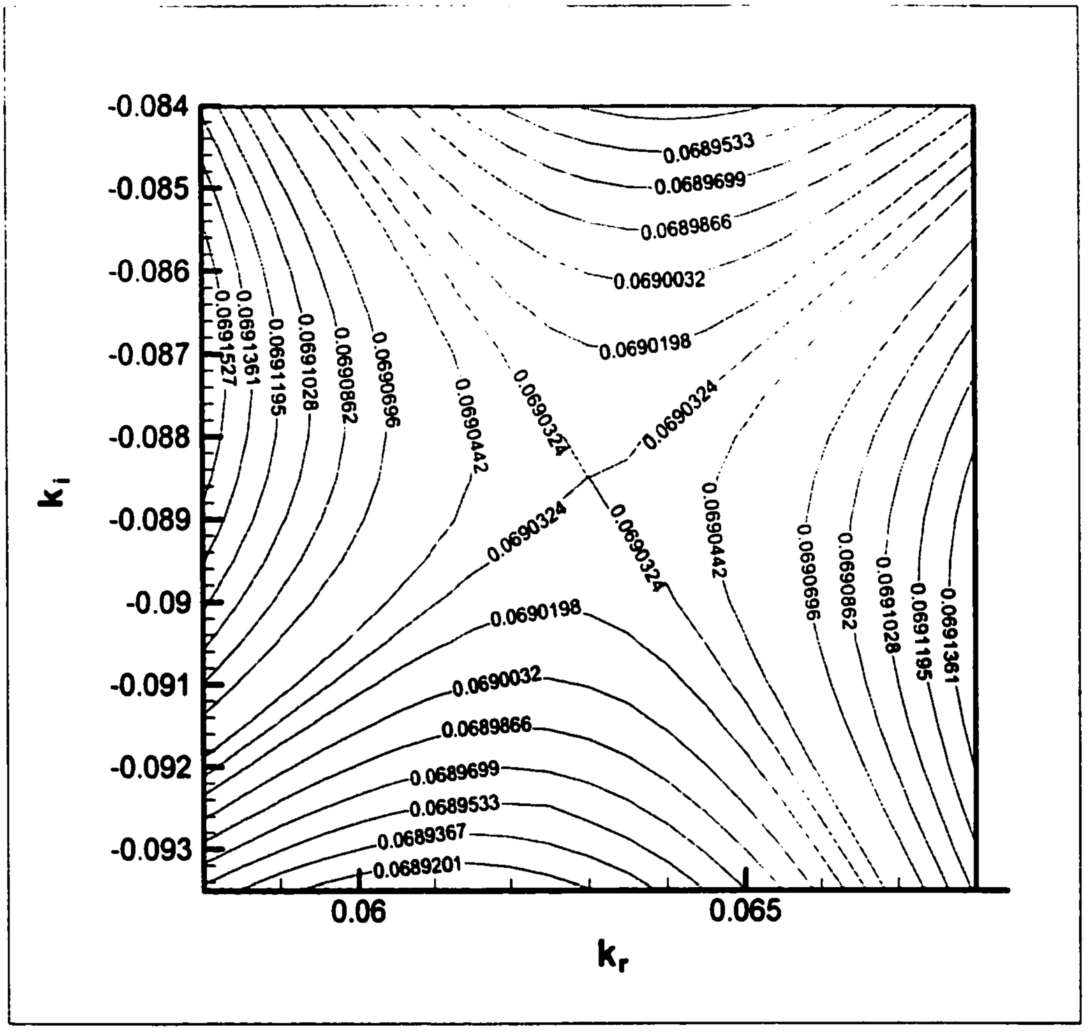

Figure A197: Contour plot of Ω_r for $R/\theta = 10$, $Fr = 10$, $\rho_j/\rho_\infty = 0.14$, $Sc = 1$, and $\Delta r = 2.5$ in the k-plane illustrating the pinch point formation

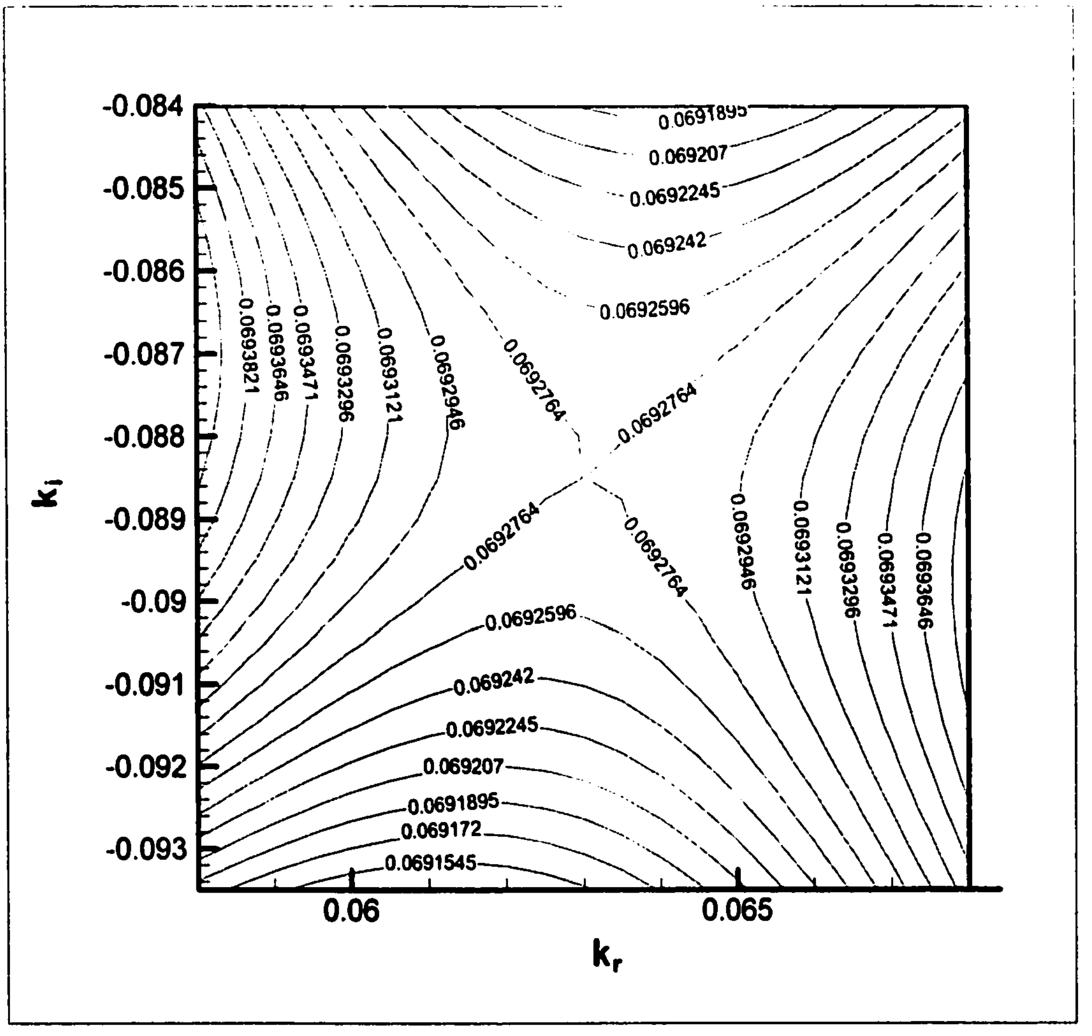

Figure A198: Contour plot of Ω_r for $R/\theta = 10$, $Fr = 5$, $\rho_j/\rho_\infty = 0.14$, $Sc = 1$, and $\Delta r = 2.5$ in the k-plane illustrating the pinch point formation

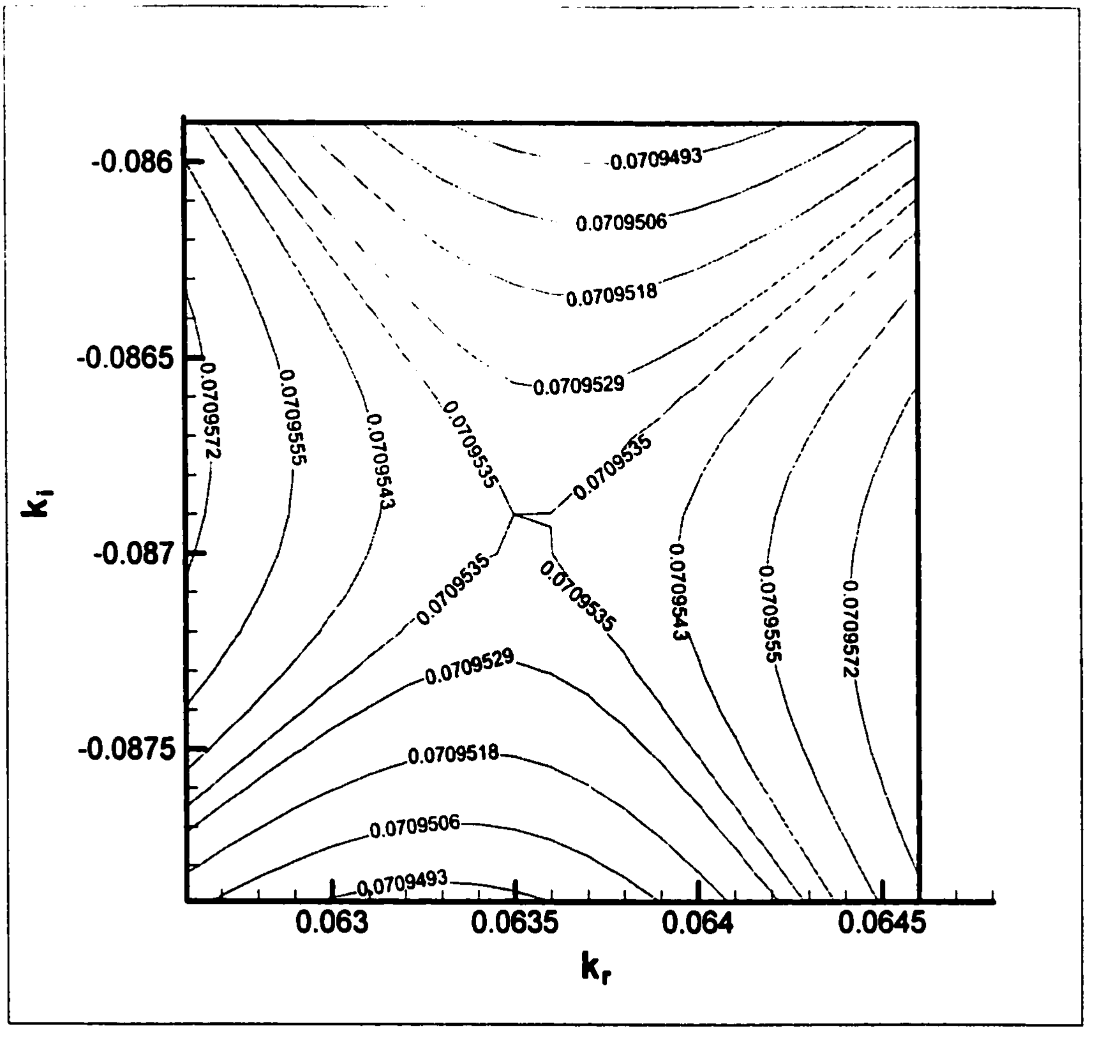

Figure A199: Contour plot of Ω_r for $R/\theta = 10$, $Fr = 2$, $\rho_j/\rho_\infty = 0.14$, $Sc = 1$, and $\Delta r = 2.5$ in the k-plane illustrating the pinch point formation

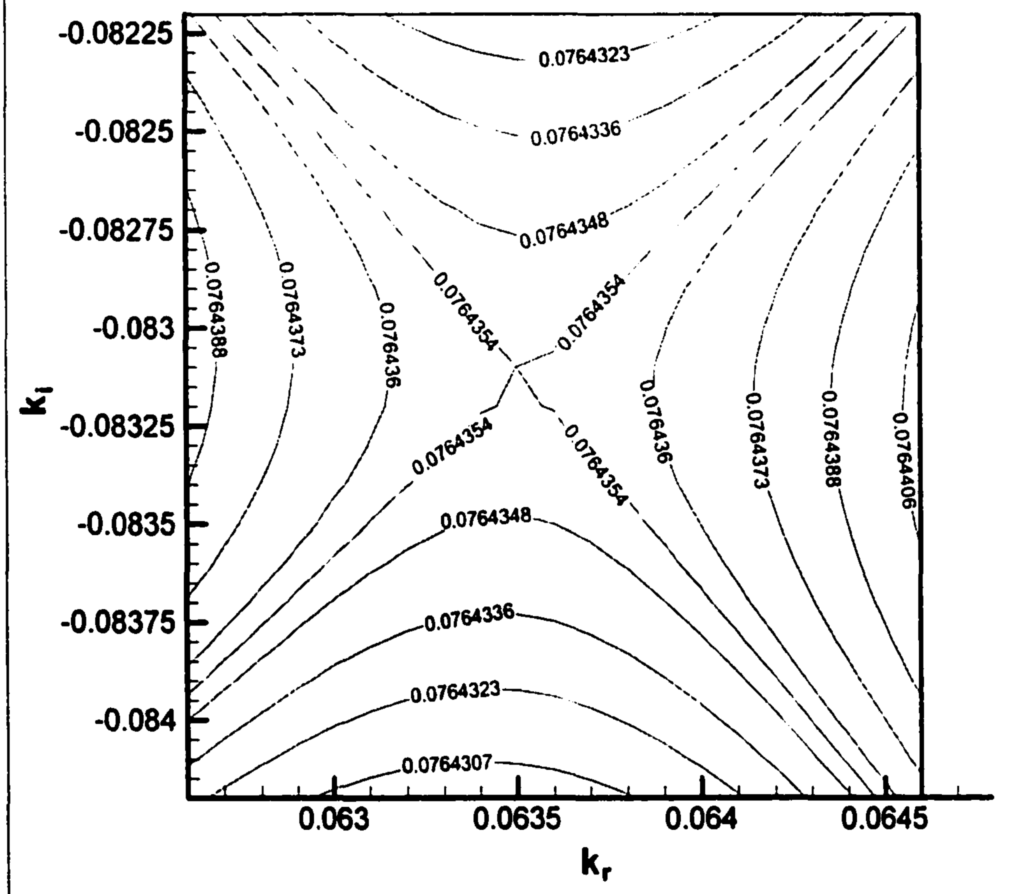

Figure A200: Contour plot of Ω_r for $R/\theta = 10$, $Fr = 1$, $\rho_j/\rho_\infty = 0.14$, $Sc = 1$, and $\Delta r = 2.5$ in the k-plane illustrating the pinch point formation

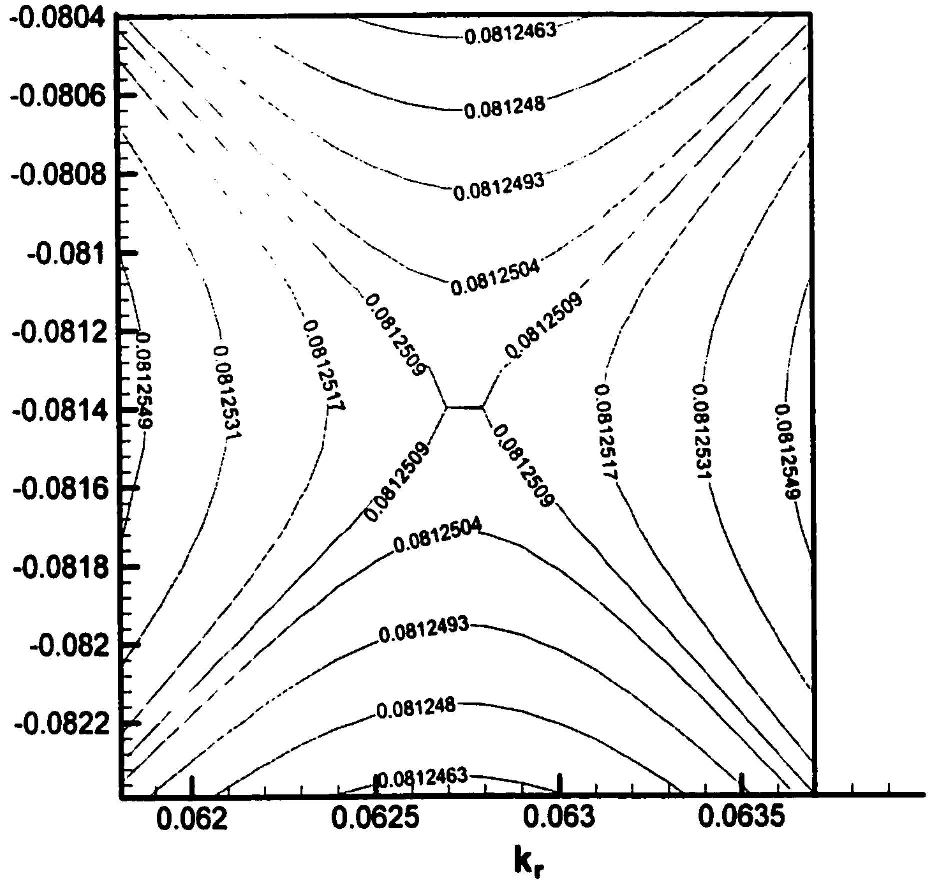

Figure A201: Contour plot of Ω_r for $R/\theta = 10$, $Fr = 0.75$, $\rho_j/\rho_\infty = 0.14$, $Sc = 1$, and $\Delta r = 2.5$ in the k-plane illustrating the pinch point formation

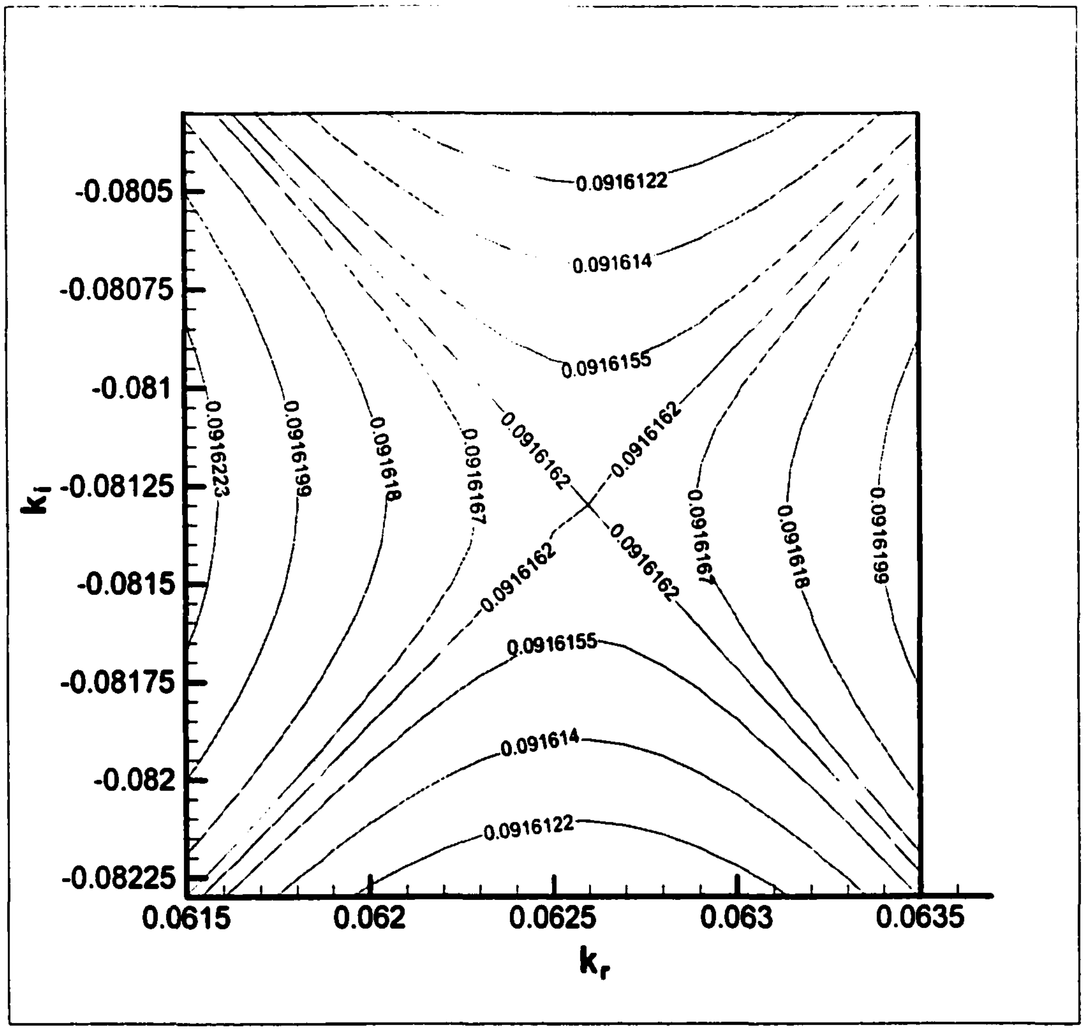

Figure A202: Contour plot of Ω_r for $R/\theta = 10$, $Fr = 0.5$, $\rho_j/\rho_\infty = 0.14$, $Sc = 1$, and $\Delta r = 2.5$ in the k-plane illustrating the pinch point formation

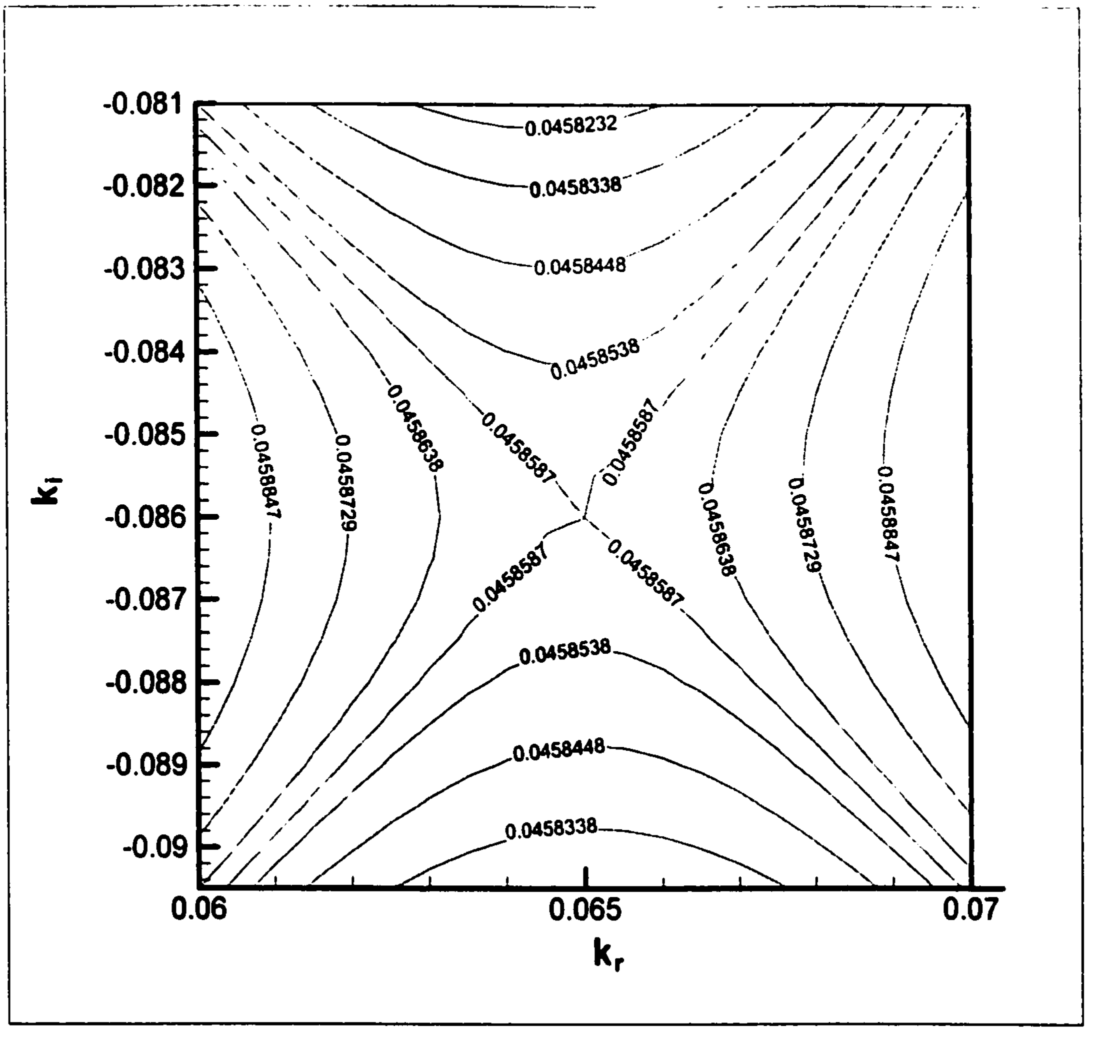

Figure A203: Contour plot of Ω_r for $R/\theta = 10$, $Fr = \infty$, $\rho_j/\rho_\infty = 0.14$, $Sc = 1$, and $\Delta r = -2.5$ in the k-plane illustrating the pinch point formation

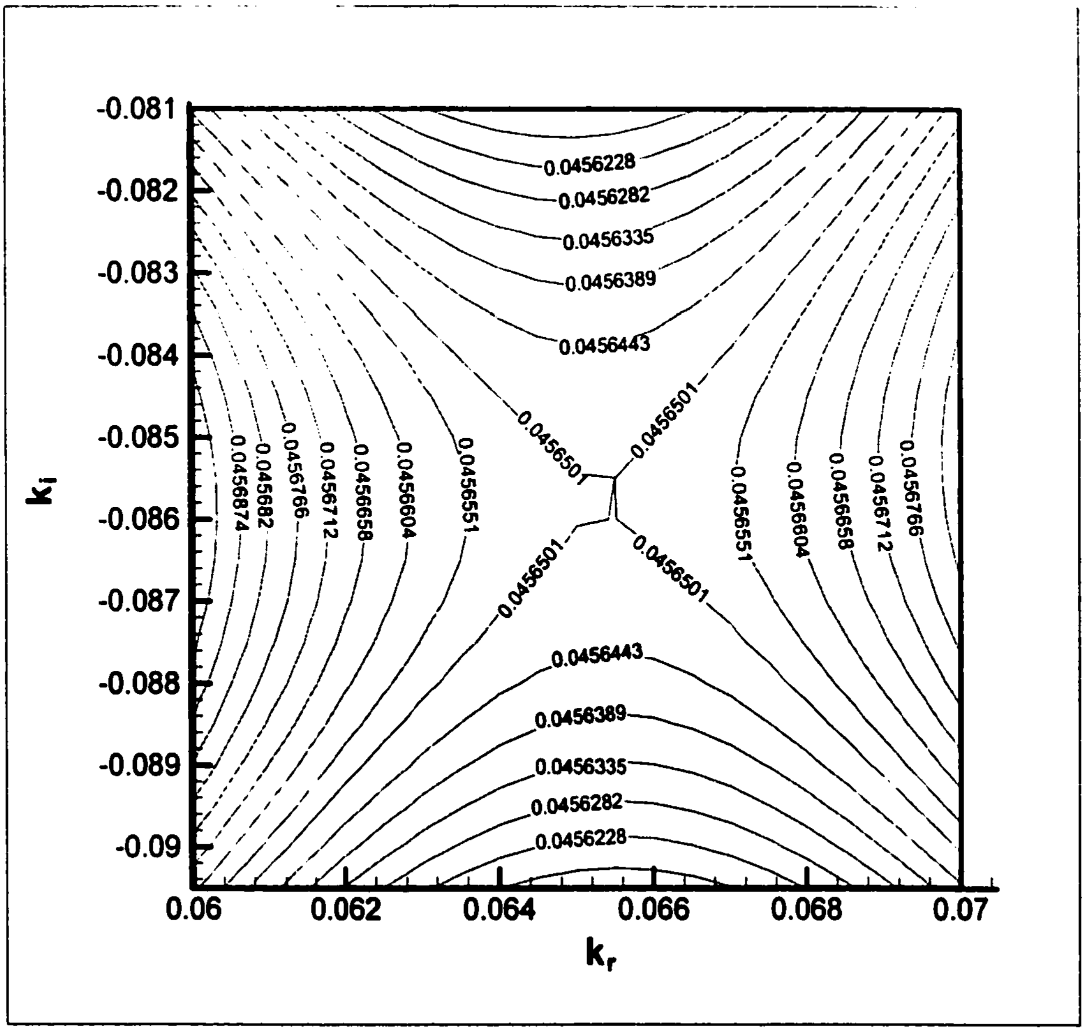

Figure A204: Contour plot of Ω_r for $R/\theta = 10$, $Fr = 10$, $\rho_j/\rho_\infty = 0.14$, $Sc = 1$, and $\Delta r = -2.5$ in the k-plane illustrating the pinch point formation

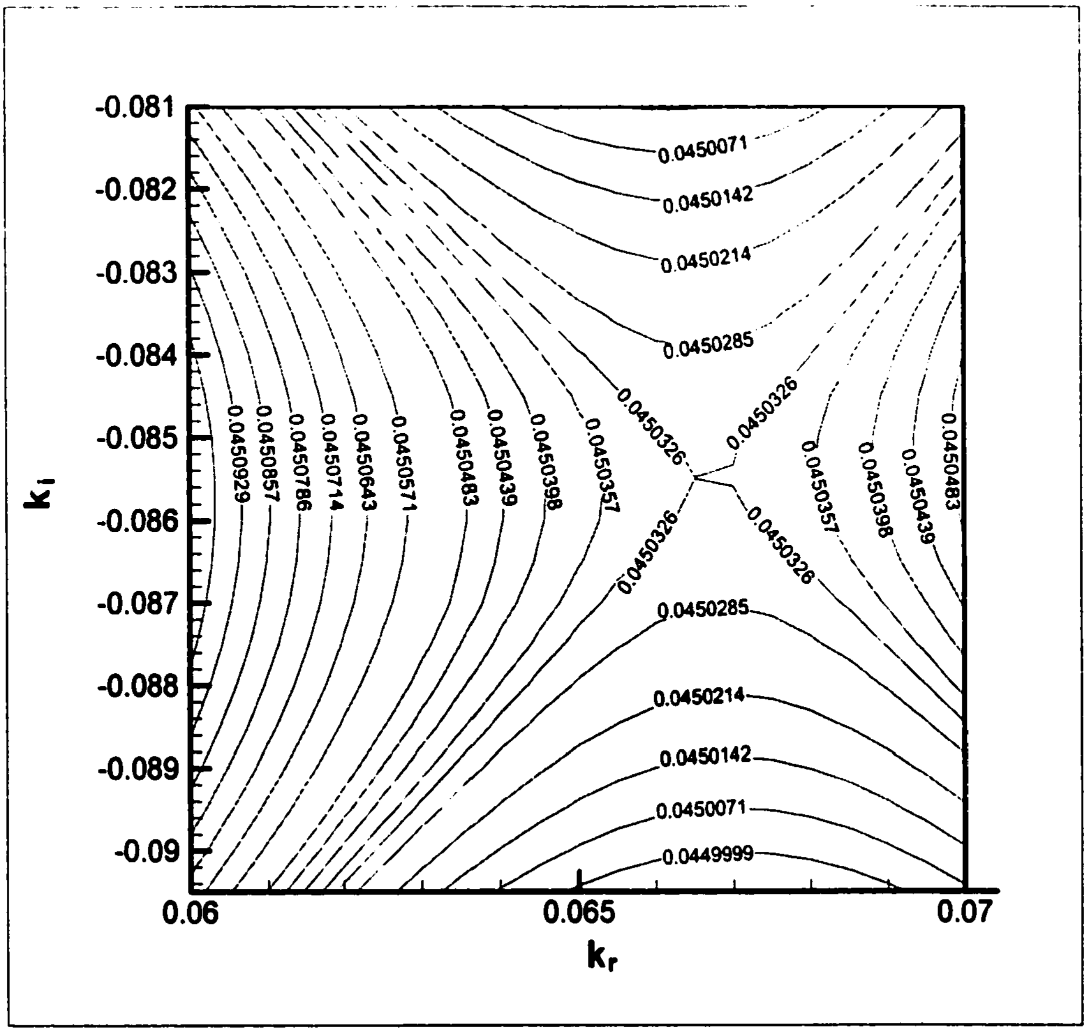

Figure A205: Contour plot of Ω_r for $R/\theta = 10$, $Fr = 5$, $\rho_j/\rho_\infty = 0.14$, $Sc = 1$, and $\Delta r = -2.5$ in the k-plane illustrating the pinch point formation

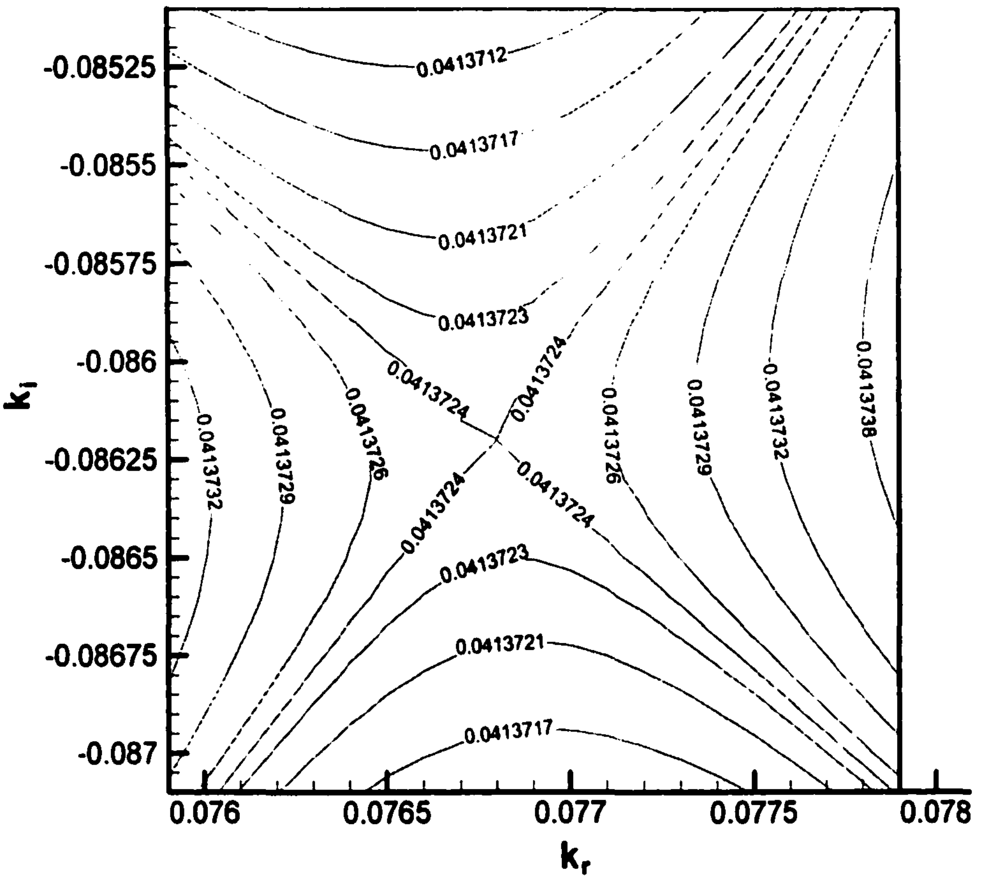

Figure A206: Contour plot of Ω_r for $R/\theta = 10$, $Fr = 2$, $\rho_j/\rho_\infty = 0.14$, $Sc = 1$, and $\Delta r = -2.5$ in the k-plane illustrating the pinch point formation

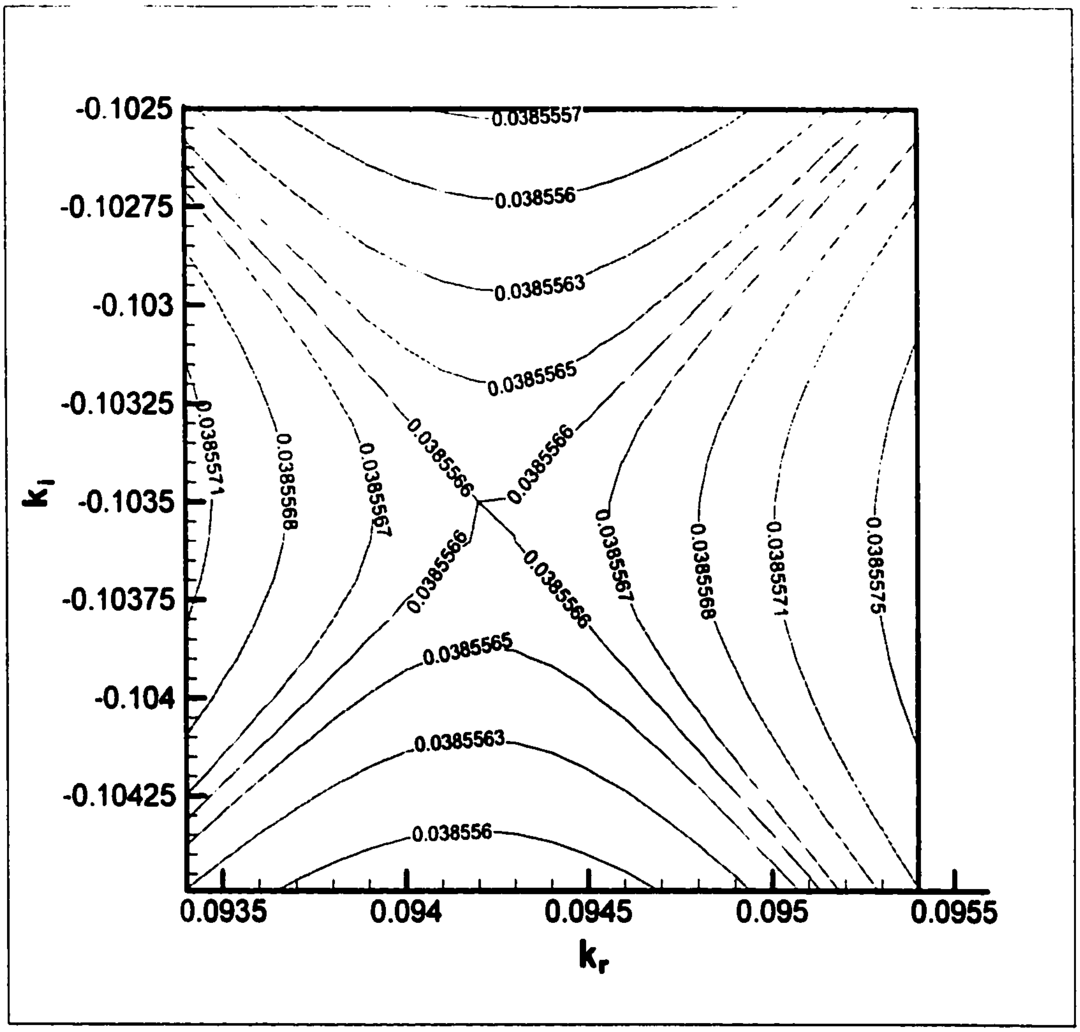

Figure A207: Contour plot of Ω_r for $R/\theta = 10$, $Fr = 1$, $\rho_j/\rho_\infty = 0.14$, $Sc = 1$, and $\Delta r = -2.5$ in the k-plane illustrating the pinch point formation

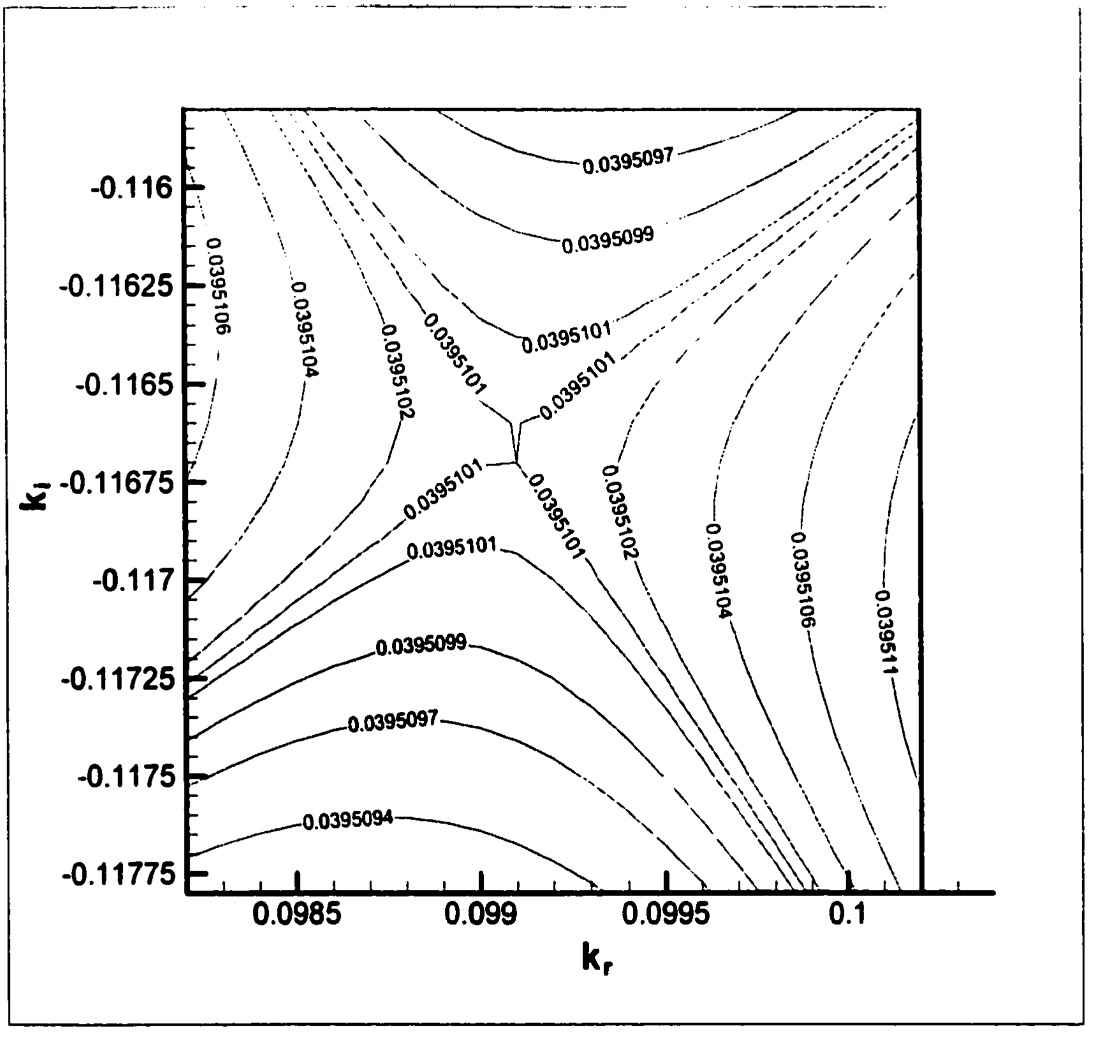

Figure A208: Contour plot of Ω_i for $R/\theta = 10$, $Fr = 0.75$, $\rho_j/\rho_\infty = 0.14$, $Sc = 1$, and $\Delta r = -2.5$ in the k-plane illustrating the pinch point formation

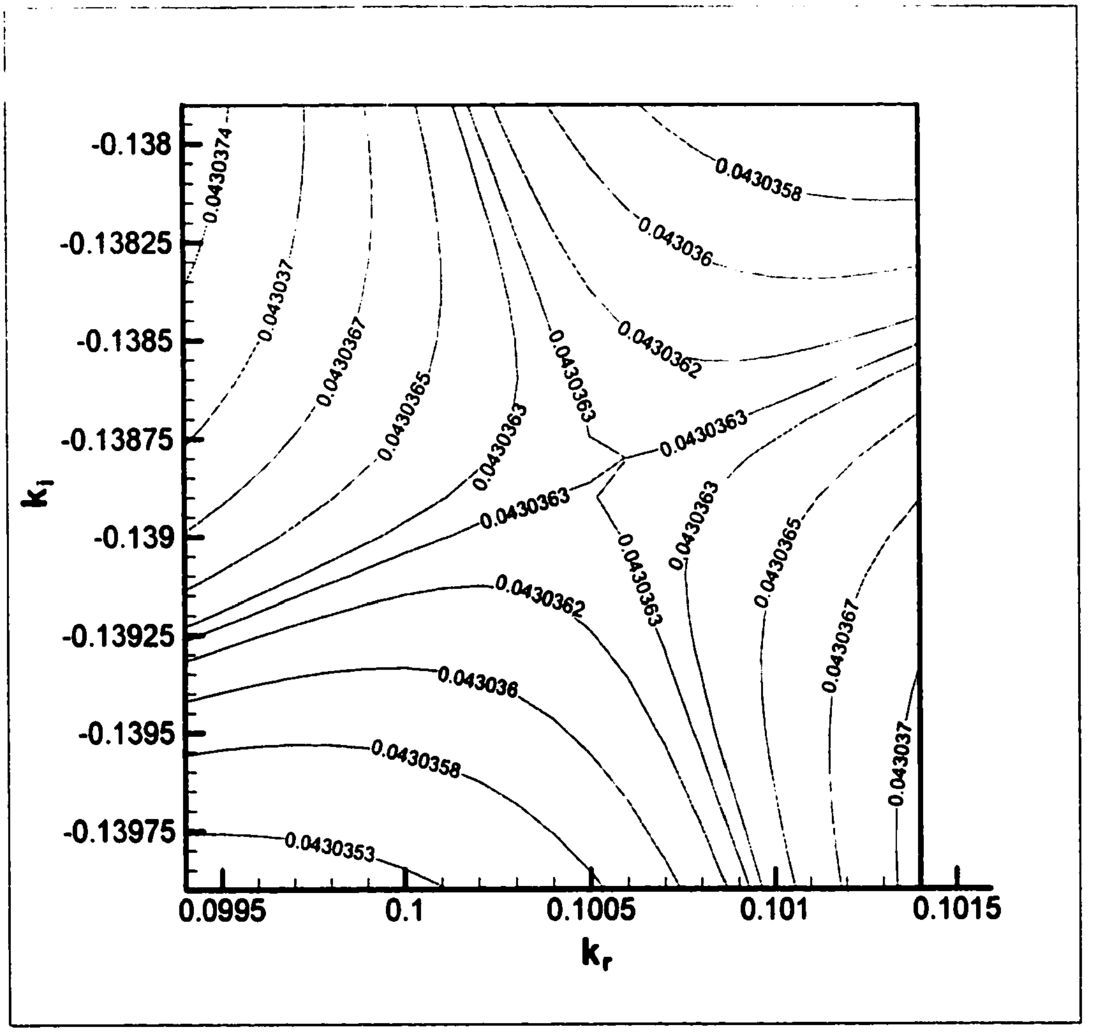

Figure A209: Contour plot of Ω_r for $R/\theta = 10$, $Fr = 0.5$, $\rho_j/\rho_\infty = 0.14$, $Sc = 1$, and $\Delta r = -2.5$ in the k-plane illustrating the pinch point formation

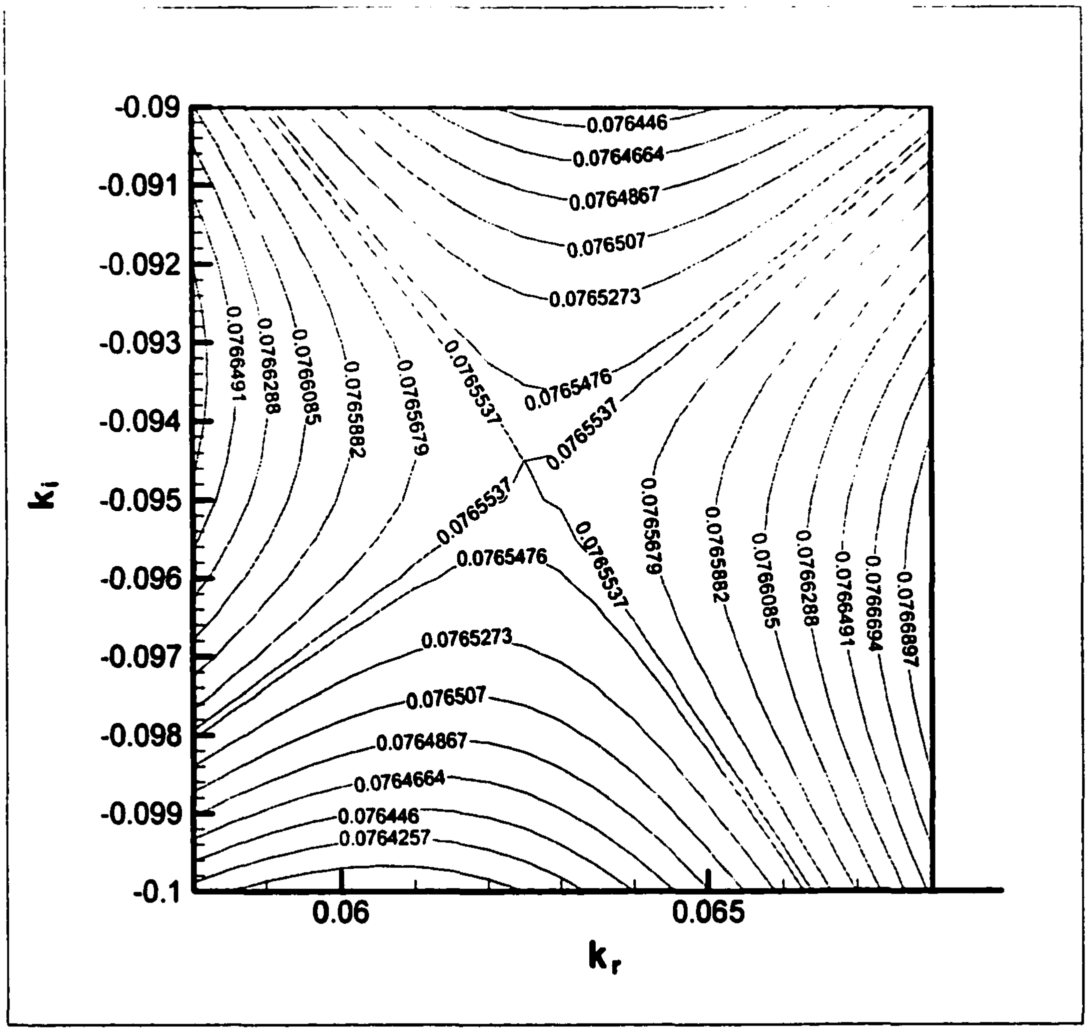

Figure A210: Contour plot of Ω_r for $R/\theta = 10$, $Fr = \infty$, $\rho_j/\rho_\infty = 0.14$, $Sc = 1$, and $\Delta r = 3.75$ in the k-plane illustrating the pinch point formation

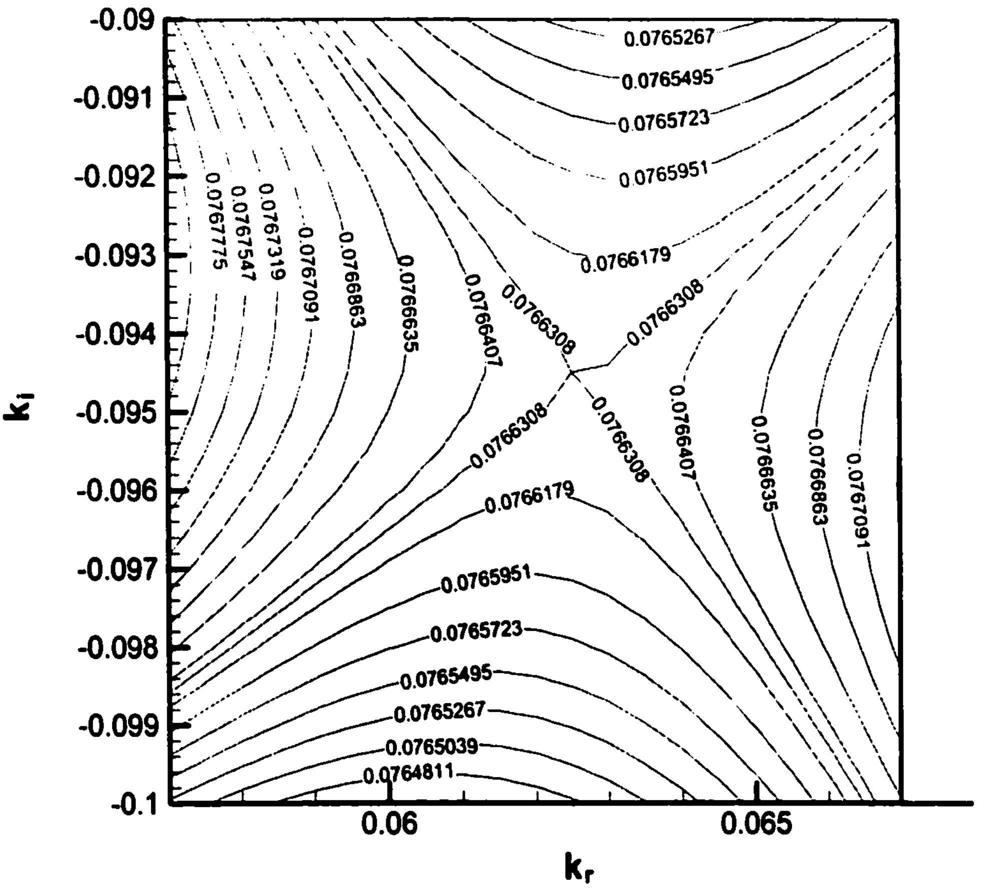

Figure A211: Contour plot of Ω_i for $R/\theta = 10$, $Fr = 10$, $\rho_j/\rho_\infty = 0.14$, $Sc = 1$, and $\Delta r = 3.75$ in the k-plane illustrating the pinch point formation

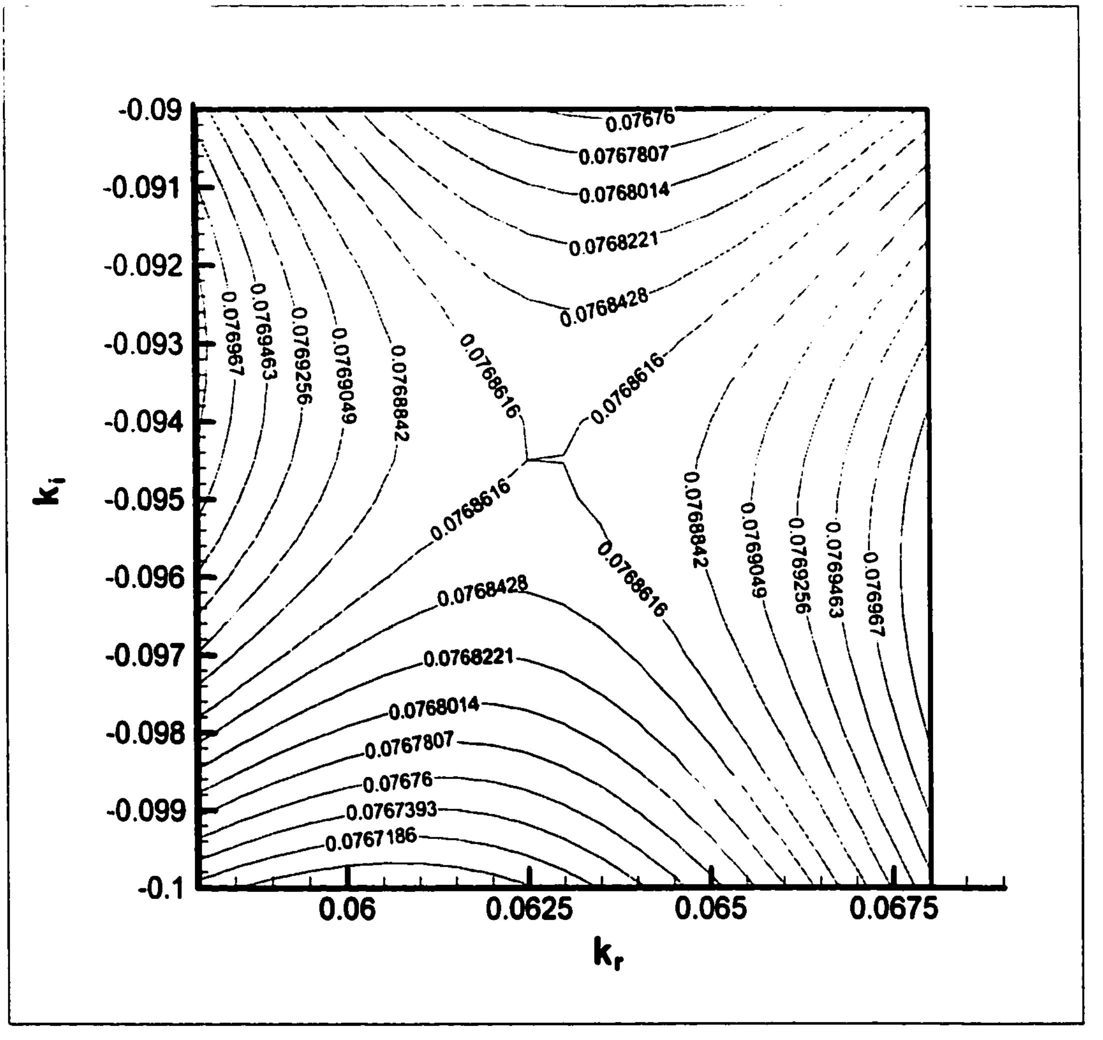

Figure A212: Contour plot of Ω_r for $R/\theta = 10$, $Fr = 5$, $\rho_j/\rho_\infty = 0.14$, $Sc = 1$, and $\Delta r = 3.75$ in the k-plane illustrating the pinch point formation

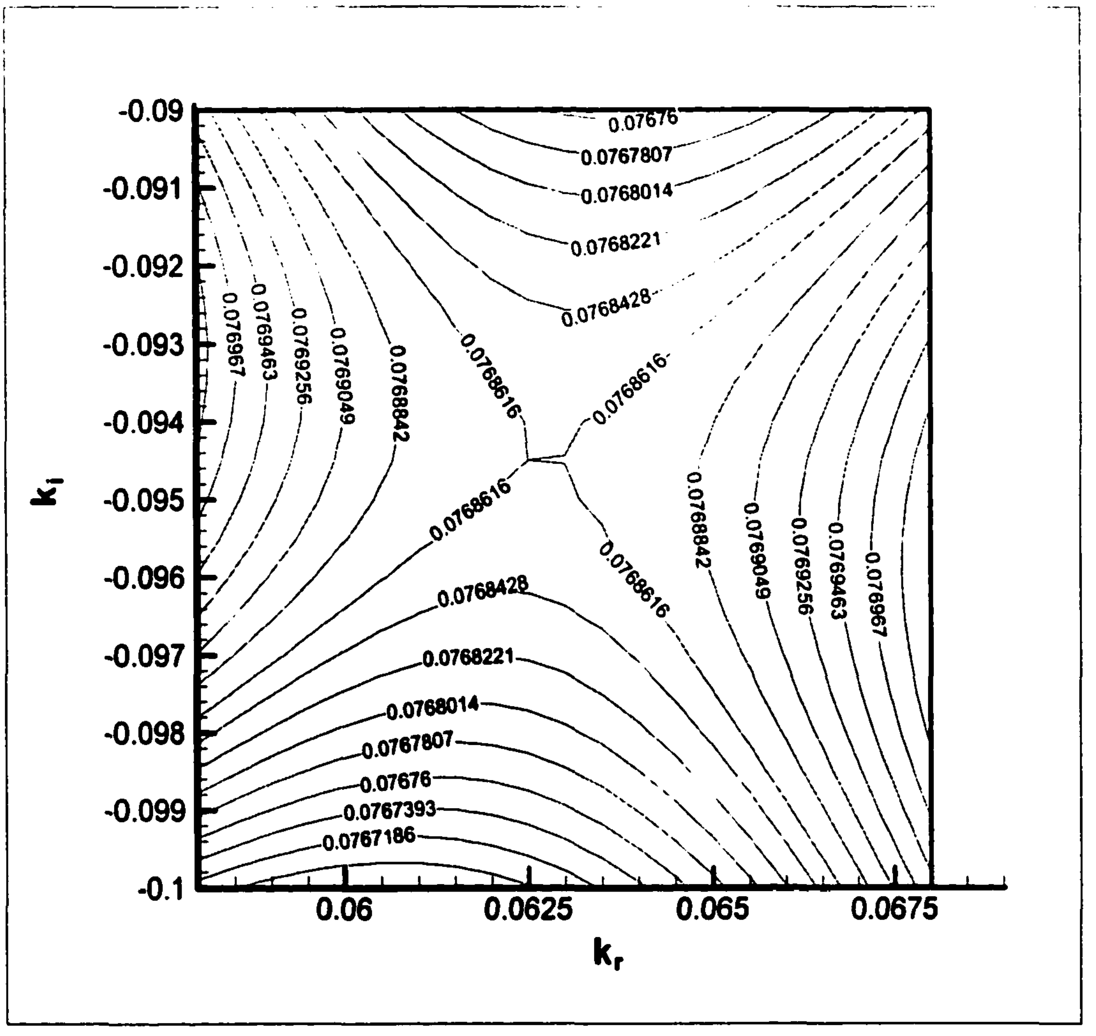

Figure A213: Contour plot of Ω_r for $R/\theta = 10$, $Fr = 2$, $\rho_j/\rho_\infty = 0.14$, $Sc = 1$, and $\Delta r = 3.75$ in the k-plane illustrating the pinch point formation

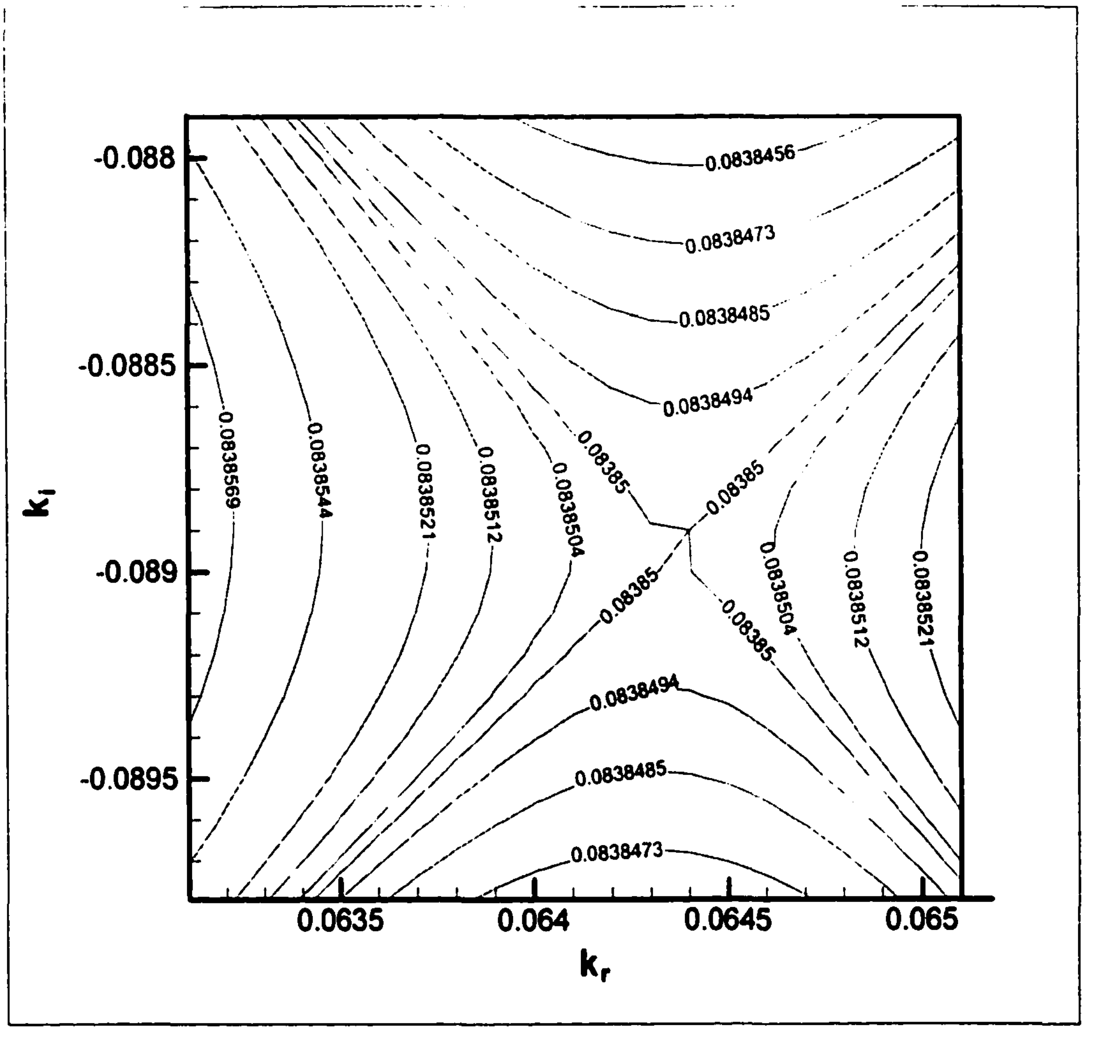

Figure A214: Contour plot of Ω_r for $R/\theta = 10$, $Fr = 1$, $\rho_j/\rho_\infty = 0.14$, $Sc = 1$, and $\Delta r = 3.75$ in the k-plane illustrating the pinch point formation

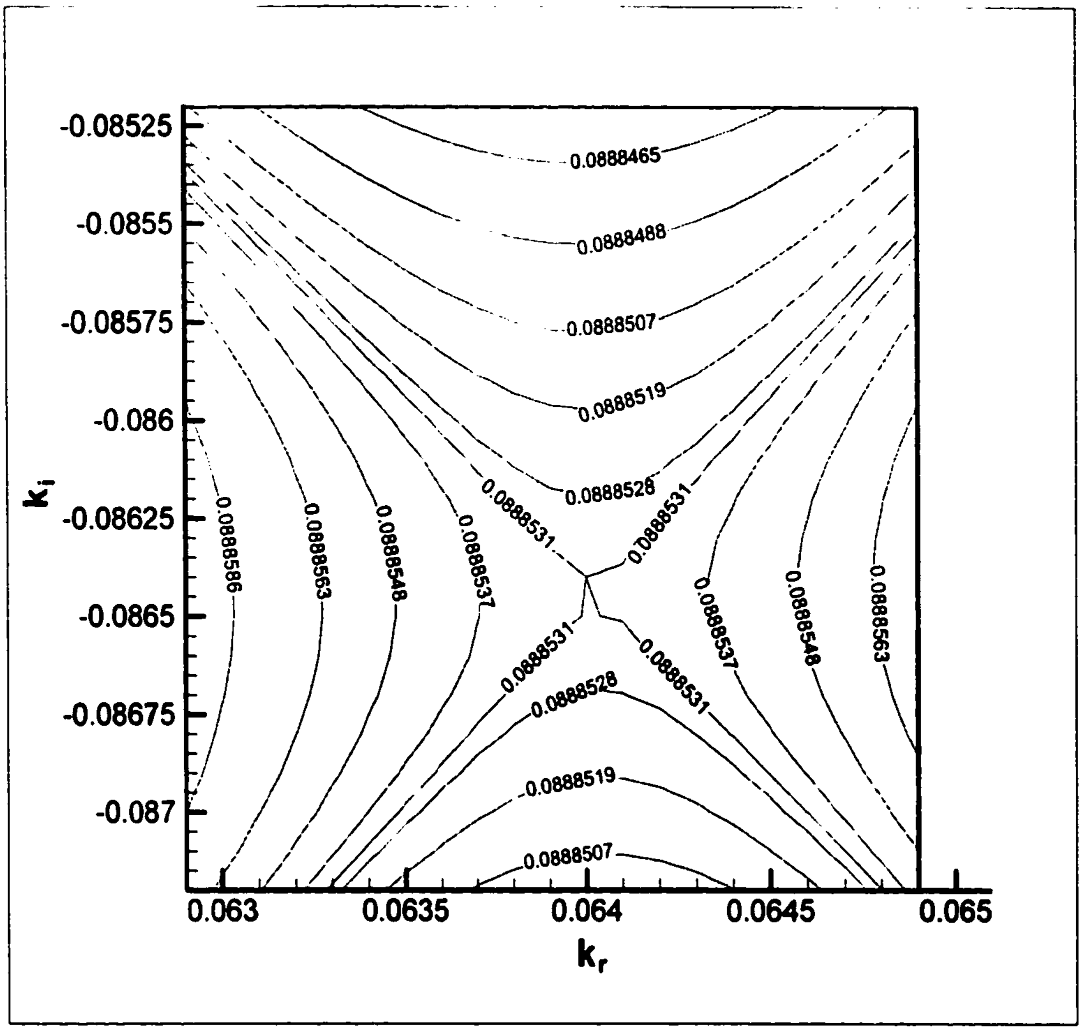

Figure A215: Contour plot of Ω_r for $R/\theta = 10$, $Fr = 0.75$, $\rho_j/\rho_\infty = 0.14$, $Sc = 1$, and $\Delta r = 3.75$ in the k-plane illustrating the pinch point formation

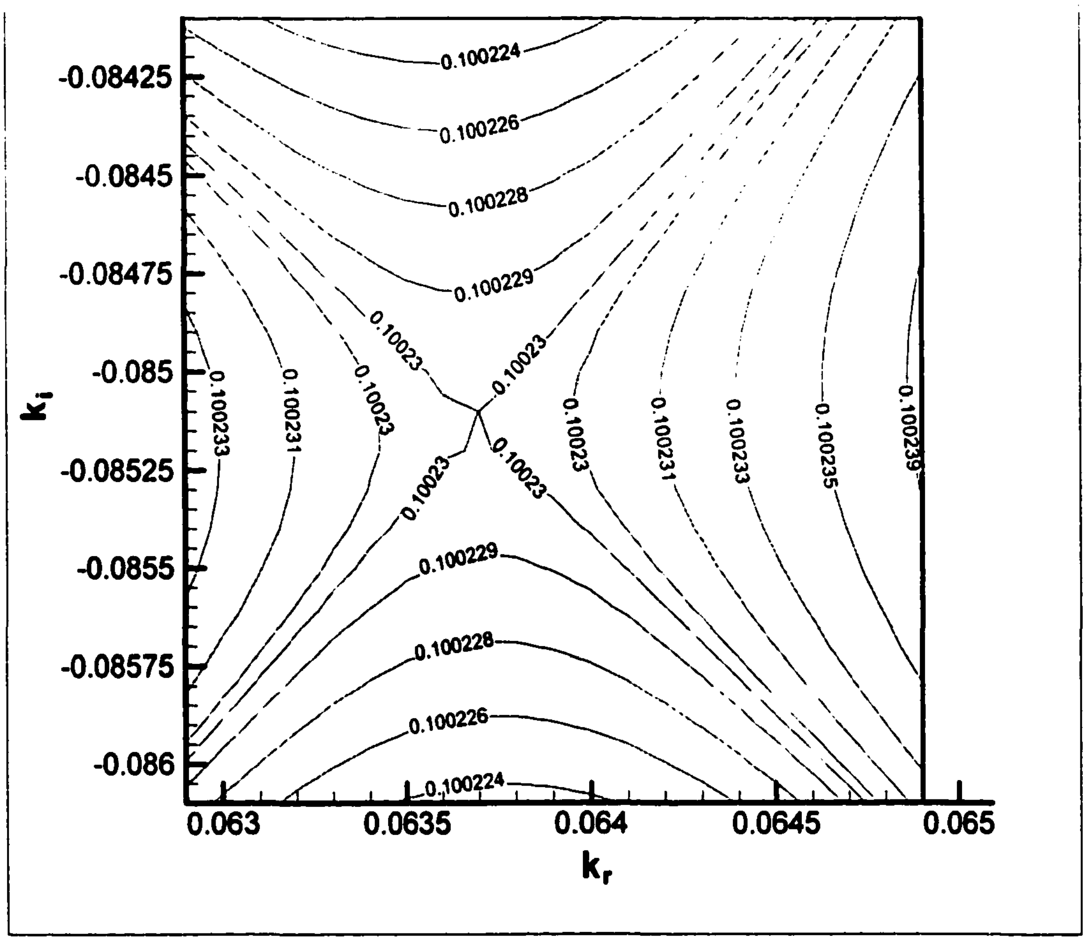

Figure A216: Contour plot of Ω_r for $R/\theta = 10$, $Fr = 0.5$, $\rho_j/\rho_\infty = 0.14$, $Sc = 1$, and $\Delta r = 3.75$ in the k-plane illustrating the pinch point formation

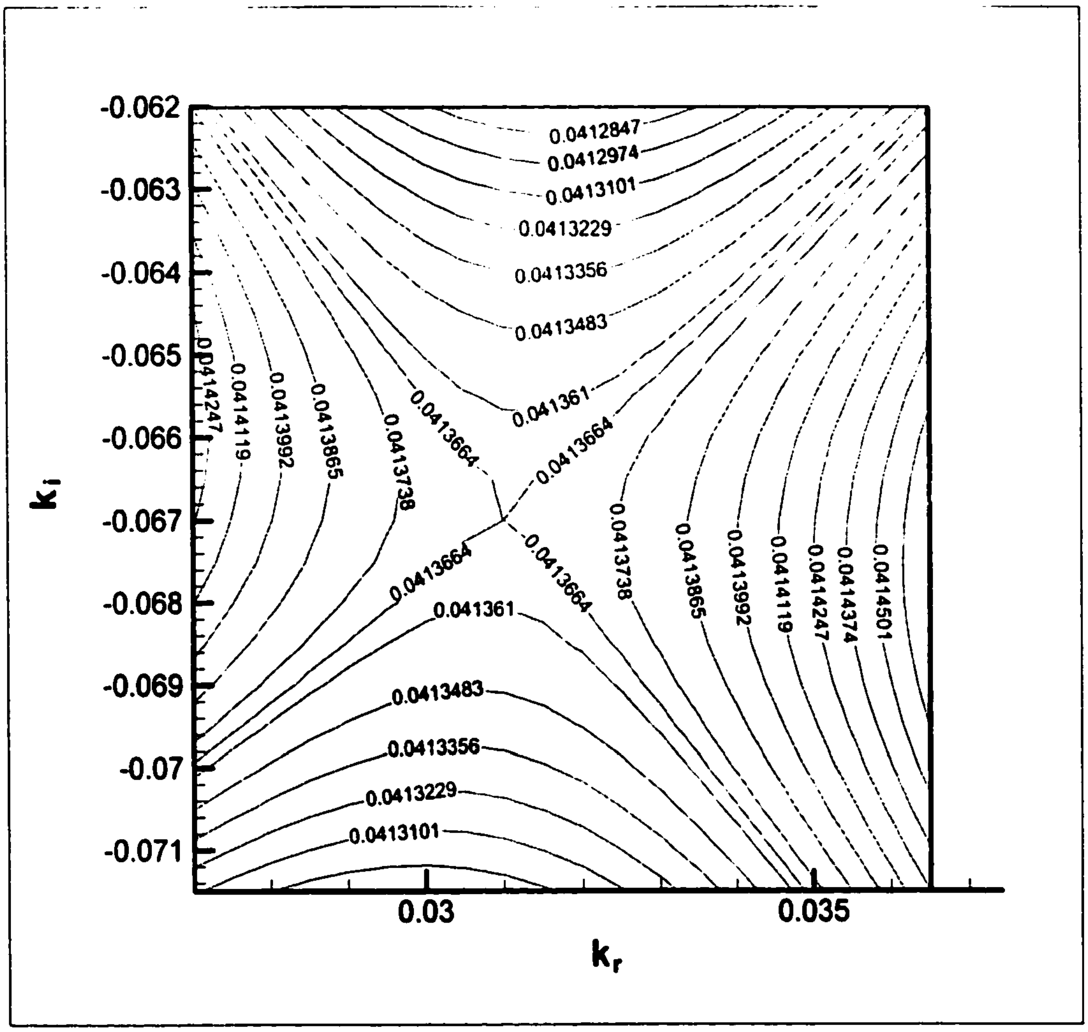

Figure A217: Contour plot of Ω_r for $R/\theta = 10$, $Fr = \infty$, $\rho_c/\rho_\infty = 0.14$, $Sc = 1$, and $\Delta r = -3.75$ in the k-plane illustrating the pinch point formation

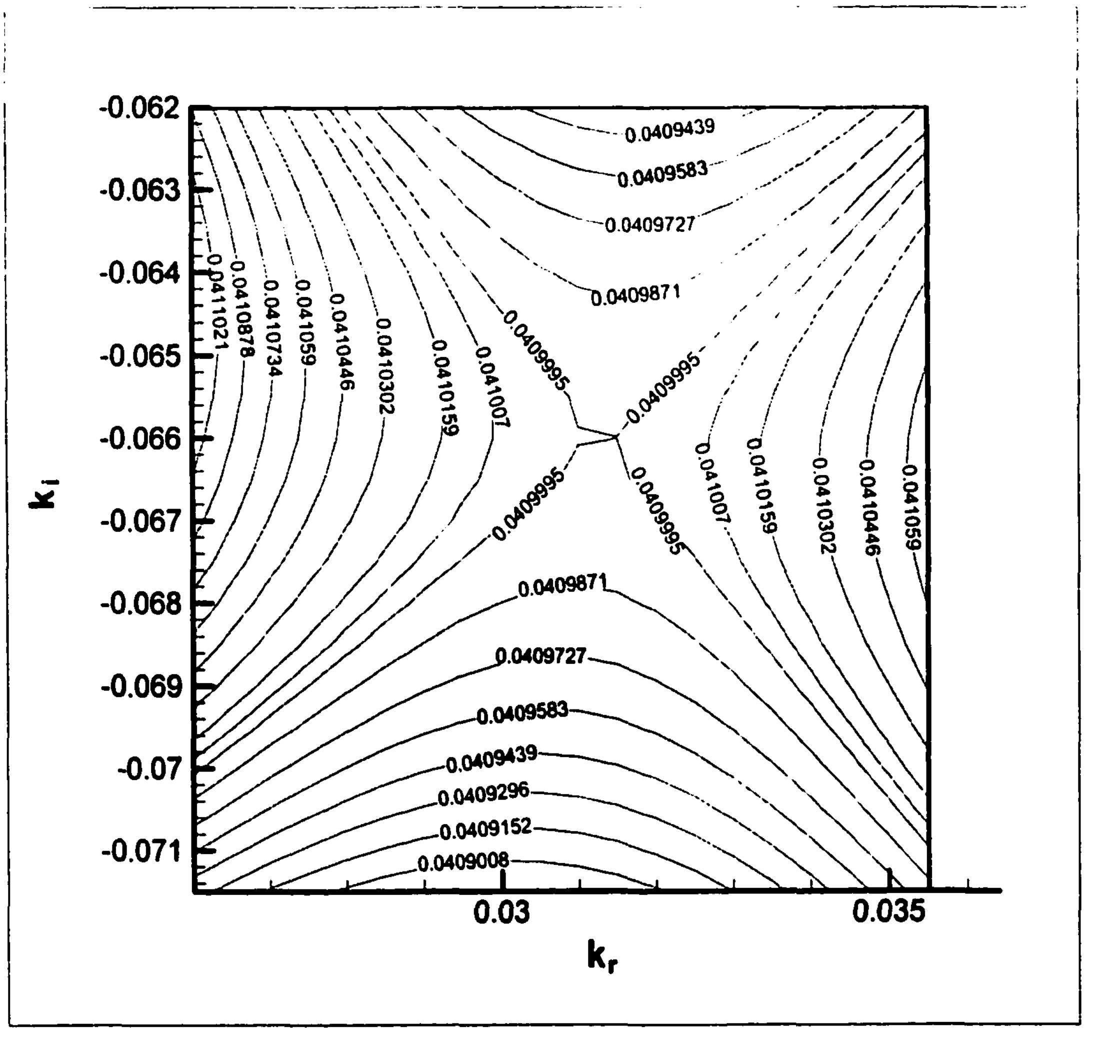

Figure A218: Contour plot of Ω_r for $R/\theta = 10$, $Fr = 10$, $\rho_j/\rho_\infty = 0.14$, $Sc = 1$, and $\Delta r = -3.75$ in the k-plane illustrating the pinch point formation

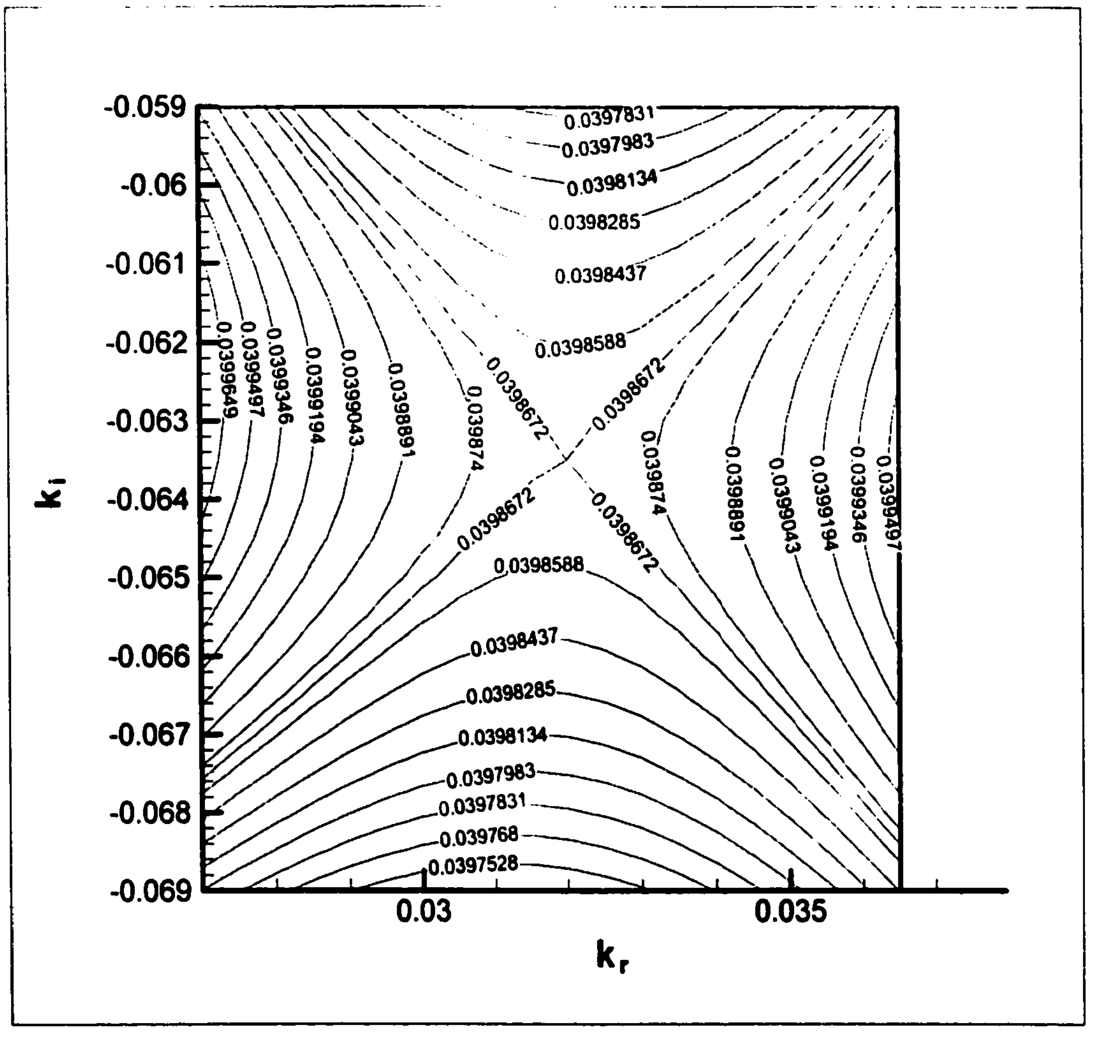

Figure A219: Contour plot of Ω_r for $R/\theta = 10$, $Fr = 5$, $\rho_j/\rho_\infty = 0.14$, $Sc = 1$, and $\Delta r = -3.75$ in the k-plane illustrating the pinch point formation

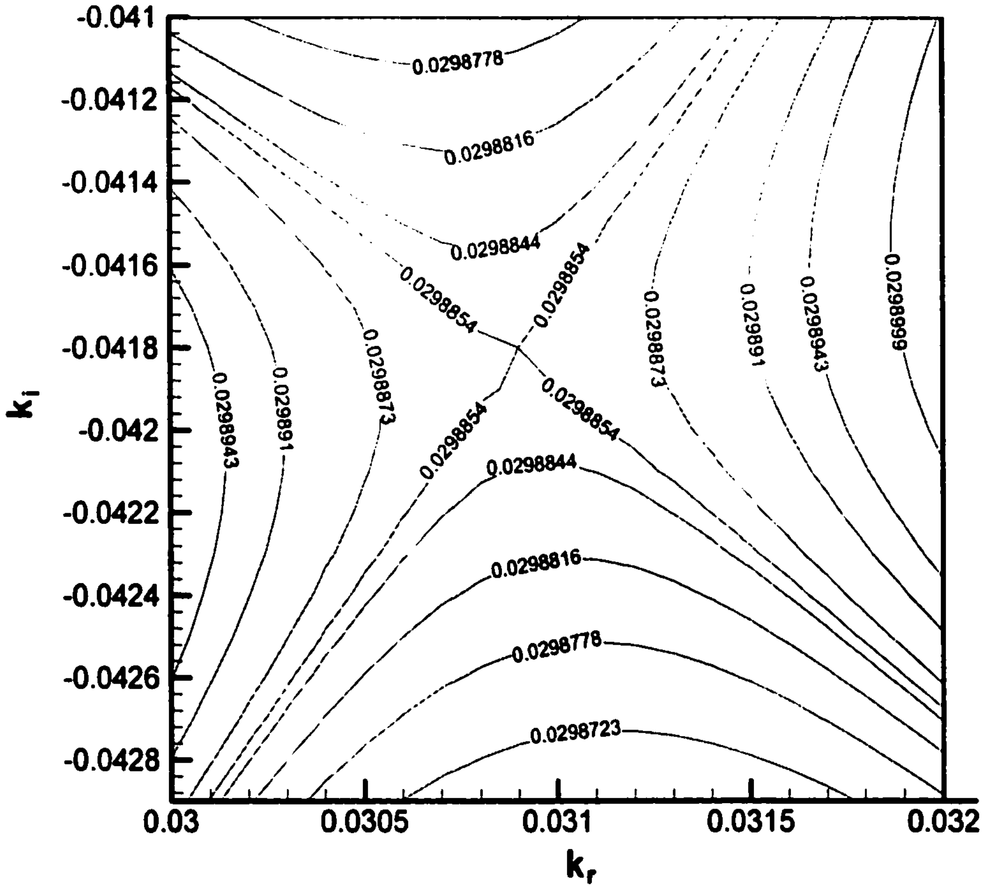

Figure A220: Contour plot of Ω_r for $R/\theta = 10$, $Fr = 2$, $\rho_j/\rho_\infty = 0.14$, $Sc = 1$, and $\Delta r = -3.75$ in the k-plane illustrating the pinch point formation

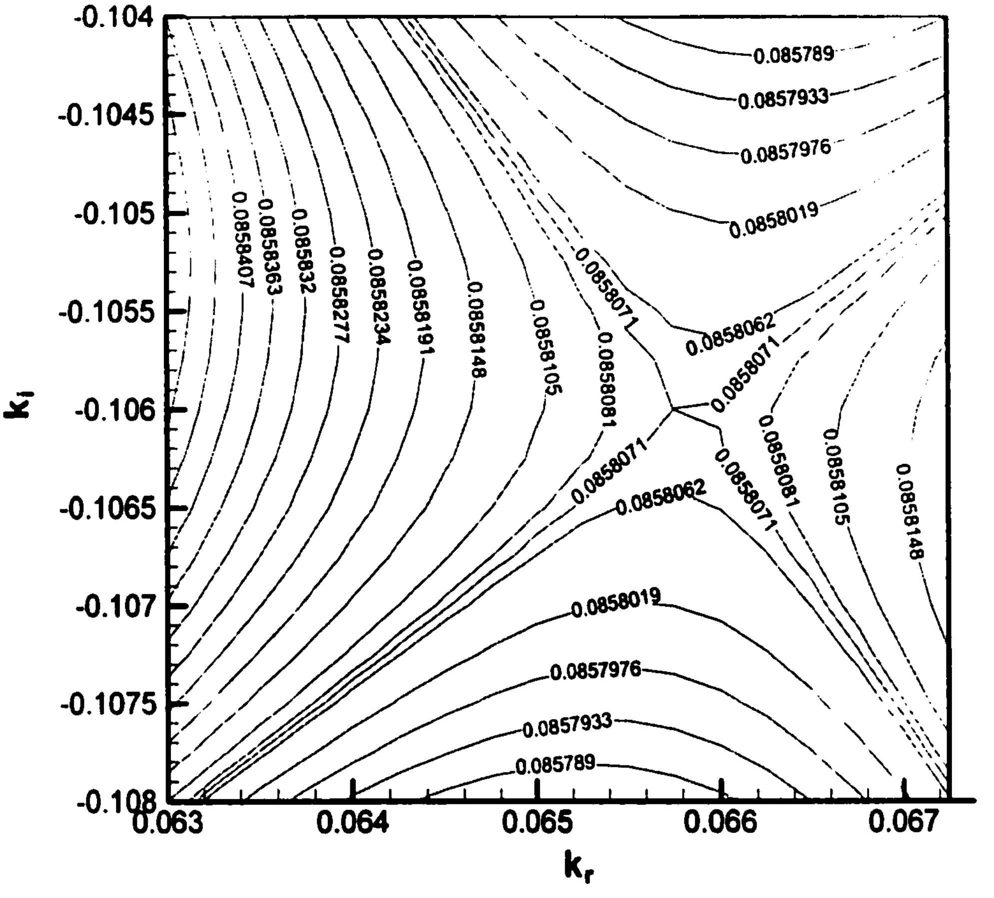

Figure A221: Contour plot of Ω_r for $R/\theta = 10$, $Fr = \infty$, $\rho_j/\rho_\infty = 0.14$, $Sc = 1$, and $\Delta r = 5$ in the k-plane illustrating the pinch point formation

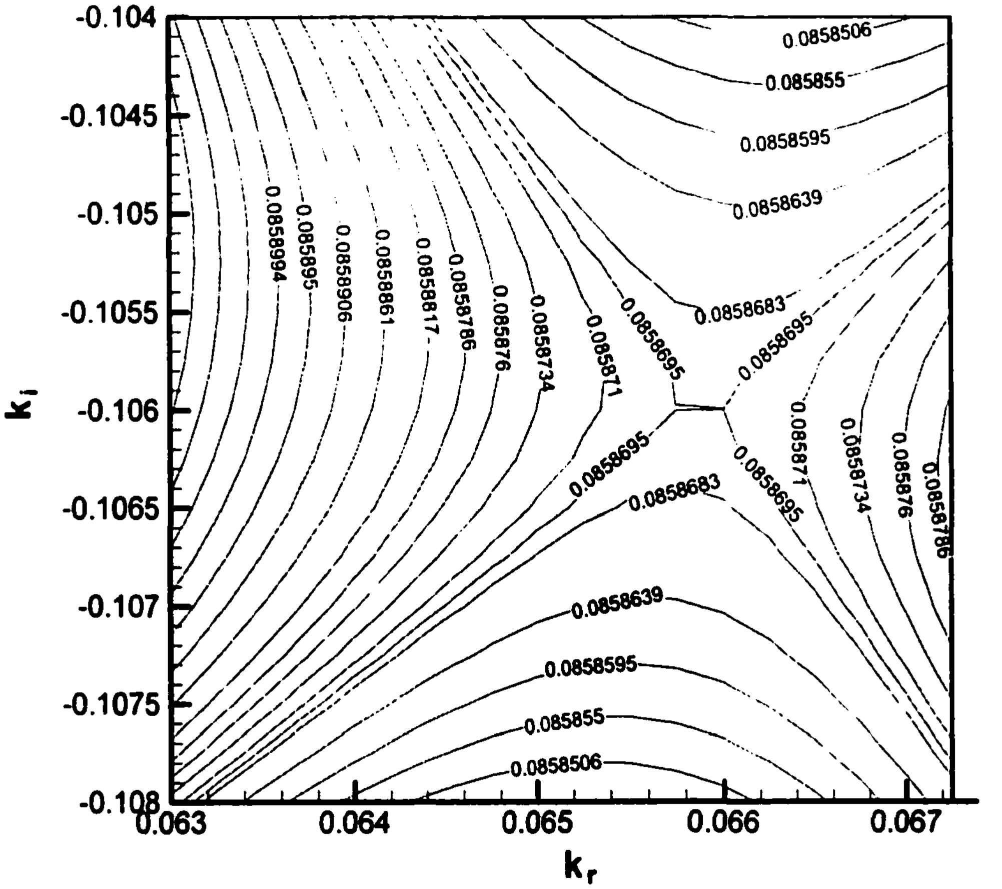

Figure A222: Contour plot of Ω_r for $R/\theta = 10$, $Fr = 10$, $\rho_j/\rho_\infty = 0.14$, $Sc = 1$, and $\Delta r = 5$ in the k-plane illustrating the pinch point formation

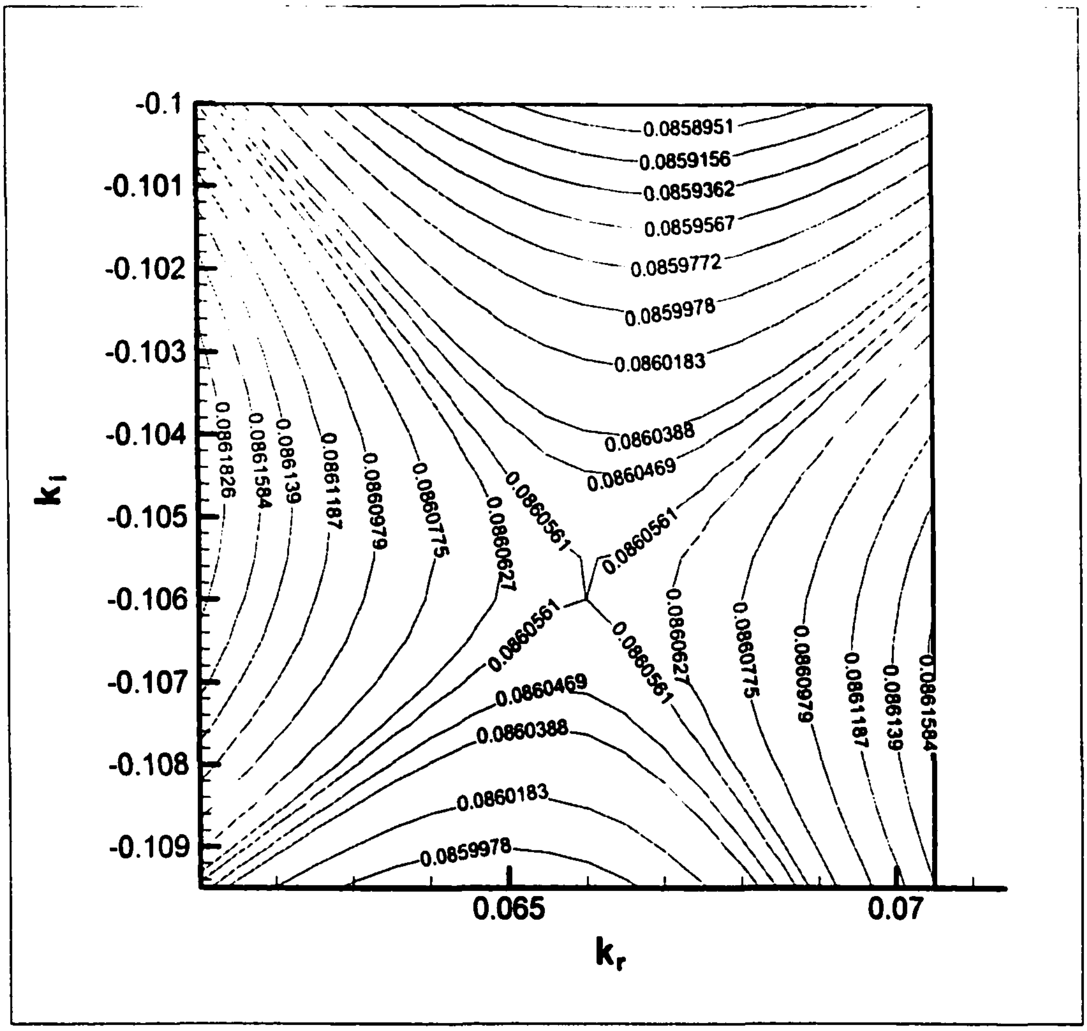

Figure A223: Contour plot of Ω_r for $R/\theta = 10$, $Fr = 5$, $\rho_j/\rho_\infty = 0.14$, $Sc = 1$, and $\Delta r = 5$ in the k-plane illustrating the pinch point formation

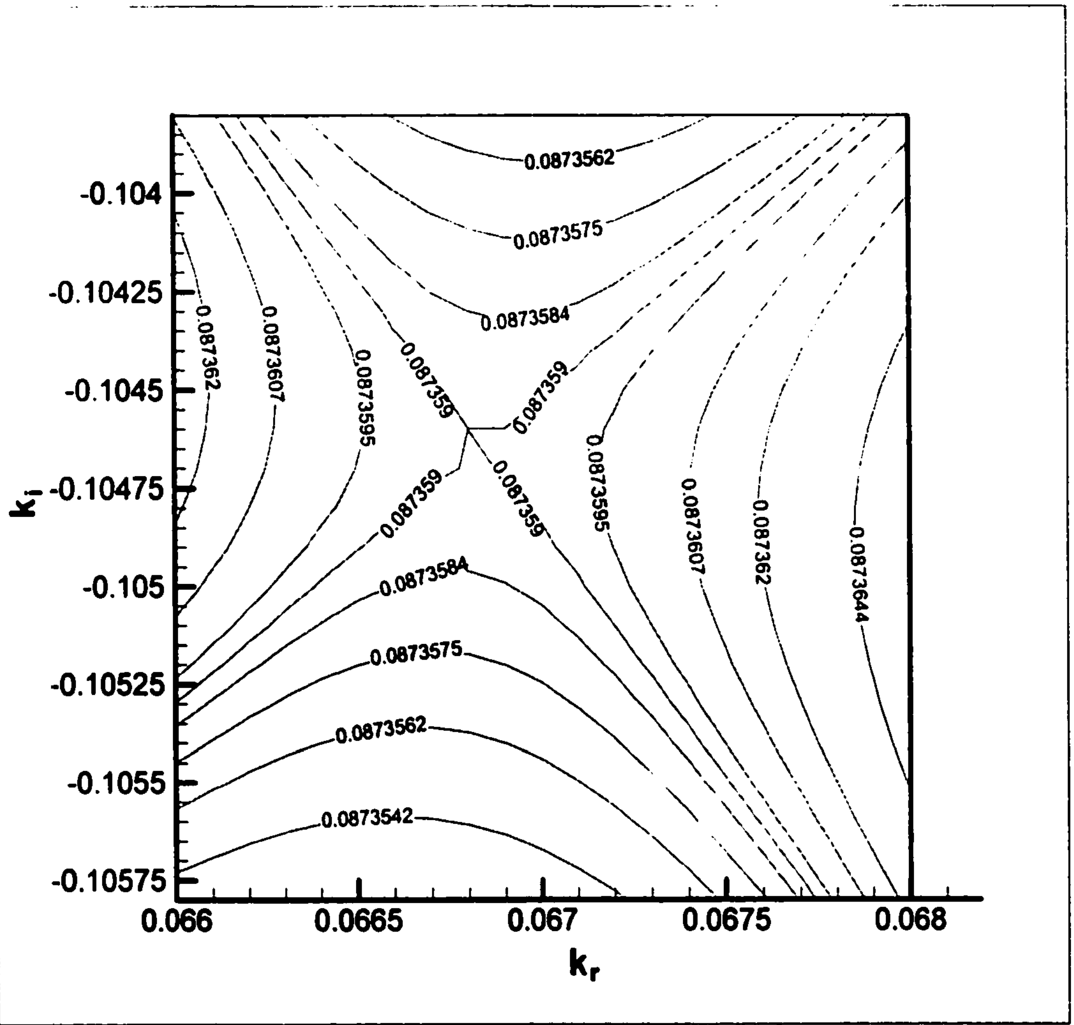

Figure A224: Contour plot of Ω_r for $R/\theta = 10$, $Fr = 2$, $\rho_j/\rho_\infty = 0.14$, $Sc = 1$, and $\Delta r = 5$ in the k-plane illustrating the pinch point formation

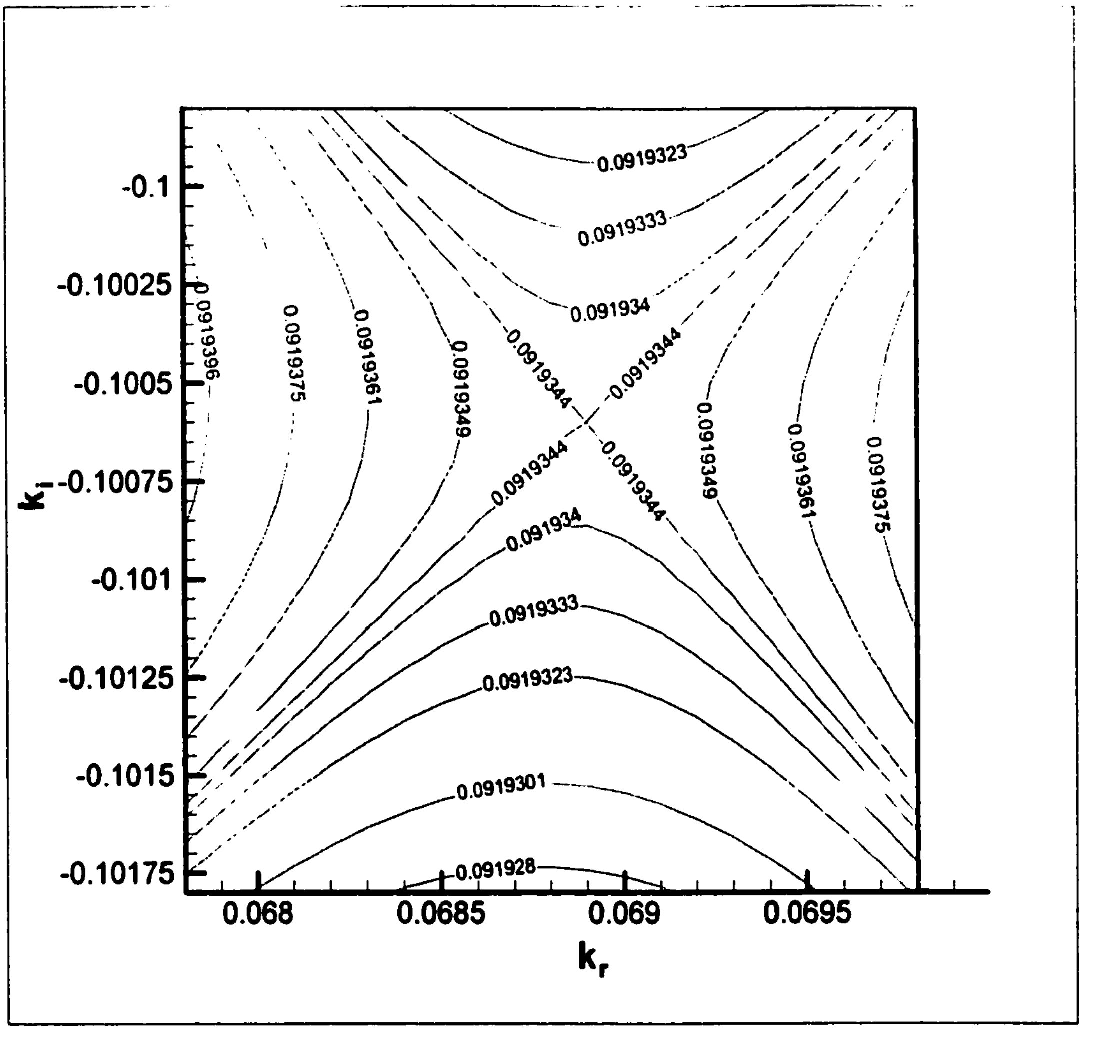

Figure A225: Contour plot of Ω_r for $R/\theta = 10$, $Fr = 1$, $\rho_j/\rho_\infty = 0.14$, $Sc = 1$, and $\Delta r = 5$ in the k-plane illustrating the pinch point formation

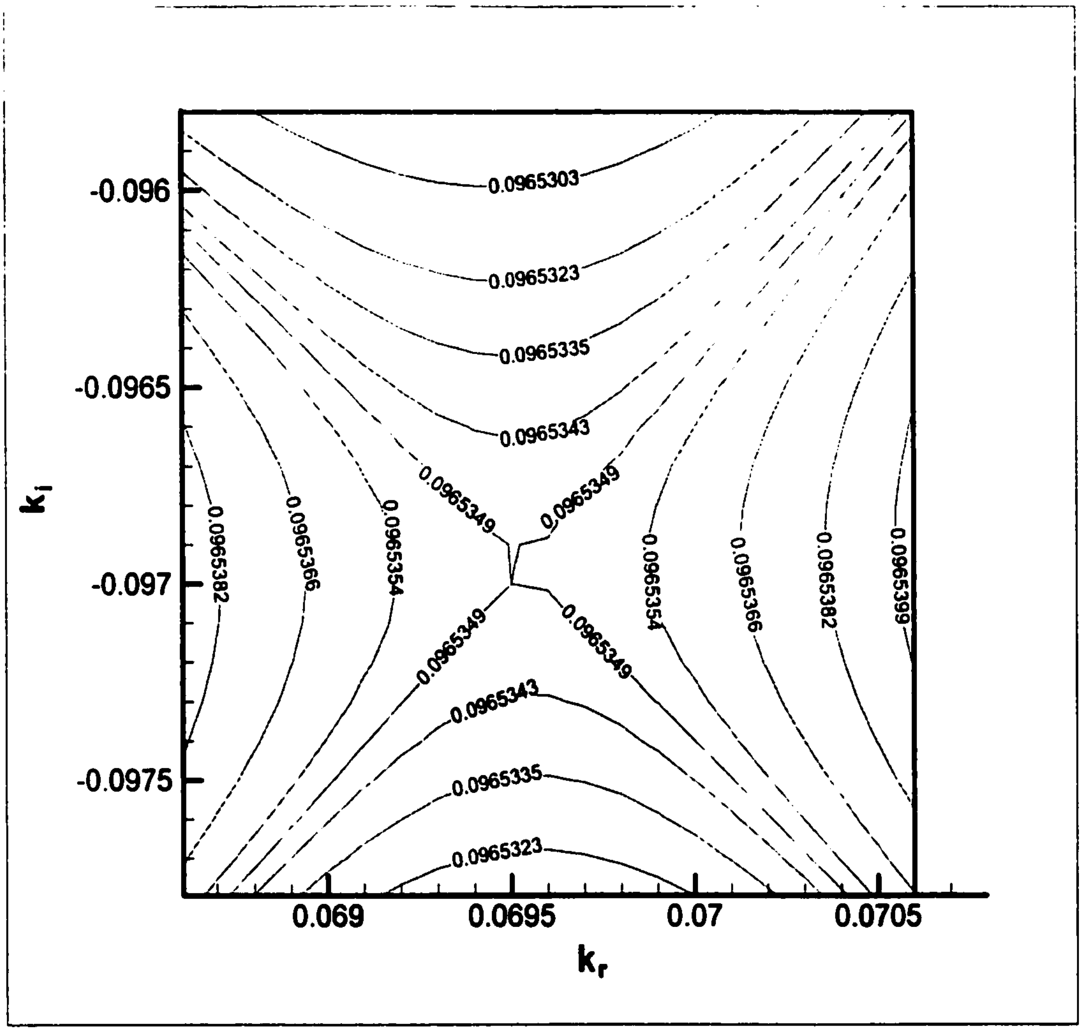

Figure A226: Contour plot of Ω_r for $R/\theta = 10$, $Fr = 0.75$, $\rho_j/\rho_\infty = 0.14$, $Sc = 1$, and $\Delta r = 5$ in the k-plane illustrating the pinch point formation

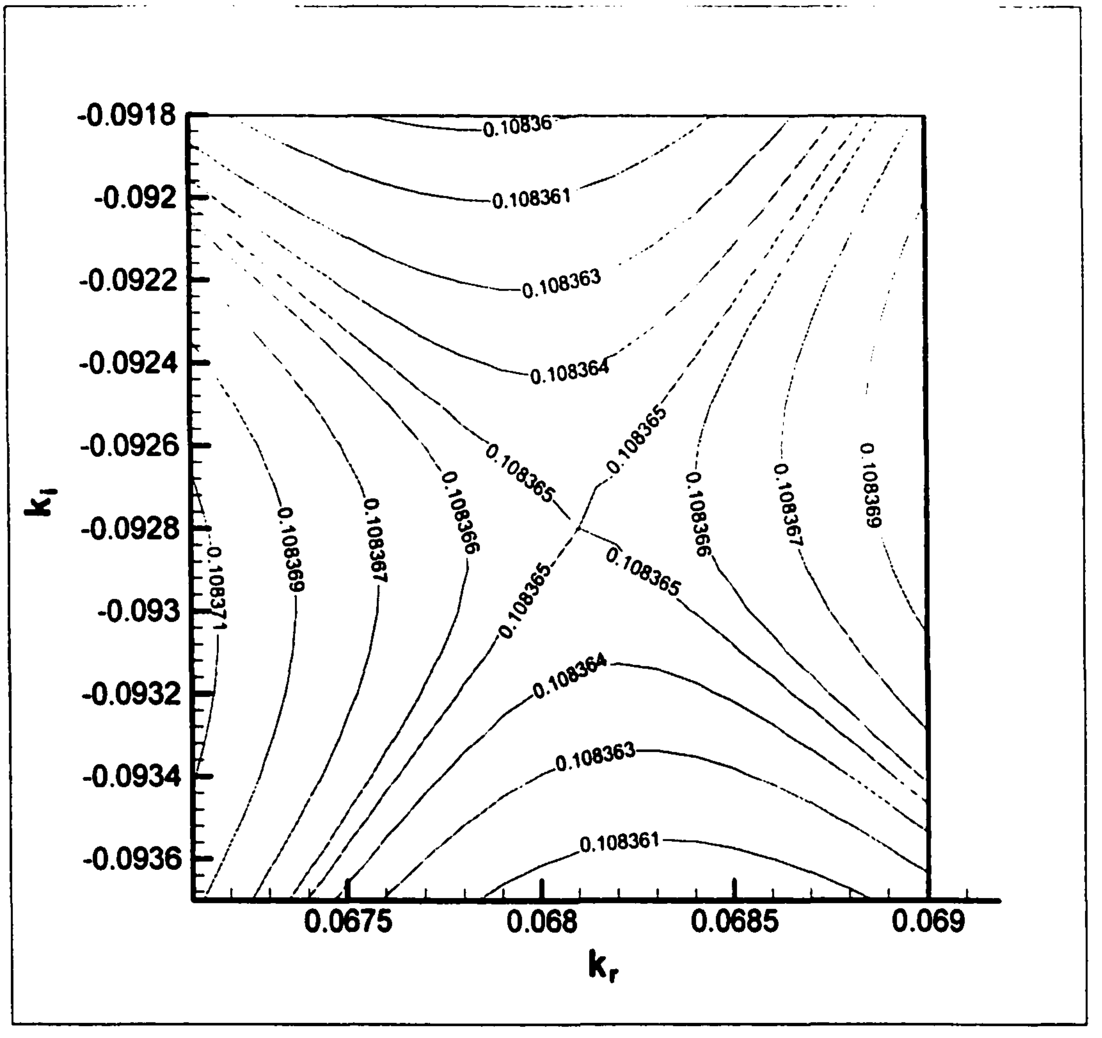

Figure A227: Contour plot of Ω_r for $R/\theta = 10$, $Fr = 0.5$, $\rho_j/\rho_\infty = 0.14$, $Sc = 1$, and $\Delta r =$ 5 in the k-plane illustrating the pinch point formation

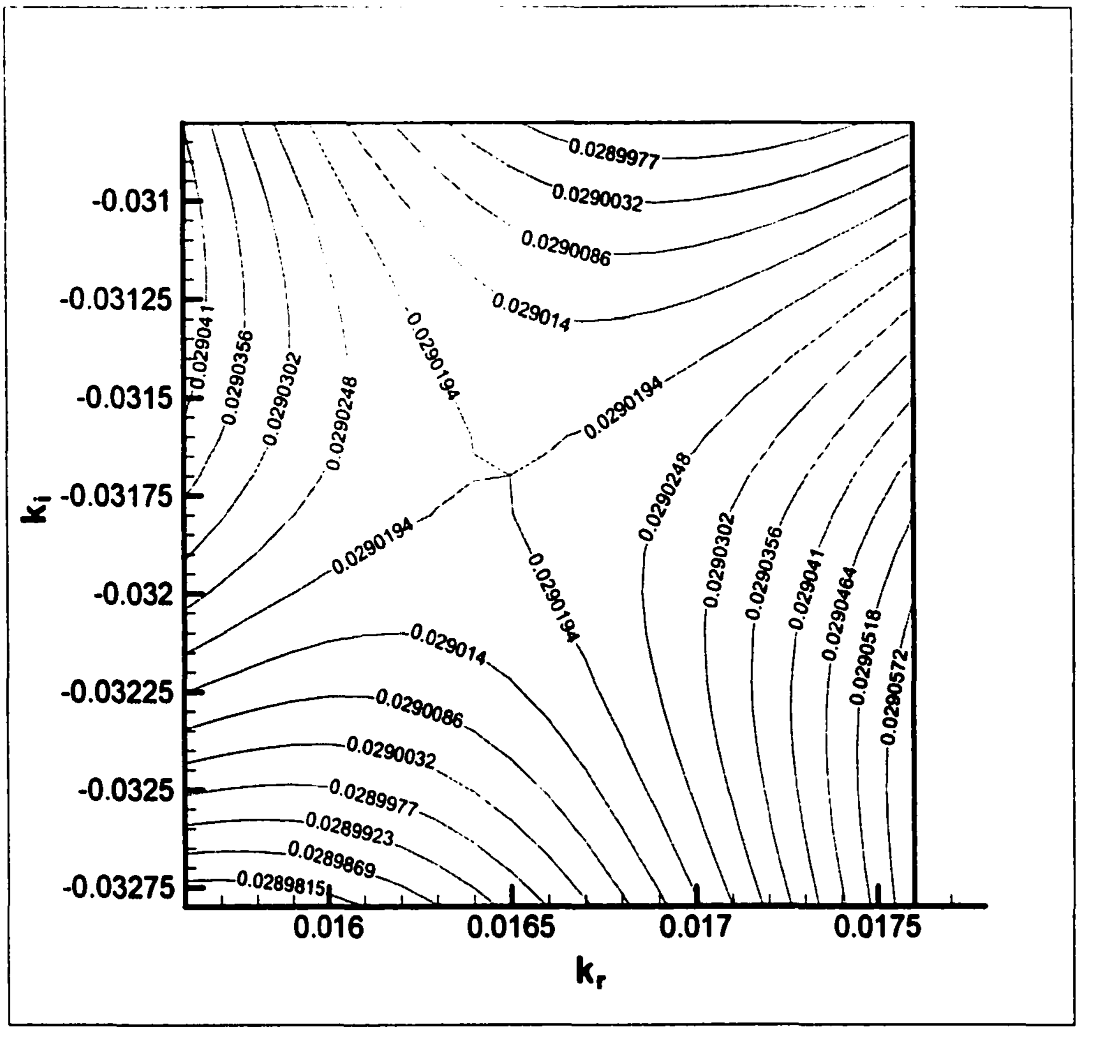

Figure 228: Contour plot of Ω_r for $R/\theta = 25$, $Fr = \infty$, $\rho_j/\rho_\infty = 0.14$, $Sc = 1.43$, and $\Delta r = 12.5$ in the k-plane illustrating the pinch point formation

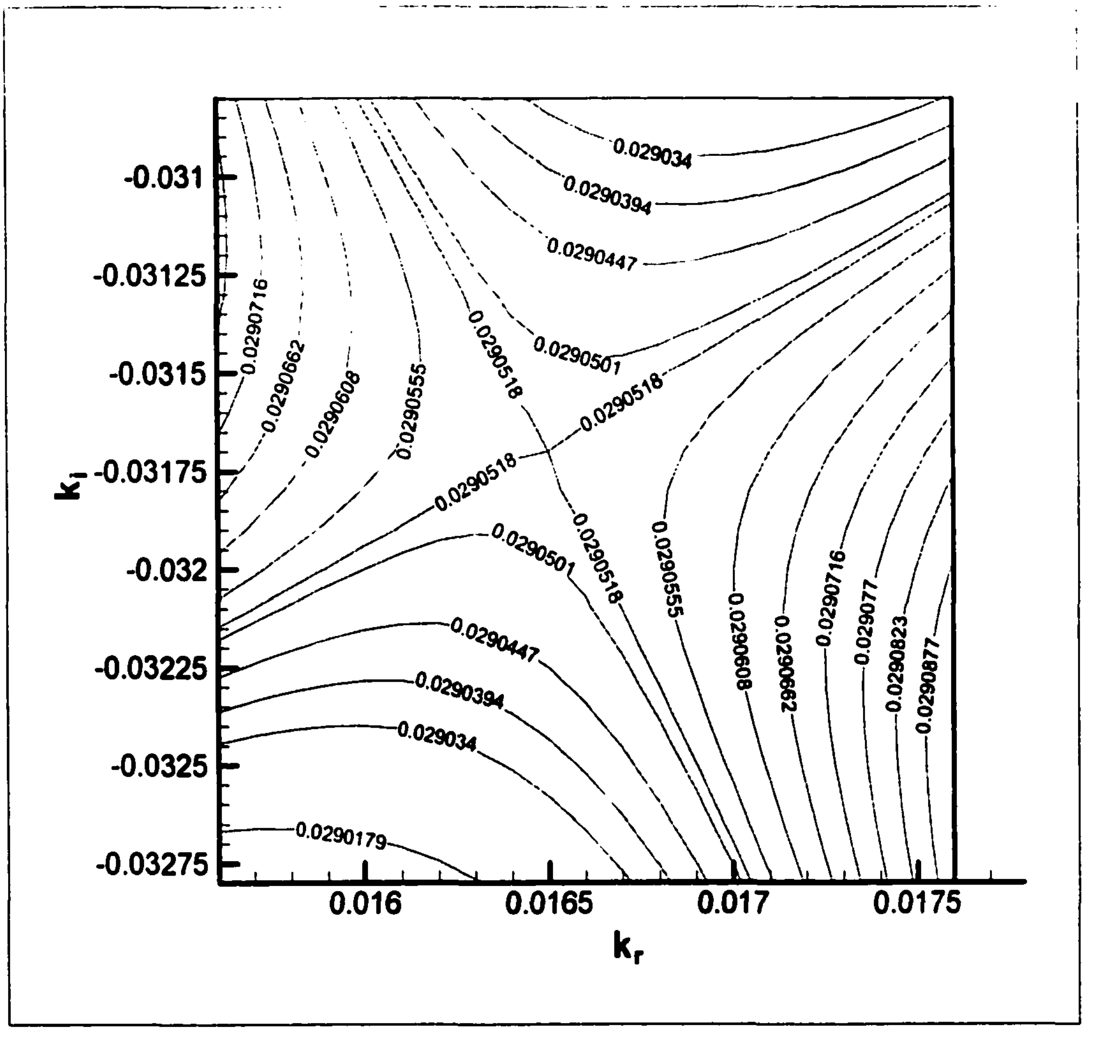

Figure 229: Contour plot of Ω_r for $R/\theta = 25$, $Fr = 10$, $\rho_j/\rho_\infty = 0.14$, $Sc = 1.43$, and $\Delta r = 12.5$ in the k-plane illustrating the pinch point formation

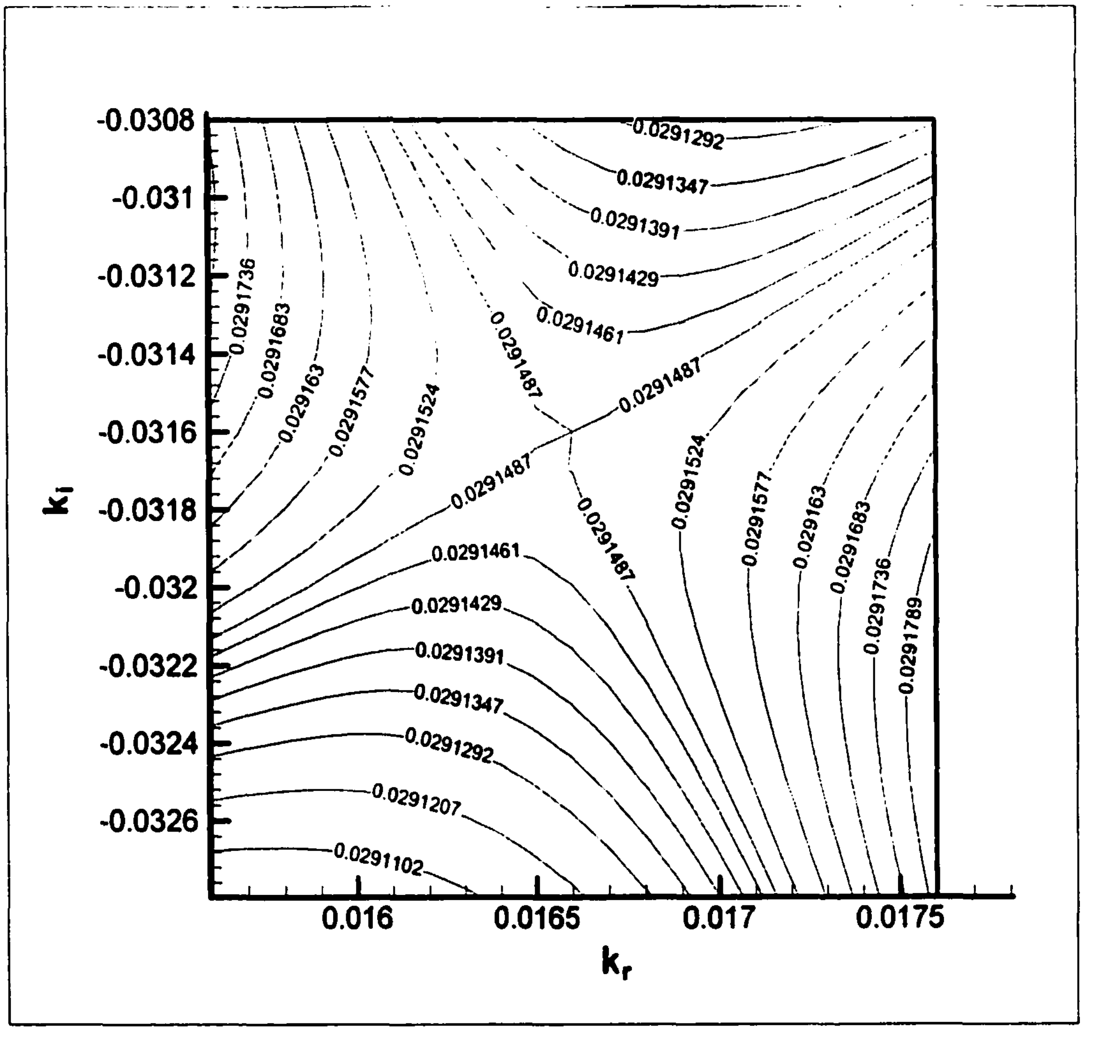

Figure 230: Contour plot of Ω_r for $R/\theta = 25$, $Fr = 5$, $\rho_j/\rho_\infty = 0.14$, $Sc = 1.43$, and $\Delta r = 12.5$ in the k-plane illustrating the pinch point formation

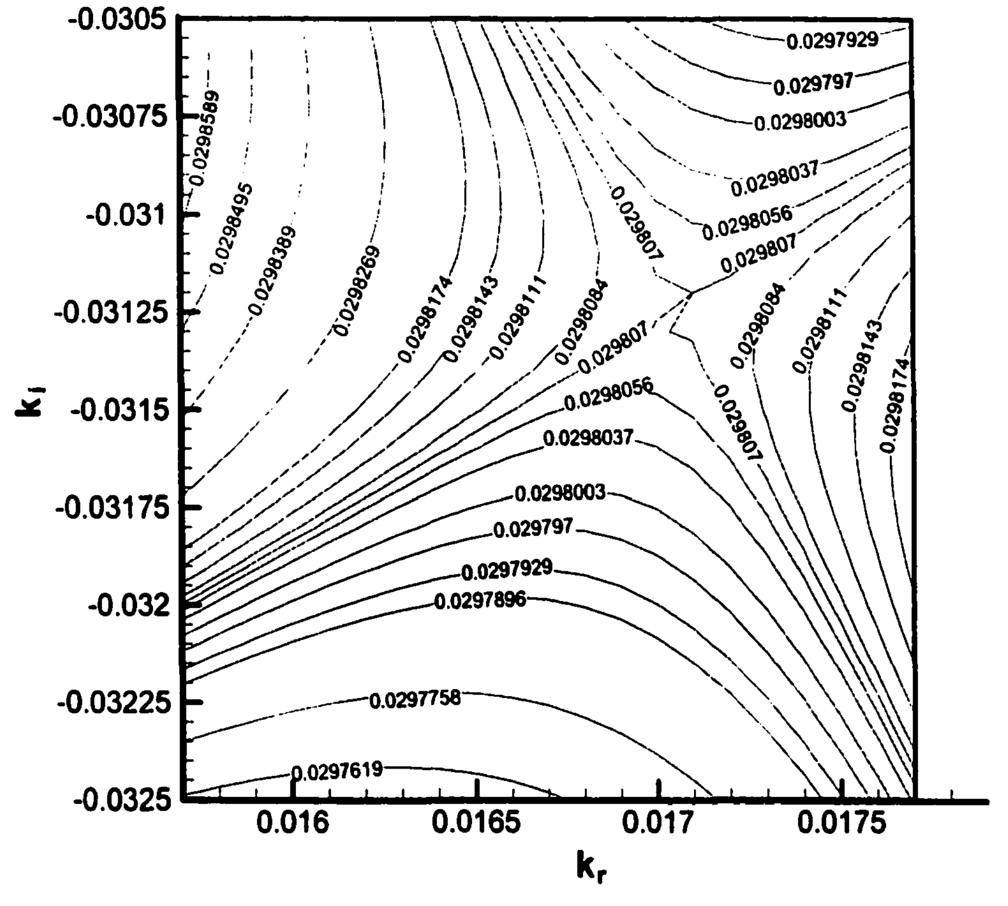

Figure 231: Contour plot of Ω_r for $R/\theta = 25$, $Fr = 2$, $\rho_f/\rho_\infty = 0.14$, $Sc = 1.43$, and $\Delta r = 12.5$ in the k-plane illustrating the pinch point formation

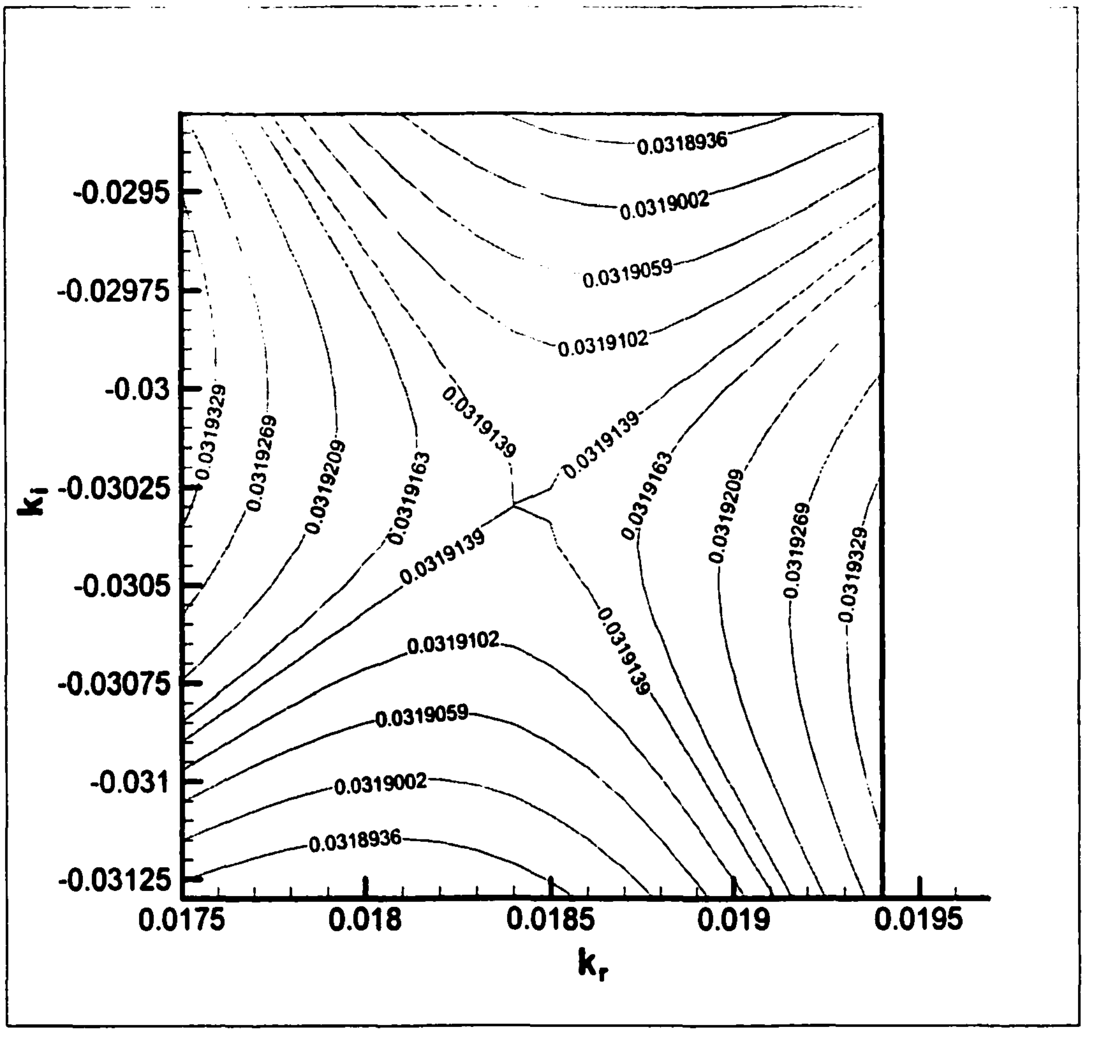

Figure 232: Contour plot of Ω_r for $R/\theta = 25$, $Fr = 1$, $\rho_j/\rho_\infty = 0.14$, $Sc = 1.43$, and $\Delta r = 12.5$ in the k-plane illustrating the pinch point formation

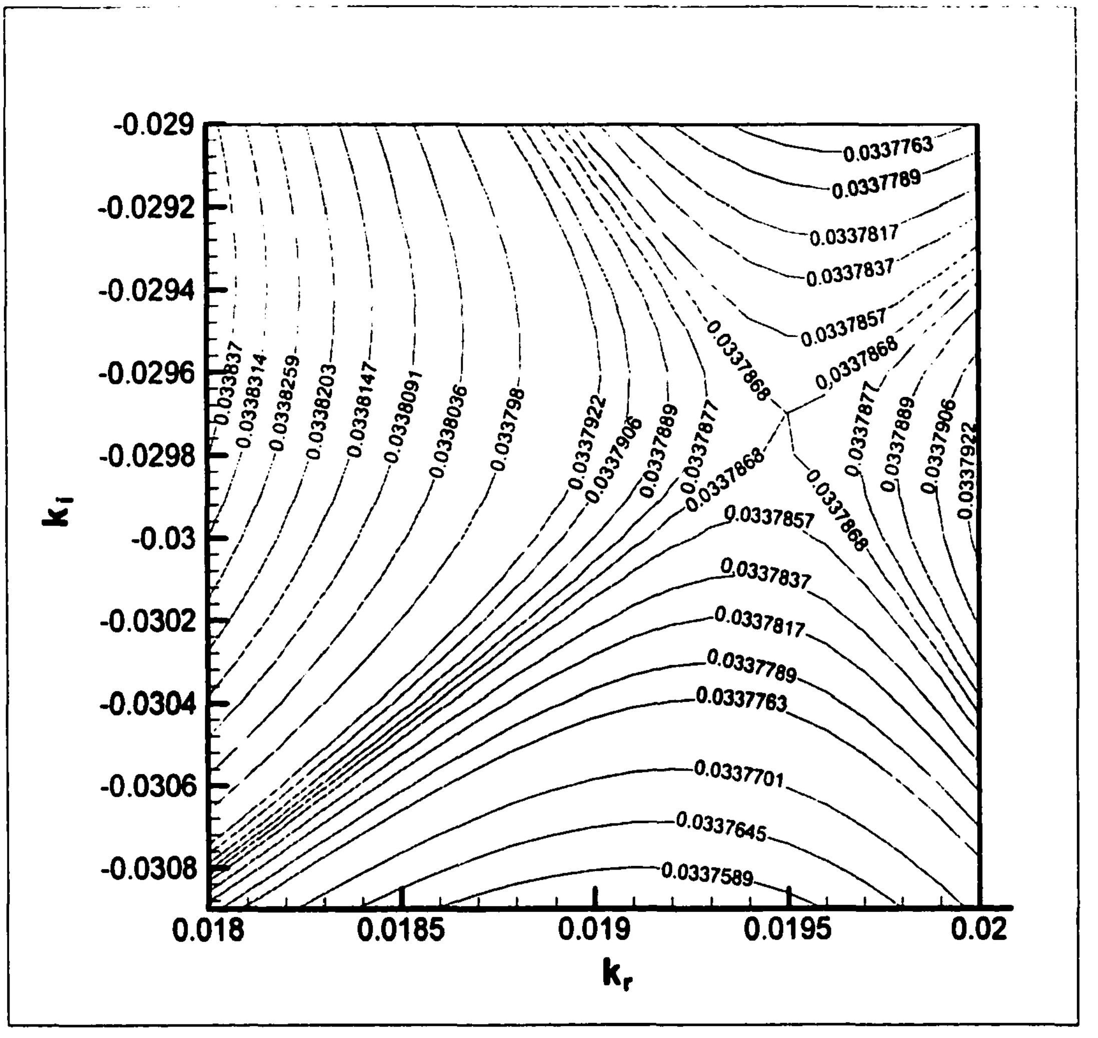

Figure 233: Contour plot of Ω_r for $R/\theta = 25$, $Fr = 0.75$, $\rho_j/\rho_\infty = 0.14$, $Sc = 1.43$, and $\Delta r = 12.5$ in the k-plane illustrating the pinch point formation

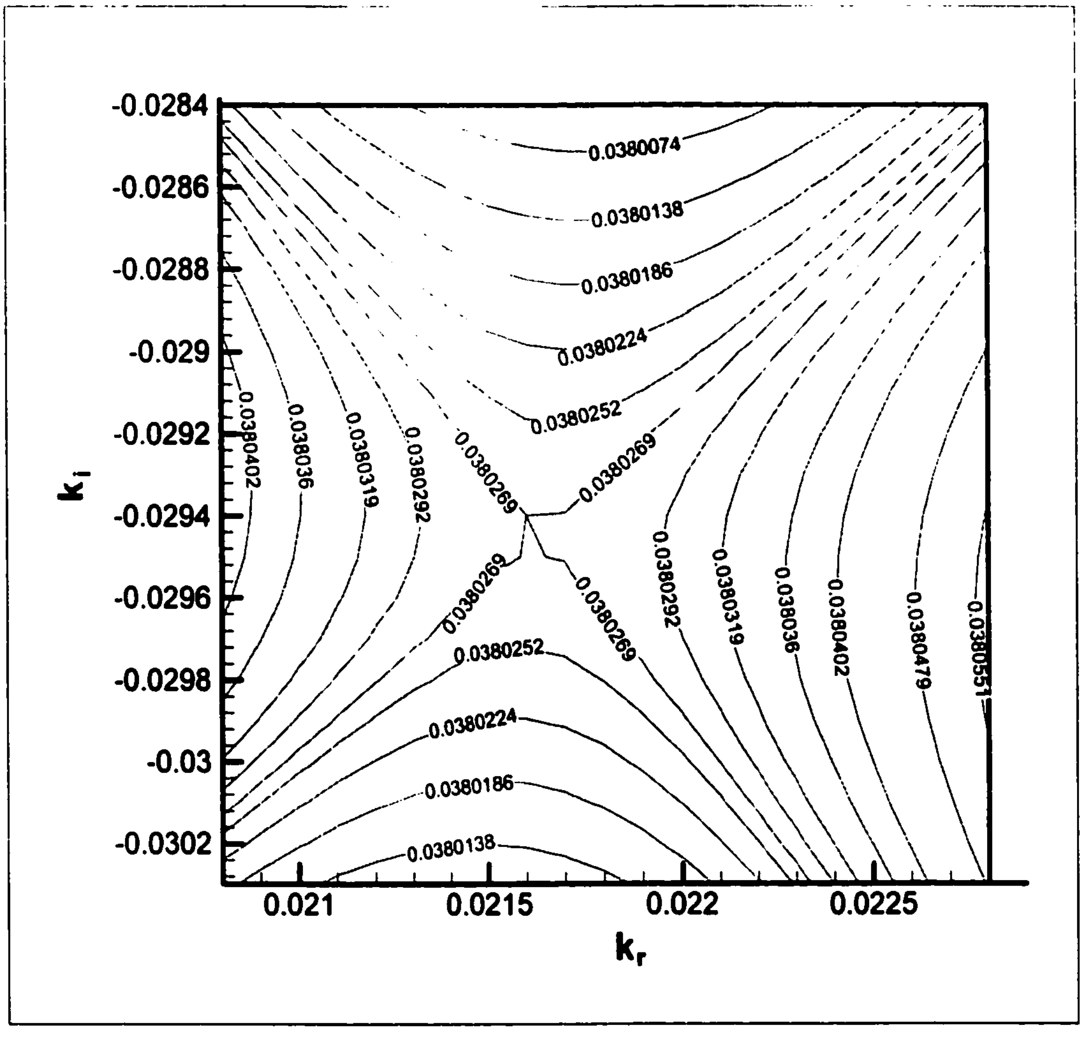

Figure 234: Contour plot of Ω_r for $R/\theta = 25$, $Fr = 0.5$, $\rho_j/\rho_\infty = 0.14$, $Sc = 1.43$, and $\Delta r = 12.5$ in the k-plane illustrating the pinch point formation

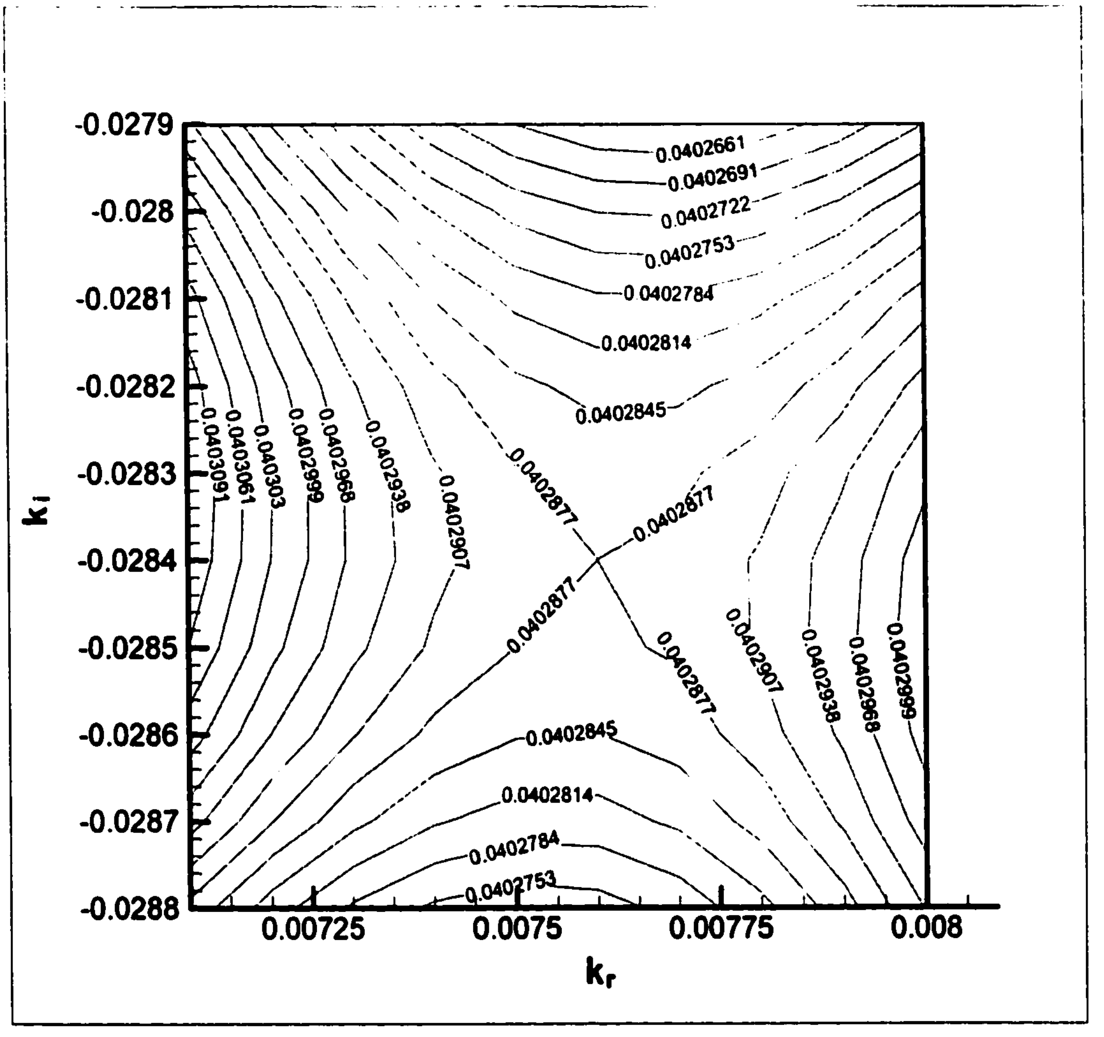

Figure 235: Contour plot of Ω_r for $R/\theta = 25$, $Fr = \infty$, $\rho_j/\rho_\infty = 0.14$, $Sc = 1.43$, and $\Delta r = 12.5$, $U_\infty/\Delta U = 1$ in the k-plane illustrating the pinch point formation

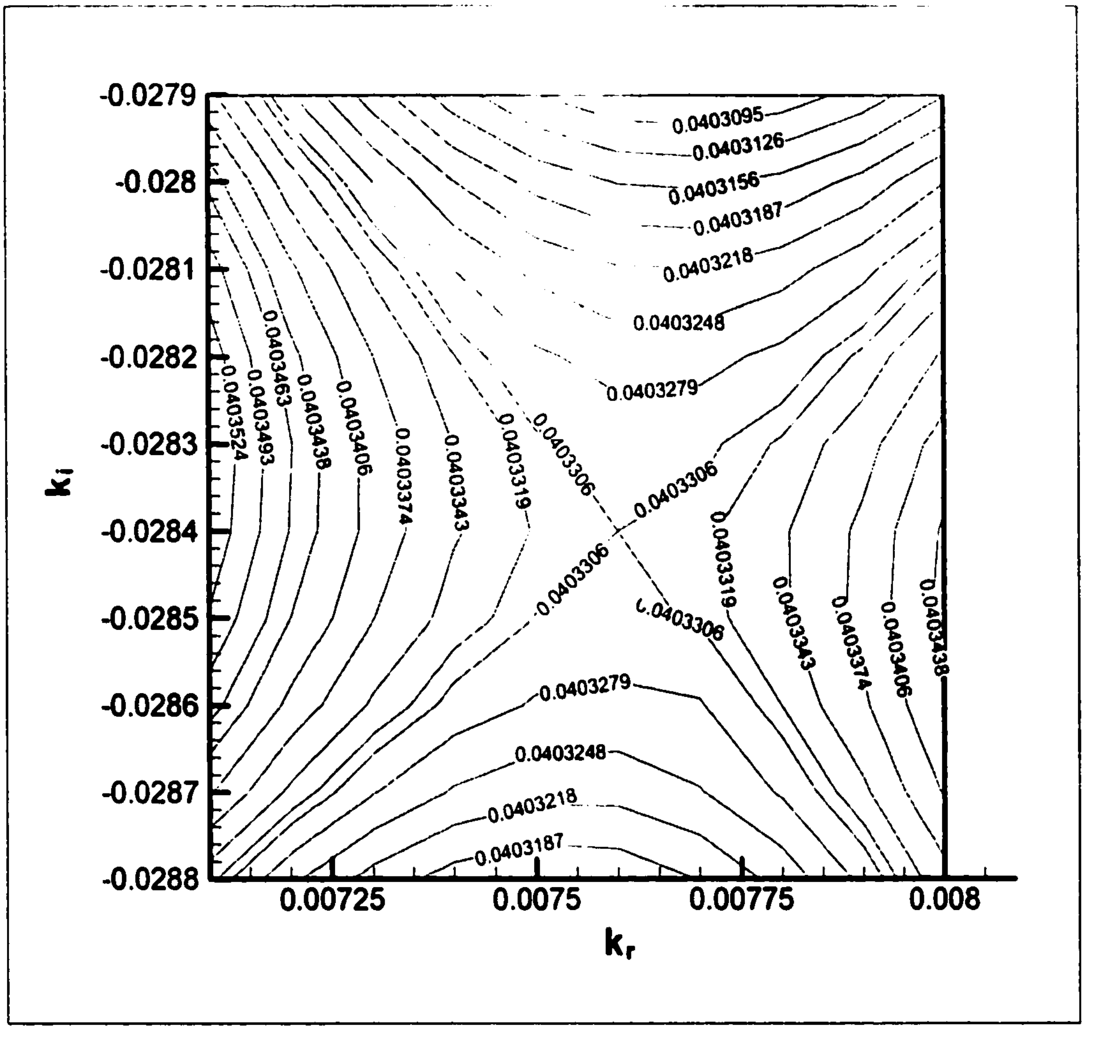

Figure 236: Contour plot of Ω_r for $R/\theta = 25$, $Fr = 10$, $\rho_j/\rho_\infty = 0.14$, $Sc = 1.43$, and $\Delta r = 12.5$, $U_\infty/\Delta U = 1$ in the k-plane illustrating the pinch point formation

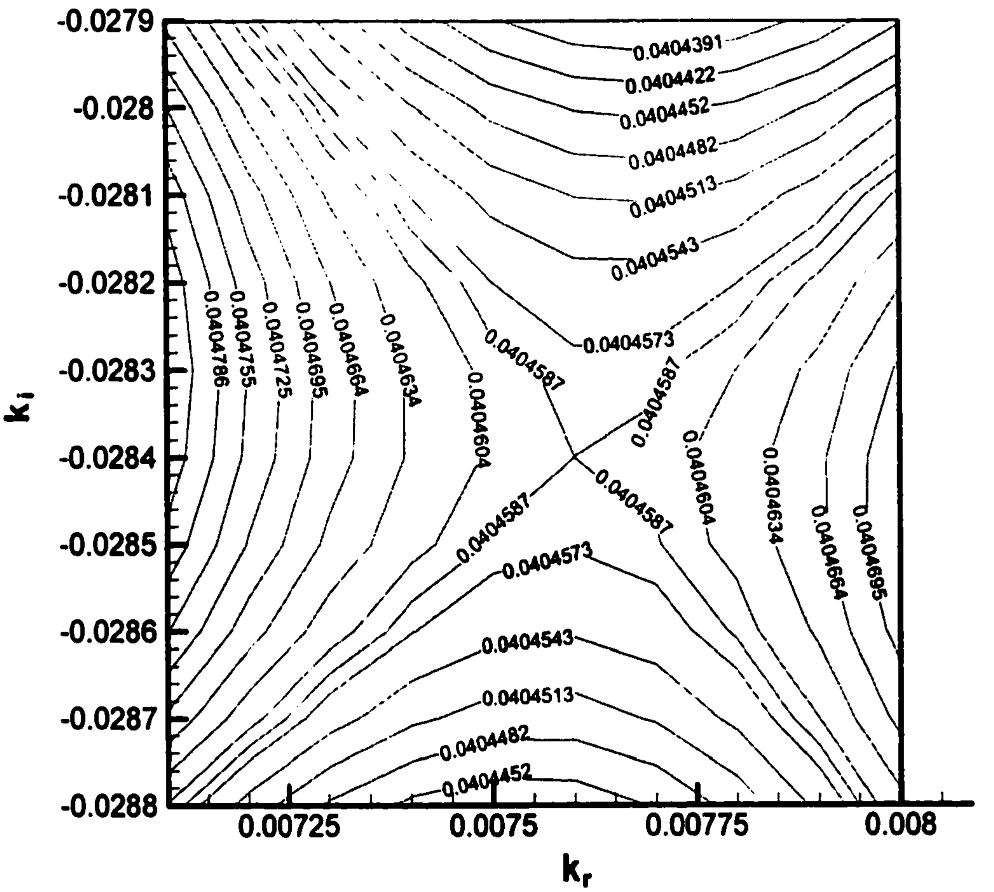

Figure 237: Contour plot of Ω_r for $R/\theta = 25$, $Fr = 5$, $\rho_j/\rho_\infty = 0.14$, $Sc = 1.43$, and $\Delta r = 12.5$, $U_\infty/\Delta U = 1$ in the k-plane illustrating the pinch point formation

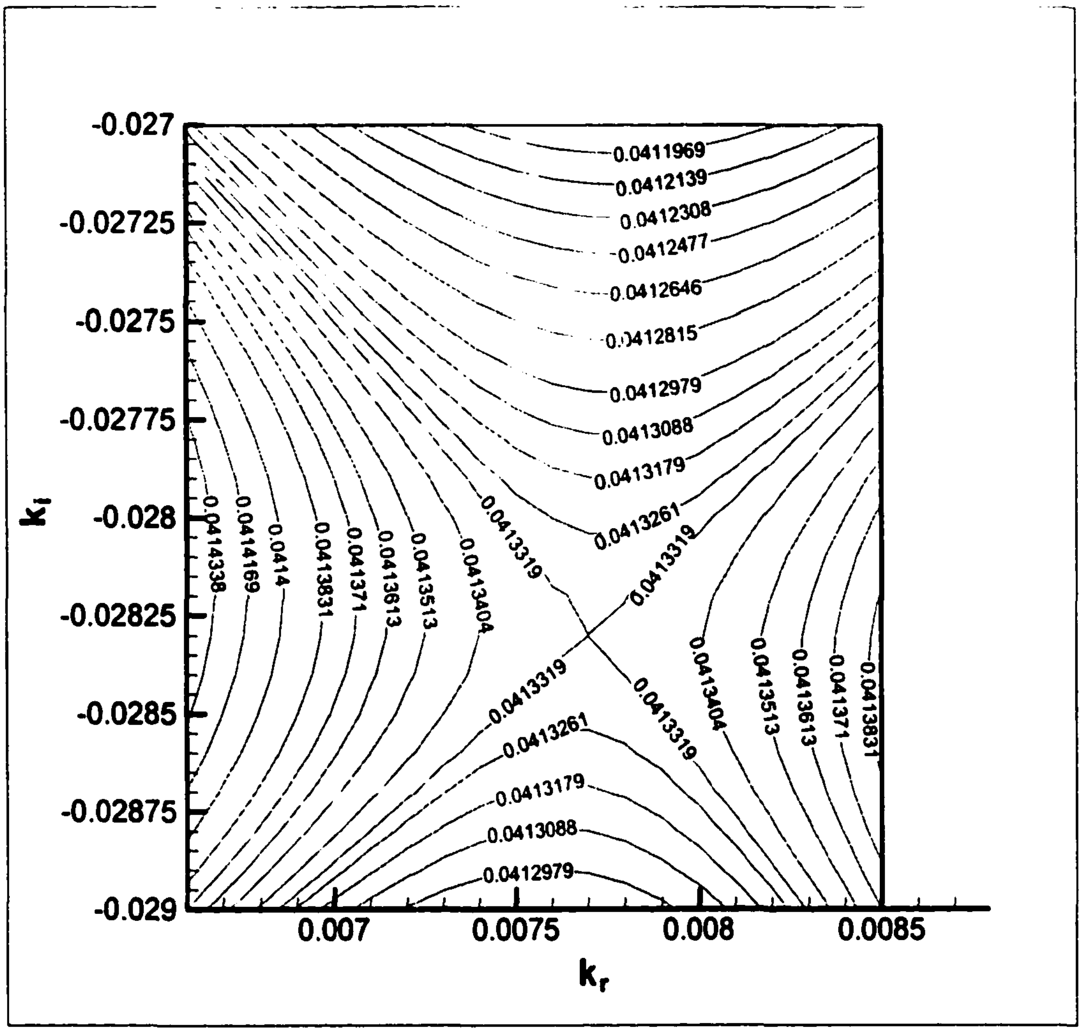

Figure 238: Contour plot of Ω_r for $R/\theta = 25$, $Fr = 2$, $\rho_j/\rho_\infty = 0.14$, $Sc = 1.43$, and $\Delta r = 12.5$, $U_\infty/\Delta U = 1$ in the k-plane illustrating the pinch point formation

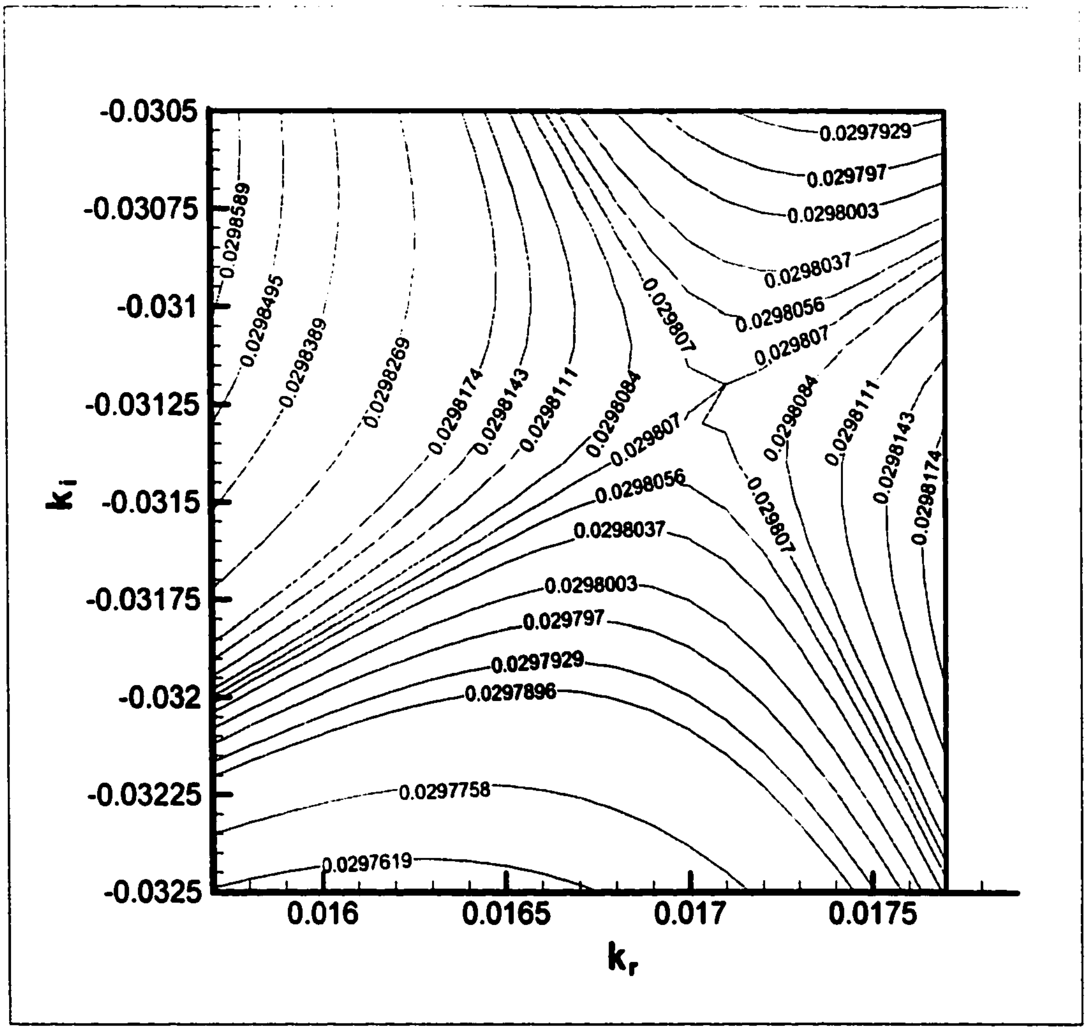

Figure 239: Contour plot of Ω_r for $R/\theta = 25$, $Fr = 1$, $\rho_j/\rho_\infty = 0.14$, $Sc = 1.43$, and $\Delta r = 12.5$, $U_\infty/\Delta U = 1$ in the k-plane illustrating the pinch point formation

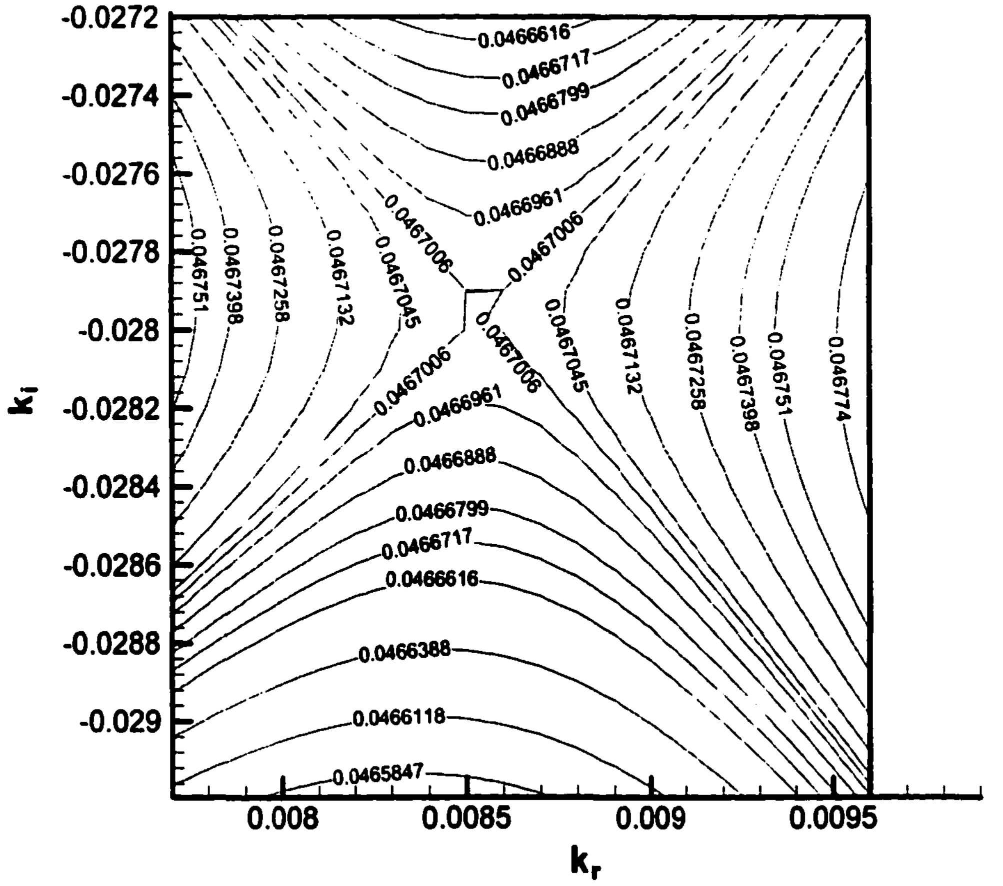

Figure 240: Contour plot of Ω_r for $R/\theta = 25$, $Fr = 0.75$, $\rho_j/\rho_\infty = 0.14$, $Sc = 1.43$, and $\Delta r = 12.5$, $U_\infty/\Delta U = 1$ in the k-plane illustrating the pinch point formation

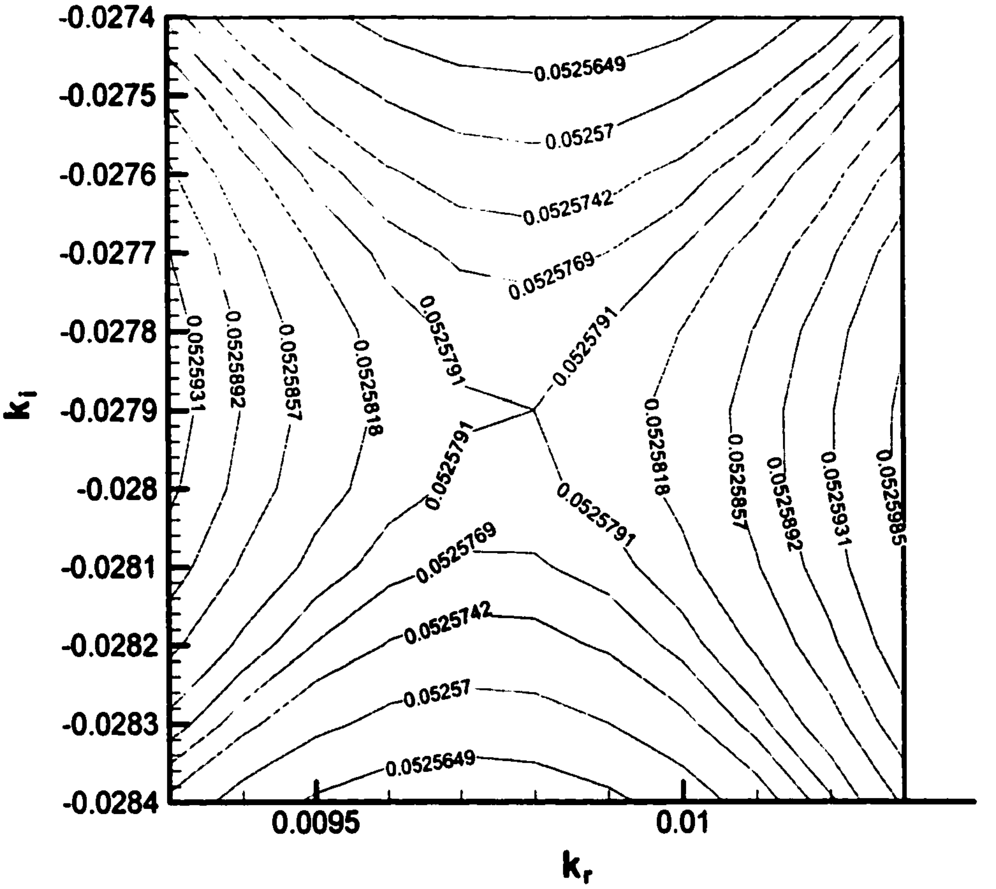

Figure 241: Contour plot of Ω_r for $R/\theta = 25$, $Fr = 0.5$, $\rho_j/\rho_\infty = 0.14$, $Sc = 1.43$, and $\Delta r = 12.5$, $U_\infty/\Delta U = 1$ in the k-plane illustrating the pinch point formation

Appendix B

Listing of Fortran and Excel Macro Codes

B1: PROGRAM RH0K

```
!       NOTE: The program is pronounced RH "zero" K
!************************************************************************
!
!   -       THIS PROGRAM FINDS THE EIGENVALUES OF A CO-FLOWING
JET
!           PROFILE; USING INVISCID TEMPORAL STABILITY ANALYSIS
!   -       A hyperbolic tangent profile is used for the density and
!           velocity profiles within the shear layer of the jet.
!************************************************************************
!
!       AXISYMMETRIC MODE: M=0 VERSION WITH NO EFFECTS OF
PARTICLES
!
!           Wavenumber = BETA (real) <-- k
!           Frequency = ALPHA (COMPLEX) <-- Ω
!************************************************************************
! RLIM = r at infinity
!       (For ROVT = 5, RLIM = 20;                 where ROVT is R/θ
!       for ROVT = 10, RLIM = 40;
!       for ROVT = 25, RLIM = 55)
! H1 = stepsize for inner integration, H2 = stepsize for outer integration
! IL1 = iterations for inner integration, IL2 = iterations for outer integration
!       (For ROVT = 5, IL1 = 800, IL2 = 2400;
!       for ROVT = 10, IL1 = 1600, IL2 = 4800;
!       for ROVT = 25, IL1 = 4000, IL2 = 4800)
! beta = k_r (real wavenumber for temporal stability analysis)

! rhoRatio = ratio of jet exit mass density to ambient gas mass density

    REAL*8     X1,H1,X2,H2, rovt, rhoRatio, Froude, kr, ki, Sc,DR
    REAL*8     kreal, kimag, wreal, wimag
    COMPLEX*16 Y1(2),Y2(2),ALPHA2(3),ALPHAM,DET1(3), ALPHA3(3)
    COMPLEX*16 YIN(2,3),YOUT(2,3),AROOT(2),RDET1,RDET2
    COMPLEX*16 RYIN1,RYIN2,RYIN3,RYIN4,RYOUT1,RYOUT2
    COMPLEX*16 RYOUT3,RYOUT4, beta
    COMPLEX*16 Z0
    real*8     XNU
    INTEGER    N, kr1, ki1
```

```
      PARAMETER (N=2)
      COMPLEX*16     CBS(N)
      EXTERNAL  DCBIS, UMACH, DCBKS
      common/given/beta,rovt,rhoRatio,Froude,Sc,DR,M

!         Initialize limits of the jet boundaries
      RLIM = 20.0d0
      H1 = 0.00625d0
      IL1 = 800
      H2 = -0.00625d0
      IL2 = 2400
!         Input data for flow stability variables and three initial guesses for ALPHA2
          M = 0
          rovt = 5.0d0
          Sc = 1.0d0               ! Vary Schimdt # (Sc) as 0.21, 0.6, 1, 1.3, 1.64
         DR = 0.0d0                ! Vary lateral shift (Δr) as -2.5, -1.25, 0, 1.25, 2.5, etc
!                                          (according to Raynal et al., 1993 => Δyi*R/θ)
!         Froude = 0.5d0           ! Comment this line for Froude = infinity
                                   !         (Also, see comment for rho7 in Subroutine
DERIVS)
          rhoRatio = 0.3d0

          beta = dcmplx(0.2d0,0.0d0)
       ALPHA2(1) = (0.1238d0,-0.0155d0)
       ALPHA2(2) = (0.1283d0,-0.0238d0)
       ALPHA2(3) = (0.1255d0,-0.0183d0)
   27 IA = 0
   23 IA = IA+1
      IF (IA.GT.3) GO TO 24
      ALPHAM = ALPHA2(IA)
      X1 = 0.0d0
      Y1(1) = (1.0d0,0.0d0)
      Y1(2) = (0.0d0,0.0d0)
      CALL RUNG1(X1,H1,Y1,IL1,ALPHAM,NIT)
      YIN(1,IA) = Y1(1)
      YIN(2,IA) = Y1(2)
      Z0 = RLIM*beta
      XNU = 0.0d0
      CALL DCBKS (XNU, Z0, N, CBS)
      Y2(1) = CBS(1)
      Y2(2) = -1.0d0*CBS(2)*beta
      X2 = RLIM
      CALL RUNG1 (X2,H2,Y2,IL2,ALPHAM,NIT)
      YOUT(1,IA) = Y2(1)
      YOUT(2,IA) = Y2(2)
```

```
      DET1(IA) = YIN(1,IA)*YOUT(2,IA)-YIN(2,IA)*YOUT(1,IA)
      WRITE(*,*) IA, ALPHA2(IA), DET1(IA)
      IF(NIT.GT.25) GO TO 26
      GO TO 23
   24 CALL PAR1 (ALPHA2,DET1,AROOT)
      NIT = NIT+1
      ALPHAM = AROOT(1)
      X1 = 0.0d0
      Y1(1) = (1.0d0,0.0d0)
      Y1(2) = (0.0d0,0.0d0)
      CALL RUNG1 (X1,H1,Y1,IL1,ALPHAM,NIT)
      RYIN1 = Y1(1)
      RYIN2 = Y1(2)
      Z0 = RLIM*beta
      XNU = 0.0d0
      CALL DCBKS (XNU, Z0, N, CBS)
      Y2(1) = CBS(1)
      Y2(2) = -1.0d0*CBS(2)*beta
      X2 = RLIM
      CALL RUNG1 (X2,H2,Y2,IL2,ALPHAM,NIT)
      RYOUT1 = Y2(1)
      RYOUT2 = Y2(2)
      RDET1 = RYIN1*RYOUT2-RYIN2*RYOUT1
      ALPHAM = AROOT(2)
      X1 = 0.0d0
      Y1(1) = (1.0d0,0.0d0)
      Y1(2) = (0.0d0,0.0d0)
      CALL RUNG1 (X1,H1,Y1,IL1,ALPHAM,NIT)
      RYIN3 = Y1(1)
      RYIN4 = Y1(2)
      Z0 = RLIM*beta
      XNU = 0.0d0
      CALL DCBKS (XNU, Z0, N, CBS)
      Y2(1) = CBS(1)
      Y2(2) = -1.0d0*CBS(2)*beta
      X2 = RLIM
      CALL RUNG1 (X2,H2,Y2,IL2,ALPHAM,NIT)
      RYOUT3 = Y2(1)
      RYOUT4 = Y2(2)
      RDET2 = RYIN3*RYOUT4-RYIN4*RYOUT3
      IF(ZABS(RDET1).LT.ZABS(RDET2))THEN
      ALPHA2(3) = ALPHA2(2)
      ALPHA2(2) = ALPHA2(1)
      ALPHA2(1) = AROOT(1)
      ELSE
```

```
      ALPHA2(3) = ALPHA2(2)
      ALPHA2(2) = ALPHA2(1)
      ALPHA2(1) = AROOT(2)
      ENDIF
      GOTO 27
   26 STOP
      END
!
!
      SUBROUTINE RUNG1 (X,H,Y,IL,ALPHA1,NIT1)
      INTEGER   NIT1
      REAL*8    H,HH,H6,X,XH, moy(2)
      COMPLEX*16 Y(2),DYDX(2),YOUT(2),YT(2),DYT(2),DYM(2)
      COMPLEX*16 ALPHA1
      N = 2
      DO 21 IM = 1,IL
      HH = H*0.5d0
      H6 = H/6.0d0
      XH = X + HH
      CALL DERIVS (X,Y,DYDX,ALPHA1)
      DO 11 I = 1,N
      YT(I) = Y(I) + HH*DYDX(I)
   11 CONTINUE
      CALL DERIVS (XH,YT,DYT,ALPHA1)
      DO 12 I = 1,N
      YT(I) = Y(I) + HH*DYT(I)
   12 CONTINUE
      CALL DERIVS (XH,YT,DYM,ALPHA1)
      DO 13 I = 1,N
      YT(I) = Y(I) + H*DYM(I)
      DYM(I) = DYT(I) + DYM(I)
   13 CONTINUE
      CALL DERIVS (X+H,YT,DYT,ALPHA1)
      DO 14 I = 1,N
      YOUT(I) = Y(I) + H6*(DYDX(I)+DYT(I)+2.00*DYM(I))
   14 CONTINUE
      DO 15 I = 1,N
      Y(I) = YOUT(I)
   15 CONTINUE
      X = X + H
   21 CONTINUE
      RETURN
      END
!
!
```

```
      SUBROUTINE DERIVS (X1,Y1,DYDX1,ALPHA)
      REAL*8 ROVT,AM,X1,U1,U2,U3,U,DU1,DU, Sc,DR
      COMPLEX*16 Y1(2),DYDX1(2),ALPHA,V1,V2
      COMPLEX*16 rho, Drho, rho1, rho2, rho3, Drho1, Drho2, rho6, rho7, beta
      REAL*8 Froude, rhoRatio
      common/given/beta,rovt,rhoRatio,Froude,Sc,DR,M
      U2 = 0.0d0
      AM = DFLOAT(M)
      IF(X1.EQ.0.0d0) THEN
      DYDX1(1) = (0.0d0,0.0d0)
      DYDX1(2) = (0.5d0,0.0d0)
      ELSE
      IF(X1.LT.1.50d0) THEN
      U = 1.0d0
      DU = 0.0d0
      ELSE
      U1 = DTANH(0.25d0*X1-0.25d0*ROVT*ROVT/X1)
      U3 = 2.0d0*U2 + 1.0d0
      U = 0.5d0*(U3-U1)
      DU1 = 1.0d0/(DCOSH(0.25d0*X1-0.25d0*ROVT*ROVT/X1))
      DU = -0.5d0*DU1*DU1*(0.25d0+0.25d0*ROVT*ROVT/X1/X1)
      ENDIF
! At an X1 less than 0.03438, rho and Drho values need to be specified otherwise
!       overflow error occurs.
  IF(X1.lt.1.0d0) THEN
      rho = rhoRatio
      Drho = 0.0d0
  ELSE
      rho3 = (rhoRatio - 1.0d0)
      rho2 = 0.5d0*(1.0d0 - DTANH(0.25d0*(X1+DR)-0.25d0*ROVT*ROVT/(X1+DR)))
      rho1 = rho2**Sc
      rho = 1.0d0 + (rho3*rho1)
      Drho1 = 1.0d0/(DCOSH(0.25d0*(X1+DR)-0.25d0*ROVT*ROVT/(X1)))
      Drho2 = (-
1.0d0)*rho3*Drho1*Drho1*(0.25d0+0.25d0*ROVT*ROVT/(X1+DR)/(X1))
      Drho = 0.5d0*Sc*Drho2*(0.5d0*(1.0d0-U1))**(Sc-1.0d0)
  ENDIF
      V1 = beta*beta+AM*AM/X1/X1
! Use for Fr = infinity. For finite values of Fr comment next line and uncomment
subsequent line.
       rho7 = (1.0d0,0.0d0)
!      rho7 = (1.0d0+((0.0d0,1.0d0)*(1.0d0/(ROVT*Froude*Froude*(((1.0d0)/rhoRatio)
                -(1.0d0))*beta*(U-alpha/beta)*(U-alpha/beta)))))
       rho6 = ((1.0d0)/rho)*Drho*rho7
       V2 = (1.0d0/X1)-(2.0d0*DU/(U-alpha/beta))-rho6
```

```
      DYDX1(1) = Y1(2)
      DYDX1(2) = V1*Y1(1)-V2*Y1(2)
    ENDIF
    RETURN
    END
!
!
     SUBROUTINE PAR1 (XC,YC,ROOT)
     COMPLEX*16 XC(3),YC(3),ROOT(2),V11,V12,A,B,C
     V11 = (YC(1)-YC(2))/(XC(1)-XC(2))-(YC(2)-YC(3))/(XC(2)-XC(3))
     A = V11/(XC(1)-XC(3))
     B = (YC(1)-YC(2))/(XC(1)-XC(2))-A*(XC(1)+XC(2))
     C = YC(1)-A*XC(1)*XC(1)-B*XC(1)
     V12 = B*B-4.0d0*A*C
     ROOT(1) = -0.5d0*B/A + SQRT(V12)*0.5d0/A
     ROOT(2) = -0.5d0*B/A - SQRT(V12)*0.5d0/A
     RETURN
     END
```

B2: PROGRAM RHOKABSWO

```
!*********************************************************************
!
!       -THIS PROGRAM FINDS THE EIGENVALUES OF A CO-FLOWING JET
!       PROFILE; USING INVISCID SPATIO-TEMPORAL STABILITY ANALYSIS
!       -       A hyperbolic tangent profile is used for the density and
!               velocity profiles within the shear layer of the jet.
!*********************************************************************
!
!       AXISYMMETRIC MODE: M=0 VERSION WITH NO EFFECTS OF
PARTICLES
!
!               Wavenumber = BETA (complex) <-- k
!               Frequency = ALPHA (COMPLEX) <-- Ω
!*********************************************************************
! RLIM = r at infinity
!       (For ROVT = 5, RLIM = 20;               where ROVT is R/θ
!       for ROVT = 10, RLIM = 40;
!       for ROVT = 25, RLIM = 55)
! H1 = stepsize for inner integration, H2 = stepsize for outer integration
! IL1 = iterations for inner integration, IL2 = iterations for outer integration
!       (For ROVT = 5, IL1 = 800, IL2 = 2400;
!       for ROVT = 10, IL1 = 1600, IL2 = 4800;
!       for ROVT = 25, IL1 = 4000, IL2 = 4800)
! beta = k_r (real wavenumber for temporal stability analysis)
! beta = (k_r,k_i) complex wavenumber for absolute stability analysis
! rhoRatio = ratio of jet exit mass density to ambient gas mass density

    REAL*8    X1,H1,X2,H2, rovt, rhoRatio, Froude, kr, ki, Sc,DR
    REAL*8    kreal, kimag, wreal, wimag
    COMPLEX*16 Y1(2),Y2(2),ALPHA2(3),ALPHAM,DET1(3), ALPHA3(3)
    COMPLEX*16 YIN(2,3),YOUT(2,3),AROOT(2),RDET1,RDET2
    COMPLEX*16 RYIN1,RYIN2,RYIN3,RYIN4,RYOUT1,RYOUT2
    COMPLEX*16 RYOUT3,RYOUT4, beta
    COMPLEX*16 Z0
    real*8    XNU
    INTEGER  N, kr1, ki1
    PARAMETER (N=2)
    COMPLEX*16      CBS(N)
    EXTERNAL  DCBIS, UMACH, DCBKS
    common/given/beta,rovt,rhoRatio,Froude,Sc,DR,M
!       Open output files
        open(1, file = 'rhok4abswoi', status = 'unknown')
        open(2, file = 'rhok4abswor', status = 'unknown')
```

```
!       Initialize limits of the jet boundaries
   RLIM = 20.0d0
   H1 = 0.00625d0
   IL1 = 800
   H2 = -0.00625d0
   IL2 = 2400
!       Input data for flow stability variables and three initial guesses for ALPHA2
        M = 0
        rovt = 5.0d0
        Sc = 1.0d0               ! Vary Schimdt # (Sc) as 0.21, 0.6, 1, 1.3, 1.64
       DR = 0.0d0                ! Vary lateral shift (Δr) as -2.5, -1.25, 0, 1.25, 2.5, etc
!                                        (according to Raynal et al., 1993 => Δyi*R/θ)
!       Froude = 0.5d0           ! Comment this line for Froude = infinity
                                 !       (Also, see comment for rho7 in Subroutine
DERIVS)
        rhoRatio = 0.3d0
        write(1,*) 'kr ', 'ki ', 'wi '
        write(2,*) 'kr ', 'ki ', 'wr '
        kr1 = 0
        ki1 = 0
        do 200 kr = 0.1335d0,0.1355d0,0.0001d0
        kr1 = kr1 + 1
        do 100 ki = 0.1785d0,0.1805d0,0.0001d0
        NIT = 1
        ki1 = ki1 + 1
        beta = dcmplx(kr,-ki)
   ALPHA2(1) = (0.1238d0,-0.0155d0)
   ALPHA2(2) = (0.1283d0,-0.0238d0)
   ALPHA2(3) = (0.1255d0,-0.0183d0)
  27 IA = 0
  23 IA = IA+1
   IF (IA.GT.3) GO TO 24
   ALPHAM = ALPHA2(IA)
   X1 = 0.0d0
   Y1(1) = (1.0d0,0.0d0)
   Y1(2) = (0.0d0,0.0d0)
   CALL RUNG1(X1,H1,Y1,IL1,ALPHAM,NIT)
   YIN(1,IA) = Y1(1)
   YIN(2,IA) = Y1(2)
   Z0 = RLIM*beta
   XNU = 0.0d0
   CALL DCBKS (XNU, Z0, N, CBS)
   Y2(1) = CBS(1)
   Y2(2) = -1.0d0*CBS(2)*beta
   X2 = RLIM
```

```
      CALL RUNG1 (X2,H2,Y2,IL2,ALPHAM,NIT)
      YOUT(1,IA) = Y2(1)
      YOUT(2,IA) = Y2(2)
      DET1(IA) = YIN(1,IA)*YOUT(2,IA)-YIN(2,IA)*YOUT(1,IA)
      WRITE(*,*) IA, ALPHA2(IA), DET1(IA)
      IF(NIT.GT.25) GO TO 26
      GO TO 23
   24 CALL PAR1 (ALPHA2,DET1,AROOT)
      NIT = NIT+1
      ALPHAM = AROOT(1)
      X1 = 0.0d0
      Y1(1) = (1.0d0,0.0d0)
      Y1(2) = (0.0d0,0.0d0)
      CALL RUNG1 (X1,H1,Y1,IL1,ALPHAM,NIT)
      RYIN1 = Y1(1)
      RYIN2 = Y1(2)
      Z0 = RLIM*beta
      XNU = 0.0d0
      CALL DCBKS (XNU, Z0, N, CBS)
      Y2(1) = CBS(1)
      Y2(2) = -1.0d0*CBS(2)*beta
      X2 = RLIM
      CALL RUNG1 (X2,H2,Y2,IL2,ALPHAM,NIT)
      RYOUT1 = Y2(1)
      RYOUT2 = Y2(2)
      RDET1 = RYIN1*RYOUT2-RYIN2*RYOUT1
      ALPHAM = AROOT(2)
      X1 = 0.0d0
      Y1(1) = (1.0d0,0.0d0)
      Y1(2) = (0.0d0,0.0d0)
      CALL RUNG1 (X1,H1,Y1,IL1,ALPHAM,NIT)
      RYIN3 = Y1(1)
      RYIN4 = Y1(2)
      Z0 = RLIM*beta
      XNU = 0.0d0
      CALL DCBKS (XNU, Z0, N, CBS)
      Y2(1) = CBS(1)
      Y2(2) = -1.0d0*CBS(2)*beta
      X2 = RLIM
      CALL RUNG1 (X2,H2,Y2,IL2,ALPHAM,NIT)
      RYOUT3 = Y2(1)
      RYOUT4 = Y2(2)
      RDET2 = RYIN3*RYOUT4-RYIN4*RYOUT3
      IF(ZABS(RDET1).LT.ZABS(RDET2))THEN
      ALPHA2(3) = ALPHA2(2)
```

```
      ALPHA2(2) = ALPHA2(1)
      ALPHA2(1) = AROOT(1)
      ELSE
      ALPHA2(3) = ALPHA2(2)
      ALPHA2(2) = ALPHA2(1)
      ALPHA2(1) = AROOT(2)
      ENDIF
      GOTO 27
   26 kreal = dreal(beta)
      kimag = dimag(beta)
      wreal = dreal(alpha2(1))
      wimag = dimag(alpha2(1))
! Print results to file(s)
      write(1,*) kreal, kimag, wimag
      write(2,*) kreal, kimag, wreal
  100 continue
  200 continue
      STOP
      END
!
!
      SUBROUTINE RUNG1 (X,H,Y,IL,ALPHA1,NIT1)
      INTEGER  NIT1
      REAL*8   H,HH,H6,X,XH, moy(2)
      COMPLEX*16 Y(2),DYDX(2),YOUT(2),YT(2),DYT(2),DYM(2)
      COMPLEX*16 ALPHA1
      N = 2
      DO 21 IM = 1,IL
      HH = H*0.5d0
      H6 = H/6.0d0
      XH = X + HH
      CALL DERIVS (X,Y,DYDX,ALPHA1)
      DO 11 I = 1,N
      YT(I) = Y(I) + HH*DYDX(I)
   11 CONTINUE
      CALL DERIVS (XH,YT,DYT,ALPHA1)
      DO 12 I = 1,N
      YT(I) = Y(I) + HH*DYT(I)
   12 CONTINUE
      CALL DERIVS (XH,YT,DYM,ALPHA1)
      DO 13 I = 1,N
      YT(I) = Y(I) + H*DYM(I)
      DYM(I) = DYT(I) + DYM(I)
   13 CONTINUE
      CALL DERIVS (X+H,YT,DYT,ALPHA1)
```

```
      DO 14 I = 1,N
      YOUT(I) = Y(I) + H6*(DYDX(I)+DYT(I)+2.00*DYM(I))
   14 CONTINUE
      DO 15 I = 1,N
      Y(I) = YOUT(I)
   15 CONTINUE
      X = X + H
   21 CONTINUE
      RETURN
      END
!
!
      SUBROUTINE DERIVS (X1,Y1,DYDX1,ALPHA)
      REAL*8 ROVT,AM,X1,U1,U2,U3,U,DU1,DU, Sc,DR
      COMPLEX*16 Y1(2),DYDX1(2),ALPHA,V1,V2
      COMPLEX*16 rho, Drho, rho1, rho2, rho3, Drho1, Drho2, rho6, rho7, beta
      REAL*8 Froude, rhoRatio
      common/given/beta,rovt,rhoRatio,Froude,Sc,DR,M
      U2 = 0.0d0
      AM = DFLOAT(M)
      IF(X1.EQ.0.0d0) THEN
      DYDX1(1) = (0.0d0,0.0d0)
      DYDX1(2) = (0.5d0,0.0d0)
      ELSE
      IF(X1.LT.1.50d0) THEN
      U = 1.0d0
      DU = 0.0d0
      ELSE
      U1 = DTANH(0.25d0*X1-0.25d0*ROVT*ROVT/X1)
      U3 = 2.0d0*U2 + 1.0d0
      U = 0.5d0*(U3-U1)
      DU1 = 1.0d0/(DCOSH(0.25d0*X1-0.25d0*ROVT*ROVT/X1))
      DU = -0.5d0*DU1*DU1*(0.25d0+0.25d0*ROVT*ROVT/X1/X1)
      ENDIF
! At an X1 less than 0.03438, rho and Drho values need to be specified otherwise
!          overflow error occurs.
    IF(X1.lt.1.0d0) THEN
      rho = rhoRatio
      Drho = 0.0d0
    ELSE
      rho3 = (rhoRatio - 1.0d0)
      rho2 = 0.5d0*(1.0d0 - DTANH(0.25d0*(X1+DR)-0.25d0*ROVT*ROVT/(X1+DR)))
      rho1 = rho2**Sc
      rho = 1.0d0 + (rho3*rho1)
      Drho1 = 1.0d0/(DCOSH(0.25d0*(X1+DR)-0.25d0*ROVT*ROVT/(X1+DR)))
```

```
    Drho2 = (-
1.0d0)*rho3*Drho1*Drho1*(0.25d0+0.25d0*ROVT*ROVT/(X1+DR)/(X1+DR))
    Drho = 0.5d0*Sc*Drho2*(0.5d0*(1.0d0-U1))**(Sc-1.0d0)
  ENDIF
    V1 = beta*beta+AM*AM/X1/X1
! Use for Fr = infinity. For finite values of Fr comment next line and uncomment
subsequent line.
     rho7 = (1.0d0,0.0d0)
!    rho7 = (1.0d0+((0.0d0,1.0d0)*(1.0d0/(ROVT*Froude*Froude*(((1.0d0)/rhoRatio)
               -(1.0d0))*beta*(U-alpha/beta)*(U-alpha/beta)))))
     rho6 = ((1.0d0)/rho)*Drho*rho7
     V2 = (1.0d0/X1)-(2.0d0*DU/(U-alpha/beta))-rho6
     DYDX1(1) = Y1(2)
     DYDX1(2) = V1*Y1(1)-V2*Y1(2)
   ENDIF
   RETURN
   END
!
!
    SUBROUTINE PAR1 (XC,YC,ROOT)
    COMPLEX*16 XC(3),YC(3),ROOT(2),V11,V12,A,B,C
    V11 = (YC(1)-YC(2))/(XC(1)-XC(2))-(YC(2)-YC(3))/(XC(2)-XC(3))
    A = V11/(XC(1)-XC(3))
    B = (YC(1)-YC(2))/(XC(1)-XC(2))-A*(XC(1)+XC(2))
    C = YC(1)-A*XC(1)*XC(1)-B*XC(1)
    V12 = B*B-4.0d0*A*C
    ROOT(1) = -0.5d0*B/A + SQRT(V12)*0.5d0/A
    ROOT(2) = -0.5d0*B/A - SQRT(V12)*0.5d0/A
    RETURN
    END
```

B3: PROGRAM Pressure

```
!***************************************************************************
!
!    -        THIS PROGRAM FINDS:
!                  Pressure distribution
!                  Derivative of the pressure distribution
!                  Axial and radial components of the velocity disturbance
!                  Azimuthal component of the vorticity
!
!             OF A CO-FLOWING JET PROFILE; using inviscid temporal and
!                  spatio-TEMPORAL ANALYSIS
!    -        A hyperbolic tangent profile is used for the density and
!             velocity profiles within the shear layer of the jet.
!***************************************************************************
!
!       AXISYMMETRIC MODE: M=0 VERSION WITH NO EFFECTS OF
!             PARTICLES
!
!             Wavenumber = BETA (complex) <-- k
!             Frequency = ALPHA (COMPLEX) <-- Ω
!*************************************************************************
! RLIM = r at infinity
!       (For ROVT = 5, RLIM = 20;              where ROVT is R/θ
!       for ROVT = 10, RLIM = 40;
!       for ROVT = 25, RLIM = 55)
! H1 = stepsize for inner integration, H2 = stepsize for outer integration
! IL1 = iterations for inner integration, IL2 = iterations for outer integration
!       (For ROVT = 5, IL1 = 800, IL2 = 2400;
!       for ROVT = 10, IL1 = 1600, IL2 = 4800;
!       for ROVT = 25, IL1 = 4000, IL2 = 4800)
! beta = k_r (real wavenumber for temporal stability analysis)
! beta = (k_r,k_i) complex wavenumber for absolute stability analysis
! rhoRatio = ratio of jet exit mass density to ambient gas mass density

    REAL*8 X1,H1,X2,H2, rovt, rhoRatio, Froude, kr, ki, Sc,DR
    REAL*8 kreal, kimag, wreal, wimag
    COMPLEX*16     Y1(2),Y2(2),ALPHA2,ALPHAM,DET1, ALPHA3
    COMPLEX*16     YIN(2),YOUT(2),AROOT(2),RDET1,RDET2, your(2)
    COMPLEX*16     RYIN1,RYIN2,RYIN3,RYIN4,RYOUT1,RYOUT2
    COMPLEX*16     RYOUT3,RYOUT4, beta, dydxour(2), dydxin(2), dydx(2)
    COMPLEX*16     dydx2(2)
    COMPLEX*16    Z0
    real*8         XNU
    INTEGER        N, kr1, ki1
```

```
      PARAMETER      (N=2)
      COMPLEX*16     CBS(N)
      EXTERNAL       DCBIS, UMACH, DCBKS
      common/given/beta,rovt,rhoRatio,Froude,Sc,DR,M
!        Open output files
          open(3, file = 'pres', status = 'unknown')
          open(4, file = 'dpres', status = 'unknown')
          open(5, file = 'distU', status = 'unknown')
          open(6, file = 'distV', status = 'unknown')
          open(7, file = 'vortict', status = 'unknown')
!        Initialize limits of the jet boundaries
      RLIM = 70.0d0
      H1 = 0.00625d0
      IL1 = 1600
      H2 = -0.00625d0
      IL2 = 9600
!        Input data for flow stability variables
          M = 0
          rovt = 10.0d0
          Sc = 1.0d0           ! Vary Schimdt # (Sc) as 0.21, 0.6, 1, 1.3, 1.64
        DR = 0.0d0             ! Vary lateral shift (Δr) as -2.5, -1.25, 0, 1.25, 2.5, etc
                                        !(according to Raynal et al., 1993 => Δy_i*R/θ)
!         Froude = 1.0d0       ! Comment this line for Froude = infinity
                               !        (Also, see comment for rho7, vorticit5, vortict6
                               and !    ucap4 in Subroutine DERIVS)
          rhoRatio = 0.99d0
!        Print column titles in output files
          write(3,*) 'r ', 'P '
          write(4,*) 'r ', 'dP '
          write(5,*) 'r ', 'ucap '
          write(6,*) 'r ', 'vcap '
          write(7,*) 'r ', 'vorticity '

!        Wavenumber and frequency data inputs
!!!!!!!!!!!!!!!!!!!!!!!!!!!!!!!!!!!!!!!!!!!!!!!!!!!!!!!!!!!!!!!!!!!!!!!!!!!!!!!!!!!!!!!
!!!! Data corresponding to saddle points from Spatio-temporal stability analysis !!!!!!!
!!!wavenumber data:
!        Fr = infinity, S = 0.99
          beta = dcmplx(0.1037d0,-0.1578d0)
!        Fr = infinity, S = 0.14
!         beta = dcmplx(0.0705d0,-0.0895d0)
!        Fr = 1, S = 0.99
!         beta = dcmplx(0.109d0,-0.1573d0)
!        Fr = 1, S = 0.14
!         beta = dcmplx(0.06975d0,-0.087d0)
```

```
!!!Frequency data:
!        Fr = infinity, S = 0.99
           ALPHA2 = dcmplx(0.116458585081395d0,-0.0183494943140852d0)
!        Fr = infinity, S = 0.14
!          ALPHA2 = dcmplx(0.0563760634536487d0,0.0180811751034121d0)
!        Fr = 1, S = 0.99
!          ALPHA2 = dcmplx(0.122705190617981d0,0.0230543121518239d0)
!        Fr = 1, S = 0.14
!   ALPHA2 = dcmplx(0.0607526089390155d0,0.0289853014057314d0)
!!!!!!!!!!!!!!!!!!!!!!!!!!!!!!!!!!!!!!!!!!!!!!!!!!!!!!!!!!!!!!!!!!!!!!!!!!!!!!!!!!!!!!!


!!!!!!!!!!!!!!!!!!!!!!!!!!!!!!!!!!!!!!!!!!!!!!!!!!!!!!!!!!!!!!!!!!!!!!!!!!!!!!!!!!!!!!!
!!!! Data corresponding to max growth rate from temporal stability analysis   !!!!!!!!!!!
!!!wavenumber data:
!        Fr = infinity, S = 0.99
!          beta = dcmplx(0.24d0,0.0d0)
!        Fr = infinity, S = 0.14
!          beta = dcmplx(0.26d0,0.0d0)
!        Fr = 1, S = 0.99
!          beta = dcmplx(0.26d0,0.0d0)
!        Fr = 1, S = 0.14
!          beta = dcmplx(0.26d0,0.0d0)
!!!Frequency data:
!        Fr = infinity, S = 0.99
!          ALPHA2 = dcmplx(0.151443957460553d0,0.0420948269233371d0)
!        Fr = infinity, S = 0.14
!          ALPHA2 = dcmplx(0.100583766110241d0,0.0510921840479045d0)
!        Fr = 1, S = 0.99
!          ALPHA2 = dcmplx(0.161649141d0,0.0833522206329646d0)
!        Fr = 1, S = 0.14
!   ALPHA2 = dcmplx(0.106925994253422d0,0.0601231139433525d0)
!!!!!!!!!!!!!!!!!!!!!!!!!!!!!!!!!!!!!!!!!!!!!!!!!!!!!!!!!!!!!!!!!!!!!!!!!!!!!!!!!!!!!!!!!
    ALPHAM = ALPHA2
    X1 = 0.0d0
    Y1(1) = (1.0d0,0.0d0)
    Y1(2) = (0.0d0,0.0d0)
    CALL RUNG1(X1,H1,Y1,IL1,ALPHAM,dydx)
    YIN(1) = Y1(1)
    YIN(2) = Y1(2)
          dydxin(1) = dydx(1)
          dydxin(2) = dydx(2)
    Z0 = RLIM*beta
          XNU = 0.0d0
          CALL DCBKS (XNU, Z0, N, CBS)
```

```
      Y2(1) = CBS(1)
      Y2(2) = -1.0d0*CBS(2)*beta
      X2 = RLIM
      CALL RUNG1 (X2,H2,Y2,IL2,ALPHAM,dydx2)
      YOUT(1) = Y2(1)
      YOUT(2) = Y2(2)
            Your(1) = Yout(1)
            Your(2) = Yout(2)
            dydxour(1) = dydx2(1)
            dydxour(2) = dydx2(2)
      Z0 = RLIM*beta
            XNU = 0.0d0
            CALL DCBKS (XNU, Z0, N, CBS)
      Y2(1) = CBS(1)
      Y2(2) = -1.0d0*CBS(2)*beta
      X2 = RLIM
      CALL RUNG2 (X2,H2,Y2,IL2,ALPHAM,yin,your,dydxin,dydxour)
            Det1 = YIN(1)*YOUT(2)-YIN(2)*YOUT(1)
   26 STOP
      END
!
!
      SUBROUTINE RUNG1 (X,H,Y,IL,ALPHA1,dydx)
            INTEGER NIT1
      REAL*8 H,HH,H6,X,XH, moy(2)
      COMPLEX*16 Y(2),DYDX(2),YOUT(2),YT(2),DYT(2),DYM(2)
      COMPLEX*16 ALPHA1
      COMPLEX*16 ucap, ucapp, vcap, ucp, vcp,vrtict1,vrtict2,vrtict3,vrtict4,vorticity

      N = 2
      DO 21 IM = 1,IL
      HH = H*0.5d0
      H6 = H/6.0d0
      XH = X + HH
      CALL DERIVS(X,Y,DYDX,ALPHA1,ucap,ucapp,vcap,vrtict1,vrtict2,vrtict3,vrtict4)
      DO 11 I = 1,N
      YT(I) = Y(I) + HH*DYDX(I)
   11 CONTINUE
      CALL DERIVS(XH,YT,DYT,ALPHA1,ucap,ucapp,vcap,vrtict1,vrtict2,vrtict3,vrtict4)
      DO 12 I = 1,N
      YT(I) = Y(I) + HH*DYT(I)
   12 CONTINUE
      CALL DERIVS(XH,YT,DYM,ALPHA1,ucap,ucapp,vcap,vrtict1,vrtict2,vrtict3,vrtict4)
      DO 13 I = 1,N
      YT(I) = Y(I) + H*DYM(I)
```

```
  DYM(I) = DYT(I) + DYM(I)
 13 CONTINUE
CALL DERIVS(X+H,YT,DYT,ALPHA1,ucap,ucapp,vcap,vrtict1,vrtict2,vrtict3,vrtict4)
  DO 14 I = 1,N
  YOUT(I) = Y(I) + H6*(DYDX(I)+DYT(I)+2.00*DYM(I))
 14 CONTINUE
  DO 15 I = 1,N
  Y(I) = YOUT(I)
       moy(I) = cdabs(y(I))
 15 CONTINUE
       write(3,*) x+H, moy(1)
       write(4,*) x+H, moy(2)
       ucp = ucap*y(1) + ucapp*y(2)
       vcp = vcap*y(2)
       write(5,*) x+H, cdabs(ucp)
       write(6,*) x+H, cdabs(vcp)
       vorticity = vrtict1 + vrtict2*y(1) + vrtict3*DYDX(2) + vrtict4*y(2)
       write(7,*) x, cdabs(vorticity)
  X = X + H
 21 CONTINUE
  RETURN
  END
!
  SUBROUTINE RUNG2 (X,H,Y,IL,ALPHA1,yn,yor,dydxin,dydxour)
  INTEGER NIT1
  REAL*8 H,HH,H6,X,XH, moy(2)
  COMPLEX*16 Y(2),DYDX(2),YOUT(2),YT(2),DYT(2),DYM(2)
  COMPLEX*16 ALPHA1, ydon(2), yn(2), yor(2), maxy2
  COMPLEX*16 dydxdon(2),dydxin(2),dydxour(2)
  COMPLEX*16 ucap, ucapp, vcap, ucp, vcp,vrtict1,vrtict2,vrtict3,vrtict4,vorticity,
  COMPLEX*16 d2P(2)
  N = 2
  DO 31 IM = 1,IL
  HH = H*0.5d0
  H6 = H/6.0d0
  XH = X + HH
  CALL DERIVS (X,Y,DYDX,ALPHA1,ucap,ucapp,vcap,vrtict1,vrtict2,vrtict3,vrtict4)
  DO 41 I = 1,N
  YT(I) = Y(I) + HH*DYDX(I)
 41 CONTINUE
 CALL DERIVS(XH,YT,DYT,ALPHA1,ucap,ucapp,vcap,vrtict1,vrtict2,vrtict3,vrtict4)
  DO 42 I = 1,N
  YT(I) = Y(I) + HH*DYT(I)
 42 CONTINUE
 CALL DERIVS(XH,YT,DYM,ALPHA1,ucap,ucapp,vcap,vrtict1,vrtict2,vrtict3,vrtict4)
```

```
  DO 43 I = 1,N
  YT(I) = Y(I) + H*DYM(I)
  DYM(I) = DYT(I) + DYM(I)
 43 CONTINUE
 CALL DERIVS(X+H,YT,DYT,ALPHA1,ucap,ucapp,vcap,vrtict1,vrtict2,vrtict3,vrtict4)
  DO 44 I = 1,N
  YOUT(I) = Y(I) + H6*(DYDX(I)+DYT(I)+2.00*DYM(I))
 44 CONTINUE
  maxy2 = ydon(2)
  DO 45 I = 1,N
  Y(I) = YOUT(I)
        ydon(I) = yout(I)*yn(I)/yor(I)
        dydxdon(I) = dydx(I)*dydxin(I)/dydxour(I)
        moy(I) = cdabs(ydon(I))
 45 CONTINUE
        write(3,*) x+H, moy(1)
        write(4,*) x+H, moy(2)
        ucp = ucap*ydon(1) + ucapp*ydon(2)
        vcp = vcap*ydon(2)
        write(5,*) x+H, cdabs(ucp)
        write(6,*) x+H, cdabs(vcp)
        vorticity = vrtict1 + vrtict2*ydon(1) + vrtict3*dydxdon(2) + vrtict4*ydon(2)
        write(7,*) x, cdabs(vorticity)
  X = X + H
 31 CONTINUE
   RETURN
   END
!
SUBROUTINE DERIVS(X1,Y1,DYDX1,ALPHA,ucap1,ucap2,vcap1,
                                                vortict1,vortict2,vortict3,vortict4)
REAL*8       ROVT,AM,X1,U1,U2,U3,U,DU1,DU, D2U, D2U1, D2U2, Sc,DR
COMPLEX*16 Y1(2),DYDX1(2),ALPHA,V1,V2
COMPLEX*16 rho,Drho,rho1,rho2,rho3,Drho1,Drho2,rho6,rho7, beta,
COMPLEX*16 D2rho,D2rho1,D2rho2,D2rho3
COMPLEX*16 denom,ucap1,ucap2,ucap3,ucap4,vcap1,vortict1,vortict2,vortict3,
COMPLEX*16 vortict4,vortict5,vortict6
REAL*8       Froude, rhoRatio
common/given/beta,rovt,rhoRatio,Froude,Sc,DR,M
   U2 = 0.0d0
   AM = DFLOAT(M)
IF(X1.EQ.0.0d0) THEN
   DYDX1(1) = (0.0d0,0.0d0)
   DYDX1(2) = (0.5d0,0.0d0)
ELSE
   IF(X1.LT.1.50d0) THEN
```

```
   U = 1.0d0
   DU = 0.0d0
 ELSE
   U1 = DTANH(0.25d0*X1-0.25d0*ROVT*ROVT/X1)
   U3 = 2.0d0*U2 + 1.0d0
   U = 0.5d0*(U3-U1)
   DU1 = 1.0d0/(DCOSH(0.25d0*X1-0.25d0*ROVT*ROVT/X1))
!!!! Derivative of the velocity profile
   DU = -0.5d0*DU1*DU1*(0.25d0+0.25d0*ROVT*ROVT/X1/X1)
   D2U1 = DSINH(0.25d0*X1-0.25d0*ROVT*ROVT/X1)
   D2U2
=(0.25d0+0.25d0*ROVT*ROVT/X1/X1)*(0.25d0+0.25d0*ROVT*ROVT/X1/X1)
!!!! Second derivative of the velocity profile
   D2U = D2U1*DU1*DU1*DU1*D2U2 +
0.25d0*DU1*DU1*ROVT*ROVT/X1/X1/X1
   ENDIF
! At an X1 less than 0.03438, rho and Drho values need to be specified otherwise
!        overflow error occurs.
IF(X1.lt.1.0d0) THEN
   rho = rhoRatio
   Drho = 0.0d0
ELSE
   rho3 = (rhoRatio - 1.0d0)
   rho2 = 0.5d0*(1.0d0 - DTANH(0.25d0*(X1+DR)-0.25d0*ROVT*ROVT/(X1+DR)))
   rho1 = rho2**Sc
   rho = 1.0d0 + (rho3*rho1)
   Drho1 = 1.0d0/(DCOSH(0.25d0*(X1+DR)-0.25d0*ROVT*ROVT/(X1+DR)))
   Drho2 = (-
1.0d0)*rho3*Drho1*Drho1*(0.25d0+0.25d0*ROVT*ROVT/(X1+DR)/(X1+DR))
!!!! Derivative of the density profile
    Drho = 0.5d0*Sc*Drho2*(0.5d0*(1.0d0-U1))**(Sc-1.0d0)
    D2rho1 = D2U1*DU1*DU1*DU1*D2U2
    D2rho2 = 0.25d0*DU1*DU1*ROVT*ROVT/X1/X1/X1
    D2rho3 = 0.25d0*(Sc-1)*DU1*DU1*DU1*DU1*D2U2/(0.5d0*(1.0d0-U1))
!!!! Second derivative of the density profile
    D2rho = (rho3*Sc*(0.5d0*(1.0d0-U1))**(Sc-1.0d0))*(D2rho1+D2rho2+D2rho3)
ENDIF
   V1 = beta*beta+AM*AM/X1/X1
! Use for Fr = infinity. For finite values of Fr comment next line and uncomment
subsequent line.
   rho7 = (1.0d0,0.0d0)
!  rho7 = (1.0d0+((0.0d0,1.0d0)*(1.0d0/(ROVT*Froude*Froude*(((1.0d0)/rhoRatio)
              -(1.0d0))*beta*(U-alpha/beta)*(U-alpha/beta)))))
   rho6 = ((1.0d0)/rho)*Drho*rho7
   V2 = (1.0d0/X1)-(2.0d0*DU/(U-alpha/beta))-rho6
```

```
      DYDX1(1) = Y1(2)
      DYDX1(2) = V1*Y1(1)-V2*Y1(2)
      denom = (beta*U - alpha)
      ucap1 = (-1.0d0)*beta/(rho*denom)
      ucap3 = (-1.0d0)*DU/(rho*denom*denom)
! Use for Fr = infinity. For finite values of Fr comment next line and uncomment
subsequent line.
      ucap4 = (0.0d0,0.0d0)
!     ucap4 = (0.0d0,1.0d0)*Drho/(rovt*Froude*Froude*(((1.0d0)/rhoRatio)
                 -(1.0d0))*rho*rho*denom*denom*denom)
      ucap2 = ucap3 + ucap4
      vcap1 = (0.0d0,1.0d0)/(rho*denom)
      vortict1 = (-1.0d0)*DU
      vortict2 = (-1.0d0)*(beta*Drho/(rho*rho*denom) +
beta*beta*DU/(rho*denom*denom))
! Use for Fr = infinity. For finite values of Fr comment next line and uncomment
subsequent line.
      vortict6 = (0.0d0,0.0d0)
!     vortict6 = ((0.0d0,1.0d0)*(Drho/(ROVT*Froude*Froude*((1.0d0/rhoRatio)-1.0d0)))
                         /(rho*rho*denom*denom*denom))
       vortict3 = DU/(rho*denom*denom) - vortict6
! Use for Fr = infinity. For finite values of Fr comment next line and uncomment
subsequent line.
       vortict5 = (0.0d0,0.0d0)
!      vortict5 = (0.0d0,1.0d0)*(1/(ROVT*Froude*Froude*((1.0d0/rhoRatio)-1.0d0)))
                         *(2*Drho*Drho/(rho*rho*rho*denom*denom*denom)
                         + 3*beta*Drho*DU/(rho*rho*denom*denom*denom*denom)
                         - D2rho/(rho*rho*denom*denom*denom))
        vortict4 = (D2rho/(rho*denom*denom) - DU*Drho/(rho*rho*denom*denom)
                         -    2*beta*DU*DU/(rho*denom*denom*denom) + vortict5)
 ENDIF
      RETURN
      END
!
      SUBROUTINE PAR1 (XC,YC,ROOT)
      COMPLEX*16      XC(3),YC(3),ROOT(2),V11,V12,A,B,C
      V11 = (YC(1)-YC(2))/(XC(1)-XC(2))-(YC(2)-YC(3))/(XC(2)-XC(3))
      A = V11/(XC(1)-XC(3))
      B = (YC(1)-YC(2))/(XC(1)-XC(2))-A*(XC(1)+XC(2))
      C = YC(1)-A*XC(1)*XC(1)-B*XC(1)
      V12 = B*B-4.0d0*A*C
      ROOT(1) = -0.5d0*B/A + SQRT(V12)*0.5d0/A
      ROOT(2) = -0.5d0*B/A - SQRT(V12)*0.5d0/A
      RETURN
      END
```

B4: Excel Macro used to format the output files from Program RHOKABSWO.f90 into the carpet format required for the TechPlot software.

```
Sub kikrFormat()
'
' kikrFormat Macro
' Macro recorded 6/21/2001 by Tony Lawson
'
'
    Range("B22:B422").Select
    Selection.Cut
    ActiveWindow.ScrollRow = 1
    Range("C2").Select
    ActiveSheet.Paste
    Range("C22:C401").Select
    Selection.Cut
    ActiveWindow.LargeScroll Down:=-1
    Range("D2").Select
    ActiveSheet.Paste
    Range("D22:D408").Select
    Selection.Cut
    ActiveWindow.LargeScroll Down:=-1
    Range("E2").Select
    ActiveSheet.Paste
    Range("E22:E438").Select
    Selection.Cut
    ActiveWindow.LargeScroll Down:=-1
    Range("F2").Select
    ActiveSheet.Paste
    Range("F22:F381").Select
    Selection.Cut
    ActiveWindow.LargeScroll Down:=-1
    Range("G2").Select
    ActiveSheet.Paste
    Range("G22:G446").Select
    Selection.Cut
    ActiveWindow.LargeScroll Down:=-1
    Range("H2").Select
    ActiveSheet.Paste
```

```
Range("H22:H363").Select
Selection.Cut
ActiveWindow.LargeScroll Down:=-1
Range("I2").Select
ActiveSheet.Paste
Range("I22:I327").Select
Selection.Cut
ActiveWindow.LargeScroll Down:=-1
Range("J2").Select
ActiveSheet.Paste
Range("J22:J331").Select
Selection.Cut
ActiveWindow.LargeScroll Down:=-1
Range("K2").Select
ActiveSheet.Paste
Range("K22:K356").Select
Selection.Cut
ActiveWindow.LargeScroll Down:=-1
Range("L2").Select
ActiveSheet.Paste
Range("L22:L286").Select
Selection.Cut
ActiveWindow.LargeScroll Down:=-1
Range("M2").Select
ActiveSheet.Paste
Range("M22:M394").Select
Selection.Cut
ActiveWindow.LargeScroll Down:=-1
Range("N2").Select
ActiveSheet.Paste
Range("N22:N311").Select
Selection.Cut
ActiveWindow.LargeScroll Down:=-1
Range("O2").Select
ActiveSheet.Paste
Range("O22:O424").Select
Selection.Cut
ActiveWindow.LargeScroll Down:=-1
Range("P2").Select
ActiveSheet.Paste
Range("P22:P351").Select
```

```
    Selection.Cut
    ActiveWindow.LargeScroll Down:=-1
    Range("Q2").Select
    ActiveSheet.Paste
    Range("Q22:Q370").Select
    Selection.Cut
    ActiveWindow.LargeScroll Down:=-1
    Range("R2").Select
    ActiveSheet.Paste
    Range("R22:R366").Select
    Selection.Cut
    ActiveWindow.LargeScroll Down:=-1
    Range("S2").Select
    ActiveSheet.Paste
    Range("S22:S88").Select
    Selection.Cut
    ActiveWindow.LargeScroll Down:=-1
    Range("T2").Select
    ActiveSheet.Paste
    Range("T22:T125").Select
    Selection.Cut
    ActiveWindow.LargeScroll Down:=-1
    Range("U2").Select
    ActiveSheet.Paste
End Sub
```